
A hierarchy of graph-based methods to study the behavior of immune cells in vivo

Doctoral Dissertation submitted to the
Faculty of Informatics of the Università della Svizzera Italiana
in partial fulfillment of the requirements for the degree of
Doctor of Philosophy

presented by
Diego Ulisse Pizzagalli

under the supervision of
Prof. Dr. Rolf Krause and Dr. Santiago Fernandez Gonzalez

March 2020

Dissertation Committee

| | |
|------------------------------------|-------------------------------------|
| Rolf Krause | ICS, USI - Switzerland |
| Santiago Fernandez Gonzalez | IRB, USI - Switzerland |
| Olaf Schenk | ICS, USI - Switzerland |
| Luca Gambardella | IDSIA, USI-SUPSI - Switzerland |
| Marcus Thelen | IRB, USI - Switzerland |
| Matteo Matteucci | DEIB, Politecnico di Milano - Italy |

Dissertation accepted on 03 March 2020

Research Advisor

Prof. Dr. Rolf Krause

Co-Advisor

Dr. Santiago Fernandez Gonzalez

PhD Program Director

The PhD program Director *pro tempore*

I certify that except where due acknowledgement has been given, the work presented in this thesis is that of the author alone; the work has not been submitted previously, in whole or in part, to qualify for any other academic award; and the content of the thesis is the result of work which has been carried out since the official commencement date of the approved research program.

Diego Ulisse Pizzagalli
Lugano, 03 March 2020

To my beloved

I am the vine, you are the branches
The Bible, John 15:5

Abstract

The immune system has a critical role in diseases of primary importance such as infections and cancer. Hence, it represents a target for novel therapeutic strategies.

However, the immune system relies on a complex network of cell-to-cell interactions which remains largely unknown, or difficult to be interpreted.

The combination of experimental data with computational methods is of paramount importance to analyze these interactions. Indeed, recently established 2-photon intravital microscopes (2P-IVM), can capture videos of cells while interacting in organs of living animals. These interactions are often associated with specific movement patterns. Hence, computer vision methods have the potential to extract knowledge from these videos by analyzing the movement of cells. Unfortunately, common analysis methods poorly apply to 2P-IVM videos capturing the cells of the immune system. This is mainly due to the complex appearance and biomechanical properties of these cells, as well as challenges introduced by *in vivo* imaging. Additionally, a lack of publicly available 2P-IVM datasets hampers the development of novel analysis methods along with data-driven studies of the immune system. Finally, common measures of cell motility, poorly describe the dynamic behavior of immune cells.

In this thesis, we address these limitations by

- Making available the first database of 2P-IVM videos and tracks of immune cells.
- Modeling as graph the content of 2P-IVM videos, from pixels to biological processes.
- Developing, refining, and applying a variety of computational methods to extract knowledge from this graph.
- Shifting the analysis of cell motility towards the recognition of cell actions, which does not necessarily require cell tracking.

This combination of microscopy data, graph-based methods, and action-based models allowed us to quantify the complex movement patterns of neutrophils, revealing different phases of the immune response to influenza vaccination.

Acknowledgements

Supervisors and colleagues. I am thankful to my supervisors *Prof. Rolf Krause*, *Dr. Santiago Fernandez Gonzalez*, *Prof. Marcus Thelen* and colleagues *Dr. Nikolaos Chatziandreou*, *Dr. Yagmur Farsakoglu*, *Dr. Miguel Palomino-Segura* who shaped the evolution of the project from its primordial-soup. *Tommaso Virgilio*, *Irene Latino*, *Daniel Molina-Romero*, *Dr. Juliana Falivene*, *Silvia Zanaga*, *Dr. Jordi Sintes*, *Nina Germic*, *Dr. Mauro Di Pilato*, *Sabrina Casella*, *Paola Antonello*, *Ilaria Pierangeli* who provided biomedical data, insights and experience. *Benedikt Thelen*, *Gabriele Rovi*, *Concetta Piazza*, *Rocco D'Antuono*, *Diego Morone*, *Dr. Davide Eynard*, *Dr. Ganna Marchenko*, *Dr. Alessandro Giusti*, *Prof. Giuseppe Pozzi*, for technical support. **Tutored students.** I am thankful to *Alain Pulfer* who inherits the project in its evolved yet chaotic form, and for sharing passion on systems biology. *Radu Theodorescu*, *Elisa Palladino* for help in LTDB. *Ilaria Arini* who accidentally named "Dijkstra algorithm" in 2016, going to be a main ingredient of the thesis. *Liudmila Karagyaur* for discussions on physics and appreciation of the Hough Transform. **USIMakers.** Community of makers which I co-founded at USI with *Dr. Ivan Elhart* and *Prof. Marc Langheinrich*. It provided the sufficiently needed amount of scientific distraction. **Italian Red Cross - Gruppo Clown Tiramisu.** This group of people provided energy and skills for stress management, team building, communication and teaching. **Beloved.** I am thankful to my *family* for having taught appreciating the beauty in the little things and for having supported my career decisions, *Madalina Mahrus* for having improved each-other, having prepared all the days my lunch-box, and transformed by weaknesses into opportunities. **Funding.** I am thankful to SystemsX.ch - the Swiss Initiative in Systems Biology - for funding (iPhD project 2013/124) and training.

Contents

| | |
|--|-------------|
| Contents | xi |
| List of Figures | xiii |
| List of Tables | xv |
| 1 Introduction | 1 |
| 1.1 The immune system and its actors | 2 |
| 1.2 Actions of immune cells, an ontology | 9 |
| 1.3 Open research questions | 19 |
| 2 State of the art methods to study immune cell behavior <i>in vivo</i> | 21 |
| 2.1 Intravital imaging pipeline | 21 |
| 2.1.1 Image acquisition | 23 |
| 2.1.2 Cell staining | 25 |
| 2.1.3 Organs and surgical models | 26 |
| 2.1.4 Cell detection | 27 |
| 2.1.5 Cell tracking | 31 |
| 2.2 Quantification of immune cell migration and interaction | 34 |
| 2.2.1 Measures to quantify cell migration and interaction | 35 |
| 2.2.2 Quantification of cell actions | 37 |
| 2.3 Relevant computer vision methods | 40 |
| 2.3.1 Superpixels | 40 |
| 2.3.2 Optical flow | 43 |

| | | |
|----------|--|------------|
| 2.3.3 | Action recognition | 45 |
| 2.4 | Clustering algorithms for data-driven research | 47 |
| 3 | Objectives of the thesis | 51 |
| 4 | LTDB, A database of videos and tracks of immune cells from intravital microscopy | 53 |
| 5 | Graph-based algorithms | 73 |
| 5.1 | A trainable, graph-based clustering algorithm | 73 |
| 5.2 | Optimized implementation of the Dijkstra algorithm on images . . | 97 |
| 5.3 | Outlook | 107 |
| 6 | Application of graph-based methods for analyzing immune cell migration and interaction | 113 |
| 6.1 | Modeling 2P-IVM data as a hierarchical graph | 113 |
| 6.2 | Grouping pixels in space and color - superpixels | 116 |
| 6.3 | Grouping pixels in time | 120 |
| 6.4 | HoT-POF: an interpretable descriptor of cell motility | 133 |
| 6.5 | Detection and quantification of neutrophil response to apoptosis . | 140 |
| 6.6 | Semi-supervised colocalization | 144 |
| 6.7 | De-bounced kiss and run analysis | 153 |
| 6.8 | Swarm detection | 156 |
| 7 | Characterization of the dynamic behavior of neutrophils following influenza vaccination | 157 |
| 8 | Conclusion, and future perspectives | 189 |
| 8.1 | Workflow and implementation | 190 |
| 8.2 | IMMUNEMAP, making 2-photon microscopy data FAIR | 192 |
| 8.3 | Experimental definition of imaging protocols | 195 |
| 8.4 | Tracking with CARE | 196 |
| 8.5 | Detection and discovery of additional cell actions | 197 |
| 8.6 | Relevance of actions | 198 |
| | Additional contributions | 229 |

Figures

| | | |
|-----|---|----|
| 1.1 | Different layers of defense of the immune system | 4 |
| 1.2 | Structure of a lymph node | 6 |
| 1.3 | Characteristics and examples of patrolling leukocytes | 11 |
| 1.4 | Characteristics and examples of directed leukocytes | 12 |
| 1.5 | Characteristics and examples of arrested leukocytes | 14 |
| 1.6 | Characteristics and examples of contact formation | 15 |
| 1.7 | Characteristics and examples of swarm formation | 18 |
| 2.1 | Image acquisition and analysis pipeline. | 22 |
| 2.2 | Two-photon point-wise excitation | 23 |
| 2.3 | Surgical models for intravital imaging | 27 |
| 2.4 | Measures to quantify cell migration and interaction | 34 |
| 3.1 | Interdisciplinary of the thesis. | 51 |
| 4.1 | LTDB - Data generation workflow | 62 |
| 4.2 | LTDB - Challenges of cell tracking | 63 |
| 4.3 | LTDB - Data organization and format | 64 |
| 4.4 | LTDB - Use cases | 65 |
| 5.1 | Clustering rules on a simplified example. | 87 |
| 5.2 | Evaluation on a synthetic dataset with heterogeneous structures | 88 |
| 5.3 | Robustness to density peak detection. | 89 |
| 5.4 | Robustness to background noise. | 90 |
| 5.5 | Application for segmentation of immune cells. | 91 |

| | | |
|------|---|-----|
| 5.6 | Recognition of different heart rhythms. | 92 |
| 5.7 | Graph structure. | 93 |
| 5.8 | Evaluation on the 12 synthetic datasets from ClustEval | 94 |
| 5.9 | Performance degradation assay with respect to number of training paths. | 95 |
| 5.10 | Benchmark on high dimensional synthetic datasets. | 96 |
| 5.11 | Results on the bonemarrow leukemia dataset. | 96 |
| 5.12 | Iterative implementation of the Dijkstra algorithm | 100 |
| 5.13 | Iterative Dijkstra algorithm - benchmark | 102 |
| 5.14 | Iterative Dijkstra - Shortest paths found at each iteration | 105 |
| 5.15 | Iterative Dijkstra - Results on 2D lattices | 106 |
| 5.16 | Clustering via Hough Transform - simplified example | 110 |
| 5.17 | Analogy with the Hough Transform | 110 |
| 5.18 | Give and receive votes | 111 |
| 6.1 | Hierarchical graph from pixels to biological knowledge | 115 |
| 6.2 | Clustering of non-convex groups of pixels in color and space | 117 |
| 6.3 | Qualitative results on 2P-IVM data | 118 |
| 6.4 | Quantitative results on BSDS | 119 |
| 6.5 | Tracking vs. Optical Flow | 120 |
| 6.6 | Optical Flow errors on 2P-IVM data | 121 |
| 6.7 | Shortest path properties as descriptor | 124 |
| 6.8 | Graph-based optical flow - proposed structure | 125 |
| 6.9 | Optical Flow - Qualitative results on a squeezing neutrophil | 126 |
| 6.10 | Optical Flow - Results on synthetic example | 126 |
| 6.11 | Optical Flow - Registration error quantification | 127 |
| 6.12 | Optical Flow as tracking predictor - accuracy (1) | 128 |
| 6.13 | Optical Flow as tracking predictor - accuracy (2) | 129 |
| 6.14 | Effect of unstable centroids | 129 |
| 6.15 | Optical Flow Ground Truth generation | 131 |
| 6.16 | Downsampling of Optical Flow | 131 |
| 6.17 | HoT-POF arechitecture | 134 |
| 6.18 | HoT-POF example: neutrophils 2PIVM | 136 |
| 6.19 | HoT-POF example: B cell colture | 137 |
| 6.20 | Apoptosis morphodynamics | 142 |
| 6.21 | Effect of an apoptotic cell on the neighborhood | 142 |
| 6.22 | Apoptosis detection via HoT-POF | 143 |
| 6.23 | Apoptosis detection performances | 143 |
| 6.24 | Colocalization challenges in 2P-IVM | 146 |

| | | |
|------|--|-----|
| 6.25 | Improving tracking of poorly visible cells | 147 |
| 6.26 | Improving tracking of non-specifically stained cells | 149 |
| 6.27 | Usage of path-based features to classify superpixels | 152 |
| 6.28 | Example of contact formation (Neutrophil-Macrophage) | 154 |
| 6.29 | Contact detection with hysteresis | 155 |
| 6.30 | De-bounced contact detection with brightness fluctuations | 155 |
| 6.31 | Swarm detection using clustering | 156 |
| | | |
| 7.1 | Neutrophil recruitment and distribution into the popliteal lymph node (PLN) after influenza vaccine administration | 178 |
| 7.2 | Production of CXCL1 and IL-1 α induce recruitment of neutrophils to the PLN in response to vaccination | 179 |
| 7.3 | Neutrophils phagocyte and transport influenza virus | 180 |
| 7.4 | Time-course of neutrophil motility | 181 |
| 7.5 | Neutrophils exhibit different actions in the early response to vaccination | 182 |
| 7.6 | Characterization of neutrophils swarm formation in the PLN after influenza vaccination | 183 |
| 7.7 | Neutrophils - Supplementary 1 | 184 |
| 7.8 | Neutrophils - Supplementary 2 | 185 |
| | | |
| 8.1 | Workflow of the PhD project | 191 |
| 8.2 | IMMUNEMAP architecture | 193 |
| 8.3 | IMMUNEMAP partners | 194 |
| 8.4 | Effect of time-step on measured cell speed | 195 |
| 8.5 | Future work - tracking as semi-supervised clustering | 196 |

Tables

| | | |
|-----|---|-----|
| 1.1 | Main types of immune cells and functions | 5 |
| 2.1 | Two-photon magnifications | 24 |
| 2.2 | State of the art methods for foreground segmentation | 30 |
| 2.3 | Track based measures to quantify cell migration and interaction | 36 |
| 2.4 | Tools to detect and quantify cell actions | 37 |
| 4.1 | LTDB - Biomechanical and technical problematics | 66 |
| 4.2 | LTDB - Dataset overview | 67 |
| 4.3 | LTDB - Channel specification | 68 |
| 4.4 | LTDB - Experimental settings | 69 |
| 4.5 | LTDB - Microscopy platforms | 70 |
| 4.6 | LTDB - Comparison of tracking operators | 71 |
| 4.7 | LTDB - File format | 72 |
| 7.1 | Gates for track-based activity recognition | 176 |
| 8.1 | IMMUNEMAP biological content | 194 |

CHAPTER 1

Introduction

Systems biology is a recently established research paradigm which combines experimental data with computational methods to observe, model and interpret complex biological processes [78].

In this thesis, we focused on the combination of microscopy data with graph-based algorithms to investigate the complexity of the immune system *in vivo*. Hence, we contribute towards the reverse engineering of biology [54].

In this chapter, we introduce the immune system describing it as a set of actors performing certain actions.

The first section "The immune system and its actors" provides a brief introduction to the cellular and molecular mechanisms involved in immunity, describing the main types of immune cells as "actors" and the dynamism of the immune system which involves cell migration.

In the second section "Actions of immune cells" we review the main actions that the immune cells can perform, both in response to an immune challenge (e.g. infection) and in homeostasis.

Lastly, in the third section, we describe the main open research questions which are partially addressed within this thesis.

The actor-action point-of-view to describe the immune system is one of the main contributions of the thesis, resulting in a novel way of analysis.

1.1 The immune system and its actors

Immunity is a word that derives from the latin expression "immunus" which meant the exemption from public duties. Later, (approx. 400 years B.C), the term immunity started to be used as protection from disease.

Although immunity has been historically associated to infective diseases, recently it became evident that the mechanisms involved in immunity, play a central role in the pathogenesis of neoplastic, autoimmune, neurodegenerative and many other diseases.

These diseases of primary importance worldwide, posing enormous health and economic challenges. Therefore, immunological research is essential for improving human health.

Indeed, while evolution conferred to humans the capabilities of defending from otherwise deadly microbes and parasites, the co-evolution of microbes and the increased possibilities of transmission still pose major risks of infection, resulting in the major cause of death in low-economy countries.

Moreover, the recently increased life span of people in high-income countries, pose the new challenge of protection from age-related diseases (WHO).

Immunity involves a complex network of interactions between cells and molecules which, together, represent the immune system. Such a network is distributed among different organs and changes over time to allow an exchange of information between its components. This dynamism is essential to promptly mount an immune response in the entire body and returning to homeostasis once an infection is resolved. Moreover, similarly to brain circuits, the network of interactions between immune cells can be remodeled to learn responding to new pathogens.

Nowadays it is clear that a functional network is essential to protect the host from pathogens, while a dysfunctional network eventually leads to disease.

The human immune system is composed of stratified lines of defense which are summarized in (Figure 1.1).

Physical barriers. The first layer of defense of the immune system is represented by the physical barriers. These involve both specific organs and tissues (i.e. skin) that avoid external pathogens to enter in the body, and chemicals that create a hostile environment for their replication (i.e. acid pH of mucosae). If a

new pathogen breaches these barriers, an immediate, but non-specific immune response can be triggered.

Blood proteins. When a pathogen is present within the body, proteins circulating in the blood can bind to its surface and rapidly neutralize its pathogenicity, potentially up to nanoseconds. These proteins include the complement system and antibodies.

Cells. The immune system involves specialized cells. These are called immune cells, also referred to as leukocytes, and represent the main actors of the immune system. These cells respond up to several days following an immune stimulus, both by interacting between them, with other cells of the host and with the pathogen.

More in detail, the earlier responders to a pathogenic challenge are typically innate immune cells. These cells have the capacity to contain and eliminate microbes in a generic way involving phagocytosis, and secretion of toxic compounds. However, certain types of infection might require a more advanced type of response to be eliminated. Indeed, organisms which were more able to tailor the immune response towards a specific pathogen had more chances to survive. This gave rise to organisms in which a second layer of protection, named adaptive immune system, exists. This second layer involves the constant selection and expansion of specific cells, and the production of proteins that specifically bind to microbial antigens (antibodies). Although this process may require up to several days to complete, it can confer protection to the host for an extended amount of time.

Vaccination artificially induce the adaptive immune response towards certain pathogens, aiming at conferring long-lasting protection to otherwise deadly infections.

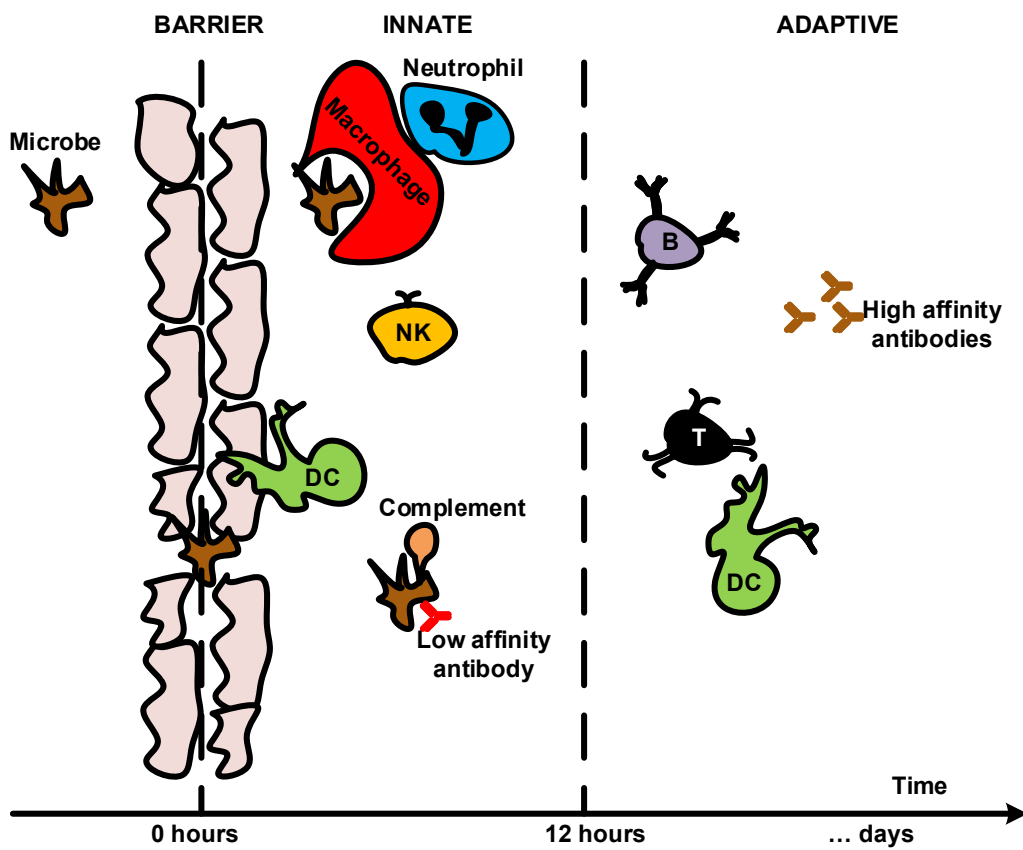


Figure 1.1. Different layers of defense of the immune system.

Type of immune cells. Immune cells are classically grouped according to their function in infectious diseases. These are summarized in Table 1.1

However, increasing evidence suggests that immune cells can execute a broad range of non-classical functions. For instance, neutrophils which are classically described as cells involved in tissue clearing and microbial containment were recently found important in shaping the adaptive immune response [145].

Additionally, the behavior of immune cells is dynamic, varying over time and in response to other changes in the tissues. To this end, in the next section, we review the literature describing the different functions associated with different immune cells in several experimental conditions.

| Type | Main cells | Description |
|--|--|--|
| Phagocytic cells | Neutrophils, Monocytes, Macrophages | Phagocytic cells primarily internalize microbes and contrast their dissemination. This might involve the creation of inflammatory conditions, tissue damage and phagocytosis of cell particles. Additionally, phagocytic cells can digest the internalized microbes and present microbial proteins (antigens) to other specialized cells. While neutrophils and monocytes typically circulate within the blood stream after being recruited from the bone marrow, macrophages are typically tissue resident cells which differentiate from monocytes. Apart from phagocytosis these cells have roles in the initiation of the immune response by secreting important molecules for the activation and recruitment of other cells to the site of infection. |
| Granulocytes | Neutrophils, Mast cells, Basophils, Eosinophils | Granulocytes are characterized by the presence of granules in the cytoplasm containing chemicals with inflammatory and/or antimicrobial activity. These cells are involved in both the innate and adaptive immune response. Additionally, they are essential in the control of parasitic infections and they are involved in several allergic diseases. While neutrophils and eosinophils are found in blood, Mast cells are found in mucosae and in the skin. Basophils can be found both in tissues and circulating in the blood. |
| Antigen Presenting Cells (APCs) | Dendritic cells, Macrophages, B cells, others | APCs have the capacity of capturing antigens and presenting these to specialized cells of adaptive immunity. For this reason, APCs are considered the bridge between the innate and the adaptive immune response. Several cells can serve as APCs. Amongst these dendritic cells have the capacity to capture microbes in peripheral tissues and transport them to the lymph node. In the lymph node, other resident APCs regulate the selection of B cells. |
| Lymphocytes | B cells, T cells, NK cells | Lymphocytes are the main cells present in the lymph. While B and T cells are the main players for adaptive immune response, NK cells are innate-like. B cells are responsible for the humoral immune response which involves the generation and secretion of proteins that specifically bind an antigen (antibodies). B cells are also involved in antigen presentation and in memory. T cells are responsible for cellular immunity. They can be divided in Cytotoxic T cells that can induce the death of stressed/infected/damaged cells, Helper T cells that produce cytokines to regulate the adaptive immune response. NK cells are involved in the lysis (via the secretion of toxic granules) of infected or tumor cells displaying an altered set of proteins on their surface. |

Table 1.1. Main types of immune cells grouped by function

Organs. Lastly, the aforementioned immune response can happen at different locations, including both the site of infection and specialized lymphoid organs. Amongst these, we focus on the lymph node (LN), as the organ in which the immune system encounters antigens and adaptive immune response take place. LNs have a compartmentalized structure that is associated with their function. Three main compartments, namely the cortex, paracortex, and medulla are generated by specific types of hematopoietic stromal cell population, which give rise to their anatomical structure [191, 237]. Different populations of lymphocytes are specifically localized in the compartments: B cells occupy the cortical follicles, T cells are recruited and confined in the paracortical region, macrophages are present in the superficial cortex and the medullary regions, and dendritic cells (DC), are associated with T cells in the paracortex and the medullary cords [267, 237]. Importantly, the existence of a prominent network of lymphatic vessels facilitates the transport of lymph-borne antigen and pathogens towards the LN [200, 237], while a network of blood vessels facilitates the recruitment of other cells from the bloodstream and their circulation through the LN. Although monocytes and neutrophils are promptly recruited to the lymph node following inflammation, tumor cells can use similar mechanisms to migrate to the lymph nodes. Hence, lymph nodes represent important sites where tumors can spread to other organs, or where tumor-antigens can trigger the development of an immune response towards the tumors.

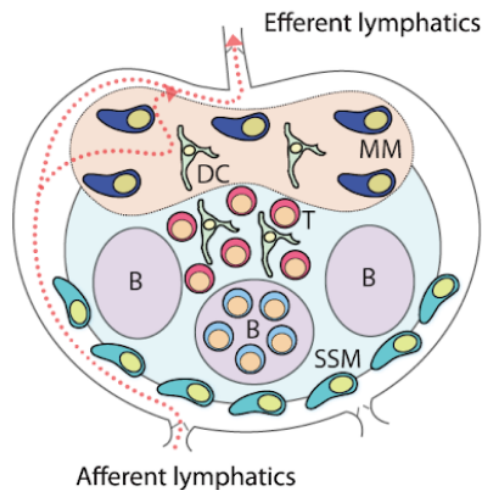


Figure 1.2. Structure of a LN. Schematic representation of the major compartments of the LN and the major immune cells populations, DC, SSM and MM stands for dendritic cells, subcapsular sinus macrophages and medullary macrophages, respectively

Cell migration. Cell migration is a topic of central biomedical significance. It is a process that involves the continuous relocation of cells in different organs, anatomical compartments, and tissues. This is involved in many pathologies including developmental and inflammatory diseases and tumor metastasis.

Amongst the multitude of cells that migrate, immune cells are amongst the most dynamic. Indeed, they continuously migrate to scan the environment, share information and interact with potential pathogens, for instance.

Immune cells engage both long-range migration and short-range migration which are essential for immunity [36]. Long-range migration includes the movement of cells from one organ to another via blood or lymph. By contrast, short-range migration happens inside specific organs or tissues.

In the presence of inflammatory or other recruiting stimuli, endothelial cells of blood and lymphatic vessels can express specific adhesion molecules to allow the extravasation of circulating immune cells. As a consequence, circulating immune cells enhance the interaction with the blood endothelium, progressively decreasing their speed. This makes the switch from a passive cell transportation to an active migration on the vessel walls, finally allowing immune cells to leave the vessel and migrating to other tissues.

From a biomechanical point of view, a force that accelerates the cell is required for migration. Immune cells actively generate this force by remodeling their cytoskeleton and adhering to the surrounding cells or structures. This process involves both intracellular and extracellular mechanisms. The former includes the continuous destruction and reconstruction of the actin filaments forming the cytoskeleton. The latter include the response to extracellular signals such as gradients of chemical compounds that can attract immune cells (chemoattractants). Chemoattractants include chemokines, cytokines, pathogen debris, lipids and degraded components [84]. Chemoattractants can polarize a cell, conferring to it an efficient shape to migrate. For instance, the exposure of chemokine gradients rapidly break the symmetry of blood-borne cells by promoting the formation of an anterior-posterior axis [244].

Attraction, remodeling are the main ingredients that confer to immune cells the capacity to migrate towards a specific direction. Indeed, migration is achieved by the cyclic expansion of the leading front (pseudopod) towards the direction of the chemoattractant and the retraction of the opposite front (uropod), resembling the migration modes of amoeba and therefore inheriting the name of

amoeboid migration" [141].

Another external mechanism that facilitates cell migration is adhesion. This involves the binding of specific molecules expressed by the migratory cells (i.e. integrins) with other molecules expressed on the surface of the surrounding cells or extracellular structures. These bindings provide anchorage and support to migration [269].

The migration of immune cells can be classified based on the direction and the type of adhesion. *Chemotaxis* and *Chemokinesis* refer respectively to cells moving towards the source of a chemotactic gradient and without a specific target (i.e. when a gradient is not present or multiple gradients exist). Similarly, *Haptotaxis* and *Haptokinesis* refer to migration modes involving high or null adhesion with the substrate.

Finally, cell migration is regulated by internal programs [101]. For instance, neutrophils regularly stop, sense the presence of chemoattractant gradients, change the direction of movement, and move towards that direction. This cyclic process involves both directional memory and refractory periods of time [101]. Additionally, this process changes according to with the cell type. For instance, while monocytes can rapidly invert their polarization axis, other leukocytes such as neutrophils are more likely to invert their direction by turning [256].

Although cell migration has been extensively described *in vitro* in chemotaxis assays, recent studies showed that cell migration *in vivo* can exhibit different patterns [172]. Therefore, it is important to investigate the behavior of immune cells under physiological conditions.

Additionally, cell migration has been extensively studied by quantifying the motility of individual cells. However, the migration patterns of a collectivity of immune cells can be difficult to interpret. To this end, Mayor and colleagues argue that the migration of immune cells could be better explained by considering cells as part of supracellular entities [232], allowing to detect and quantify cell migration at a higher scale [233].

1.2 Actions of immune cells, an ontology

Immune cells perform a broad range of biological functions which are associated with migratory and interaction patterns.

Indeed, an increasing number of studies identified recurrent movement patterns of immune cells and associated these to specific biological functions. This is in contrast to previous studies *in vitro* where the movement of immune cells was classically modeled as particles following either a directional or random motion.

In this section, we report these patterns from the literature, and we refer to them as actions considering immune cells as active and dynamic objects able to perform different actions over time [211].

This point of view has some advantages with respect to the standard way of analysis. Firstly, it facilitates the interpretation of cell movement by identifying meaningful and previously described patterns. Secondly, it bridges immunology with the computer vision field, where actions are routinely used to quantify the movement of humans.

An action can be defined as the modification of the environment performed by an actor. Actions are typical of animals and humans which can sense the environment and modify it according to their needs.

Similarly, cells respond to chemical stimuli and perform actions at tissutal level. For instance, thanks to their migratory capacity, they can relocate within tissues and organs and give rise to relevant immunological reactions [265].

Patrolling

Definition. Patrolling is an activity of motile immune cells associated with extensive monitoring of tissues [18]. Patrolling cells exhibit long tracks in a confined area which results in low directionality. Moreover, the direction of patrolling cells is not correlated to flow direction (i.e. blood) or other external forces that could transport the cells [35]. The speed of patrolling cells instead varies according to the cell type, conditions, and anatomical site. For instance, patrolling monocytes exhibited a speed of 36 $\mu\text{m}/\text{min}$ in the endothelium of carotid arteries and 9 $\mu\text{m}/\text{min}$ in the mesenteric venules [35] while patrolling B cells exhibit a speed of 6 $\mu\text{m}/\text{min}$ in the lymph node follicles.

Biological relevance and cases.

Continuous screening of pathogens. The endothelium of blood vessels is continuously monitored by patrolling monocytes [35, 259, 18, 17]. These cells can recognize infection and damage signals via Toll-Like Receptors (TLR), which are cellular receptors binding to proteins expressed by several pathogens. Indeed, TLR triggers a rapid response of monocytes, with tissue invasion and differentiation into macrophages [18]. Additionally, patrolling monocytes promote the recruitment and activation of neutrophils in acute inflammation [79] and initiate a local neutrophil response via a TLR7-dependent paracrine secretion of pro-inflammatory cytokines, such as IL-1 β , CXCL1, TNF, CCL3, or IL-6 [35, 39]. Neutrophils patrolling in the blood can adhere to the endothelial walls [133, 201], and get promptly recruited in the inflammation site within a few hours.

Tumor immunosurveillance. Within the tumor microenvironment, patrolling monocytes were also associated to immunosurveillance, rapidly detecting tumor material via CX3CR1 [104], establishing interactions with metastasizing cells, and promoting recruitment and activation of NK cells in an animal model of lung carcinoma [104].

Similarly, within the LN, NK cells exhibit a patrolling pattern while searching for cognate targets and transformed cells [87]. By contrast to other cells, while patrolling NK cells form transient cell to cell contacts for the clearance of MHC-mismatched targets [87].

Maximize antigen encountering. In the lymph node, patrolling B cells continuously survey subcapsular macrophages and follicular dendritic cells for surface-displayed antigen or soluble antigens in their environment [56]. Moreover, within the germinal centers (GC), patrolling B cells exhibited a probing, dendritic morphology that gives them a larger surface area and greater opportunity for antigen encountering [56]. Similarly, Beuneu and colleagues [26] report that NK cells maintain a patrolling behavior during priming, suggesting that the patrolling pattern is an efficient strategy for sensing and integrating cytokine signals in the vicinity of multiple DCs.

Also within lymphatic capillaries, DCs [113], CD4 + effector and memory T cells [241] were associated with patrolling behavior. Considering that lymphatic capillaries transport antigens to the lymph node, this further suggests a role of the patrolling pattern for antigen encountering.

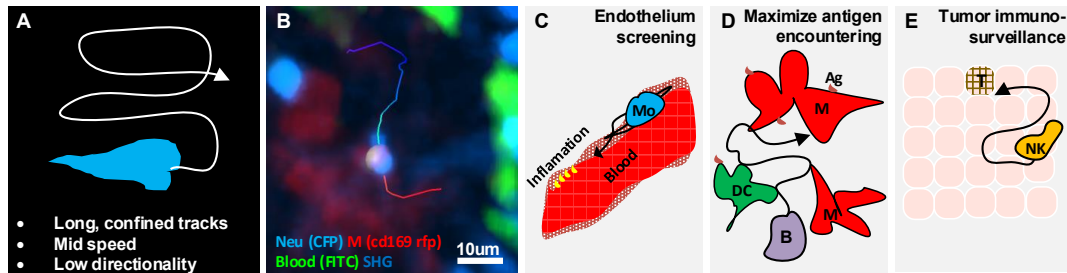


Figure 1.3. Characteristics and examples of patrolling leukocytes. **A.** Sketch showing the characteristic long tracks confined in an area, which are associated to a mid speed and low directionality (high confinement). **B.** 2P-IVM micrograph showing a patrolling neutrophil (light blue) migrating between macrophages (red) in the subcapsular sinus of a lymph node following infection. **C.** Sketch showing a monocyte (Mo) patrolling the endothelium of blood vessels. **D.** Sketch showing a B cell patrolling in the lymph node to survey antigen presenting cells (M: macrophages, DC: dendritic cells). **E.** Sketch showing a natural killer (NK) patrolling for immuno-surveillance in tissue with a tumor cell (T).

Directed migration

Definition. Directional migration is associated with the movement of cells towards a target. Such a target must exist for a sufficient amount of time to bias the migration. This happens when a chemical cue is located within a delimited spatial region, driving the migration toward the source. Directed migration is opposed to undirected migration, which reflects the movement toward a non-specific, or rapidly changing, target. Cells undergoing directed migration exhibit high directionality and possibly high speeds.

Biological relevance and case.

Response to chemotactic gradients. As leukocytes sense a biased signal, they move toward its source to mediate a plethora of functions, such as tissue repair [60], microbial detection [60], cell priming, and other cell-to-cell interactions [84]. Neutrophils exhibit a directed migration pattern while migrating toward an inflammation site such as epithelial injuries [198], inflammation [122] and infection [230]. Although studied with less frequency, other leukocytes migrate accordingly to a directional pattern. Macrophages perform directed migration in interstitial tissue in response to bacterial infection or tissue injury [275].

Influence of anatomical structures. The architecture of organs and tissues can influence cell movements, conferring properties of directed migration. Within the lymph node, recruited B cells and T cells migrate following directed trajectories to relocate precisely in their respective areas [84]. B cells can also migrate

from the follicle area to the interface with the T cell zone to increase the probability of contact with the T cells [84]. Dendritic cells, even mostly known to be sessile, do migrate from the dermal interstitial space to the afferent lymphatics [151].

In a model of ovarian carcinoma, CD8+ T cells exhibited a directed migration pattern along collagen fibers as if they were migrating in a conduit [30]. By contrast, in the paracortical area of the LN, T cells exhibited a highly non-directed migration, which is probably an efficient way of movement to avoid obstacles in complicated microenvironments [127].

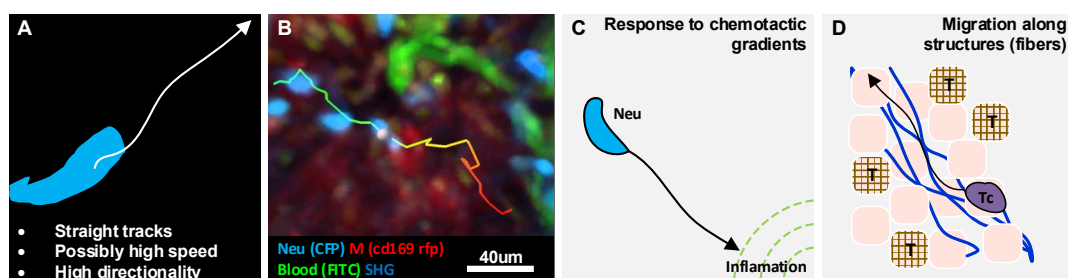


Figure 1.4. Characteristics and examples of directed leukocytes. A. Sketch showing the characteristic straight tracks associated to a high directionality and possibly high speed. B. 2P-IVM micrograph showing a neutrophil (light blue) exhibiting directed migration towards the subcapsular sinus area of a lymph node following infection. C. Sketch showing a neutrophil (Neu) directed towards the source of a chemotactic gradient. D. Sketch showing a T cell (Tc) moving with directed migration while following collagen fibers (blue structures) between tumor cells (T).

Arresting

Definition. An immune cell is said to arrest when it does not move for a sufficiently large amount of time. Indeed, the migration of immune cells involves cyclic stop-and-go periods [101]. Hence, to define a cell as arrested, an observation time larger than the period of the stop and go cycle is required.

Additionally, considering that a cell can keep a certain motility, a threshold on the speed or displacement is required for the definition of arrested cells. Friedl and Weigelin [84] reviewed the interstitial migration patterns of immune cells and described arrested cells with a speed less than a threshold (i.e. 1 $\mu\text{m} / \text{min}$).

Biological relevance and cases. Arresting is an action of immune cells associated with both adhesive interactions and to specific internal states of cells.

Adhesive interactions during recruitment. Friedl and colleagues reviewed the migratory patterns of several types of leukocytes, describing that during recruitment, integrin-dependent adhesive interactions with stromal cells are associated with the arresting of leukocytes. This in line with the more recent studies by [113] where arrested T cells were observed in the lymphatics.

Arresting during activation. In neutrophils, arresting was associated with the oxidative burst [134], which is a state in which reactive oxygen species are generated. This occurs both during phagocytosis and in response to soluble antigens [46]. Beuneu and colleagues [26] report that NK cells do not arrest while being activated by dendritic cells. However, NK cells were reported arrested in the medullary part of the lymph-node [75] following influenza vaccination. Although these arrested NK cells were forming stable contacts with macrophages, this behavior was not associated with NK-mediated lysis. Therefore we consider that it might represent a different activation pattern.

Arresting during intracellular communication and signaling. Effective intracellular communication requires arresting. This is supported by Germain and colleagues [89] describing that the regulation of speed by T cells is essential during priming to adhere to DCs and forming swarms of T cell around individual DCs. Similarly, Qi et al.[218] report that B cells arrest on DCs inducing intracellular calcium signaling.

Arresting during killing. The formation of stable contacts with a target cell is one of the most described reasons for a cell to arrest. For instance, CD8+ T cells arrest during the formation of the cytotoxic synapses with target tumor cells and resume migrating after killing the target [128, 29].

Contact formation

Definition. Cellular contacts are defined as the absence of a space (empty pixels) between cells [190].

Biological relevance and cases. Being the distance between cells in contact sufficiently small, a precise exchange of chemical stimuli is possible. Therefore, contact formation is a form of precise cell-to-cell communication that allows, for instance, the encountering of protein clusters on the cell surface [186, 68], initiate the innate immune response [75], and guide the adaptive immune response

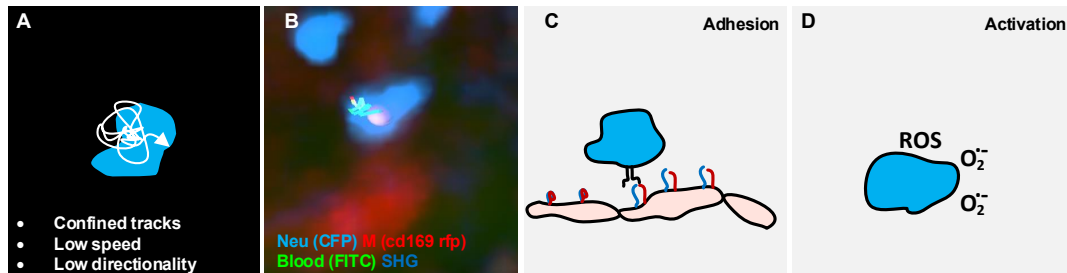


Figure 1.5. Characteristics and examples of arrested leukocytes. A. Sketch showing the track of an arrested cell, associated to a low speed and high confinement. B. 2P-IVM micrograph showing a neutrophil (light blue) arresting in proximity of a macrophage (red) in the subcapsular sinus area of a lymph node following infection. C. Sketch showing a neutrophil (Neu) arresting during an adhesive interaction with an epithelial cell layer. D. Sketch showing a neutrophil arresting during the production of reactive oxygen species.

[270].

Immunological synapses. One of the most well-studied cases of contact formation is the immune synapse occurring between DCs and T Cells in the lymph node. DCs play a crucial role in initiating the immune cell response [32], as they scan the surrounding environment in search for antigens to capture and present to naive T cells [32]. At first, T cells would engage many short-lived contacts with the surrounding DCs, reducing their pace due to the multiple interactions [174]. Upon successful encounter between T cells and antigen-presenting DCs, long-term and stable contacts occur and T cell arrest. This leads to the activation of T cells, which finally recover motility and proliferate.

In an OT-I model, a comparison between antigen-specific CD8+ T Cells and polyclonal CD8+ T revealed that already 18 h after immunization, antigen-specific cells significantly decreased their speed from 14 $\mu\text{m}/\text{min}$ to 3 $\mu\text{m}/\text{min}$, followed by the formation of stable interactions with DCs [132]. By contrast, polyclonal CD8+ T cells maintained the same initial speed [132].

This is in agreement with the study by Thorsten and colleagues where different phases of TCs-DCs interaction were associated with different contact duration [172]. Additionally, contacts between T cells and DCs can happen in other organs and compartments such as the lymphatic capillaries of the ear skin [113].

Integration of multiple signals. NKs, form short-term contacts with DCs by recognizing IL-15 (expressed on the surface of DCs) in addition to soluble signals. By contrast to *in vitro* observations, where long-lasting contacts between NKs and DCs were observed, *in vivo* acquisitions in the LN revealed that NK cells maintain a motile behavior during their activation [26]. This yields to the formation

of brief contacts with a duration of 1-3 min, suggesting an efficient strategy to sense and integrate cytokine signals in the vicinity of multiple DCs.

Cytotoxic synapses and lysis. Cytotoxic T leucocytes (CTL) can establish cytotoxic synapses with other cells which eventually yield to cell death [69]. Cytotoxic synapses formed by CD8+ T cells, also known as "death kiss", relies on a shared molecular mechanism with CD4+ T cell immunological synapses [69]. However, CD8+ T cell synapses seem to be more stable and efficient in killing the target [22]. Two known killing mechanisms involve binding of FasL to Fas, resulting in apoptotic death by caspase activation [247]. The second mechanism involves Ca²⁺ dependent release of perforin and granzymes, yielding to activation of different apoptotic pathways [247]. The latter mechanism is faster and more diffused since it does not require specific receptors [69]. Common targets of CTLs are virus-infected cells or transformed cells. However, CTLs killing efficiency was reported to be affected by the affinity for the ligand, possibly resulting in slow killing [69]. *In vivo*, CTLs were observed to kill tumoral B cells at a rate of 2.4 cells per hour [173].

NK cells form contacts to lyse target cells through degranulation. In the context of tumor cell lysis, NK-mediated lysis can happen either via contacts of long duration with a single NK or via multiple short contacts with several NK cells which are associated with increased NK activation [26].

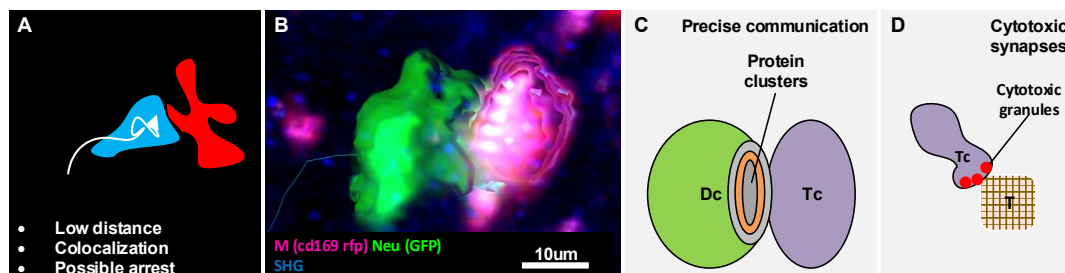


Figure 1.6. Characteristics and examples of contact formation. **A.** Sketch showing the morphodynamics of contact formations, characterized by a low distance between two cells, and the possible overlapping of colors. **B.** 2P-IVM micrograph showing a neutrophil (green) establishing a contact with a macrophage (violet). 3D reconstructions are shown to highlight the shape of the cells during the formation of the contacts. **C.** Sketch showing a T cell (Tc) forming an immunological synapse with a Dendritic cell (Dc), with a cluster of proteins in the contact area. **D.** Sketch showing a T cell (Tc) accumulating cytotoxic granules in contact with a tumor cell (T).

Swarming

Definition. Swarming is an activity that involves a collectivity of immune cells clustering in a defined space or moving towards a common target in a coordinated manner [49].

Biological relevance and cases. The swarming process was extensively described for neutrophils, observed to form aggregates in inflamed tissues in a way reminiscent of the swarming intelligence exhibited by social insects [49]. Kienle and colleagues attribute two main functions to the swarming process: Host protection and tissue disruption.

Host protection. Swarm formation was reported in infection models as a strategy to contain pathogens and protecting the host. Indeed, the presence of pathogens induces the release of signals that can trigger the formation of swarms in neutrophils [230]. These swarms yielded to the confinement of pathogens in isles where microbicidal compounds concentrate [130]. In the case of sterile photo burning [122] and needle damage [198], neutrophils formed abrupt and long-lasting clusters of large dimensions, suggesting a role of these cells in the remodeling and repair of the tissue.

Altering organ architecture and shaping the immune response The formation of swarms can alter the architecture of immune organs. For instance, the swarms formed by neutrophils were reported to disrupt the network of resident macrophages in the subcapsular sinus (SCS) area of the lymph node in parasitic infection models [53, 130, 49]. Considering that these macrophages are important to contain [153] or promoting [189] the spread of pathogens, and to activate adaptive immunity [44, 153], the alteration of this layer by swarms might influence the immune response.

Cell death is known to induce chemotaxis of phagocytic cells [221, 95] which was reported to induce the formation of neutrophil swarms with a size proportional to the number of death cells [140]. In viral infection models, macrophages resident in the SCS area of the lymph node were reported to undergo cell death followed by the release of cytokine storms and formation of neutrophil swarms [214]. This suggests an association of swarming with cell death and tissue remodeling. However, remains to be better investigated if neutrophil swarms are the cause or the consequence of the disruption of the macrophage network. Interestingly, NKs were also observed to form swarms in the SCS area of the lymph node and interact with resident cd11b+ cells. However, the accumulation

of NK cells in the SCS area was linked to another function, which is the promotion of their activation by specific antigen-presenting cells (APCs) [103].

Other cell types such as T cells were reported to form swarms around APCs following immunization. Since most of the interactions in the swarms were maintained over time, the authors highlighted that stable swarms may keep newly arrived T cells at the boundaries of the swarm, limiting their interaction with DCs [32].

From the above-listed swarm triggers, it emerges that swarms are linked with specific biological functions during inflammation. Neutrophil swarms have tissue cleaning and remodeling functions, they are involved in wound repair, and are believed to prevent pathogen spread to nearby tissues [130]. Other cell types, as seen for the NKs, may resort to swarming mechanisms to efficiently promote the encounter with APCs in a fast and directed fashion.

Swarming formation in neutrophil. One of the most characterized cases of swarm formation involves neutrophils. This was reported to follow five distinct phases in infected lymph nodes [130]. In the first phase, a self-contained number of patrolling neutrophils detect tissue injury and chemotactically migrate toward the injury site. In the second phase, recruitment is amplified through secondary cell death as supported in [140]. In this phase, neutrophils are characterized by increased speed and directionality. In the third stage, further amplification is mediated by leukotriene B4 (LTB4) released by neutrophils, promoting long-distance chemotaxis up to a 300 μm [140]. In this stage, swarm size increases in a seemingly feed-forward manner [130], leading to the accumulation of a large cell number. In the fourth stage, neutrophils slow down to form stable clusters: increased local interactions, as well as integrin based displacement, stabilize the aggregate. Neutrophils remodel and seal the damaged tissue and finally, in the fifth phase, they disperse leading to the resolution of the previously established swarms. Swarms have been classified according to their size and persistence [49]. Transient swarms have less than 150 cells and they are reported to last up to 40 minutes, while larger swarms counting up to 300 cells can last even hours [49]. Duration and swarm size were linked to the severity of the damage, with extended lesions recruiting thousands of neutrophils involved in swarms lasting for days [130].

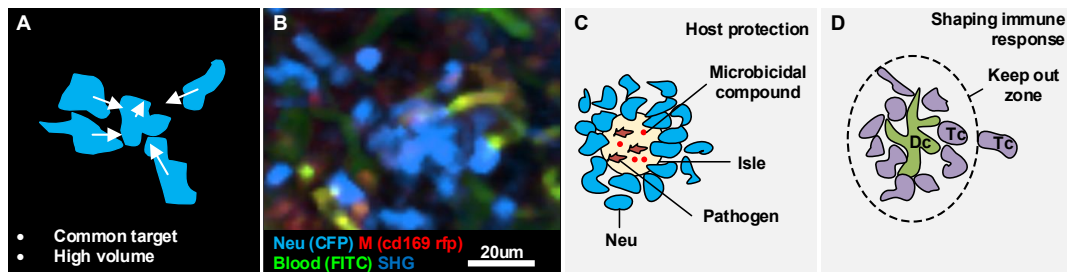


Figure 1.7. Characteristics and examples of swarm formation. **A.** Sketch showing the tracks cells towards a common target, resulting in the accumulation of cells in a confined area (high density). **B.** 2P-IVM micrograph showing a neutrophil swarm (light-blue) following infection into the subcapsular area of a lymph node. **C.** Sketch showing a swarm of neutrophils (Neu) to contain pathogens in an isle enriched with microbicidal compounds. **D.** Sketch showing a swarm of T cell (Tc) accumulating around an antigen presenting dendritic cell (Dc) and preventing other Tc to interact with the Dc.

1.3 Open research questions

As described in the previous sections, the immune system involves a complex network of cell-to-cell interaction patterns which remains largely unexplored. Regarding cell actions, although a list was provided, several remain unknown. This is especially relevant for innate immune cells. Indeed, while the majority of the studies focuses on adaptive immunity, composed by cells highly effective and highly specialized, the role of generic and non-specialized immune cells remained secondary until recent studies highlighted their capacity to shape the adaptive component.

One promising investigation method is given by 2-photon intravital microscopy (2P-IVM). This technique is described in Chapter 2 and allows to observe the behavior of immune cells in organs of living animals.

The main scientific questions to be solved from a biomedical point of view are

- Which migration and interaction patterns occur under defined experimental conditions (i.e. infection, vaccination, inflammation, tumor, and autoimmunity)?
- Which of these patterns are associated with an effective or ineffective immune response?
- How immune cells migrate and interact in different organs and tissues?

In principle, these questions can be solved thanks to the availability of efficient methods for mining biomedical data machine learning [268]. Unfortunately, there is both a lack of data and methods focused on the migration and interaction of immune cells in 2P-IVM videos.

CHAPTER 2

State of the art methods to study immune cell behavior in vivo

In this chapter, we give an overview of the state-of-the-art methods to study the migration and interaction of immune cells in organs living organisms. We initially focus on intravital microscopy as the main tool to visualize cell behavior and acquire data, Then, we focus on the methods to analyze the acquired data, discuss their pitfalls and peculiarities.

Additionally, we discuss the application of methods from computer vision and pattern recognition which are relevant for the analysis of intravital microscopy data but are not specifically designed for this task.

2.1 Intravital imaging pipeline

The standard imaging pipeline (see Figure 2.1) includes the acquisition of images, using a specific microscope, in a surgically exposed organ of an anesthetized animal. This process is repeated over time to acquire videos. Subsequently, cells are detected and tracked within the videos and their movement quantified.

Unfortunately, within the pipeline noise in the input data can be amplified, leading to inaccurate or even non-reproducible results.

Indeed, imaging artifacts and the complex biomechanical properties of immune cells hamper automatic cell detection and tracking. Errors in detection and tracking, significantly affect the measures used for quantifying cell migration and in-

teraction. Although average measure can be computed to smooth errors, biologically relevant information can be lost during the averaging process.

As a consequence, manual curation of results is required. This task is time-consuming and introduces user bias, with a possible negative impact on reproducibility and usability of imaging software [40].

Therefore, robust computational and data analysis methods are required to foster image-driven immunological research.

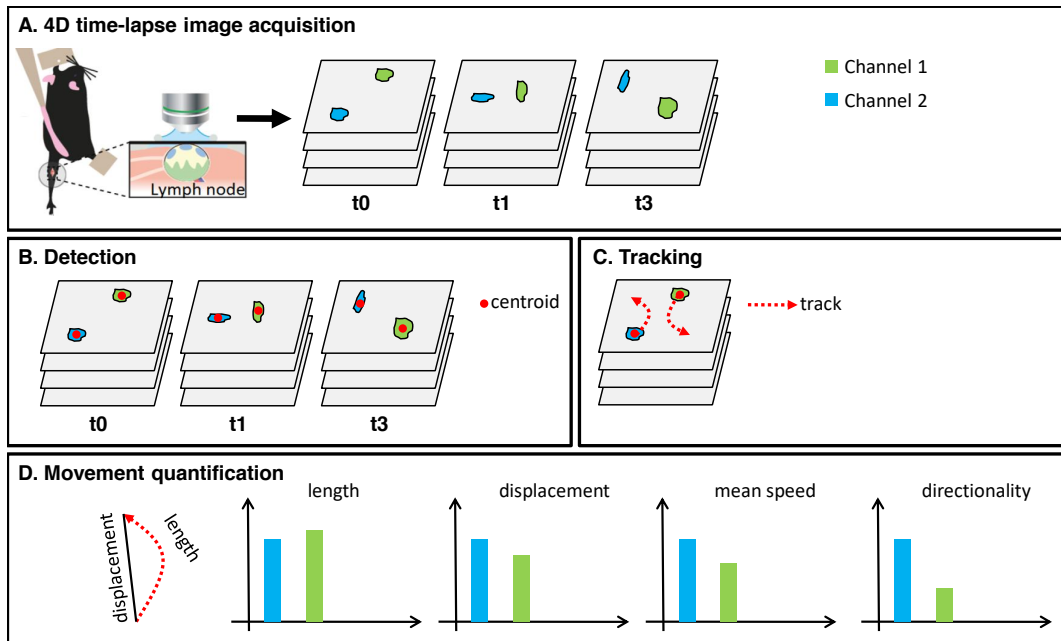


Figure 2.1. Image acquisition and analysis pipeline.

2.1.1 Image acquisition

Two-photon intravital video microscopy (2P-IVM) is the gold standard to acquire time-lapse images of immune cells in organs of living organisms [107, 237].

2P-IVM uses photons to excite fluorescence in the sample. Then, a scanner captures the emitted fluorescence and converts it into a digital image. While other fluorescence microscopy techniques stimulate the sample using a single high-energy photon, emitted by a laser in the visible spectrum, 2P-IVM uses two low-energy photons, emitted by an infrared laser. Due to the increased wavelength, infrared photons penetrate the sample at remarkable depth and reduced scattering. This allows 2P-IVM to obtain a point-like excitation of the sample. This point-wise excitation and emitted fluorescence acquisition are repeated for all the points in a plane, then the plane is moved to a different depth. A visual example is provided in Figure 2.2. The fluorescence emitted by the sample is captured by a photo-detector, which is located outside the sample. Therefore emitted fluorescence undergoes diffraction and diffusion throughout the sample.

By repeating the process over time, 2P-IVM acquires 4D data (3D volumes over time, hereafter videos).

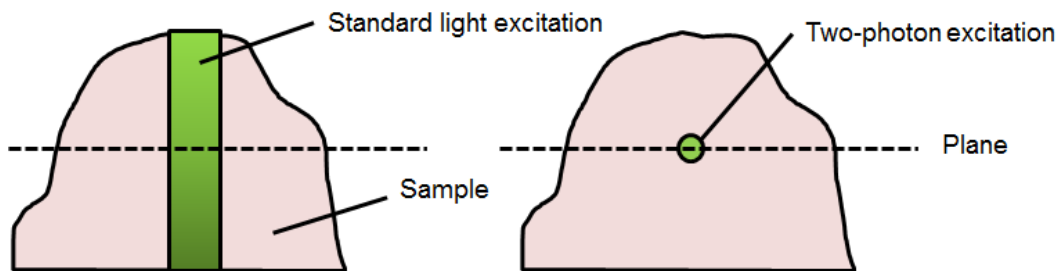


Figure 2.2. Point-wise excitation reduces photoburning and scattering.

Magnification. 2P-IVM platforms can acquire images with different magnification by using different objectives. A suitable magnification is chosen according with the type of study to be performed. We empirically identified the magnifications reported in Table 2.1 to be useful to study different immune processes.

Spatial resolution. The resolution of 2P-IVM is different according to the platform used. On average images are discretized with a pixel size from 0.1 to 1 μm in a matrix of 512x512 pixels. These can be low magnification (1mm x 1mm)

| Magnification | Useful to study | Limitations |
|-------------------------------|--|---|
| 10x ~1x1 mm | Overall positioning of cells throughout an organ Differences in regions / compartments Recruitment of cells and biodistribution of molecules | Inaccurate cell morphology Too many cells for single-cell tracking Presence of non-translational deformations |
| 25x ~500x500 μm | Collective and individual cell motility Cell-to-cell interactions Cell migration associated with anatomical structures | Might require a previous low-magnification, or different attempts to identify an appropriate area to be imaged. |
| 40x ~300x300 μm | Motility of single cells to a few number of cells. Morphodynamics | Animal movement affects the majority of field of view Possibly too few cells for statistically-driven results |

Table 2.1. Magnifications used to investigate different immunological processes.

images to see the overall dynamics in an organ with an increased number of cells, or high magnifications ($200\mu\text{m} \times 200\mu\text{m}$) to see the spatiotemporal interactions of few cells.

The distance between planes (z dimension) is one order higher, from 1 to $10 \mu\text{m}$. Typically a volume of $50\mu\text{m}$, with 10 planes is acquired.

Temporal resolution and video duration. 2P-IVM is typically configured to acquire a z-stack every 30 seconds when capturing videos of immune cells. This setup varies according to the experimental conditions. To image fast cells, the time step between z-stack acquisitions can be lowered up to 10 seconds. For slow processes, time-step can be increased to several minutes.

General limits exist on the temporal resolution. While in principle fast acquisitions can be achieved, this will induce phototoxicity in the sample with an unpredictable effect on the experiment. Therefore, this is not typically done.

This temporal resolution is just sufficient to capture fast migrating immune cells such as neutrophils. However, it does not guarantee an overlap between objects in two subsequent time points. Moreover, aliasing can be introduced by faster movements, such as the flow of cells in blood vessels and the movement of the animal. To this end, it is essential that the animal is anesthetized and immobilized appropriately [237].

Acquisitions time can last from a few minutes to several hours. Typically, videos of one hour are recorded for better file management.

Due to the possible drift of the organ over time, real-time stabilization techniques [254] play a critical role for the successful imaging over long periods.

Bit depth. Although state-of-the-art microscopes can use a bit depth of 14bits, the signal excursion is typically limited by amplification noise. In a collection of videos from different laboratories, the Signal to Noise Ratio (S.N.R.) is assessed to 17 ± 15 , exhibiting high variability from experiment to experiment [212].

2.1.2 Cell staining

2P-IVM requires fluorescent samples. Although certain molecules of living organisms are capable of spontaneously emitting fluorescence (i.e. auto-fluorescence), like, for instance, the collagen fibers, the great majority of the cells and tissues need to be labeled with fluorescent markers to be visible in 2P-IVM acquisitions. The most common labeling methods are

- Genetically modified (GM) animals
- *In vitro* labelling with fluorescent dyes
- Administration of fluorescent antibodies

GM animals, which are predominately murine models, have specific cells expressing a fluorescent protein. They are obtained by genetically encoding a probe into the sequence of a cell structure, like a protein. For instance, ubiquitin C, which is a protein constitutively expressed throughout all the cells and tissues, can be made fluorescent by inserting in its gene the sequence of the reporter Green Fluorescent Protein (GFP). As a result, all the cells of these mice, which are called UBC-GFP, emit fluorescence in the spectrum of the GFP [226].

The sequence of fluorescent proteins such as GFP usually was identified from bioluminescent organisms such as corals and jellyfishes [135].

Although it is possible to perform imaging in a reporter GM animal, some challenges could make it not practical, like the relatively limited availability and high cost of commercial reporter strains. Therefore, a common alternative approach is to inject into a recipient wild type mouse (i.e. not fluorescent) fluorescent cells, previously labeled *in vitro* using commercial dyes. Then, imaging is done into the recipient animal. According to the experimental settings, a sufficient amount of time is required prior to imaging for the cells to distribute throughout the tissues. This technique has the advantage that it reduces the costs and limitations of GM animal models. Additionally, it allows distinguishing different cell types, by injecting at the same time a combination of cells labeled in different colors or isolated from different transgenic reporter mice. Although the injection of labeled cells in the bloodstream reflects the normal recruitment path of leukocytes from blood, additional effects must be taken into consideration during the anal-

ysis of results. These include the limited persistence of cells in the bloodstream (non-continuous recruitment), the possible stress and activation of cells due to the injection.

Non-fluorescent cells can be also tagged *in vivo* using conjugated antibodies. Antibodies are very efficient in binding cells or structures and after injection in a living organism, they can specifically attach to their target. However, the efficiency of this labeling method depends on the kinetics of the distribution of every single antibody throughout the tissues. A disadvantage of dyes and antibodies methods is that the fluorescence signal can be altered by a not uniform distribution of the fluorophores in the substrate, resulting in entire cells or parts of them which are more intense than others. Such a problem is overcome using genetic models, in which fluorophores are homogeneously distributed.

From our observations of immune cells, we noticed that phagocytic immune cells (i.e. neutrophils) labeled with fluorescent dyes or antibodies present non-uniform fluorescence, with possible internalization and high concentration into the lysosomes.

2.1.3 Organs and surgical models

2P-IVM can be performed into organs and tissues of living animals with great depth (500 μm to 1 mm) [237].

Immune cells have been observed in both immune-related organs such as the lymph nodes, bone marrow, spleen [237], vessels such as blood capillaries, venules and arterioles [243], lymphatics [119], and other internal organs such as the central nervous system [205], liver [86, 97], pancreas [144], gastro-intestinal tract [123] and skin [8] amongst others.

2P-IVM requires an appropriate surgical strategy to expose and access the organ of interest, guaranteeing at the same time immobility, low tissue damage and minimization of the inflammation associated with surgery. Indeed, insufficient immobility of the organ of interest may irreversibly alter the acquisition and make the analysis not possible. Thus, very efficient organ exposure and immobilization are required. On the other hand, too invasive surgery could cause damage of blood or lymphatic vessels, which impairs the quality of fluorescent signals, cells recruitment, and reliability of the data.

Different organ features, like anatomical localization and movements, affect the probability of success of the surgery and subsequent acquisition. For instance,

imaging of intrathoracic organs remains challenging, mainly because of their anatomic inaccessibility, the large tissue displacement during breathing cycles, and of the loss of negative pressure in the thorax once opened that makes the organs collapsing [237]. Thus, it is clear that the establishment of advanced surgical protocols is critical for successful 2P-IVM imaging. For example, we recently proposed a surgical model to perform 2P-IVM imaging in the mouse trachea [207].

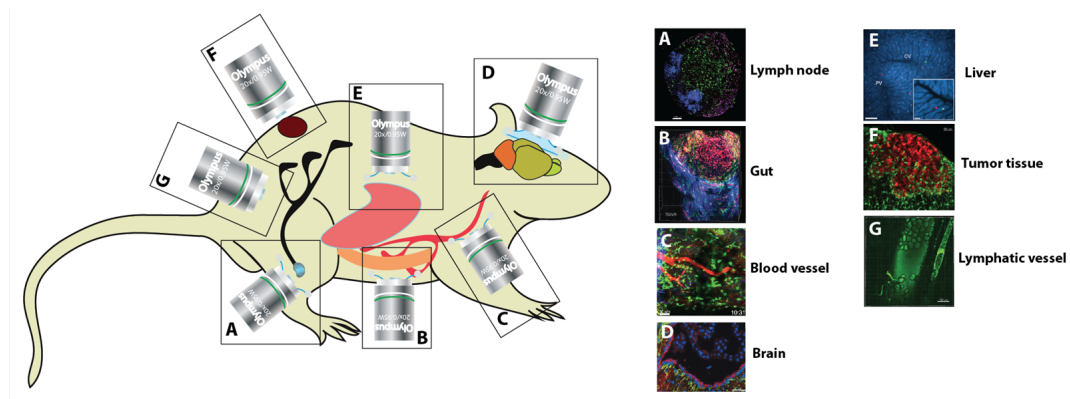


Figure 2.3. Surgical models adapted to perform intravital imaging.

2.1.4 Cell detection

Automatic cell detection includes two different tasks: Detecting which pixels are of a cell and which not. Associating these pixels to different cells.

These two tasks are typically achieved by:

- Separating foreground from background.
- Reconstructing the shape of cells.
- Separating, merging or excluding objects with size-based constraints.

Methods for foreground segmentation

The goal of these methods is to separate cells of interest from the background or other cells. Usually, another image in which only the cells of interest are visible is generated. This image can be either a binary mask, or it can have the original bit-depth of the 2P-IVM acquisition having each pixel a brightness equal to the original image for the foreground and 0 for the background, or a value proportional to the likelihood of the pixel to be foreground.

Manual thresholding. The most widely used method to separate the background from the foreground is manual thresholding. This assumes that the background has a lower brightness than the foreground. Classical bioimaging software such as Imaris (Bitplane) asks the user as the first step to set a brightness threshold to exclude the background from the cells of interest. This threshold is typically global in space and time. Although a global threshold cannot deal with brightness variations in space and time, nor exclude a background with high brightness, it can be easily tuned. Indeed, users can immediately see the generated images and tune this parameter intuitively until visual satisfactory results are obtained. Unfortunately, this threshold has to be modified from experiment to experiment, requiring an expert user that knows how cells should visually look. The high dependence of this approach on individually defined parameters (i.e. the threshold) lowers reproducibility and introduces bias.

Otsu thresholding. Otsu thresholding [203] is a method typically applied to automatically suggest an initial threshold. Let $I : \mathbb{N}^d \rightarrow \mathbb{N}$, $I(\vec{x}) = v$ be a digital image that maps a pixel at coordinates \vec{x} to a value v . Let t be a threshold. We define two classes a, b for pixels whose value is below or above the threshold t . Then we define σ_{class}^2 as the variance of the values in a class. Otsu method iterates through all the possible threshold values t and selects t^* that minimizes the intra-class variance. Otsu demonstrates that t^* also maximizes the inter-class variance

$$t^* = \arg \min_t W_a \sigma_a^2(t) + W_b \sigma_b^2(t)$$

where W_a and W_b are weight factors depending on the number of pixels in each class.

Despite its wide use, in our evaluation, the threshold computed using the Otsu method required further manual adjustment for 2P-IVM images where brightness is not uniform.

Supervised pixel classification. Supervised machine learning is applied to classify pixels in background and foreground, based on examples provided by the user.

This task is either done pixel-by-pixel by classical machine learning methods such as Support Vector Machines and Random Forest classifiers, or end-to-end, which is transforming the input image to an output image. This is typically achieved by deep neuronal networks with convolutional layers.

Amongst the available software, Ilastik [236] pioneered pixel classification by brushing. The Software allows the user to draw lines on 3D images in xy, xz and

yz planes. Each line can be assigned to a different class. Then a random forest classifier is trained for multi-class classification.

To classify pixels into different classes, the user is required to select useful features. These include:

- Color intensity (Local, or in an averaged neighbor computed via blurring).
- Edges and Brightness variation (computed at multiple scales via Difference of Gaussians (DoG) or Laplacian of Gaussians (LoG)).
- Textures (i.e. Structure Tensor Eigenvalues (STE) and Hessian of Gaussian Eigenvalues (HGE)).

The advantage of Ilastik is the live preview that allows the user to quickly visualize the predicted output and selectively correcting the errors on the regions with important mistakes. This turns in providing more training points where the classifier produces mistakes, therefore it represents an interactive way of tuning the training. Considering the training as an optimization problem that minimizes the cumulative prediction error, redistributing the points where errors are biologically relevant allows driving the optimization process towards biologically meaningful solutions. Similarly to Ilastik, Trainable Weka Segmentation [14] and other software based on pixel classification exist.

Additionally, fully-convolutional neuronal networks that convert an input image to a desired target image have been recently proposed. By using transfer learning and data augmentation these techniques can be applied to datasets with a limited number of annotations [74]. However, these have not been tested on 2P-IVM datasets yet.

On the other hand, the generic features might not be appropriate for classifying pixels of 2P-IVM acquisitions of immune cells. This is especially relevant when considering videos where the temporal component can be used to distinguish pixels with certain movement patterns.

Despite the recent success of methods based on deep neuronal networks with convolutional layers, a sufficiently extended dataset for training and validation is still not available. Therefore, transfer learning methods could represent a valid choice to port existing methods trained on other datasets to the 2P-IVM community.

Co-localization. Colocalization is a widely used technique to build a channel that includes objects of a certain color. Considering that 2P-IVM has multiple acquisition channels, the emitted fluorescence can overlap. Moreover, multiple staining could be the only possibility to separate different objects from the back-

ground.

To achieve this task, methods can be grouped into three different classes:

- Manual thresholding and rules (i.e. channel 1 lower than threshold 1 and channel 2 rather than threshold 2)
- Clustering (i.e. grouping points in color space).
- Supervised classification (similarly to pixel classification, considering features from distinct channels).

Table 2.2 summarizes the pros and the cons of the afore mentioned methods.

| Method | Pros | Cons |
|--|--|--|
| Manual thresholding | Easy to understand / tune. Immediate results. | Requires adaptation over time and space. |
| Otsu (unsupervised) | Good for initial guess. | Requires adaptation over time and space. Typically done on single channels. Hard to tune. |
| Supervised pixel classification | Tune by examples. Handles multiple colors | Lack of features specific for 2P-IVM data and datasets. |

Table 2.2. State of the art for foreground segmentation.

2.1.5 Cell tracking

Cell tracking is the problem of finding the position of each cell at each time point. State of the art methods for cell tracking can be grouped into two broad classes

- Tracking by detection (space) and subsequent linking (time).
- Tracking in space-time connected data.
- Tracking using deep learning.

Due to the limited number of methods specifically developed for tracking immune cells in 2P-IVM observations, we report in this section algorithms that have been applied for cell tracking in other microscopy techniques and evaluated at an international challenge for cell tracking (CTC) [253, 166]. Moreover, we include some promising generic object tracking algorithms that have been applied to other contexts.

Detection and association

In this paradigm, cells are first detected in each frame of the video, then linked over time.

Cell detection. We refer to cell detection as the problem of finding the centroid of a cell. This may include the segmentation of the cell shape itself.

Cell detection usually happens, after the application of image pre-processing and foreground segmentation. The pixels of the foreground are grouped into different cells according to intensity[148] and texture features[6]. The most used pixel grouping methods are based on size filtering for object separation, clustering algorithms, region growing or region merging.

Cell linking. Subsequently, a linking strategy is used to find the most likely cell correspondence between frames [166]. This has been approached by heuristics such as nearest-neighbor linking, overlap-based label propagation and by graph-based methods [253]. While nearest-neighbor and overlap-based methods assume small movement, graph-based methods can be used to model more complex scenarios such as large motion, object appearance/disappearance, and tracks of limited duration.

Graph-based methods. In graph-based methods, the track of a cell is generally modeled as a path on a graph, where nodes are the detected objects from all the time points while edges are the possible transitions. Tracking is achieved via the constrained minimization of a path-cost function, which typically includes

the weighted sum of the considered edges and penalization for non-admissible motions.

While this can be achieved for every single track independently, a globally optimal solution that considers all the tracks can be computed, by solving a linear program [120] or more efficiently by solving the K-shortest path problem on a probabilistic occupancy map [25]. Other global-optimization approaches included flow integer programming [249], multiple-hypothesis tracking [47], dynamic programming [156], and coupled minimum-cost flow [204]. In these formulations, constraints such as flow conservation, or motion feasibility can be imposed.

Unfortunately, errors in the detection impact on the linking accuracy. These can include detection of non-cellular objects, misdetection of a cell, entering and exiting of cells from the field of view.

In [25], these errors were modeled as special nodes on a graph where objects can appear or disappear. Other methods use filters and motion models to correct the results [253]. We consider that these errors can be mitigated by the usage of supervised machine learning methods for pixel classification [236] and cell detection [146].

Hybrid approaches. Interestingly, the locations of objects which are not necessarily detected can be also included in a graph. Let us define $G(V, E, w)$ a generic weighted graph G connecting two nodes $(v_i, v_j) \in V$ via an edge $e_{i,j} \in E$ with cost $w_{i,j} \in \mathbb{R}$. V corresponds to the object locations in space and time. These can be restricted to the locations identified by a cell detector or can include all the possible locations of a discrete space-time grid. Berclaz and Fua [25] associated with each node a probability of object occupancy and include the finding of the true occupancy in the objective function of a linear problem.

Space-time connected tracking

In the model evolution paradigm, an initial contour (or 3d mesh) is evolved towards the shape of a cell by minimizing a proper energy functional. Usually, a data term and a regularization term are included in the energy functional to drive the contour towards desired properties. Such a strategy allowed the reconstruction of object shapes even in images without edges [42]. Despite the possibility of applying this method in space-time connected data, it is mostly implemented by using the contour detected in one frame as a starting point for the next frame [67, 278, 66, 70, 149, 164], as described by Maska and colleagues [166].

Apostoloff and colleagues [12, 13] exploited special spatio-temporal structures, namely T-junctions, to recover the position of occluded and interacting objects.

Tracking using deep learning

Recently developed machine learning methods exhibited remarkable performances for tracking multiple objects [195, 175]. These methods processed either single frames or temporal windows to extract the tracks. These promising methods were not applied for microscopy until recently where deep learning was applied in combination with graph-based modeling of tracking errors [184]. However, their adaptation for tracking immune cells in 2P-IVM data remains to be done.

2.2 Quantification of immune cell migration and interaction

In this section, we give an overview of the main methods and measures used to quantify the behavior of dynamic immune cells. These can be divided into measures to quantify the general motility (i.e. migration), cell-to-cell interaction and complex immunological processes.

Amongst these measures, some require cells to be accurately tracked for sufficiently long time intervals. We refer to these measures as track-based.

Step-based measures instead, only require cells to be tracked for brief periods.

Lastly, cell-free measures can be computed without tracking all the cells. While the former type is generally applied, the latter remains poorly applied or not applied. In Figure 2.4, we summarize the measures most widely used in 2P-IVM studies and we include (red) novel measures that were developed within this thesis.

| | | General cell motility | | | Cell-to-cell interaction | | |
|---------------|---|--------------------------------|--------------------------------------|---|------------------------------------|---|--|
| | | Can you track the cells? | | | Can you track the cells? | | |
| | | Well | So-so | No | Well | So-so | No |
| Measures | Average motility | General motility | General motility | General motility | Preferential migration | Influence of other objects (i.e non trackable DCs) | Count of areas with multiple colors |
| | •Track length | •Instantaneous speed | •Pixel velocity | •Distance to a point | •Color variation | •Region-based contact detection | |
| | •Displacement | | | •Angle to a point | •Color variation on blurred images | | |
| Analysis | •Track Speed Mean | Dynamism | Recruitment / hot areas | Recruitment / hot areas | Influence of other cells | | |
| | •Directionality | • Optical flow | •Pixel density | •Distance transform | •Distance to the closest point | | |
| | | Recruitment / hot areas | Track-free action recognition | | of another cell | | |
| | Dynamism | •Average cell count | | Contacts | •Centroid correlation | | |
| | •Speed Variation | •Average cell density | | •Contact duration | | | |
| | •Arrest coefficient | | | •Number of contacts | | | |
| | •Regime variation | | | | | | |
| | •HoT-POF | | | | | | |
| | Recruitment | | | | | | |
| | •Cell count | | | | | | |
| •Cell density | | | | | | | |
| | Comparison of different conditions / cells | | | Influence of other cells | | | |
| | •Average dot plots + statistical tests | | | •Scatter plot: speed vs. distance | | | |
| | Identification of different cell populations | | | Influence of internalized material | | | |
| | •Scatter plots | | | •Scatter plot: speed vs. color intensity | | | |
| | •Clustering | | | Influence of non trackable but close objects | | | |
| | Dynamism | | | •Scatter plot: speed vs. color intensity (blurred) | | | |
| | •Action quantification | | | Formation of swarms | | | |
| | •Time series analysis | | | •Heatmap with pixel density | | | |
| | Spatial information | | | •Heatmap with optical flow intensity | | | |
| | •Heatmap / windmap | | | | | | |

Figure 2.4. Quantification of cell migration and interaction - measures

2.2.1 Measures to quantify cell migration and interaction

Beltman and colleagues [24] provide a review on the possible measures to describe cell migration, distinguishing two classes: *track-based* and *step-based*. Despite the former measures are computed on the entire duration of each track and can describe the overall motility of a cell for the entire period of observation, one error in a single time point can compromise the entire measure. The latter are computed amongst adjacent time points only (step), limiting the temporal propagation of errors. Despite the robustness to tracking errors, these measures remain instantaneous and loose descriptive power for long term processes.

To describe these measures more precisely, let us define the following quantities. Let $\Gamma : \mathbb{N} \rightarrow \mathbb{R}$, $\Gamma(t) = x$ be the track of a cell, mapping a time instant t , $t_0 \leq t \leq T$ to a coordinate x . Let $dt[\text{min}]$ be the time step.

Then, using this formulation in (Table 2.3) we summarize the most used track-based measures to quantify general cell motility (Table 2.3, A), dynamic behavior (Table 2.3, B), and interaction (Table 2.3, C).

Step-based measures can be derived by the ones listed in (Table 2.3), by computing them on a track fragment instead of than the entire track.

| A. General motility | | | |
|--------------------------|---|--|---|
| Measure | Description | Usage | Computed as (if available) |
| Track length | Length of the path followed by the cell | Migratory vs. stationary cells | $L = \sum_{t=\tau_0}^{T-1} \Gamma(t+1) - \Gamma(t) _2$ |
| Track duration | Time interval in which the track exists | Exclude short tracks Indicate the presence of tracking errors | $Td = (T - 1)dt$ |
| Track Speed Mean | Track length / Track duration | Varies amongst cell and conditions | $S = \frac{L}{T - 1}$ |
| Total Displacement | Length of the vector connecting the first position of the cell to the last position of the cell | A cell that oscillates around a point can have a long track but has a small displacement | $D = \Gamma(T) - \Gamma(t_0) _2$ |
| Directionality | Displacement / Length | Preferential migratory direction | $dir = D/L$ |
| Corrected straightness | Penalization of short tracks | Penalization of short tracks | $dir \sqrt{T - 1}$ |
| Mean Square Displacement | Displacement vs time | Random vs. directional migration | $MSD(t) = \frac{1}{T-1} \sum_{t=0}^{T-1} \Gamma(t) - \Gamma(0) ^2$ |
| Arrest Coefficient | % of time the cell moves with low speed (i.e. < 2um / min) | Interaction, cell death etc. | $a.c. = \frac{\sum_{t=0}^{T-1} \chi(v(t))^2}{(T-1)}$ $\chi(k) = \begin{cases} 0 & k > th \\ 1 & otherwise \end{cases}$ |

| B. Dynamic behavior | | | |
|---------------------|--|----------------------------------|--|
| Measure | Description | Usage | Computed as (if available) |
| Arrest Coefficient | % of time the cell moves with low speed (i.e. < 2um / min) | Interaction, cell death etc. | $\frac{\sum_{t=0}^{T-1} \chi(v(t))^2}{(T-1)}$ $\chi(k) = \begin{cases} 0 & k > th \\ 1 & otherwise \end{cases}$ |
| Angle distribution | Distribution of the angles between adjacent segments | Preferential migratory direction | |
| Angle to a point | Distribution of the angles between a segment and a target | Direction towards a target | |
| Speed variation | Variation of the speed with respect to the mean in a time interval | Dynamism of a cell | $\sigma S = std[s(a), \dots, s(a+n)]$ $s(t) = \frac{ \Gamma(t+1) - \Gamma(t) _2}{dt}$ |

| C. Interaction | | | |
|-------------------------------------|---|---|---|
| Measure | Description | Usage | Computed as (if available) |
| Distance to the closest other cells | Minimum distance of one cell from another cell of different type | Analysis of spatial organization | |
| Centroid correlation | Correlation between the arrays of positions of two objects | Transportation of particles within a cell; Movement associated to an external constraint. Influence of two cells. | |
| Number of contacts | Number of times that a cell forms a contact with another cell or object. | Distibguish between repeated/isolated contacts | Number of times that the distance between a cell and another object is below a threshold. |
| Contact duration | Amount of time that two cells, or a cell and another object remain in contact | Distibguish between brief/long-lasting contacts | Number of consecutive time points that the distance between a cell and another object is below a threshold. |
| Fluorescence intensity | Variation of the color of one cell | Interaction between a cell and another cell or object of different color | Colocalization of cells with different colors |

Table 2.3. Track-based measures to quantify cell motility, behavior and interaction

2.2.2 Quantification of cell actions

In this section, we report the available software and methods to quantify cell actions. Generally, available imaging software offers plugins to track cells and compute standard motility measures. These measures can be used to detect actions as reported in (Table 2.4). Moreover, we report from the literature the methods and tools used to characterize specific cell actions.

| Actions | Tools | How to use | Requires surfaces | Requires tracking |
|--------------------------|---------------------------------|---|-------------------|-------------------|
| Patrolling | Imaris | After having tracked each cell, use the Filter tool to select tracks with sufficiently high Track Length, and with mid – low Track Straightness. | NO | YES |
| | Icy, QuantEV | Launch the QuantEV plugin (track processor), Select tracks whose confinement ratio distribution is skewed towards the right. | NO | YES |
| | Fiji. Trajectory classifier | Run the Trajectory classifier for TrackMate plugin, analyze the tracks, and select cells classified as subdiffusive. | NO | YES |
| Directed | Microsoft Excel, Matlab, Imaris | Import in Microsoft Excel, Matlab or a similar program the standard track measures such as Track Duration and Track Straightness from Imaris. Exclude short tracks (i.e. < 300s) or add a rule to compute normalized Track Straightness. Select cells whose (normalized) Track Straightness is close to 1. | OPTIONAL | YES |
| | Icy, QuantEV | Launch the QuantEV plugin (track processor), Select tracks whose confinement ratio distribution is skewed towards the left. | NO | YES |
| | Fiji, Trajectory classifier | Run the Trajectory classifier for TrackMate plugin, analyze the tracks, and select cells classified as directed/active motion. | NO | YES |
| Arresting | Imaris, Arrest Coefficient XT | Select the cells of interest, launch the plugin, define a speed threshold to consider a cell arrested. The plugin computes the arrest coefficient and counts the number of stops for each cell/ | OPTIONAL | YES |
| | Icy, QuantEV | Launch the QuantEV plugin (track processor), Select tracks whose lifetime is sufficiently high, and total path length sufficiently low. | NO | YES |
| Contact formation | Imaris, Kiss and Run XT | Launch the plugin, define a distance threshold to detect a contact (i.e. 2 um) and select two surfaces (i.e. two types of cells) to compute contact number and duration for each single cell. | YES | OPTIONAL |
| | Imaris, Colocalization, Matlab | To detect contacts between cells of different color, launch the Coloc functionality to create an imaging channel specific for the contacts. Create a surface on this new channel and export the number of surfaces to count contacts. Smoothing can be applied to enhance contact detection with minimal overlap. | NO | NO |
| Swarming | Matlab/R, etc | Import cell tracks, compute the correlation of tracks, select tracks whose correlation is high | NO | YES |
| | Matlab/R, etc | Import cell tracks, compute regions with high cell density and correlated movement | NO | YES |
| | Imaris | Reconstruct a surface on the cell of interest, with large smoothing. Divide the surface volume by the typical cell volume to overestimate cells in the swarm. Apply smoothing to fill gaps | NO | NO |

Table 2.4. Tools to detect and quantify cell actions

Quantification of patrolling cells. The motility coefficient [228, 36], was used to describe the behavior of patrolling cells. However, in [113, 241] this coefficient exhibits large variance. Additionally, the Mean Square Displacement analysis on the trajectories of patrolling cells indicates a random-like movement while several studies demonstrate that immune cells do not follow a random migration [36]. Therefore, we consider these coefficients poorly descriptive of the patrolling behavior and we suggest that other parameters such as the angle or speed distribution are considered together with application-specific measures.

Quantification of directed cells. Beltman et al. extensively discuss the measures to quantify immune cell migration. Amongst these, the confinement ratio, or meandering index, is the distance between the first and the last point of the trajectory divided by the length of the total displacement of a cell [24]. However, meandering indexes are comparable if cells had similar track durations. Otherwise, normalization techniques are required. Additionally, the distribution of turning angles is indicative of directed migration when the distribution is skewed toward small angles (indicating that the cell trajectory does not deviate abruptly). We consider that the distribution of the turning angles should be complementary to the meandering index, as a trajectory with no preferential angle may have a high meandering index if the cell travels more distance in a certain direction. While a trajectory with a low meandering index may have a skewed turning angles distribution.

From a visual representation, the plotting all cell trajectories with a common origin can help as well to visually detect a preferential directionality.

Sometimes directed migration may not be immediately obvious from the trajectories of the cells, as even cells going toward a specific region may display patterns reminiscent of random migration [24]. In such cases, it is useful to evaluate the migration of the whole cell population with respect to a referential. For instance, by evaluating the turning angles with respect to a region of interest, or by computing the distance over time between the cells and the referential point. In the latter case, a decrease of the distance for the majority of the cells hints for directed migration.

Quantification of arresting cells.. The arresting action of a cell is typically quantified through the arrest coefficient [24]. This coefficient measures the amount of time in which a cell migrates with a speed below a defined threshold (typically $2 \text{ } \mu\text{m} / \text{min}$). An arrested cell has a high arrest coefficient while a cell that does

not arrest has a low arrest coefficient. However, the value of the arrest coefficient depends on the track length. Therefore, tracks (or track fragments) with similar lengths should be compared, otherwise, normalization strategies are required for comparative studies.

Quantification of contacts.. In contact formation, four aspects are commonly investigated: cells involved the contact, contact duration, number of contacts and function of the contact. To quantify the aforementioned measures contacts must be detected in the video sequence. This is commonly achieved by three different strategies based either on distance, colocalization or manual annotation. In distance-based methods, the surface of cells is reconstructed. Then, a distance threshold between pixels or centroids is defined and applied to detect contacts between cells that are sufficiently close, as implemented in the Kiss and Run plugin of Imaris (Bitplane) and described by Beltman and colleagues [24]. However, in the case of immunological synapses, the average distance between synaptic membranes is around 100 nm [136]. Considering that this is below the resolution of 2P-IVM and cells might not be reconstructed accurately, we suggest using a pixel-distance threshold greater than the microscope spatial resolution. While centroids can be annotated without the reconstruction of the cell surface, the definition of a centroid-distance threshold may be inaccurate due to the high non-convex shape of immune cells [212]. On the other side, surface reconstruction might be hampered by the presence of cell-to-cell contacts themselves [212]. By contrast, colocalization can be used to detect contacts between cells labeled in different colors, without the need for surface reconstruction [177]. Indeed, contacts can be detected as areas in which both colors are present. Alternatively, contacts between T cells and DCs were manually annotated by imaging experts as in [113]. Although manual annotation is the only possibility to detect contacts in complex datasets, this method remains time-consuming and subject to human error and bias. Therefore, more robust detection methods are required. Other methods detect contacts from other parameters (i.e. speed) whose variation is likely to be associated with a contact. In [177], contacts associated with arresting were estimated from the time-series of the instantaneous speed. In conclusion, a key factor to consider when estimating the number of contacts and contact duration is that they may be subjected to under/overestimation [23].

Quantification of cell swarms. To quantify swarm dynamics in case of localized tissue damage, the distance between the location of tissue damage and each cell can be measured at different time points. Cells whose distance decreases more

than a certain threshold were considered as members of the swarm [198, 140]. These curves describe the dynamism of the swarming process, unveiling for instance cells that promptly arrive at the damaged tissue, or cells recruited at a later time point [198].

For other cases, where a target point is not defined other approaches were used. In [49], volumetric reconstruction allowed to monitor the swarm growth over time by reconstructing a surface around the entire swarm, and measuring its volume. By dividing the swarm volume by the mean neutrophil volume it was possible to estimate the number of swarming neutrophils. Additionally, the volume of the swarm over time provides insights on the different phases of swarming, including initiation, growing and reaching of a plateau [49].

Additionally, a heat map of cell velocity and density can be constructed as described in [134] generating a spatiotemporal visualization of cellular aggregation revealing that neutrophil migration and clustering were non-uniform and regulated by short-lived local chemotactic gradients.

In summary, swarming quantification strategies were based on the two assumptions of directed migration and increased density. However, swarming behavior encapsulates the idea of cells collaborating for the same purpose in a coordinated way. These properties could be considered to detect swarms in regions with specific image features, and to quantify swarm dynamics as a collective cell migration process [232].

2.3 Relevant computer vision methods

In this section, we describe relevant methods applied in computer vision although not specifically for microscopy data analysis.

2.3.1 Superpixels

Superpixels are defined as groups of pixels with a similar appearance. Representing an image with superpixels enables the subsequent application of advanced computer vision methods on a reduced number of points. For microscopy images, superpixels are applied as the first step for segmentation and motion analysis [10]. In these applications, superpixels both speeded up computation and increased accuracy with better boundary adhesion.

Superpixel identification has been formulated as an unsupervised machine learning problem. Hence, clustering algorithms are found at the core of state-of-the-art methods [239]. Amongst these, a simple-linear-iterative-clustering algorithm

is used in SLIC [3] to compute superpixels with linear computational complexity and memory usage. SLIC finds its basis in the K-MEANS clustering algorithm [155] and introduces a novel definition of similarity between two pixels that weights the color distance (usually, in the Lab color space) and the Euclidean distance in space. SLIC has been also applied to microscopy images (i.e. electron microscopy) with superior performances respect to previously described methods [3]. Let $I : \mathbb{R}^2 \rightarrow \mathbb{R}^3$ $I(x, y) = (l, a, b)$ be an image that maps the pixel at coordinates (x, y) to the Lab color space (l, a, b) . then the distance between two pixels $p_0, p_1 \in I$ is defined as

$$d_s(p_0, p_1) = d_{lab}(p_0, p_1) + \frac{1}{\alpha} d_{xy}(p_0, p_1)$$

$$d_{xy}(p_0, p_1) = \sqrt{(x_1 - x_0)^2 + (y_1 - y_0)^2}$$

$$d_{lab}(p_0, p_1) = \sqrt{(l_1 - l_0)^2 + (a_1 - a_0)^2 + (b_1 - b_0)^2}$$

The parameter α allows to weight the spatial distance and is used to control the compactness of the superpixels.

An initial set of seeds $C_o \in I$ is then created by choosing a finite number of points distributed regularly over the image. Then, SLIC associates each pixel to the closest seed. Considering that seeds are distributed in the image, this operation is done efficiently in a local search window for each seed.

Once this has been done for all the pixels, SLIC updates the position of the seeds to be the center of mass of the identified clusters.

Then the process is repeated until a convergence criterion is satisfied.

This is the same principle behind the k-means algorithm.

Despite the efficiency and the broad applicability of this method, the limitations of k-means are inherited. Firstly it is not possible to identify highly non-convex clusters. Secondly, according to the value of the parameter α , different weight is given to color difference. Despite α can be tuned to compensate for different excursions of the image brightness and to control regularity, it acts only as a scale, without solving the problem of separating non-convex clusters with a, possibly non-existent, hyperplane. Moreover, the definition of α parameter is often left to the user.

Other clustering algorithms (i.e. spectral clustering, watershed or density-based clustering) and metrics have been used for superpixel identification.

Model evolution has also been implemented in methods such as Turbo Pixels and Eikonal Region Growing Clustering, where the contours from an initial set of seeds are evolved to minimize specific energy functionals.

Graph-based methods have also been proposed to find superpixels as a graph partitioning problem. This has been achieved either via the bottom-up merging of nodes, path-finding, or best cut identification. An extensive review of additional methods, together with an accurate evaluation methodology is provided in [197] [239].

Stutz and colleagues [239] report the following requirements for superpixels, which are agreed by most authors in the Computer Vision community

- **Partition capability.** Superpixels should define a disjoint partitioning of an image which assigns each pixel to one, and only one, partition.
- **Connectivity.** Superpixels are expected to represent connected sets of pixels, meaning that it is possible to draw a line on the image, from a pixel x to a pixel y both belonging to the same superpixel, without drawing over other superpixels.
- **Boundary Adherence.** Superpixels should preserve the boundaries of objects present in an image (i.e. not including parts of different objects).
- **Compactness, Regularity, and Smoothness.** In the absence of image boundaries, superpixels should be compact, placed regularly and exhibit smooth boundaries.
- **Efficiency.** Superpixels should be generated efficiently by algorithms ideally able to run in real-time on video streams.
- **Controllable Number of Superpixels.** The number of generated superpixels should be controllable.

Amongst the most used evaluation metrics are Boundary Recall and Undersegmentation Error, for which a ground truth is used for comparison. Boundary Recall measures check that a border of a superpixel is detected within a fixed distance d from a border annotated in the ground truth. Undersegmentation error instead evaluates the portions in which a superpixel is divided with respect to the ground truth.

The ground truth can be provided by existing datasets of natural images such as the Berkeley Segmentation Dataset (BSDS500). This includes a set of natural images (2d, RGB) together with object contours which were manually annotated by multiple, independent operators.

Although superpixels are highly efficient for camera-based images and other microscopy techniques, their application to 2P-IVM images of immune cells remains challenging. The main problems are 3D data with large anisotropy, blurred borders, presence of non-convex shapes, and high brightness variations.

2.3.2 Optical flow

Optical Flow, hereafter OF, is a technique to compute the apparent movement of single pixels in image sequences.

Optical Flow relaxes the concept of object. Hence, it does not require object detection nor tracking to quantify the movement in a video.

Since its introduction in 1981 [110], Optical Flow (OF) found applications in a broad range of Computer Vision tasks and biomedical imaging. Among these, Rodrigues *et al.* [224, 223] computed Optical Flow to link the flow of red blood cells in vessels to cardiovascular diseases, Baron *et al.* [20] applied OF to capture the expansion, contraction and the twisting motion of the heart imaged by cardiac MRI, Xu *et al.* [271] combined OF with a motion model to track tumors in the respiratory tract during breathing. Remarkably, Amat *et al.* [10] provided a robust and novel formulation of OF for fluorescence microscopy which allowed the analysis of movement in largely deforming samples, such as developing embryos.

Unfortunately, OF exhibits two major impairments for 2P-IVM investigations of the immune system.

Firstly, the apparent movement of pixels should be linked to the current knowledge of immunological processes, which is mainly defined at a cellular-level of abstraction rather than at a pixel-level.

Secondly, the assumption of brightness constancy and small displacements found in the original formulation of OF (and several successive improvements) might not hold.

To explain this more precisely, let us make the following definitions.

- $d \in \mathbb{N}$ $d = \begin{cases} 2 + 1 & \text{time-sequence of 2D images,} \\ 3 + 1 & \text{time-sequence of 3D images} \end{cases}$
- $v \in \mathbb{R}$ a brightness value (assuming grayscale imaging data)
- $\vec{x}_p \in \mathbb{N}^d$, $\vec{x}_p = [x_1, \dots, x_{d-1}, t]$
space-time coordinates of a point, i.e. $\vec{x}_p = [x, y, t]$
- $I : \mathbb{N}^d \rightarrow \mathbb{R}$, $I(\vec{x}) = v$
a d -dimensional image, mapping a point at coordinates \vec{x} (in space-time) to a brightness value v
- $U : \mathbb{N}^d \rightarrow \mathbb{R}^{d-1}$, $U(\vec{x}) = \vec{u}_x = [\Delta x_1, \dots, \Delta x_{d-1}, 1]$
A displacement field, mapping each point \vec{x} at time t , to a point at coordinates $\vec{x} + \vec{u}_x$, which is at time $t + 1$

Now, it is possible to define Optical Flow as the generic problem of finding the displacement field U .

The original formulation [110] solves this problem by assuming brightness constancy. This means that a point at time t can move in the image at time $t + 1$, but maintains the same brightness value.

$$I(\vec{x}) = I(\vec{x} + \vec{u}_x) \quad (2.1)$$

With the assumption of sufficiently small displacements, the linear approximation of the right-hand by Taylor's expansion yields to the *Optical Flow constraint*.

$$I(\vec{x}) = I(\vec{x}) + \nabla I U(\vec{x}) + H.O.T. \quad (2.2)$$

or, ignoring higher order terms,

$$\nabla I U(\vec{x}) = 0 \quad (2.3)$$

Equation 2.3 defines an equation with $d - 1$ unknowns of the type $\frac{\partial I}{\partial x_1} \Delta x_1 + \dots + \frac{\partial I}{\partial x_{d-1}} \Delta x_{d-1} + \frac{\partial I}{\partial x_d} 1 = 0$ for each pixel, leading to an undetermined system. In the Optical Flow formulation by Lukas-Kanade, a solution is found via Least Squares [154].

Regularization methods have been proposed in order to choose a solution with desirable properties, such as smoothness. An optimal U^* can be computed by minimizing an energy functional such as

$$E = E_D + \lambda E_S \quad (2.4)$$

where E_D is the left-hand of equation 2.3, E_S a regularizing term and the parameter λ controls the impact of regularization. In [110], E_S has been defined as a quadratic penalty term on the gradient of the solution, disallowing large discontinuities in the flow.

$$E(u) = \int_{\Omega} \underbrace{(I(\vec{x}) - I(\vec{x} + U(\vec{x})))^2}_{\text{data term}} d\vec{x} + \lambda \int_{\Omega} \underbrace{\|\nabla U(\vec{x})\|^2}_{\text{smoothness term}} d\vec{x}$$

More recent works, [273, 208] used different regularization techniques to allow for flow discontinuities and increasing robustness to noise.

However, Equation 2.3 is only valid in a sufficiently small and local neighborhood. Errors can be introduced in the presence of large displacements, textureless areas, or displacements along the exact direction of an edge. These problematics have been addressed in a number of works. Amongst these, rich descriptors (such as HoG and SIFT) were used rather than brightness value to match points

within a variational optical flow model [34].

Coarse-to-fine approaches also shown an increased accuracy on sequences with large displacements [43]. These include a pyramidal decomposition of images with TV-L1 regularization for the computation of OF[208] or clustering of pixels in space-time (temporal superpixels) [43]. Recently, Amat and colleagues [10] got remarkable results by applying Markov Random Fields [10] in a coarse-to-fine estimation of Optical Flow in microscopy images. This enabled to quantify the movement of cells in the development of embryos captured by confocal and light-sheet microscopy. Despite the initial assumption that optical flow can be applied without the detection of objects, the Amat method relies on the prior identification of a binary mask for excluding the background.

The aforementioned methods exhibit limitations for quantifying the behavior of immune cells in 2P-IVM images. This is especially relevant when fast migrating cells or rapid movement of the animal are captured with a limited temporal resolution, which results in large temporal derivatives. Moreover, imaging artifacts do not allow to match pixels by assuming brightness constancy.

Recently, deep learning has been applied to estimate optical flow. These methods benefited from the existence of large datasets for training, consisting of computer-simulated videos together with the Optical Flow ground truth. Amongst the deep learning-based methods, EpicFlow, DeepFlow, FlowNet use neuronal networks with convolutional layers to find the correspondence between points in adjacent images. The problem of large displacements has been addressed by multiple-stream architectures such as FlowNet2 and FlowNet3 [118, 116] which integrate distinct convolution paths. Each path separately computes optical flow with small or large displacements, then a final stage merges the results.

Although promising, the application (or transferring) of these methods to 2P-IVM data remains not done. One reason can be the poor availability of 2P-IVM data to the computer vision community.

2.3.3 Action recognition

Action recognition has been largely applied to videos of humans. However, no or few attempts have been made for dynamic microscopy data. Therefore, we report the principal methods that have been used to recognize actions in videos of humans that we consider important in the context of cell-action recognition. Generally, action recognition was achieved by describing an image sequence (or a portion of image sequence) with features, which were used to classify the pres-

ence or the absence of a certain action. We refer to "Features" as a vector describing the content of an image (or an image portion). Amongst the principal features for action recognition are

- Silhouette representation [272]
- Motion history images [264, 58]
- Space-time interest points [33, 142]
- Dense trajectories [261, 260]

Action recognition methods can be divided according to the level of abstraction used to represent a video. At a high level of abstraction, we consider methods that represent a video as a graph, where nodes represent interesting points while edges the relationships between the points [5, 262, 108]. These methods can be adapted to videos in which interesting points are meaningful and can be detected, or estimated (i.e. parts of the body, object centroids, collision points). However, the efficiency of an object detector is critical to avoid the inclusion of non-desired points (i.e. coming from the background) in the graph. This, in turn, might require extended datasets with annotated objects for training the detector, or the adaptation of pre-trained models for application-specific tasks.

At a mid-level of abstraction, we consider methods grouping the trajectories of multiple pixels into "action parts" or "flow words". These entities can be identified based on the similarity of motion and appearance of different pixels. These relationships between entities can be modeled at a higher level of abstraction, for instance, using a graph [219].

At a lower level of abstraction, methods are dealing with spatio-temporal volumes. For instance, a video can be partitioned into several subvolumes, and each subvolume represented by a feature vector [260]. A classifier is then used to classify the content of each sub-volume. This is typically achieved by representing the volume using handcrafted and holistic features including bag of words, dense trajectories, and motion boundary descriptors as reviewed in [108].

More recently, deep neuronal networks have been proposed for action recognition. These can be grouped into three main architectures [229]:

- Two-stream
- Space-time connected
- Recurrent

Two-stream architectures [76, 234] combine the output of two distinct networks to predict an action. While one network works with spatial data (i.e. images), the other works with temporal data which are commonly produced by dense motion estimation algorithms such as Optical Flow.

By contrast, network architectures working on space-time connected data make use of 3D convolutions to recognize patterns in space-time such as ConvNet

[125, 246], without requiring the prior computation of Optical Flow. Therefore, Optical Flow can be learned by the network if needed for action recognition. On the other side, if Optical Flow has to be learned, it may reflect as a more difficult training [229].

Recurrent neuronal networks and long short-term memory networks (LSTM) networks were also applied for action recognition with significant improvement over previously described methods for detecting long-term human actions in common video datasets [252].

2.4 Clustering algorithms for data-driven research

Clustering is a key technique to interpret datasets obtained from empirical studies [121], including but not limited to biomedical research.

Essentially, clustering algorithms aim at automatically grouping related points in a dataset.

The identified groups can indicate the presence of multiple phenomena (i.e. populations) in the dataset. Moreover, the structure of each group (hereafter, shape) can indicate the relationship between the included points.

Being clustering a problem without a unique solution, results depend on different metrics for point-to-point similarity and rules for point-to-cluster association. However, metrics and rules generally restrict the set of admissible solutions. As a consequence, when metrics and rules are not chosen appropriately, clustering artifacts are introduced. This is especially relevant when analyzing datasets which have points from populations with arbitrary and heterogeneous structure.

Point-based methods.. For example, common implementations of the broadly used K-MEANS algorithm [155] use the Euclidean-distance as metric for point-to-point similarity and point-to-cluster association. Despite the efficiency of K-MEANS in clustering linearly-separable groups (i.e. globular-like), artifacts can be introduced when attempting to separate non-convex and nested shapes.

Density-based methods.. Interestingly, methods based on density overcome these limitations. Arbitrary shapes are reconstructed according to a density-connectivity criterion. For example, DBSCAN[73] considers two points belonging to the same cluster if sufficiently many points, in a neighborhood, are common (density reachable). As a result, the association rule of DBSCAN correctly identifies clusters with any shape having sufficient density. However, when two or more clusters are present and sufficiently close, a wide density reachability threshold

may join them while an excessively strict threshold may fail in detecting the clusters. Generally, algorithms like DBSCAN depend on a density-connectivity threshold which can be difficult to adapt for specific datasets and applications. Recently, Rodriguez and Laio [225] proposed a remarkable strategy that achieves Clustering by finding Density Peaks (CDP). CDP addresses the limitations of DBSCAN by initially finding density peaks and using them to separate clusters. Density peaks are considered as points surrounded by sufficiently many points with lower density. These neighbors with lower density make density peaks distant. Therefore, CDP identifies density peaks by detecting the outliers of a density-distance plot. This task can be performed either automatically or manually by a user visually inspecting the density-distance plot. Due to the simplicity of this rule, CDP can be applied whenever density can be measured which holds in a wide range of applications. Once peaks are identified, each one CDP assigns them a unique label representing a cluster.

However, the association rule of CDP for the remaining points consists of inheriting the label of the closest point with a higher density, which ends in being a density peak. Although this general rule applies to any cluster shape, cases remain where such a local criterion is not optimal.

Graph-based methods.. Graph-based methods achieve clustering by finding the best set of edges in a graph that both connect points in the same group and disconnect points amongst different groups. Amongst these, spectral methods achieve a graph partitioning by studying the eigenfrequencies of the matrices describing the graph. Spectral methods [257] are coordinate free and can identify non-convex clusters.

Let $G(V, E)$ be a graph with $V = \{v_i | i = 1, \dots, n\}$ the set of nodes and $E = \{e_{i,j} | v_i \text{ connected to } v_j\}$ the set of edges.

The goal is to find a partition $V = V_+ \cup V_-$ that separates the set of nodes into two subsets minimizing the cut cost.

Spectral methods achieve graph partitioning by analyzing the eigenvectors of the graph Laplacian.

Let W be the $\|V\| \times \|V\|$ adjacency matrix where $W_{i,j} = 1$ if node i is connected to node j .

Let $L = D - W$ be the graph Laplacian where D is a diagonal matrix having $D_{i,j} = \sum_i W_i \quad \forall j$.

The cost associated to a partitioning can be formulated as the number of edges between the partitions.

An efficient way [77] is to define $x \in \mathbb{R}^N$ as a vector such that

$$x_i = \begin{cases} +1, & \text{if } i \in V_+ \\ -1, & \text{if } i \in V_- \end{cases}$$

and finding the optimal x that minimizes the energy functional

$$J(x) = \# \text{ edges between } V_+ \text{ and } V_- = \frac{1}{4} x^T L x$$

While this problem is NP-hard if treated as a discrete optimization problem, its continuous relaxation has a minimum which is easy to find.

Indeed, $J(x)$ is minimized by $x^* = \begin{cases} +1, & \text{if } u_2(i) < 0 \\ -1, & \text{if } u_2(i) \geq 0 \end{cases}$

where u_2 is the eigenvector associated to the second eigenvalue of L , named Fiedler eigenvector [77]. While intersecting clusters represented a problem for spectral clustering, a recently proposed method based on local principal component analysis allowed to overcome this limitation [15].

Other clustering algorithms for biomedical data analysis, including additional density based and graph-based methods are extensively reviewed and benchmarked by Wiwie and colleagues [268]. Indeed, they provide a platform (clus-tEval) with a shared collection of datasets and evaluation protocols for a sound comparison amongst different methods.

CHAPTER 3

Objectives of the thesis

This thesis contributes to image-driven immunological research using an interdisciplinary approach which involves the exchange of data, methods, and problems between the immunological and the computational research communities.

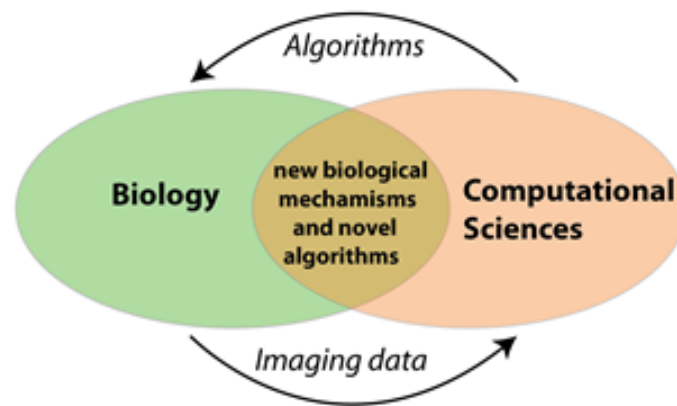


Figure 3.1. Interdisciplinary of the thesis. In this project, the discovery of new biological mechanisms from complex imaging data, and the development of novel algorithms for data analysis, are enabled by the exchange of data, methods, and needs between the biological and computational research communities.

To this end, we address the following points to facilitate the application of data analysis methods to 2-photon intravital microscopy (2P-IVM) data.

- Making available a dataset of 2P-IVM data, along with their manual analysis from imaging experts.
- Developing methods and tools for automatically analyzing 2P-IVM data.
- Applying the developed methods and tools, to extract biomedical knowledge from 2P-IVM data.

Additionally, this thesis has the objective of proposing a paradigm shift in the analysis of cell movement, which the change from considering cells as motile but inanimate particles, to considering them as active objects performing actions.

CHAPTER 4

LTDB, A database of videos and tracks of immune cells from intravital microscopy

In this chapter we present the Leukocyte Tracking Database (LTDB) which was developed within this thesis to compensate a lack of publicly available 2P-IVM data.

We consider this project essential to foster the development of Computer Vision methods for 2-photon intravital microscopy of leukocytes. Additionally, it represents a first step towards the application of data-mining methods for data-driven immunological research.

This project has been Published on July 2018 at Scientific Data

<http://www.nature.com/articles/sdata2018129>

<https://doi.org/10.1038/sdata.2018.129>

LTDB was made possible by establishing an international network of laboratories providing 2P-IVM data. In the Future work section we discuss the extension of LTDB towards a comprehensive Atlas of 2P-IVM observations. This will enable large-scale analysis including data that span different organs and experimental conditions. This extension will be supported by an approved grant from the Swiss National Science Foundation (BioLink, 2019).

Introduction and results

Despite the existence of specialized imaging software packages such as Imaris (Bitplane), Volocity (PerkinElmer) and FIJI[227], the automatic analysis of immune cell migration[24] in 2P-IVM data is problematic. Challenges are introduced at each stage of the previously described pipeline and arise both from the complex biomechanical properties of leukocytes and from technical artifacts of *in vivo* imaging (Table 4.1 and Figure 4.2a). More specifically, high plasticity of cell shape, sustained speed and frequent contacts, set a limit on the capacity of detecting and tracking cells for long time periods [279]. Additionally, technical artifacts such as the variation and non-uniform diffraction of the light emitted by fluorescently- tagged cells or the physiological movement of the sample due to peristalsis, breathing or pulsing of blood vessels, further challenge the automatic analysis. Therefore, additional steps such as image pre-processing, tuning of software parameters and manual curation of tracks, are required to improve tracking results. As a consequence, usability of imaging software is reduced [40], bias introduced and the reproducibility of the results is compromised. An example is provided in (Figure 4.2b) where the Track Speed Mean, Directionality, Track length and Track duration were computed for the entry LTDB017a (Data Citation 1). These values exhibited highly significant differences ($p \leq 0.0001$) between automatically-generated vs. manually-generated tracks.

Providing the scientific community with datasets interpreted by experts is essential to foster the development of data science methods.

Considering the challenges posed by tracking immune cells in 2P-IVM videos, a sufficiently extended dataset and tracking ground truth are needed to benchmark and validate tracking algorithm. However, any publicly available dataset was present. Despite several international cell tracking challenges were organized in the past, and they allowed to highlight the properties of different tracking algorithms, the provided data did not include videos nor tracks of immune cells observed *in-vivo*.

Therefore, we made available a leukocyte tracking database, namely "LTDB", that includes 2P-IVM videos of immune cells, together with their relative tracks. A collaboration with four international research groups was established to acquire videos captured in different experimental conditions and by different microscopy platforms. 38 videos are manually annotated by experts. Each video contains one or more challenges for the automatic analysis (Table 4.2), and captured the behaviour of one or more cell populations (Table 4.3) in response to different

stimuli (Table 4.4). 4.1

All the videos and tracks are made available as individual files or as a spatio-temporal database (Figure 4.3a) which was optimized for faster access to data and metadata (Figure 4.3b).

The expected usage of LTDB is to serve as a ground truth for the validation of tracking algorithms (Figure 4.4a). Differences with respect to the ground truth can be evaluated using, for instance, a metric that accounts for complete tracking graph comparison [165].

LTDB further aims at being a training dataset for supervised machine learning methods. Indeed, in light of the recent application of deep learning for object detection and tracking in highly variable scenarios [146, 195, 175], LTDB can provide the large number of images-tracks pairs required for the training of predictive models (Figure 4.4b). In this case, broad imaging conditions may support the generalization capabilities of these methods.

Although LTDB was provided to primarily enhance tracking algorithms, the database embeds biomedical knowledge. To this end, data-mining and image-based systems biology methods can be applied to correlate images, tracks and metadata for investigating properties of the immune system in health and disease (Figure 4.4c).

Methods

Imaging data generation. Experiments were performed by four research groups using three customized two-photon microscopy platforms (Table 4.5). Either the splenic or the lymph-node surgical models were used for acquisition (Fig 1a). Videos were acquired from 26 unique experiments, to observe the interplay of neutrophils, B cells, T cells and natural killer cells in innate or adaptive immune responses (Table 4.4).

Data pre-processing. No image processing was applied to the provided videos. RAW images were also used for manual tracking. Cropping of large 4D volumes in space and/or time was performed for the entries of the case study collection to focus on the area of interest.

Manual tracking. Centroids of cells were manually annotated and linked over time, using the "Spots drawing" tool from Imaris (Bitplane). This process was performed by a group of three operators who tracked all the cells independently, redundantly and in three different locations without seeing the results produced

by each other. In order to maximize track duration, cells were tracked also if partially visible. Tracks were interrupted only when cells completely disappeared. For specific studies, tracks of partially visible cells, migrating close to the boundaries of the field of view, can be excluded a posteriori by the user. Videos with ID (LTDB001 to LTDB020) have the maximum number of visible cells tracked. Videos in the Case Study collection (CS001 to CS018), instead, have only selected and challenging cells tracked.

Consensus tracking ground truth generation. Multiple independent annotations and tracks were merged into the consensus ground truth provided along with the dataset using a majority-voting scheme. This process was performed manually by a fourth expert using the "Unify" functionality of Imaris. The Matlab script `LTDBCheck.m` was used to facilitate track matching, detecting common errors and highlighting conflictive situations. Two tracks were said likely to "match" (i.e. referring to the same cell) if their annotations were closer than $10\mu\text{m}$ for at least N time instants. N was defined as the minimum between the track duration and 10. Conflictive situations were detected as tracks matching for only certain time instants but not for the entire track duration. These includes a) tracks with an annotation in a far position by mistake, b) a longer track matching with one or multiple shorter tracks, c) two tracks matching for N instants but having different initial and/or final positions (i.e. track switches for closely interacting cells) amongst others. Tracks with a duration shorter than 4 time instants were also inspected manually. Due to the high plasticity of cells these criteria were used only to facilitate the work of the fourth expert who had to manually merge multiple tracks as follows: If at least two operators agreed on the direction of a cell, the track was included in the dataset (i.e. two matching tracks having the same duration and detected in the same frames). If two operators tracked a cell, but the track duration was different, the points annotated only by one operator were evaluated, confirmed or discarded by the fourth expert. When two operators could not agree on the direction of a cell, the following method was applied. If the fourth expert or the Matlab script identified an evident tracking error (i.e. cells not annotated by mistake, unrealistic jumps or broken tracks) the error was corrected and the tracks were merged. For real conflictive situations (i.e. track switching for closely interacting cells) the experts were asked to meet and discuss the most appropriate solution. If still the majority consensus could not be reached, and only in this case, tracks were interrupted. Finally, the position of cell centroids included in the ground truth was not averaged but selected as the centroid closer to the mean. Although this choice may produce less

smooth tracks, it avoids to position a centroid outside non-convex cells.

These criteria together with the manual merging of tracks and re-evaluation of tracking conflicts, allowed to include the maximum number of tracks for the longest possible period of time.

Animal models. The mouse strains included in this study are specified in Table 4.6.

Prior to imaging, mice were anesthetized with a cocktail of Ketamine (100 mg/Kg) and Xylazine (10 mg/Kg) as previously described [172]. All animals were maintained in specific pathogen-free facilities at the Institute for Research in Biomedicine (Bellinzona, CH), Theodor Kocher Institute (Bern, CH) and Massachusetts General Hospital (Boston, MA). All the experiments were performed according to the rules and regulations of the local authorities and approved by the institutional animal committees: Swiss Federal Veterinary Office, Research Animal Care of the Massachusetts General Hospital, MGH Institutional Animal Care and Use Committee (IACUC).

Code availability. To facilitate the usage of LTDB, the following Matlab code is provided, under the GPL v3 Open Source licence, at <http://www.ltdb.info/downloads/> or via Git-Hub at <https://github.com/IRB-LTDB/>.

`LTDBReadTracks.m` Reads the tracks contained in a CSV file.

`LTDBReadImages.m` Reads the 4D images contained in the TIFF files.

`LTDBExampleQuery.m` Provides an example for querying the locally installed database.

`XLTDBImportTracks.m` Imports tracks as spots in Imaris.

`LTDB2CTC.m` Exports LTDB tracks in the format used for the Cell Tracking Challenge described in [253, 166], mainly for evaluation with the methods proposed in [253].

`LTDBCheck.m` Checks for common tracking errors (i.e. annotations deleted by mistakes, broken tracks and overlapping tracks).

`EstimateDSMeasures.m` Estimates the measures in (Table 4.2) regarding the dataset complexity.

`LTDBCheck.m` and `EstimateDSMeasures.m` make use of the following libraries: `ImarisReader` <https://github.com/PeterBeemiller/ImarisReader> to read Imaris files and `bwdistsc` [180] to efficiently estimate the distance of each pixel from the closest centroid.

Data Records

Data included in this work (Videos and Tracks) are available through *figshare* (Data Citation 1) under the CC-BY open data license.

Images resulting from 2P-IVM are contained in two zip archives with name `TIFFS_LTDB001_LTDB020.zip` for the videos with ID 001 to 020, and `TIFFS_CS001_CS018.zip` for the videos in the case study collection with ID 001 to 018. In these archives, a folder for each video contains 4D images as TIFF files.

Tracks resulting from the consensus tracking ground truth generation, are contained in the archive `GT_TRACKS.zip`

A dump of the SQL database used to organize data and metadata is provided in `LTDB.sql`.

The following supplementary files are available through *figshare* (Data Citation 1). For a quicker preview, each is available in a H264 encoded MP4 file named `<VideoID>.mp4`.

A snapshot of all the videos is contained in the archive `SNAPSHOTS.zip` respectively named `<VideoID>.png`

Individual tracks produced by different operators are provided in the supplementary archive `operator_individual_tracks.zip` and named `<VideoID>_<TrackID>_<OpID>.csv`. In this case `<OpID>` is the ID of the operator (OP1, OP2 or OP3).

Technical Validation

Imaging data. Imaging data were captured from organs of living animals using either the splenic or the popliteal lymph node surgical models (Figure 4.1a and Table 4.4) which are typical for 2P-IVM investigations of the immune system [237]. Cells involved in both innate and adaptive responses were included in the dataset. Videos 12, 13, 14 (Data Citation 1) come from recently published 2P-IVM studies [194, 231, 160]. To represent data generated by multiple laboratories in different experimental settings [171], LTDB includes videos with different size, resolution, sampling rate and challenges for the automatic analysis (Table 4.2), acquired by three different microscopy platforms (Table 4.5). Moreover, cells were labelled with different fluorescent tags and detected by multiple channels (Table 4.3).

The following measures were computed to estimate the complexity of each video:

signal to noise ratio (SNR), minimum distance between two cells (Dist) and number of cells per time instant. Since the proposed dataset is centroid-based rather than segmentation-based, SNR was estimated by adapting the definitions proposed in [253] with the following heuristic. Let $c_{i,t}$ be the centroid position of cell i at time t . For each pixel v in the current frame, the distance to the closest centroid was computed as $d_v = \min(\|v - c_{i,t}\|) \forall i$. Then, considering a typical cell diameter of $10\mu m$, each pixel v was defined as foreground (FG - inside a cell) or background (BG - outside a cell) according to (Equation 1). This assumption allowed to sample a sufficient number of points in each video to estimate the aforementioned measures. (Table 4.2) summarizes the average values of each video while the additional script `EstimateDSMeasures.m` can be used to compute the values for each time instant.

$$v \in FG \implies d_v < 4\mu m \quad v \in BG \implies d_v > 20\mu m \quad (4.1)$$

$$SNR = \frac{\|avg(FG) - avg(BG)\|}{std(BG)} \quad (4.2)$$

Tracks. The consensus tracking ground truth provided with LTDB includes 728 unique tracks composed of 44722 instantaneous annotations. On average, each track is composed by 61 annotations. This varying with the track duration. The total observation time included in LTDB amounts to the equivalent of 260 hours for a single cell.

Common tracking errors (i.e. cells not annotated by mistake, broken tracks or jumps in the z-axis) as well as conflicts produced by multiple operators were detected by executing the Matlab script `LTDBCheck.m` provided in the code availability section.

Individual operators produced 1850 tracks (113807 annotations) which were merged into the 728 tracks of the consensus tracking ground truth. The performances of each operator with respect to the consensus ground truth is reported in (Table 4.7). To this end, the TRA [253] measure was computed. This measure includes a complete comparison of tracks represented as an acyclic oriented graph [165]. In order to estimate this measure, the ground truth and the individual tracks were converted in the format described in [253] and evaluated using the `TRAMeasure` software provided along. However, that software and methodology matches a cell in the ground-truth with a cell in the track to be evaluated, when they overlap more than 50% in space. Being our dataset centroid-based a difference of 1 pixel would made the matching not possible. Hence, considering the typical cell diameter, we approximated a sphere around each of the

centroids. The tolerance radius of the spheres was at maximum of $10\mu m$ and was truncated in case of two centroids closer than $10\mu m$. The script `LTDB2CTC.m` was used to export the LTDB tracks in the acyclic oriented graph format described in [166, 253].

Usage Notes

The expected use case scenario of LTDB is the evaluation of results produced by a cell tracking algorithm (Figure 4.3a). Considering a generic cell tracking algorithm as an input-output system that reads an image sequence and outputs the tracks, LTDB can be used both as a source of images and as a ground truth for comparing the output.

To assess the overall performances of a cell tracking algorithm, we direct the user of LTDB towards the entries `LTDB001` to `LTDB020`. To test the behaviour of an algorithm on specific cases instead, we recommend the user with the videos in the Case Study collection `CS001` to `CS018` that facilitates manual investigation and debugging having a reduced number of cells.

4D images are provided as uint16 TIFF files. File names were structured as `<VideoID>_Txxx_Cxxx_Zxxx.tiff` where

`<VideoID>` is either `LTDB001` to `LTDB020` or `CS001` to `CS018`

the suffix `xxx` after T, C, Z indicates time instant, channel number, and depth level respectively spanning from 000 to 999 maximum.

Images with a lower bit depth were stored as uint16 without any scaling. If needed, for normalization the bit-depth of each video can be found in (Table 4.2).

Tracks are provided in the CSV Format described in (Table 4.7) and named `<VideoID>_<TrackID>_GT.csv`.

For videos with only one cell population `<TrackID>` is "a", while for videos with two cell populations tracked it is either "a" or "b". These suffixes correspond to the suffixes used in (Table 4.2).

The synthetic example with ID `SQUARE` was added to the dataset. This provides a test-case for software having different coordinate systems. A parallelogram of $5 \times 5 \times 10 \mu m$ is positioned in the first frame close to the origin used for LTDB videos, corresponding to the bottom($x=0$), left($y=0$), deepest($z=0$) corner of the 3D volume. This parallelogram migrates along the y-axis.

In order to evaluate tracking performances we provide a Matlab script `LTDB2CTC.m` to export LTDB tracks as the acyclic oriented graph representation [165] used in the Cell Tracking Challenge described in [253, 166]. This allows the usage of the

accurate methodology and software provided by the aforementioned authors to compare computed tracks vs. ground truth.

For detecting cell populations visible in more than one channel (Table 4.2 and Table 4.3) we encourage the usage of a co-localization method based on supervised machine learning such as Ilastik [236] or Trainable Weka Segmentation [14].

For discriminative machine learning models, it is worth noticing that all the cells of the videos LTDB001 to LTDB020 which are expected to be visible in the indicated channels were tracked. Other objects such as background, cell debris or additional cell populations were not tracked.

In the context of big-data analysis, (Figure 4.3c) LTDB represents a resource to compare the biological properties of tracks (i.e. speed, directionality) amongst different experimental conditions. A review of the possible measures that could be computed from the tracks is provided in [24].

The SQL database `ltdb.sql` can be installed optionally and for instance using the MySQL database management system. Queries to retrieve videos of interest (i.e. associated to a specific challenge, type of cell or site of imaging) can be addressed to the locally installed database. Additionally, a web interface was set up to facilitate search, preview and download of videos and it is accessible at <http://www.ltdb.info/>

Figures

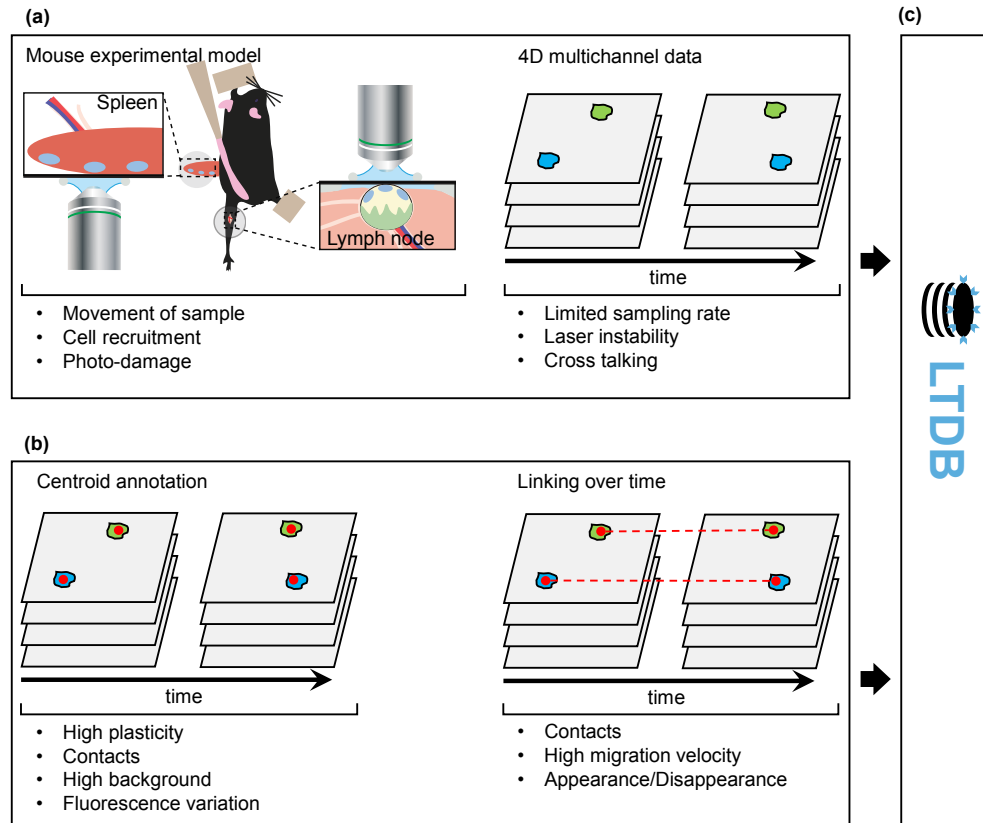


Figure 4.1. Data generation workflow. (a) *in vivo* imaging acquisition (left) Surgically exposed tissues from an anaesthetized and immobilized mouse are subjected to 2P-IVM. (right) 4D data composed by z-stack of parallel image planes are acquired at different time points for multiple channels. (b) Cell detection and tracking (left) Cells are detected and the centroid position annotated the image series (red dots). Subsequently, (right) centroids are associated over time producing the cell tracks. For each phase of the imaging pipeline are reported specific problematics that affect cell tracking. c. Database. Both 4D imaging data and cell tracks are included in LTDB.

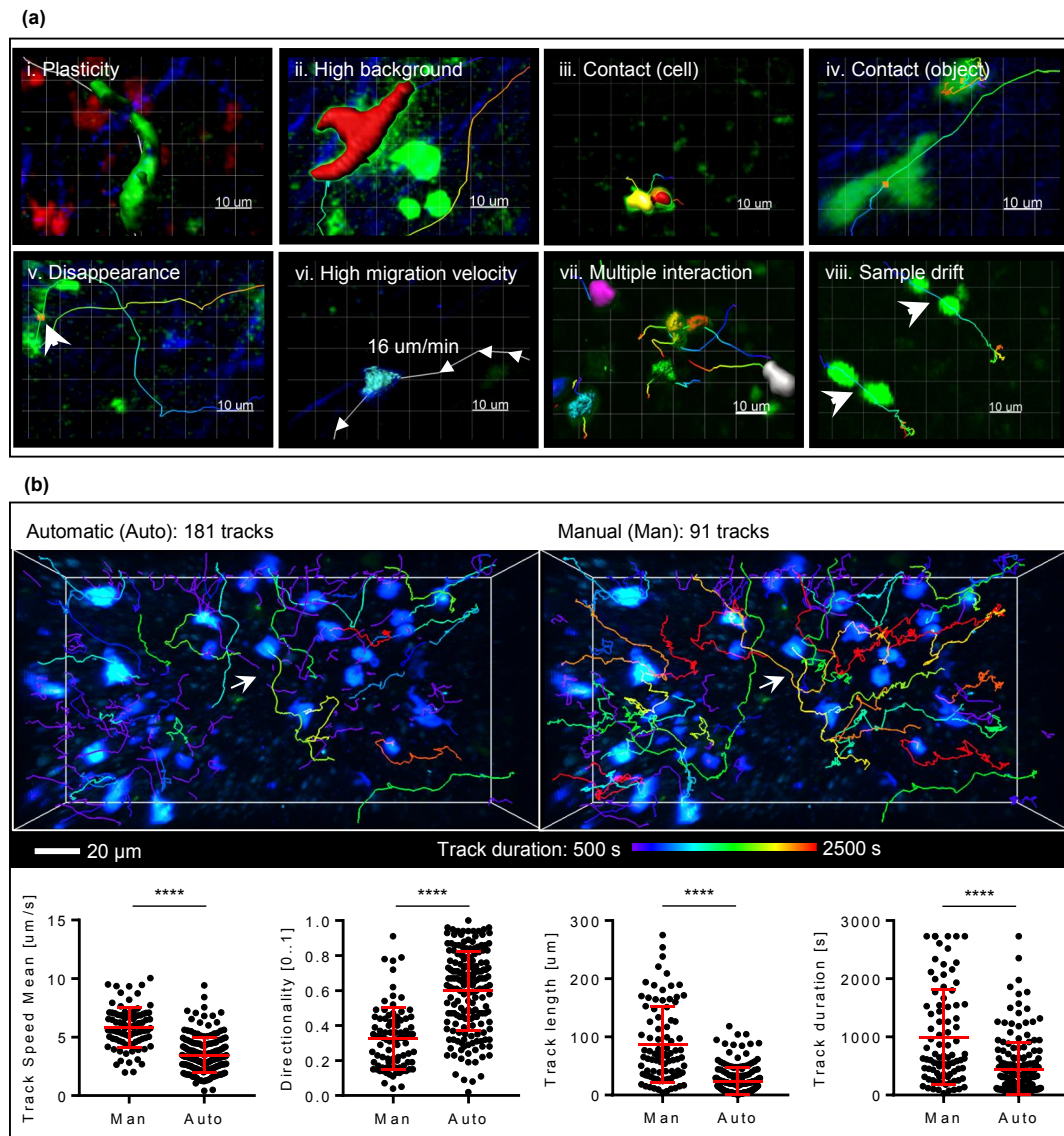
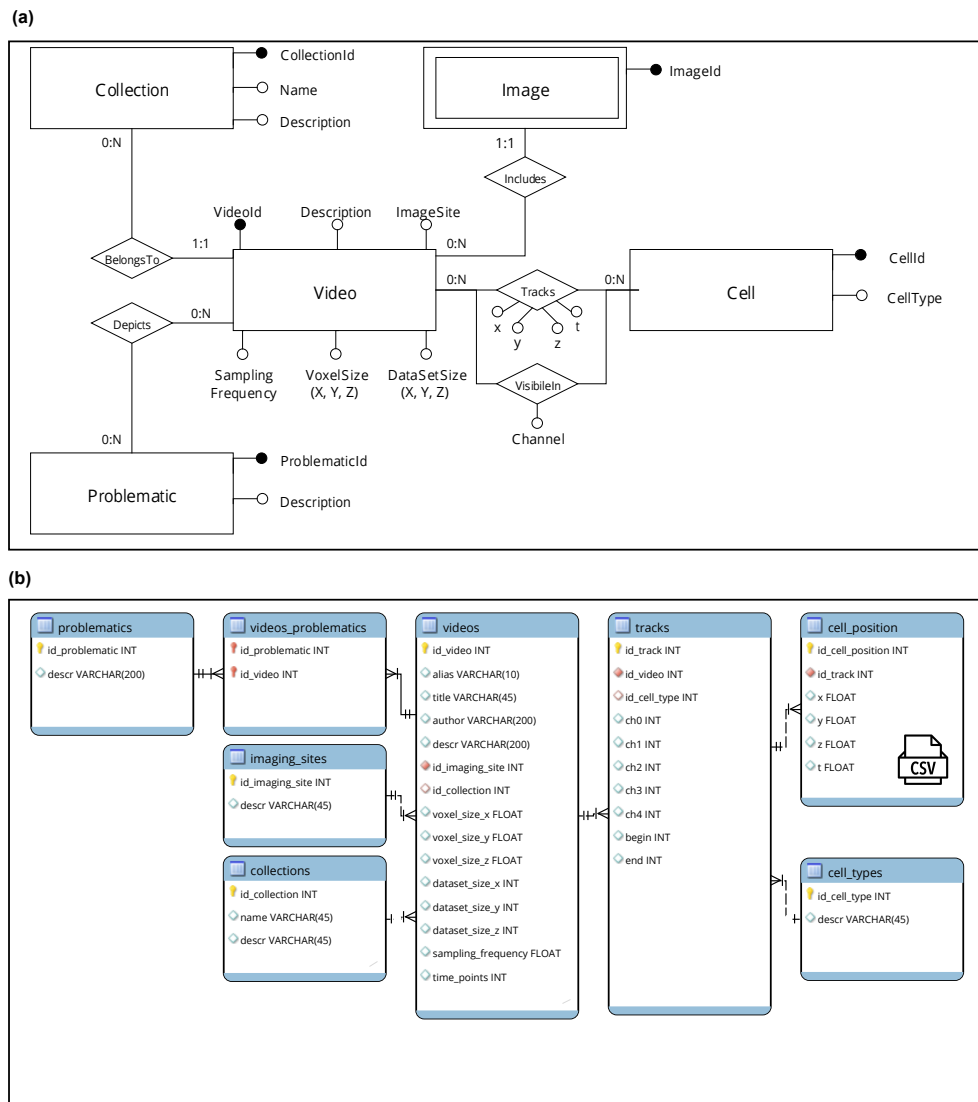


Figure 4.2. Tracking challenges. (a) Example case studies (i-viii) Representative snapshots of selected 2P-IVM micrographs from problematic cases indicated in the upper part of the picture. (i) Surface reconstruction (SR) (green) of a T cell with uropodia. (ii) SR (red) of a T cell migrating with pseudopodia on a high background. (iii) SR (yellow, red) of two neutrophils forming a brief contact. (iv) Centers of mass (red dots) of a T cell forming a brief contact with a non motile object. (v) Estimated center of mass (red dot) of a T cell close to a boundary of the field of view. (vi) SR (blue) of a rapidly migrating Neutrophil. Arrows indicate cell displacement. (vii) SR (colored objects) of Neutrophils forming multiple contacts. (viii) Tracks (colored lines) of two B cells. (b) **Effect of tracking errors** Tracking errors limit research reproducibility, significantly ($p \leq 0.0001$) affecting the typical readouts from 2P-IVM experiments. The figures (top-left and top-right) and the graphs (bottom) compare the manual tracks presented in *LTDB017_a* vs. the tracks generated automatically by Imaris. Automatic tracks were interrupted when the software could not detect or link cells, yielding to the creation of an increased number of shorter tracklets.



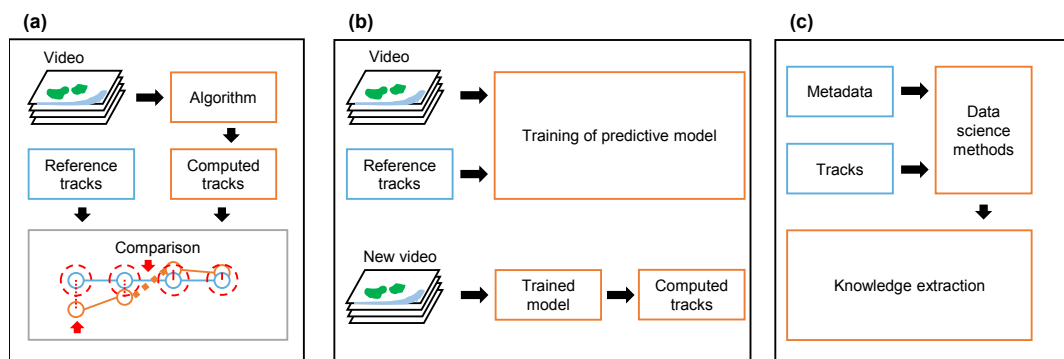


Figure 4.4. Typical usage scenarios. (a) **Evaluation of a tracking algorithm.** LTDB videos are provided as input to a tracking algorithm. Computed tracks can be compared with respect to the ground-truth tracks using a methodology of choice such as the complete graph comparison [253, 165]. In the example red arrows indicate errors where a cell was detected not sufficiently close, and when a track was interrupted. (b) **Machine learning dataset.** LTDB videos and tracks can potentially be used in the context of supervised machine learning as training and validation dataset. The generated predictive model can be generalized and used to track new videos. (c) **Resource for big data analysis.** Properties of leukocyte migration in different experimental conditions can potentially be discovered by the application of pattern recognition on LTDB metadata and tracks.

Tables

| Problem | Description | Effect on cell detection and tracking |
|---|--|---|
| Plasticity (Pla) | High variability in cell shape, such as elongation and formation of projections | Parts of the same cell not detected or associated to other cells |
| Contact (Con) | Close proximity of two cells with the same color | Cells merged in a single object. Track interrupted or switched |
| High background or low signal to noise ratio (BG) | Background or other objects (collagen fibers, auto-fluorescence, cell debris) appear in the same channel of cells with a similar brightness | Inaccurate cell detection, track interruption, tracking of third objects |
| Fluorescence variation (Flu) | The intensity of fluorescent cells changes during acquisition. Reasons include photo-bleaching and migration in different areas of the tissue | Inaccurate cell detection and track interruption |
| High migrating velocity (Vel) | Migration velocity greater than the cell size in a time step (absence of overlap) | Track interruption and aliasing if assumptions for interpolation rules for poorly visible cells are not correct. Deformation of cell shapes. |
| Appearance and Disappearance (A/D) | Sudden or progressive appearance/disappearance of a cell, either close to the boundaries of the field of view or in proximity to a blood or lymphatic vessel | Track duration is less or equal than the length of the video. Tracking errors if interpolation rules for poorly visible cells are not correct |
| Movement of the sample (Mov) | Shifting, drifting or fluctuations of the sample due to the movement of the animal or insufficient isolation from breathing, peristalsis and heartbeat | Non-rigid deformation of the tissue, discontinuities in tracks |
| Microscope instability (Ins) | Noise introduced either by oscillations in the laser power or in the sensitivity of the photo-detectors, resulting in bands or bright spots | Detection of larger or smaller objects. Appearance of the background, disappearance of cells. |
| Large areas (Lar) | Non-uniform brightness | Frequent detection and tracking errors if parameters are not adjusted locally. Increased computational time |
| Channel specificity (Spe) | Emitted spectrum is captured in more than one channel | Mis-detection and increased contacts with the background |
| Density (Den) | High number of cells in close proximity | Track switching for tightly interacting cells and mis-detection |

Table 4.1. Biomechanical and technical problems. Description of the main problems for automatic cell detection and tracking. In brackets it is reported the abbreviation used to refer at each specific problem.

| CS | DATASET SIZE | | | | VOXEL SIZE | | | D. TYPE | | SNR | | | | COMPLEXITY | | CHALLENGES | | | | | | | | | | |
|-------|--------------|-----|----|-----|------------|---|----|---------|---|------|------|------|-----|------------|----|------------|-----|----|-----|-----|-----|-----|-----|-----|-----|-----|
| | W | H | D | T | xy | z | t | bit | C | CH0 | CH1 | CH2 | CH3 | DIST | AT | Pla | Con | BG | Flu | Vel | A/D | Mov | Ins | Lar | Spf | Den |
| 001_a | 127 | 83 | 11 | 31 | 1.15 | 4 | 15 | 12 | 4 | 0.1 | 0.6 | 7.7 | 0.3 | | 1 | x | | | | x | | | | | | |
| 002_a | 116 | 87 | 11 | 120 | 1.15 | 4 | 15 | 12 | 4 | 0.2 | 1.0 | 11.5 | 0.2 | | 1 | x | | | x | | | | | | | |
| 003_a | 116 | 86 | 11 | 120 | 1.15 | 4 | 15 | 12 | 4 | 0.2 | 0.6 | 9.6 | 0.3 | | 1 | x | x | x | | | x | | | | | |
| 004_a | 279 | 197 | 18 | 20 | 0.50 | 2 | 60 | 14 | 3 | 14.4 | 0.1 | 17.0 | | | 1 | x | | | | x | | | | | x | |
| 005_a | 241 | 200 | 14 | 29 | 0.43 | 3 | 32 | 14 | 1 | 78.3 | | | | 12 ± 3 | 1 | | x | | | | | | | | | |
| 006_a | 124 | 134 | 11 | 120 | 1.15 | 4 | 15 | 12 | 4 | 0.1 | 0.8 | 9.7 | 0.2 | 50 ± 19 | 2 | x | x | | | | | | | | | |
| 007_a | 300 | 320 | 14 | 29 | 0.43 | 3 | 32 | 14 | 1 | 38.4 | | | | 11 ± 4 | 12 | | x | x | | | | | | | | |
| 008_a | 124 | 112 | 10 | 119 | 0.80 | 2 | 25 | 14 | 1 | 52.0 | | | | 36 ± 9 | 2 | | | | | | | x | | | | |
| 009_a | 108 | 76 | 11 | 115 | 0.80 | 2 | 25 | 14 | 2 | 38.3 | 1.3 | | | 10 ± 2 | 4 | | x | | | | | | | | | |
| 010_a | 148 | 279 | 18 | 26 | 0.50 | 2 | 60 | 14 | 3 | 2.5 | 0.5 | 3.0 | | 14 ± 6 | 3 | x | x | | | | | | | | x | |
| 011_a | 218 | 187 | 16 | 60 | 0.85 | 2 | 30 | 14 | 3 | 6.6 | 0.4 | 0.2 | | 47 ± 25 | 3 | x | | x | | | x | | | | | |
| 012_a | 105 | 69 | 14 | 61 | 0.47 | 4 | 20 | 12 | 1 | 4.3 | | | | 13 ± 16 | 2 | | | | | | | | | | | |
| 013_a | 256 | 144 | 14 | 39 | 0.27 | 2 | 30 | 14 | 3 | 29.3 | 0.2 | 20.9 | | | 1 | x | | | | | | | | | x | |
| 014_a | 142 | 115 | 13 | 242 | 0.80 | 3 | 15 | 8 | 3 | 20.4 | 1.7 | 8.2 | | 50 ± 12 | 3 | x | | | x | | x | | | | | x |
| 015_a | 279 | 116 | 10 | 220 | 0.50 | 3 | 12 | 8 | 3 | 0.5 | 12.6 | 0.8 | | | 1 | | | x | x | | | | | | | |
| 016_a | 279 | 116 | 10 | 220 | 0.50 | 3 | 12 | 8 | 3 | 2.8 | 0.4 | 6.5 | | | 1 | x | x | x | | | x | | | | | x |
| 017_a | 163 | 132 | 10 | 128 | 0.50 | 3 | 12 | 8 | 3 | 8.1 | 1.7 | 9.2 | | 28 ± 14 | 2 | x | x | | | | | | | | | x |
| 018_a | 143 | 135 | 14 | 60 | 0.56 | 3 | 30 | 14 | 4 | 2.8 | 0.1 | 0.2 | 0.1 | 10 ± 2 | 11 | x | x | | | | | | x | | | |
| LTDB | W | H | D | T | xy | z | t | bit | C | CH0 | CH1 | CH2 | CH3 | DIST | AT | Pla | Con | BG | Flu | Vel | A/D | Mov | Ins | Lar | Spf | Den |
| 001_a | 556 | 556 | 18 | 60 | 0.50 | 2 | 60 | 14 | 3 | 4.0 | 0.3 | 4.9 | | 15 ± 7 | 12 | x | x | x | | x | | | | | x | x |
| 002_a | 556 | 556 | 18 | 59 | 0.50 | 2 | 60 | 14 | 3 | 3.5 | 0.3 | 4.7 | | 13 ± 5 | 14 | x | x | x | | x | | | | | x | x |
| 003_a | 391 | 352 | 20 | 71 | 0.50 | 2 | 13 | 14 | 3 | 14.3 | 0.2 | 6.9 | | 20 ± 14 | 6 | | | | x | | | x | | | | x |
| 004_a | 555 | 555 | 14 | 135 | 0.80 | 3 | 15 | 8 | 3 | 10.7 | 1.2 | 11.3 | | 36 ± 12 | 7 | | x | x | x | | | x | | | x | x |
| 004_b | 555 | 555 | 14 | 135 | 0.80 | 3 | 15 | 8 | 3 | 6.6 | 16.7 | 5.7 | | 29 ± 36 | 1 | | x | x | | | | x | | | | |
| 005_a | 555 | 555 | 15 | 131 | 0.80 | 3 | 15 | 8 | 3 | 8.6 | 2.2 | 11.3 | | 43 ± 14 | 7 | | x | x | x | | | | | | x | x |
| 005_b | 555 | 555 | 15 | 131 | 0.80 | 3 | 15 | 8 | 3 | 6.6 | 11.0 | 5.2 | | 83 ± 27 | 2 | | x | x | x | | | | | | x | |
| 006_a | 555 | 555 | 14 | 138 | 0.80 | 3 | 15 | 8 | 3 | 4.9 | 1.1 | 10.9 | | 120 ± 10 | 3 | x | | | x | | | | | | | x |
| 007_a | 555 | 555 | 15 | 93 | 0.80 | 3 | 15 | 8 | 3 | 3.5 | 1.1 | 8.7 | | 34 ± 6 | 8 | | x | x | x | | | | | | x | x |
| 007_b | 555 | 555 | 15 | 93 | 0.80 | 3 | 15 | 8 | 3 | 21.9 | 3.1 | 6.1 | | 15 ± 5 | 29 | | x | x | x | | | | | | x | x |
| 008_a | 524 | 518 | 14 | 39 | 0.27 | 2 | 30 | 14 | 3 | 15.8 | 0.1 | 8.5 | | | 1 | | | | | | | | x | | x | |
| 009_a | 391 | 352 | 20 | 23 | 0.50 | 2 | 14 | 14 | 3 | 10.0 | 0.1 | 5.8 | | 55 ± 15 | 4 | | | | x | | | | | x | | x |
| 010_a | 555 | 555 | 10 | 120 | 0.80 | 2 | 30 | 14 | 2 | 2.9 | 42.9 | | | 16 ± 2 | 23 | | | | x | | | | | | x | |
| 011_a | 725 | 725 | 10 | 45 | 0.38 | 2 | 40 | 14 | 2 | 40.1 | 1.1 | | | 16 ± 2 | 9 | | | | x | | | | | | | |
| 012_a | 512 | 512 | 11 | 89 | 1.15 | 4 | 15 | 12 | 4 | 0.7 | 8.5 | 0.1 | 0.0 | 80 ± 6 | 4 | x | | | x | x | | | | | x | |
| 012_b | 512 | 512 | 11 | 89 | 1.15 | 4 | 15 | 12 | 4 | 0.1 | 1.9 | 11.5 | 0.1 | 16 ± 5 | 39 | x | x | x | x | | | | | | x | x |
| 013_a | 512 | 512 | 11 | 120 | 1.15 | 4 | 15 | 12 | 4 | 0.0 | 0.5 | 15.4 | 0.2 | 10 ± 3 | 58 | x | x | x | x | | | | | | x | x |
| 014_a | 257 | 257 | 11 | 241 | 0.60 | 4 | 15 | 12 | 4 | 0.1 | 0.5 | 0.2 | 3.2 | 14 ± 6 | 6 | x | x | x | x | | | | | | | x |
| 014_b | 257 | 257 | 11 | 241 | 0.60 | 4 | 15 | 12 | 4 | 4.8 | 0.2 | 0.2 | 0.1 | 12 ± 3 | 14 | x | x | x | x | | | | | | | x |
| 015_a | 523 | 523 | 16 | 61 | 0.38 | 4 | 20 | 14 | 4 | 0.1 | 35.3 | 6.3 | 0.1 | 20 ± 5 | 12 | x | x | x | x | x | | | | | x | |
| 016_a | 379 | 355 | 10 | 220 | 0.50 | 3 | 12 | 8 | 3 | 5.7 | 0.9 | 12.6 | | 11 ± 4 | 15 | x | x | x | | | | | | | x | x |
| 017_a | 404 | 214 | 14 | 183 | 0.50 | 3 | 15 | 8 | 3 | 14.7 | 1.0 | 31.8 | | 9 ± 2 | 33 | x | x | x | | | | | | | x | x |
| 017_b | 404 | 214 | 14 | 183 | 0.50 | 3 | 15 | 8 | 3 | 0.9 | 8.4 | 0.4 | | 12 ± 3 | 18 | x | x | x | x | | | | | | x | x |
| 018_a | 555 | 555 | 22 | 36 | 0.80 | 3 | 42 | 14 | 2 | 0.2 | 68.2 | | | 104 ± 9 | 5 | | | | | | | | x | x | | |
| 019_a | 430 | 409 | 22 | 80 | 0.80 | 3 | 30 | 14 | 3 | 4.2 | 0.4 | 11.3 | | 32 ± 21 | 6 | | | | x | | | | | | x | x |
| 020_a | 351 | 354 | 11 | 60 | 0.80 | 3 | 30 | 14 | 4 | 1.0 | 7.6 | 1.6 | 0.1 | | 1 | | | | | | | x | | | | |

Table 4.2. Dataset overview Overview of the size and complexity of each video-track entry of LTDB. The columns in the group DATASET_SIZE report the digital size of the 4D data (W: width, H: height, D: Depth, T: number of time instants). The columns in group VOXEL_SIZE express the physical size of each pixel(xy: along the axes x and y [um], z: distance between two image planes [um], t: time interval between to time instants [s]). The columns in the group D.TYPE (Data type) report the bit depth (bit), and the number of channels included. The columns in the group SNR report the average (over time) of the Signal to Noise Ratio (SNR) for each channel in the video. When a cell population is not visible in a specific channel these values tends to 0 (empty if the channel does not exist in the current video). The SNR values of the channels in which a cell population is expected to be visible are in bold. The columns in COMPLEXITY group report the average minimum distance between cells (DIST) and the average number of cell present in each time instant (AT). The columns in the CHALLENGES group report the main challenges (bold x) and the secondary challenges included (regular x). Pla: high plasticity, Con: contacts, BG: high background/low SNR/presence of cell debris, Flu: fluorescence variation, Vel: high migration velocity, A/D: appearing/disappearing objects, Mov: movement of the sample, Ins: instabilities of the laser, Lar: large areas, Spf: channel specificity, Den: high density.

| VideoID | CH0 | CH1 | CH2 | CH3 |
|---------|--|-------------------------|---------------------------------|-------------------------------|
| CS001 | BG(FR) | Tc(CMTMR) | a:Tc(HIV-GFP) | Coll |
| CS002 | BG(FR) | Tc(CMTMR) | a:Tc(HIV-GFP) | Coll |
| CS003 | BG(FR) | Tc(CMTMR) | a:Tc(HIV-GFP) | Coll |
| CS004 | a:Ne(UBC-CFP) , Dc(CD11c YFP) | Vaccine | a:Ne(UBC-CFP) , Coll | |
| CS005 | a:Ne(UBC-GFP) | | | |
| CS006 | BG(FR) | Tc(CMTMR) | a:Tc(HIV-GFP) | Coll |
| CS007 | a:Ne(UBC-GFP) | | | |
| CS008 | a:Ne(UBC-GFP) | | | |
| CS009 | a:Ne(UBC-GFP) | | | |
| CS010 | a:Ne(UBC-CFP) , Dc(CD11c YFP) | Vaccine | a:Ne(UBC-CFP) , Coll | |
| CS011 | a:Ne(UBC-GFP) , BG | BG | Coll, BG | |
| CS012 | a:Tc(CFSE) | | | |
| CS013 | a:Ne(UBC-CFP) , Dc(CD11c YFP) | Vaccine | a:Ne(UBC-CFP) , Coll | |
| CS014 | a:Ne(UBC-GFP) | Vaccine | a:Ne(UBC-CFP) , Coll | |
| CS015 | a:Ne(UBC-CFP) , Dc(CD11c YFP), AF | Ne(CMTMR), AF | a:Ne(UBC-CFP) , Coll, AF | |
| CS016 | a:Ne(UBC-CFP) , Dc(CD11c YFP), AF | Ne(CMTMR), AF | a:Ne(UBC-CFP) , Coll, AF | |
| CS017 | a:Ne(UBC-CFP) , Dc(CD11c YFP), AF | Ne(CMTMR), AF | a:Ne(UBC-CFP) , Coll, AF | |
| CS018 | a:NK(NCR1 GFP) , Mp(CD169 Pe) | Mp(Cd169 Pe) | Vaccine | Coll |
| LTDB001 | a:Ne(UBC-CFP) , Dc(CD11c YFP) | Vaccine | a:Ne(UBC-CFP) , Coll | |
| LTDB002 | a:Ne(UBC-CFP) , Dc(CD11c YFP) | Vaccine | a:Ne(UBC-CFP) , Coll | |
| LTDB003 | a:Ne(UBC-CFP) , Dc(CD11c YFP) | Vaccine | a:Ne(UBC-CFP) , Coll | |
| LTDB004 | Ne(UBC-GFP), a:Ne(UBC-CFP) , AF | b:Ne(CMTMR) , AF | a:Ne(UBC-CFP) , Coll, AF | |
| LTDB005 | Ne(UBC-GFP), a:Ne(UBC-CFP) , AF | b:Ne(CMTMR) , AF | a:Ne(UBC-CFP) , Coll, AF | |
| LTDB006 | a:Ne(UBC-CFP) , Dc(CD11c YFP) | Vaccine, BG | a:Ne(UBC-CFP) , Coll | |
| LTDB007 | b:Ne(UBC-GFP) , a:Ne(UBC-CFP) , AF | Ne(CMTMR), AF | a:Ne(UBC-CFP) , Coll, AF | |
| LTDB008 | a:Ne(UBC-CFP) , Dc(CD11c YFP) | Vaccine | a:Ne(UBC-CFP) , Coll | |
| LTDB009 | a:Ne(UBC-CFP) , Dc(CD11c YFP) | Vaccine | a:Ne(UBC-CFP) , Coll | |
| LTDB010 | Ne(UBC-GFP), BG | a:Bc(CTV) | | |
| LTDB011 | a:Ne(UBC-GFP) , BG | Bc(CD19 RFP) | | |
| LTDB012 | BG(FR) | a:Tc(CMTMR) | b:Tc(HIV-GFP) | Coll |
| LTDB013 | BG(FR) | Tc(CMTMR) | a:Tc(HIV-GFP) | Coll |
| LTDB014 | b:Bc(Bodipy 650) | Tc(H2B-RFP) | Tc(NFAT-GFP) | a:Bc(Ag+ Hoechst33342) |
| LTDB015 | Tc(CMAC) | a:Tc(CFSE) | Tc(CMTMR) | HEV(Meca-633) |
| LTDB016 | a:Ne(UBC-CFP) , Dc(CD11c YFP) | Ne(CMTMR), AF | a:Ne(UBC-CFP) , Coll, AF | |
| LTDB017 | a:Ne(UBC-CFP) , Dc(CD11c YFP) | Ne(CMTMR), AF | a:Ne(UBC-CFP) , Coll, AF | |
| LTDB018 | Dc(CD11c YFP) | a:NK(CMTMR) | | |
| LTDB019 | a:NK(CTV) , Dc(CD11c YFP) | Vaccine | a:NK(CTV) | |
| LTDB020 | BG | a:NK(CMTMR) | BG | Coll |

Table 4.3. Channel specification. Description of which cell population is expected to be visible in each channel of the provided videos. Bold indicates the cells that have been tracked. Brackets reports the type of staining used. The prefix a: or b: is used to indicate which is the corresponding tracking file (e.g. for video 04, b:N.(CMTMR) means that the tracks relative to the neutrophils labelled with CMTMR are in 04b.csv). Legend: Bc = B cells, Tc = T cells, Ne = neutrophils, Dc = dendritic cells, NKs= natural killer cells, Mp = macrophages, AF = auto-fluorescence, BG = background, Coll = collagen.

| VideoID | Site of Imaging | Immune stimulus | Group | Ref. |
|---------|----------------------|-------------------------------|---------------|--------|
| CS001 | popliteal lymph node | HIV-infected humanized T cell | T.M. / T.T.M. | [5,30] |
| CS002 | popliteal lymph node | HIV-infected humanized T cell | T.M. / T.T.M. | [5,30] |
| CS003 | popliteal lymph node | HIV-infected humanized T cell | T.M. / T.T.M. | [5,30] |
| CS004 | popliteal lymph node | Influenza Vaccine | S.F.G. | |
| CS005 | spleen | Vaccinia Virus | S.F.G. | |
| CS006 | popliteal lymph node | HIV-infected humanized T cell | T.M. / T.T.M. | [5,30] |
| CS007 | spleen | Vaccinia Virus | S.F.G. | |
| CS008 | spleen | Ovalbumin | S.F.G. | |
| CS009 | spleen | Ovalbumin | S.F.G. | |
| CS010 | popliteal lymph node | Influenza Vaccine | S.F.G. | |
| CS011 | popliteal lymph node | Influenza Vaccine | S.F.G. | |
| CS012 | popliteal lymph node | Steady State | J.V.S. | |
| CS013 | popliteal lymph node | Influenza Vaccine | S.F.G. | |
| CS014 | popliteal lymph node | Influenza Vaccine | S.F.G. | |
| CS015 | popliteal lymph node | Influenza Vaccine | S.F.G. | |
| CS016 | popliteal lymph node | Influenza Vaccine | S.F.G. | |
| CS017 | popliteal lymph node | Influenza Vaccine | S.F.G. | |
| CS018 | popliteal lymph node | Influenza Vaccine | S.F.G. | |
| LTDB001 | popliteal lymph node | Influenza Vaccine | S.F.G. | |
| LTDB002 | popliteal lymph node | Influenza Vaccine | S.F.G. | |
| LTDB003 | popliteal lymph node | Influenza Vaccine | S.F.G. | |
| LTDB004 | popliteal lymph node | Influenza Vaccine | S.F.G. | |
| LTDB005 | popliteal lymph node | Influenza Vaccine | S.F.G. | |
| LTDB006 | popliteal lymph node | Influenza Vaccine | S.F.G. | |
| LTDB007 | popliteal lymph node | Influenza Vaccine | S.F.G. | |
| LTDB008 | popliteal lymph node | Influenza Vaccine | S.F.G. | |
| LTDB009 | popliteal lymph node | Influenza Vaccine | S.F.G. | |
| LTDB010 | spleen | Ovalbumin | S.F.G. | |
| LTDB011 | spleen | Ovalbumin | S.F.G. | |
| LTDB012 | popliteal lymph node | HIV-infected humanized T cell | T.M. / T.T.M. | [5,30] |
| LTDB013 | popliteal lymph node | HIV-infected humanized T cell | T.M. / T.T.M. | [5,30] |
| LTDB014 | popliteal lymph node | Ovalbumin | T.M. | [7] |
| LTDB015 | popliteal lymph node | Steady State | J.V.S. | |
| LTDB016 | popliteal lymph node | Influenza Vaccine | S.F.G. | |
| LTDB017 | popliteal lymph node | Influenza Vaccine | S.F.G. | |
| LTDB018 | popliteal lymph node | Influenza Vaccine | S.F.G. | |
| LTDB019 | popliteal lymph node | Influenza Vaccine | S.F.G. | |
| LTDB020 | popliteal lymph node | Influenza Vaccine | S.F.G. | |

Table 4.4. Experimental settings. Experimental conditions for each video. Ref. indicates the references for videos which are part of published works. The acronyms under the Group column correspond to S.F.G.: Santiago Fernandez Gonzalez group, T.M. / T.T.M.: Thorsten Mempel and Thomas T. Murooka group, J.V.S.: Jens V. Stein group

| Microscope | Equipment | Format | VideoID |
|---|--|-----------------|---|
| TrimScope (LaVision BioTec GmbH) | Ti:Sapphire lasers (Chameleon Ultra I, Chameleon Ultra II, Coherent Inc.), Optical parametric oscillator (Chameleon Compact OPO, Coherent Inc.), with 1010-1340nm emission and 690-1080nm output wavelength. | 14 bits, 8 bits | CS004, CS005, CS007-CS011, CS013-CS018 LTDB001-LTDB011, LTDB016-LTDB020 |
| Ultima IV multiphoton microscope (Bruker Systems) | DeepSee and MaiTai Ti:Sapphire lasers (Newport/Spectra-Physics) tuned between 850 and 990 nm. | 12 bits | CS001-CS003, CS006; LTDB012-LTDB014 |
| TrimScope (LaVision BioTec GmbH) | MaiTai Ti:Sapphire laser (Spectraphysics) tuned to 780 or 840 nm. Trimscope I based on BX50WI fluorescence microscope (LaVisionBiotec). | 14 bits | CS012 LTDB015 |

Table 4.5. Microscopy platforms. Technical specifications of the 2P-IVM microscopy platforms used to generate each video.

| CS | TRA | | | Track duration | | | | Number of tracks | | | |
|---------|------|------|------|----------------|-----|-----|-----|------------------|-----|-----|-----|
| | OP1 | OP2 | OP3 | GT | OP1 | OP2 | OP3 | GT | OP1 | OP2 | OP3 |
| 001_a | 1.00 | 0.87 | 0.86 | 30 | 30 | 30 | 30 | 1 | 1 | 1 | 1 |
| 002_a | 0.90 | 0.98 | 1.00 | 119 | 119 | 79 | 119 | 1 | 1 | 2 | 1 |
| 003_a | 0.99 | 0.99 | 1.00 | 118 | 117 | 118 | 118 | 1 | 1 | 1 | 1 |
| 004_a | 1.00 | 1.00 | 1.00 | 18 | 18 | 18 | 18 | 1 | 1 | 1 | 1 |
| 005_a | 0.99 | 1.00 | 1.00 | 22 | 22 | 22 | 22 | 2 | 2 | 2 | 2 |
| 006_a | 1.00 | 0.96 | 0.95 | 119 | 119 | 118 | 119 | 2 | 2 | 2 | 2 |
| 007_a | 0.61 | 1.00 | 0.69 | 26 | 27 | 26 | 28 | 13 | 7 | 13 | 8 |
| 008_a | 1.00 | 0.99 | 0.99 | 111 | 111 | 90 | 91 | 2 | 2 | 3 | 3 |
| 009_a | 1.00 | 1.00 | 1.00 | 114 | 114 | 114 | 114 | 4 | 4 | 4 | 4 |
| 010_a | 1.00 | 0.99 | 0.99 | 25 | 25 | 22 | 22 | 3 | 3 | 4 | 4 |
| 011_a | 0.84 | 1.00 | 0.75 | 37 | 44 | 37 | 35 | 6 | 4 | 6 | 5 |
| 012_a | 0.85 | 1.00 | 0.93 | 15 | 16 | 14 | 16 | 9 | 7 | 10 | 8 |
| 013_a | 1.00 | 1.00 | 0.98 | 38 | 38 | 38 | 38 | 1 | 1 | 1 | 1 |
| 014_a | 0.38 | 0.95 | 0.96 | 185 | 179 | 88 | 203 | 4 | 1 | 9 | 5 |
| 015_a | 1.00 | 0.97 | 0.98 | 184 | 184 | 179 | 180 | 1 | 1 | 1 | 1 |
| 016_a | 0.97 | 0.97 | 1.00 | 155 | 153 | 157 | 155 | 1 | 1 | 1 | 1 |
| 017_a | 1.00 | 1.00 | 1.00 | 116 | 116 | 116 | 116 | 2 | 2 | 2 | 2 |
| 018_a | 1.00 | 0.59 | 0.48 | 42 | 40 | 52 | 42 | 15 | 16 | 7 | 7 |
| LTDB | OP1 | OP2 | OP3 | GT | OP1 | OP2 | OP3 | GT | OP1 | OP2 | OP3 |
| 001_a | 0.91 | 0.92 | 0.78 | 32 | 29 | 38 | 30 | 22 | 22 | 17 | 19 |
| 002_a | 0.91 | 0.86 | 0.92 | 33 | 30 | 35 | 36 | 26 | 28 | 21 | 24 |
| 003_a | 0.96 | 0.69 | 0.99 | 46 | 49 | 53 | 38 | 9 | 8 | 5 | 11 |
| 004_a | 0.78 | 0.78 | 0.78 | 92 | 87 | 93 | 88 | 10 | 10 | 8 | 9 |
| 004_b | 0.91 | 1.00 | 0.83 | 82 | 75 | 82 | 68 | 2 | 2 | 2 | 2 |
| 005_a | 0.39 | 0.65 | 0.96 | 77 | 130 | 92 | 83 | 12 | 2 | 6 | 11 |
| 005_b | 0.88 | 1.00 | 0.76 | 130 | 130 | 130 | 130 | 2 | 2 | 2 | 2 |
| 006_a | 0.50 | 0.50 | 0.99 | 137 | 137 | 137 | 137 | 3 | 1 | 1 | 3 |
| 007_a | 0.78 | 0.80 | 0.65 | 60 | 56 | 58 | 71 | 12 | 11 | 11 | 8 |
| 007_b | 0.82 | 0.95 | 0.86 | 82 | 78 | 76 | 82 | 32 | 28 | 33 | 30 |
| 008_a | 1.00 | 1.00 | 1.00 | 38 | 38 | 38 | 38 | 1 | 1 | 1 | 1 |
| 009_a | 0.97 | 1.00 | 0.84 | 21 | 20 | 21 | 22 | 4 | 4 | 4 | 3 |
| 010_a | 0.79 | 0.96 | 0.90 | 111 | 119 | 106 | 77 | 26 | 19 | 26 | 35 |
| 011_a | 0.50 | 0.84 | 1.00 | 36 | 44 | 33 | 37 | 11 | 4 | 10 | 11 |
| 012_a | 0.65 | 0.84 | 0.90 | 41 | 49 | 36 | 40 | 83 | 48 | 89 | 83 |
| 012_b | 0.94 | 0.99 | 0.93 | 81 | 78 | 56 | 77 | 4 | 4 | 7 | 5 |
| 013_a | 0.71 | 0.94 | 0.76 | 84 | 83 | 77 | 87 | 82 | 62 | 85 | 65 |
| 014_a | 0.69 | 0.92 | 0.99 | 82 | 119 | 69 | 84 | 20 | 9 | 22 | 20 |
| 014_b | 0.61 | 0.62 | 0.98 | 70 | 56 | 101 | 73 | 49 | 39 | 22 | 50 |
| 015_a | 0.88 | 0.95 | 0.99 | 25 | 30 | 30 | 24 | 30 | 22 | 24 | 32 |
| 016_a | 0.52 | 0.93 | 0.93 | 81 | 135 | 79 | 73 | 43 | 13 | 42 | 46 |
| 017_a | 0.83 | 0.86 | 0.91 | 68 | 77 | 67 | 76 | 89 | 67 | 80 | 78 |
| 017_b | 0.41 | 0.75 | 0.79 | 49 | 56 | 50 | 56 | 68 | 31 | 56 | 50 |
| 018_a | 1.00 | 0.49 | 0.97 | 35 | 35 | 31 | 27 | 5 | 5 | 6 | 9 |
| 019_a | 0.99 | 0.81 | 0.59 | 44 | 38 | 51 | 44 | 12 | 14 | 10 | 7 |
| 020_a | 0.98 | 1.00 | 0.93 | 31 | 30 | 31 | 29 | 2 | 2 | 2 | 2 |
| average | 0.84 | 0.89 | 0.90 | 71 | 74 | 68 | 70 | 17 | 12 | 15 | 15 |

Table 4.6. Comparison of tracking operators. Differences between the tracks produced by individual operators and the consensus ground truth, for all the videos in LTDB. Values of the TRA measure [253] close to 1 means the accurate matching of the operators tracks with respect to the consensus ground truth while lower values indicates tracking differences.

| | | | | | |
|--------------------------|--|--|--|--|--|
| Row 1 | LTDB_ID [string] <i>video identifier</i> | dx [um] <i>voxel size (x)</i> | dy [um] <i>voxel size (y)</i> | dz [um] <i>voxel size (z)</i> | dt [s] <i>time interval</i> |
| Row 2 | ch0 [bool] <i>visible in channel 0</i> | ch1 [bool] <i>visible in channel 1</i> | ch2 [bool] <i>visible in channel 2</i> | ch3 [bool] <i>visible in channel 3</i> | ch4 [bool] <i>visible in channel 4</i> |
| Rows 3 to end | ID [INT] <i>unique track identifier</i> | x [um] <i>position (x)</i> | y [um] <i>position (y)</i> | z [um] <i>position (z)</i> | t [INT] <i>time instant</i> |

Table 4.7. Structure of the CSV track file. The position of the centroids of all the cells tracked in a video was saved in a ASCII CSV file. Columns are delimited by the semicolon separator and rows are terminated by CR LF. The first row reports the identifier of the video, including the eventual suffix "a" or "b". The second to the fifth columns report the pixel size (dx,dy,dz) and the time interval (dt). The second row specifies in which channel (Ch) cells appear in the video. From the third to the last row, the coordinates of cells are saved. The first column represents the unique identifier of a track, not varying for the entire track duration. The second to fifth columns (x, y, z, t) represent the position of the cell with respect to the top-up-left most corner of the z-stack at a specific time point. Coordinates are expressed in μm while the time point is an integer number.

CHAPTER 5

Graph-based algorithms

In this chapter we describe algorithms that we proposed to analyze biomedical datasets represented as a graph. Then, in the next chapter we apply these algorithms to analyze the behavior of leukocytes in 2P-IVM data.

5.1 A trainable clustering algorithm based on shortest paths from density peaks

In this section we propose a novel algorithm that facilitates the collaboration between machines and humans in the analysis of complex biomedical datasets.

This work has been developed in the period 2016-2018 and published on October 30th 2019 at Science Advances.

<http://advances.sciencemag.org/content/5/10/eaax3770/>

Abstract

Clustering is a technique to analyze empirical data, with a major application for biomedical research. Essentially, clustering finds groups of related points in a dataset. However, results depend on both metrics for point-to-point similarity and rules for point-to-group association. Non-appropriate metrics and rules can

lead to artifacts, especially in case of multiple groups with heterogeneous structure. In this work, we propose a clustering algorithm that evaluates the properties of paths between points (rather than point-to-point similarity) and solves a global optimization problem, finding solutions not obtainable by methods relying on local choices. Moreover, our algorithm is trainable. Hence, it can be adapted and adopted for specific datasets and applications by providing examples of valid and invalid paths to train a path classifier. We demonstrate its applicability to identify heterogeneous groups in challenging synthetic datasets, segment highly nonconvex immune cells in confocal microscopy images, and classify arrhythmic heartbeats in electrocardiographic signals.

Introduction

Clustering algorithms aim at automatically grouping points. This task is critical for extracting knowledge from complex datasets of unlabeled data, which are commonly produced by empirical studies [121] and are impossible to analyze manually [268]. The identified groups can indicate the presence of multiple phenomena (i.e. populations) in the dataset. Moreover, the structure of each group (hereafter, shape) can indicate the relationship between the included points. Being clustering a problem without a unique solution, results depend on different metrics for point-to-point similarity and rules for point-to-cluster association. However, metrics and rules generally restrict the set of admissible solutions. As a consequence, when metrics and rules are not chosen appropriately, clustering artifacts are introduced. This is especially relevant when analyzing datasets which have points from populations with arbitrary and heterogeneous structure.

For example, common implementations of the broadly used K-MEANS algorithm [155] use the Euclidean-distance as metric for point-to-point similarity and point-to-cluster association. Despite the efficiency of K-MEANS in clustering linearly-separable groups (i.e. globular-like), artifacts can be introduced when attempting to separate non-convex and nested shapes.

Interestingly, methods based on density overcome these limitations. Arbitrary shapes are reconstructed according to a density-connectivity criterion. For example, DBSCAN[73] considers two points belonging to the same cluster if sufficiently many points, in a neighborhood, are common (density reachable). As a result, the association rule of DBSCAN correctly identifies clusters with any shape having sufficient density. However, when two or more clusters are present and in close proximity, a wide density reachability threshold may join them while an excessively strict threshold may fail in detecting the clusters. Generally, algorithms like DBSCAN depend on a density-connectivity threshold which can be difficult

to adapt for specific dataset and applications.

Recently, Rodriguez and Laio [225] proposed a remarkable strategy that achieves Clustering by finding Density Peaks (CDP). CDP addresses the limitations of DBSCAN by initially finding density peaks and using them to separate clusters. Density peaks are considered as points surrounded by sufficiently many other points with lower density. Hence, the distance between two density peaks should be higher than the distance between another arbitrary point and its closer point with a higher density.

Based on this intuition, CDP identifies density peaks by detecting the outliers of a density-distance plot. This task can be performed either automatically or manually by inspecting the density-distance plot. Due to the simplicity of this rule, CDP can be applied whenever density can be measured which holds in a wide range of applications. Once peaks are identified, CDP assigns them a unique label representing a cluster.

However, the association rule of CDP for the remaining points consists of inheriting the label of the closest point with a higher density, which ends in being a density peak. Although this generic rule is applicable to any cluster shape, cases remain where such a local criterion is not optimal (i.e. it associates a point disregarding how the others point are associated).

In this work, we propose to substitute the local association rule of CDP with the solution of a global optimization problem on a graph, bringing two main contributions. Firstly, a global vision on the dataset allows finding globally-optimal solutions not identifiable with a local choice. Secondly, we evaluate path-properties rather than point-to-point differences. This allows defining path-cost functions which can be generically meaningful (i.e. large gaps penalization). Additionally, by providing examples of valid and invalid paths, a path classifier can be trained. This is used for easily adopting and adapting the proposed method to specific tasks and datasets, by providing examples rather than tuning parameters, within a semi-supervised approach for data analysis.

We evaluate the proposed method (both with a generic path cost function and with a trainable path classifier) on synthetic datasets designed to challenge clustering algorithms [268]. Then, we provide two applications for analyzing real biomedical data. The first is the segmentation of highly non-convex immune cells in confocal microscopy (grouping pixels in space). The second is the identification of different types of arrhythmia in ECG signals.

Our method obtained clustering results not obtainable by DBSCAN nor CDP

In conclusion, our method exploits network information [88] and the integration of possibly existing knowledge in line with a theory-guided-data-science paradigm [126]. We consider it as a step towards machines (fast, operation-based) capable of working collaboratively with humans (slow, practice-based) [121].

Comparison with CDP on a simplified dataset

In CDP, a point is associated with the closest point with a higher density. This local rule takes place regardless of how the other points are associated and there exist cases where artifacts are introduced. An example is illustrated in (Figure 5.1, A) where a long-thin projection of a non-globular cluster and a second globular-like cluster are in close proximity. The estimated point-density (Figure 5.1, B) and the distance to the closest point with a higher density (Figure 5.1, C), are used to find density-peaks in a density-distance plot (Figure 5.1, D). For a generic point x , the association rule of CDP connects it to the wrong density peak q (Figure 5.1, D - white arrows). By contrast, our algorithm computes the path optimally connecting x to a density peak, which turns out to be p (Figure 5.1, F - white arrows). Although local heuristics would not consider that path (i.e. longer, non-smooth density variation), our algorithm identifies it by solving a shortest path problem in which paths having multiple small gaps rather than fewer but larger gaps are preferred. This has been expressed using a minimax path cost function (Figure 5.1, G). As a result, the thin portion of the cluster is correctly associated by our algorithm (Figure 5.1, H-I). We consider the differences on this example relevant. Indeed, analyzing the cuts introduced by the two algorithms (Figure 5.1 - dashed lines), CDP introduces a visually non-realistic cut, without the possibility of specifying how a cut should (or should not) be. By contrast, our algorithm obtained a visually-realistic boundary by specifying desired path properties. The same result can be obtained using CDP to initially identify multiple smaller clusters (i.e. selecting more density peaks) and subsequently applying a graph-based algorithm to join them. However, this would require to select density peaks which are less emerging from the density-distance plot. Moreover, it would require to specify how to join sub-clusters at a higher level of abstraction (subgroup-to-subgroup similarity). Our algorithm solves this issue at the root and allows to specify how to group points at a lower level of abstraction which is useful when pair-wise to path-wise knowledge is available.

Algorithm for global optimization

We consider clustering as the problem of associating each point to a density peak with the optimal set of paths. This problem is modeled as a Single Source Shortest Path (SSSP) on a graph (Figure 5.1, F and Figure 5.7). A globally optimal solution is computed by the Dijkstra's SSSP algorithm [61], adopting a customized path-cost function.

For explaining this more in detail, let us make some definitions.

Let $G(V, E, w)$ be a weighted graph where a node $v \in V$ is connected to another node $u \in V, v \neq u$ through an edge $e_{v,u} \in E$ with an associated cost $w_{v,u} : E \rightarrow \mathbb{R}_+$. $w_{u,v}$ is a distance metric (i.e. Euclidean distance).

Let ρ_v be the density of a given node $v \in V$, defined as the number of points in a weighted neighborhood. See [225] for an implementation where a Gaussian kernel is used to estimate ρ_v .

Let $\delta_v = \min \|v - u\| \forall u \in V \text{ s.t. } \rho_u > \rho_v$. Which is the distance of v to the closest point u with a higher density.

Let $P_\tau \subset V$, $P_\tau = \{v | v \in V, \rho_v > \tau_\rho \cap \delta_v > \tau_d\}$,

where $0 < \tau_\rho < \max(\rho), 0 < \tau_d < \max(\delta)$ are two arbitrary thresholds. We call the points in the set P_τ density peaks, i.e. nodes whose local density and distance to the closest point with a higher density are both sufficiently high.

Let s be a fictitious node added to G and connected to each density peak with an edge having a negligible cost ϵ (Figure 5.7).

The goal is to find the SSSP towards all the points with s as source, corresponding to the minimal spanning tree having s as root.

Let $\Gamma = \{s, \dots, x\}$ be the shortest path connecting the starting node s to an arbitrary point x . It is possible to show for reductio ad absurdum (Supplementary proof 1) that x is reached, passing through a single density peak (and possibly intermediate points). In this case, x belongs to the cluster containing p .

Let $w_{i,j}$ be the Euclidean distance between two nodes. If G is fully connected, the usage of a path-cost function that sums the cost of edges in the path does not penalize large gaps nor the problem of associating x to the closest but possibly not optimal peak p . Therefore, we describe the position of x with respect to a density peak, by evaluating the path connecting them. Properties of the path, such as mediating elements [80], textures[90], density patterns, or user-defined metrics, can be used to associate a meaningful cost.

The Dijkstra's SSSP algorithm can be adopted to compute the shortest paths on graphs if the path-cost is not decreasing when extending a path. Being $\xi : \mathbb{G} \rightarrow$

\mathbb{R} , $\xi(\Gamma) = c$ the cost of a path $\Gamma \in \mathbb{G}$ the following should be guaranteed:

$$\xi(\Gamma = \{s, x_i\}) \leq \xi(\Gamma' = \{s, x_i, x_{i+1}\}) \quad (5.1)$$

Several functions respect (1). Amongst these, cumulative functions sum the weights of edges included in the path $\xi_p(\Gamma) = \sum_{i,j \in \Gamma} (|w_{i,j}|^p)^{\frac{1}{p}}$. Values of $p \geq 1$ penalize edges with high cost, preferring (if possible) alternative multiple edges with lower cost. Generally $p > 1$ acts a regularizer, preferring edges with similar value.

When $p \rightarrow +\infty$, the total cost of a path is given by the edge with maximum cost in the path. This metric is used in the *minimax* formulation which defines for a generic path Λ the cost $\xi_{\text{inf}}(\Lambda)$ as $\max(w_{i,i+1}), i, i+1 \in \Lambda$. Λ is "*minimax*" if its cost is minimum with respect to all the existing paths from the same source to the same destination.

$$\Gamma \text{ "minimax" if } \xi_{\text{inf}}(\Gamma) \leq \xi_{\text{inf}}(\Lambda) \quad \forall \Lambda \neq \Gamma$$

Trainable path cost function

The Dijkstra algorithm incrementally extends a set of shortest-paths by evaluating the cost of the possible extensions. We exploited this behavior and used a custom function for computing the cost of an extended path, based on the last path fragment. Let $\Gamma_1 = \{s, x_1, x_2, \dots, x_{n-w}, \dots, x_n\}$ be a path from s to x_n with associated cost c_1 . The cost of the extended path $\Gamma_2 = \{s, x_1, x_2, \dots, x_{n-w}, \dots, x_n, x_{n+1}\}$ can be evaluated by means of a function that considers the cost until x_n (corresponding to c_1), and the path fragment

$x_{n-w}, \dots, x_n, x_{n+1}$, where $w+1$ is the number of nodes in the fragment. In the original formulation of the Dijkstra algorithm this is computed by adding to c_1 the cost of the edge from x_n to x_{n+1} . Instead, we propose to evaluate properties of a fragment including w nodes (more than one). Therefore, this fragment can be evaluated by a path classifier trained on a fixed number of elements.

Amongst the possible features to describe such a path-fragment, we propose the density profile as the ordered density values of the nodes in the fragment.

This opens the possibility to integrate existing knowledge in a supervised learning approach to prefer certain paths with respect to others by training a path classifier providing examples of admissible and non-admissible paths.

Reconstruction of heterogeneous synthetic shapes

To benchmark the proposed algorithm we benefit from the availability of the ClustEval platform [268] which provides synthetic datasets specifically designed to challenge clustering algorithms, together with an evaluation methodology. Amongst these datasets, we report the comparison with respect to other common methods on an example categorized as difficult, which visually contains heterogeneous structures (i.e. two globular-like clusters, surrounded by one thin-elongated cluster) (Figure 5.2, A). Our method achieves comparable performances to state of the art algorithms when the generic minimax path cost function is used (Figure 5.2, A, B - orange columns).

However, our method outperforms the other algorithms when trained with examples of valid and invalid paths (Figure 5.2, A, B - blue columns). In this example, 25 fragments of good and 25 fragments of bad paths composed by 5 points respectively (Figure 5.2, C), were automatically generated from the ground truth and were described using the density of points as feature vector (Figure 5.2, D). In comparison to CDP, our method allowed to correctly cluster the outermost elongated structure while still keeping separate the two central globular clusters. We provide two scripts to train the algorithm. In *demo_trainable.m* (Supplementary data file 2) we provide the code for training the algorithm from an available (but not necessarily complete) ground truth. In *demo_interactive.m* instead, a GUI allows a user to visually inspect the dataset and annotate valid/invalid paths. A video showing an example of interactive training is provided in Supplementary video 1. Quantitative results on the remaining datasets included in ClustEval are provided in (Figure 5.8, A). Amongst these, in (Figure 5.8, B) we zoom in another challenging dataset where the trainable version of the algorithm allowed to cluster heterogeneous groups. A performance degradation assay with respect to the number of training paths and the length of the path fragments is provided in (Figure 5.9).

Robustness to density peak detection. Results of the proposed algorithm depend on the initial identification of density peaks. Figure 5.3 includes a performance assay, evaluating the F1-score of the proposed method with respect to an artificial perturbation on the position of density peaks (Figure 5.3, A). On the example *04_fu_flame* from ClustEval [268], the proposed method tolerates perturbations up to the 30% of the dataset size, without decrease in performance (Figure 5.3, B). Above this level, the algorithm exhibited a variable and generally decreasing behavior which was dependent on the position of the peaks with respect to the conformation of the dataset. More precisely, when two seeds were

randomly assigned to points in the same cluster, an undesired partition was introduced, lowering the performances. Perturbations keeping seeds in two separated clusters are better tolerated (Figure 5.3, C).

The identification of density peaks depends on the setting of the threshold parameters τ_ρ and τ_δ . These two parameters can be set to select only the outliers of a density-distance plot, see [225], (Figure 5.3, D). Variations from the optimal values that do not select additional points as density peaks keep the maximum achievable performance. Variations that include additional points, result in the identification of an increased number of clusters, lowering the performance with respect to the ground truth labels (Figure 5.3, E).

Noise handling. The proposed method can identify points which are suitable to be considered as noise, by analyzing the path connecting them to a cluster. This can be achieved, for instance by introducing a cut-off threshold on the path-cost. When using a trainable path-cost function, examples of paths including noisy points can be used to penalize these connections. Automatic thresholding methods such as Otsu thresholding [203] can be used to set the cut-off distance. Considering that a density profile can be used as path-descriptor, this strategy is in line with the criterion of DBSCAN which considers as noise those points not density-reachable from a cluster.

A benchmark of the proposed method in the presence of background noise is reported in Figure 5.4. To this end, a synthetic probability distribution with 3 density peaks and a uniform background with different probability was generated (Figure 5.4, A). The proposed method exhibited average better results than CDP with a decreased slope of the F1-score with respect to the background noise level (Figure 5.4, B). With a low level of background noise, both a minimax path-cost function and a trained path-cost function achieved similar performances (Figure 5.4, C-E). For higher levels of noise, a path-cost function trained to associate high cost to paths including noise (Figure 5.4, F-H) yielded to an improved recognition of background.

Application on biomedical data

Segmentation of immune cells in confocal microscopy. Microscopy images are considered challenging spatiotemporal biomedical datasets [253, 166]. This is particularly relevant for images of immune cells which exhibit high plasticity, both globular and non-globular shapes, possibly in contact [212, 24]. Considering segmentation as a grouping task, the aforementioned properties represent

challenges for clustering algorithms (i.e. heterogeneous shapes in close proximity). Moreover, they remain challenging for state-of-the-art bioimaging software which requires manual correction of results, lowers usability [40] and compromising reproducibility.

Here, we apply our clustering algorithm for grouping pixels. We assume that other image processing tasks such as background-removal have been already executed with specific software such as Ilastik [236], Trainable Weka Segmentation [14] or Imaris (Bitplane). Qualitative results are presented in (Figure 5.5). Similarly to the example of (Figure 5.1), in (Figure 5.5, A) the local association rule of CDP yields to the wrong association of a thin dendrite (i) but correctly separates touching cells (ii). In (Figure 5.5, B) DBSCAN correctly reconstructs the shape of dendritic cells but does not separate touching cells. In (Figure 5.5, C) our algorithm, penalizing large gaps in the paths, connects the pixels to the correct density peaks in both the cases.

In this example, training the algorithm does not increase performances significantly. In fact, these are limited because more than necessary density peaks are identified as starting points. As a consequence, some cells are split into multiple parts. To merge these sub-clusters, a different metric can be used for computing the δ measure for each peak. Alternatively, methods for merging multiple clusters such as [170] can be applied for post-processing.

Identification of different heart rhythms. Long-term electrocardiographic (ECG) records are widely used to capture the dynamic behavior of the heart, which may change over time and exhibit different rhythms. Here, we applied clustering analysis to automatically identify different rhythms in a complex ECG record showing various types of arrhythmia [91]. Arrhythmia affects the distance between heartbeats (Figure 5.6, A). To this end, we described each heartbeat with two parameters corresponding to the distance (in seconds) from the previous (RR1) and the next (RR2) heartbeat. These two parameters are similar in sinus rhythms (Figure 5.6, B) and vary linearly according to the heart rate. However, in the presence of extra-systoles these may change. Indeed, extra-systoles are beats which stay closer to the previous beat and are possibly followed by a long pause. There are two main types of extra-systoles: atrial and ventricular. The second has an increased alteration of the distances. Life-threatening arrhythmias such as ventricular tachycardia and flutter, result in extremely short distances between beats (Figure 5.6, C-D), compromising the pump function of the heart. In results presented in (Figure 5.6, E), our algorithm identified 6 different rhythms. Similarly to the ground truth (manually annotated by a group of cardiologists),

our algorithm identified groups corresponding to ventricular flutter (brown), isolated ventricular extra-systoles (red), isolated atrial extra-systoles (orange) and right bundle branch block (blue). By contrast, the algorithm identified two different subtypes (instead of one) of sinus beats, one associated with lower heart rate (gold) and one associated with higher heart rate (green).

With respect to CDP, our algorithm removed an unrealistic boundary that was cutting a piece of the ventricular extra-systole cluster (red). In CDP, these beats were joined by mistake to the normal beats (green), while in our algorithm they are correctly joined with the ventricular extrasystole group (red).

The trained version further allowed to find a group of mixed atrial-ventricular extra-systoles which were associated by mistake to the normal beats by the untrained version.

Discussion

The proposed method inherits the advantages of density-based clustering methods but, using a global association rule, is able to overcome the limitations of local connectivity rules. This is in line with the work by Tenenbaum *et al.* [242], which uses global optimization (i.e. shortest path computation) to represent the global structure of a dataset in a lower dimensional coordinate system. Indeed, clustering can be interpreted as a special case of dimensionality reduction, where points are represented by a single discrete coordinate corresponding to the assigned label.

The application of the proposed method requires the initial detection of density peaks as described in [225]. Despite this step may hamper the application to datasets where density-peaks do not exist, CDP demonstrated broad applicability to challenging datasets [268] where density peaks become easily identifiable as outliers, with high density and high distance, in a density-distance plot. Outliers of the density-distance plot can be selected as points above two thresholds τ_ρ and τ_δ . These thresholds can be set either manually by inspecting the density-distance plot, or automatically (i.e. via Otsu thresholding [203]), or to meaningful values for applications where the expected cluster size and density are known. Alternatively, points can be ranked according to a score and the top N points selected as density-peaks (N = number of desired clusters). Additionally, a combined approach based on thresholding and ranking can be adopted. There might be cases in which density peaks are not obvious to identify. This can happen in the presence of clusters composed of multiple sub-clusters. Peaks of these sub-clusters may arise in the density-distance plot. In this case, a hierar-

chical approach is suggested.

Recently, Du *et al.* [63] proposed an approach that facilitates the identification of density peaks using the graph-distance to compute δ . Indeed, two points in the same cluster are more likely to be connected by a path with low cost. Density peaks which are in distinct clusters instead are more likely to be connected by a path with high cost. Hence, the graph-distance of density peaks is likely to be higher than the graph-distance of arbitrary non-peaks points in the same cluster, resulting in higher values of δ for density peaks.

The proposed method generalizes to high dimensional dataset if they can be represented as a graph and a point-density can be estimated. Common methods to estimate point-density rely on Euclidean distance to define a neighborhood. However, Euclidean distance loses significance with increasing number of variables [4]. Hence, it should be computed only in a sufficiently restricted neighborhood. Figure 5.10 reports a benchmark on synthetically generated datasets including multidimensional distributions using Euclidean-distance as metric to build the graph. The proposed algorithm exhibits comparable performances to CDP.

Arbitrary non-negative metrics for edge cost are supported by the proposed methods. Figure 5.11 reports an application on real high dimensional data from the bonemarrow leukemia dataset [268, 187]. Such a dataset includes the gene expression level of 999 genes from 38 samples of patients with three different types of leukemia. The proposed method correctly identified three groups with comparable performances to CDP. In this case the graph was built with an edge cost derived from the Spearman correlation.

Alternatively, graph-pruning can be used together with a cumulative Euclidean path-cost function to limit the connectivity of each node within a restricted neighborhood.

Methods for dimensionality reduction can further be used for data pre-processing. Amongst these, global and non-linear approaches, such as Isomap [242], are preferable with respect to PCA for highly non-convex datasets.

The proposed path-based formulation supports the expression of a path-cost by evaluating path-properties. A non-decreasing path-cost function allows solving the proposed clustering problem using the Dijkstra Single Source Shortest Path algorithm. Amongst the possible path-cost functions, minimax penalizes paths with large gaps which is a generically desired property. Other non-linear functions can be designed for specific tasks..

Dijkstra's SSSP algorithm exhibits a lower than quadratic computational complexity which can be reduced for sparse graphs. Moreover, it does not require to store the adjacency matrix on memory and can be speeded up by adopting heuristics for optimal path-finding or graph partitioning techniques. Therefore, we consider this method suitable to be adapted and optimized for specific applications.

Lastly, existing knowledge can be integrated by defining an appropriate path-cost function which can be obtained, for instance, by training a path classifier with examples provided by humans or available ground truths. Therefore, it represents an intermediate method between machine and human computation for tasks that would benefit from a collaborative effort [37, 121].

Data generation

For data shown in Figure 5.5, immunofluorescence confocal microscopy was performed using a Leica TCS SP5 microscope, with sequential acquisition to limit signal cross-talking. A murine trachea was collected and fixed in 4% paraformaldehyde at 4°C for 1 h. Tracheas were cut in two halves along the long axis. Pieces were placed on a microscopy slide and embedded in Fluoromount[®] Aqueous Mounting Medium (Sigma Aldrich). 3D images were acquired using a HCX PL APO CS 20X/0.7 oil immersion objective, z-step was 1 μm for a total depth ranging from 50 μm to 112 μm . The bioimaging software Bitplane Imaris (v 9.2.1) was used for computing the 2D maximum intensity projections (MIP) and for manual cell segmentation. The same software (Coloc functionality) has been used to exclude the background and creating a channel containing only the points belonging to Cd11c-GFP+ cells. This dataset along with the ground truth is provided in (Supplementary data file 1) using the same format described in [268]. The dataset presented in (Figure 5.1) is also provided in (Supplementary data file 1).

Implementation

The proposed algorithm was implemented in Matlab r2017b. A demo for both the generic (minimax) and trainable algorithms are provided respectively in *demo_generic.m* and *demo_trainable.m* in (Supplementary data file 2). Moreover, an interactive example where the user can visually draw examples of valid paths and invalid paths on a 2d dataset is provided in *demo_interactive.m* and in (Supplementary Video 1).

The Dijkstra SSSP Algorithm, which is at the core of the proposed method, was implemented using vectorization and outperforming the *graphshortestpath()* routine distributed with the Bioinformatics toolbox of Matlab r2017b.

The following libraries have been used:

- DensityClust.m - Implementation of the CDP clustering algorithm
fileexchange/53922-densityclust
- dbscan.m - Implementation of the DBSCAN clustering algorithm
<https://www.peterkovesi.com/matlabfns/Misc/dbscan.m>
- FitCSVM - Implementation of a Supported Vector Machine classifier
Matlab bioinformatics Toolbox

Path classifier

In the example provided in (Figure 5.2, C-E) a Support Vector Machine with RBF Kernel was trained on 25 desired paths and 25 non-desired path fragments. Results can be reproduced and training data can be generated using the Matlab script *demo_trainable.m* provided in (Supplementary data file 2).

Evaluation

For the quantitative benchmarking of the proposed method with respect to the ground truth, the F1-score and the Jaccard Index (J) were computed according with [268]. These were defined as follows. $F1 = 2*(Recall*Precision)/(Recall+Precision)$. $J = TP/(TP + FN + FP)$, where TP are the True Positives, FN the False Negatives, FP the False Positives and TN the True Negatives. $Recall = (TP)/(TP + FN)$, $Precision = TP/(TP + FP)$.

Supplementary proof 1 - unique cluster assignation

We want to demonstrate that only a single density peak is included in the shortest path from the dummy node s to a generic point x . Let \mathbb{G} be the set of all the possible paths on the graph provided in (Figure 5.7), where a starting node s is connected only to a set of nodes P , namely "density peaks", with a negligible cost $\epsilon \in \mathbb{R}_+$, $\epsilon \rightarrow 0$. Now, let us assume the existence of a shortest-path $\Gamma = \{s, P_1, a, P_2, b, x\}$ from s to x such that two density peaks P_1 and P_2 are included. We encounter a contradiction since the cost of the sub-path $\{s, P_1, a, P_2\}$ is always greater than the cost of directly connecting $\{s, P_2\}$.

Therefore, Γ is not a shortest path.

This proof is valid under the assumption that the cost of a generic path $\Gamma \in \mathbb{G}$ is

evaluated by means of a non-decreasing function $\xi : \mathbb{G} \rightarrow \mathbb{R}$, $c = \xi(\Gamma)$, $\xi(\Gamma_1) \leq \xi(\{\Gamma_1, \Gamma_2\}) \quad \forall \Gamma_2 \in \mathbb{G}$.

Figures

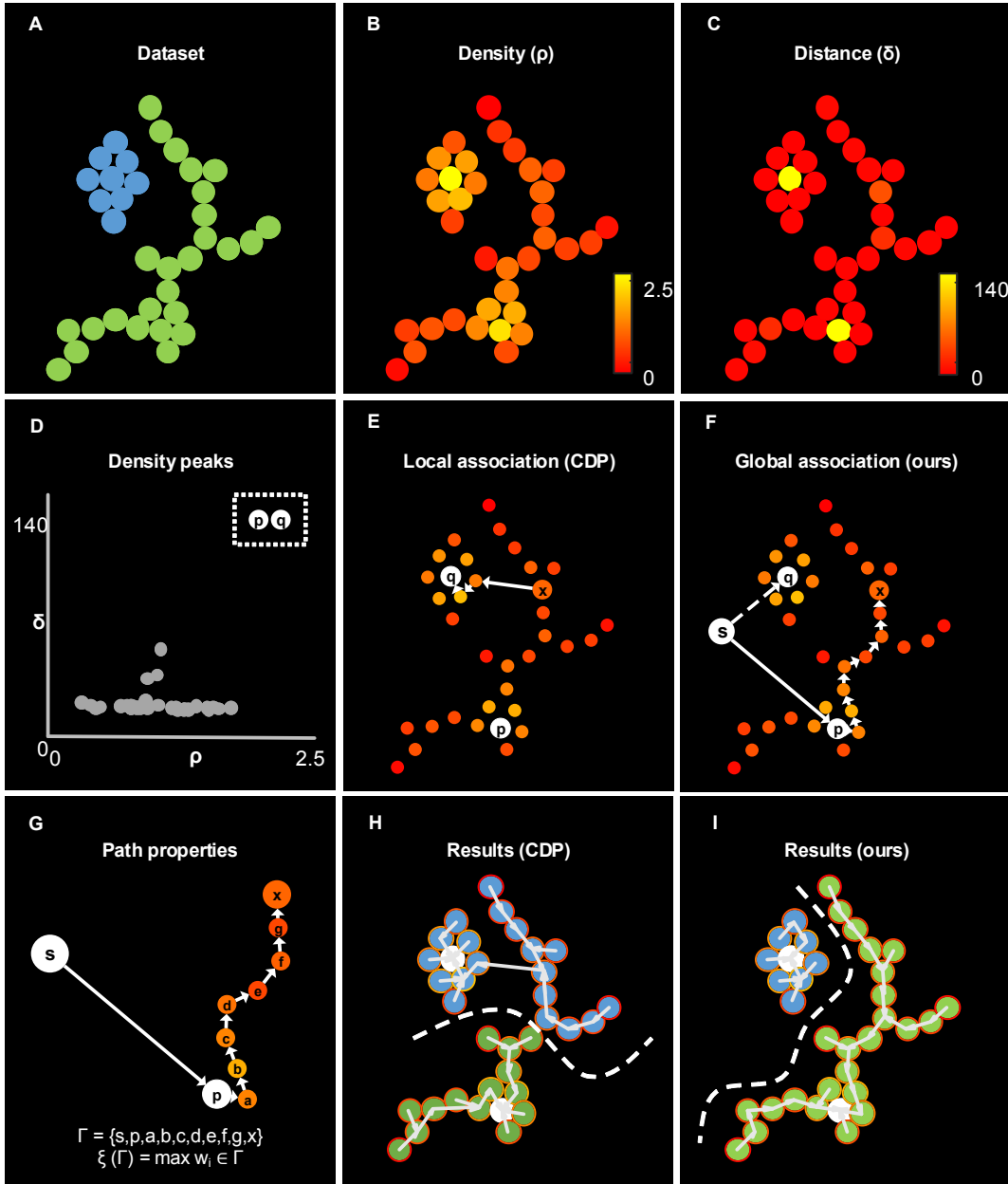


Figure 5.1. Association rules on a simplified example. **A.** Raw data-points in a 2d space. **B.** Color-coded point density (ρ). **C.** Color-coded distance to the closest point with a higher density (δ). **D.** Density-distance plot for selecting density peaks (dashed box), characterized as outliers with sufficiently high density and distance. In this case, the density peaks correspond to the points p, q in E-F. **E.** Local association rule of CDP connecting a point x , to the closest point with higher density, until this is a density peak. This happens regardless of the other connections. **F.** Global association rule of the proposed method, which computes the optimal path to connect a starting node s to a generic point x , passing by density peaks. **G.** The path from S , via p , to x can be evaluated according to its properties, such as the maximum gap included. **H.** Color-coded results of CDP. **I.** Color-coded results of the proposed algorithm.

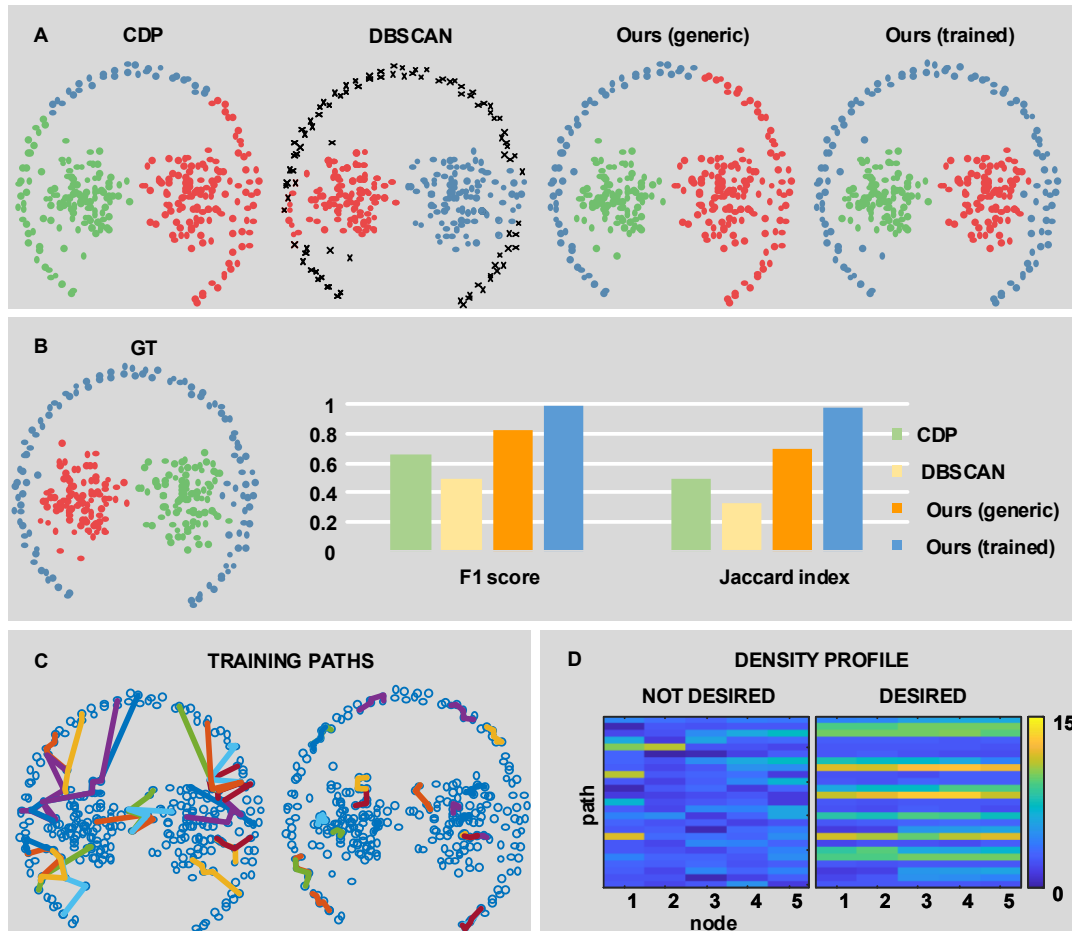


Figure 5.2. Evaluation on a synthetic dataset with heterogeneous structures. A-B. The performances of the proposed method are evaluated on the synthetic dataset *01_chang_pathbased* provided in ClustEval [268]. This includes groups with heterogeneous structures (i.e. a thin-elongated structure surrounding two globular-like structures). Our method, with a generic mini-max path cost function, partially improved the results produced by CDP and DBSCAN (A-B) with respect to the ground truth. By contrast, by training a path classifier, the algorithm achieved full performances with an F1 score ≥ 0.99 and a Jaccard index ≥ 0.98 . C. Training paths composed of 25 examples of desired paths and 25 examples of undesired paths. D. Path features corresponding to the density profile (vector including the density of the nodes in the path).

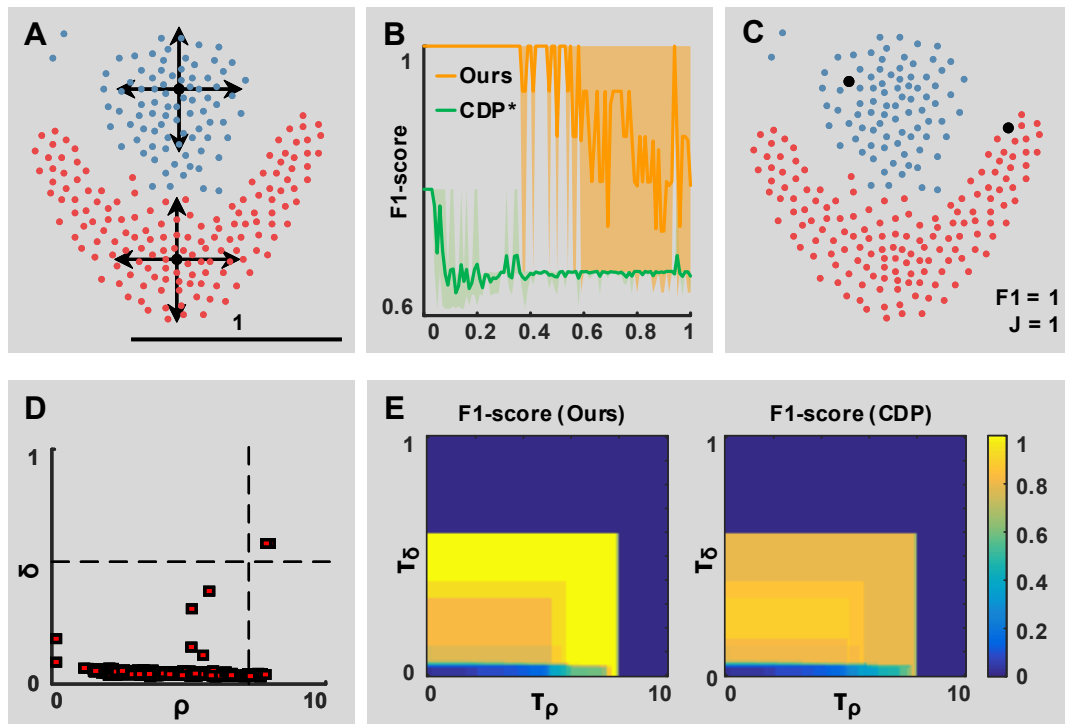


Figure 5.3. Robustness to density peak detection. **A.** Color coded ground truth including two clusters in close proximity (red and blue) from the synthetic dataset *04_fu_flame* provided in ClustEval. Points colored in black are the identified density peaks, which are used as seeds by the proposed algorithm. The position of seeds is perturbed by a displacement of max ± 1 (black line). **B.** Performance degradation with respect to the maximum perturbation. Results are obtained with $n = 5$ replicas with a random perturbation direction. CDP* refers to a modified version of CDP, forced to associate points to the perturbed seeds. **C.** Color coded results of the proposed method using the seeds colored in black. **D-F** Robustness to the setting of τ_ρ and τ_δ parameters. The optimal settings of the parameters (E) identifies two outliers of the δ - ρ graph. (E-F) Variations from the optimal settings include additional sub-clusters, lowering the performances of the algorithm.

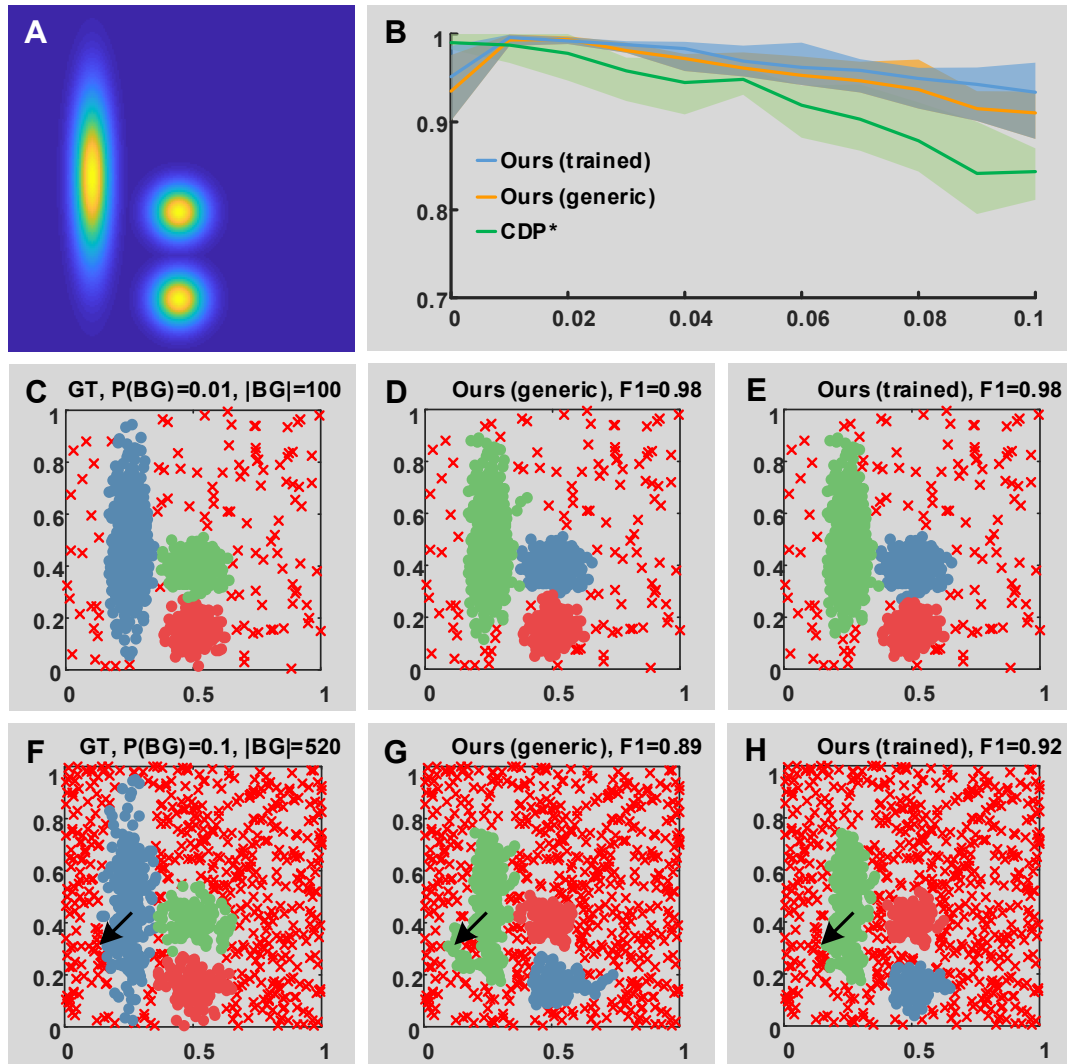


Figure 5.4. Robustness to background noise. **A.** Synthetic probability distribution from which point distributions are drawn. Lighter areas have the maximum probability. The area in blue is a background with uniform probability from 0 to 0.1, corresponding to a number of points from 10% to 52% of the total. **B.** Quantitative performance degradation assay with respect to the value of background probability. 1000 points are drawn from the probability distribution in (A), varying the background uniform probability from 0 to 0.1. For each level of background probability, $n = 5$ replicates are generated. Bold lines refer to the mean of the F1-score amongst the replicates, while the shaded lines correspond to the range. Three peaks were selected using γ ranking [225]. **C-E.** Qualitative results with a background probability of 0.01, corresponding to 900 points from the clusters and 100 points in the background. Cluster labels are color coded. Red x correspond to noise. **F-H.** Qualitative results with a background probability of 0.1, corresponding to 480 points from the true clusters and 520 points in the background. Arrows indicate an aggregation of points in the background. The trained algorithm detects those points as noise.

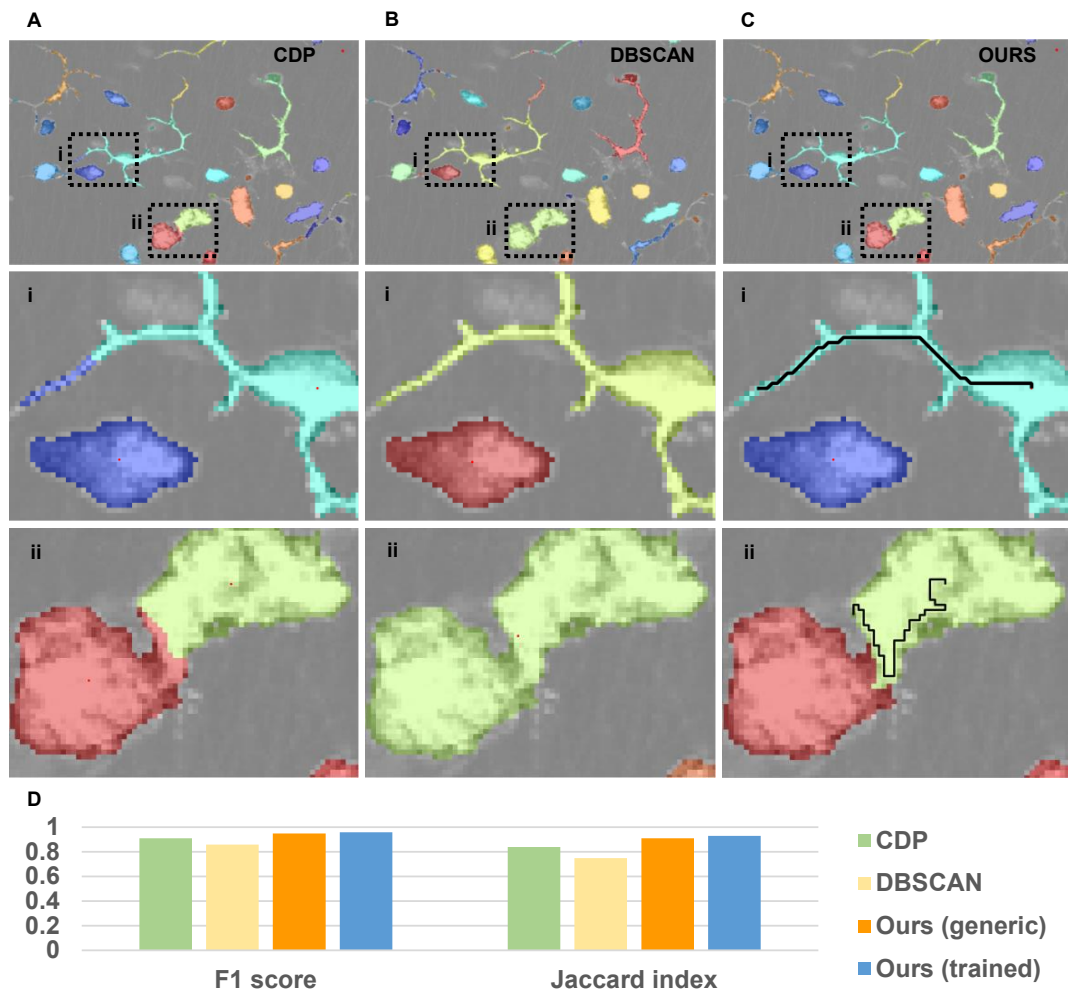


Figure 5.5. Application for segmentation of immune cells. A-C. Qualitative results (color-coded labels) produced by different density-based clustering algorithms for clustering pixels in space. Images show a confocal microscopy acquisition of murine immune cells, labeled with CD11c+ GFP. CDP (A) using a Euclidean metric correctly separates touching cells but associates a piece of dendrite to the wrong cell. DBSCAN (B) correctly reconstructs the shape of dendritic cells but is not able to separate touching cells with the same density-reachability criterion. The proposed method (C) correctly associates the dendrite of the dendritic cell and separates the touching cells. Black lines indicate the optimal path followed by the algorithm, from the cell centroid (density peak) to a point in the dendrite and in the touching region respectively. D. Quantitative performances. The F1 score and the Jaccard index are computed with respect to the ground truth. Here the trained version of the algorithm achieved similar performances to the generic version. These are bounded because of the separation of cells with increased size, into multiple sub-clusters.

Supplementary figures

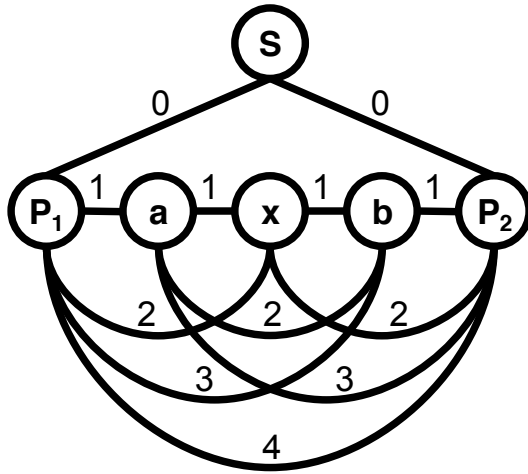


Figure 5.7. Graph structure. Each density peak P_i is connected to a dummy node s with a negligible cost ϵ . All the remaining points $\{a, b, \dots\}$ are connected on a graph that guarantees their reachability from s . Despite in this example we provide a fully connected graph, the proposed algorithm supports sparse/pruned graphs guaranteeing this condition. Additionally, the algorithm supports non-negative edge costs which can be derived from an arbitrary point-to-point distance (i.e. Euclidean distance)

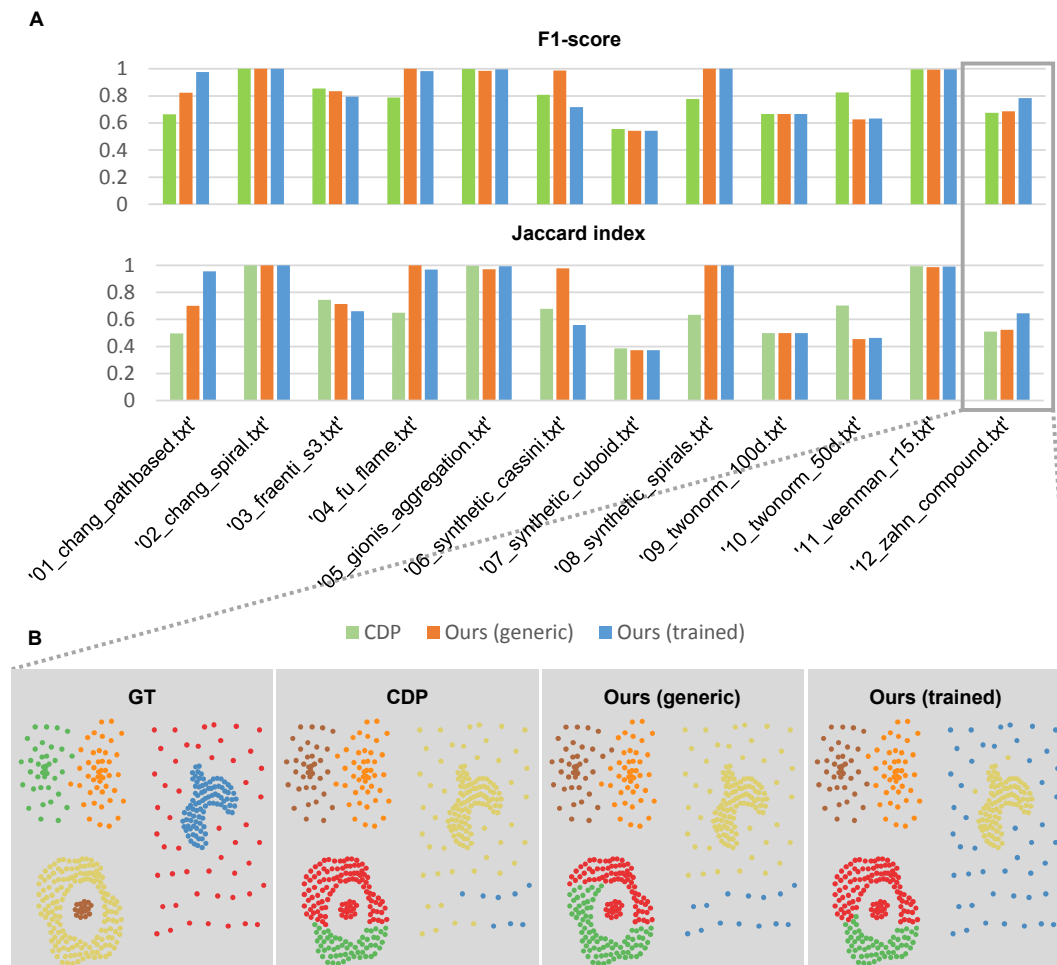


Figure 5.8. Full evaluation on the 12 synthetic datasets of ClustEval. **A.** Quantitative results. **B.** Qualitative results on `zahn_compound` dataset including heterogeneous shapes.

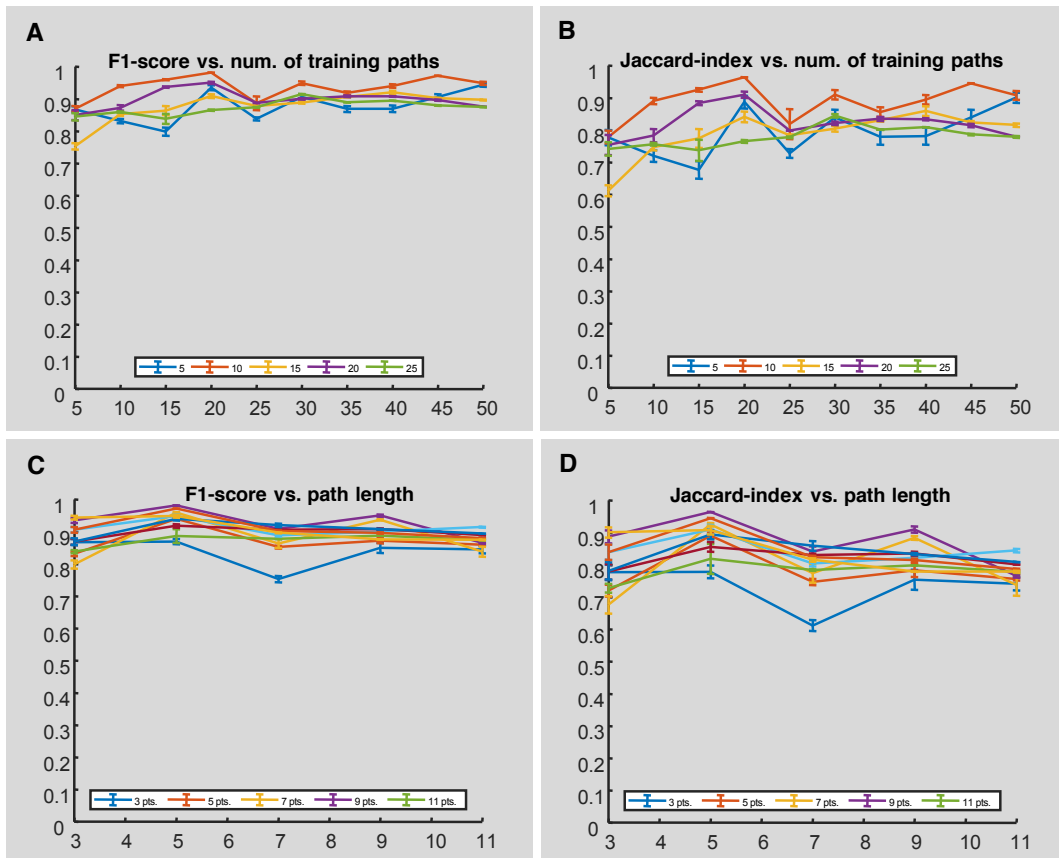


Figure 5.9. Performance degradation assay with respect to number of training paths. (A-B) and to the number of points in each fragment (path length) (C-D) on the dataset *01_chang_pathbased*. Mean and standard deviations using 5 different runs of the algorithms with the same parameters, but with random paths are provided.

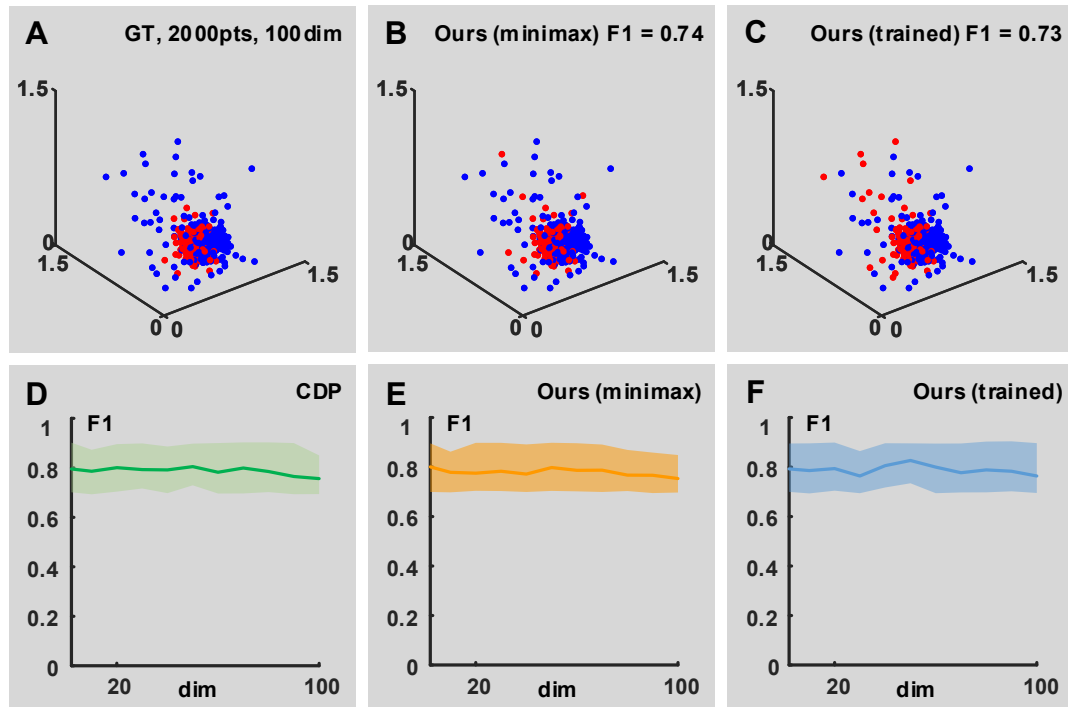


Figure 5.10. Benchmark on high dimensional synthetic datasets. (A-C) Results on a synthetic generated dataset of 2000 points and 100 dimensions with two clusters. Three dimensions are shown. (D-F) F1-score varying the dimensionality. For each dimension, 15 datasets with two clusters of different size and position were generated. Bold lines refer to the mean F1-score, the shaded areas the range of CDP (D), proposed method using a generic minimax path cost function (E), and the proposed method trained with random paths (F).

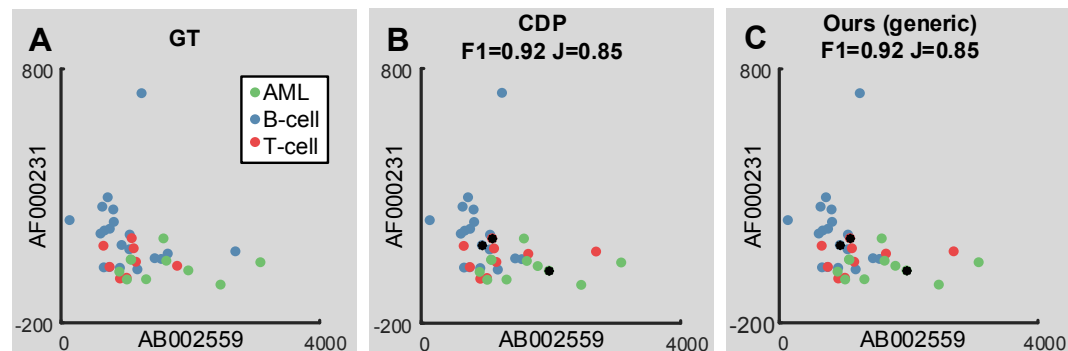


Figure 5.11. Results on the bonemarrow leukemia dataset. (A-C) The proposed method was evaluated on a high dimensional dataset containing the expression of 999 genes on 38 samples from patients with three different types of leukemia (AML - Acute Myeloid Leukemia, B and T cell leukemia). (A) Representation of two dimensions out of 999 with color coded points according with the Ground Truth (GT) provided in [268, 187]. (B,C) Quantitative and qualitative results of CDP and the proposed methods using a minimax path cost function. In this example edge-cost derived from the Spearman correlation is used.

5.2 An iterative, parallel and cache-friendly implementation of the Dijkstra shortest path algorithm on images

In this section, we propose an optimized implementation of the Dijkstra Single Source Shortest Path (SSSP) algorithm on images, which can be represented as a rectangular lattice.

Finding the shortest path from one node (source) to multiple other nodes on an image is a relevant task in computer vision. Focusing on biomedical applications, in the previous section we described how the usage of shortest paths from density peaks can improve the segmentation of non-convex cells in fluorescence microscopy images [212]. On light-microscopy images, Uhlman *et al.* developed a plugin for ImageJ (DiversePathJ) to identify the skeleton of worms, following the shortest path from the head to the tail of the worms [251]. Instead, Ghidoni and colleagues proposed the usage of the Dijkstra SSSP algorithm to compute a descriptor that was used for classifying textures in medical images [90].

While the Dijkstra SSSP algorithm can be computed on a generic graph with non-negative edge costs [61], images exhibit a regular structure that can be exploited to optimize computation.

Let $G(V, E, w)$ be a generic, fully connected, weighted graph with $|V|$ nodes and $|E|$ edges. The naive implementation of the Dijkstra algorithm has a computational complexity of $O(|V|^2)$. This is due to the task of finding the minimum in an unsorted array of size $|V|$, which has a complexity $O(|V|)$ and is repeated for all the nodes of the graph. By using queues such as min-heap or Fibonacci heaps, the computational complexity of the algorithm on a generic graph can be reduced to $O(|E| + |V| \log |V|)$.

However, this theoretical computational complexity does not count for data locality which has a huge impact on the time required for accessing memory.

Indeed, the Dijkstra SSSP algorithm successively selects a node to explore, as the node that is reached with the minimum cost and is not explored yet.

This rule can introduce jumping from one node to another arbitrary node. Considering the storage of the graph as an array on memory, this can introduce frequent cache-miss. Moreover, parallel implementations of the algorithm that assign partitions of the graph to different cores might require communication to handle these jumps or more advanced strategies as reviewed in [235].

Heuristics such as A* and the Jump Point Search [105] allowed to speed-up the computation by one order of magnitude on generic graphs and two orders of magnitude on regular grids, by avoiding to explore unnecessary nodes.

Similarly, we propose an efficient implementation of the Dijkstra SSSP algorithm on for rectangular lattices, based on the intuition that a target node t can be reached from a source node s only by crossing horizontal and vertical edges. Therefore, we evaluated the possibility of computing shortest paths, by evaluating independently orthogonal directions and by iteratively updating the results.

The proposed strategy brings two advantages. Firstly, from a memory access point of view, it accesses nodes sequentially, which is more cache-friendly strategy than accessing elements randomly. This is relevant when implementing the algorithm as the edge cost of rectangular lattices with $H \times W$ nodes can be stored on memory on two 2D matrices of size $(H-1, W)$ for vertical edges, and size $(H, W-1)$ for horizontal edges.

Secondly, at each step, different columns can be assigned to different processors without any need for communication. Once all the columns have been updated, results will be updated along the rows, in the next step. This only requires to wait until all the columns have been processed before starting the propagation along the rows.

Description of the algorithm. Based on the intuition that a path includes only vertical and horizontal edges, the algorithm computes the shortest path between one source and all the other nodes on an image with fewer instructions.

Let us define the following variables

- H = height of the lattice
- W = width of the lattice
- s_i, s_j = coordinates of the start node in the lattice ($1 \leq s_i \leq H, 1 \leq s_j \leq W$)
- S = index of the start node = $(s_j-1) \cdot H + s_i$
- $BED[i,j]$: best distance to reach the node at coordinates (i,j) , initialized to $+\infty$
- $PRED[i,j]$: predecessor of the node at coordinates (i,j) , initialized to null
- $UPD[i,j]$: matrix to keep node of which nodes have been updated. initialized to false.

The algorithm starts by updating the best distance of the starting node, $BED[S] = 0$ and the predecessor of S , $PRED[S] = S$.

Now the iterative approach starts, doing at each iteration, for each column

- Select the nodes $U[]$ whose best distance has been updated in the previous

iteration.

- For each nodes u in $U[]$
- Compute the cost to reach any node x in the same column of u as $c[x] = \text{BED}[u] + w_{uv} + \dots + w_{wx}$, which is the sum of the adjacent edges from u up to x (x above u , in the column), or the sum of the edges from u down to x (x below u , in the column).
- If $c[x] < \text{BED}[x]$
 - $\text{BED}[x] = c[x]$
 - $\text{PRED}[x] = x + 1$ (x above u), or $\text{PRED}[x] = x - 1$ (x below u).
 - $\text{UPD}[x] = \text{true}$
- Transpose the BED, PRED, and UPD matrices.

The algorithm stops when any update is done.

Computational complexity In each column, the algorithm resembles the original Dijkstra algorithm, checking whether a node can be reached with less cost. For simplicity, let us consider a square lattice of size $N \times N$. A column has \sqrt{N} nodes. Executing the naive implementation of the Dijkstra SSSP algorithm on a single column would lead to a cost of $O(\sqrt{N}^2) = O(N)$. This is repeated for all the columns, K iterations (Figure 5.12). Therefore, the total computational complexity of the method is $O(n\sqrt{n}K)$.

(Figure 5.12) reports the comparison of the proposed method with the classical implementation Dijkstra algorithm, showing the different ways in which costs are updated.

Application on 2D images. Similarly to a regular grid, we consider a 2D image to be a graph with limited and fixed connectivity. More precisely, each pixel is connected to the four pixels which are closer in space (up, down, right, left). By contrast to a regular grid, the cost of each edge depends on the brightness difference between two pixels.

Let us define an image as a matrix $I \in \mathbb{R}^N \times N$. The cost of the edge connecting each pixel to its superior/inferior and left/right neighbor can be efficiently computed by optimized instructions for finite differencing, such as *diff* in Matlab. This yields to the creation of two matrices including the gradient components along orthogonal axes, thus the edge costs.

In (Figure 5.15, C-D) we report the algorithm executed on two example images containing visual structures such as a text, and a flat logo. The algorithm exhibited a faster convergence as the shortest path in large areas with uniform color can be identified with two iterations.

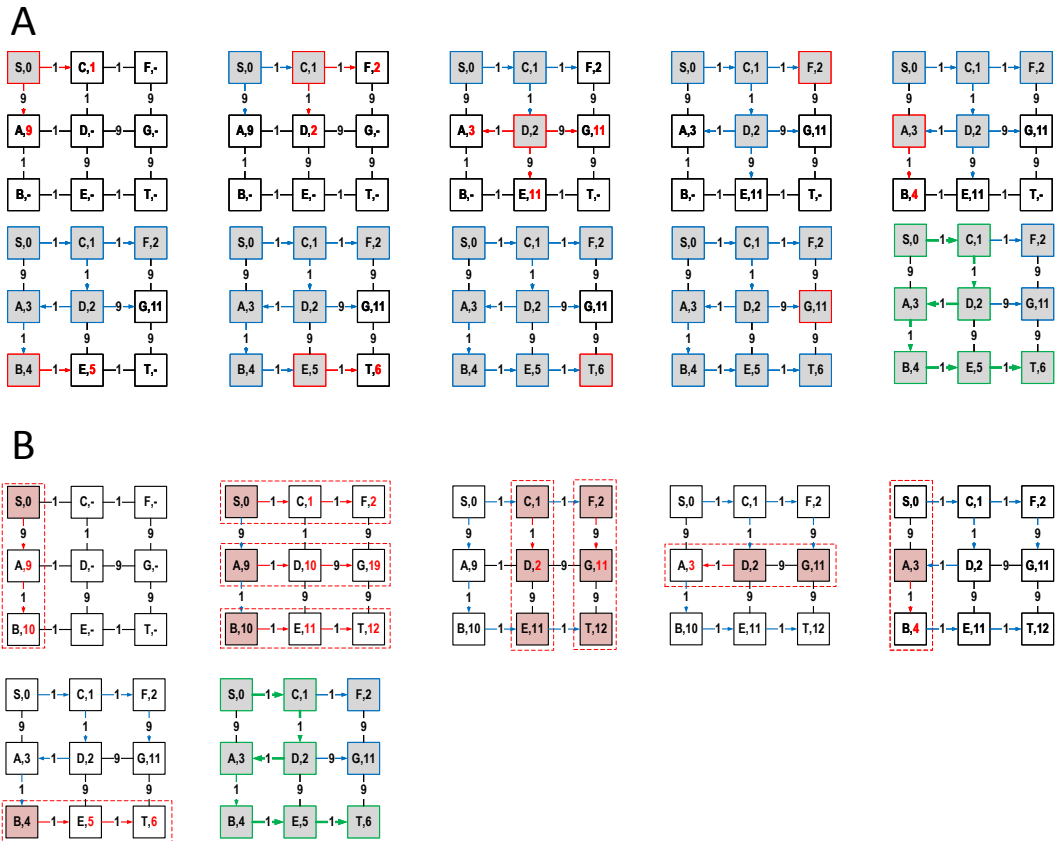


Figure 5.12. Iterative implementation of the Dijkstra algorithm

A. The classical algorithm selects the node reached with minimum cost and not yet selected. Then it updates the distance of the nodes connected to this node. B. Each column is processed independently, then the process is repeated on the rows and then on the columns.

Number of iterations. The number of iterations K vary according to the starting node and the graph. However, after a sufficient number of iterations, the algorithm finds shortest paths with the same cost of the original version, which coincide if unique shortest paths exist (Figure 5.15, A).

Empirically, we found that the number of iterations depend on the number of turns that a path includes. $K = 1$ when a shortest-path in the solution is straight (i.e. does not include edges from different columns or rows). When an edge crossing two adjacent columns (or rows) is included, K increases at least by 1. Empirically, on graphs with random edge cost (Figure 5.15, A-B, E), K was proportional, but less, than \sqrt{N} . On graphs derived from images containing structures and areas with uniform intensity, the algorithm converged with less iterations (Figure 5.15, C-D). Therefore, the time required for running the algorithm is variable. However, parallel turning points are computed in parallel. Moreover,

K can be set to a maximum number of iterations. Indeed, the algorithm retains anytime properties. After the first two iterations (required to initialize the path-cost to all the nodes), at each iteration, the algorithm always computes a better solution and can be stopped at any time to obtain a sub-optimal solution. Convergence to the optimal solution is reached as demonstrated in Proof 1.

Parallelism and benchmarking. At each iteration, the proposed algorithm processes columns independently. When an iteration is completed, the algorithm reads the transposed matrix of edge costs. This can be computed before starting the algorithm, without the need for transposing at each iteration.

During an iteration, there is no need for communication between processes since each column reads and updates the values of the nodes (and edges) in the same column only. Therefore, parallelism is maximized inside each iteration. By contrast, each iteration has to wait until all the columns are processed. We benchmark the algorithm with respect to the classical implementation of the Dijkstra SSSP algorithm, showing a significant speedup both when processing columns sequentially (Figure 5.13, A - blue line) or gaining an additional 3.5x speedup for sufficiently large graphs by assigning different columns to different cores (Figure 5.13, A-B, green line).

Cache-friendly. Let us assume that a matrix with a sufficiently high number of elements is organized on the main memory column-wise (Matlab/FORTRAN notation) on a system that uses a set-associative cache. When an element at position i, j is accessed, the elements at position $i \dots i + \text{CL}$ are loaded into the cache where CL is the size of cache line. Therefore, accessing those data will be much faster than accessing a random element of the matrix not in the cache.

As a consequence, successively accessing elements in columns on the matrix results in increased cache-hit than accessing elements row-wise or randomly.

Proof of correctness. In this proof, we demonstrate that the path computed by the algorithm is the shortest path.

Let us define a lattice $\mathbb{L}_4 \in \mathbb{G}(V, E, w)$ as a graph with limited connectivity, in which an arbitrary node $a \in V$ is connected to each of its upper, lower, left and right neighbors b with an edge $(a, b) \in E$ having a non-negative cost $w_{a,b} \in \mathbb{R}_+$. An arbitrary path $\Gamma(s, t) \in \mathbb{L}_4$ is an ordered sequence of nodes connecting s to t $\Gamma = \{s, a, b, \dots, t\}$.

The cost of a path can be evaluated by means of a path-cost function $\xi : \mathbb{G} \rightarrow$

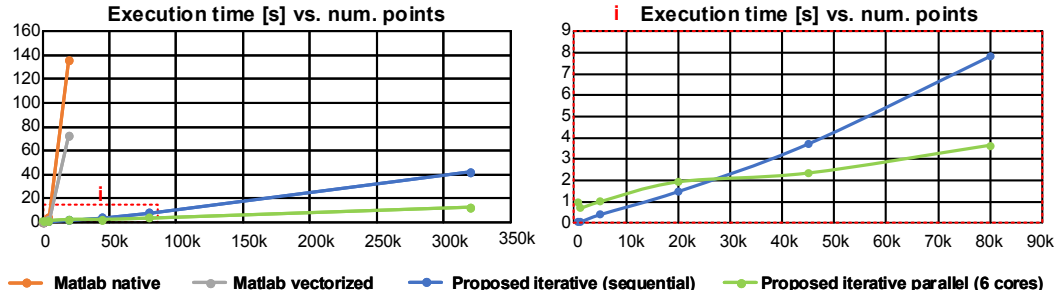


Figure 5.13. Benchmarking the iterative and parallel implementation of the Dijkstra algorithm A. Comparison of the proposed iterative method (blue: sequential, yellow: parallel) w.r.t. the classical implementation of the Dijkstra algorithm provided by the Matlab Bioinformatics toolbox (r2017b) and an optimized implementation [213] using SIMD instructions. The proposed implementation allowed to tract image sizes that were poorly tractable by the classical implementation. **B.** Comparison of the proposed iterative methods on a machine with 6 cores (Intel Xeon E5-1650 v3), processing columns in sequential order (blue line) or in parallel by 6 threads (orange line). The parallel method achieves a 3.5x speedup when a sufficiently large graph is used.

$$\mathbb{R}_+, \quad \xi(\Gamma) = c.$$

For this proof, let us consider the following path-cost functions $\xi(\Gamma) = \sum_{(i,j) \in \Gamma} w_{i,j}$. However, the following demonstrations are valid for every non-decreasing path-cost function, as described in the previous section.

Lemma 1. *Every sub-path of a shortest path is a shortest path.*

Let us define a shortest path as $\Gamma^* = \{s, \dots, a, \dots, b, \dots, t\}$ and assume ab absurbum that there exists another sub-path between the intermediate nodes $I(a, b)$, which is more convenient. If such a path existed, $\Gamma^*(s, t)$ would not be shortest. More formally, let $\Gamma^*(s, t)$ be the shortest path from a node s to a node t and let $\Gamma(s, t)$ be an arbitrary path between the same nodes.

Since Γ^* is optimal, $\xi(\Gamma^*) \leq \xi(\Gamma) \quad \forall \Gamma \neq \Gamma^*$.

Let I^* be a sub-path of $\Gamma^* = \{s, a, I^*, b, t\}$ and let us assume that exists a sub-path $I \neq I^*$ such that $\xi(I) < \xi(I^*)$.

Considering that the cost of an arbitrary path Γ can be decomposed as

$$\xi(\Gamma) = w_{sa} + \xi(I) + w_{bt} = \xi(I) + K \quad \text{where } K \geq 0,$$

derives that $\xi(\Gamma^*) = \min \xi(\Gamma) = \min(\xi(I) + K) = \min(\xi(I)) = \xi(I^*)$. Hence, I is a shortest path.

Corollary 1. *Sub-paths of a shortest path including only vertical and horizontal edges are shortest-path*

Let us consider the sub-paths of $\Gamma^*(s, t)$ that include only vertical or only hori-

zontal edges. Each of these paths is a sub-path of a shortest path, therefore it is a shortest path.

Hence, every shortest path on L_4 can be decomposed into vertical and horizontal sub-paths, which are shortest-paths.

Lemma 2. *At iteration K , the algorithm finds the shortest paths containing at maximum $K-1$ turns.* Let us consider an iteration as composed by both the propagation of path-costs in the vertical and in the horizontal directions. We refer to the vertical and horizontal steps of the k -th iteration as "kv" or "kh".

Let us also consider a starting node A and a target node T .

The algorithm starts by assigning a path-cost to $A = 0$. This means that if the target node $T = A$, the algorithm already identified the solution at the first step. Since edge costs are non-negative, and path-cost functions non-decreasing, an other path would have a greater cost. Hence, all the shortest-paths with 0 edges will be identified at this step.

By contrast, any other target node $T \neq A$, would require additional iterations as the algorithm does not know yet the path nor the cost to reach the remaining nodes (Figure 5.14, dashed lines).

At the end of iteration 1v, the algorithm computes the path-cost of the nodes in the same column of A , by summing the edge weights from A . This means that if a target node T is connected to A by means of a shortest-path including only vertical edges (T in the same column of A), such a path is found at iteration 1v. Similarly, at iteration 1h, the algorithm finds shortest paths from A to a target node T on the same row of A . This means that all the straight shortest-paths (with < 1 turns) will be identified at the completion of iteration 1.

Additionally, at iteration 1h the algorithm identifies L-shaped paths, which are formed by a vertical sub-path (in the same column of A) and a horizontal sub-path (in the same row of the target node). If these paths are optimal, they will not change at later iterations as their associated cost will be minimum.

At iteration 2v, the algorithm compares if an arbitrary node, is reached with a lower cost following a vertical edge from a neighbor. Hence, it compares if the solution found at iteration 1h can be improved by substituting a horizontal edge, with a vertical edge, potentially introducing a turn. This means that the algorithm finds at the end of iteration 2, all the paths with < 2 turns.

By induction, at the end of each iteration, the algorithm can potentially substitute a vertical edge with a horizontal edge, introducing a turn if this provides a better solution. Hence it finds shortest paths with $K-1$ turns at the completion of iteration K .

This process is represented in Figure 5.14

Proof. *The algorithm finds the optimal combination of shortest sub-paths.* Although a shortest-path can be decomposed in a sequence of shortest sub-paths including only vertical and horizontal edges (from now on, vertical and horizontal components), it remains to be demonstrated that the algorithm finds the optimal combination of these components.

Let us start demonstrating the correctness of the algorithm on a simplified lattice with 4 nodes where the shortest path from A to D has to be found (Figure). Let us assume that the path A,B,D is the optimal one. At the first iteration, the algorithm finds that B is reached with a better distance, from A. At the second iteration, the algorithm finds that C is reached with a better distance from A, and D is reached with a better distance from B. At the third iteration, the algorithm finds that D is already reached with the best distance, as it could be reached from C with a worse distance. Focusing on the comparisons that the algorithm does, to reach the point D the algorithm compares the paths ACD and ABD, excluding ACD, which is the only other possible alternative.

On a lattice with an arbitrary number of nodes, a point P can be reached only by 4 neighbors (L,M,N,O). Considering that these four neighbors can be connected to the starting node with four paths (w,x,y,z), the algorithm compares at each iteration, the costs of the paths wLP, xMP, yNP, zOP. Hence, if the cost of a neighbor was improved in the previous iteration, the predecessor of P will be updated. For the Lemma 2, the cost of the predecessor is updated at iteration K-1, if and only if, a shortest-path with K-2 turns connects the predecessor to the starting node. Hence, after a sufficient number of iterations, the algorithm finds the shortest path and converges when the shortest path with the maximum numbers of turns have been identified.

Conclusion and discussion. The proposed algorithm allows computing the shortest path on images in $O(n\sqrt{n}K)$ maximizing the sequential access to data and bringing a significant speedup with respect to other implementations.

As proposed in queue-based implementations of the Dijkstra algorithm, further optimization can be obtained by keeping a queue of the updated nodes at each iteration. This would allow exploring nodes only in the restricted neighborhood of the updated nodes in the next iteration.

The proposed method can generalize to N-dimensional images. A path in an N-dimensional represented as a hyper-lattice, will be composed of edges parallel to one direction only. Hence, by selecting orthogonal directions at each iteration

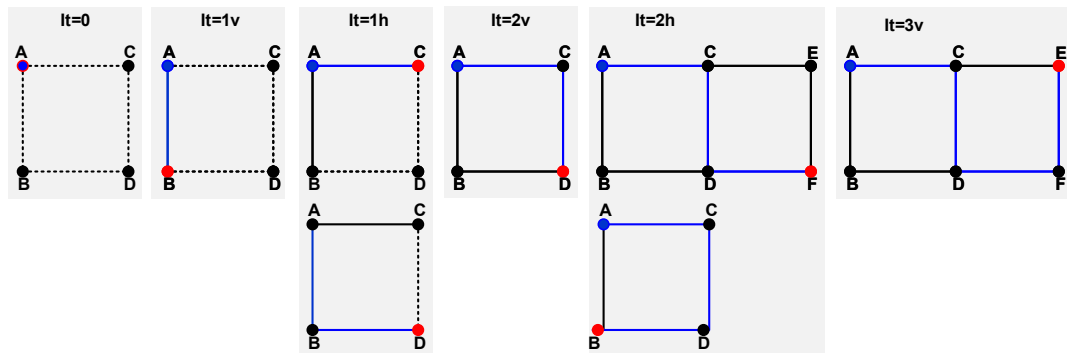


Figure 5.14. Types of shortest-paths found at each iteration At iteration n , the algorithm finds shortest paths with at maximum $n - 1$ turns. $It=nv$ or $It=nh$ refer to the step in which distances are propagated vertically (v) or horizontally (h) at the n -th iteration. Blue node indicate the starting node. Red node indicate the target node. Dashed lines indicate edges which have not been evaluated yet at the current iteration. Continuous line indicate edges which have been already evaluated at the current iteration and are either not considered in the currently found shortest path (black) or considered (blue).

these paths can potentially be found. However, when dealing with anisotropic images, appropriate path-cost functions must be used. Indeed, as proposed in the previous section, a meaningful, non-decreasing path cost can be adopted for applying the proposed method to specific tasks.

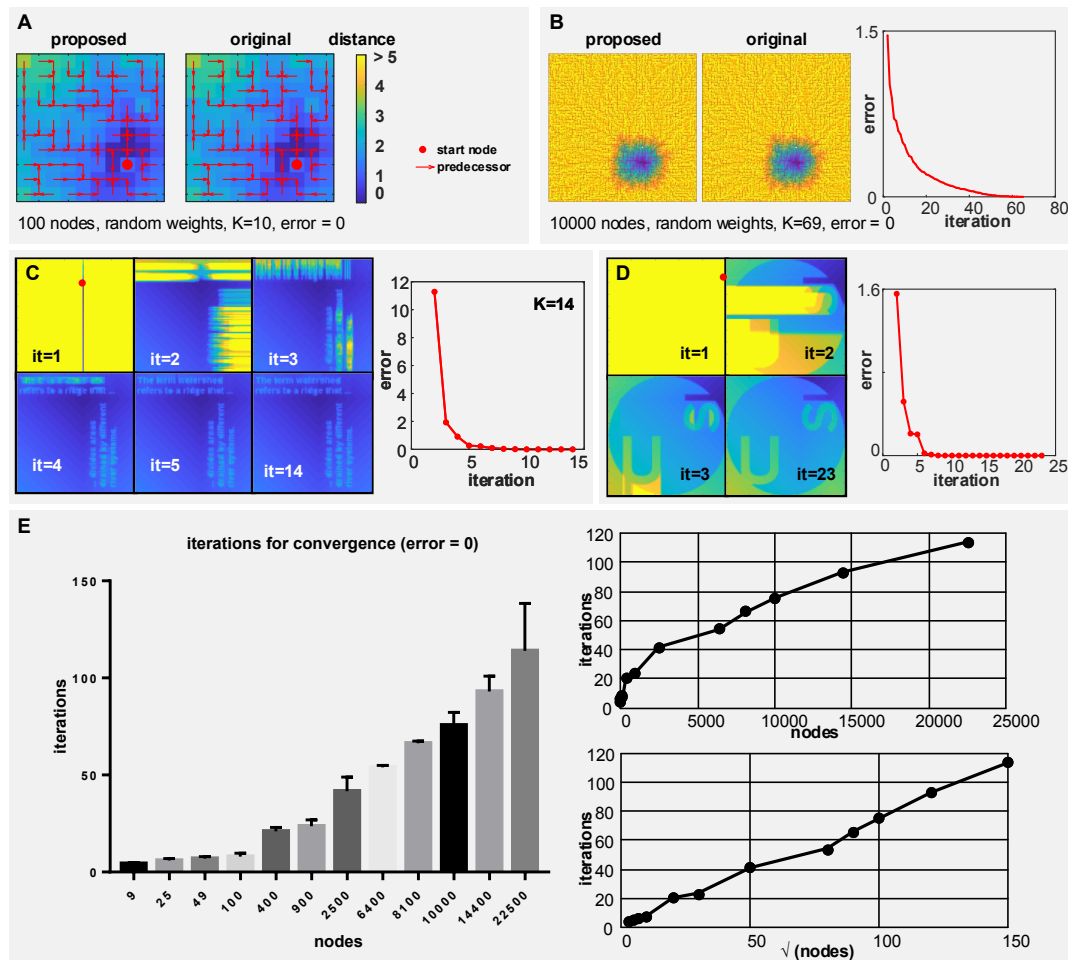


Figure 5.15. Results of the iterative algorithm on different examples. **A.** Color coded lattice of 100 nodes. Colors indicate the shortest-path distance from a random starting node (red dot). Red arrows indicate the predecessor of each node. Weights on the edges of the lattice are random. **B.** Color coded lattice with 10000 nodes and random edge weight, showing qualitative no-difference between the proposed and the original algorithm (left), and a decreasing error at each iteration, which reaches 0 after 69 iterations (right). **C.** Results on an image containing structures (text) showing successive refinements of the shortest-path distance (left, color coded) and decreasing error at each iteration (right). **D.** Results on an image containing structures (USI logo) showing successive refinements of the shortest-path distance (left, color coded) and decreasing error at each iteration (right). **E.** Benchmark on lattice with different size and random edge weights, showing a number of iterations increasing with the size of the lattice, following a linear trend with the width (or height) of the lattice $\sqrt{\text{nodes}}$. ($n = 3$ replicas for each lattice size. Mean and SD are shown).

5.3 Outlook

In the previous two sections we described how graph-based algorithms can be applied for clustering, and optimized for regular graphs such as images. We have identified a series of improvements that could make the proposed methods more accurate, faster, or easier to be applied.

- **Remove the need of initial density peak detection.** This would allow the application of the method when density peaks are difficult to identify. In the next subsection, we report a preliminary study in which we use each point as a potential density peak and detect clusters solving an Hough-like inverse problem.
- **Avoid computing Shortest path when points are density-reachable.** More precisely, from a point x with known shortest path distance d , DBSCAN can be used to group points which are density reachable from x , and their shortest path distance approximated. This would allow to save the computation of the exact shortest path on graphs which are sufficiently dense to be most likely a cluster.
- **Usage of multiple edges between two nodes.** The only requirement to apply the Dijkstra SSSP algorithm works is the usage of a path cost function which is non decreasing. This generally implies that edge costs should be non negative, when using cumulative euclidean distances as path-cost functions. This property holds also for graphs in which two nodes are connected with multiple edges. Hence, the algorithm allows to define the similarity between two points with more than one metric. The algorithm can select which of the metric is more convenient to be considered.

In a preliminary study on the bonemarrow leukemia dataset (with 39 samples described by 9999 variables), we used two different distance metrics between node: Euclidean distance and Spearman correlation. Then, we applied the clustering algorithm proposed in 4.1, on this graph with multiple edges between the same nodes. The algorithm exhibited an increased accuracy (F1 = 0.95, J = 0.90) with respect to using a single edge (F1 = 0.92, J = 0.85). These results outperform all the other methods evaluated in ClustEval [268] benchmark (max F1 = 0.94, J = 0.87). Hence, it is a promising method whose applicability can be investigated when different distance metrics can be applied.

Clustering by giving and receiving, a Hough-like inverse problem. In this section we consider a cluster (group) as a set of shortest paths on a graph. Then,

we propose a novel clustering algorithm that finds groups of nodes, by applying a voting scheme which finds its basis in the Hough-Transform, a method originally developed in the 1960s for multiple line detection.

Indeed, the Hough-Transform generates for each point all the possible lines passing from a point and selects the most common. then, it votes for the most common lines. Similarly, we generate all the possible shortest paths from one point and to that point.

Amongst the possible voting strategies, we implemented a scheme relying on the definition of a group. More precisely, in social sciences, a group was defined as a set of individuals in which each member gives to, and receives from, the other members [19]. Hence, we evaluate for each point, how it gives and how it receives to a set of admissible groups, then we select the most adequate groups.

Clustering can be interpreted as an optimization problem whose solution is a grouping. Given a set of N points $x_i \in \mathbb{R}^d, i = \{1, \dots, N\}$, clustering minimizes the cost function $\sum_{i=1}^N \sum_{j=1}^K d(x_i, c_k) L_{i,k}$ where the Boolean labeling matrix $L_{i,k}$ associates a point x_i to a cluster c_k while d represents a distance function, such as the Euclidean distance from the cluster centroid [155]. Hence, clustering finds how groups are structured.

Let us call the clustering problem as the direct problem \mathbb{A} , for which a unique solution does not exist.

Now, let us define a problem \mathbb{B} as the inverse problem of \mathbb{A} for which a solution can be computed more efficiently. One possibility solution a Hough-like numerical scheme can be applied on a graph.

One possibility is to interpret \mathbb{B} as a data-generation process which is, given a precise structure (i.e. described by an equation), generate the points spanned by that structure.

This definition uses the solution of the direct problem as input (a structure which we consider the same as a group), while its solution can be computed simply by evaluating a function numerically.

To implement this scheme, L can be interpreted as the adjacency matrix of a bipartite graph connecting K clusters to N data points. This matrix can be converted in its connected-component form M , where $m_{i,j} = 1 \iff \{x_i, x_j\} \in c_k$.

Now, the precise structure (corresponding to the input of \mathbb{B}), can be represented as $m_{i,j} = 1$, meaning that x_i, x_j belong to the same cluster.

Hence, assuming that the pairs i, j are given to define a structure, the points belonging to that structure can be generated, for instance by computing the shortest path from x_i to x_j on the undirected graph G .

By generating a sufficient number of i, j pairs and relative shortest paths, a voting procedure can be setup to choose the clusters conformations.

This setup is present in the *Hough Transform* (HT) and its derivations [64] which allowed to find multiple lines in noisy data. The basis of HT is, for each data-point p , generate all of the admissible lines passing through p , then vote for the most commons.

Considering that, the shortest path between two points on a graph is unique (except for the case of shortest paths with the same cost), the proposed inverse clustering problem correspond to the line detection faced by HT.

Hence, structures are modeled using two parameters (node pairs), similarly to the parameters to describe a line in the original Ht formulation.

This gains relevance considering the computational complexity of HT which is exponential in the number of parameters.

We evaluated the possibility to use Hough-like voting to identify multiple structures in a dataset. For an arbitrary point i , we computed the shortest path to K closest points in a neighborhood, corresponding to K leaves of the minimum spanning tree having i as root. Edges between pairs of node in the tree receive a vote.

After repeating the voting a sufficient number of times, we computed a threshold, to cut edges in the graph with lower votes. This gives eventually rise to a graph partitioning corresponding to clustering.

However, the aforementioned voting scheme does not consider if an edge is included because a point j is reached from a shortest path from point i , or the opposite. Considering the social definition of a group, this might represent an important aspect to be evaluated. Hence, we divided the votes in two groups. For each point we defined a "Give-set" and a "Receive-set". The Give-set of point i is formed by the K closest leaves of the minimum spanning tree having root in i . By contrast, the Receive-set of point i , includes the points from which a generated minimum spanning tree has i as leaf.

A first result of this definition is the identification of outliers, as points giving to others, but receiving (Figure 5.18, B,D). Then, it allowed to identify "balanced groups", which are groups in which both giving and receiving are conserved.

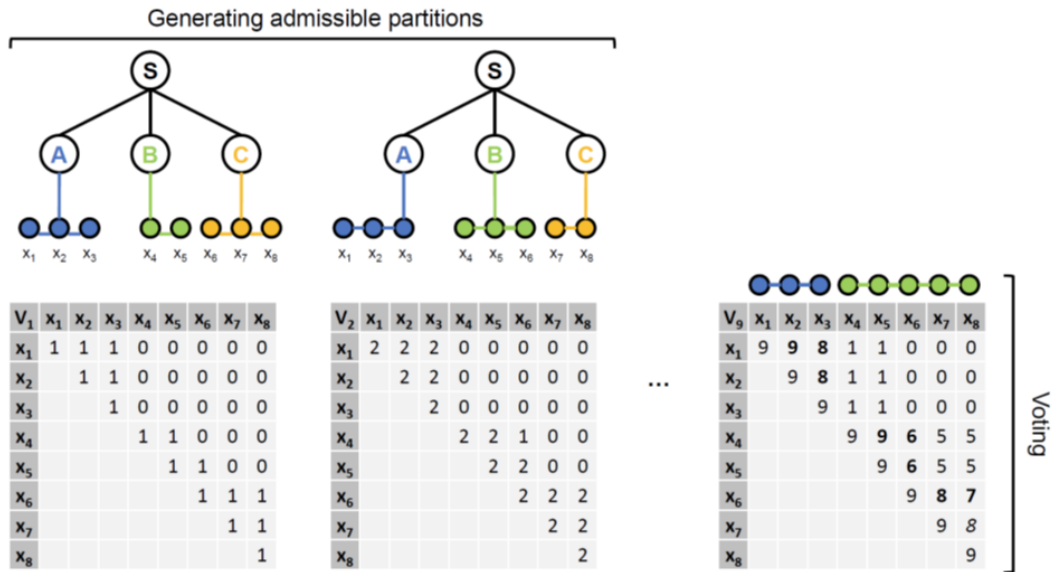


Figure 5.16. Simplified example on a 1d dataset using different seeds.

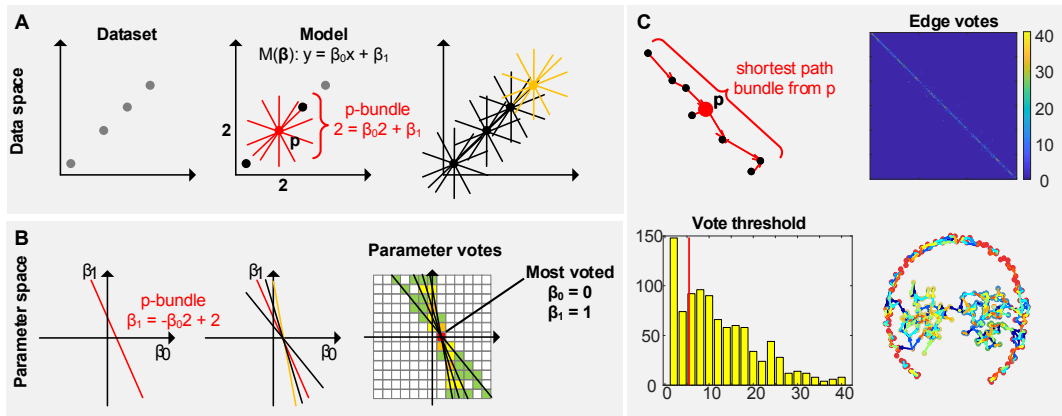


Figure 5.17. Analogy with the Hough Transform. A-B. Example showing a dataset composed by four points in the data space (A), is transformed into four lines in the parameter space (B). A discretized parameter space is used to count votes.

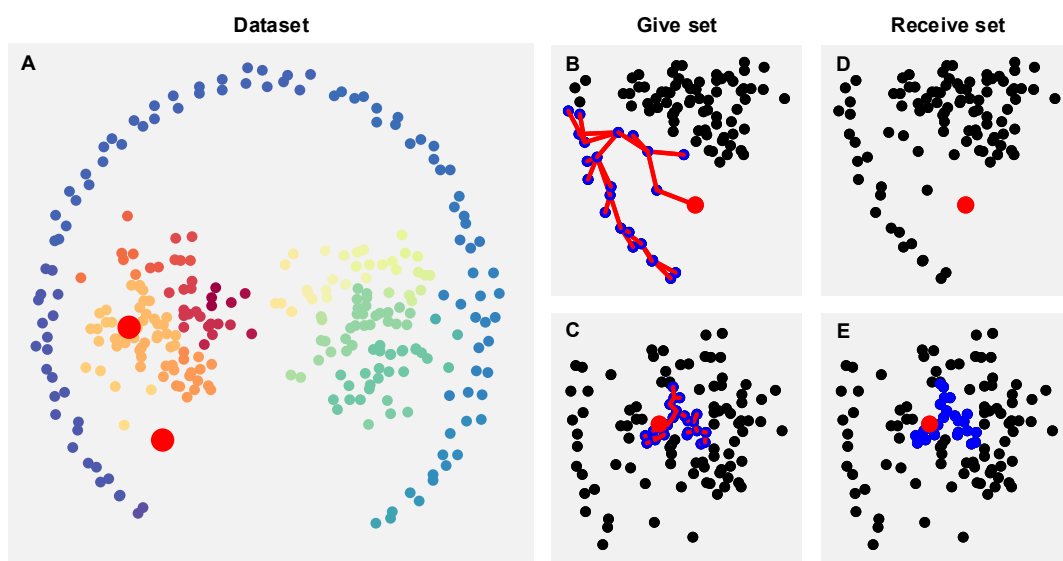


Figure 5.18. Clustering results using give and receive voting. A. Color-coded clustering results on a non convex dataset. Red dots indicate two arbitrary points. B-C. Give set of two arbitrary points. D-E. Receive set of two arbitrary points, showing an isolated point not receiving from any other point in the neighborhood.

CHAPTER 6

Application of graph-based methods for analyzing immune cell migration and interaction

In this chapter, we discuss the application of graph-based methods and to analyze the behavior of immune cells from 2-photon intravital microscopy (2P-IVM) data. Initially, we propose a hierarchical representation of 2P-IVM data, connecting images to biological knowledge.

Then, we propose some improvements to apply computer vision methods on 2P-IVM data. More precisely we consider the tasks of co-localization, segmentation, and movement analysis as the problems of grouping points in color, space and time respectively.

Lastly, we propose a set of tools to analyze the behavior of immune cells, with a focus on action recognition.

6.1 Modeling 2P-IVM data as a hierarchical graph

Graphs are versatile data structures that allow modeling physical processes at different levels of abstractions.

Considering that one main goal of models is the interpretation of complex physical processes, graphs allow studying how nodes are connected. Hence, a graph can be used to map, and find the connections between experimental data and knowledge.

Within this thesis, we represent microscopy data obtained via 2P-IVM as a space-

time connected and hierarchical graph. This graph (represented in 6.1)) represents the scene included in microscopy videos, modeling the relationships from pixels to biomedical knowledge.

More precisely, at the bottom-most lowest level, nodes represent every single pixel while edges represent admissible displacements of pixels between adjacent frame (corresponding to Optical Flow).

At a higher level, group pixels are grouped into superpixels [239] and *flow words* [50]. These groups potentially correspond but are not limited to, cells. Edges at this level represent the admissible displacements of flow-words. Paths at this level of abstraction potentially correspond to cell tracks.

The height of this data structure can be further extended to group flow words into biologically relevant movement patterns, for instance by using action recognition techniques based on machine learning [45, 199, 57]. These patterns potentially correspond to the actions described in Chapter 1. Additional actions and biological processes can be discovered by applying data-mining methods on this data structure.

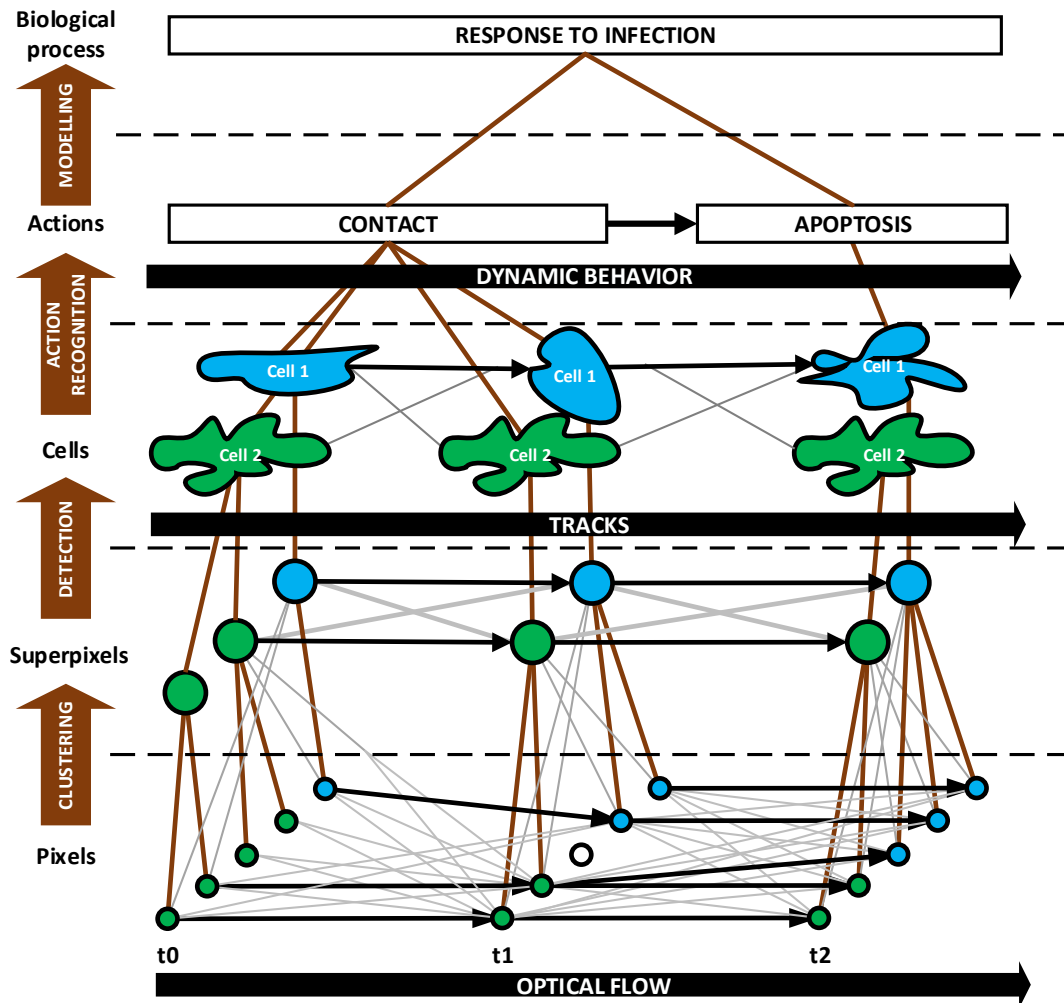


Figure 6.1. Proposed hierarchical graph representation of the microscopy scene, from pixels (bottom) to biomedical knowledge (up).

6.2 Grouping pixels in space and color - superpixels

Superpixels are groups of pixels with similar appearance, and sufficiently close. Representing an image with superpixels, rather than single pixels, demonstrated convenient for the subsequent application of computer vision methods.

However, superpixel identification is not trivial, especially when images include objects with non-convex shapes, or exhibit a variable brightness.

In this section, we propose an improvement to SLIC (a widely used superpixel method), using graph-based metrics for pixel clustering. This allowed decomposing 2P-IVM images in superpixels, with improved adherence to the boundaries of non-convex cells and increased robustness to brightness variations.

Introduction and results. Superpixels have been recently applied to microscopy images of developing embryos [10] and epithelial cells [277]. In both cases, superpixels speeded up and improved the accuracy of cell segmentation and movement analysis methods.

Superpixel identification is typically formulated as an unsupervised machine learning problem. Hence, clustering algorithms are typically found at the core of superpixel methods [239]. One of the most used methods is SLIC [3] (Simple Linear Iterative Clustering), which shows linear computational complexity and broad applicability. For other superpixel algorithms see Chapter 2.

SLIC finds its basis in the K-MEANS clustering algorithm [155], defining the distance between two pixels as the weighted euclidean distance in color and space. Being the color-distance of pixels in the RGB color-space very different from the differences perceived by the human eye, SLIC computes the color-Euclidean distance in the Lab color space which is perceptually more uniform.

Let $I : \mathbb{R}^2 \rightarrow \mathbb{R}^3$ $I(x, y) = (l, a, b)$ be an image that maps the pixel at coordinates (x, y) to a color in the Lab space (l, a, b) . Then, the distance between two pixels p_0, p_1 in space and color is defined as

$$\begin{aligned} d_s(p_0, p_1) &= d_{lab}(p_0, p_1) + \frac{1}{\alpha} d_{xy}(p_0, p_1) \\ d_{xy}(p_0, p_1) &= \sqrt{(x_1 - x_0)^2 + (y_1 - y_0)^2} \\ d_{lab}(p_0, p_1) &= \sqrt{(l_1 - l_0)^2 + (a_1 - a_0)^2 + (b_1 - b_0)^2} \end{aligned} \quad (6.1)$$

The parameter α weights the spatial distance and is used to control the compactness of the superpixels. Then, for an initial set of seeds $Ck \in I$, SLIC associates each pixel to the closest seed. Considering that seeds are distributed in the im-

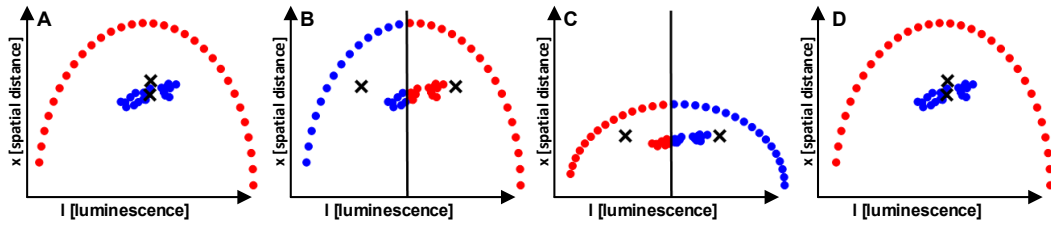


Figure 6.2. Clustering of non-convex groups of pixels in color and space. A simplified dataset where points are represented by one space coordinate (x) and one color coordinate (l). **A.** ground truth composed by one non-convex cluster (red) and one globular-like cluster (blue). **B.** SLIC (K-MEANS) with the color weight $\alpha = 1$ associates the points to the Euclidean-closest centroids. This results in a partition of the points with a linear boundary (solid line) that cannot separate non-convex clusters. **C.** SLIC with the color weight $\alpha = 2$, this parameter acts as a scaling coefficient on the color axis and results in a small change of slope of the separating linear boundary, which does not solve the issue of separating non-convex clusters. **D.** Results of the proposed algorithm using the cost of the shortest path, connecting two points on a graph with limited connectivity as distance metric.

age, this operation is done efficiently in a local search window for each seed. Once this has been done, SLIC updates the position of the seeds to the center of mass of each identified cluster. Then the process is repeated until a convergence criterion is satisfied.

Despite the efficiency and the generic applicability of SLIC, the limitations of K-MEANS are inherited. Figure 6.2 shows the behavior of K-MEANS in a simplified example with 2 clusters (Figure 6.2, A) where points are described by a one-dimensional spatial coordinate x and by a one-dimensional color coordinate l (luminescence).

Indeed, clustering artifacts can be introduced by K-MEANS in the presence of non-convex structures (Figure 6.2, B). Although the value of the parameter α compensates for different excursions of the image brightness and allows to control regularity, α acts only as a scale parameter (Figure 6.2, C). Hence, it does not solve the problem of separating non-convex clusters with a, possibly non-existent, hyperplane. Moreover, the definition of this parameter is often left to the user, reducing the reproducibility of results.

In this work, we use graph-based measure for pixel-to-pixel similarity rather than a linear combination of spatial and color distances.

More precisely, we select N seeds regularly distributed on the image. Then, we assign each other points to the seed connected with the shortest path. Once this has been done, we update the position of the seeds, and repeat the process until convergence, or until a maximum number of iteration is reached.

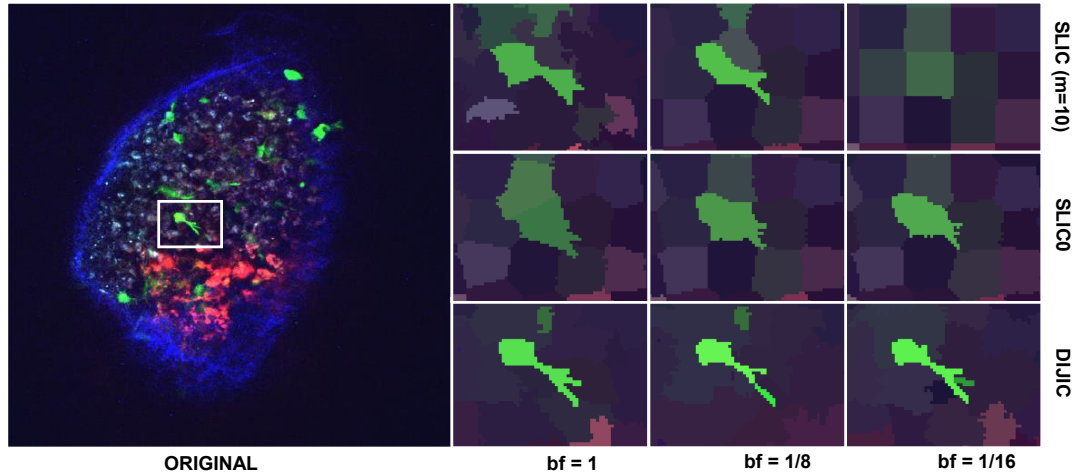


Figure 6.3. Qualitative results of the proposed algorithm on 2P-IVM images of immune cells. **A.** full-size (480x480 pixel) image captured in a murine lymph node presenting CX3CR1-GFP dendritic cells (green), subcapsular-sinus macrophages (red), collagen (blue) and other auto-fluorescent cells (mixed colors). **B.** Zoom-in showing the superpixel reconstructed on a dendritic cell by different algorithms (rows: 1-SLIC, 2-SLIC0, 3-OURS), in response to brightness variation (left to right). The color of superpixels is the average color of the pixels included. While SLIC and SLIC-0 loose boundary adherence in response to brightness decrease, the proposed algorithm maintained the shape of the dendritic cell.

This corresponds to applying K-MEANS, with a geodesic distance. On a simplified synthetic example (Figure 6.2, D), the method allowed us to separate two non-convex clusters correctly.

Additionally, we used a rectangular lattice to represent images like a graph in which each pixel is a node connected to the 4 spatially closer pixels. We used color difference as edge cost. This moved the spatial distance term, from the similarity metric to a constraint in the structure of the graph. Hence, the cost of paths is computed on this structure without any linear combination of color and spatial distances.

Having removed the spatial term from the similarity function, increased robustness to brightness variations with respect to SLIC. as shown in (Figure 6.3), where a brightness variation was simulated on a real 2P-IVM acquisition. Even by varying the brightness by a 16x factor, the proposed method computed superpixels with better adherence to the boundaries of a highly non-convex dendritic cell with respect to SLIC, or SLIC-0.

Since a segmentation ground truth for 2P-IVM images is not available, we eval-

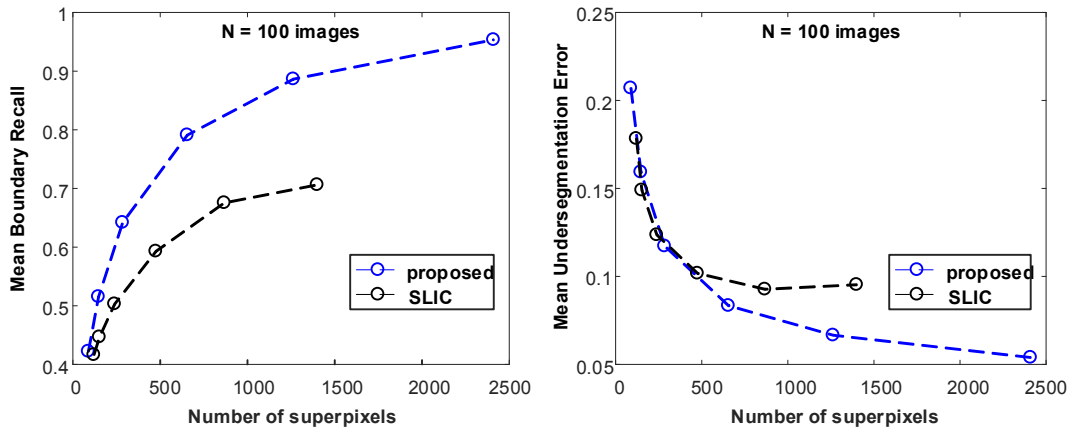


Figure 6.4. Quantitative results of the proposed algorithm on the Berkeley Segmentation Dataset. The performance of the proposed method was evaluated with respect to the ground truth of $n=100$ images in which the boundaries of objects were manually annotated by a pool of humans (Berkeley Segmentation Dataset - BSDS). The proposed method achieved a superior Boundary Recall and a lower Undersegmentation Error compared to SLIC.

uated the performances of the proposed method on the Berkeley Segmentation Dataset (BSDS) [162], using a common superpixel benchmarking tool [197]. This benchmark included natural images whose contours were manually annotated by humans. The proposed method exhibited a higher boundary recall and a lower undersegmentation error with respect to SLIC (Figure 6.4).

In conclusion, the usage of a path-based distance metric allowed improving performances of SLIC and its application on a challenging 2P-IVM acquisition.

Additionally, as described in Chapter 5.1, supervised machine learning can be applied define application-specific path-cost function.

Regarding the computational complexity of the method, although the computation of shortest paths require is more expensive than computing euclidean distances, the complexity depends on the neighborhood size for each seed. Indeed, in SLIC only a limited number of nodes can be reached from each seed. Using N seeds, connected to maximum K pixels, the computational cost of the method, in the worst case is $O(N(K^2))$. Further optimizations can be achieved by heap-based implementations of the Dijkstra algorithm, or methods exploiting regularities of the lattice as described in Chapter 5.2.

6.3 Grouping pixels in time

Optical Flow (OF) is an estimated deformation to transform an image at time t_i to an image at time t_{i+1} .

In the context of 2P-IVM data analysis, OF has the potential to estimate cellular morphodynamics without the requirement of cell tracking nor segmentation. Hence, it represents a promising method to extract knowledge from microscopy videos (Figure 6.5).

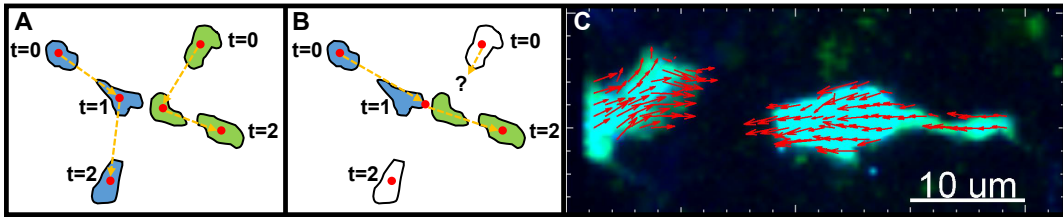


Figure 6.5. Tracking vs. Optical Flow **A.** Sketch showing the correct tracking of two cells. **B.** Sketch showing tracking errors introduced by a detection error, which turns into measurement errors. **C.** 2P-IVM micrograph showing two neutrophils that are going to establish a contact. Optical flow vectors (red arrows) are computed without requiring cell tracking nor cell detection.

However, computing OF is an ill-posed problem that admits several solutions. Unfortunately, most of the existing strategies to compute these solutions are tailored for natural images captured by digital cameras, which are substantially different from the images of immune cells obtained via 2P-IVM. As a consequence, the deformations estimated by available OF methods on 2P-IVM data are not realistic.

In this section, we describe a method to improve the accuracy of OF estimation on 2P-IVM data using graph-based metrics and clustering.

Preliminary results showed a more realistic estimated deformation, and lower image registration error on challenging videos with rapidly migrating neutrophils. Moreover, results suggested the possibility to use clustering in space-time for joint segmentation and movement estimation.

However, the behavior of the proposed method was unstable and poorly controllable. These issues can be potentially addressed using semi-supervised clustering (see Discussion paragraph).

Evaluation of existing methods. In a preliminary evaluation, classical OF methods such as [110, 154], and methods based on TV-L1 regularization [124] esti-

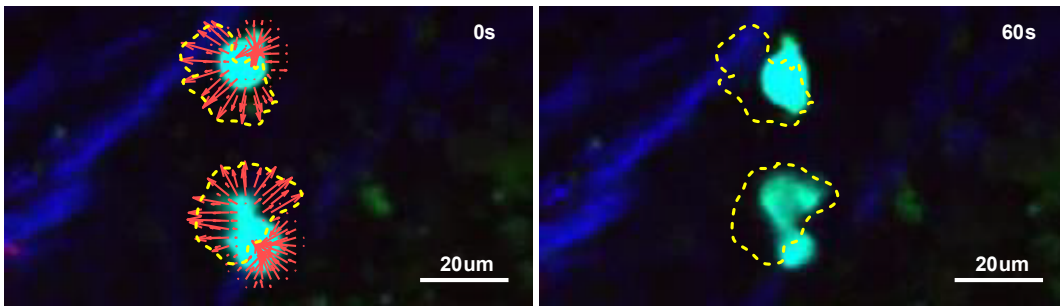


Figure 6.6. Optical Flow errors on 2P-IVM data. 2P-IVM micrographs showing CFP neutrophils (light blue) at two different time points. Optical Flow (red arrows) estimated a deformation from the image at 0s to the image at 60 s, (yellow line) that is not realistic, including non-matching object contours, and empty flow in the inner part of the cell where textures are lacking.

mated non-realistic deformations when applied on 2P-IVM data (Figure 6.6). The main challenges are due to the lack of textures, large displacements and brightness variations which are typically found in microscopy images acquired *in vivo*. These void the assumptions of classical OF methods, which are small displacements and brightness constancy, as described in Chapter 2.

As a result, these methods computed null displacement vectors in areas lacking textures such as the inner part of a moving cell, or too large displacement vectors on the boundaries of the cells, or too smoothed flows (Figure, 6.6). Tuning of software parameters did not allow us to obtain realistic flows (i.e. showing non-admissible biomechanical properties of cells).

Recently proposed strategies to compute OF on complex videos were based on a coarse decomposition of each frame in superpixels. These methods exhibited increased accuracy for both microscopy data lacking textures [10], and natural images with large displacements [34]. In our evaluation, from a visual perspective, the method proposed by Amat and colleagues [10] (hereafter, Amat method) was the one showing more realistic flows on 2P-IVM videos of migrating cells. Indeed, the computed displacement vectors matched the amoeboid motility of cells which is characterized by the expansion of pseudopodia, and contraction of uropodia.

However, the Amat method relies on a superpixel decomposition based on SLIC which might be not accurate for 2P-IVM data as described in the previous section. Additionally, it requires a segmentation mask that might be difficult to obtain. Moreover, in the presence of large displacements, the method computed flows which were far from realistic and poorly oriented towards the real migra-

tion direction of the cells.

Quantitatively, we evaluated the capacity of Optical Flow methods to predict the centroid displacement of a cell, as the mean of optical flow vectors included in the cell volume. The Amat method resulted in the one with lower estimation error. However, on videos sampled at 60 s, on average, this error was $15\mu\text{m}$ which is more than the typical diameter of a cell.

To this end, we developed a method that

- Uses a coarse decomposition of the images (similarly to the Amat method).
- Uses a rich pixel descriptor that captures morphological properties.
- Can compute Optical Flow by minimizing a global optimization problem.

More precisely, the proposed method describes an arbitrary pixel, as a point positioned inside a group of pixels with a centroid (Figure 6.7). This means that a pixel is not described only by its brightness value, but by a rich descriptor that embeds morphological properties.

Then, we compute OF by grouping (in time) points with similar descriptors. This is achieved by matching nodes on a bipartite graph as shown in (Figure 6.8).

Although this method assumes an initial grouping in space, and subsequently associates points in time, a clustering algorithm can be used for the simultaneous grouping in space-time, using a specific path-cost function.

Hence, this approach can potentially be applied to identify OF from spatio-temporal structures. Additionally, considering that groups of pixels can correspond to objects (or object parts), this method has the potential to perform object detection and movement estimation simultaneously.

However, due to the highly variable content of microscopy images, and the difficulty of adapting clustering algorithms to the different cases, we did not achieve this goal of joint detection and movement estimation, which remains possible from a theoretical point of view. Moreover, this is supported by the algorithms which we recently developed and described in Chapter 5.

Initial guess by clustering. Similarly to the Amat method, we initially computed a binary mask to exclude the background from the analysis. Then, an initial grouping of pixels was obtained through the density-based clustering algorithm described in [225] (hereafter, CDP). The advantage of CDP is that only a parameter τ_δ must be set to define the minimum distance between the cluster centers. This value can be set as the typical cell diameter to force clusters to correspond to cells, or to a lower value to group sub-cellular components.

More in detail, for each pixel i , the density ρ_i was computed as

$$\rho_i = \sum_j \chi(d_{ij} - d_c)$$

where $\chi(x) = 1$ if $x < 0$, 0 otherwise. Hence, ρ_i is equal to the number of points that are closer than a distance threshold d_c to the point i . Subsequently, for each pixel, the minimum distance δ_i to any other point with higher density was computed.

$$\delta_i = \min_{j:\rho_j > \rho_i} d_{ij}$$

If p is the point with the highest density ρ_p in a cluster, then, if another point q with higher density $\rho_q > \rho_p$ exists, it should necessarily belong to another cluster, meaning that δ_i should be sufficiently high. Hence, the method separates in distinct clusters, points having a $\delta_i > \tau_\delta$, which are called density peaks, yielding to one density peak for each cluster.

Local descriptor. We defined a descriptor of each pixel in a cluster, based on the shortest path that connects it to the density peak. Such a path has been computed on a graph with limited connectivity, using the Dijkstra single-source shortest path algorithm from a starting node S to all the nodes, imposing the passage from density peaks, as described in Chapter 4.1. The minimax path cost function was used.

The edge cost between two nodes i, j , in the same frame, was defined as the linear combination of the Euclidean distance in space and the brightness difference.

$$w_{i,j} = \alpha \|x_i - x_j\|_2 + \beta \|I(x_i) - I(x_j)\|_2$$

Different terms, such as density or image gradient magnitude can be included in the edge cost to consider other image features. However, these might require the tuning of additional parameters.

By contrast, representing an image on a rectangular lattice allowed us to get rid of pixel coordinates. Hence, we considered only the color difference and we avoided the need of tuning the parameters α, β .

Once shortest-paths from density peaks were computed, the density profile of each path was computed as a descriptor for each pixel.

Being $\Gamma(s, t) = s, p, v_0, v_1, \dots, t$ the shortest path connecting the starting node s ,

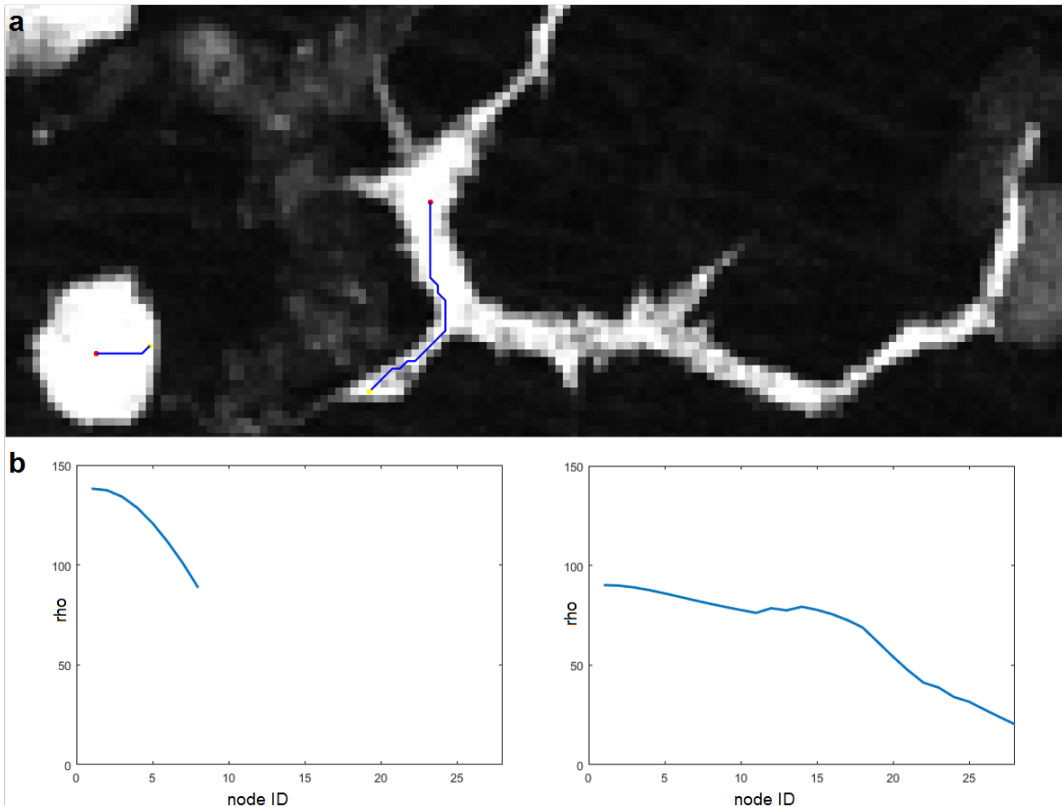


Figure 6.7. Shortest path as local descriptor A. The shortest path (blue line) connecting a pixel to a density peaks (red dots) has been computed by executing Dijkstra algorithm on a frame modeled as a regular lattice. **B.** Density profile of the two paths outlined in a)

to the target node t , via a density peak p and intermediate nodes v , we defined the density profile D_Γ as the ordered density values of the nodes in the path $\Gamma = D_\Gamma = \{\rho_p, \rho_{v_0}, \rho_{v_1}, \dots, \rho_t\}$.

Such a path descriptor is outlined in figure 6.7 and has the goal to match pixels which have a similar density and positioning in the cluster.

Additionally, we described each pixel with a vector representing its position with respect to the cluster centroid, with the aim of facilitating the matching of pixels in symmetric objects.

Point matching. We defined two points at coordinates x_i, x_j and at adjacent time instants $t_i, t_{j=i+1}$ "matched" if the apparent movement of the pixel at x_i is towards the pixel at x_j .

To find these pairs of nodes, we matched the density profiles of points at adjacent time steps, representing them on a bipartite graph as shown in (Figure 6.8, B).

To match density profiles of paths with different length, each density profile was rescaled to a vector of fixed length.

Amongst the methods for matching, it is possible to choose between local heuristics (such as nearest neighbor search), or global optimization methods such as maximal weighted matching, or shortest path from a fictitious node S , to the all the pixels in a space-time connected graph (6.8, A).

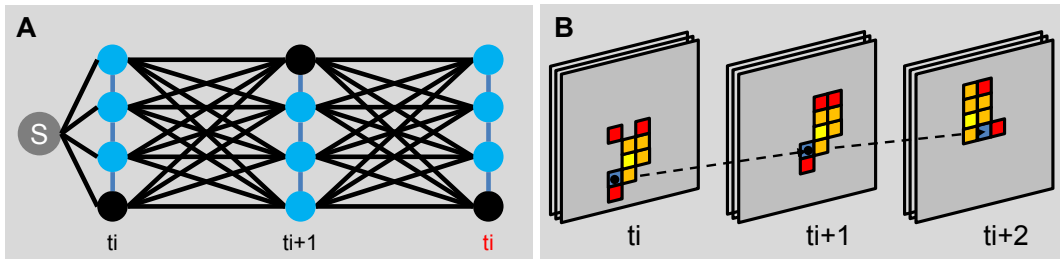


Figure 6.8. Graph-based optical flow - symmetric structure A. Symmetric graph showing the pixels at different time points (nodes), possible transitions (black edges) and possible grouping in space (blue edges). S is a fictitious starting node. **B.** Color coded example, where color indicate the value of the proposed descriptor, arrows the best matching between two points.

Results using nearest neighbor search. By using the nearest neighbor heuristic that selects for each pixel at time $t_i + 1$, the edge with minimum cost to a pixel at time t_i , without any constraint nor global optimization techniques, we obtained an increased accuracy with respect to other methods, both visually on a case study of a squeezing neutrophil (Figure 6.9), on a synthetic case study with large displacements and deformation challenges (Figure 6.10), and quantitatively in image registration for a 2P-IVM video with 60 frames (Figure 6.11).

Despite this promising improvement, the local rule used in this approach fails to deal with more complex cases, where a global view on the problem is needed. For instance, in case of expanding or contracting objects, there might be pixels that do not necessarily have a matching element, or that should be matched to more than one pixel. An example is shown in (Figure 6.10), where unfeasible displacements, associated with the contraction of the object, were computed. Similar errors would arise in the presence of appearing or disappearing objects too.

To solve these issues, a global optimization method such as maximum weighted matching on bipartite graph [83], or the Dijkstra shortest path on a symmetric version of the graph were tested. Results using the latter method are reported in (Figure 6.11).

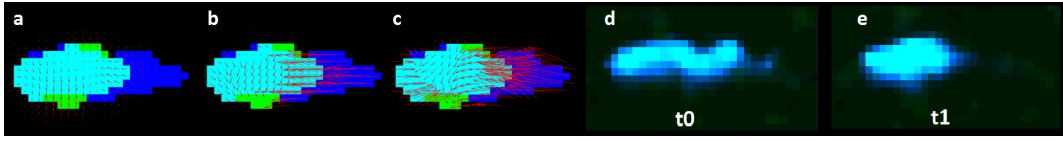


Figure 6.9. OF results on a squeezing neutrophil A. Classical OF with TV-L1 regularization [124] shows null displacement vectors in areas of uniform color and smoothed arrows outside the cell. **B.** Coarse OF by [10] shows a non-smooth deformation. **C.** Proposed approach. **D-E.** 2P-IVM snapshot showing a neutrophil at time 0 (0s), also outlined in blue in A-C and at time 1 (60s), also outlined in green in A-C.

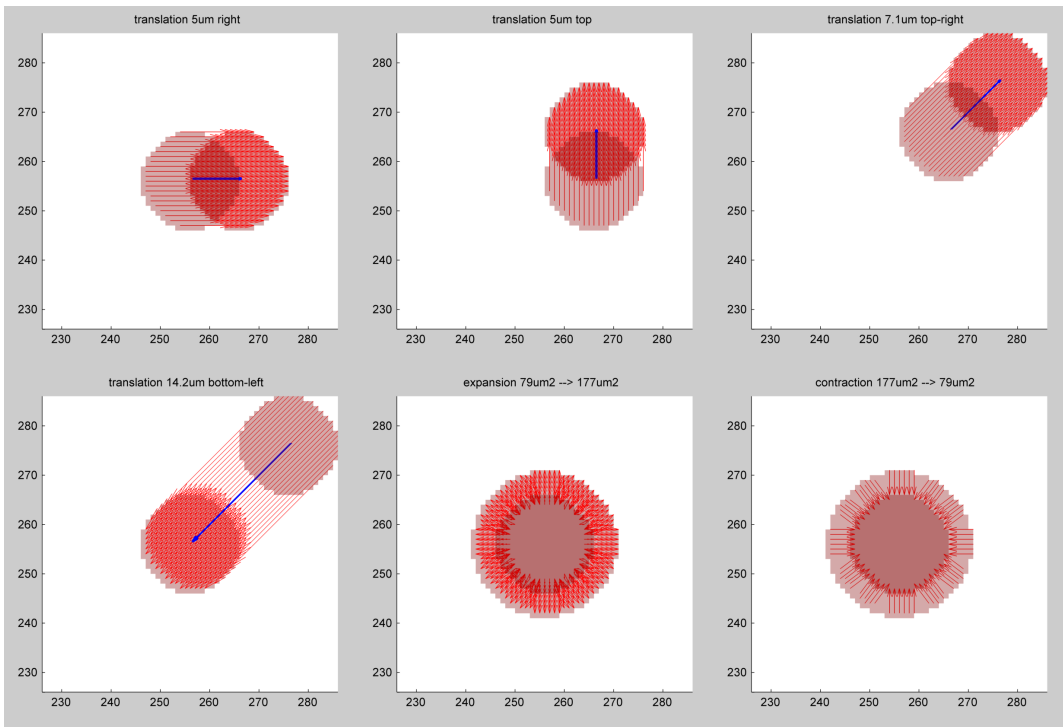


Figure 6.10. OF results on a synthetic example. The proposed approach was tested on synthetic image of a circle undergoing different transformations. Red arrows represent the OF vectors while the blue arrow indicates the overall predicted movement of the flow word.

Quantitative comparison using a tracking ground truth. The proposed method was used to estimate the movement of cells in videos which included large displacements (rapid migration), brightness variations, and non-convex cell shapes. Its performances were evaluated with respect to a ground truth composed of manually-annotated cell tracks, and compared to the Amat method. To do this, a binary mask was applied to the RAW microscopy images to exclude points in the background. This binary mask was common for both the methods and computed using a fixed color intensity thresholding (Coloc functionality of Imaris).

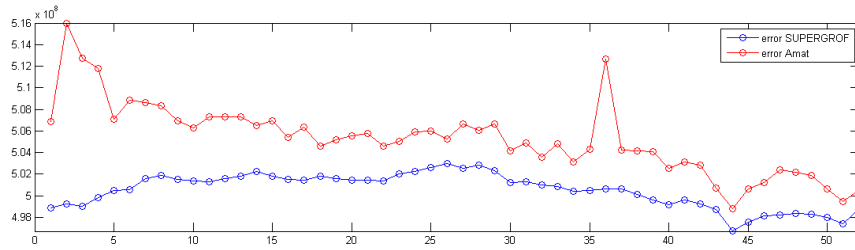


Figure 6.11. Error in image registration. Our approach (blue) has been evaluated vs. [10] in image registration on the video LTDB001. Each pixel of a frame at time t was translated by the estimated OF vector. Then, this translated image was compared to the real image at time $t+1$. Comparison was done as the sum of all the pixel brightness differences.

Clustering via CDP [225], with a distance threshold = $5\mu m$ was used to group pixels at each time frame (excluding points in the background). Considering that each cluster potentially corresponds to a cell, at each time point we performed clustering, and estimated the position of cells as the centroids of the clusters.

Then, the nearest neighbor was used for point matching, yielding to a displacement vector for each pixel. The average displacement of each cluster was estimated by averaging the displacement vectors of the pixels belonging to the cluster. This potentially corresponds to the movement of each cell between adjacent time points, hence we consider it as a movement predictor.

Then, we defined the following two metrics to measure the errors in predicting the cell movements

- IPE: Initial Point Error [μm]. This error measures the distance of a cell in the ground truth, from the closest identified cluster centroid. The average distance of all the cells in the ground truth is reported.
- EPE: End Point Error [μm]. This error measures the distance between the real position of a cell at time t_{i+1} with respect to the predicted position from time t_i . The average distance for all the cells in a frame is reported.

Since the same binary mask was used for applying the Amat method and the proposed method, the same clusters were considered for the comparison, hence the methods have the same IPE

On a video of 16 frames, including two migrating neutrophils, IPE was on average below the typical cell diameter while the proposed method exhibited a significantly lower EPE compared to Amat (Figure 6.13).

However, results were critically affected by the initial guess of cell positions by clustering. Indeed, if a point is associated with different centroids at time t_0 and t_1 , different descriptors for the point will be computed at different time

points. Hence, point matching is hampered. This effect was visible on a challenging video of 86 frames, with highly motile cells undergoing brightness variation from frame to frame. A large IPE (greater than the typical cell diameter) and EPE were introduced by the presence of unstable centroids (6.14, A). Similarly to [34], one solution is to over-decompose the image, identifying more centroids than needed. Then only the centroids that exist in both two adjacent frames can be considered. (Figure 6.14, B).

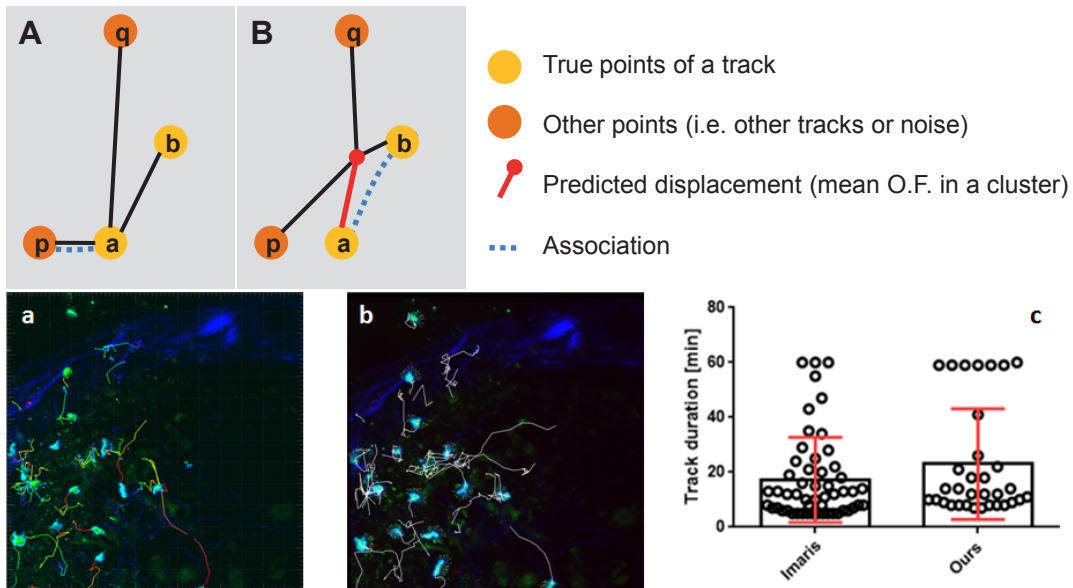


Figure 6.12. Tracking using predictors. The proposed approach was used to estimate a local predictor of cell movement as the mean of OF vectors. Such a predictor was used in combination with a nearest neighbor search algorithm to track cells in time. **A-B.** Association of two points without and with prediction. **C-D.** Qualitative results on the video LTDB001 without and with predictions (lines indicates compute tracks). **E.** Quantitative comparison showing increased track duration.

Discussion. The proposed method partially addressed the limitations of Optical Flow in some cases. However, additional work is required to make the behavior of this method more stable and less affected by the performances of the initial clustering.

A possibility is represented by semi-supervised clustering algorithms, which can be used to group points in space-time.

A performance increase was obtained in image registration and movement prediction with respect to other classical Optical Flow methods, on some challenging

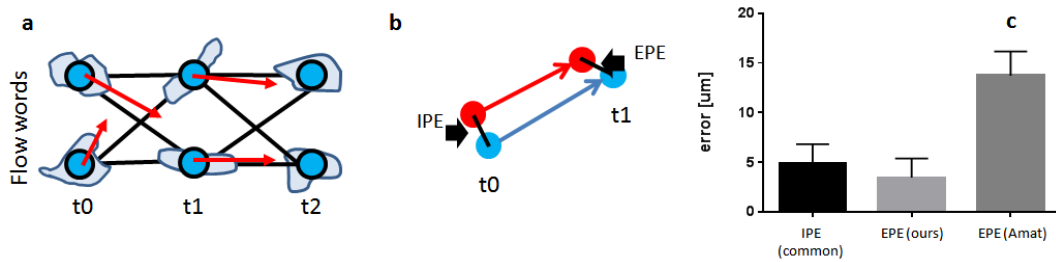


Figure 6.13. Prediction accuracy vs. manual ground truth. **A.** Optical Flow was computed on 60 adjacent images from LTDB001 using the proposed method (ours) and Amat method [10]. Both were compared with respect to the tracking ground truth. Pixels were grouped into flow words by CDP and the position of the centroid estimated as cluster barycenter (blue dots). Predictors (red arrows) were estimated as the mean of the optical flow vectors in the cluster. **B.** Two metrics were used to evaluate the prediction accuracy of the methods with respect to the ground: Initial Point Error (IPE) and End Point Error (EPE). IPE is the distance between the estimated cell centroid and the real cell centroid at each time step. EPE is the distance of the predicted point at the next time instant, with respect to the real displacement. Our approach has been evaluated vs. the mean of OF vectors generated by Amat. **C.** Quantitative results showing a decreased EPE for the proposed method.

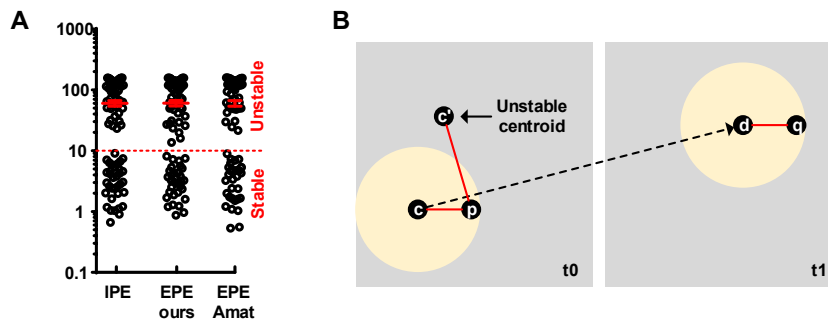


Figure 6.14. Effect of unstable centroids. **A.** Optical Flow was computed on 86 adjacent images from LTDB005 using the proposed method (ours) and Amat method [10]. The centroids of objects were identified by applying CDP with a constant distance threshold = $10\mu m$. Large Initial Point Error (IPE) and End Point Error (EPE) were introduced when centroids were not stable between adjacent frames. **B.** Proposed solution showing the association of one point p at time t_0 to two possible centroids, one stable c , and one unstable c' . The point can be described by means of two descriptors (red line). At time t_1 the point q is associated to the centroid d . A matching between p and q is possible considering the centroids c and d , suggesting that c' was unstable.

2P-IVM videos.

Although these measures suggest a better estimated flow, several flows could give rise to the same performance score. For example, the movement of a cell that does not move can be estimated with maximum accuracy both by a method that computes null OF vectors and by a method that computes orthogonal OF vectors.

Hence, an Optical Flow ground truth is needed to compare the real displacement of every single pixel rather than an average precision.

Recently developed methods based on deep learning achieved remarkable performances in estimating OF on videos with large displacements [117]. This was possible thanks to the availability of synthetically generated datasets providing image-pairs along with OF ground truth.

Unfortunately, such a dataset include objects with totally different morphologies, textures, and movement from cells observed via 2P-IVM.

Recently proposed methods to simulate the movement of cells in microscopy videos [266] represent another possibility to create such a ground truth. However, these simulated videos do not include the main challenges of *in vivo* imaging.

2P-IVM Optical Flow dataset. To compensate for the lack of data, which is needed to validate and adapt OF methods for 2P-IVM, we acquired a set of videos using special experimental conditions. These conditions allowed to estimate a ground truth using classical OF methods.

More in detail, we minimized the major sources of errors which are due to the movement of the sample (i.e. due to breathing), and the large time steps. This optimal scenario was achieved by performing imaging in the popliteal lymph node (PLN) after the animal death. Interestingly, we observed that neutrophils kept migrating *ex-vivo* in the PLN for several hours. By contrast, all the other (unwanted) movements were removed.

Additionally, we maximized the sampling frequency of the microscope pushing it at the construction limits, regardless of photo-induced tissue injury. This allowed us to record 3D videos with a time step from 2s to 5s. In total, we recorded 8 videos, providing 749 pairs of volumes at adjacent time points.

Generation of realistic videos and OF ground truth. Without large drifts and with sufficiently small time steps, brightness constancy was better preserved. This turned into smaller derivatives in space and time, supporting the application of classical optical flow formulations relying on first-order approximations. Therefore, we could estimate Optical Flow by applying the Horn-Shunck Optical flow method, with correction for 3D anisotropy and quadratic regularization.

Then, we downsampled (in time) frames and optical flow vectors, generating

videos having realistic acquisition settings along with Optical Flow ground-truth (Figure 6.15).

Frames were downsampled by dropping one time point every ten time points.

Optical flow vectors were downsampled via pixel tracking.

The quality of the proposed dataset was evaluated by computing (for both the original flows and the downsampled flows) a registration error (Figure 6.16).

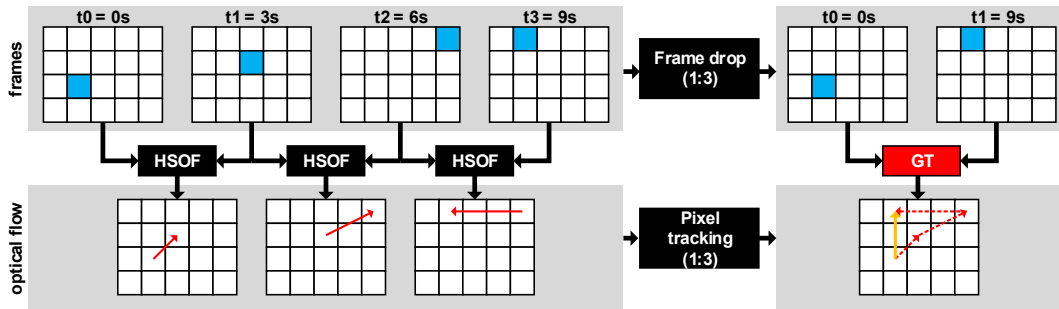


Figure 6.15. Optical Flow Ground Truth generation.

High-Speed Optical Flow (HSOF) is computed using the Horn-Shunck method between adjacent frames of the original video. Frames are dropped with a 1:K ratio to generate the downsampled video. Optical Flow vectors are joined over K frames using pixel-tracking with the head-to-tail method (bottom, right).

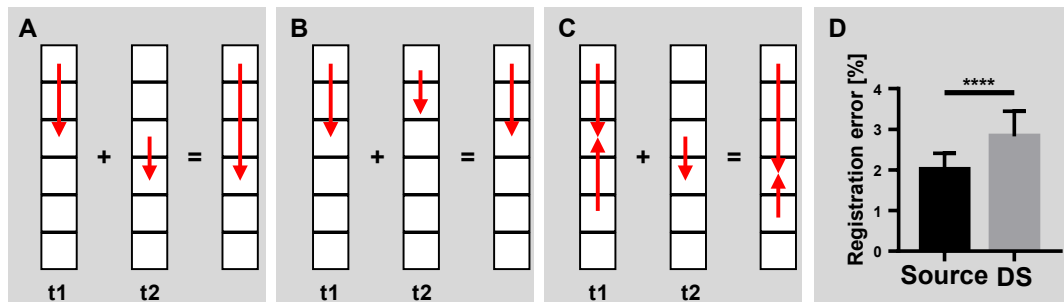


Figure 6.16. Downsampling accuracy of Optical Flow.

A-C. Different cases for pixel tracking. D Comparison of image registration accuracy using the full videos and the generated downsampled ground truth.

This dataset has the main purpose of bringing to 2P-IVM the powerfulness of supervised machine learning methods for estimating Optical Flow. More precisely, the main expected usage is for validation of existing methods, or for transfer learning.

Data augmentation strategies can be implemented in meaningful ways, simulating realistic changes in the videos. These include

- Non-uniform brightness variation (simulating the non-uniform diffraction)

- Virtually introduced distortions (simulating the movement of the tissue)
 - Virtual drift (simulating the drift of the entire sample outside the field of view).
- Interestingly, data augmentation to estimate optical flow in 2D, can be performed by projecting the 3D volume to different planes. Considering the limited resolution and size of the image along the z-axis, we empirically found that projections on a plane, rotated by a maximum of ± 30 with respect to the xy-plane, are meaningful.

Additional acquisitions (for instance with other types of cells, or in other organs) should be performed to include more generic cases of cell migration. Although neutrophils are amongst the most motile cells in the lymph node, their biomechanical properties might differ from other cell types (i.e. monocytes). Therefore, the acquisition of additional videos might be important for validating the generalization capability of trained OF methods on other cell types. However, an appropriate acquisition setting remains to be identified. We speculate that organoids models, or *ex-vivo* organs in culture might represent a choice.

This dataset is publicly available at <http://www.ltdb.info/2pof>

6.4 HoT-POF: an interpretable descriptor of cell motility

In this section we propose a novel descriptor of cell motility, namely HoT-POF. This method combines the advantages of cell tracking and Optical Flow. Indeed, cell tracking allows following the position of cells over time while Optical Flow allows evaluating the instantaneous changes in morphology. The combination of these information allowed us to represent the complex cellular morphodynamics associated to different migration modes *in vitro*, and different cell actions *in vivo*.

Introduction and results

In computer vision, movement descriptors are largely applied to summarize the content of videos, representing the movement of objects with a limited number of values rather than a large number of pixels.

Amongst the available descriptors, Histogram of Oriented Optical Flow (HOOF) methods have been successfully applied in computer vision for human action recognition [45], video surveillance [163] and anomaly detection [52] amongst others. HOOF computes an histogram of N bins from the optical flow vectors, by counting the number of vectors oriented in a certain direction. Additionally, it weights the counts according with the length of the vectors [45]. HOOF has the theoretical advantage of being a generic technique that can be applied to any type of video regardless of the content. Additionally, it does not require object tracking which might be difficult for certain objects such as cells in 2P-IVM videos.

However, HOOF is an instantaneous quantification of the video which describes the movement between adjacent frames. Hence, a single HOOF might not capture long-term dynamics spanning multiple frames.

By contrast, object tracking allows describing the movement of an object for the entire duration of a track.

However, when quantifying the migration of objects via track-based measures, information can be lost. Indeed, analyzing only the centroid of an object loses the morphological changes of the surface. Additionally, common measures computed on long tracks might average different behaviors. Lastly, long tracks are difficult to obtain when multiple objects are present and these potentially include tracking errors.

In this work, we combine HOOF with cell tracking to analyze immune cell migration. We compute Optical Flow between the adjacent frames of a microscopy

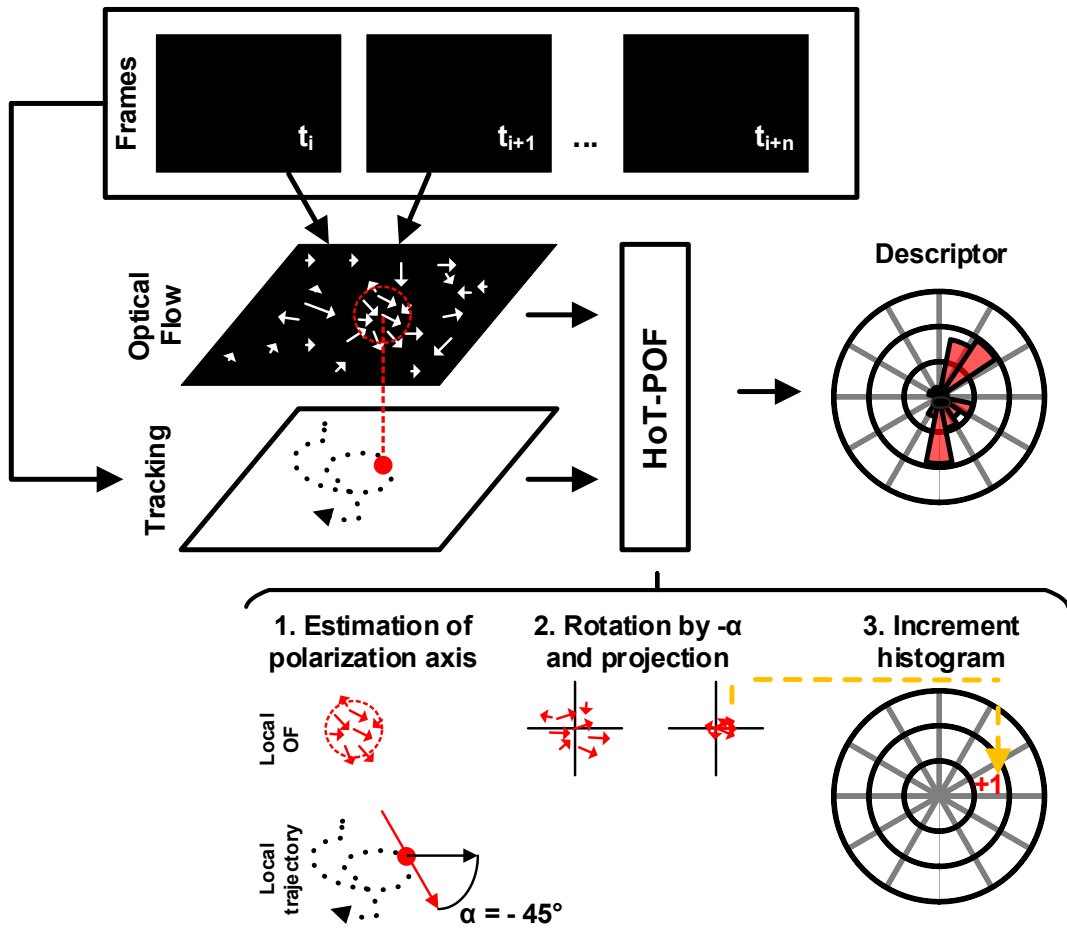


Figure 6.17. HoT-POF architecture. (up) Instantaneous Optical Flow computed between adjacent frames, and cell tracks spanning multiple frames, are combined by HoT-POF to generate a motility descriptor. (down) For each point of a track (red dot), the Optical Flow in a local neighborhood and the local trajectory are estimated. Then, Optical Flow is rotated towards the direction of movement, projected and a polar histogram is incremented.

video, and cell tracking across all the frames of the video.

Then, we describe cellular morphodynamics via a novel descriptor, namely HoT-POF which stands for Histogram of Tracklet-Projected Optical Flow.

HoT-POF Descriptor. Given a microscopy video, the Optical Flow vectors of the entire video, and the track of a cell, we computed HoT-POF as shown in Figure 6.17, and described as follows.

Data: N: number of bins of the histogram
Track: $2 \times T$ array with the position (2D) of a cell at each time $0 < t < T$
r: Radius of a circular neighborhood
Result: k HoT-POF descriptors
Divide each track into k tracklets (using a track splitting method)
foreach *tracklet* **do**
 Initialize an HoT-POF vector of N elements to 0
 foreach *point of the tracklet* **do**
 Define a circular neighborhood of radius r (i.e $5\mu m$)
 Select the Optical Flow vectors in the circular neighborhood
 Compute/estimate the local displacement of the cell centroid
 Compute α as the angle of the displacement
 Rotate the Optical Flow vectors by $-\alpha$
 Compute HOOF on the rotated vectors with N bins
 Merge the HOOF counts to the HoT-POF vector (i.e. by adding
 the counts or by taking the maximum count for each bin)
 end
end

Algorithm 1: How to compute HoT-POF for a track.

HoT-POF captures the morphodynamics of different cell actions *in vivo*.

HoT-POF was computed on 2P-IVM data of neutrophils 24 hours following influenza infection in the draining lymph node. At this time point, neutrophils are expected both to clear the tissue from leftovers of dead cells and to undergo cell death too.

By applying HoT-POF it was possible to detect different morphological changes of cells associated with different biological actions. In Figure 6.18 we report four examples of neutrophils performing four different activities. These actions were characterized by different morphological changes which were visible by the HoT-POF descriptor.

Additionally, the proposed descriptor provided insights on how cell migration occurs. In migrating cells (Figure 6.18 A,C) the presence of orthogonal vectors indicates the expansion of the pseudopodia (vectors with 0 angle w.r.t cell polarization axis) and the contraction of the orthogonal sides (vectors with 90 and 180 angles).

HoT-POF differentiates between haptotaxis and haptokinesis *in vitro*. HoT-POF was computed on time-lapse images of an *in vitro* culture of B cell lymphoma migrating on a substrate of endothelial cells. Amongst the different migration

patterns of cells *in vitro*, two known patterns are haptotaxis and haptokinesis, indicating respectively the adhesive or non-adhesive migration (further details are reported Chapter 1). The former involves high binding to the substrate, conferring plasticity and formation of cell protrusions. By contrast, the latter involves less plasticity.

Hot-POF confirmed the differences between these types of migration. Figure 6.19 reports an example of three manually labeled cells.

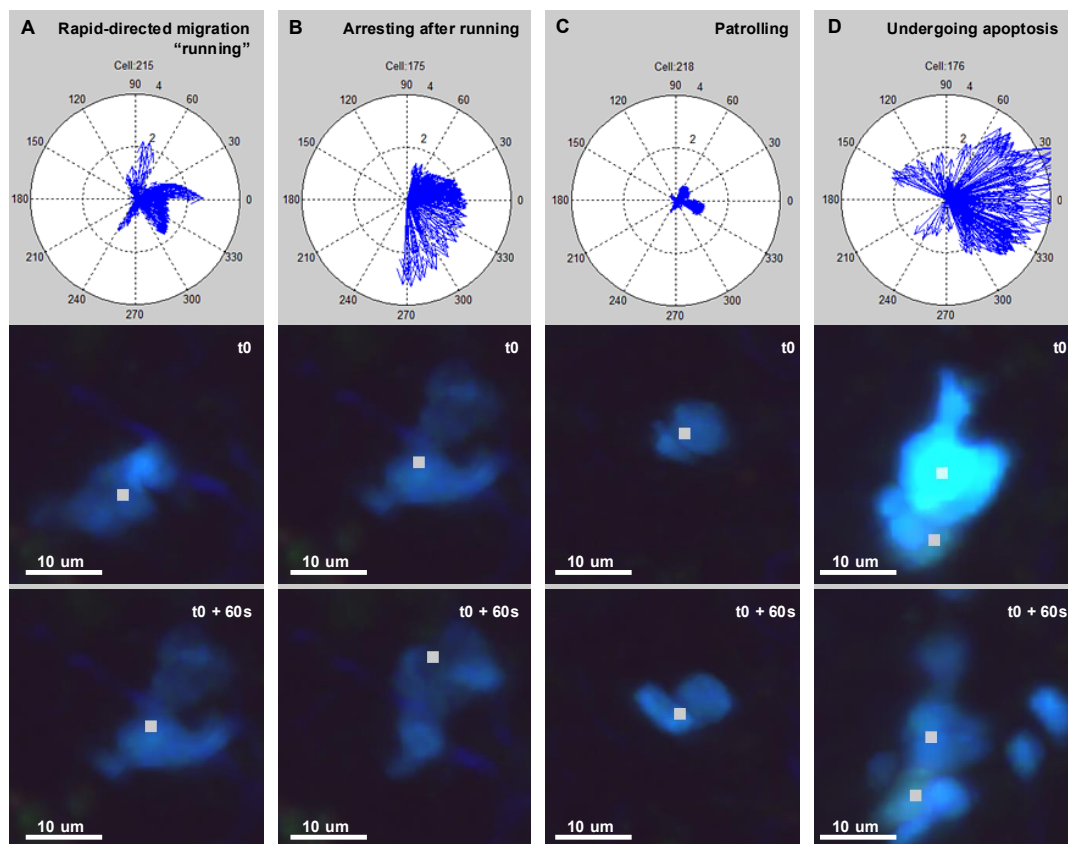


Figure 6.18. HoT-POF descriptor and 2P-IVM micrographs of neutrophils performing different actions *in vivo*. **A.** Neutrophil rapidly migrating with high directionality. **B.** Arresting after the rapid migration. **C.** Neutrophil patrolling an area with confined migration and low speed. **D.** Neutrophil undergoing apoptosis. The 0 angle corresponds to the direction of movement of the cell. In this example we included all the Optical Flow vectors instead of the counts for visualization purposes.

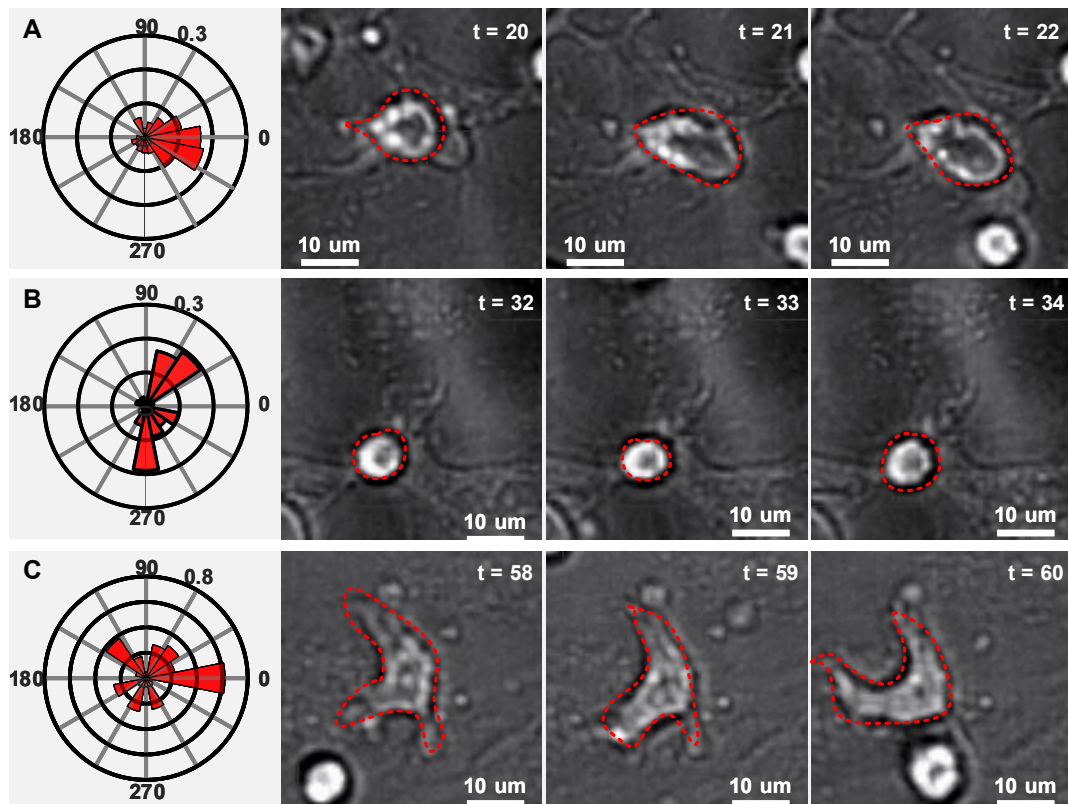


Figure 6.19. HoT-POF descriptor and transmitted light micrographs of B cell lymphoma migrating on a substrate of epithelial cells *in vitro*. **A.** B cell undergoing amoeboid migration with adhesion and formation of pseudopodia. **B.** B cell non-adhering to the substrate, with an associated bright halo and round shape. **C.** B cell with high plasticity but null migration, strongly adhering to the substrate. The 0 angle corresponds to the direction of the movement of the cell. In this example, we included the percentage (0...1) of the vectors in each bin of the polar histogram.

Discussion

The proposed method allowed to capture cellular morphodynamics both *in vivo* and *in vitro* using two different imaging modalities (fluorescence and transmitted light).

Compared to standard measures to quantify cell migration, HoT-POF provides insights on the underlying actions of immune cells.

However, considering that a cell changes action over time (see Chapter 6), HoT-POF should be computed on a sufficiently limited track fragment. To this end, we suggest dividing tracklets when a cell stops. This criterion agrees with the described migration model of granulocytes [101] which include repeated stops in which the cell decide the polarization direction.

The polarization axis of a cell was estimated to rotate the optical Flow vectors towards the direction of movement. The direction of movements can be computed either as the local displacement of a track or as the average angle of the Optical Flow vectors.

We suggest using the former modality when tracking can be performed with sufficient precision. However, when using manual tracking, noise in the positioning of cell centroids can be introduced [212]. To compensate this issue we estimated the local movement direction on 5 time points and we applied smoothing via a moving averaging window to the coordinates of cell centroids (window width = 3 time points).

Amongst the few methods available to compute Optical Flow on microscopy images, we applied the method proposed by Amat and colleagues. Although this method supports large displacements it requires a binary mask on the objects of interests. We estimated this mask using a global thresholding method which is generically good but not precise in the presence of non-uniform illumination. To avoid this problem, more recent methods based on supervised machine learning for either foreground segmentation or optical flow computation can be applied and are compatible with the proposed descriptor.

Methods

Imaging. *in vivo* videos of neutrophils were acquired via a customized up-right two-photon platform (TrimScope, LaVision BioTec). Two-photon probe excitation and tissue second-harmonic generation (SHG) were obtained with a set of two tunable Ti:sapphire lasers (Chameleon Ultra I, Chameleon Ultra II, Coherent) and an optical parametric oscillator that emits in the range of 1,010 to 1,340 nm (Chameleon Compact OPO, Coherent), with output wavelength in the range of 690-1,080 nm.

Imaging was performed in a transgenic CD11c-YFP animal [151] while fluorescent neutrophils were isolated from the bone marrow of a CK6/ECFP animal [100] and injected intra-ocularly in the bloodstream.

in vitro videos of migratory B cells were acquired via an ImageXpress Micro 4 widefield microscope using direct light. Cells were incubated on a substrate of epithelial cells

Mice. All the animals used for *in vivo* imaging were bred in-house. Mice were maintained under specific pathogen-free conditions at the Institute for Research

in Biomedicine, Bellinzona and used following the Swiss Federal Veterinary Office guidelines.

All animal experiments were performed following the Swiss Federal Veterinary Office guidelines and authorized by the relevant institutional committee (Commissione cantonale per gli esperimenti sugli animali, Ticino) of the Cantonal Veterinary with authorization numbers TI28/17, TI02/14, and TI07/13.

Optical Flow. Optical Flow was computed using the method proposed by Amat and colleagues [10]. A coarse-to-fine pyramidal decomposition of the images was computed using 4 different scales (downsampling = 0, 2, 4, 8). 2d grayscale images were obtained as the mean projection of all the imaging channels. The initial binary mask required by the method was computed using Otsu thresholding on the generated 2d images.

Cell tracking. Cells were tracked manually using the Spots functionality of Imaris (version 7.7.2 Oxford Instruments).

Tracklet creation. A track was decomposed into tracklets of variable length. Each tracklet started when the cell was stopped. We considered a cell stopped when its speed was less than $1.32\mu\text{m}/\text{min}$.

6.5 Detection and quantification of neutrophil response to apoptosis

In this section we report on a novel method based on the aforementioned HoT-POF descriptor, to detect apoptotic cells in 2P-IVM data.

Additionally, we briefly report the observed effect of neutrophil apoptosis on the other cells following influenza infection and photodamage.

Introduction and results. Apoptosis is a type of programmed cell death which is vital for the development and survival of multicellular organisms, being involved in recognition, response, and removal [96].

Dysfunctions in apoptosis may result in developmental diseases, tumor and autoimmunity [72].

Apoptosis is generally characterized by specific morphological characteristics [72], including shrinking of the nucleus and blebbing of the cell membrane yielding to the fragmentation of the cell (Figure 6.20).

To this end, apoptosis represents one cellular action that can be detected from imaging data.

Although apoptosis is considered a silent type of cell death, which happens to eliminate cells without creating inflammation, apoptotic cells have the capacity to release signals just before dying. These signals can be of two types: "find-me" and "keep-out" [96]. While the former can be chemoattractants for certain cell types, the latter can inhibit the migration of other cell types.

Since this process happens *in vivo*, where a multitude of signals are present, microscopy together with appropriate computational methods are of paramount importance of its quantification.

In this work, we applied HoT-POF to identify apoptotic neutrophils in 2P-IVM videos and we characterize the effect of this event on the other cells in a model of influenza infection.

We observed that neutrophils undergo apoptosis in the popliteal lymph node, 24 hours post-vaccination with UV-inactivated influenza virus.

Apoptotic neutrophils localized mostly in the subcapsular sinus, in association with the debris of previously death macrophages which underwent necrosis as described in our previous work [44].

Apoptotic neutrophils displayed a shrinkage of their shape, blebbing and fragmentation (Figure 6.21, A).

Following apoptosis, we found that other neutrophils are recruited towards the

site of apoptosis. This accumulation is transient, starting from 1000s after apoptosis, reaching a plateau after 3000s and disappearing after 4000s approximately (Figure 6.21, B).

Additionally, we observed that neutrophils distant up to 200 μ m from the apoptotic site, rapidly respond by changing their motility in less than 300s. Indeed, these cells undergo a sudden change in direction towards the apoptotic site. This results in a peak of low directionality, followed by a peak of high directionality (Figure 6.21, C). Lastly, by analyzing at the variance of cell directionality, we could observe that apoptosis acts as synchronization for the neighboring neutrophils which display similar movement patterns.

By applying HoT-POF the characteristic morphology of apoptotic cells was captured by a wide distribution of the Optical Flow vectors (Figure 6.22, up). By contrast, the responding cells displayed long and directed tracks, with an HoT-POF descriptor mainly oriented towards the migration axis.

Additionally, we used HoT-POF in combination with an SVM classifier to distinguish between apoptotic and non-apoptotic cells. This was achieved by using a total of 9 training and 9 validation track fragments, which were previously labeled in two classes by imaging experts.

The classifier was able to distinguish between the two classes with performances shown in (Figure 6.23).

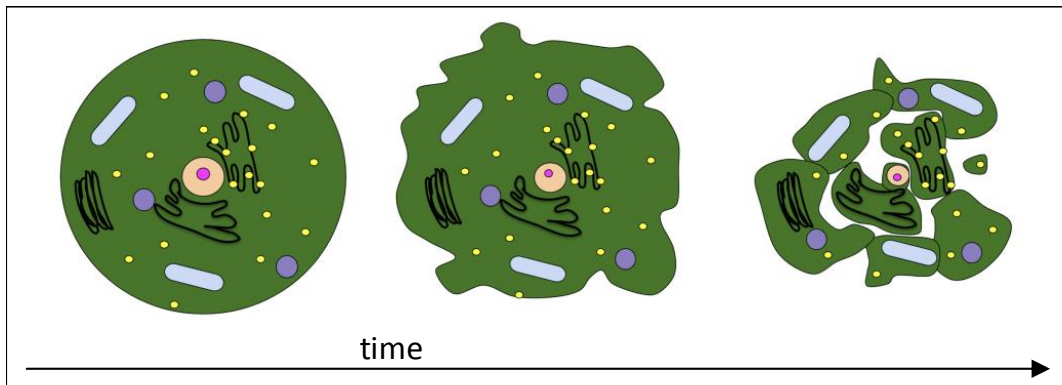


Figure 6.20. Morphological characteristic of apoptotic cell death including shrinkage of the nucleus, blebbing and fragmentation. Image adapted from Jordynmill [CC-BY-SA]

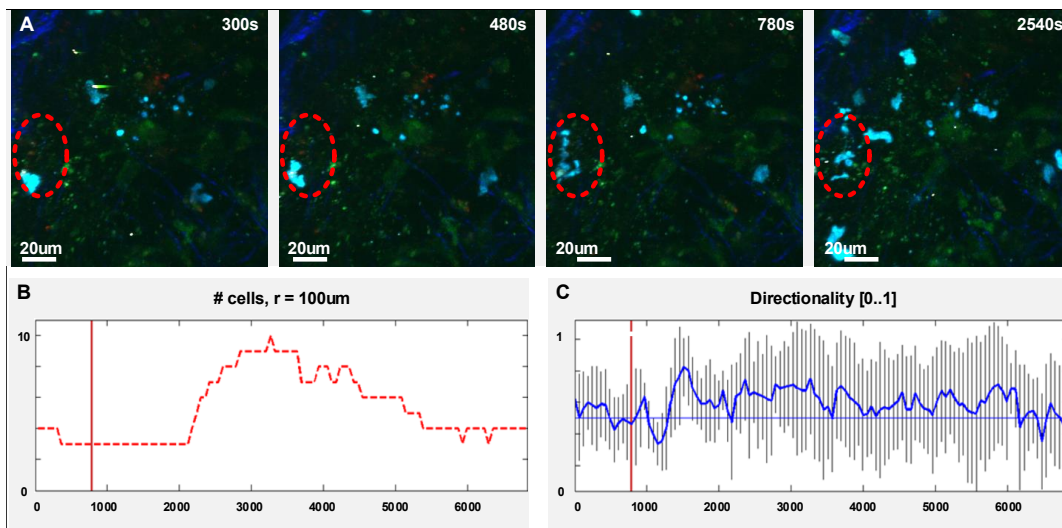


Figure 6.21. Neutrophil apoptosis 24 hours post influenza vaccination. A. 2P-IVM snapshots at different time points showing a CFP (blue) neutrophil undergoing apoptosis (dashed red line). The other neutrophils in the field of view respond by migrating towards the apoptotic site. B. Cell number in a circular neighborhood of radius $100\mu m$ over time showing an increase after the apoptotic event (red line). C. Average directionality of cells over time, showing a substantial change after the apoptotic event (red line). Cells initially decrease directionality, then exhibit high directionality. Vertical bars indicate the standard deviation. After the apoptotic event, the standard deviation is reduced.

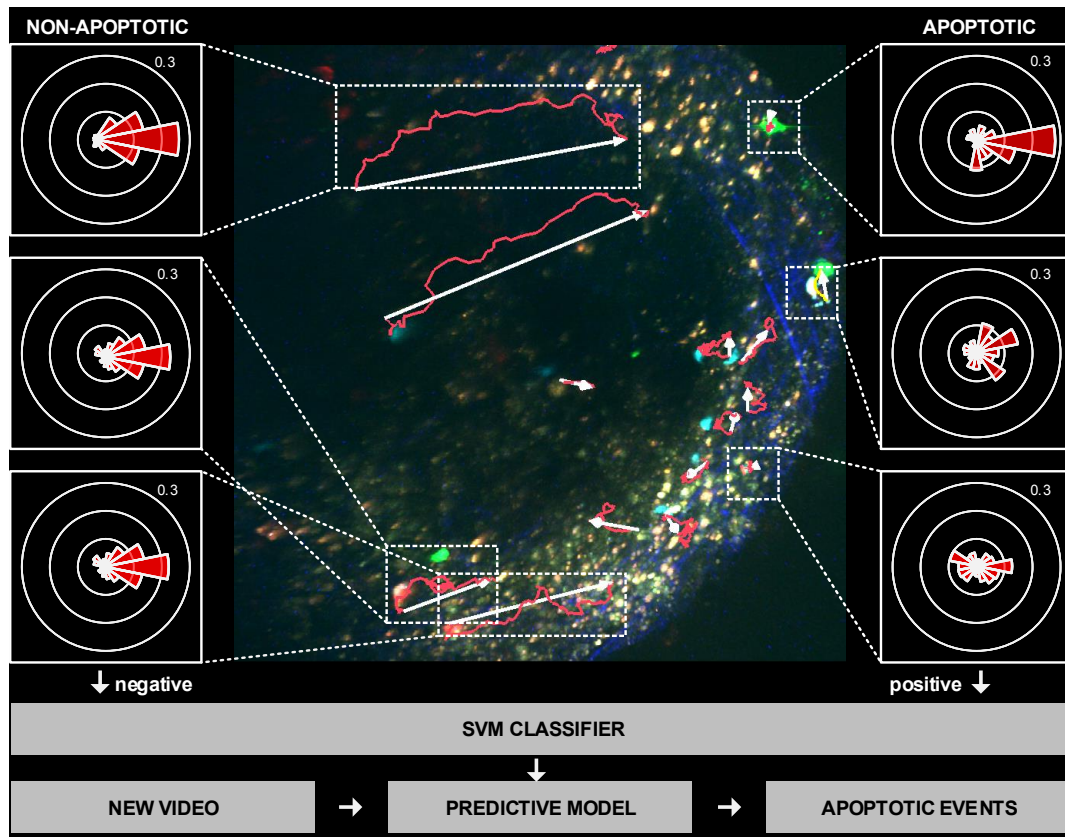


Figure 6.22. Framework for apoptosis detection and example on LTDB005. (up) The HoT-POF descriptor is computed on different tracks of both non-apoptotic and apoptotic cells. (low) A classifier (i.e. SVM) can be trained to distinguish between the two classes by providing negative and positive examples of cells undergoing apoptosis. Once trained, the classifier can be applied to the tracks of other videos to detect apoptotic events.

| | | predicted | |
|--------------|----------|-----------|----------|
| | | negative | positive |
| ground truth | negative | TN=6 | FN=2 |
| | positive | FP=2 | TP=8 |

Figure 6.23. Performances of apoptosis detection using HoT-POF on LTDB005. n = 18 cells were classified via SVM using HoT-POF descriptors on the entire cell track.

6.6 Semi-supervised machine learning facilitates colocalization and tracking

One of the most difficult task for the automatic analysis of cell migration and interaction in 2P-IVM data is the recognition of the cells of interest with respect to other cells and background.

Although an imaging expert may know how a cell should appear, this knowledge is difficult to be expressed as criteria (such as brightness thresholds). Challenges are introduced by the possible low specificity of acquisition channels which may include multiple cell populations, the presence of objects in the background with a similar appearance to the cells of interest, the high plasticity of immune cells, and the high variability between different samples. Hence, both manual curation of results and tuning of bioimaging software parameters among different experiments, are commonly required.

In this section, we describe a method based on semi-supervised machine learning to facilitate colocalization. In line with recently proposed approaches for pixel classification, the method requires the user to draw some lines on the cells of interest and some line on the other objects/background.

Although state-of-the-art methods use these lines to select a sufficient number of points for pixel classification, we consider that lines embed knowledge, not only on which pixel belongs to a class or which pixel belongs to another class but also on how pixels within the same object are connected. Hence, the proposed method exploits both pixel-wise and connectivity-wise information from the annotations to create an additional imaging channel that is specific for the cells of interest. The usage of this method increased tracking accuracy on a dataset of challenging 2P-IVM videos of leukocytes.

Introduction

2P-IVM requires a fluorescent sample. For methods to make a biological sample fluorescent (hereafter labeling) see Chapter 2. In brief, these are based on markers that emit fluorescence at a specific wavelength following excitation by 2-photon. The most common labeling methods involve the usage of genetically modified (GM) animals which express fluorescent proteins on certain cells, *in vitro* labeling with fluorescent dyes or administration of fluorescent antibodies.

When multiple cell populations are imaged, it is desirable to acquire multiple acquisition channels to distinguish different populations. This can be achieved by using different fluorescent labeling (each population with a specific emission

wavelength), in combination with a set of optical filters to acquire wavelength-specific channels. Such a combination of labeling and filter set is critical to distinguish a cell population from another and background.

Indeed, if cells are poorly visible, or similar to other objects, errors in cell detection can be introduced. These can subsequently compromise tracking and affect the final measurements.

Unfortunately, fluorescently labeled immune cells often appear in more than one acquisition channel or exhibit bizarre appearance. This is due either to the broad emission spectrum of the used fluorescent markers (Figure 6.24, A) or to the incorporation of fluorescent material acquired, for instance, via phagocytosis. The effect of phagocytosis is often visible when phagocytic cells (i.e. neutrophils) are labeled *in vitro* with the formation of bright spots in the lysosomes due to the accumulation of the marker (Figure 6.24, B).

Additionally, the fluorescence emitted by cells undergoes diffraction throughout the sample, introducing a brightness variation in space (Figure 6.24, C). Brightness variation and artifacts can further be introduced by photo-damage and insufficient isolation of animal movements (Figure 6.24, D). Lastly, auto-fluorescent objects, such as background and collagen fibers can appear in the same acquisition channels of cells with similar intensity (Figure 6.24, E).

Therefore, specific image processing techniques are required to generate specific channels where only the cells of interests are visible.

However, the multiple aforementioned challenges hamper the usage of generic colocalization methods. Brightness thresholds to separate the background from the cells of interest should be adapted among different areas of the same acquisition and different experiments. This reduces the usability of specialized imaging software packages such as Imaris (Bitplane inc.) and introduces research bias.

Although morphological information can in principle be taken into account to distinguish immune cells from the background, their high plasticity and commonly non-convex shapes introduce additional challenges to consider all the possible cases.

In this work, we propose an imaging processing method based on semi-supervised machine learning. This approach facilitates the transmission of knowledge on the appearance of cells from an imaging expert to a computer, in line with recently proposed methods for clustering [213]. This knowledge is then exploited to create an additional imaging channel which is more specific for the cells of interest. The usage of this channel improved tracking accuracy on challenging 2P-IVM videos from the Leukocyte Tracking Database [212]. Additionally, the proposed

method allows using the same mathematical model to analyze different samples of the same experiment. These are for instance videos from samples labeled using the same markers, but at different time points or in different animals. By providing examples of desired cells across all the samples, the computer automatically identifies the common parameters for the analysis. Hence, it does not require to adapt brightness thresholds from experiment to experiment, with a positive impact on the reproducibility of results.

The application of the method is supported by a user-friendly software with a graphical interface that allows selecting which features to use according to the videos to be analyzed. Such software is available as a plugin for Imaris at <http://www.ltdb.info/tools>.

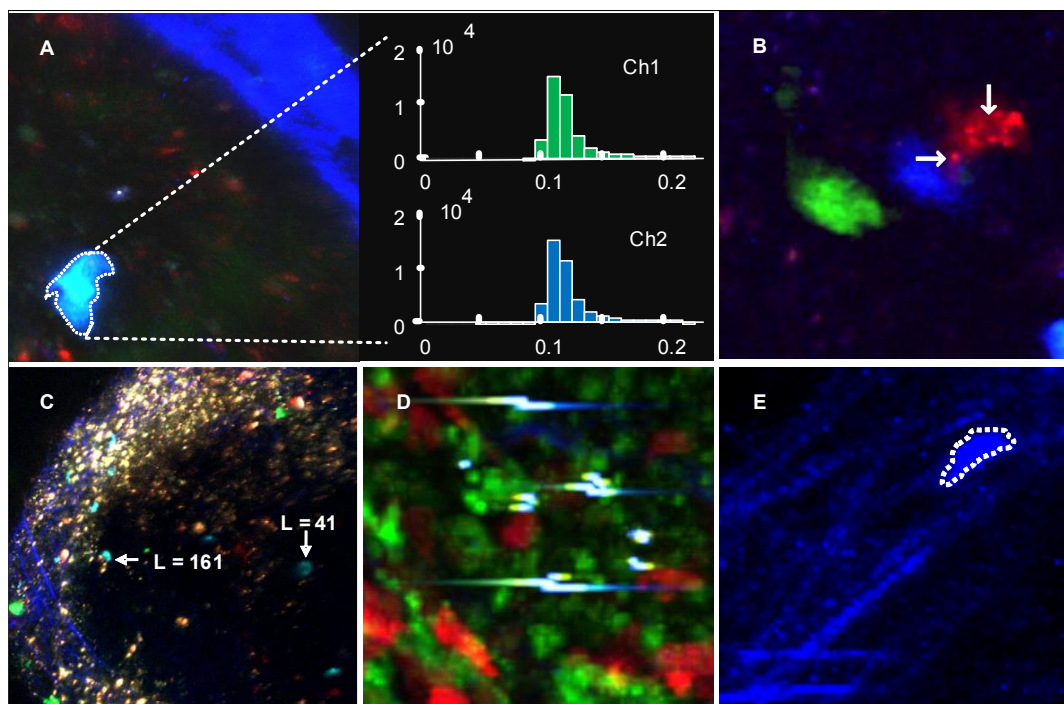


Figure 6.24. Challenges in 2P-IVM imaging of immune cells. **A.** CFP neutrophils emitting fluorescence in two acquisition channels with similar intensities. **B.** Neutrophils constitutively expressing GFP (green), CFP (blue) or labelled *in vitro* with CMTMR die (red). The CMTMR labelled cell shows non-uniform brightness and accumulation of fluorescent die in the lysosomes. **C.** Non spatially-uniform brightness showing a decrease of luminance (L) towards the bottom-right part of the image. **D.** Imaging artifacts due to saturation which were introduced by the movement of the animals and surgery defects. **E.** CFP neutrophil with elongated shape migrating on collagen fibers.

Results

Color features improve tracking of poorly visible cells. The method was applied on the video 10 from LTDB, which included B cells labeled with CTV (red) migrating in the spleen of a mouse with a green-autofluorescent background (Figure 6.25, A). Although the signal to noise ratio of the video is very high (> 43) and the majority of the cells appear bright, their brightness can vary over time because of the challenges previously described. This variability introduces tracking errors when cells temporarily appeared with a brightness level similar to the background, interrupting tracks and creating multiple track fragments of short duration (Figure 6.25, B, C blue). By contrast, the proposed method learned to distinguish poorly visible cells from the background. By using the imaging channel generated by the method, tracks were computed without errors (Figure 6.25, B, C yellow).

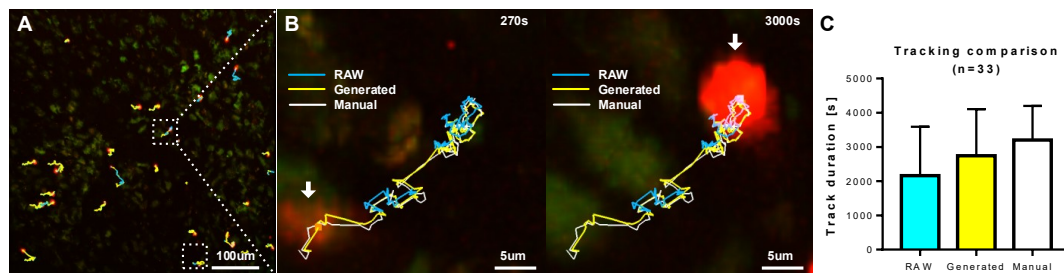


Figure 6.25. Tracking improvements for poorly visible cells. **A.** 2P-IVM micrograph showing CTV B cells (high red) in the spleen, migrating over an autofluorescent background visible (green/low red). **B** Sequence of micrographs, showing a cell appearing with different brightness levels. Lines are the tracks obtained with different methods, showing errors of automatic tracking using RAW data (blue line) when a cell appeared with low brightness (red arrow). By contrast, the tracks obtained using the generated colocalization channel (yellow line), correspond to manual tracking (white line). **C.** Comparison of the track duration on the entire video.

Color features improve separation of CFP cells from SHG background and GFP. Certain fluorescent cells are visible in multiple acquisition channels. The proposed method was applied to analyze the movement of neutrophils, adoptively transferred from a CK6/ECFP animal [100] to a CD11c/GFP animal [238] (Figure 6.26, A). Additionally, the acquired data included viral particles labeled with the DiD fluorescent dye [143].

In the videos acquired via 2P-IVM, the emitted spectrum of neutrophils was captured by two imaging channels centered on the green and blue wavelengths. However, these channels captured also the fluorescence from the CD11c/GFP

cells and the auto-fluorescence of collagen (second harmonic generation). The result was an overlap of the fluorescence emitted by the two cell populations and collagen (Figure 6.26, B) which resulted in poorly separable distributions (Figure 6.26, C). Additionally, the acquired videos exhibited spatially non-uniform brightness and brightness variation over time.

To separate neutrophils from the other cells and collagen fibers, each pixel was described using a set of features including the color of the pixel, the average color in a small circular neighborhood of radius = $3\mu m$, and the average color in a larger circular neighborhood of radius = $7\mu m$.

20 annotations were added by an imaging expert on the cells of interest, and 20 annotations on the other cells/background.

These annotations were used to classify every single pixel, creating an additional imaging channel which is specific for the neutrophils (Figure 6.26, D).

The usage of the computed colocalization channel improved the accuracy of cell tracking. Although differences in track duration are not statistically significant (Figure 6.26, E), the colocalization channel excluded unwanted objects such as not-motile pieces of collagen fibers (background) and GFP cells (Figure 6.26, F). Moreover, it improved the detection of poorly visible cells (Figure 6.26, G).

Path-features separate cells from cell debris. The annotations provided by the user in form of a line (Figure 6.27, A, yellow and red lines) were exploited, not only to detect pixels belonging to foreground or background but also to decompose images into superpixels (Figure 6.27, A, white lines). Considering a cell as a group of pixels, a line drawn between the pixels of the cell contains information on how these pixels are connected [213]. We used this information to find the optimal parameters to decompose an image into superpixels using SLIC [2]. Indeed, an error measure was estimated by counting how many superpixels were crossed by lines of multiple classes (Figure 6.27, B). Then, the compactness parameter of SLIC was optimized by minimizing the error estimate using sequential search.

A coarse decomposition on images into superpixels allowed to classify superpixels instead of single pixels, benefiting of the superpixel properties of boundary adherence and faster execution. The desired class (or target brightness value when using a linear prediction) can be estimated using the annotations provided by the user. If a superpixel is crossed by a line of desired objects, then its target value was set to 1. If a superpixel is crossed by a line of undesired objects, then its target value was set to 0. If a superpixel is crossed by multiple lines of different classes, then its value corresponds to the weighted average of the different

classes (Figure 6.27, C).

Considering an image as a graph, having pixels as vertices and color differences as edges, shortest-paths on the image are useful to analyze its content [90, 213]. To this end, we described each superpixel as a set of shortest-path between arbitrary points inside the superpixel (Figure 6.27, D, up). A support vector machine was then trained to classify each path independently. The final predicted class for each superpixel was given by a consensus voting on the classes of the paths inside the superpixel, using, for instance, the median of the predicted value (Figure 6.27, D, low).

This method allowed to distinguish between superpixels containing cells and particles of disrupted cells (Figure 6.27, E).

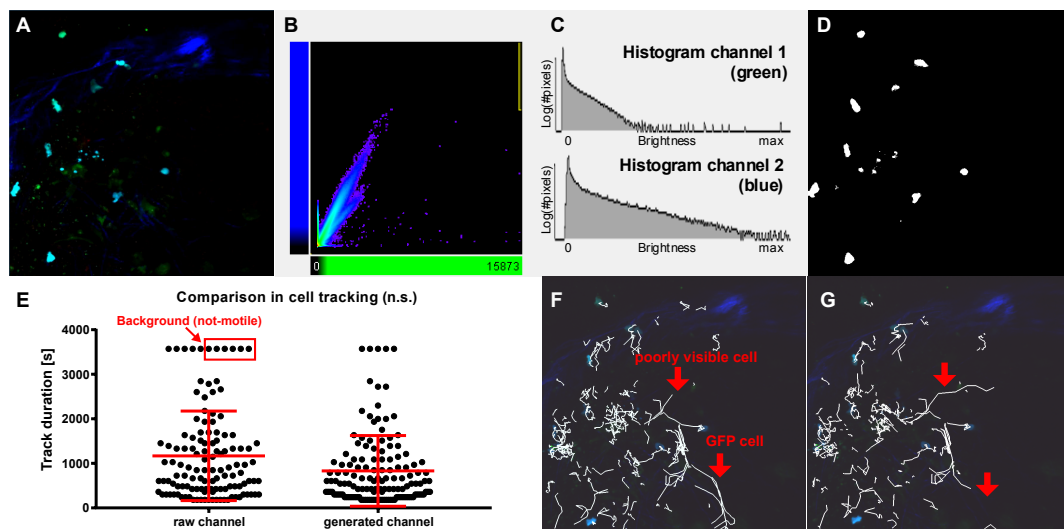


Figure 6.26. Improving tracking of non-specifically stained cells using pixel-wise features. **A.** 2P-IVM micrograph showing CFP neutrophils (light blue) in the popliteal lymph node of a CD11c/GFP animal (green) with collagen structures (blue - SHG) and viral particles (red - DiD). **B** Scatter plot showing the intensity of each pixel in two acquisition channels. The central tails are cells appearing in more than one imaging channel. **C.** Histogram of pixel intensity in two acquisition channels. **D.** Results (binary mask) of pixel classification. **E.** Comparison of track duration when using the raw channels or the generated channel. **F.** Tracks (white lines) obtained using the original imaging channels including errors (red arrows). **G.** Tracks (white lines) obtained using the generated colocalization channel specific for CFP cells.

Discussion

The proposed method relies on brushing, in line with other tools such as Ilastik [236] and Trainable WEKA Segmentation [14], asking the user to hand-draw

some lines on interesting points (i.e. on some cells of interest) and other lines on non-interesting points (i.e. other cells, background, etc.). By contrast to the aforementioned tools, the proposed method exploits the provided information differently. More precisely, the annotations provided by the user (which are in the form of a line), are used to build a graph-based representation of the microscopy data.

Such a graph is used by the proposed method to compute specific features to face the challenges of 2P-IVM videos of immune cells.

Then, machine learning is applied to the graph to find a mathematical model that maps every single pixel to a scalar value, expressing how much it is likely to be part of the generated imaging channel. Once this model has been obtained, it can be applied to the entire video. Considering annotations from multiple videos, the method has the potential to be applied to process multiple videos without requiring parameters tuning.

Recently proposed approaches based on neuronal networks with convolutional layers such as U-NET [74] achieved remarkable performances for cell detection in microscopy data, using only limited annotations from the user. With respect to these approaches, the proposed method uses hand-crafted features. Although this choice is less generic and might not be optimal, it allows the user to choose the more appropriate features to face specific challenges in 2P-IVM imaging of the immune system.

The selection of training points for supervised cell segmentation is typically left to the user. We identified that when adding to the training set background points which are in proximity to the cells of interest obtained a sharper response of the pixel classifier at the boundaries.

Methods

Intravital two-photon microscopy. Deep tissue imaging was performed on a customized up-right two-photon platform (TrimScope, LaVision BioTec). Two-photon probe excitation and tissue second-harmonic generation (SHG) were obtained with a set of two tunable Ti:sapphire lasers (Chameleon Ultra I, Chameleon Ultra II, Coherent) and an optical parametric oscillator that emits in the range of 1,010 to 1,340 nm (Chameleon Compact OPO, Coherent), with output wavelength in the range of 690-1,080 nm.

Mice. All animals were bred in-house or acquired from Janvier labs (C57BL/6). Mice were maintained under specific pathogen-free conditions at the IRB, Bellinzona and used following the Swiss Federal Veterinary Office guidelines. CD11c-GFP [238], CK6/ECFP [100]. All animal experiments were performed following the Swiss Federal Veterinary Office guidelines and authorized by the relevant institutional committee (Commissione cantonale per gli esperimenti sugli animali, Ticino) of the Cantonal Veterinary with authorization numbers TI28/17, TI02/14, and TI07/13.

Pixel-wise classification. Each pixel is classified as foreground or background, based on a predictive model trained on a few landmarks provided by the users. The predictive model is generated by training a Supported Vector Machine binary classifier using the radial basis function kernel. color features of each pixel, and in a circular neighborhood were used.

Superpixel-wise classification. Videos were initially decomposed in superpixels using SLIC [2]. SLIC was applied on each slice of the 3d stack independently. A fixed number of 1000 superpixels was used for the results reported in Figure 6.27. Compactness was automatically determined by the method, minimizing the number of paths of different classes in each superpixel. Each superpixel was described employing $K = 5$ paths. Each path was described as the color-sequence of the vertices. Paths shorter, or longer than 8 points, were interpolated to 8 points using average smoothing.

Implementation. The proposed method was entirely written in Matlab (Mathworks) as an extension for the bioimaging software Imaris and tested on the versions 7.7.2 to 9.3.1.

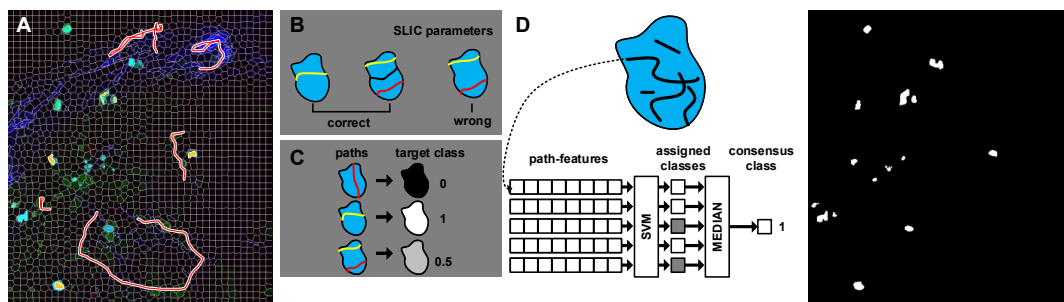


Figure 6.27. Path-based features for superpixel classification. **A.** 2P-IVM micrograph showing CFP neutrophils (light blue) in the popliteal lymph node of a CD11c/GFP animal (green) with collagen structures (blue - SHG) and viral particles (red - DiD). Yellow and red lines are the annotations provided by the users for desired and undesired points respectively. White lines are the borders of superpixel decomposition **B** The correctness of a superpixel decomposition is evaluated by minimizing the number of lines of a different class (yellow, red) in the same superpixel. **C.** Each superpixel is associated with a target value as the weighted average of the contained annotations. **D.** Path-based superpixel descriptor. (up) a superpixel is described as a set of paths. (low) each path is classified independently. then, the superpixel is classified as the mean of the classified paths. **E.** Output of superpixel classification, showing the disappearance of superpixels associated with cell debris (blebs).

6.7 De-bounced kiss and run analysis

De-bouncing is a technique to avoid multiple on-off transitions in electronic circuits due to noise. This is achieved by modeling on and off as two possible states and imposing the transition between the two states via distinct paths.

In this section, we describe a technique that uses de-bouncing to improve the detection of contacts between multiple cells.

The importance of cell-to-cell contacts is described in Chapter 1. In brief, this interaction of immune cells allows a precise exchange of information such as encountering clusters of proteins on the cell surface. Additionally, contacts are relevant for cell-mediated lysis. An example is provided in Figure 6.28 where a motile neutrophil forms a contact with a resident macrophage in the subcapsular sinus of the lymph node following influenza vaccination.

Unfortunately, contact detection in 2P-IVM data has some challenges. To describe these more in details let us define

- $t \in \mathbb{R}$: a time instant.
- $X_i(t) \in \mathbb{R}^{V \times 3}$: The pixels of a cell i at time t .
- "off": the state in which a is not in contact with any another cell
- "on": the state in which a cell is in contact with at least one other cell.
- τ : distance threshold [μm].
- $d(t) = \min \|X_i(t) - X_j(t)\| \forall j \neq i$: the minimum distance between the cell i and any other cell. Distance refers to the distance between two pixels.
- τ : an arbitrary distance threshold

Methods based on the distance between cells such as the Kiss and Run plugin of Imaris (Bitplane ag), typically detect a contact when $d(t) < \tau$.

However, the threshold τ is not robust to noise and imaging artifacts. Indeed, oscillations of laser power, as well as surface reconstruction errors, make the shape of cells highly variable over time. This turns into a high variability of the measured distance between cells. In our acquisitions this variation is in the order of μm , which is in the same order of cell diameter.

In this work, we modeled the on and off states as nodes on a graph, which are reached by different paths rather than thresholding (Figure 6.29a). Indeed, we defined a hysteresis window W that allows detecting the establishment and termination of contacts, with an adjustable threshold that depends on the history (Figure 6.29b). A distance greater than $\tau + W$ is required to terminate a contact,

while to initiate a contact a distance below $\tau - W$ is required.

This allows keeping the contact when the noise alters $d(t)$. The method makes the arbitrary choice of τ more robust and does not require smoothing over time. W can be chosen according to the reconstruction errors present in the images.

The method was used to detect rapid and transient contacts between neutrophils and dendritic cells in a murine trachea [207], exhibiting the ability to compensate fluctuations in cell reconstruction as well as the ability to detect brief contacts (Figure 6.30).

This method has been implemented in Matlab (r2017b) and released as a plugin for Imaris (Bitplane, v7.7.2).

In our future work, we will evaluate methods that do not require surface reconstruction for contact detection. These include an approach based on supervised machine learning for region classification. To this end, a dataset of manually annotated contacts is under development.

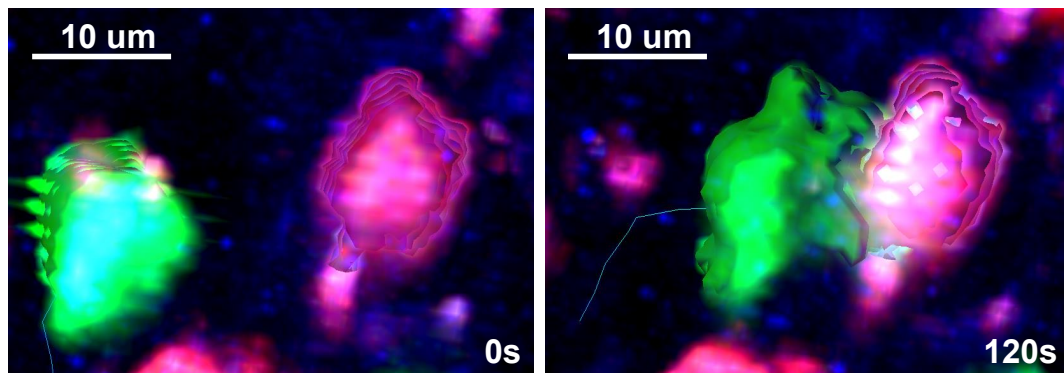


Figure 6.28. Example of contact formation (Neutrophil-Macrophage). 2P-IVM micrographs showing a motile neutrophil (UBC/GFP, green) forming a contact with a macrophage (CD169/RFP - red) in the subcapsular area of a lymph node. This sequence is extracted from the video LTDB007 [212]

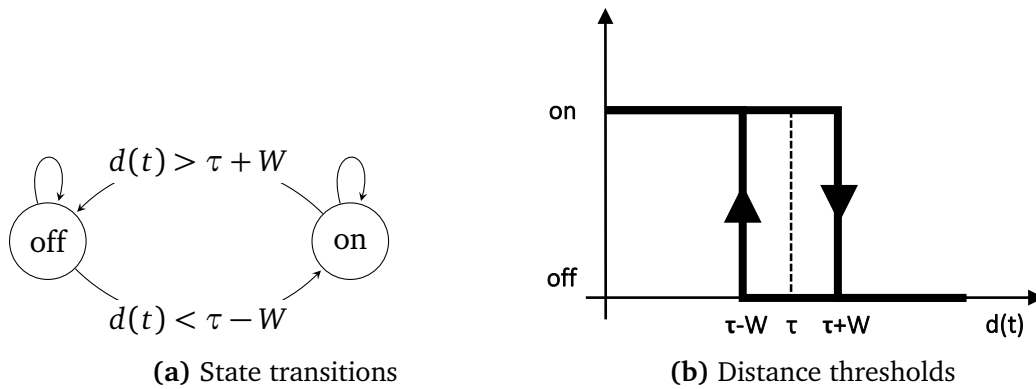


Figure 6.29. Contact detection with hysteresis. The transition between a not-in-contact state (off) and a in-contact state (on) requires two distinct distance constraints, associated with two different thresholds, to be satisfied.

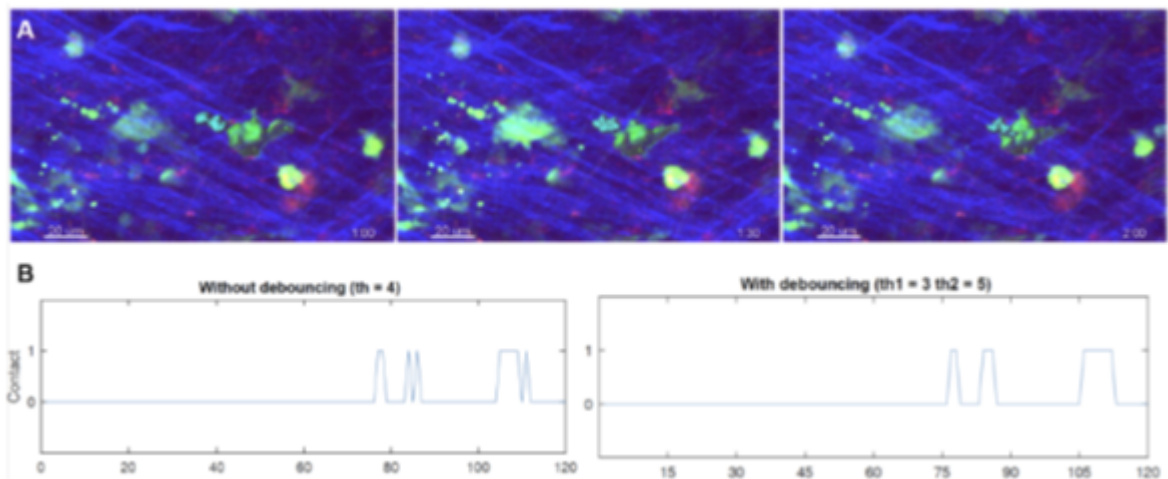


Figure 6.30. A. Brightness fluctuation. B. Contacts detected without de-bouncing (left) and with de-bouncing (right).

6.8 Swarm detection

Swarming is a supra-migration pattern of cells which results in the accumulation of cells in a specific area. Swarming involves the recruitment of cells towards the swarm itself, resulting in growth over time. Moreover, the swarm can migrate with motility patterns which are different from the motility of single cells.

The tracking of single cells in a swarm is challenging due to the numerous contacts and the loss of cell borders. Therefore, methods that do not require the tracking of single cells, are preferable to quantify swarm dynamics. Amongst these, methods based on intensity thresholding or manual annotation are typically used as described in Chapter 2.

Here, we propose the usage of clustering to identifying swarms as groups of connected pixels.

In Figure (fig:swarmboxes) report preliminary results obtained by using DBSCAN, with a meaningful density reachability threshold. This method has been released as a plugin for Imaris (Bitplane, v7.7.2).

Although the proposed method allowed to detect swarms by setting defined parameters, the number of cells in the tissue might be very different according to the experimental conditions. Moreover, the usage of colocalization for generating a specific channel for the cells of interests is required.

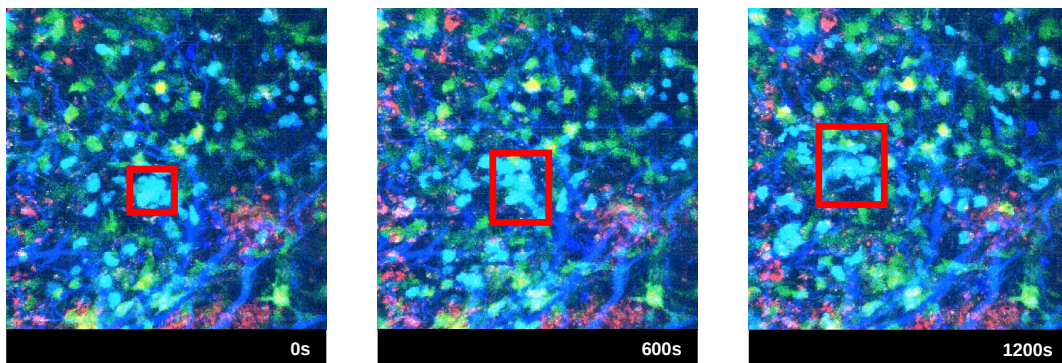


Figure 6.31. Swarm (red box) of neutrophils (light-blue), detected with a cell free approach based on clustering.

CHAPTER 7

Characterization of the dynamic behavior of neutrophils following influenza vaccination

Key computational aspects. We mapped a set of distinct actions to a set of different movement patterns. Then, we solved the inverse problem of associating one movement pattern to an action.

Key bioimaging aspects. This is one of the first studies using cell actions to quantify the behavior of cells.

We revealed important difference in cell actions over time which were not appreciable using standard motility measures.

Additionally, we applied cell-free methods(Optical Flow) to detect areas of high motility in the lymph node without requiring cell tracking.

Key biological aspects. The early response of neutrophils to influenza vaccination occurs in distinct phases. The dynamic behavior of these cells suggests a role in shaping the adaptive immune response, although other studies support that neutrophil depletion do not affect quantity nor affinity of antibody production.

In this chapter we report a study in which we applied the proposed methods, in combination with other imaging and molecular techniques to characterized the dynamic behavior of neutrophils in response to influenza vaccination.

We revealed for the first time, distinct activities performed by neutrophils in the early response to vaccination (< 12h). Additionally, we identified distinct phases and areas in the lymph node where these activities have place.

These findings support that neutrophils may have important implications in the shaping of adaptive immune response to viral infections.

This study has been published at *Frontiers in Immunology* on November 2019
<https://www.frontiersin.org/articles/10.3389/fimmu.2019.02621/full>

Neutrophils are amongst the first cells to respond to inflammation and infection. Although they play a key role in limiting the dissemination of pathogens, the study of their dynamic behavior in immune organs remains elusive. In this work, we characterize *in vivo* the dynamic behavior of neutrophils in the mouse popliteal lymph node after influenza vaccination with UV-inactivated virus. To achieve this, we used an image-based systems biology approach to detect the motility patterns of neutrophils and to associate them to distinct actions. We described a prominent and rapid recruitment of neutrophils to the PLN following vaccination, which was dependent on the secretion of the chemokine CXCL1 and the alarmin molecule IL-1 α . In addition, we observed that the initial recruitment occurred mainly via high endothelial venules located in the paracortical and interfollicular regions of the PLN. The analysis of the spatial-temporal patterns of neutrophil migration demonstrated that, in the initial stage, the majority of neutrophils display a patrolling behavior, followed by the formation of swarms in the subcapsular sinus of the PLN, which were associated with macrophages in this compartment. Finally, we observed, using multiple imaging techniques, that neutrophils phagocytize and transport influenza virus particles. These processes might have important implications in the capacity of these cells to present viral antigens.

Introduction

The innate immune system plays a critical role in protecting the host during the first hours that follow a new insult [7]. This process involves complex cell-to-cell and cell-to-pathogen interactions that are essential for the early recognition of the pathogen and the initiation of the adaptive immune response [145]. Although several advances have been made in linking the behavior of innate immune cells to the efficiency of the immune response [109], many questions remain open. This is mainly due to the dynamic nature of the aforementioned interaction patterns, which change over time and are distributed in space [169].

The lymph node (LN) has been the preferred organ to investigate *in vivo* the complexity of cell behavior and cell dynamics in relation to immune functions [237]. This organ is highly compartmentalized and is composed of specific regions, which facilitate the coordination of the innate and adaptive immune responses. Indeed, the architecture of the LN further promotes the dynamics of immune cell interactions, such as antigen trafficking between macrophages from different regions, which is critical for the final effector response [41, 44, 75, 115, 189], and the capture and presentation of antigen by LN resident dendritic cells (DC) [93, 245]. The migration of different cell populations to the specific regions of the LN follows a complex balance of chemokine gradients that orchestrate its architecture. For instance, CCL21 and CXCL12 act on the vascular endothelium to promote the recruitment of leukocytes via high endothelial venules (HEV) [82, 193]. After the extravasation process, CXCL13 and CCL19-21 direct B and T cells towards the B-cell follicle and the T-cell zone, respectively [9, 55, 81, 92, 98, 150].

Among the innate cells that migrate to the LN in inflammatory conditions, neutrophils constitute the first line of defense against pathogens [49, 157]. These cells have important immunological functions, such as the secretion of antimicrobial compounds [210], and play a key role in tissue cleaning and remodeling [133]. Neutrophils are abundant in the circulation in their mature form and are rapidly recruited from the bone marrow upon inflammation [85, 167] via post-capillary vessels [94, 182] or lymphatics [16, 94, 102, 222]. Neutrophil recruitment to the site of infection is a highly regulated process that involves the initial secretion of pro-inflammatory factors, released by activated macrophages and DC, which regulate the expression of adhesion molecules from vascular endothelial cells [133, 147]. Among the different inflammatory cytokines that have shown to be involved in this process, the interleukin-1 (IL-1) family [62, 159, 176] and the tumor necrosis factor (TNF) are some of the best-characterized [16]. In addition, many other chemokines and receptors are known to be involved [139].

Once recruited to the inflamed tissue, neutrophils can interact with lymphocytes and antigen-presenting cells (APC) influencing the adaptive immune response [133, 158, 183]. This was demonstrated in different inflammatory conditions in which neutrophils released B cell-stimulating molecules, such as BAFF or CD40L [217], or induced T cell proliferation and activation [158, 183, 258]. T cell response can be further orchestrated by neutrophils influencing both DC priming and T cell function via NETosis or release of granules [179]. Moreover, recent evidence has indicated that neutrophils can cooperate with DC, transporting anti-

gens to the site of T cell activation or acting as APC [1, 65, 157].

While the initial recruitment of neutrophils from blood has been extensively characterized [28], their post-recruitment behavior remains widely unknown. One of the few actions previously described regards the formation of aggregates or swarms [49]. This process involves the coordinated migration of cells towards a common target [49, 130, 134]. During the formation of swarms, the first neutrophils that are recruited can trigger a cascade of secondary chemoattractants, which amplify the recruitment of other neutrophils in a feed-forward manner [265]. The main signals triggering neutrophil influx and swarm formation were associated with tissue injury [122, 198]. However, in infection models other factors such as pathogen-derived compounds [230], or molecules released by dying neutrophils [140] can trigger swarm formation. The role of neutrophil swarms has been linked with microbicidal activity, tissue remodeling, and protection of uninfected tissues (45). However, it is unclear how individual neutrophils behave in the swarming environment. Recent studies using infection models have shown that neutrophil swarm growth is correlated with the removal of subscapular sinus macrophages [49]. This suggests an interplay between the two populations and a possible involvement of the resident cell population in the initiation and regulation of the process.

To better investigate the behavior of neutrophils following influenza vaccination, imaging techniques are of paramount importance. Among the available imaging methods, 2-photon intravital microscopy (2P-IVM), allows the long-term observation of cells in tissues of living animals. For this reason, in the last two decades, 2P-IVM has become an essential tool for the observation of immune-related mechanisms *in vivo*, highlighting unprecedented mechanisms related to cell migration and cell-to-cell interaction [237]. However, an interdisciplinary approach is required to analyze the imaging data generated by this technique. Indeed, the recently established image-based systems biology approach [78] combines microscopy data with computational methods to describe, quantify, and interpret complex biological processes, from imaging data. This combination of methods allowed for instance to uncover different T cell receptor signalling patterns [188] or different types of migration patterns [185] from the tracks of immune cells.

In this work, we employ a cutting-edge imaging analysis methodology to characterize *in vivo* the dynamics of neutrophil recruitment and their migratory patterns following vaccination with UV-inactivated influenza virus. Thus, we highlight the interaction of early recruited neutrophils with the resident macrophage popula-

tion involved in antigen capturing. Finally, we report how neutrophil behavior changes over time, using a new mathematical model that maps recurrent motility patterns of neutrophils to biological functions.

Results

Neutrophils are recruited to the draining lymph node via blood following influenza vaccination

To study the dynamics of neutrophil recruitment to the popliteal lymph node (PLN) we evaluated the total number of Ly6G+CD11b+ cells by flow cytometry during the first 24 h following footpad administration of influenza vaccine (UV-inactivated influenza virus, strain A/Puerto Rico/8/34). We observed a rapid increase in the number of neutrophils, reaching a peak at 12 h post vaccination (p.v.) (Figures 1A, B). Moreover, we found that the recruitment coincided with an increase in the expression of the early activation marker CD69 in these cells (Figure 7.1C). However, we found that, once in the LN, neutrophils downregulate the expression of the chemokine receptor CXCR4, one of the key regulators of leukocyte trafficking (Figure 7.1D). In addition, we also detect loss and shedding of the receptors CD44, CD62L, and CD49d, which are constitutively expressed in resting neutrophils (Supplementary Figure 7.1B-E). To better characterize the recruitment process, we performed confocal microscopy and quantified the presence of these cells in different areas of the PLN at 3 h p.v. (Figure 7.1E). We observed that, at this early time, neutrophils accumulate in the medullary and interfollicular areas (Figure 7.1F). Next, to evaluate if the recruitment occurs via the blood vessels or the lymphatic system, we monitored *in vivo* the process using intravital 2-photon and electron microscopy. Quantitative analysis of the 2-photon movies acquired in the paracortical blood vessels of LysM-GFP mice showed a prominent increase in the number of neutrophils during the first 2 h p.v. (Figure 7.1H). In addition, we observed the presence of multiple hotspots [114] in the wall of high endothelial venules (HEVs), suggesting a relevant role of these areas in the observed recruitment (Figure 7.1G, Supplementary Movie 1). To confirm this observation, we performed electron microscopy in a PLN HEV, which clearly showed neutrophils associated with the blood vessel endothelium as early as 2 h p.v. (Supplementary Figure 7.1A). Interestingly, intravital imaging of the lymphatic vessels, which drain the area in which the vaccine was administered (Figure 7.1I), showed a progressive increase in the number of neutrophils inside the lymphatic vessels during the first 4 h p.v. (Figure 7.1I, Supplemen-

tary Movie 2). However, this process appeared to be slower than the recruitment that occurs via blood, as we could not detect any neutrophil in the lumen of the lymphatic vessels during the first 2 h p.v. (Figure 7.1J).

The recruitment of neutrophils to the LN involves the cytokine IL-1 α and the chemokine CXCL1

In a previous study, we observed that the necrotic death of the LN macrophages after the administration of influenza vaccine was followed by the release of the potent inflammatory cytokine IL-1 α [44]. In this work, we confirmed that IL-1 α reaches an early peak (6 h) following vaccination and returns to basal levels at 24 h p.v. (Figure 7.2A). Moreover, we found that IL-1RKO animals show a significant inhibition of neutrophil recruitment in the PLN (Figure 7.2B). To confirm that IL-1 α was involved in neutrophil recruitment, we injected a dose of 1 μ g of recombinant IL-1 α in the mouse footpad, and observed that the injection of this cytokine alone was able to induce the recruitment of neutrophil in the draining PLN at 12 h p.v. (Figure 7.2D). In a previous work, we also observed that influenza vaccination induced a fast increase of the chemokine CXCL1 [44], a well-known inducer of neutrophil recruitment [216]. Therefore, to investigate whether the production of this chemokine was associated with LN macrophages, we measured the secretion of CXCL1 in animals in which LN macrophages (CD169-DTR + Diphtheria toxin) or monocytes (CCR2KO) had been depleted. We observed that, in both cases, the levels of CXCL1 were significantly reduced at 12 h p.v. compared to the control group (Figure 7.2C). However, CXCL1 levels were not completely abrogated. Interestingly, we also observed that the type-I interferon response following vaccination was necessary for the secretion of this chemokine, as IFNAR1KO animals showed a prominent inhibition of the levels of CXCL1 at 12 h p.v. (Figure 7.2C). Moreover, we also observed that IFNAR1KO animals display lower number of resident macrophages (Supplementary Figure 7.1H-I), while CCR2KO did not show any difference (Supplementary Figure 7.1G). However, DTX-treated CD169-DTR mice exhibited a complete depletion of LN macrophages after the administration of the toxin (Supplementary Figure 7.1F). Besides, footpad administration of recombinant CXCL1 (0.5 μ g/fp) alone was able to induce a significant recruitment of neutrophils in the popliteal LN (Figure 7.2D). However, we observed significant differences in the effect that both molecules had on the activation of neutrophils. Recombinant CXCL1, but not IL-1 α , was able to induce the expression of the early activation marker CD69 in the recruited neutrophils (Figure 7.2E). However, neutrophils recruited after IL-1 α adminis-

tration showed higher levels of MHC II compared to the ones recruited following treatment with CXCL1 (Figure 7.2F).

Neutrophils phagocytize and transport influenza virus

To examine the capacity of neutrophils to phagocytize UV-inactivated influenza virus (UV-PR8), we performed electron microscopy. Indeed, results showed that a number of neutrophils phagocytized necrotic vesicles containing the UV-PR8 particles (Figure 7.3A, Supplementary Figure 7.1J). To quantify the percentage of neutrophils that phagocytized the virus, we labeled inactivated influenza virus with the lipophilic dye DiO and performed flow cytometric analysis. We found that 15 % of the neutrophils were positive at 12 h p.v. (Figure 7.3B). Finally, to assess the capacity of neutrophils to transport phagocytized influenza particles, we performed 2P-IVM in LysM-GFP mice. The dual tracking of DiO-UV-PR8 and LysM-GFP neutrophils confirmed that, after phagocytosis, neutrophils were able to transport the phagocytized virus within the LN during 7 h (Figure 7.3C, representative track, Supplementary Movie 3). A volumetric reconstruction further confirmed that viral particles were internalized, with a distance from the cell centroid smaller than the cell radius (Figure 7.3D).

Neutrophils change their motility soon after being recruited to the LN

To identify the areas of the LN with higher activity, we acquired low-magnification 2P-IVM movies (Figure 7.4A) in a non-fluorescent recipient animal by adoptively transferring neutrophils from a CK6/ECFP donor. Moreover, to visualize the vasculature and the LN macrophages, we administered fluorescein isothiocyanate-dextran (200 kDa) and CD169-PE antibody, respectively. Initially, we imaged an area located in the paracortex of the LN (Figure 7.4A, dashed line), characterized by a high vascularization and active recruitment of neutrophils. Representative snapshots of the acquired movies are shown in Figure 7.4B-D, while the tracks of the analyzed cells are plotted in Figure 7.4E-G. A qualitative analysis of cell migration showed that at 30 min p.v. neutrophils generated long tracks in four main directions, which were associated with their movement inside the blood vessels (Figure 7.4E, Supplementary Movie 4). Once outside the blood vessel (75 min p.v.), neutrophils did not follow any preferential direction (Figure 7.4F, Supplementary Movie 4), while at later time points (135 min p.v.) they displayed a collective migration directed towards an area in which cells started to

cluster (Figure 7.4G, Supplementary Movie 4). Next, we quantified cell migration by computing measures based on entire tracks (Figure 7.4H). We observed a significant change in neutrophil motility occurring within 30-75 minutes p.v.. Indeed, neutrophils at 30 min p.v. were faster, more directional and traveled longer distances with a lower arrest coefficient, compared to later time points. However, no significant difference was observed between 75 and 135 min. These findings, using track-based measures, confirmed a change in the overall motility only after recruitment. Nevertheless, the analysis of the instantaneous speed of neutrophils showed a high variance (Figure 7.4I, left), which was associated with a variable mean over time (Figure 7.4I, right, black line). The observed variability in speed arises from both the differences between distinct cells at the changes of speed that a single neutrophil undergoes over time. An example is provided in Figure 7.4J, where the track of a neutrophil (left) and the plot of the instantaneous speed (right) over time are shown. This example shows the transition between two distinct behaviors that are characterized by low speed and high speed, respectively.

Neutrophils change actions over time

To describe the long-term and time-varying behavior of each individual neutrophil, we defined, according to previous studies [18, 84, 130, 138], five distinct cellular actions based on the motility patterns visually identifiable in the videos (Figure 7.5A). We named them as flowing, arrested, patrolling, directed migration and swarming (Figure 7.5A). To detect these actions from imaging data, we divided the track of each neutrophil into multiple fragments (tracklets). Then, we computed morphological and motility measures on each of them. By defining a gating strategy on these measures, each tracklet was associated with an action (Figure 7.5B). Considering each tracklet as a data-point, the proposed gating strategy identified five distinct populations corresponding to the different actions (Figure 7.5C). Following this analysis, we observed that neutrophils perform different actions at different time points (Figure 7.5D). At homeostasis, neutrophils were mostly flowing. Hence, circulating within blood vessels with high speed and directionality (Supplementary Figure 7.2, Supplementary Movie 8). Then, during the first 30 min p.v. neutrophils were mostly associated with capillaries, displaying both flowing and directed migration. This behavior changed when neutrophils started to migrate within the LN (30 to 75 min p.v.), displaying primarily patrolling, directed, and arrested behaviors. Other neutrophils exhibited a temporarily directed migration. Finally, at 2 h p.v., cluster formation was the predominant neutrophil behavior. This was associated with temporar-

ily directed migration of neutrophils either towards a swarm under formation or from a previously formed swarm to another target. In addition, a small population of neutrophils was arrested (Figure 7.5D). These results confirmed that the time-varying motility of neutrophils can be represented as a sequence of distinct actions which, in turn, are associated with distinct biological processes.

Following vaccination neutrophils form swarms in the SCS associated with SCS macrophages (SSM)

To identify the areas in the LN with high cell motility we performed low magnification (10X) 2P-IVM, which allowed the visualization of the whole organ (Figure 7.6A, Supplementary Movie 5). Cells were tracked for a period of 30 min and the percentage of cells migrating from one region to another was computed. We found that at early time p.v. most of the neutrophil migration occurred between the interfollicular (IF) and the SCS areas (Figure 7.6B). To evaluate the presence of areas associated with high neutrophil motility, we measured the average pixel velocity by optical flow, a computer vision method that does not require cell tracking [124]. The results showed the presence of hotspots with high motility, which are depicted as lighter areas in the pixel velocity heat map (Figure 7.6C). These hotspots were localized in the SCS and IF area. Interestingly, the hotspots were associated with the regions where swarms were formed (Figure 7.6D-E). To fully characterize neutrophils swarming behavior, we recorded movies in the SCS region of the LN using different magnifications. Low magnification movies from LysM-GFP mice showed that neutrophils formed large and multiple swarms in association with regions enriched with macrophages (Figure 7.6F, Supplementary Movie 6). Such swarms grew in size over time (Figure 7.6G). Furthermore, neutrophils involved in the swarms often changed their directionality from one cluster to another (Figure 7.6F). In mathematical terms, the average dynamic of the observed swarms was best described by a sigmoidal function (Figure 7.6H), suggesting that swarm formation undergoes an initial steady state, a growing phase and a plateau before its resolution. Moreover, we observed that the decreasing swarms showed a resolution period of approximately 30 min. To better visualize individual neutrophil behavior, as well as possible interactions with resident macrophages, we acquired high-magnification videos starting from 5-7 h p.v.. These videos confirmed that swarm formation occurs in proximity to SSM (Figure 7.6I, Supplementary Movie 7), with highly directed and skewed trajectories (Figure 7.6J), and the majority of the cells approaching the center of the swarm (Figure 7.6K). Moreover, using high-magnification 3D reconstruction and

EM, we confirmed that neutrophils were located in close proximity to SSM clusters (Figure 7.6L-M). To investigate the involvement of SSM in the formation of swarms we quantified the accumulation of neutrophils in areas proximal or distal to SSM. Interestingly, the number of neutrophils fluctuated over time outside the SCS area (Figure 7.6N). By contrast, it constantly increased in areas rich in macrophages (Figure 7.6O) exhibiting the sigmoidal growth rate observed during swarm formation.

Discussion

In this study, we investigated *in vivo* the behavior of neutrophils that are recruited to the draining LN following influenza vaccine administration. Neutrophil recruitment has been previously described in several infection models [28, 49, 102, 140, 152]. However, despite the critical role of these cells in pathogen clearance and the initiation of the inflammatory response, their specific behavior upon vaccination remains poorly studied. In this work, we observed a rapid recruitment of activated and mature neutrophils in response to vaccination with an inactivated influenza virus. Although the role of neutrophils against influenza has been extensively studied in the lung [250], this is the first time that their behavior is characterized in the draining LN in the early response to influenza vaccine administration.

The way neutrophils enter the LN remains controversial. Different studies have suggested that neutrophils get recruited mainly via the HEV [28, 122]. However, other authors have stated that neutrophils access the LN mainly via the lymphatic vessels [16, 102, 222]. Our data suggested that influenza vaccination induces an initial recruitment of neutrophils via HEV, followed by a minor, secondary wave through the lymphatics that drain directly from the injection site to the sentinel LN. It is tempting to speculate that the type of recruitment might influence the function of the recruited cells. However, future experiments need to be performed to study differences in the behavior and the function of neutrophils that arrive through different routes. In addition, we found that a percentage of neutrophils downregulates the expression of CXCR4, a marker known to be involved in neutrophil mobilization from the bone marrow and trafficking through the circulation to the site of inflammation [71, 161]. Moreover, consistently with neutrophils activation, we detected a downregulation of multiple cell surface-receptors linked with leucocyte trafficking and accumulation [129, 131]. By contrast, these receptors were expressed at high levels in resting neutrophils

[248].

Neutrophil localization within the LN after pathogen challenge is tightly linked to their specific function. In a previous study we observed that macrophages, located within the subcapsular sinus (SCS) and the medullary area of the LN, capture and retain influenza virus following vaccination. Interestingly, in both the areas, macrophages undergo necrosis-like cell death after viral capture that leads to their progressive decline [44]. Our study demonstrated that neutrophils migrate towards the SCS progressively, probably in response to chemoattractant signals released by the necrotic macrophages, as suggested by other models based on infection [49, 122]. Among the different signals released by the necrotic macrophages, IL-1 α is one of the most potent [44]. In this work, we have demonstrated that IL-1 α and its receptor IL-1R are involved in the initial recruitment of neutrophils to the LN. Other authors have previously confirmed the role of IL-1 β and IL-1R in the recruitment of neutrophils to the infection site [27, 168, 176]. However, we could not observe any significant secretion of IL-1 β or activation of the inflammasome pathway in the LN following influenza vaccine administration [44]. Therefore, we can conclude that the observed absence of neutrophil recruitment in the IL-1R-defective mice was associated with IL-1 α released by macrophages.

Moreover, we confirmed that CXCL1, a mouse homolog of human IL-8, was also involved in the recruitment of neutrophils to the LN. The source of this chemokine needs to be further investigated but we speculate that DC and activated macrophages could be the main producers [21, 59]. Indeed, the secretion of CXCL1 was almost abolished in mice lacking type-I interferon (IFN) receptors, suggesting an important role of LN macrophages and DC, the main producers of IFN, in this process. Thus, absence of IFN-I signaling in IFNARKO mice partially reduced the total number of CD169+ macrophages compared to the control, although it did not significantly impair the number of medullary macrophages. However, the specific elimination of macrophages reduced only partially the expression of CXCL1. Interestingly, our findings demonstrated that subcutaneous administration of IL-1 α and CXCL1 induced the mobilization of neutrophils toward the LN. Nevertheless, we showed that CXCL1 induced the expression of CD69, a marker associated with the early activation, while IL-1 α administration increased the expression of MHCII, suggesting a potential role of neutrophils in antigen presentation, as previously described in other models [255, 258]. Neutrophils are sensitive to a vast array of chemoattractants that regulate their migration and infiltration to inflamed tissues. Indeed, Chou et al. [48], previously

described this process as a cascade that require a multitude of chemokines, such as MIP-1 α , MIP-1 β and MIP-2. Therefore, will be of interest to explore the complex nature of signals that mediate neutrophils recruitment post influenza vaccination.

In the early phases of recruitment, we found that neutrophils exhibited significant differences, resulting in reduced speed, directionality, and displacement, while increased arrest coefficient. These findings suggest that the recruited neutrophils actively migrate and increase cell-to-cell interactions. Previous studies have associated the increase in the arresting of neutrophils with the oxidative burst (20) in which reactive oxygen species are generated. Antigen presentation might also influence the speed of neutrophils. Indeed, other authors have reported that neutrophils can serve as antigen presenting cells (APC) during influenza infection in mice [112, 145, 240]. In support of the notion that neutrophils might act as APC in the context of influenza vaccination, we observed that they actively phagocytize influenza particles, which were previously associated with necrotic macrophages. Moreover, we could observe an increase in the expression of MHCII in these cells after exposure to IL-1 α which is released by the dying macrophages [44]. However, it is not clear if the APC function of neutrophils might occur in the LN or, as suggested by other authors [202], in other immune-relevant organs, such as the spleen. In support of the former, we observed that neutrophils are able to transport influenza particles for long distances in the LN [106]. This suggests that neutrophils can carry viral particles to specific areas as described for other infection models [38, 196, 220]. Therefore, the potential capacity of the neutrophils to transport viral particles to other organs, as well as the capability of these cells to function as APC, need to be further investigated.

Our findings supported that neutrophil behavior is a dynamic process, with significant differences observed already within the first 3 h p.v.. These findings were in agreement with previous *in vitro* studies in which the motility of neutrophils was found to change within minutes in response to both external (i.e. chemical gradients) and internal factors (i.e. directional memory) [101].

Among the different actions that occur within the first few hours after vaccination, we identified the formation of swarms, which is a process previously associated with tissue injury [140, 198]. In this study, we showed that neutrophils swarms are formed in the SCS, co-localizing with the resident SSM population. The characterization of swarm dynamics showed consistent growth rates, sug-

gesting that they are comparable to smaller transient swarms observed in other infection models [49]. Regarding the factors that generate this behavior, tissue injury, neutrophil secondary cell death and the release of the chemoattractant LTB4 have been previously proposed as triggers of swarm formation [140]. Although LTB4 is mainly secreted by neutrophils, macrophages can also produce this molecule [140]. These observations, along with our *in vivo* evidence of swarms association with SSM, suggest a close association between the two populations. In previous studies, swarm formation in the SCS was linked with the removal of resident SSM [133]. We speculate that macrophage death contributes to the initiation, amplification, and stabilization of neutrophil swarming and recruitment via the release of different chemoattractants, such as IL-1 α . However, the redundancy in the recruitment process of neutrophils, with the involvement of more than 30 chemokine receptors [139], makes the effect of a single molecule difficult to be distinguished from other cues that regulate neutrophil chemotaxis.

Regarding the swarm dynamics, a direct correlation between swarm size and tissue injury severity has previously been shown [209]. Furthermore, the number of neutrophil secondary death is also proportional to the swarm size [140]. It would be compelling to determine whether influenza vaccination induces the death of neutrophils in a way similar to the previously described macrophage death [44].

The quantification of the spatio-temporal migration and interaction patterns of cells from 2P-IVM data presents specific challenges. These arise from the difficulties both in cell tracking and in describing a complex biological system by means of numerical values. The difficulties in cell-tracking, arise from both the textureless appearance and the complex biomechanical properties of neutrophils, including high plasticity and formation of contacts. These problems are amplified by the high number of cells that need to be tracked. To facilitate individual tracking, the number of fluorescently-labeled cells can be reduced by performing an adoptive transfer of a limited number of fluorescently labeled cell to a non-fluorescent recipient animal. This justifies the differences in cell number between the experimental setup using LysM-GFP transgenic model or the adoptive transfer of CFP-neutrophils into wild type animals prior to imaging shown in Figure 7.1 and in Figure 7.6 respectively.

In this study, we described an alternative way to analyze cell motility in 2P-IVM videos when single cells cannot be tracked. Indeed, by computing pixel velocity, we identified the areas in the LN, called hotspots, in which cells were more active.

The advantage of pixel-based measures with respect to track-based measures is that neither manual nor automatic single-cell tracking is required. Therefore, this allows the analysis of videos with a high number of cells.

The quantification of neutrophil behavior from 2P-IVM data is further challenged by the lack of mathematical models that make their motility patterns interpretable. Although optical probes can be used to transform a biological function into a light signal, their application for 2P-IVM remains challenging [31].

To address this issue, we developed a new method of analysis that brings two main advantages with respect to the previously used methods: capturing the time-varying motility of cells and making results interpretable. Indeed, the available methods to assess cell motility can lose information during the averaging process [101]. Additionally, although several measures of cell motility were defined [24], the connection of their values to a biological meaning remains to be addressed by the investigator. When applied to our data, the standard track-based measures did not capture significant differences in neutrophil behavior. However, the new method of analysis, proposed in Figure 7.5, identified distinct actions, which changed over time, indicating clear differences in the functions of the analyzed cells. Although in this study we defined five distinct actions of neutrophils, alternative actions could be also defined in future studies, such as apoptosis or NETosis [196], amongst others.

The proposed method allowed to perform a dynamic *in situ* cytometric analysis as proposed in previous studies [31, 188] where distinct phenotypes of cells were identified in 2P-IVM data. However, a set of gates correlating phenotypes to actions were not defined previously. By contrast, our action-based model allowed to define a precise set of gates to interpret the results. It would be compelling to define an extended list of actions that neutrophils can perform or automatically unravel populations of cells expressing distinct phenotypes using data mining methods such as clustering algorithms [213, 268]. Additionally, advanced computer vision methods can be applied to detect more complex behaviors, both on shorter and longer periods of time considering other parameters such as cell morphology, context, and space-time structures. This is in line with recent works that aim to recognize cellular motion phenotypes in *in vitro* cultures [277] or human actions using deep machine learning methods [276].

In conclusion, to analyze the complex dynamics of neutrophils in intravital imaging data, an interdisciplinary effort is required. By combining different imaging methodologies, molecular techniques, and pattern recognition methods, we identified distinct behaviors of neutrophils in the early response to influenza vac-

ination. These behaviors are the expression, of the biological mechanisms that follow influenza vaccination. In addition, we identified an interaction between neutrophil and macrophages, which might be important in terms of the capacity of the former to capture and present antigen.

Methods

Mice. All animals were bred in-house or acquired from Janvier labs (C57BL/6). Mice were maintained under specific pathogen-free conditions at the Institute for Research in Biomedicine, Bellinzona and used in accordance with the Swiss Federal Veterinary Office guidelines. The following transgenic mice were used: LysM-GFP [51], IL-1R KO [137], TLR3 KO, Myd88 KO [111], CCR2 KO, IFNAR KO [192], CD169DTR [181], CD11c-YFP [151], CK6/ECFP [100], UBC-GFP [226]. All strains were on C57BL/6 background. All animal experiments were performed in accordance with the Swiss Federal Veterinary Office guidelines and authorized by the relevant institutional committee (Commissione cantonale per gli esperimenti sugli animali, Ticino) of the Cantonal Veterinary with authorization numbers TI28/17, TI02/14 and TI07/13.

Virus production inactivation and labeling. Influenza virus strain A/PR/8/34 was grown for 3 days in the allantoic cavity of 10-day embryonated chicken eggs. To remove cellular debris the allantoic fluid was harvested and centrifuged at 3000 rpm for 30 min. Virus was subsequently purified twice in a discontinuous sucrose gradient at 25,000 rpm for 90 min. Virus stocks were quantified by tissue culture infective dose assay (TCID₅₀). To be inactivated, viral suspensions were placed under the UV lamp at a distance of 15 cm for 15 min. For the labeling of UV-inactivated influenza virus, 50 mg/ml of DiD or DiO dye was added to the viral suspension and incubated for 20 min at RT. After that, virus was subsequently purified by centrifugation as mentioned before.

Antigen administration and injections. 10⁶ plaque-forming units (PFU) of inactivated virus per footpad in a final volume of 10 μ L were injected into anesthetized mice at different time points prior to LN collection. Macrophage depletion from CD169DTR mice was established by intraperitoneal (i.p.) injection of 10 μ g/kg of diphtheria toxin (Sigma-Aldrich) a day before vaccination. Recombinant murine IL-1 α (1 μ g/fp) and murine CXCL1 (0.5 μ g/fp) were reconstituted in sterilized PBS and injected in a final volume of 10 μ l 12 h before LN collection. For *in vivo* labeling of cells, mice received subcutaneous injection of

1 μ g of fluorescently-labeled α CD21/35, α F4/80 and α CD169/footpad (Biolegend), 3 h before image acquisition. To label the blood vessel mice were injected intravenously with 70 kDa Rhodamin B isothiocyanate-Dextran or Fluorescein isothiocyanate-Dextran solution as described before [206].

Flow cytometry. Neutrophil influx to the PLN was monitored using flow cytometry. PLN were collected, disrupted with tweezers, and digested for 10 min at 37 °C in an enzyme mix composed of DNase I (0.28 mg/ml, Amresco), dispase (1 U/mL, Corning), and collagenase P (0.5 mg/mL, Roche) in calcium- and magnesium-free PBS (PBS-) followed by a stop solution composed of 2 mM EDTA (Sigma-Aldrich) and 2% heat-inactivated filter-sterilized fetal calf serum (Thermo Fisher Scientific) in PBS- (Sigma-Aldrich). Fc receptors were blocked (α CD16/32, Biolegend) followed by surface staining and analyzed by flow cytometry on a LSRFortessa™ (BD Biosciences). Dead cells were excluded using ZombieAcqua fixable viability dye (Biolegend) and data were analyzed using FlowJo software (TriStar Inc).

Antibodies. In this study cell suspension was isolated from harvested organs and immunostained with various combinations of the following fluorescence-conjugated antibodies: α B220 (RA3-6B2), α CD3 (17A2), α CD11b (M1/70), α CD69 (H1.2F3), α I-A/I-E (M5/114.15.2), α Ly-6G (1A8), α CD21/CD35 (7E9), α F4/80 (BM8), α CD169 (3D6.112), α CD16/32 (93) (all from Biolegend).

Cytoplex assay. The concentration of various cytokines and chemokine in the lymph was determined by LEGENDPlex assays (Mouse Proinflammatory Chemokine Panel and Mouse Inflammation Panel; Biolegend) according to manufacturer instructions. Briefly, popliteal LNs were collected and carefully disrupted in 75 μ L ice-cold phosphate buffer, minimizing cell rupture. The suspension was centrifuged at 1,500 rpm for 5 min, and the supernatant was collected. 25 μ L supernatant was used for the protocol following the manufacturer instructions. Samples were analyzed by flow cytometry on an LSRFortessa (BD Biosciences), and data were analyzed using LEGENDPlex software (BioLegend).

Immunohistology and microscopy. Mice were euthanized, PLN harvested and fixed in 4 % PFA at 4 °C for 4-6 h. Organs were embedded in 4 % low gelling agarose (Sigma-Aldrich) and 50 μ m sections were cut with Leica VT1200S vibratome (Leica Microsystems), blocked with proper sera and stained with the indicated antibodies in 0.05 % Tween-20 in 0.5 % BSA PBS- for two days at 4

°C shaking. More details are reported in the antibodies section. Immunofluorescence confocal microscopy was performed using a Leica TCS SP5 confocal microscope (Leica Microsystems). Micrographs were acquired in sequential scans and merged to obtain a multicolor image. Images were processed using Imaris software (Bitplane AG).

Electron microscop. PLN were collected and fixed in 2 % formaldehyde 2.5 % glutaraldehyde in 0.1 M sodium cacodylate buffer (pH 7.4) overnight at 4 °C. LN were washed in 0.05 M maleate buffer (pH 5.15) and stained for 2 h in 1 % uranyl acetate in maleate buffer. The samples were dehydrated by incubation for 15 minutes in ethanol water (60 %, 90 %, 100 %) and embedded in Epon.

Intravital two-photon microscopy. Deep tissue imaging was performed on a customized up-right two-photon platform (TrimScope, LaVision BioTec). Two-photon probe excitation and tissue second-harmonic generation (SHG) were obtained with a set of two tunable Ti:sapphire lasers (Chameleon Ultra I, Chameleon Ultra II, Coherent) and an optical parametric oscillator that emits in the range of 1,010 to 1,340 nm (Chameleon Compact OPO, Coherent), with output wavelength in the range of 690-1,080 nm.

Imaging was performed in the PLN as previously described[178].

Image analysis and data processing. Cell detection, tracking and volumetric reconstruction from 4D 2P-IVM data were performed using Imaris (Oxford Instruments, v7.7.2). Raw data generated from Imaris were further processed and analyzed with a custom Matlab script. Cell tracks were generated semi-automatically and curated to correct errors (i.e. jumps or non detected cells). Tracks with a duration less than 5 points or 300 s were excluded from the analysis. Videos were stabilized using the drift correction functionality when needed, compensating for translational-drift only and by cropping the largest common area in the videos. Standard measures of cell motility were computed using Imaris. These include Track duration (time interval between the first and the last time points in which a cell is tracked), Track Length (total length of the cell trajectory), Track Speed Mean (Track length / Track duration), Track Displacement (length of the vector from the first to the latest centroid position of the cell), Track Straightness (Track Displacement / Track Length), Speed (instantaneous speed computed between adjacent time points).

Spectral unmixing. An additional imaging channel, specific for the cells of interest was generated by classifying each pixel as foreground or background. This was

achieved using the Coloc functionality of Imaris in combination with a custom supervised machine learning method for pixel classification implemented in Matlab as described in [215]. This method trains a Supported Vector Machine (SVM) to classify pixels as background or foreground on the basis of examples provided by the user. A minimum of 20 and a maximum of 60 training points were provided for each video. To differentiate between background and foreground the following features were used: Local color, Gaussian-weighted average color in a neighborhood ($\sigma = 3 \mu\text{m}, 7 \mu\text{m}$).

Quantification of cell density in High Endothelial Venules (HEV) and Lymphatic vessels (LV). The density of neutrophils in a vessel presented in Figure 7.1 is defined as the ratio of the number of cells inside a vessel and the volume of the vessel itself. The density of neutrophils in HEV was computed at different time points inside a selected HEV which was visible for the entire duration of the acquisition (3 hours). HEV were labeled by the i.v injection of 70 kDa Rhodamine B isothiocyanate-Dextran. Cells inside the HEV were manually counted every 300s. The volume of the HEV was estimated as the volume of a cylinder, by measuring the average diameter in the xy plane and the average height along z and the length of the vessel. The density of neutrophils in LV at the injection site were computed in a LV visible for the entire duration of the acquisition (4 hours). Draining LV were labeled by the subcutaneous injection of DiD-labeled virus and 70 kDa Rhodamine B isothiocyanate-Dextran. Cells were detected and counted automatically using the Spots function of Imaris. The volume of the LV was estimated via volumetric reconstruction using the Surfaces tool of Imaris.

Estimation of distance of the virus particle with respect to cell centroid.

To confirm the internalization of the viral particles by neutrophils, the distance of the particles from the cell centroid was computed and compared to the cell radius. Cell radius was estimated via volumetric reconstruction of the cell surface and computed as the radius of a sphere having the same volume of the cell. Pixel velocity. The average velocity of pixels presented in (Figure 7.6, A) was estimated via a custom Matlab script that computes optical flow as described in [124]. Only the channel where the neutrophils were visible was used for optical flow estimation. To address the lack of texture of immune cells which leads to an aperture problem, Tikhonov regularization was used while computing the flow (Tikhonov constant = 40). Additionally, outliers were removed by Gaussian smoothing ($\sigma = 7$) followed by the saturation of the bottom 1 % and the top 1 % of all pixel velocity values (set to the minimum and maximum values

respectively).

Pixel velocity. The average velocity of pixels presented in (Figure 7.6, A) was estimated via a custom Matlab script that computes optical flow as described in [124]. Only the channel where the neutrophils were visible was used for optical flow estimation. To address the lack of texture of immune cells which leads to an aperture problem, Tikhonov regularization was used while computing the flow (Tikhonov constant = 40). Additionally, outliers were removed by Gaussian smoothing ($\sigma = 7$) followed by the saturation of the bottom 1 % and the top 1 % of all pixel velocity values (set to the minimum and maximum values respectively).

Activity recognition. Gating strategy. We mapped a biological meaning (actions) to specific ranges of instantaneous motility measures. This allowed both to describe the dynamic behavior of neutrophils as a series of actions and provided a suggestion on the biological function of each neutrophil at different time points. However, the problem of identifying one action from a range of measures (gate) is an ill-posed problem which often arises when characterizing a complex biological system from experimental data [99]. Indeed, not all the possible actions are known and several actions might exhibit similar motility measures leading to an undetermined solution. To solve this issue, we defined gating thresholds that minimize the overlap between distinct actions and we selected one action out of the multiple possible solutions, based on an arbitrary priority order. Although the gates used to detect actions are subjected to the bias of the investigator, these can be easily adapted according to the experimental settings and based on a priori knowledge.

Software implementation A custom Matlab script (Supplementary Data File 1) was used to automatically compute instantaneous motility measures and detect actions. This script decomposes each track into track fragments (tracklets) with a fixed duration of 500 s (approximated to 17 time points with a sampling interval of 30 s). From a track with total duration $T_d \geq 17$ time points, $K = (T_d - 17) + 1$ tracklets were extracted by a sliding window. For the analysis of neutrophils actions in homeostatic conditions and due to the high speed of cells flowing in large blood vessels, the time window was reduced to 5 time points and the sampling interval of the microscope decreased to 20s. Then, the script computes the following measures on each tracklet. Displacement: distance between the initial and the final points of the tracks. Speed: track length / track duration. Straightness: displacement / track length. Arrest coefficient is typically defined

as the percentage of time in which a cell moves below a certain speed threshold. However, being the tracklets of short duration this results in a limited number of admissible percentages. Additionally, a sharp threshold may introduce artifacts. Therefore, we computed arrest coefficient by using a sigmoidal thresholding function defined as follows.

$$ac = \frac{\sum i = 1^k 1 - \frac{1}{e^{1+s(k)-\tau}}}{ac0}$$

where $\tau = 2\mu m/\text{min}$ is a speed threshold and $ac0 = k - \frac{k}{e^{1-\tau}}$ is the arrest coefficient of a cell having a constant speed of $0\mu m/\text{min}$

Based on the aforementioned parameters, each tracklet was associated to one of the following activities:

- "Arrested": Cell which does not move (i.e. interacting / adhering / death), exhibiting low speed, low directionality, low displacement and high arrest coefficient.
- "Patrolling": Cell which moves, covering a large area of tissue, with medium speed and directionality.
- "Directed": Cell which moves towards a target exhibiting high speed and directionality (high displacement and low arrest coefficient)
- "Flowing": Cell which flows inside the capillaries of blood vessels in the LN. A flowing cell exhibits extremely high speed and directionality

Tracklet-to-action association was implemented by means of fixed thresholds corresponding to different gates defined in table 7.1.

| <i>evaluated on 500 s</i> | | Arrested | Patrolling | Directed | Flowing | Swarming |
|----------------------------------|-----|-----------------|-------------------|-----------------|----------------|-----------------|
| speed [um/min] | min | 0 | 2 | 6 | 10 | - |
| | max | 7 | 8 | 25 | 300 | - |
| straightness [0..1] | min | 0 | 0.1 | 0.3 | 0.5 | - |
| | max | 0.3 | 0.5 | 1 | 1 | - |
| arrest coefficient [0..1] | min | 0.7 | 0.1 | 0 | 0 | - |
| | max | 1 | 0.8 | 0.2 | 0.2 | - |
| displacement [0..1] | min | 0 | 4 | 8 | 50 | - |
| | max | 15 | 20 | 80 | 300 | - |
| volume [um³] | min | - | - | - | - | 2000 |

Table 7.1. Gates for track-based activity recognition. Each activity (row) is mapped to a specific range (min-max) of motility parameters (columns). Values refer to tracklets with duration of 500s.

The detection of cells involved in a swarm (swarming) was achieved via a volumetric reconstruction. For the videos in Figure 7.4 with adoptively transferred CK6/ECFP neutrophils, swarms were considered as surfaces with a minimum volume of $2 \times 10^3 \mu\text{m}^3$. The number of cells in a swarm was estimated by dividing the swarm volume by the volume of a single cell (assumed to $1 \times 10^3 \mu\text{m}^3$ without spaces between cells).

Swarm quantification. To quantify the size and the growth rate of swarms we defined both a cell density and an overall directionality criteria. More precisely, we detected swarms in regions where cells accumulated and where most trajectories pointed to. The "surfaces" functionality of Imaris was used to reconstruct the volume of swarms, selecting the marching cube algorithm with either a user-defined brightness threshold in (low-magnification videos - Figure 7.6C) or by manually defining a region of interest around the swarm in (high magnification videos - Figure 7.6I). Neutrophils involved in the swarm were manually tracked until the end of the videos or when they merged to emerging swarms.

Statistics. Results were expressed as mean \pm standard deviation (SD). All statistical analyses were performed in Prism8 (Graphpad Software, La Jolla, USA). Means among two groups were compared with two-tailed t-test. Means among three or more groups were compared with one-way ANOVA with Dunn multiple comparison post-test.

Software availability and usage. The source code of the program to quantify the actions of immune cells from their tracks is provided in Supplementary Data File 1. This program requires the tracks of the cells to be exported from Imaris to an Excel file. After this has been done, it is possible to open the program in Matlab, enter the location of the Excel file, and executing the program. The plots counting the actions will be automatically created. To facilitate this process, and to avoid the requirement of Matlab, the software will be further distributed as an open source plug-in for common imaging software at <http://www.ltdb.info/tools> and <https://github.com/IRB-LTDB/tools>

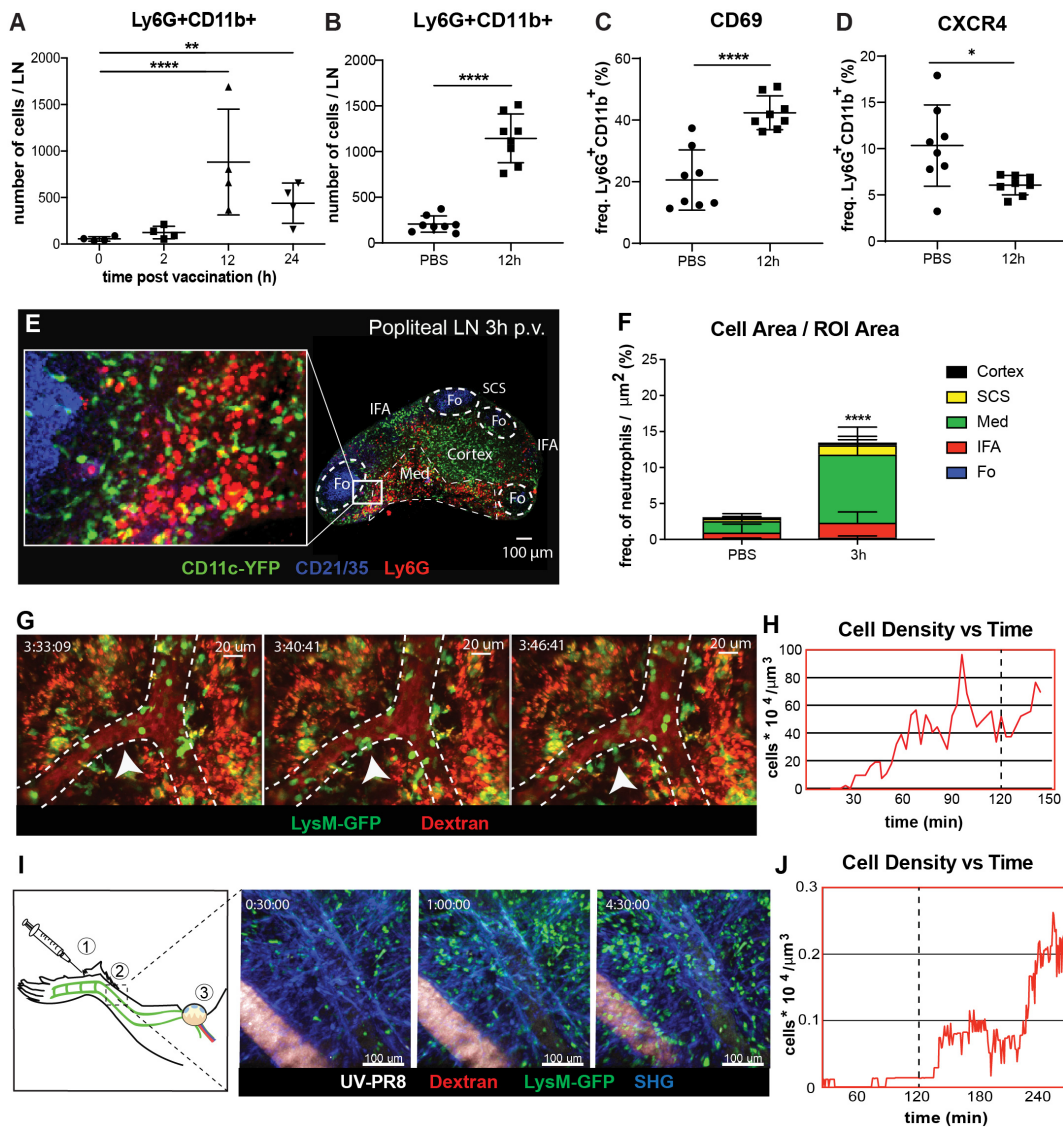


Figure 7.1. Neutrophil recruitment and distribution into the popliteal lymph node (PLN) after influenza vaccine administration. (A) Kinetic of neutrophil recruitment into the LN during the first 24 h following UV-inactivated influenza virus injection (UV-PR8). (B) Flow cytometric analysis showing the recruitment of neutrophils (Ly6G+ CD11b+) at 12 h post vaccination (p.v.). Percentages of CD69+ (C) and CXCR4+ (D) cells out of all neutrophils at 12 h p.v. compared with non-vaccinated controls. (E) Representative confocal microscopy of LN section showing the distribution of Ly6G+ neutrophils (red) in the LN at 3 h p.v. in a CD11c-YFP animal. (F) Quantification plots showing the distribution of neutrophils in the medullary (Med), interfollicular area (IFA), T cell zone (Cortex), follicle (Fo) and subcapsular sinus (SCS) areas of the LN at 3 h p.v. (G) Sequential 2-photon intravital (2P-IV) micrographs showing the recruitment of LysM-GFP neutrophils (green). Blood vessels (red) are labeled by i.v. injection of Rhodamine B isothiocyanate-Dextran. White arrow indicate hotspot. (H) Time series showing increasing density of neutrophils inside high endothelial venules (HEVs) of the PLN following vaccination. I, (left) Schematic drawing of the mouse footpad showing the injection site (1), the imaged area (2) and the lymphatic drainage towards the PLN (3). I, (right) Sequential 2P-IV micrographs showing the recruitment of LysM-GFP inside the lymphatic vessel in the injection site following UV-PR8 administration (I, right). (J) Time series showing density of neutrophils inside the draining lymphatic vessel. In all figures, the presented data are representative of at least three independent experiments. Results are given as mean \pm SD. ns $p > 0.05$; * $p < 0.05$; ** $p < 0.01$; **** $p < 0.0001$.

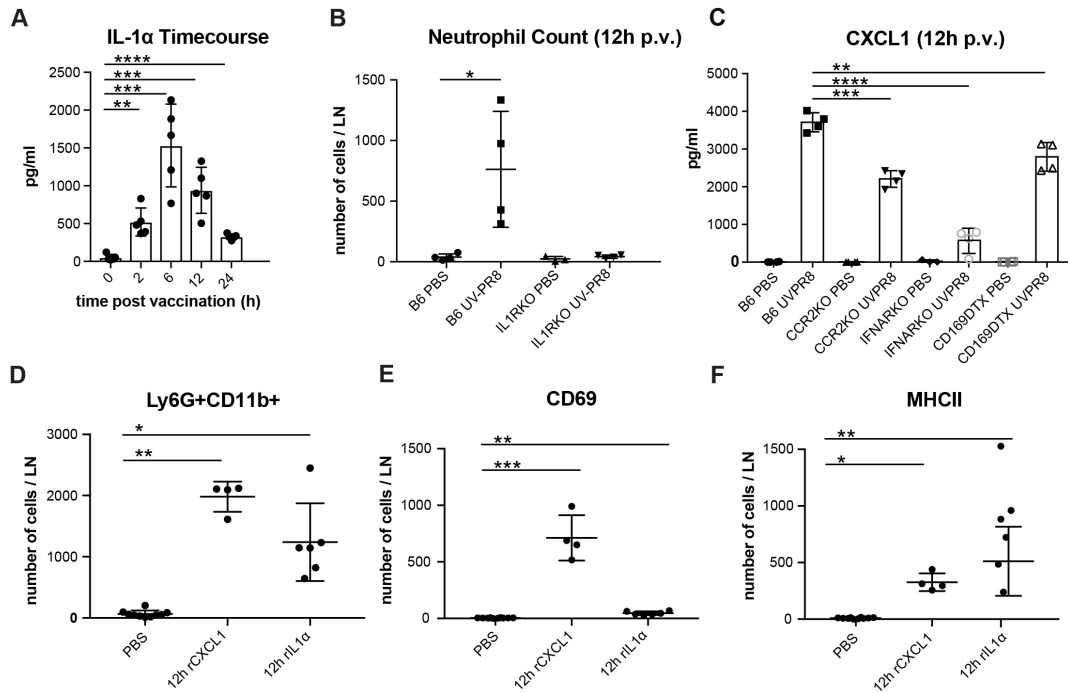


Figure 7.2. Production of CXCL1 and IL-1 α induce recruitment of neutrophils to the PLN in response to vaccination. A) Time course showing the secreted IL-1 α in the PLN at 0, 2, 6, 12 and 24 h following vaccination. B) Flow cytometric analysis showing the recruitment of neutrophils in the LN in B6 and IL-1R-deficient mice at 12 h p.v.. C) Cytoplex analysis showing the production of CXCL1 in the LN at 12 h p.v. in CCR2 KO, IFNAR KO, and CD169DTR mice compared to B6 controls. Flow cytometric analysis showing the total neutrophils count (D), and the expression of CD69 (E) and MHCII (F) after administration of recombinant IL-1 α and CXCL1. In all figures, the presented data are representative of at least three independent experiments. Results are given as mean \pm SD. ns $p > 0.05$; * $p < 0.05$; ** $p < 0.01$; *** $p < 0.001$; **** $p < 0.0001$.

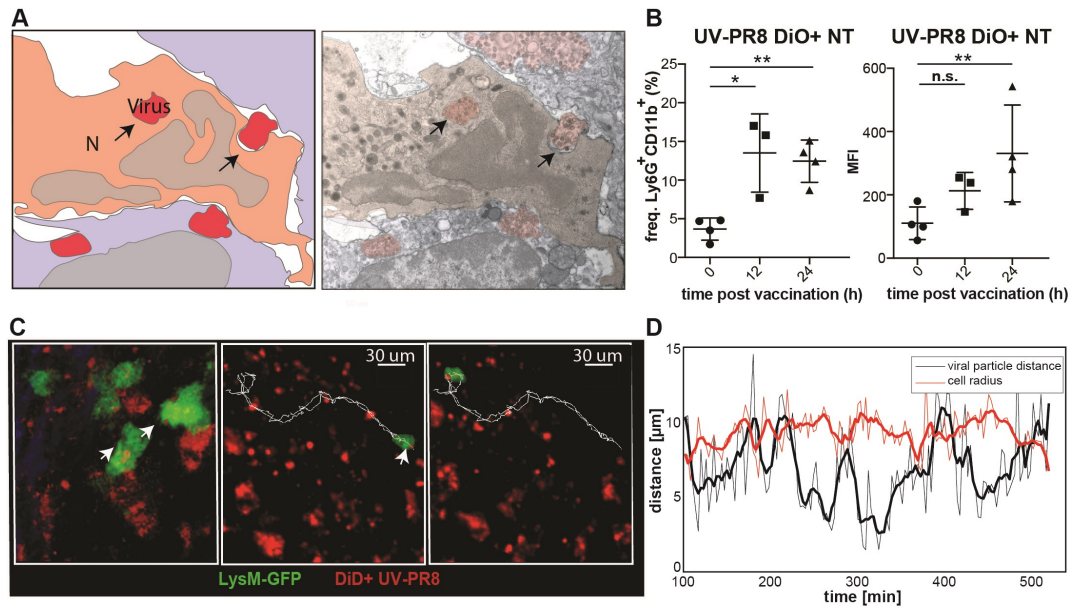


Figure 7.3. Neutrophils phagocyte and transport influenza virus. A) Schematic drawing (left) of an electron micrograph (right) showing neutrophils in the SCS phagocytizing UV-inactivated influenza virus at 2 h p.v.. B) Flow cytometric analysis indicating the percentage of neutrophils positive for influenza vaccine (DiO labeled, left) and the corresponding MFI analysis (right). C) Intravital 2-photon micrograph showing a LysM-GFP neutrophil (green) phagocytizing DiD labeled UV-PR8 (red) (left). Intravital 2-photon timelapse showing the correlation between the tracks from a UV-PR8 positive vesicle and the neutrophil (right). D) Distance of the viral particles from the cell centroid (black line), compared to the cell radius (red line). Results are given as mean \pm SD. ns $p > 0.05$; * $p < 0.05$; ** $p < 0.01$.

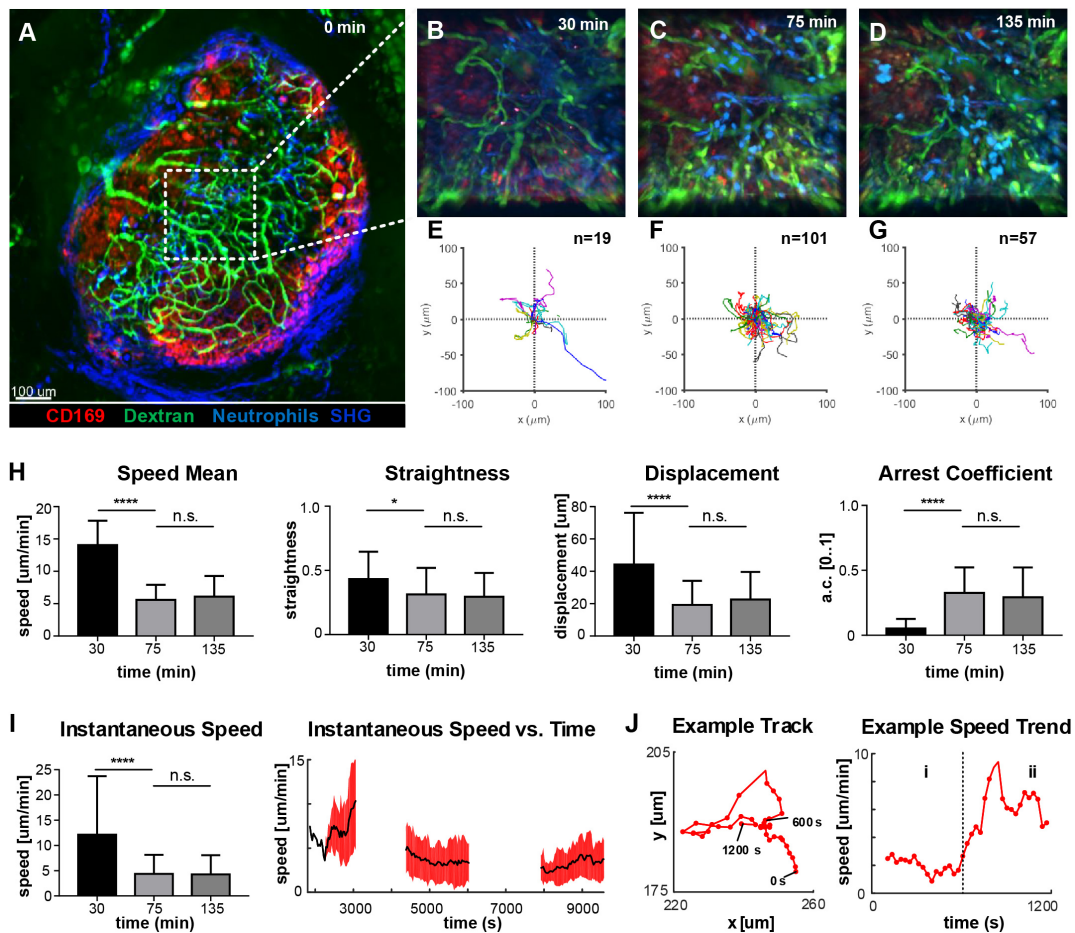


Figure 7.4. Time-course of neutrophil motility. A) Low-magnification 2P-IVM micrograph showing the structure of the PLN including vascular network (Fluorescein isothiocyanate-Dextran), CD169+ macrophages (red), collagen scaffold (Second Harmonic Generation - blue) and neutrophils (light-blue) adoptively transferred from a CK6/ECFP animal. Image was acquired immediately after vaccine injection. B-D) Snapshots of representative LN areas at different time points. E-G) Plots of cell tracks with common origin showing four preferential migratory directions at 30 min, more equally distributed directionalities at 75 minutes and a tendency towards the 1st and 4th quadrants at 135 minutes. The number of tracks is 19, 101, 57 respectively. H) Cell motility quantification using tracks mean speed, straightness, displacement and arrest coefficient. I) Boxplots of Instantaneous speed (left) exhibiting high variance at early time points. Instantaneous speed time series (right) showing distinct trends at different time points. J) Representative track (left) acquired at 135 min and the associated time series of the instantaneous speed (right). The same cell exhibits two different trends characterized by low speed (i) and high speed (ii). Results are given as mean \pm SD. ns $p > 0.05$; * $p < 0.05$; *** $p < 0.001$; **** $p < 0.0001$.

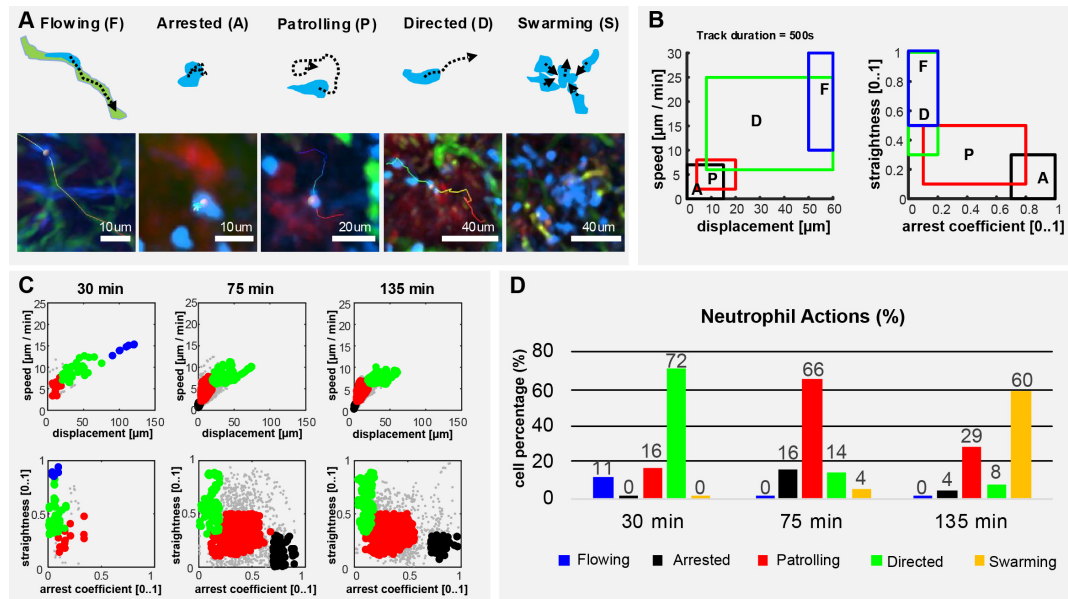


Figure 7.5. Neutrophils exhibit different actions in the early response to vaccination. A) Graphic representation (up) and 2P-IVM micrographs showing different neutrophil actions in response to influenza vaccination: flowing "F" neutrophils moving inside blood vessels, with long and straight following the vessel structure. Arrested neutrophils "A" exhibit confined tracks and short displacement. Patrolling neutrophils "P" have long, non-straight tracks associated with extensive tissue monitoring. Directed neutrophils "D" exhibit straight tracks with lower migration speed compared to flowing neutrophils. Swarming neutrophils (S) form cell aggregates with high density and large volume. B) Gating strategies used to define and identify the actions according to cell speed, displacement, straightness and arrest coefficient on track fragments of fixed length (500s). C) Classification of track fragments at different time intervals (arrested: black, patrolling: red, directed: green, flowing: blue). D) Time-course plot showing the percentage of cells performing each of the actions over time, according to our gating strategy.

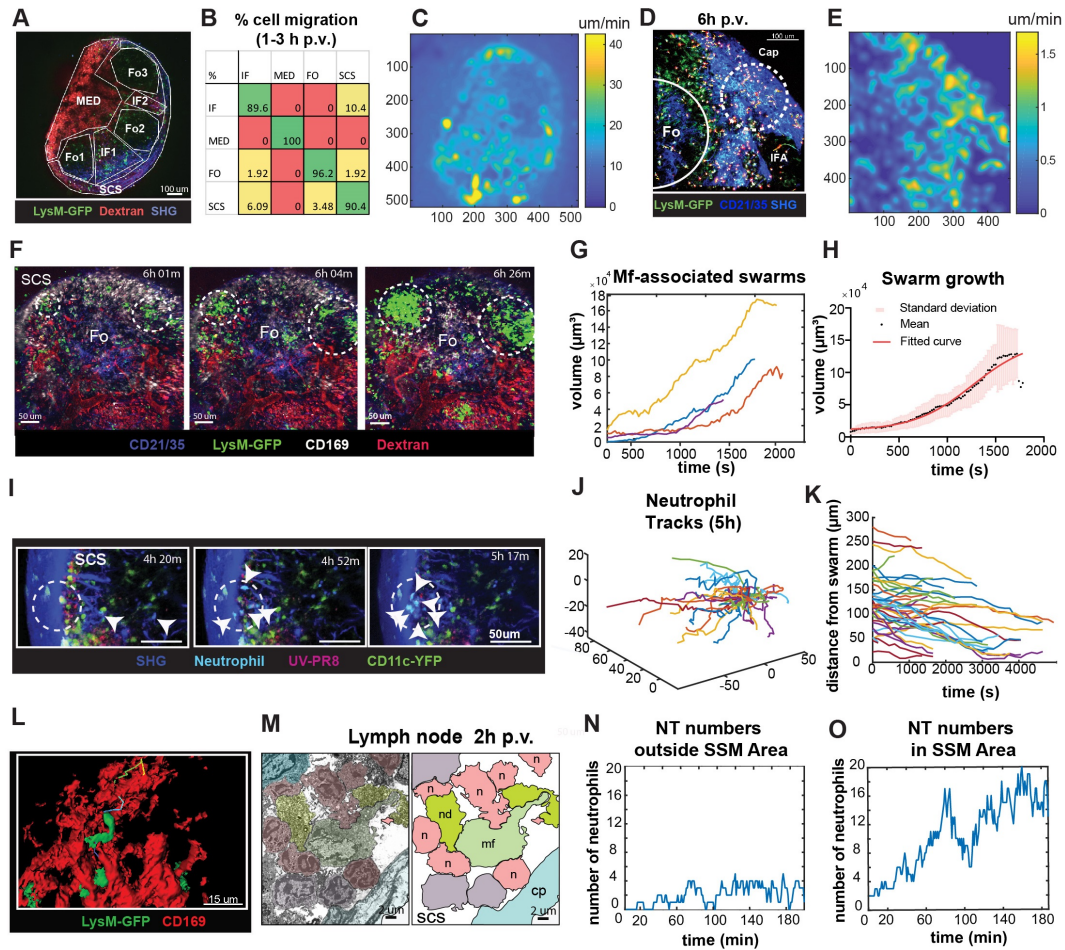


Figure 7.6. Characterization of neutrophils swarm formation in the PLN after influenza vaccination. A) Low magnification 2P-IVM micrograph showing the PLN of a LysM-GFP animal at 3 h p.v. Seven different areas are identified according to their anatomical structure and cell populations: SCS, follicles (Fo1-3), interfollicular areas (IF1-2) and medullary area (MED). B) Transition matrix showing the migration of cells across different areas. The value at the *i*-th row and *j*-th column refers to the percentage of cells that migrated from the *i*-th to the *j*-th area. Values on the diagonal refer to the percentage of cells that remained in the same area. C) Pixel velocity heatmap, showing hotspots with high motility. D) 2P-IVM micrograph showing the IF and SCS areas at 6 h p.v. Cap refers to the collagen capsule. Dashed lines indicate hotspots toward which cells migrate with high motility. E) Pixel velocity heatmap showing hotspots with high motility (yellow). F) Sequence of micrographs at 6 h p.v. showing the formation of multiple LysM-GFP neutrophils swarms in the SCS in close proximity to CD169+ macrophages (white). G) Swarm volumes over time observed at 6 h p.v.. Volumetric data built according to fluorescence intensity thresholding. H) Sigmoid fit to previous swarm volume ($R = 0.652$) showing their averaged growth phase. I) Sequence of micrographs with 25x magnification in the SCS showing CFP-expressing neutrophils initiating a swarm at 5 h p.v.. J) Trajectories of 5h p.v. swarm plotted from the same origin. K) Time-course distances from the swarm center at 5h p.v.. L) High magnification 3D reconstruction of LysM-GFP neutrophils interacting with CD169 macrophage network (red) in the SCS region. M) Colored transmission electron micrograph (left) and schematic drawing (right) showing the interaction of different neutrophils (n) with a macrophage (mf) in the SCS of the LN at 2h p.v.. Number of neutrophils vs. time showing an oscillatory trend in an area without macrophages (N), and an increasing trend indicative of swarming in an area associated with macrophages (O).

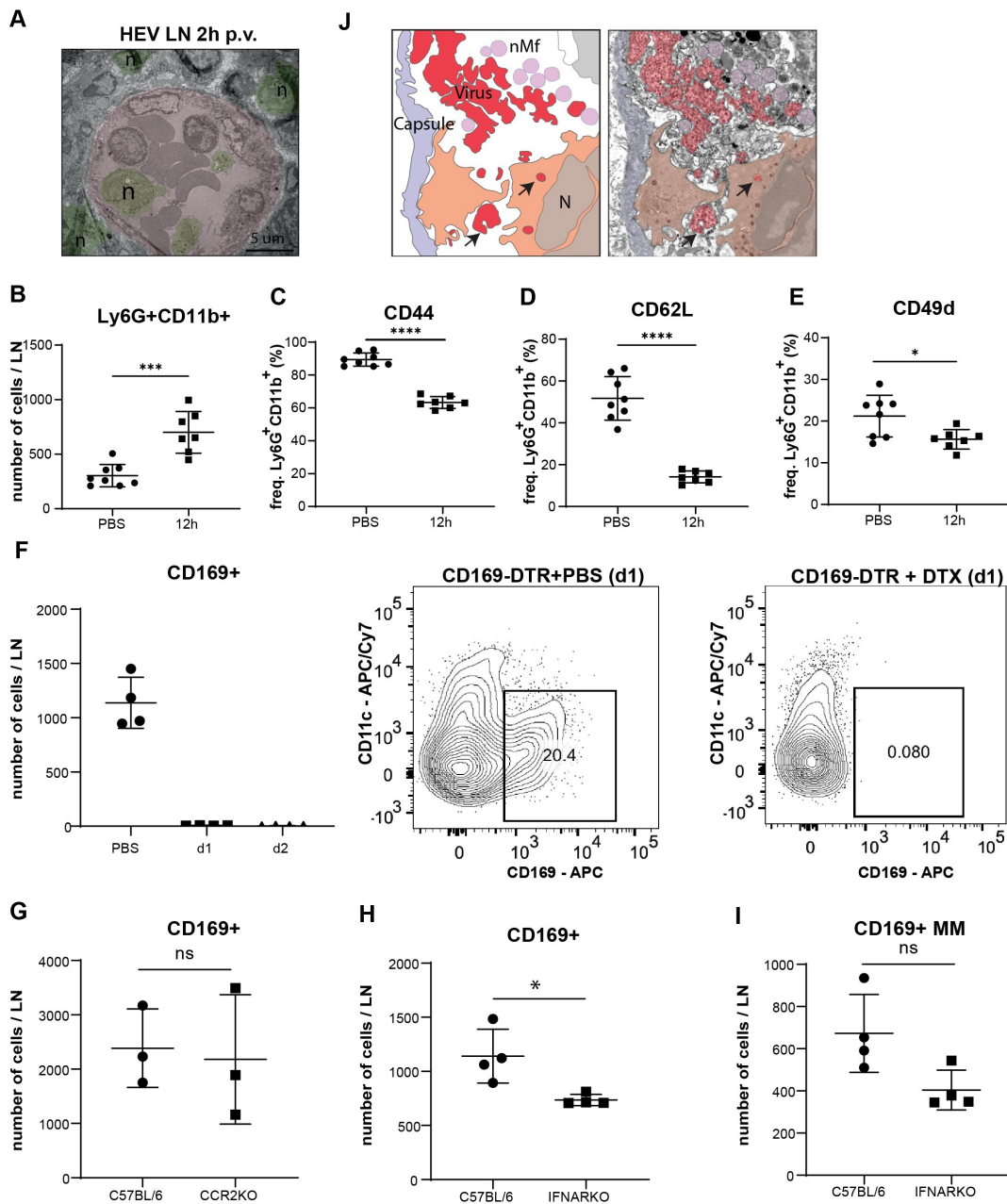


Figure 7.7. Supplementary 1. A) Scanning electron micrograph showing an association between neutrophils (n) and HEV at 2 h post vaccination (p.v.). The lumen of the blood vessel is marked in red. B) Flow cytometric analysis showing the recruitment of neutrophils (Ly6G⁺CD11b⁺) at 12 h p.v. Percentages of CD44⁺ (C), CD62L (D) and CD49d⁺ (E) cells out of all neutrophils at 12 h p.v. compared with non-vaccinated controls. (F) Absolute numbers of CD169⁺ cells in the lymph node of DT treated CD169-DTR mice (left) and representative density dot plot showing the gating for CD169⁺CD11c^{intlow} macrophage population (right). Quantification of CD169⁺ macrophages in CCR2KO (G) and IFNARKO mice (H). I) Total number of CD169⁺F4/80⁺ medullary macrophages in IFNARKO mice. J) Schematic drawing (left) of an electron micrograph (right) showing neutrophils in the SCS phagocytizing UV-inactivated influenza virus at 2 h p.v..

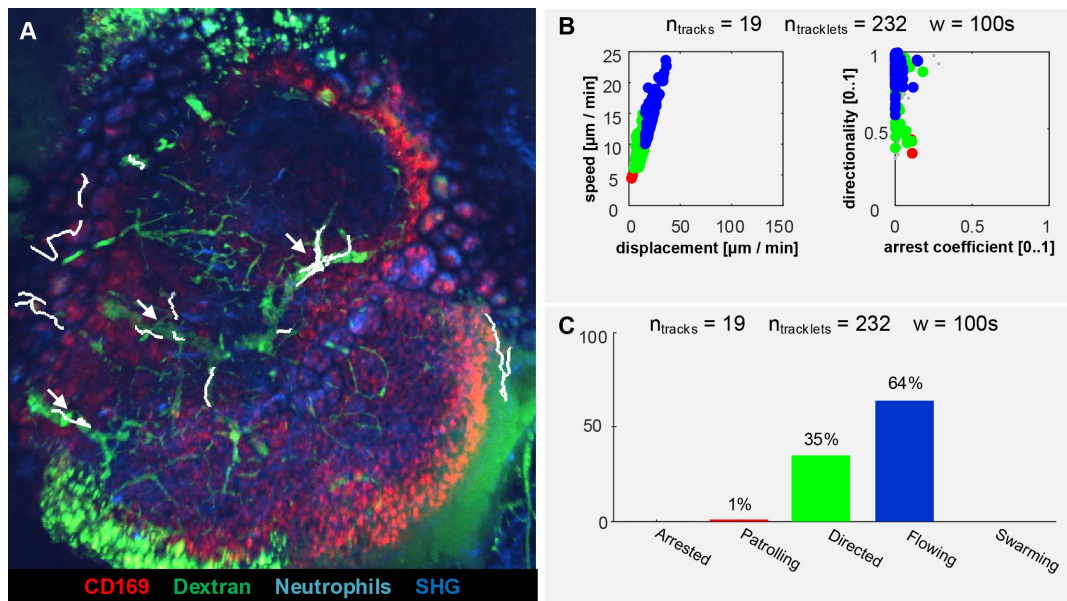


Figure 7.8. Supplementary 2.A) 2P-IVM micrograph showing the vascular structure of the popliteal lymph node and the tracks of neutrophils (white lines) prior to vaccination. Only neutrophils visible for at least 100s and migrating within the lymph node are tracked. Actions performed by the tracked neutrophils corresponding to distinct motility values (B) mainly associated to flowing (C).

Supplementary Movie 1 - Recruitment of neutrophils from blood vessels. 4D 2P-IVM video acquired in the LN showing LysM-GFP neutrophils (green) recruited via blood vessels (labeled with i.v. injection of Rhodamin B isothiocyanate-Dextran - red, dashed line). Arrow indicates a hotspot where neutrophils accumulate during extravasation.

<https://ndownloader.figshare.com/files/19118750>

Supplementary Movie 2 - Recruitment of neutrophils from lymphatic vessels. 4D 2P-IVM video acquired in the site of injection, showing LysM-GFP neutrophils (green) recruited via lymphatic vessels (red) that draining to lymph node. UV-PR8 is labeled in FR (white). Collagen fibers are visible by second harmonic generation (SHG, blue).

<https://ndownloader.figshare.com/files/19118762>

Supplementary Movie 3 - Neutrophils phagocytize influenza virus particles. 4D 2P-IVM video acquired in the LN showing an interaction between LysM-GFP neutrophils (green) and viral aggregates (UV-PR8-DiO, red). Lines indicate the tracks of a neutrophil and a viral aggregate.

<https://ndownloader.figshare.com/files/19118774>

Supplementary Movie 4 - Migration of neutrophils in the LN at 30, 75 and 135 minutes post vaccination. Neutrophils (light-blue) adoptively transferred from a CK6/ECFP animal perform different actions in the LN over time. The vascular network is labeled via i.v. injection of Fluorescein isothiocyanate-Dextran (green), macrophages are labeled via CD169-PE antibody (red). Collagen scaffold is visible via Second Harmonic Generation (SHG, blue).

<https://ndownloader.figshare.com/files/19118786>

Supplementary Movie 5 - Neutrophil migration in different areas of the LN. 4D 2P-IVM video acquired using a low magnification (10x) showing the migration of LysM-GFP neutrophils (green) in the different areas of the LN. Collagen scaffold is visible via Second Harmonic Generation (SHG, blue).

<https://ndownloader.figshare.com/files/19118798>

Supplementary Movie 6 - Swarm formation after vaccination. 4D 2P-IVM video showing the formation of multiple LysM-GFP neutrophils swarms (green) in the SCS in close proximity to CD169-AF647 macrophages (white). Blood vessels are labeled via i.v. dextran injection (red). Collagen scaffold is visible via Second Harmonic Generation (SHG, blue).

<https://ndownloader.figshare.com/files/19118810>

Supplementary Movie 7 - Swarm formation associated with dying macrophages. 4D 2P-IVM video showing swarm formation after vaccination. CFP-expressing neutrophils (light-blue) are adoptive transfer into CD11c-YFP (green) animal prior vaccine injection. UV-PR8 is labeled with DiD labeling dye (red). Dashed line indicates the subcapsular sinus area and arrows indicate recruited neutrophils.

<https://ndownloader.figshare.com/files/19118822>

Supplementary Movie 8 - Neutrophil migration in homeostasis. Neutrophils (light-blue) adoptively transferred from a CK6/ECFP animal flow within the blood vessels of the lymph node. Vascular network labeled via i.v. injection of Fluorescein isothiocyanate-Dextran (green), macrophages are labeled via CD169-PE antibody (red) while the collagen scaffold is visible via Second Harmonic Generation (SHG, blue).

<https://ndownloader.figshare.com/files/19118834>

CHAPTER 8

Conclusion, and future perspectives

Within this thesis, we combined computational methods, with two-photon microscopy to study the behavior of immune cells *in vivo*. We contributed to bridging the gap between computer vision and immunology, by exchanging data, methods, and problems.

The meeting point between the two fields is the proposed graph-based representation of microscopy data. Indeed, the content of videos was modeled through a graph with multiple levels of abstractions: from single pixels to cell actions.

Taken independently, each level targets different biological questions and requires specific computer vision methods. Of main relevance is the cell action level which represents a paradigm shift from considering cells as inanimate particles which move more or less randomly, to considering them as active objects performing actions with relevant biological meaning.

Taken as a whole, the graph allowed decomposing, and studying complex biological processes such as the collective migration of immune cells in response to an infection.

Hence, this thesis represents a step towards image-driven systems immunology.

8.1 Workflow and implementation

The work presented in this thesis originated from the need for better tools for tracking immune cells in 2P-IVM videos.

However, computer vision methods established for tracking humans or objects in videos, could not be directly applied to 2P-IVM data because of the differences in the appearance of cells and the limited amount of data available.

To this end, approximately one year was dedicated to the creation of a Leukocyte Tracking Database, which was published at *Scientific Data* on July 2018.

The main issue for tracking was the high variability of 2P-IVM experiments. Despite a researcher known how a cell should appear and move, the variability between different cells and experimental conditions, make their detection and tracking difficult for a computer. This gap of knowledge between humans and computers is not specific for this task, but common when biomedical datasets have to be analyzed. Indeed, medicine and biology are disciplines largely based on empirical knowledge. This knowledge can be difficult to be exchanged between computers and researchers. To this end, we worked on a method that allows the collaborative analysis of biomedical datasets. This yielded to a novel clustering algorithm which was published at *Science Advances* on October 2019 providing applications in several domains including immunology, cardiology, and oncology.

In the meanwhile, it became evident that the main problem was not only the tracking of immune cells but also the quantification of cell movements since the measures to quantify tracks poorly described the dynamic behavior of immune cells.

Indeed, state of the art measures considered cells as inanimate particles, describing whether they were fast/slow, directional or moving randomly. Additionally, when computing average measures, information about the dynamic behavior of cells was lost. To this end, the project moved towards action-based modeling of cell behavior. Indeed, by considering cells as active objects, performing distinct actions it was possible to explain the high variance exhibited by the standard measures, as published in a study at *Frontiers in Immunology* on November 2019.

Following this direction, methods to detect actions can be developed without necessarily the need for cell tracking.

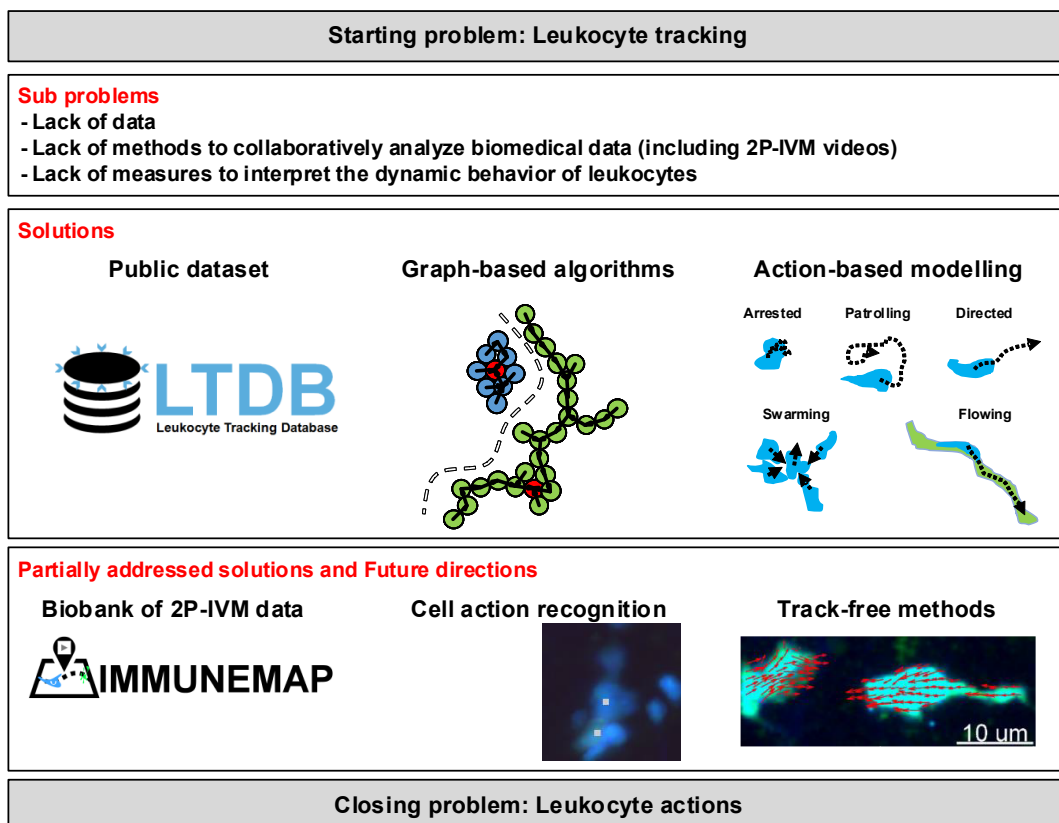


Figure 8.1. Workflow of the PhD project

Software and tools

Within this thesis, several tools and scripts were developed to facilitate the analysis of the data produced by Gonzalez's lab.

Some of these were implemented as plugins for bioimaging software and made to the community via GitHub at <https://github.com/IRB-LTDB/scripts> and <https://www.ltdb.info/tools>.

Plugins (XTensions) for the bioimaging software Imaris.

- XTSVMColoc - Performs supervised colocalization.
- XTSwarmDetection - Detects cell swarms (track-free).
- XTOfHeatMap - Creates an heatmap with motility intensity (track-free)
- XTFDHTransform - Converts phase contrast microscopy to fluorescence-like videos.
- XTCountActions - Detects and counts actions of cells (track-based).
- XTLTDBDetectSegments - Detects common errors of manual tracking.

8.2 IMMUNEMAP, making 2-photon microscopy data FAIR

The Leukocyte Tracking Database (LTDB) proposed in this thesis, provides a collection of challenging 2P-IVM videos with the primary aim to foster the development and validation of computer vision methods.

Moreover, it represents a first step towards the application of data mining methods to extract biomedical knowledge from microscopy videos. However, a larger number of videos is required to perform large-scale investigations that consider different experimental conditions, and possibly data from multiple laboratories. Indeed, the following issues should be considered:

- Each video captures a limited (spatiotemporal) window to observe a systemic reaction.
- A single research group can generate a restricted amount of data, in specific organs and experimental conditions, due to the high cost and time required for the acquisition and analysis of the videos.
- Currently, research institutes keep data and metadata in biobanks which are not interoperable nor accessible.
- Public microscopy datasets (i.e. Cell Image Library) do not include a comprehensive amount of 2P-IVM data.

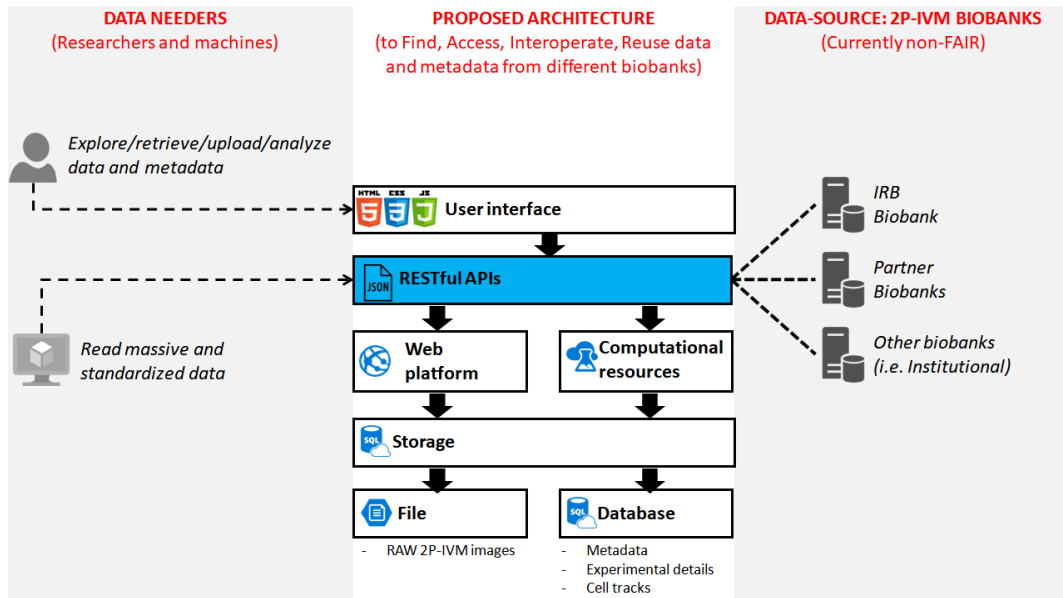


Figure 8.2. Proposed IT infrastructure based on a cloud architecture. The access to RAW imaging data and structured metadata will be provided via a web platform that supports a user interface and RESTful APIs. These will be used by data needers (visitors and applications) to retrieve content from data-sources which are the biobanks involved in the project. The content from the linked biobanks will be either copied into optimized cloud storage or made available to the system via APIs. In both cases, data retrieval will happen using the same APIs. Lastly, computational resources available on the cloud will be used for analyzing both data and metadata. These will keep results up to date and will allow executing knowledge extraction algorithms on the cloud.

- Data analysis (i.e. computer vision and pattern recognition) methods are not sufficiently validated on 2P-IVM data.

Therefore, there is a lack of 2P-IVM data, which hampers a complete vision of the immune system.

To fill the gap we secured a BIOLINK grant, from the Swiss National Science Foundation (SNF) to develop IMMUNEMAP: a cloud architecture to make data from a large network of laboratories Findable, Accessible, Interoperable and Reusable (FAIR), as shown in Figure 8.2. We will start focusing on two main experimental conditions: infection, and cancer, by collecting data from eight project partners (Table 8.1, Figure 8.3. Then, we will make the system open for the submission of 2P-IVM data.

We retain that the proposed project is crucially needed to support data-driven immunological research. Moreover, we consider that this platform would be a precious source of information, saving time and research costs.

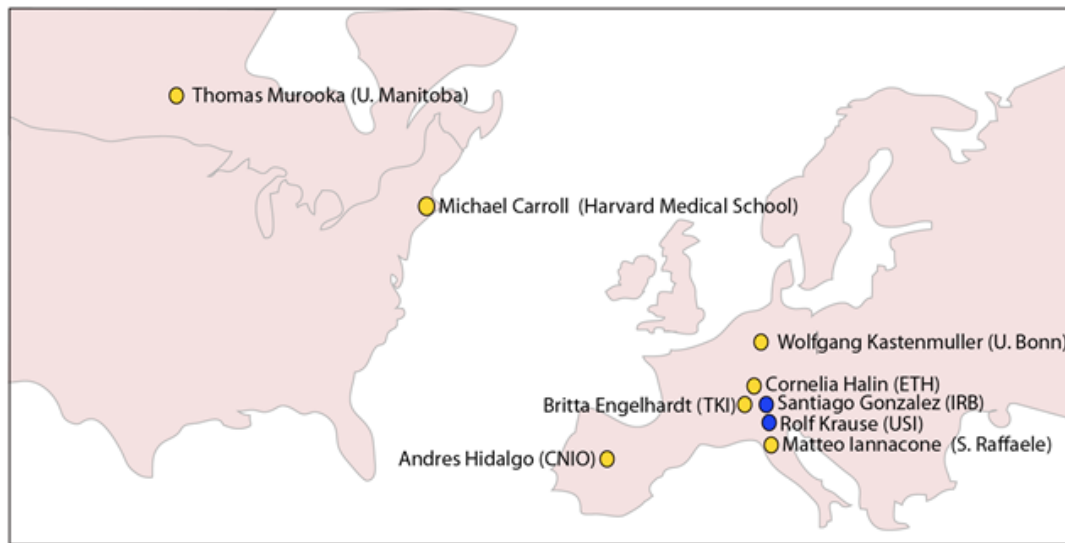


Figure 8.3. Schematic drawing showing the international dimension of the biobanks participating in this project. Blue color indicates the project applicants and yellow color indicate the project partners..

| <i>Biobank (PI name)</i> | <i>Institution</i> | <i>Intravital technique</i> | <i>Type of cells imaged / site of imaging</i> | <i>Experimental conditions</i> |
|--------------------------|-----------------------------|----------------------------------|--|--|
| Gonzalez | IRB, Switzerland | 2-Photon, Confocal, Fluorescence | Neutrophils, NK, Macrophages, T, B/ Lymph node, Spleen, trachea, Skin. | Inflammation, Vaccination, Infectious Diseases, Cancer |
| Murooka | U. of Manitoba, Canada | 2-Photon | T, DC/Lymphoid tissue, Skin | Infectious diseases |
| Engelhardt | TKI, Switzerland | 2-Photon, Confocal | T, Microglia/Brain, Spinal cord microvessels | Autoimmunity, Cancer |
| Hidalgo | CNIC, Spain | 2-Photon, Confocal, Fluorescence | Neutrophils/Blood vessels | Cell migration, Inflammation |
| Iannacone | ISF, Italy | 2-Photon, Confocal | NK, T, Monocytes, Macrophages/ Liver, Lymph node | Inflammation, Infectious Diseases, Cancer |
| Kastenmuller | U. of Bonn, Germany | 2-Photon | T, DC/ Lymph node | Inflammation |
| Carroll | Harvard Medical School, USA | 2-Photon, Confocal, Fluorescence | B, T, Macrophages, DC/Lymph node, Spleen | Autoimmunity, Infectious diseases, Vaccination |
| Halin | ETH, Switzerland | 2-Photon, Confocal, | T, DC/lymphatic vessels, lymph nodes, Skin | Inflammation |

Table 8.1. Specifics of the initial data included in IMMUNEMAP which are provided by the project partners. The name of the biobank in the first column is given following the surname of the Principal Investigator of the group.

8.3 Experimental definition of imaging protocols

The biomedical knowledge that can be extracted from 2P-IVM data is critically dependent on the entire imaging pipeline.

To this end, we aim at establishing a protocol that describes the best acquisition settings for different experimental conditions.

Indeed, the acquisition settings of 2P-IVM vary across different microscopes, studies or even within the same experiment. In a preliminary evaluation, we found that the temporal sampling rate critically impacts the measured speed of cells. In the work by Aoshi and colleagues [11] for instance, the time step was set to 30 s or 45 s.

Considering a track as a piece-wise linear approximation of the real cell-trajectory, it gives an underestimation of the track length. Therefore large time-steps may cancel the content of high frequencies, resulting in shorter track lengths and lower speeds.

However, this information loss is dependent on the spectrum of the movement, which varies according to the different actions performed by the cells. To evaluate this phenomenon we used a dataset with 68 tracks of highly motile neutrophils, exhibiting multiple different actions. These tracks were captured with a time step of 15 s. Then, we performed the downsampling of the tracks and measured the track mean speed. Interestingly, we noticed a decrease in the track mean speed from $6.5\mu\text{m}/\text{min}$ to $3\mu\text{m}/\text{min}$, with the major curvature from 15 s to 45 s (Figure 8.4).

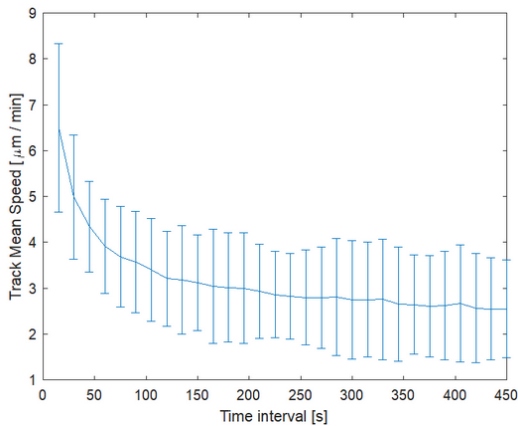


Figure 8.4. Effect of acquisition time interval on measured cell speed. The plot shows the average speed of 68 neutrophils from the video LTDB017. Speed was computed by downsampling the tracks of the cells by different factors corresponding to different acquisition time intervals.

8.4 Tracking with CARE

Content-Aware Restoration (CARE) is a recent application of deep learning to restore microscopy images corrupted by noise (i.e. arising from a large point spread function) [263]. This was achieved by training an end-to-end fully convolutional neuronal network using noisy images as inputs and images without noise as output.

During the development of LTDB, we collected an extensive amount of tracks affected by errors and we manually corrected them. Similarly to the dataset used for CARE, the tracks from LTDB can potentially be used to train a neuronal network to predict corrected tracks from a set of tracks affected by noise.

Moreover, the proposed trainable clustering algorithm can be applied to achieve this task by grouping pixels in space-time.

In a preliminary study, we applied the proposed clustering algorithm to group separately pixels in space, then cell centroids only in time. Results on the challenging video LTDB017 confirmed that this method can potentially be applied for cell tracking (Figure 8.5).

Additionally, a hybrid approach combining deep learning, with graph-based methods for cell tracking has recently been proposed by Moen and colleagues [184].

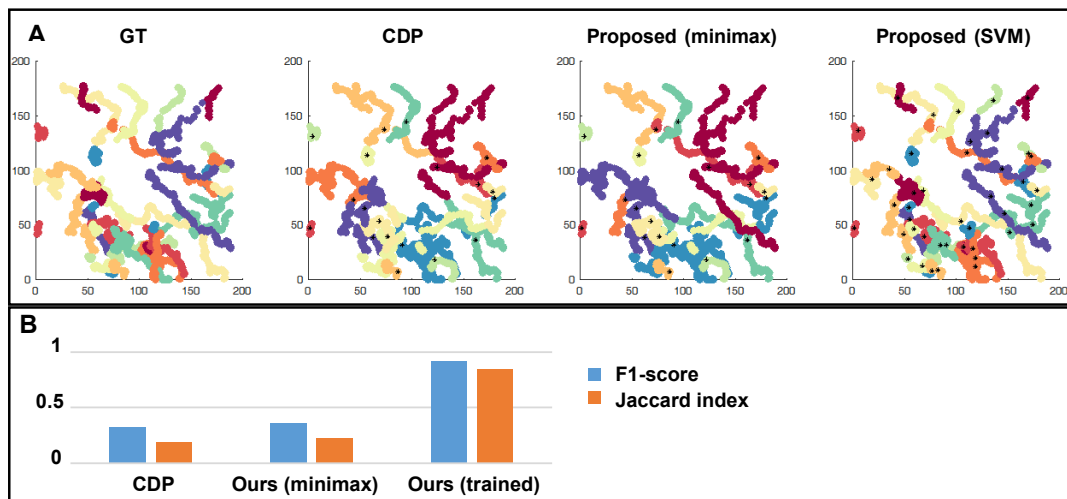


Figure 8.5. Preliminary work using semi-supervised clustering for cell tracking. **A.** Tracks color-coded according to the manual ground truth (GT) or the clustering results of different density-based clustering algorithms: CDP proposed using a minimax path-cost function, and proposed using a trained model (Support Vector Machine). **B.** Quantitative comparison with respect to the ground truth showing an increased F1 score (blue) and Jaccard Index (orange) of the proposed method using path-training.

8.5 Detection and discovery of additional cell actions

Within this thesis, we proposed to model the behavior of immune cells as the dynamic transitions between a defined set of states (actions). We detected these actions by mapping track fragments (tracklets) to a predefined set of action names. However, this requires at least a partial tracking of cells. A future perspective is represented by detecting regions where relevant biological actions take place without the need for tracking. Although the proposed HoT-POF method could be used for this task (i.e. by computing it on a sliding region), recently developed methods based on deep learning for human action recognition represent a promising way to achieve this task also for cells [274]. To this end, we started developing a framework for detecting cell actions. This includes: a dataset of annotated regions, a data-augmentation strategy based on volume rotation and projection, a region classifier, and a biologically-relevant validation.

Additionally, the usage of clustering algorithms can discover new cell actions. In a preliminary study, we applied the CDP algorithm to automatically group the tracklets of migrating neutrophils described in Chapter 7. The algorithm found 3 main groups of tracklets, which highly overlapped the definitions of "patrolling", "arrested", and "directed" assigned by imaging experts. This paves the way for recognizing unknown cell actions, which is especially relevant considering that not all the possible cell actions have been characterized in the literature.

An alternative approach is represented by the detection of changes in cell behavior. This corresponds to detect the action of changing action, which applies even if not all the possible actions are known.

In a preliminary experiment, we relied on the intuition that the future movement pattern of a cell can be predicted from the past if the cell keeps moving in the same way.

Therefore, we detect action-changes when future movement patterns cannot be predicted accurately from the past. With this assumption, we identified abrupt changes in the movement of neutrophils following photo-burning, as well as neutrophils arresting during the extravasation from the bloodstream.

However, other behavioral changes which are not associated with abrupt changes will require more advanced methods (i.e. time-series segmentation).

8.6 Relevance of actions

In this thesis, we demonstrated that neutrophils perform distinct actions over time following influenza vaccination. Indeed, the proposed quantification of actions over time allowed to interpret the dynamic behavior of neutrophils which was not captured by the standard measures of motility.

A further step would be represented by the combination of intravital imaging data with molecular techniques such as optical probes or gene expression profiles. This combination could provide a way to better interpret the meaning of cell actions.

This quantification method can generalize to other types of cells, as well as to other experimental models in which cell actions can be linked to a prognostic value.

Bibliography

- [1] ABDALLAH, D. S. A., EGAN, C. E., BUTCHER, B. A., AND DENKERS, E. Y. Mouse neutrophils are professional antigen-presenting cells programmed to instruct T h1 and T h17 T-cell differentiation. *International Immunology* 23, 5 (2011), 317–326.
- [2] ACHANTA, R., SHAJI, A., SMITH, K., LUCCHI, A., FUA, P., AND SUSSTRUNK, S. SLIC Superpixels. *EPFL Technical Report 149300*, June (2010), 15.
- [3] ACHANTA, R., SHAJI, A., SMITH, K., LUCCHI, A., FUA, P., AND SÜSSTRUNK, S. SLIC superpixels compared to state-of-the-art superpixel methods. *IEEE transactions on pattern analysis and machine intelligence* 34, 11 (2012), 2274–2282.
- [4] AGGARWAL, C. C., HINNEBURG, A., AND KEIM, D. A. On the surprising behavior of distance metrics in high dimensional space. In *International conference on database theory* (2001), Springer, pp. 420–434.
- [5] AGGARWAL, J., AND RYOO, M. Human activity analysis. *ACM Computing Surveys* 43, 3 (apr 2011), 1–43.
- [6] AL-KOFAHI, O., RADKE, R. J., GODERIE, S. K., SHEN, Q., TEMPLE, S., AND ROYSAM, B. Automated cell lineage construction: a rapid method to analyze clonal development established with murine neural progenitor cells. *Cell cycle* 5, 3 (2006), 327–335.

- [7] ALBERTS, B., JOHNSON, A., LEWIS, J., RAFF, M., ROBERTS, K., AND WALTER, P. Innate immunity. In *Molecular Biology of the Cell. 4th edition*. Garland Science, 2002.
- [8] ALI, N., ZIRAK, B., RODRIGUEZ, R. S., PAULI, M. L., TRUONG, H.-A., LAI, K., AHN, R., CORBIN, K., LOWE, M. M., SCHARSCHMIDT, T. C., ET AL. Regulatory t cells in skin facilitate epithelial stem cell differentiation. *Cell* 169, 6 (2017), 1119–1129.
- [9] ALLEN, C. D., AND CYSTER, J. G. Follicular dendritic cell networks of primary follicles and germinal centers: Phenotype and function, feb 2008.
- [10] AMAT, F., MYERS, E. W., AND KELLER, P. J. Fast and robust optical flow for time-lapse microscopy using super-voxels. *Bioinformatics* 29, 3 (2013), 373–380.
- [11] AOSHI, T., ZINSELMAYER, B. H., KONJUFCA, V., LYNCH, J. N., ZHANG, X., KOIDE, Y., AND MILLER, M. J. Bacterial entry to the splenic white pulp initiates antigen presentation to cd8+ t cells. *Immunity* 29, 3 (2008), 476–486.
- [12] APOSTOLOFF, N., AND FITZGIBBON, A. Learning spatiotemporal T-junctions for occlusion detection. In *Computer Vision and Pattern Recognition, 2005. CVPR 2005. IEEE Computer Society Conference on (2005)*, vol. 2, IEEE, pp. 553–559.
- [13] APOSTOLOFF, N., AND FITZGIBBON, A. W. Automatic video segmentation using spatiotemporal T-junctions. *Bmvc* (2006), 1089–1098.
- [14] ARGANDA-CARRERAS, I., KAYNIG, V., RUEDEN, C., ELICEIRI, K. W., SCHINDELIN, J., CARDONA, A., AND SEBASTIAN SEUNG, H. Trainable Weka Segmentation: a machine learning tool for microscopy pixel classification. *Bioinformatics* 33, 15 (2017), 2424–2426.
- [15] ARIAS-CASTRO, E., LERMAN, G., AND ZHANG, T. Spectral clustering based on local pca. *The Journal of Machine Learning Research* 18, 1 (2017), 253–309.
- [16] AROKIASAMY, S., ZAKIAN, C., DILLIWAY, J., WANG, W., NOURSHARGH, S., AND VOISIN, M. B. Endogenous TNF α orchestrates the trafficking of neutrophils into and within lymphatic vessels during acute inflammation. *Scientific Reports* (2017).

- [17] AUDOY-RE, J., SOULET, D., ZHOU, H., KUBES, P., AND VALLIE, L. Rod-Shaped Monocytes Patrol the Brain Vasculature and Give Rise to Perivascular Macrophages under the Influence of Proinflammatory Cytokines and Angiopoietin-2. *Journal of Neuroscience* 28, 41 (2008), 10187–10199.
- [18] AUFFRAY, C., FOGG, D., GARFA, M., ELAIN, G., JOIN-LAMBERT, O., KAYAL, S., SARNACKI, S., CUMANO, A., LAUVAU, G., AND GEISSMANN, F. Monitoring of Blood Vessels and Tissues by a Population of Monocytes with Patrolling Behavior. *Science* 317, 5838 (aug 2007), 666–670.
- [19] BALES, R. F. *Interaction process analysis; a method for the study of small groups*. Addison-Wesley, 1950.
- [20] BARON, J. L. Experience with 3D optical flow on gated MRI cardiac datasets. In *Computer and Robot Vision, 2004. Proceedings. First Canadian Conference on* (2004), IEEE, pp. 370–377.
- [21] BARRY, K. C., FONTANA, M. F., PORTMAN, J. L., DUGAN, A. S., AND VANCE, R. E. IL-1 α Signaling Initiates the Inflammatory Response to Virulent *Legionella pneumophila* In Vivo . *The Journal of Immunology* (2013).
- [22] BEAL, A. M., ANIKEEVA, N., VARMA, R., CAMERON, T. O., VASILIVER-SHAMIS, G., NORRIS, P. J., DUSTIN, M. L., AND SYKULEV, Y. Kinetics of Early T Cell Receptor Signaling Regulate the Pathway of Lytic Granule Delivery to the Secretory Domain. *Immunity* 31, 4 (oct 2009), 632–642.
- [23] BELTMAN, J. B., HENRICKSON, S. E., VON ANDRIAN, U. H., DE BOER, R. J., AND MARÉE, A. F. Towards estimating the true duration of dendritic cell interactions with T cells. *Journal of Immunological Methods* 347, 1-2 (aug 2009), 54–69.
- [24] BELTMAN, J. B., MARÉE, A. F. M., DE BOER, R. J., M MARÉE, A. F., DE BOER, R. J., MARÉE, A. F. M., AND DE BOER, R. J. Analysing immune cell migration. *Nature reviews. Immunology* 9, 11 (2009), 789–798.
- [25] BERCLAZ, J., FLEURET, F., TURETKEN, E., FUA, P., TÜRETKEN, E., AND FUA, P. Multiple object tracking using k-shortest paths optimization. *IEEE transactions on pattern analysis and machine intelligence* 33, 9 (2011), 1806–1819.
- [26] BEUNEU, H., DEGUINE, J., BREART, B., MANDELBOIM, O., DI SANTO, J. P., AND BOUSSO, P. Dynamic behavior of NK cells during activation in lymph nodes. *Blood* 114, 15 (oct 2009), 3227–3234.

- [27] BIONDO, C., MANCUSO, G., MIDIRI, A., SIGNORINO, G., DOMINA, M., LANZA CARICCIO, V., MOHAMMADI, N., VENZA, M., VENZA, I., TETI, G., AND BENINATI, C. The interleukin-1 β /CXCL1/2/neutrophil axis mediates host protection against group B streptococcal infection. *Infection and immunity* 82, 11 (nov 2014), 4508–17.
- [28] BOGOSLOWSKI, A., BUTCHER, E. C., AND KUBES, P. Neutrophils recruited through high endothelial venules of the lymph nodes via PNA α intercept disseminating *Staphylococcus aureus*. *Proceedings of the National Academy of Sciences* 115, 10 (mar 2018), 2449–2454.
- [29] BOISSONNAS, A., FETLER, L., ZEELBERG, I. S., HUGUES, S., AND AMIGORENA, S. In vivo imaging of cytotoxic T cell infiltration and elimination of a solid tumor. *The Journal of Experimental Medicine* 204, 2 (feb 2007), 345–356.
- [30] BOUGHERARA, H., MANSUET-LUPO, A., ALIFANO, M., NGÔ, C., DAMOTTE, D., LE FRÈRE-BELDA, M.-A., DONNADIEU, E., AND PERANZONI, E. Real-Time Imaging of Resident T Cells in Human Lung and Ovarian Carcinomas Reveals How Different Tumor Microenvironments Control T Lymphocyte Migration. *Frontiers in Immunology* 6 (oct 2015).
- [31] BOUSSO, P., AND MOREAU, H. D. Functional immunoimaging: the revolution continues. *Nature Reviews Immunology* 12, 12 (dec 2012), 858–864.
- [32] BOUSSO, P., AND ROBESY, E. Dynamics of CD8 $^{+}$ T cell priming by dendritic cells in intact lymph nodes. *Nature Immunology* 4, 6 (jun 2003), 579–585.
- [33] BREGONZIO, M., GONG, S., XIANG, T., ET AL. Recognising action as clouds of space-time interest points. In *CVPR (2009)*, vol. 9, pp. 1948–1955.
- [34] BROX, T., AND MALIK, J. [2011][3]Large Displacement Optical Flow Descriptor Matching in Variational Motion Estimation.pdf. *TPAMI* 33, 3 (2011), 1–14.
- [35] BUSCHER, K., MARCOVECCHIO, P., HEDRICK, C. C., AND LEY, K. Patrolling Mechanics of Non-Classical Monocytes in Vascular Inflammation. *Frontiers in Cardiovascular Medicine* 4, December (dec 2017), 1–10.
- [36] CAHALAN, M. D., AND PARKER, I. Choreography of Cell Motility and Interaction Dynamics Imaged by Two-Photon Microscopy in Lymphoid Organs. *Annual Review of Immunology* 26, 1 (apr 2008), 585–626.

- [37] CALEGARI, G. R. E., NASI, G., AND CELINO, I. Human Computation vs . Machine Learning : an Experimental Comparison for Image Classification. *Journal of Human Computation* (2018), 13–30.
- [38] CAMP, J. V., AND JONSSON, C. B. A role for neutrophils in viral respiratory disease, may 2017.
- [39] CARLIN, L. M., STAMATIADIS, E. G., AUFRAY, C., HANNA, R. N., GLOVER, L., VIZCAY-BARRENA, G., HEDRICK, C. C., COOK, H. T., DIEBOLD, S., AND GEISSMANN, F. Nr4a1-Dependent Ly6Clow Monocytes Monitor Endothelial Cells and Orchestrate Their Disposal. *Cell* 153, 2 (apr 2013), 362–375.
- [40] CARPENTER, A. E., KAMENSKY, L., AND ELICEIRI, K. W. A call for bioimaging software usability. *Nature methods* 9, 7 (2012), 666.
- [41] CARRASCO, Y. R., AND BATISTA, F. D. B Cells Acquire Particulate Antigen in a Macrophage-Rich Area at the Boundary between the Follicle and the Subcapsular Sinus of the Lymph Node. *Immunity* 27, 1 (jul 2007), 160–171.
- [42] CHAN, T. F., AND VESE, L. A. Active contours without edges. *IEEE Transactions on image processing* 10, 2 (2001), 266–277.
- [43] CHANG, J., WEI, D., AND FISHER, J. W. A video representation using temporal superpixels. *Proceedings of the IEEE Computer Society Conference on Computer Vision and Pattern Recognition* (2013), 2051–2058.
- [44] CHATZIANDREOU, N., FARSAKOGLU, Y., PALOMINO-SEGURA, M., D’ANTUONO, R., PIZZAGALLI, D. U., SALLUSTO, F., LUKACS-KORNEK, V., UGUCCIONI, M., CORTI, D., TURLEY, S. J., LANZAVECCHIA, A., CARROLL, M. C., AND GONZALEZ, S. F. Macrophage Death following Influenza Vaccination Initiates the Inflammatory Response that Promotes Dendritic Cell Function in the Draining Lymph Node. *Cell Reports* 18, 10 (mar 2017), 2427–2440.
- [45] CHAUDHRY, R., RAVICHANDRAN, A., HAGER, G., AND VIDAL, R. Histograms of oriented optical flow and binet-cauchy kernels on nonlinear dynamical systems for the recognition of human actions. In *computer vision and pattern recognition, 2009. CVPR 2009. IEEE Conference on* (2009), IEEE, pp. 1932–1939.

- [46] CHEN, S.-C., ZHAO, T., GORDON, G. J., AND MURPHY, R. F. Automated image analysis of protein localization in budding yeast. *Bioinformatics* 23 (2007), 66–71.
- [47] CHENOUEARD, N., BLOCH, I., AND OLIVO-MARIN, J.-C. Multiple hypothesis tracking for cluttered biological image sequences. *IEEE transactions on pattern analysis and machine intelligence* 35, 11 (2013), 2736–3750.
- [48] CHOU, R. C., KIM, N. D., SADIK, C. D., SEUNG, E., LAN, Y., BYRNE, M. H., HARIBABU, B., IWAKURA, Y., AND LUSTER, A. D. Lipid-Cytokine-Chemokine Cascade Drives Neutrophil Recruitment in a Murine Model of Inflammatory Arthritis. *Immunity* 33, 2 (aug 2010), 266–278.
- [49] CHTANOVA, T., SCHAEFFER, M., HAN, S.-J., VAN DOOREN, G. G., NOLLMANN, M., HERZMARK, P., CHAN, S. W., SATIJA, H., CAMFIELD, K., AARON, H., STRIEPEN, B., AND ROBEY, E. A. Dynamics of Neutrophil Migration in Lymph Nodes during Infection. *Immunity* 29, 3 (sep 2008), 487–496.
- [50] CIPTADI, A., GOODWIN, M. S., AND REHG, J. M. Movement pattern histogram for action recognition and retrieval. In *European Conference on Computer Vision* (2014), Springer, pp. 695–710.
- [51] CLAUSEN, B. E., BURKHARDT, C., REITH, W., RENKAWITZ, R., AND FÖRSTER, I. Conditional gene targeting in macrophages and granulocytes using LysMcre mice. *Transgenic Research* 8, 4 (aug 1999), 265–277.
- [52] COLQUE, R. V. H. M., CAETANO, C., DE ANDRADE, M. T. L., AND SCHWARTZ, W. R. Histograms of Optical Flow Orientation and Magnitude and Entropy to Detect Anomalous Events in Videos. *IEEE Transactions on Circuits and Systems for Video Technology* (2017).
- [53] COOMBES, J. L., CHARSAR, B. A., HAN, S.-J., HALKIAS, J., CHAN, S. W., KOSHY, A. A., STRIEPEN, B., AND ROBEY, E. A. Motile invaded neutrophils in the small intestine of *Toxoplasma gondii*-infected mice reveal a potential mechanism for parasite spread. *Proceedings of the National Academy of Sciences* 110, 21 (2013), E1913–E1922.
- [54] CSETE, M. E., AND DOYLE, J. C. Reverse Engineering of Biological Complexity. *Science* 295, 5560 (mar 2002), 1664–1669.
- [55] CYSTER, J. G. Chemokines and cell migration in secondary lymphoid organs. *Science (New York, N.Y.)* 286, 5447 (dec 1999), 2098–102.

- [56] CYSTER, J. G., AND ALLEN, C. D. B Cell Responses: Cell Interaction Dynamics and Decisions. *Cell* 177, 3 (2019), 524–540.
- [57] DALAL, N., TRIGGS, B., AND SCHMID, C. Human detection using oriented histograms of flow and appearance. In *European conference on computer vision* (2006), Springer, pp. 428–441.
- [58] DAVIS, J. W. Hierarchical motion history images for recognizing human motion. In *Proceedings IEEE Workshop on Detection and Recognition of Events in Video* (2001), IEEE, pp. 39–46.
- [59] DE FILIPPO, K., HENDERSON, R. B., LASCHINGER, M., AND HOGG, N. Neutrophil Chemokines KC and Macrophage-Inflammatory Protein-2 Are Newly Synthesized by Tissue Macrophages Using Distinct TLR Signaling Pathways. *The Journal of Immunology* (2008).
- [60] DE OLIVEIRA, S., ROSOWSKI, E. E., AND HUTTENLOCHER, A. Neutrophil migration in infection and wound repair: going forward in reverse. *Nature Reviews Immunology* 16, 6 (jun 2016), 378–391.
- [61] DIJKSTRA, E. W. A note on two problems in connexion with graphs. *Numerische Mathematik* 1, 1 (1959), 269–271.
- [62] DINARELLO, C. A. Overview of the IL-1 family in innate inflammation and acquired immunity, jan 2018.
- [63] DU, M., DING, S., XU, X., AND XUE, Y. Density peaks clustering using geodesic distances. *International Journal of Machine Learning and Cybernetics* 9, 8 (Aug 2018), 1335–1349.
- [64] DUDA, R. O., AND HART, P. E. Use of the hough transformation to detect lines and curves in pictures. *Communications of the ACM* 15, 1 (1972), 11–15.
- [65] DUFFY, D., PERRIN, H., ABADIE, V., BENHABILES, N., BOISSONNAS, A., LIARD, C., DESCOURS, B., REBOULLEAU, D., BONDUELLE, O., VERRIER, B., VAN ROOIJEN, N., COMBADIÈRE, C., AND COMBADIÈRE, B. Neutrophils transport antigen from the dermis to the bone marrow, initiating a source of memory CD8+ T cells. *Immunity* 37, 5 (nov 2012), 917–29.
- [66] DUFOUR, A., SHININ, V., TAJBAKSH, S., GUILLÉN-AGHION, N., OLIVOMARIN, J.-C., AND ZIMMER, C. Segmenting and tracking fluorescent cells

- in dynamic 3-D microscopy with coupled active surfaces. *IEEE Transactions on Image Processing* 14, 9 (2005), 1396–1410.
- [67] DUFOUR, A., THIBEAUX, R., LABRUYERE, E., GUILLEN, N., AND OLIVOMARIN, J.-C. 3-D active meshes: fast discrete deformable models for cell tracking in 3-D time-lapse microscopy. *IEEE Transactions on Image Processing* 20, 7 (2011), 1925–1937.
- [68] DUSTIN, M. L., CHAKRABORTY, A. K., AND SHAW, A. S. Understanding the Structure and Function of the Immunological Synapse. *Cold Spring Harbor Perspectives in Biology* 2, 10 (oct 2010), a002311–a002311.
- [69] DUSTIN, M. L., AND LONG, E. O. Cytotoxic immunological synapses. *Immunological Reviews* 235, 1 (apr 2010), 24–34.
- [70] DZYUBACHYK, O., VAN CAPPELLEN, W. A., ESSERS, J., NIESSEN, W. J., AND MEIJERING, E. Advanced level-set-based cell tracking in time-lapse fluorescence microscopy. *IEEE transactions on medical imaging* 29, 3 (2010), 852–867.
- [71] EASH, K. J., MEANS, J. M., WHITE, D. W., LINK, D. C., MERMED, J. J., AND DEXTER, T. M. CXCR4 is a key regulator of neutrophil release from the bone marrow under basal and stress granulopoiesis conditions. *Blood* 113, 19 (may 2009), 4711–9.
- [72] ELMORE, S. Apoptosis: a review of programmed cell death. *Toxicologic pathology* 35, 4 (2007), 495–516.
- [73] ESTER, M., KRIEGEL, H.-P., SANDER, J., XU, X., AND OTHERS. A density-based algorithm for discovering clusters in large spatial databases with noise. In *Kdd* (1996), vol. 96, pp. 226–231.
- [74] FALK, T., MAI, D., BENSCH, R., ÇIÇEK, Ö., ABDULKADIR, A., MARRAKCHI, Y., BÖHM, A., DEUBNER, J., JÄCKEL, Z., SEIWALD, K., ET AL. U-net: deep learning for cell counting, detection, and morphometry. *Nature methods* 16, 1 (2019), 67.
- [75] FARSAKOGLU, Y., PALOMINO-SEGURA, M., LATINO, I., ZANAGA, S., CHATZIANDREOU, N., PIZZAGALLI, D. U., RINALDI, A., BOLIS, M., SALLUSTO, F., STEIN, J. V., AND GONZALEZ, S. F. Influenza Vaccination Induces NK-Cell-Mediated Type-II IFN Response that Regulates Humoral Immunity in an IL-6-Dependent Manner. *Cell Reports* 26, 9 (feb 2019), 2307–2315.e5.

- [76] FEICHTENHOFER, C., PINZ, A., AND ZISSERMAN, A. Convolutional two-stream network fusion for video action recognition. In *Proceedings of the IEEE conference on computer vision and pattern recognition* (2016), pp. 1933–1941.
- [77] FIEDLER, M. A property of eigenvectors of nonnegative symmetric matrices and its application to graph theory. *Czechoslovak Mathematical Journal* 25, 4 (1975), 619–633.
- [78] FIGGE, M. T., AND MURPHY, R. F. Image-based systems biology. *Cytometry Part A* 87, 6 (jun 2015), 459–461.
- [79] FINSTERBUSCH, M., HALL, P., LI, A., DEVI, S., WESTHORPE, C. L. V., KITCHING, A. R., AND HICKEY, M. J. Patrolling monocytes promote intravascular neutrophil activation and glomerular injury in the acutely inflamed glomerulus. *Proceedings of the National Academy of Sciences* 113, 35 (aug 2016), E5172–E5181.
- [80] FISCHER, B., AND BUHMANN, J. M. Path-based clustering for grouping of smooth curves and texture segmentation. *IEEE Transactions on Pattern Analysis and Machine Intelligence* 25, 4 (2003), 513–518.
- [81] FÖRSTER, R., BRAUN, A., AND WORBS, T. Lymph node homing of T cells and dendritic cells via afferent lymphatics. *Trends in immunology* 33, 6 (jun 2012), 271–80.
- [82] FÖRSTER, R., DAVALOS-MISSLITZ, A. C., AND ROT, A. CCR7 and its ligands: balancing immunity and tolerance. *Nature reviews. Immunology* 8, 5 (may 2008), 362–71.
- [83] FRANK, A. On kuhn’s hungarian method—a tribute from hungary. *Naval Research Logistics (NRL)* 52, 1 (2005), 2–5.
- [84] FRIEDL, P., AND WEIGELIN, B. Interstitial leukocyte migration and immune function. *Nature Immunology* 9, 9 (2008), 960–969.
- [85] FURZE, R. C., AND RANKIN, S. M. Neutrophil mobilization and clearance in the bone marrow, 2008.
- [86] GAERTNER, F., AHMAD, Z., ROSENBERGER, G., FAN, S., NICOLAI, L., BUSCH, B., YAVUZ, G., LUCKNER, M., ISHIKAWA-ANKERHOLD, H., HENNEL, R., ET AL. Migrating platelets are mechano-scavengers that collect and bundle bacteria. *Cell* 171, 6 (2017), 1368–1382.

- [87] GARROD, K. R., WEI, S. H., PARKER, I., AND CAHALAN, M. D. Natural killer cells actively patrol peripheral lymph nodes forming stable conjugates to eliminate MHC-mismatched targets. *Proceedings of the National Academy of Sciences* 104, 29 (2007), 12081–12086.
- [88] GERBER, S., AND HORENKO, I. Improving clustering by imposing network information. *Science advances* 1, 7 (2015), e1500163.
- [89] GERMAIN, R. N., ROBEY, E. A., AND CAHALAN, M. D. A Decade of Imaging Cellular Motility and Interaction Dynamics in the Immune System. *Science* 336, 6089 (jun 2012), 1676–1681.
- [90] GHIDONI, S., NANNI, L., BRAHNAM, S., AND MENEGATTI, E. Texture descriptors based on dijkstra’s algorithm for medical image analysis. In *Studies in health technology and informatics*. IOS, 2014, pp. 74–82.
- [91] GOLDBERGER, A. L., AMARAL, L. A., GLASS, L., HAUSDORFF, J. M., IVANOV, P. C., MARK, R. G., MIETUS, J. E., MOODY, G. B., PENG, C.-K., AND STANLEY, H. E. Physiobank, physiotoolkit, and physionet: components of a new research resource for complex physiologic signals. *Circulation* 101, 23 (2000), e215–e220.
- [92] GONZALEZ, S. F., DEGN, S. E., PITCHER, L. A., WOODRUFFE, M., HEESTERS, B. A., AND CARROLL, M. C. Trafficking of B cell antigen in lymph nodes. *Annual review of immunology* 29 (2011), 215–33.
- [93] GONZALEZ, S. F., LUKACS-KORNEK, V., KULIGOWSKI, M. P., PITCHER, L. A., DEGN, S. E., KIM, Y.-A., CLONINGER, M. J., MARTINEZ-POMARES, L., GORDON, S., TURLEY, S. J., AND CARROLL, M. C. Capture of influenza by medullary dendritic cells via SIGN-R1 is essential for humoral immunity in draining lymph nodes. *Nature Immunology* 11, 5 (may 2010), 427–434.
- [94] GORLINO, C. V., RANOCCHIA, R. P., HARMAN, M. F., GARCÍA, I. A., CRESPO, M. I., MORÓN, G., MALETTO, B. A., AND PISTORESÍ-PALENCIA, M. C. Neutrophils Exhibit Differential Requirements for Homing Molecules in Their Lymphatic and Blood Trafficking into Draining Lymph Nodes. *The Journal of Immunology* 193, 4 (aug 2014), 1966–1974.
- [95] GREGORY, C. D., AND POUND, J. D. Cell death in the neighbourhood: direct microenvironmental effects of apoptosis in normal and neoplastic tissues. *The Journal of Pathology* 223, 2 (jan 2011), 178–195.

- [96] GREGORY, C. D., AND POUND, J. D. Cell death in the neighbourhood: direct microenvironmental effects of apoptosis in normal and neoplastic tissues. *The Journal of pathology* 223, 2 (2011), 178–195.
- [97] GUIDOTTI, L. G., INVERSO, D., SIRONI, L., DI LUCIA, P., FIORAVANTI, J., GANZER, L., FIOCCHI, A., VACCA, M., AIOLFI, R., SAMMICHELI, S., ET AL. Immunosurveillance of the liver by intravascular effector cd8+ t cells. *Cell* 161, 3 (2015), 486–500.
- [98] GUNN, M. D., NGO, V. N., ANSEL, K. M., EKLAND, E. H., CYSTER, J. G., AND WILLIAMS, L. T. A B-cell-homing chemokine made in lymphoid follicles activates Burkitt’s lymphoma receptor-1. *Nature* 391, 6669 (feb 1998), 799–803.
- [99] GUZZI, R., COLOMBO, T., AND PACI, P. Inverse Problems in Systems Biology: A Critical Review. Springer New York, 2018, pp. 69–94.
- [100] HADJANTONAKIS, A.-K., MACMASTER, S., AND NAGY, A. Embryonic stem cells and mice expressing different GFP variants for multiple non-invasive reporter usage within a single animal. *BMC biotechnology* 2, 1 (2002), 11.
- [101] HALLETT, M. B. *The Neutrophil: Cellular Biochemistry and Physiology*. CRC Press, 1989.
- [102] HAMPTON, H. R., BAILEY, J., TOMURA, M., BRINK, R., AND CHTANOVA, T. Microbe-dependent lymphatic migration of neutrophils modulates lymphocyte proliferation in lymph nodes. *Nature Communications* 6, 1 (nov 2015), 7139.
- [103] HAN, S.-J., VAN ROOIJEN, N., RAULET, D. H., AND ROBEY, E. A. Infection-induced regulation of natural killer cells by macrophages and collagen at the lymph node subcapsular sinus. *Cell Reports* 2, 1 (Jul 2012), 124–135.
- [104] HANNA, R. N., CEKIC, C., SAG, D., TACKE, R., THOMAS, G. D., NOWYHED, H., HERRLEY, E., RASQUINHA, N., MCARDLE, S., WU, R., PELUSO, E., METZGER, D., ICHINOSE, H., SHAKED, I., CHODACZEK, G., BISWAS, S. K., AND HEDRICK, C. C. Patrolling monocytes control tumor metastasis to the lung. *Science* 350, 6263 (nov 2015), 985–990.
- [105] HARABOR, D., AND GRASTIEN, A. The JPS Pathfinding System. *Fifth Annual Symposium on Combinatorial Search* (2012), 207–208.

- [106] HASHIMOTO, Y., MOKI, T., TAKIZAWA, T., SHIRATSUCHI, A., AND NAKANISHI, Y. Evidence for Phagocytosis of Influenza Virus-Infected, Apoptotic Cells by Neutrophils and Macrophages in Mice. *The Journal of Immunology* 178, 4 (feb 2007), 2448–2457.
- [107] HELMCHEN, F., AND DENK, W. Deep tissue two-photon microscopy. *Nature methods* 2, 12 (2005), 932–940.
- [108] HERZIG, R., LEVI, E., XU, H., GAO, H., BROSH, E., WANG, X., GLOBERSON, A., AND DARRELL, T. Spatio-Temporal Action Graph Networks. *arXiv* (dec 2018).
- [109] HICKMAN, H. D., BENNINK, J. R., AND YEWDELL, J. W. Caught in the Act: Intravital Multiphoton Microscopy of Host-Pathogen Interactions. *Cell Host & Microbe* 5, 1 (jan 2009), 13–21.
- [110] HORN, B. K. P., AND SCHUNCK, B. G. Determining optical flow. *Artificial Intelligence* 17, 1-3 (1981), 185–203.
- [111] HOU, B., REIZIS, B., AND DEFRANCO, A. L. Toll-like Receptors Activate Innate and Adaptive Immunity by using Dendritic Cell-Intrinsic and -Extrinsic Mechanisms. *Immunity* 29, 2 (aug 2008), 272–282.
- [112] HUFFORD, M. M., RICHARDSON, G., ZHOU, H., MANICASSAMY, B., GARCÍA-SASTRE, A., ENELow, R. I., AND BRACIALE, T. J. Influenza-Infected Neutrophils within the Infected Lungs Act as Antigen Presenting Cells for Anti-Viral CD8+ T Cells. *PLoS ONE* 7, 10 (oct 2012).
- [113] HUNTER, M. C., TEIJEIRA, A., MONTECCHI, R., RUSSO, E., RUNGE, P., KIEFER, F., HALIN, C., AND ANGELI, V. Dendritic Cells and T Cells Interact Within Murine Afferent Lymphatic Capillaries. *Frontiers in Immunology* 10, March (2019), 1–11.
- [114] HYUN, Y.-M., CHOE, Y. H., PARK, S. A., AND KIM, M. LFA-1 (CD11a/CD18) and Mac-1 (CD11b/CD18) distinctly regulate neutrophil extravasation through hotspots I and II. *Experimental & Molecular Medicine* 51, 4 (apr 2019), 39.
- [115] IANNAcone, M., MOSEMAN, E. A., TONTI, E., BOSURGI, L., JUNt, T., HENRICKSON, S. E., WHELAN, S. P., GUIDOTTI, L. G., AND VON ANDRIAN, U. H. Subcapsular sinus macrophages prevent CNS invasion on peripheral infection with a neurotropic virus. *Nature* 465, 7301 (jun 2010), 1079–1083.

- [116] ILG, E., CICEK, O., GALESSO, S., KLEIN, A., MAKANSI, O., HUTTER, F., AND BROX, T. Uncertainty estimates and multi-hypotheses networks for optical flow. In *Proceedings of the European Conference on Computer Vision (ECCV)* (2018), pp. 652–667.
- [117] ILG, E., MAYER, N., SAIKIA, T., KEUPER, M., DOSOVITSKIY, A., AND BROX, T. FlowNet 2.0: Evolution of optical flow estimation with deep networks. In *Proceedings of the IEEE conference on computer vision and pattern recognition* (2017), pp. 2462–2470.
- [118] ILG, E., SAIKIA, T., KEUPER, M., AND BROX, T. Occlusions, motion and depth boundaries with a generic network for disparity, optical flow or scene flow estimation. In *Proceedings of the European Conference on Computer Vision (ECCV)* (2018), pp. 614–630.
- [119] JACKSON, D. G. Leucocyte trafficking via the lymphatic vasculature - mechanisms and consequences. *Frontiers in immunology* 10 (2019).
- [120] JIANG, H., FELS, S., AND LITTLE, J. J. A linear programming approach for multiple object tracking. In *2007 IEEE Conference on Computer Vision and Pattern Recognition* (2007), IEEE, pp. 1–8.
- [121] JORDAN, M. I., AND MITCHELL, T. M. Machine learning: Trends, perspectives, and prospects. *Science* 349, 6245 (jul 2015), 255–260.
- [122] KAMENYEVA, O., BOULARAN, C., KABAT, J., CHEUNG, G. Y. C., CICALA, C., YEH, A. J., CHAN, J. L., PERIASAMY, S., OTTO, M., AND KEHRL, J. H. Neutrophil Recruitment to Lymph Nodes Limits Local Humoral Response to *Staphylococcus aureus*. *PLOS Pathogens* 11, 4 (apr 2015), e1004827.
- [123] KAO, J. Y., ZHANG, M., MILLER, M. J., MILLS, J. C., WANG, B., LIU, M., EATON, K. A., ZOU, W., BERNDT, B. E., COLE, T. S., ET AL. *Helicobacter pylori* immune escape is mediated by dendritic cell-induced treg skewing and th17 suppression in mice. *Gastroenterology* 138, 3 (2010), 1046–1054.
- [124] KARLSSON, S. M., AND BIGUN, J. Lip-motion events analysis and lip segmentation using optical flow. In *2012 IEEE Computer Society Conference on Computer Vision and Pattern Recognition Workshops* (jun 2012), IEEE, pp. 138–145.

- [125] KARPATY, A., TODERICI, G., SHETTY, S., LEUNG, T., SUKTHANKAR, R., AND FEI-FEI, L. Large-scale video classification with convolutional neural networks. In *Proceedings of the IEEE conference on Computer Vision and Pattern Recognition* (2014), pp. 1725–1732.
- [126] KARPATNE, A., ATLURI, G., FAGHMOUS, J. H., STEINBACH, M., BANERJEE, A., GANGULY, A., SHEKHAR, S., SAMATOVA, N., AND KUMAR, V. Theory-guided data science: A new paradigm for scientific discovery from data. *IEEE Transactions on Knowledge and Data Engineering* 29, 10 (2017), 2318–2331.
- [127] KATAKAI, T., AND KINASHI, T. Microenvironmental Control of High-Speed Interstitial T Cell Migration in the Lymph Node. *Frontiers in Immunology* 7 (may 2016).
- [128] KAWAKAMI, N., AND FLÜGEL, A. Knocking at the brain’s door: intravital two-photon imaging of autoreactive T cell interactions with CNS structures. *Seminars in Immunopathology* 32, 3 (sep 2010), 275–287.
- [129] KHAN, A. I., KERFOOT, S. M., HEIT, B., LIU, L., ANDONEGUI, G., RUFFELL, B., JOHNSON, P., AND KUBES, P. Role of CD44 and Hyaluronan in Neutrophil Recruitment. *The Journal of Immunology* 173, 12 (dec 2004), 7594–7601.
- [130] KIENLE, K., AND LÄMMERMANN, T. Neutrophil swarming: an essential process of the neutrophil tissue response. *Immunological Reviews* 273, 1 (2016), 76–93.
- [131] KISHIMOTO, T. K., JUTILA, M. A., BERG, E. L., AND BUTCHER, E. C. Neutrophil Mac-1 and MEL-14 adhesion proteins inversely regulated by chemotactic factors. *Science* 245, 4923 (1989), 1238–1241.
- [132] KITANO, M., YAMAZAKI, C., TAKUMI, A., IKENO, T., HEMMI, H., TAKAHASHI, N., SHIMIZU, K., FRASER, S. E., HOSHINO, K., KAISHO, T., AND OKADA, T. Imaging of the cross-presenting dendritic cell subsets in the skin-draining lymph node. *Proceedings of the National Academy of Sciences* 113, 4 (jan 2016), 1044–1049.
- [133] KOLACZKOWSKA, E., AND KUBES, P. Neutrophil recruitment and function in health and inflammation, 2013.
- [134] KREISEL, D., NAVA, R. G., LI, W., ZINSELMAYER, B. H., WANG, B., LAI, J., PLESS, R., GELMAN, A. E., KRUPNICK, A. S., AND MILLER, M. J. In vivo

- two-photon imaging reveals monocyte-dependent neutrophil extravasation during pulmonary inflammation. *Proceedings of the National Academy of Sciences* (2010).
- [135] KREMERS, G.-J., GILBERT, S. G., CRANFILL, P. J., DAVIDSON, M. W., AND PISTON, D. W. Fluorescent proteins at a glance. *J Cell Sci* 124, 2 (2011), 157–160.
- [136] KRUMMEL, M. F., AND CAHALAN, M. D. The Immunological Synapse: a Dynamic Platform for Local Signaling. *Journal of Clinical Immunology* 30, 3 (may 2010), 364–372.
- [137] LABOW, M., SHUSTER, D., ZETTERSTROM, M., NUNES, P., TERRY, R., CULLINAN, E. B., BARTFAI, T., SOLORZANO, C., MOLDAWER, L. L., CHIZZONITE, R., AND MCINTYRE, K. W. Absence of IL-1 signaling and reduced inflammatory response in IL-1 type I receptor-deficient mice. *The Journal of Immunology* 159, 5 (sep 1997), 2452 LP – 2461.
- [138] LAM, P.-Y., AND HUTTENLOCHER, A. Interstitial leukocyte migration in vivo. *Current opinion in cell biology* 25, 5 (oct 2013), 650–8.
- [139] LÄMMERMANN, T. In the eye of the neutrophil swarm-navigation signals that bring neutrophils together in inflamed and infected tissues. *Journal of Leukocyte Biology* 100, 1 (jul 2016), 55–63.
- [140] LÄMMERMANN, T., AFONSO, P. V., ANGERMANN, B. R., WANG, J. M., KASTENMÜLLER, W., PARENT, C. A., AND GERMAIN, R. N. Neutrophil swarms require LTB4 and integrins at sites of cell death in vivo. *Nature* (2013).
- [141] LÄMMERMANN, T., AND SIXT, M. Mechanical modes of ‘amoeboid’ cell migration. *Current Opinion in Cell Biology* 21, 5 (oct 2009), 636–644.
- [142] LAPTEV, I. On space-time interest points. *International journal of computer vision* 64, 2-3 (2005), 107–123.
- [143] LEE, H., ALT, C., PITSILLIDES, C. M., PUORISÄÄHAAG, M., AND LIN, C. P. In vivo imaging flow cytometer. *Optics express* 14, 17 (2006), 7789–7800.
- [144] LEE, M., DOWNES, A., CHAU, Y.-Y., SERRELS, B., HASTIE, N., ELFICK, A., BRUNTON, V., FRAME, M., AND SERRELS, A. In vivo imaging of the tumor and its associated microenvironment using combined cars/2-photon microscopy. *IntraVital* 4, 1 (2015), e1055430.

- [145] LELIEFELD, P. H. C., KOENDERMAN, L., AND PILLAY, J. How Neutrophils Shape Adaptive Immune Responses. *Frontiers in Immunology* 6 (sep 2015).
- [146] LEMPITSKY, V, AND ZISSERMAN, A. Learning to count objects in images. In *Advances in Neural Information Processing Systems* (2010), pp. 1324–1332.
- [147] LEY, K., LAUDANNA, C., CYBULSKY, M. I., AND NOURSHARGH, S. Getting to the site of inflammation: The leukocyte adhesion cascade updated. *Nature Reviews Immunology* 7, 9 (2007), 678–689.
- [148] LI, F., ZHOU, X., MA, J., AND WONG, S. T. C. Multiple nuclei tracking using integer programming for quantitative cancer cell cycle analysis. *IEEE transactions on medical imaging* 29, 1 (2010), 96–105.
- [149] LI, K., MILLER, E. D., CHEN, M., KANADE, T., WEISS, L. E., AND CAMPBELL, P. G. Cell population tracking and lineage construction with spatiotemporal context. *Medical image analysis* 12, 5 (2008), 546–566.
- [150] LIAN, J., AND LUSTER, A. D. Chemokine-guided cell positioning in the lymph node orchestrates the generation of adaptive immune responses, 2015.
- [151] LINDQUIST, R. L., SHAKHAR, G., DUDZIAK, D., WARDEMANN, H., EISENREICH, T., DUSTIN, M. L., AND NUSSENZWEIG, M. C. Visualizing dendritic cell networks in vivo. *Nature Immunology* 5, 12 (dec 2004), 1243–1250.
- [152] LOPEZ, S., MARCO, A. J., PRATS, N., AND CZUPRYNSKI, C. J. Critical Role of Neutrophils in Eliminating *Listeria monocytogenes* from the Central Nervous System during Experimental Murine Listeriosis. *Infection and Immunity* 68, 8 (aug 2000), 4789–4791.
- [153] LOUIE, D. A. P, AND LIAO, S. Lymph Node Subcapsular Sinus Macrophages as the Frontline of Lymphatic Immune Defense. *Frontiers in Immunology* 10 (feb 2019).
- [154] LUCAS, B. D., KANADE, T., ET AL. An iterative image registration technique with an application to stereo vision. In *Proceedings of the Seventh International Joint Conference on Artificial Intelligence* (1981), Vancouver, British Columbia.

- [155] MACQUEEN, J., ET AL. Some methods for classification and analysis of multivariate observations. In *Proceedings of the fifth Berkeley symposium on mathematical statistics and probability* (1967), vol. 1, Oakland, CA, USA., pp. 281–297.
- [156] MAGNUSSON, K. E. G., AND JALDÉN, J. A batch algorithm using iterative application of the Viterbi algorithm to track cells and construct cell lineages. In *Biomedical Imaging (ISBI), 2012 9th IEEE International Symposium on* (2012), IEEE, pp. 382–385.
- [157] MALETTO, B. A., ROPOLO, A. S., ALIGNANI, D. O., LISCOVSKY, M. V., RANOCCHIA, R. P., MORON, V. G., AND PISTORESI-PALENCIA, M. C. Presence of neutrophil-bearing antigen in lymphoid organs of immune mice. *Blood* 108, 9 (nov 2006), 3094–102.
- [158] MANTOVANI, A., CASSATELLA, M. A., COSTANTINI, C., AND JAILLON, S. Neutrophils in the activation and regulation of innate and adaptive immunity. *Nature Reviews Immunology* (2011).
- [159] MANTOVANI, A., DINARELLO, C. A., MOLGORA, M., AND GARLANDA, C. Interleukin-1 and Related Cytokines in the Regulation of Inflammation and Immunity. *Immunity* 50, 4 (apr 2019), 778–795.
- [160] MARANGONI, F., MUROOKA, T. T., MANZO, T., KIM, E. Y., CARRIZOSA, E., ELPEK, N. M., AND MEMPEL, T. R. The transcription factor NFAT exhibits signal memory during serial T cell interactions with antigen-presenting cells. *Immunity* 38, 2 (2013), 237–249.
- [161] MARTIN, C., BURDON, P. C., BRIDGER, G., GUTIERREZ-RAMOS, J. C., WILLIAMS, T. J., AND RANKIN, S. M. Chemokines acting via CXCR2 and CXCR4 control the release of neutrophils from the bone marrow and their return following senescence. *Immunity* (2003).
- [162] MARTIN, D., FOWLKES, C., TAL, D., AND MALIK, J. A database of human segmented natural images and its application to evaluating segmentation algorithms and measuring ecological statistics. In *Proc. 8th Int'l Conf. Computer Vision* (July 2001), vol. 2, pp. 416–423.
- [163] MARTÍNEZ, F., MANZANERA, A., AND ROMERO, E. A Motion Descriptor Based on Statistics of Optical Flow Orientations for Action Classification in Video-Surveillance. *Communications in Computer and Information Science* 346 (2012), 267–274.

- [164] MAŠKA, M., DANĚK, O., GARASA, S., ROUZAUT, A., MUÑOZ-BARRUTIA, A., AND ORTIZ-DE SOLÓRZANO, C. Segmentation and Shape Tracking of Whole Fluorescent Cells Based on the Chan–Vese Model. *IEEE transactions on medical imaging* 32, 6 (2013), 995–1006.
- [165] MATULA, P. P., MASKA, M., SOROKIN, D. V., MATULA, P. P., ORTIZ-DE SOLÓRZANO, C., KOZUBEK, M., MAŠKA, M., SOROKIN, D. V., MATULA, P. P., ORTIZ-DE SOLÓRZANO, C., AND KOZUBEK, M. Cell tracking accuracy measurement based on comparison of acyclic oriented graphs. *PloS one* 10, 12 (2015), e0144959.
- [166] MAŠKA, M., ULMAN, V. V., SVOBODA, D., MATULA, P. P., MATULA, P. P., EDERRA, C., URBIOLA, A., ESPAÑA, T. S., VENKATESAN, S., BALAK, D. M. W., KARAS, P., BOLCKOVÁ, T., TA, M., TREITOVÁ, Š., CARHEL, C., CORALUPPI, S., HARDER, N., ROHR, K., MAGNUSSON, K. E. G., JALDÉ N, J., BLAU, H. M., DZYUBACHYK, O., KÁŽÍŽ EK, P., HAGEN, G. M., PASTOR-ESCUREDO, D., JIMENEZ-CARRETERO, D., LEDESMA-CARBAYO, M. J., MUÑOZ-BARRUTIA, A., MEIJERING, E., KOZUBEK, M., ORTIZ-DE-SOLORZANO, C., MAŠKA, M., ULMAN, V. V., SVOBODA, D., MATULA, P. P., MATULA, P. P., EDERRA, C., URBIOLA, A., ESPAÑA, T., VENKATESAN, S., BALAK, D. M. W., AND OTHERS. A benchmark for comparison of cell tracking algorithms. *Bioinformatics* 30, 11 (2014), 1609–1617.
- [167] MAYADAS, T. N., CULLERE, X., AND LOWELL, C. A. The Multifaceted Functions of Neutrophils. *Annual Review of Pathology: Mechanisms of Disease* (2013).
- [168] MAYER-BARBER, K. D., AND YAN, B. Clash of the Cytokine Titans: counter-regulation of interleukin-1 and type I interferon-mediated inflammatory responses. *Cellular & Molecular Immunology* 14, 1 (jan 2017), 22–35.
- [169] MEDYUKHINA, A., TIMME, S., MOKHTARI, Z., AND FIGGE, M. T. Image-based systems biology of infection. *Cytometry Part A* 87, 6 (2015), 462–470.
- [170] MEHMOOD, R., EL-ASHRAM, S., BIE, R., DAWOOD, H., AND KOS, A. Clustering by fast search and merge of local density peaks for gene expression microarray data. *Nature Publishing Group* (2017).
- [171] MEIJERING, E., CARPENTER, A. E., PENG, H., HAMPRECHT, F. A., AND OLIVOMARIN, J.-C. Imagining the future of bioimage analysis. *Nature biotechnology* 34, 12 (2016), 1250.

- [172] MEMPEL, T. R., HENRICKSON, S. E., AND VON ANDRIAN, U. H. T-cell priming by dendritic cells in lymph nodes occurs in three distinct phases. *Nature* 427, 6970 (jan 2004), 154–159.
- [173] MEMPEL, T. R., PITTET, M. J., KHAZAIE, K., WENINGER, W., WEISSLEDER, R., VON BOEHMER, H., AND VON ANDRIAN, U. H. Regulatory T Cells Reversibly Suppress Cytotoxic T Cell Function Independent of Effector Differentiation. *Immunity* 25, 1 (2006), 129–141.
- [174] MEMPEL, T. R., SCIMONE, M. L., MORA, J. R., AND VON ANDRIAN, U. H. In vivo imaging of leukocyte trafficking in blood vessels and tissues. *Current Opinion in Immunology* 16, 4 (aug 2004), 406–417.
- [175] MILAN, A., REZATOFIHI, S. H., DICK, A., REID, I., AND SCHINDLER, K. Online multi-target tracking using recurrent neural networks. *arXiv preprint arXiv:1604.03635* (2016).
- [176] MILLER, L. S., O’CONNELL, R. M., GUTIERREZ, M. A., PIETRAS, E. M., SHAHANGIAN, A., GROSS, C. E., THIRUMALA, A., CHEUNG, A. L., CHENG, G., AND MODLIN, R. L. MyD88 mediates neutrophil recruitment initiated by IL-1R but not TLR2 activation in immunity against *Staphylococcus aureus*. *Immunity* (2006).
- [177] MILLER, M. J., WEI, S. H., HEJAZI, A. S., PARKER, I., AND CAHALAN, M. D. T cell repertoire scanning is promoted by dynamic dendritic cell behavior and random T cell motility in the lymph node. *Proceedings of the National Academy of Sciences* 101, 4 (2004), 998–1003.
- [178] MILLER, M. J., WEI, S. H., PARKER, I., AND CAHALAN, M. D. Two-photon imaging of lymphocyte motility and antigen response in intact lymph node. *Science (New York, N.Y.)* 296, 5574 (jun 2002), 1869–73.
- [179] MINNS, D., SMITH, K. J., AND FINDLAY, E. G. Orchestration of Adaptive T Cell Responses by Neutrophil Granule Contents. *Mediators of Inflammation* 2019 (mar 2019), 1–15.
- [180] MISHCHENKO, Y. A function for fast computation of large discrete Euclidean distance transforms in three or more dimensions in Matlab. *Signal. Image and Video Processing* 9 (2015), 19.

- [181] MIYAKE, Y., ASANO, K., KAISE, H., UEMURA, M., NAKAYAMA, M., AND TANAKA, M. Critical role of macrophages in the marginal zone in the suppression of immune responses to apoptotic cell-associated antigens. *The Journal of Clinical Investigation* 117, 8 (aug 2007), 2268–2278.
- [182] MIYASAKA, M., AND TANAKA, T. Lymphocyte trafficking across high endothelial venules: Dogmas and enigmas, 2004.
- [183] MÓCSAI, A. Diverse novel functions of neutrophils in immunity, inflammation, and beyond, jul 2013.
- [184] MOEN, E., BORBA, E., MILLER, G., SCHWARTZ, M., BANNON, D., KOE, N., CAMPLISSON, I., KYME, D., PAVELCHEK, C., PRICE, T., KUDO, T., PAO, E., GRAF, W., AND VAN VALEN, D. Accurate cell tracking and lineage construction in live-cell imaging experiments with deep learning. *bioRxiv* (2019).
- [185] MOKHTARI, Z., MECH, F., ZITZMANN, C., HASENBERG, M., GUNZER, M., AND FIGGE, M. T. Automated characterization and parameter-free classification of Cell tracks based on local migration behavior. *PLoS ONE* 8, 12 (2013).
- [186] MONKS, C. R. F., FREIBERG, B. A., KUPFER, H., SCIAKY, N., AND KUPFER, A. Three-dimensional segregation of supramolecular activation clusters in T cells. *Nature* 395, 6697 (sep 1998), 82–86.
- [187] MONTI, S., TAMAYO, P., MESIROV, J., AND GOLUB, T. Consensus clustering: a resampling-based method for class discovery and visualization of gene expression microarray data. *Machine learning* 52, 1-2 (2003), 91–118.
- [188] MOREAU, H. D., LEMAÎTRE, F., TERRIAC, E., AZAR, G., PIEL, M., LENNON-DUMENIL, A.-M., AND BOUSSO, P. Dynamic In Situ Cytometry Uncovers T Cell Receptor Signaling during Immunological Synapses and Kinapses In Vivo. *Immunity* 37, 2 (aug 2012), 351–363.
- [189] MOSEMAN, E. A., IANNAcone, M., BOSURGI, L., TONTI, E., CHEVRIER, N., TUMANOV, A., FU, Y.-X., HACOEN, N., AND VON ANDRIAN, U. H. B Cell Maintenance of Subcapsular Sinus Macrophages Protects against a Fatal Viral Infection Independent of Adaptive Immunity. *Immunity* 36, 3 (mar 2012), 415–426.
- [190] MRASS, P., TAKANO, H., NG, L. G., DAXINI, S., LASARO, M. O., IPARRAGUIRRE, A., CAVANAGH, L. L., VON ANDRIAN, U. H., ERTL, H. C., HAYDON, P. G., AND WENINGER, W. Random migration precedes stable target

- cell interactions of tumor-infiltrating T cells. *The Journal of Experimental Medicine* 203, 12 (nov 2006), 2749–2761.
- [191] MUELLER, S. N., AND GERMAIN, R. N. Stromal cell contributions to the homeostasis and functionality of the immune system. *Nature Reviews Immunology* 9, 9 (sep 2009), 618–629.
- [192] MULLER, U., STEINHOFF, U., REIS, L., HEMMI, S., PAVLOVIC, J., ZINKER-NAGEL, R., AND AGUET, M. Functional role of type I and type II interferons in antiviral defense. *Science* 264, 5167 (jun 1994), 1918–1921.
- [193] MULLER, W. A. Mechanisms of Leukocyte Transendothelial Migration. *Annual Review of Pathology: Mechanisms of Disease* (2011).
- [194] MUROOKA, T. T., DERUAZ, M., MARANGONI, F., VRBANAC, V. D., SEUNG, E., VON ANDRIAN, U. H., TAGER, A. M., LUSTER, A. D., AND MEMPEL, T. R. Hiv-infected t cells are migratory vehicles for viral dissemination. *Nature* 490, 7419 (2012), 283–287.
- [195] NAM, H., AND HAN, B. Learning multi-domain convolutional neural networks for visual tracking. In *Proceedings of the IEEE Conference on Computer Vision and Pattern Recognition* (2016), pp. 4293–4302.
- [196] NAUMENKO, V., TURK, M., JENNE, C. N., AND KIM, S.-J. Neutrophils in viral infection. *Cell and tissue research* 371, 3 (mar 2018), 505–516.
- [197] NEUBERT, P., AND PROTZEL, P. Superpixel Benchmark and Comparison. *Tu-Chemnitz.De* (2012), 1–12.
- [198] NG, L. G., QIN, J. S., ROEDIGER, B., WANG, Y., JAIN, R., CAVANAGH, L. L., SMITH, A. L., JONES, C. A., DE VEER, M., GRIMBALDESTON, M. A., MEEUSEN, E. N., AND WENINGER, W. Visualizing the neutrophil response to sterile tissue injury in mouse dermis reveals a three-phase cascade of events. *Journal of Investigative Dermatology* 131, 10 (2011), 2058–2068.
- [199] NIGAM, I., VATSA, M., AND SINGH, R. Leap signature recognition using hoof and hot features. In *Image Processing (ICIP), 2014 IEEE International Conference on* (2014), IEEE, pp. 5012–5016.
- [200] NITSCHKE, C., GARIN, A., KOSCO-VILBOIS, M., AND GUNZER, M. 3D and 4D imaging of immune cells in vitro and in vivo. *Histochemistry and Cell Biology* 130, 6 (dec 2008), 1053–1062.

- [201] NOURSHARGH, S., AND ALON, R. Leukocyte Migration into Inflamed Tissues. *Immunity* 41, 5 (nov 2014), 694–707.
- [202] NOURSHARGH, S., RENSHAW, S. A., AND IMHOFF, B. A. Reverse Migration of Neutrophils: Where, When, How, and Why? *Trends in immunology* 37, 5 (2016), 273–286.
- [203] OTSU, N. A threshold selection method from gray-level histograms. *IEEE transactions on systems, man, and cybernetics* 9, 1 (1979), 62–66.
- [204] PADFIELD, D., RITTSCHER, J., AND ROYSAM, B. Coupled minimum-cost flow cell tracking for high-throughput quantitative analysis. *Medical image analysis* 15, 4 (2011), 650–668.
- [205] PAI, S., DANNE, K. J., QIN, J., CAVANAGH, L. L., SMITH, A., HICKEY, M. J., AND WENINGER, W. Visualizing leukocyte trafficking in the living brain with 2-photon intravital microscopy. *Frontiers in cellular neuroscience* 6 (2013), 67.
- [206] PALOMINO-SEGURA, M., AND GONZALEZ, S. F. Two-Photon Intravital Imaging of Leukocytes in the Trachea During Pneumococcal Infection. In *Streptococcus pneumoniae*. Springer, 2019, pp. 183–194.
- [207] PALOMINO-SEGURA, M., VIRGILIO, T., MORONE, D., PIZZAGALLI, D., AND GONZALEZ, S. Imaging cell interaction in tracheal mucosa during influenza virus infection using two-photon intravital microscopy. *Journal of Visualized Experiments* 2018, 138 (2018).
- [208] PÉREZ, J. S., MEINHARDT-LLOPIS, E., AND FACCILOLO, G. TV-L1 optical flow estimation. *Image Processing On Line* 2013 (2013), 137–150.
- [209] PETERS, N. C., EGEN, J. G., SECUNDINO, N., DEBRABANT, A., KAMHAWI, S., LAWYER, P., FAY, M. P., GERMAIN, R. N., AND SACKS, D. In vivo imaging reveals an essential role for neutrophils in Leishmaniasis transmitted by sand flies. *Science* 321, 5891 (2009), 970–974.
- [210] PETRI, B., PHILLIPSON, M., AND KUBES, P. The Physiology of Leukocyte Recruitment: An In Vivo Perspective. *The Journal of Immunology* (2008).
- [211] PITTET, M. J., GARRIS, C. S., ARLAUCKAS, S. P., AND WEISSLEDER, R. Recording the wild lives of immune cells. *Science immunology* 3, 27 (sep 2018), eaaq0491.

- [212] PIZZAGALLI, D. U., FARSAKOGLU, Y., PALOMINO-SEGURA, M., PALLADINO, E., SINTES, J., MARANGONI, F., MEMPEL, T. R., KOH, W. H., MUROOKA, T. T., THELEN, F., STEIN, J. V., POZZI, G., THELEN, M., KRAUSE, R., AND GONZALEZ, S. F. Leukocyte Tracking Database, a collection of immune cell tracks from intravital 2-photon microscopy videos. *Scientific Data* 5 (2018), 1–13.
- [213] PIZZAGALLI, D. U., GONZALEZ, S. F., AND KRAUSE, R. A trainable clustering algorithm based on shortest paths from density peaks. *Science Advances* 5, 10 (oct 2019), eaax3770.
- [214] PIZZAGALLI, D. U., LATINO, I., PULFER, A., PALOMINO-SEGURA, M., VIRGILIO, T., FARSAKOGLU, Y., KRAUSE, R., AND GONZALEZ, S. F. Characterization of the dynamic behavior of neutrophils following influenza vaccination. *Frontiers in Immunology* 10 (2019), 2621.
- [215] PIZZAGALLI, D. U., THELEN, M., GONZALEZ, S. F., AND KRAUSE, R. Semi-supervised machine learning facilitates cell colocalization and tracking in 2-photon microscopy. *BioRxiv* (2019).
- [216] PRUENSTER, M., MUDDE, L., BOMBOSI, P., DIMITROVA, S., ZSAK, M., MIDDLETON, J., RICHMOND, A., GRAHAM, G. J., SEGERER, S., NIBBS, R. J. B., AND ROT, A. The Duffy antigen receptor for chemokines transports chemokines and supports their promigratory activity. *Nature immunology* 10, 1 (jan 2009), 101–8.
- [217] PUGA, I., COLS, M., BARRA, C. M., HE, B., CASSIS, L., GENTILE, M., COMERMA, L., CHORNY, A., SHAN, M., XU, W., MAGRI, G., KNOWLES, D. M., TAM, W., CHIU, A., BUSSEL, J. B., SERRANO, S., LORENTE, J. A., BELLOSILLO, B., LLORETA, J., JUANPERE, N., ALAMEDA, F., BARÓ, T., DE HEREDIA, C. D., TORÁN, N., CATALÀ, A., TORREBADELL, M., FORTUNY, C., CUSÍ, V., CARRERAS, C., DIAZ, G. A., BLANDER, J. M., FARBER, C. M., SILVESTRI, G., CUNNINGHAM-RUNDLES, C., CALVILLO, M., DUFOUR, C., NOTARANGELO, L. D., LOUGARIS, V., PLEBANI, A., CASANOVA, J. L., GANAL, S. C., DIEFENBACH, A., ARÓSTEGUI, J. I., JUAN, M., YAGÜE, J., MAHLAOU, N., DONADIEU, J., CHEN, K., AND CERUTTI, A. B cell-helper neutrophils stimulate the diversification and production of immunoglobulin in the marginal zone of the spleen. *Nature Immunology* 13, 2 (feb 2012), 170–180.

- [218] QI, H., CANNONS, J. L., KLAUSCHEN, F., SCHWARTZBERG, P. L., AND GERMAIN, R. N. SAP-controlled T-B cell interactions underlie germinal centre formation. *Nature* 455, 7214 (oct 2008), 764–769.
- [219] RAPTIS, M., KOKKINOS, I., AND SOATTO, S. Discovering discriminative action parts from mid-level video representations. In *2012 IEEE Conference on Computer Vision and Pattern Recognition* (jun 2012), IEEE, pp. 1242–1249.
- [220] RATCLIFFE, D., MIGLIORISI, G., AND CRAMER, E. Translocation of influenza virus by migrating neutrophils. *Cellular and molecular biology* 38, 1 (feb 1992), 63–70.
- [221] RAVICHANDRAN, K. S. Find-me and eat-me signals in apoptotic cell clearance: progress and conundrums. *The Journal of Experimental Medicine* 207, 9 (aug 2010), 1807–1817.
- [222] RIGBY, D. A., FERGUSON, D. J. P., JOHNSON, L. A., AND JACKSON, D. G. Neutrophils rapidly transit inflamed lymphatic vessel endothelium via integrin-dependent proteolysis and lipoxin-induced junctional retraction. *Journal of Leukocyte Biology* (2015).
- [223] RODRIGUES, V., RODRIGUES, P. J., PEREIRA, A. I., AND LIMA, R. Automatic tracking of red blood cells in micro channels using opencv. vol. 1558, pp. 594–597.
- [224] RODRIGUES, V., RODRIGUES, P. J., PEREIRA, A. I., LIMA, R., RODRIGUES, VÂNIA, RODRIGUES, ., PEDRO J, PEREIRA, A. I., LIMA, AND RUI. Automatic cell tracking method based on optical flow tuned by template matching. In *I Encontro de Jovens Investigadores IPB* (2013).
- [225] RODRIGUEZ, A., AND LAIO, A. Clustering by fast search and find of density peaks. *Science* 344, 6191 (jun 2014), 1492–1496.
- [226] SCHAEFER, B. C., SCHAEFER, M. L., KAPPLER, J. W., MARRACK, P., AND KEDL, R. M. Observation of Antigen-Dependent CD8+ T-Cell/ Dendritic Cell Interactions in Vivo. *Cellular Immunology* 214, 2 (dec 2001), 110–122.
- [227] SCHINDELIN, J., ARGANDA-CARRERAS, I., FRISE, E., KAYNIG, V., LONGAIR, M., PIETZSCH, T., PREIBISCH, S., RUEDEN, C., SAALFELD, S., SCHMID, B., AND OTHERS. Fiji: an open-source platform for biological-image analysis. *Nature methods* 9, 7 (2012), 676–682.

- [228] SELMECZI, D., MOSLER, S., HAGEDORN, P. H., LARSEN, N. B., AND FLYVBJERG, H. Cell Motility as Persistent Random Motion: Theories from Experiments. *Biophysical Journal* 89, 2 (aug 2005), 912–931.
- [229] SEVILLA-LARA, L., LIAO, Y., GÜNEY, F., JAMPANI, V., GEIGER, A., AND BLACK, M. J. On the integration of optical flow and action recognition. In *German Conference on Pattern Recognition (2018)*, Springer, pp. 281–297.
- [230] SHANNON, J. G., BOSIO, C. F., AND HINNEBUSCH, B. J. Dermal Neutrophil, Macrophage and Dendritic Cell Responses to *Yersinia pestis* Transmitted by Fleas. *PLoS Pathogens* 11, 3 (2015), 1–19.
- [231] SHARAF, R., MEMPEL, T. R., AND MUROOKA, T. T. Visualizing the Behavior of HIV-Infected T Cells In Vivo Using Multiphoton Intravital Microscopy. *HIV Protocols* (2016), 189–201.
- [232] SHELLARD, A., AND MAYOR, R. Supracellular migration - beyond collective cell migration. *Journal of Cell Science* 132, 8 (apr 2019), jcs226142.
- [233] SHELLARD, A., SZABÓ, A., TREPAT, X., AND MAYOR, R. Supracellular contraction at the rear of neural crest cell groups drives collective chemotaxis. *Science* 362, 6412 (oct 2018), 339–343.
- [234] SIMONYAN, K., AND ZISSERMAN, A. Two-stream convolutional networks for action recognition in videos. In *Advances in neural information processing systems* (2014), pp. 568–576.
- [235] SINGH, D. P., AND KHARE, N. A study of different parallel implementations of single source shortest path algorithms. *International Journal of Computer Applications* 54, 10 (2012).
- [236] SOMMER, C., STRAEHLE, C., KÖTHE, U., AND HAMPRECHT, F. A. Ilastik: Interactive learning and segmentation toolkit. In *2011 IEEE international symposium on biomedical imaging: From nano to macro* (2011), IEEE, pp. 230–233.
- [237] STEIN, J. V., AND GONZALEZ, S. F. Dynamic intravital imaging of cell-cell interactions in the lymph node. *Journal of Allergy and Clinical Immunology* 139, 1 (2017), 12–20.
- [238] STRANGES, P. B., WATSON, J., COOPER, C. J., CHOISY-ROSSI, C.-M., STONEBRAKER, A. C., BEIGHTON, R. A., HARTIG, H., SUNDBERG, J. P., SERVIC, S.,

- KAUFMANN, G., ET AL. Elimination of antigen-presenting cells and autoreactive t cells by fas contributes to prevention of autoimmunity. *Immunity* 26, 5 (2007), 629–641.
- [239] STUTZ, D., HERMANS, A., AND LEIBE, B. Superpixels: An evaluation of the state-of-the-art. *Computer Vision and Image Understanding* 166 (2018), 1–27.
- [240] TATE, M. D., BROOKS, A. G., READING, P. C., AND MINTER, J. D. Neutrophils sustain effective CD8 + T-cell responses in the respiratory tract following influenza infection. *Immunology and Cell Biology* 90, 2 (feb 2012), 197–205.
- [241] TEIJEIRA, A., HUNTER, M. C., RUSSO, E., PROULX, S. T., FREI, T., DEBES, G. F., COLES, M., MELERO, I., DETMAR, M., ROUZAUT, A., AND HALIN, C. T Cell Migration from Inflamed Skin to Draining Lymph Nodes Requires Intralymphatic Crawling Supported by ICAM-1/LFA-1 Interactions. *Cell Reports* 18, 4 (jan 2017), 857–865.
- [242] TENENBAUM, J. B. A Global Geometric Framework for Nonlinear Dimensionality Reduction. *Science* 290, 5500 (dec 2000), 2319–2323.
- [243] THAKUR, M., PFEILER, S., STARK, K., MEGENS, R., JOSHI, U., WEBER, C., MASSBERG, S., AND ENGELMANN, B. Pancreatic tumor microvesicles invade immune cells via cd36 and distinctly promote tumor-associated deep vein thrombosis. *Hämostaseologie* 39, S 01 (2019), P14–1.
- [244] THELEN, M., AND STEIN, J. V. How chemokines invite leukocytes to dance. *Nature immunology* 9, 9 (2008), 953–959.
- [245] THOMAS, S. N., ROHNER, N. A., AND EDWARDS, E. E. Implications of lymphatic transport to lymph nodes in immunity and immunotherapy. *Annual review of biomedical engineering* 18 (2016), 207–233.
- [246] TRAN, D., BOURDEV, L., FERGUS, R., TORRESANI, L., AND PALURI, M. Learning spatiotemporal features with 3d convolutional networks. In *Proceedings of the IEEE international conference on computer vision* (2015), pp. 4489–4497.
- [247] TRAPANI, J. A., AND SMYTH, M. J. Functional significance of the perforin/granzyme cell death pathway. *Nature Reviews Immunology* 2, 10 (oct 2002), 735–747.

- [248] TSUDA, Y., TAKAHASHI, H., KOBAYASHI, M., HANAFUSA, T., HERNDON, D. N., AND SUZUKI, F. Three different neutrophil subsets exhibited in mice with different susceptibilities to infection by methicillin-resistant *Staphylococcus aureus*. *Immunity* 21, 2 (aug 2004), 215–226.
- [249] TURETKEN, E., WANG, X., BECKER, C. J., HAUBOLD, C., AND FUA, P. Network Flow Integer Programming to Track Elliptical Cells in Time-Lapse Sequences. *IEEE Transactions on Medical Imaging* (2016).
- [250] UEKI, H., WANG, I.-H., FUKUYAMA, S., KATSURA, H., DA SILVA LOPES, T. J., NEUMANN, G., AND KAWAOKA, Y. In vivo imaging of the pathophysiological changes and neutrophil dynamics in influenza virus-infected mouse lungs. *Proceedings of the National Academy of Sciences* 115, 28 (jul 2018), E6622–E6629.
- [251] UHLMANN, V., HAUBOLD, C., HAMPRECHT, F. A., AND UNSER, M. Diversepathsj: diverse shortest paths for bioimage analysis. *Bioinformatics (Oxford, England)* 34, 3 (February 2018), 538–540.
- [252] ULLAH, A., AHMAD, J., MUHAMMAD, K., SAJJAD, M., AND BAIK, S. W. Action Recognition in Video Sequences using Deep Bi-Directional LSTM with CNN Features. *IEEE Access* 6, November (2017), 1155–1166.
- [253] ULMAN, V. V., MAŠKA, M., MAGNUSSON, K. E. G., RONNEBERGER, O., HAUBOLD, C., HARDER, N., MATULA, P. P., MATULA, P. P., SVOBODA, D., RADOJEVIC, M., OTHERS, SMAL, I., ROHR, K., JALDÉN, J., BLAU, H. M., DZYUBACHYK, O., LELIEVELDT, B., XIAO, P, LI, Y., CHO, S. Y., DUFOUR, A. C., OLIVO-MARIN, J. C., REYES-ALDASORO, C. C., SOLIS-LEMUS, J. A., BENSCH, R., BROX, T., STEGMAIER, J., MIKUT, R., WOLĘ, S., HAMPRECHT, F. A., ESTEVES, T., QUELHAS, P., DEMIREL, Ö., MALMSTRÖM, L., JUG, F., TOMANCAK, P., MEIJERING, E., MUÑOZ-BARRUTIA, A., KOZUBEK, M., AND ORTIZ-DE-SOLORZANO, C. An objective comparison of cell-tracking algorithms. *Nature methods* 14, 12 (2017), 1141.
- [254] VLADYMYROV, M., ABE, J., MOALLI, F., STEIN, J. V., AND ARIGA, A. Real-time tissue offset correction system for intravital multiphoton microscopy. *Journal of Immunological Methods* 438 (2016), 35–41.
- [255] VOISIN, M.-B., AND NOURSHARGH, S. INVITED REVIEW Neutrophil trafficking to lymphoid tissues: physiological and pathological implications. *Journal of Pathology J Pathol* 247 (2019), 662–671.

- [256] VOLPE, S., THELEN, S., PERTEL, T., LOHSE, M. J., AND THELEN, M. Polarization of migrating monocytic cells is independent of pi 3-kinase activity. *PLoS One* 5, 4 (2010).
- [257] VON LUXBURG, U. A tutorial on spectral clustering. *Statistics and computing* 17, 4 (2007), 395–416.
- [258] VONO, M., LIN, A., NORRBY-TEGLUND, A., KOUŘ, R. A., LIANG, F., AND LORÉ, K. Neutrophils acquire the capacity for antigen presentation to memory CD4+ T cells in vitro and ex vivo. *Blood* 129, 14 (2017), 1991–2001.
- [259] WAIT, E., WINTER, M., BJORNSSON, C., KOKOVAY, E., WANG, Y., GODERIE, S., TEMPLE, S., AND COHEN, A. R. Visualization and correction of automated segmentation, tracking and lineaging from 5-D stem cell image sequences. *BMC Bioinformatics* (2014).
- [260] WANG, H., KLASER, A., SCHMID, C., AND LIU, C.-L. Action recognition by dense trajectories. In *CVPR 2011* (jun 2011), IEEE, pp. 3169–3176.
- [261] WANG, H., KLÄSER, A., SCHMID, C., AND LIU, C.-L. Dense trajectories and motion boundary descriptors for action recognition. *International journal of computer vision* 103, 1 (2013), 60–79.
- [262] WANG, L., AND SAHBI, H. Directed acyclic graph kernels for action recognition. In *The IEEE International Conference on Computer Vision (ICCV)* (December 2013).
- [263] WEIGERT, M., SCHMIDT, U., BOOTHE, T., MÜLLER, A., DIBROV, A., JAIN, A., WILHELM, B., SCHMIDT, D., BROADDUS, C., CULLEY, S., ROCHA-MARTINS, M., SEGOVIA-MIRANDA, F., NORDEN, C., HENRIQUES, R., ZERIAL, M., SOLIMENA, M., RINK, J., TOMANCAK, P., ROYER, L., JUG, F., AND MYERS, E. W. Content-aware image restoration: pushing the limits of fluorescence microscopy. *Nature Methods* 15, 12 (dec 2018), 1090–1097.
- [264] WEINLAND, D., RONFARD, R., AND BOYER, E. Free viewpoint action recognition using motion history volumes. *Computer vision and image understanding* 104, 2-3 (2006), 249–257.
- [265] WENINGER, W., BIRO, M., AND JAIN, R. Leukocyte migration in the interstitial space of non-lymphoid organs. *Nature reviews. Immunology* 14, 4 (2014), 232.

- [266] WIESNER, D., SVOBODA, D., MAŠKA, M., AND KOZUBEK, M. Cytovacq: a web-interface for simulating multi-dimensional cell imaging. *Bioinformatics* (2019).
- [267] WILLARD-MACK, C. L. Normal Structure, Function, and Histology of Lymph Nodes. *Toxicologic Pathology* 34, 5 (aug 2006), 409–424.
- [268] WIWIE, C., BAUMBACH, J., AND RÖTTGER, R. Comparing the performance of biomedical clustering methods. *Nature Methods* 12, 11 (2015), 1033–1038.
- [269] WOLĘ K., MÜLLER, R., BORGMANN, S., BRÖCKER, E.-B., AND FRIEDL, P. Amoeboid shape change and contact guidance: T-lymphocyte crawling through fibrillar collagen is independent of matrix remodeling by MMPs and other proteases. *Blood* 102, 9 (nov 2003), 3262–9.
- [270] XIE, J., TATO, C. M., AND DAVIS, M. M. How the immune system talks to itself: the varied role of synapses. *Immunological Reviews* 251, 1 (jan 2013), 65–79.
- [271] XU, Q., HAMILTON, R. J., SCHOWENGERDT, R. A., ALEXANDER, B., AND JIANG, S. B. Lung tumor tracking in fluoroscopic video based on optical flow. *Medical physics* 35, 12 (2008), 5351–5359.
- [272] YAMATO, J., OHYA, J., AND ISHII, K. Recognizing human action in time-sequential images using hidden markov model. In *Proceedings 1992 IEEE Computer Society conference on computer vision and pattern recognition* (1992), IEEE, pp. 379–385.
- [273] ZACH, C., POCK, T., AND BISCHOF, H. A duality based approach for real-time TV-L 1 optical flow. In *Joint Pattern Recognition Symposium* (2007), Springer, pp. 214–223.
- [274] ZHANG, S., WEI, Z., NIE, J., HUANG, L., WANG, S., AND LI, Z. A Review on Human Activity Recognition Using Vision-Based Method. *Journal of Healthcare Engineering* 2017 (2017), 1–31.
- [275] ZHANG, Y., BAI, X.-T., ZHU, K.-Y., JIN, Y., DENG, M., LE, H.-Y., FU, Y.-F., CHEN, Y., ZHU, J., LOOK, A. T., KANKI, J., CHEN, Z., CHEN, S.-J., AND LIU, T. X. In Vivo Interstitial Migration of Primitive Macrophages Mediated by JNK-Matrix Metalloproteinase 13 Signaling in Response to Acute Injury. *The Journal of Immunology* 181, 3 (aug 2008), 2155–2164.

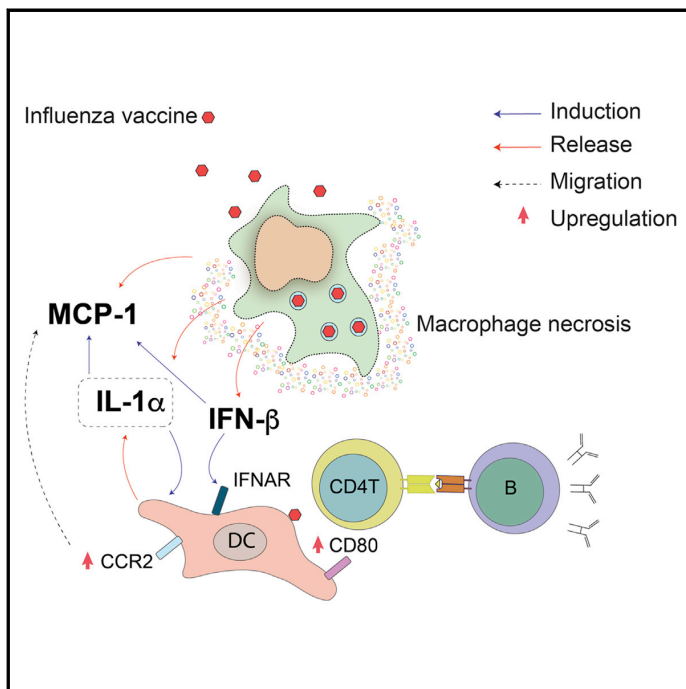
-
- [276] ZHANG, Y., ZHANG, Y., ZHANG, Z., BAO, J., AND SONG, Y. Human activity recognition based on time series analysis using U-Net. *arXiv preprint* (2018).
- [277] ZHOU, F. Y., RUIZ-PUIG, C., OWEN, R. P., WHITE, M. J., RITTSCHER, J., AND LU, X. Motion sensing superpixels (MOSES) is a systematic computational framework to quantify and discover cellular motion phenotypes. *eLife* 8 (feb 2019).
- [278] ZIMMER, C., LABRUYERE, E., MEAS-YEDID, V., GUILLEN, N., AND OLIVOMARIN, J.-C. Segmentation and tracking of migrating cells in videomicroscopy with parametric active contours: A tool for cell-based drug testing. *IEEE transactions on medical imaging* 21, 10 (2002), 1212–1221.
- [279] ZIMMER, C., ZHANG, B., DUFOUR, A., THÉBAUD, A., BERLEMONT, S., MEAS-YEDID, V., AND MARIN, J.-C. On the digital trail of mobile cells. *IEEE Signal Processing Magazine* 23, 3 (2006), 54–62.

Additional contributions

Cell Reports

Macrophage Death following Influenza Vaccination Initiates the Inflammatory Response that Promotes Dendritic Cell Function in the Draining Lymph Node

Graphical Abstract



Authors

Nikolaos Chatziandreou,
Yagmur Farsakoglu,
Miguel Palomino-Segura, ...,
Antonio Lanzavecchia, Michael C. Carroll,
Santiago F. Gonzalez

Correspondence

santiago.gonzalez@irb.usi.ch

In Brief

The mechanism by which inflammation influences the antibody response to vaccines is unclear. Chatziandreou et al. found that lymph node macrophages are key players in the initiation of the IL-1 α -mediated inflammatory response that follows influenza vaccination.

Highlights

- Lymph node macrophages undergo necrosis after vaccination
- Subcapsular sinus macrophage disappearance is mediated by TLR7
- Macrophage death induces the activation and relocation of CD11b⁺ dendritic cells
- IL-1 α -mediated inflammation is essential for B cell responses



CrossMark

Chatziandreou et al., 2017, Cell Reports 18, 2427–2440
March 7, 2017 © 2017 The Author(s).
<http://dx.doi.org/10.1016/j.celrep.2017.02.026>

CellPress

Macrophage Death following Influenza Vaccination Initiates the Inflammatory Response that Promotes Dendritic Cell Function in the Draining Lymph Node

Nikolaos Chatziandreou,^{1,9} Yagmur Farsakoglu,^{1,9} Miguel Palomino-Segura,¹ Rocco D'Antuono,¹ Diego Ulisse Pizzagalli,^{1,2} Federica Sallusto,^{1,3} Veronika Lukacs-Kornek,⁴ Mariagrazia Ugucioni,^{1,5} Davide Corti,⁶ Shannon J. Turley,⁷ Antonio Lanzavecchia,^{1,3} Michael C. Carroll,⁸ and Santiago F. Gonzalez^{1,10,*}

¹Institute for Research in Biomedicine, Università della Svizzera Italiana, via Vincenzo Vela 6, 6500 Bellinzona, Switzerland

²Institute of Computational Science, Università della Svizzera Italiana, via G. Buffi 13, 6900 Lugano, Switzerland

³Institute for Microbiology, ETH Zurich, Wolfgang-Pauli-Strasse 10, 8093 Zurich, Switzerland

⁴Department of Internal Medicine II, Saarland University Medical Centre, 66424 Homburg, Germany

⁵Department of Biomedical Sciences, Humanitas University, Via Manzoni 113, 20089 Rozzano-Milan, Italy

⁶Humabs BioMed SA, 6500 Bellinzona, Switzerland

⁷Cancer Immunology, Genentech, South San Francisco, CA 94080, USA

⁸Department of Pediatrics, Harvard Medical School and PCMM, Boston Childrens Hospital, Boston, MA 02115, USA

⁹Co-first author

¹⁰Lead Contact

*Correspondence: santiago.gonzalez@irb.usi.ch
<http://dx.doi.org/10.1016/j.celrep.2017.02.026>

SUMMARY

The mechanism by which inflammation influences the adaptive response to vaccines is not fully understood. Here, we examine the role of lymph node macrophages (LNMs) in the induction of the cytokine storm triggered by inactivated influenza virus vaccine. Following vaccination, LNMs undergo inflammasome-independent necrosis-like death that is reliant on MyD88 and Toll-like receptor 7 (TLR7) expression and releases pre-stored interleukin-1 α (IL-1 α). Furthermore, activated medullary macrophages produce interferon- β (IFN- β) that induces the autocrine secretion of IL-1 α . We also found that macrophage depletion promotes lymph node-resident dendritic cell (LNDC) relocation and affects the capacity of CD11b⁺ LNDCs to capture virus and express co-stimulatory molecules. Inhibition of the IL-1 α -induced inflammatory cascade reduced B cell responses, while co-administration of recombinant IL-1 α increased the humoral response. Stimulation of the IL-1 α inflammatory pathway might therefore represent a strategy to enhance antigen presentation by LNDCs and improve the humoral response against influenza vaccines.

INTRODUCTION

Lymph node macrophages (LNMs) are increasingly subject to investigation with a particular focus on their role in the initiation of the immune response (Gray and Cyster, 2012). LNMs can be

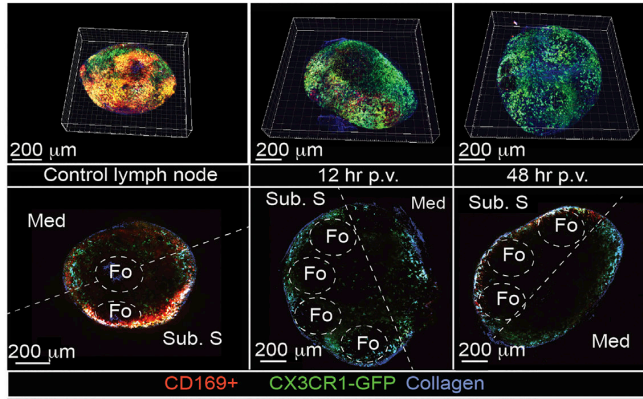
classified as subcapsular sinus or medullary macrophages (SSMs and MMs, respectively) according to their anatomical position, expression of different surface markers, and function (Kuka and Iannacone, 2014).

Located in proximity to the lymph node (LN) follicles, SSMs are important components of the innate defense barrier, acting as “flypaper” that prevents the dissemination of lymph-borne pathogens, including viruses (Farrell et al., 2015; Iannacone et al., 2010; Junt et al., 2007; Moseman et al., 2012; Winkelmann et al., 2014), bacteria (Kastenmüller et al., 2012) and parasites (Chtanova et al., 2008). In addition to their role in containing infectious agents, SSMs are known for their capacity to present intact antigen to B cells in the proximal follicles (Carrasco and Batista, 2007; Gaya et al., 2015; Junt et al., 2007; Phan et al., 2007, 2009) and processed antigen to T cells (Hickman et al., 2008). However, the factors that affect the ability of SSMs to recycle intact antigen or process and present it through the major histocompatibility complex (MHC) are yet to be elucidated. Considering the important role of SSMs as antigen-presenting cells (APCs), it has been suggested that they may compete with LN-resident dendritic cells (LNDCs) for antigen capture and presentation to T or B cells (Gonzalez et al., 2010). MMs are known for their high phagocytic capacity that is greater than that of SSMs, and their expression of endosomal degradative enzymes (Kuka and Iannacone, 2014). However, their relevance in the initiation of immune responses is poorly understood mainly due to the lack of suitable methods for their specific depletion.

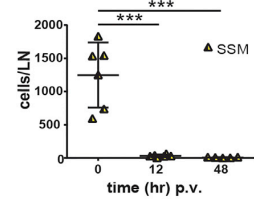
The ability of LNDCs to capture antigen and induce T cell responses has been documented previously (Gerner et al., 2015; Gonzalez et al., 2010; Hickman et al., 2008; Mempel et al., 2004; Sung et al., 2012; Woodruff et al., 2014). However, the exact location at which antigen presentation occurs and the role that LNMs play in dendritic cell (DC) activation remain



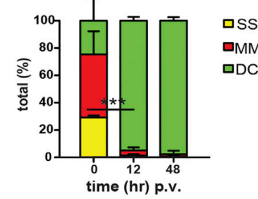
A 3D 2-photon reconstruction of popliteal LN p.v.



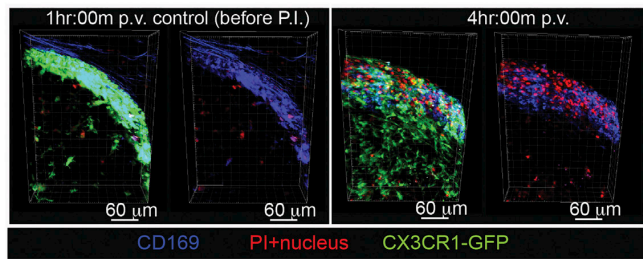
B 3D reconstruction analysis.



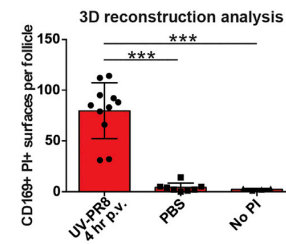
C % cell population in LN.



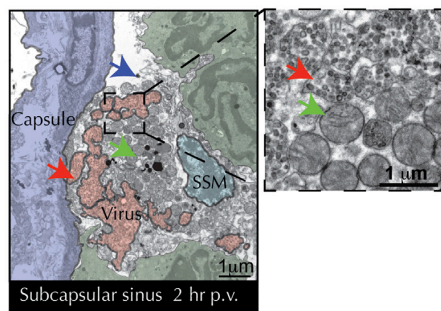
D 3D 2-photon reconstruction of popliteal LN in vivo stained with PI.



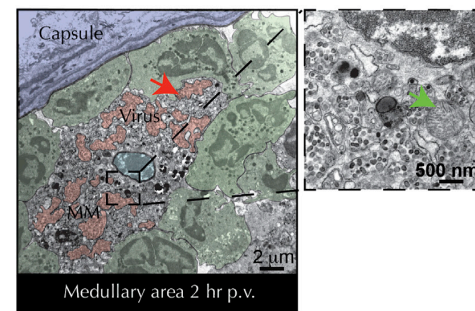
E 3D reconstruction analysis.



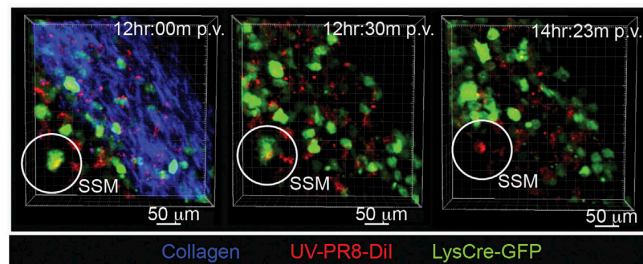
F TEM of SSM at 2hr p.v.



G TEM of MM at 2hr p.v.



H 2-photon intravital microscopy of SSM undergoing necrosis.



(legend on next page)

controversial. In addition to the well-characterized DC-T cell interaction in the LN cortex (Mempel et al., 2004), recent studies have suggested alternative areas in which this may occur. Woodruff and colleagues (Woodruff et al., 2014) described the relocation of DCs from the paracortex to the medullary area following vaccination. In addition, the interfollicular regions adjacent to the subcapsular sinus appear to be a preferred area for the priming of CD8⁺ (Gerner et al., 2015; Hickman et al., 2008; Sung et al., 2012) and CD4⁺ (Gerner et al., 2015; Woodruff et al., 2014) T cells by DCs. Despite the established role of DCs in acquiring antigen, not much is known about the molecular mechanisms that lead to their activation and positioning in lymphoid tissues and the role that LN macrophages have in these processes. Cytokines secreted by macrophages in response to antigen, such as type I interferons (IFNs), have been postulated to participate in the activation of DCs (Moseman et al., 2012; Sung et al., 2012) through a mechanism that involves the induction of CXCR3 ligands (Asselin-Paturel et al., 2005). However, a better understanding of the function of type I IFNs in the LN and their contribution to DC function is required.

In this study, we report that LNMs initiate an inflammatory response that leads to the activation of CD11b⁺ LNDCs through an interleukin-1 α (IL-1 α)-mediated process, which is essential for the elicitation of the humoral response against influenza vaccine.

RESULTS

Influenza Vaccination Induces LN Macrophage Activation and Promotes Cell Death

To examine macrophage responses to UV-inactivated influenza virus vaccine (UV-PR8) in the popliteal LN, we employed different imaging techniques, including two-photon (2PM), electron microscopy (EM), and confocal microscopy. Three-dimensional (3D) reconstructions from 2PM images of the popliteal LN cortical area (Figure 1A) showed a significant decrease in the number of SSMs at 12 and 48 hr post-vaccination (p.v.) (Figure 1B). Additionally, the percentage of SSMs and MMs was reduced over time, whereas the percentage of DCs increased significantly (Figure 1C).

To further investigate the type of SSM death, we used in vivo staining with propidium iodide (PI) followed by 2PM imaging of LNs explanted at 4 hr p.v. (Figure 1D). 3D reconstruction analysis revealed a clear increase of PI⁺ SSMs in vaccinated groups

compared to PBS-treated controls (Figure 1E), highlighting further the necrotic nature of SSM disappearance. To better examine the morphological features of the dying cells, EM was performed at 2 hr p.v., which revealed signs of necrosis in both SSMs (Figure 1F) and MMs (Figure 1G), including loss of plasma membrane integrity, mitochondria swelling, and chromatin condensation. Multiple endosomes containing viral particles were also detected in the cytoplasm of the observed cells, demonstrating their active phagocytic nature. To confirm SSM disappearance in vivo, we performed intravital 2PM on LysMCre-GFP mice. We observed that SSMs (sessile and large) that internalized UV-PR8 underwent cellular death, as evidenced by the loss of fluorescence, which is associated with the disruption of the plasma membrane. Moreover, dying SSMs did not form any blebs that are typically present in apoptotic cells (Figure 1H; Movie S1).

Using multicolor flow cytometric analysis, we assessed LN macrophage numbers in response to vaccination. A full description of the applied gating strategy is provided in Figure S1A. We found that the numbers of both SSMs and MMs were reduced by UV-PR8 administration by 12 hr p.v. (Figure 2A). We also observed that SSMs and MMs became rapidly activated following vaccine administration, as measured by the prominent upregulation of the early activation marker CD69 (Figures 2B and 2C, respectively; Figure S1B). Importantly, we observed that LNMs disappeared within the first 3 hr p.v. (Figures 2D and 2E) and remained absent for at least 1 week in the case of SSMs (Figure 1F) and 3 days in the case of MMs (Figure 1G).

The observed death mechanism was not exclusively associated with viral antigen, as SSM and MM numbers were also significantly reduced after vaccination with heat-inactivated *Streptococcus pneumoniae* (Figures S1C and S1D).

SSM Disappearance Is Dependent on Viral Internalization, TLR7 Recognition, and MyD88 Signaling, while MM Death Is Not

Having observed LNM disappearance, it was of interest to identify the factors involved in this phenomenon. To evaluate the role of viral entry in the observed death mechanism, we pretreated mice with two different anti-influenza antibodies: the neutralizing antibody H36-7 that binds specifically to the globular head of the viral hemagglutinin (HA) molecule of the PR8 H1N1 strain, thus preventing its interaction with the sialic acid (SA) of the target cell and blocking viral entry (Staudt and Gerhard, 1983), and

Figure 1. LN Macrophages undergo Necrosis-like Death after Influenza Vaccination

(A) The top panels show representative 3D reconstructions from 2PM images of popliteal LN from UV-PR8-administered CX3CR1-GFP reporter mice (green) at 12 and 48 hr p.v. (middle and right panels, respectively) following in vivo staining with anti-CD169-PE and anti-CD21/35-PB antibodies. The left panels show the unvaccinated control. The bottom panels present cross sections from the corresponding 3D reconstructions in the top panels. SSMs are indicated in yellow.

(B) Quantitative analysis of 2PM data showing SSM disappearance ($n \geq 5$ LN).

(C) Changes in the percentages of SSMs (CD169⁺, CX3CR1⁺), MMs (CD169⁺, CX3CR1⁻), and DCs (CD169⁻, CX3CR1⁺) in the LN at 12 and 24 hr p.v. ($n \geq 4$ LN).

(D) Representative 3D reconstruction from 2PM images of LN from CX3CR1-GFP reporter mice at 4 hr p.v. LN was stained in vivo with anti-CD169-PB antibody and PI.

(E) Quantitative analysis of 2PM from LN follicular areas showing the increase in number of PI⁺ CD169⁺ macrophages in the subcapsular sinus at 4 hr p.v. ($n \geq 10$ follicles).

(F and G) Representative electron micrograph of a SSM (F) and MM (G) at 2 hr p.v. In both cases, clear signs of necrosis, including loss of plasma membrane integrity (blue arrow), mitochondria swelling (green arrow), and multiple phagocytic vesicles with virus (red arrow, with higher magnification in the right panel), are evident.

(H) Intravital 2PM sequence from LysMCre-GFP reporter mice (green) showing SSM disappearance at 12 hr p.v. with Dil-labeled UV-PR8 (red) (Movie S1). Med, medullary area; Sub. S, subcapsular sinus area; Fo, follicle; MM, medullary macrophage; DC, dendritic cell.

In all figures, the presented data are representative of at least three independent experiments ($n \geq 3$). * $p < 0.1$; ** $p < 0.01$; *** $p < 0.001$. Error bars, SD.

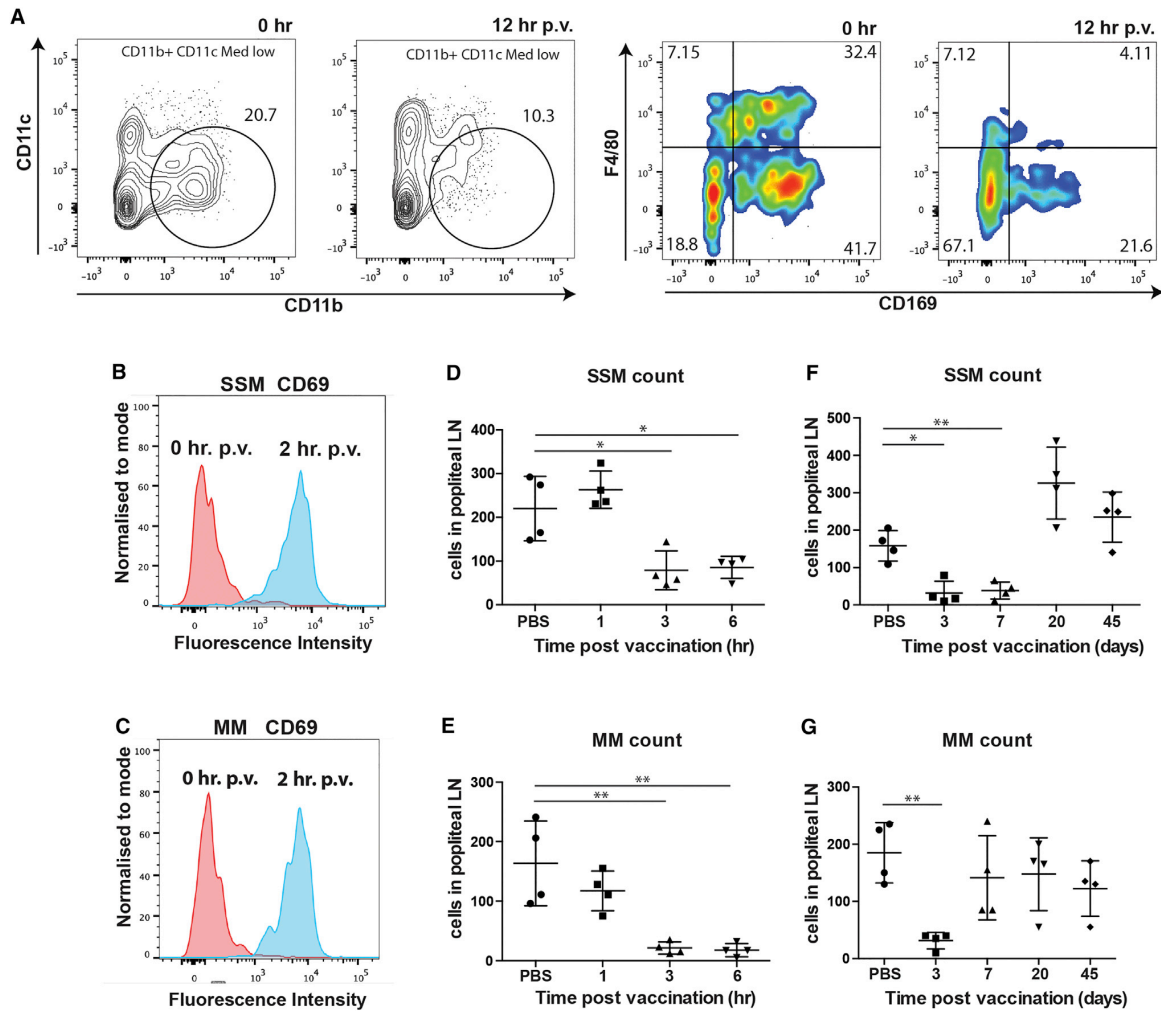


Figure 2. LN Macrophages Get Rapidly Activated and Are Absent from the LN during the First 3 Days p.v.

(A) Representative scatterplots from flow cytometric analysis of popliteal LNs showing an evident reduction of SSMs defined as CD3(–)/B220(–)/Ly6G(–)/Ly6C(–)/CD11c(inter./low)/CD11b(high)/MHCII(+)/F4/80(–)/CD169(+) in the popliteal LN at 12 hr p.v.

(B) Representative histogram of fluorescence intensity indicating differences in surface expression of the early activation marker CD69 in SSMs and MMs (C) at 2 hr. p.v. (blue) in comparison with the PBS-injected group (red).

(D–G) Flow cytometric analysis showing the rapid disappearance of SSMs (D) and MMs (E) following vaccine administration (10^5 PFU/footpad) and their reappearance at day 20 and day 7 p.v., respectively (F and G).

In all figures, the presented data are representative of at least three independent experiments ($n \geq 3$). * $p < 0.1$; ** $p < 0.01$; *** $p < 0.001$. Error bars, SD.

the anti-fusion antibody FI6 that binds to the stem of the HA molecule, preventing the fusion of the virus with the endosome (Corti et al., 2011). Strikingly, immunization with H36-7 effectively prevented p.v. SSM death, while pretreatment with FI6 did not (Figure 3A), confirming that the SA-HA interaction and subsequent viral internalization is required for SSM death to be induced. In contrast, MM death was not prevented by H36-7 (Figure 3B), suggesting that virus internalization is not required for MMs to disappear. Moreover, SSM and MM disappearance was

dependent on vaccine dosage, with complete depletion being induced with 10^5 plaque-forming units (PFUs) per footpad (Figures 3C and 3D). In an attempt to induce inflammation without the presence of virus, we administered alum, an adjuvant known for its proinflammatory properties. We observed that alum alone led to a significant reduction in the number of MMs (Figure S2G), while the number of SSMs remained unaffected (Figure S2F).

A previous study suggested that following parasitic infection, SSMs disappeared due to infiltrated neutrophils (Chtanova

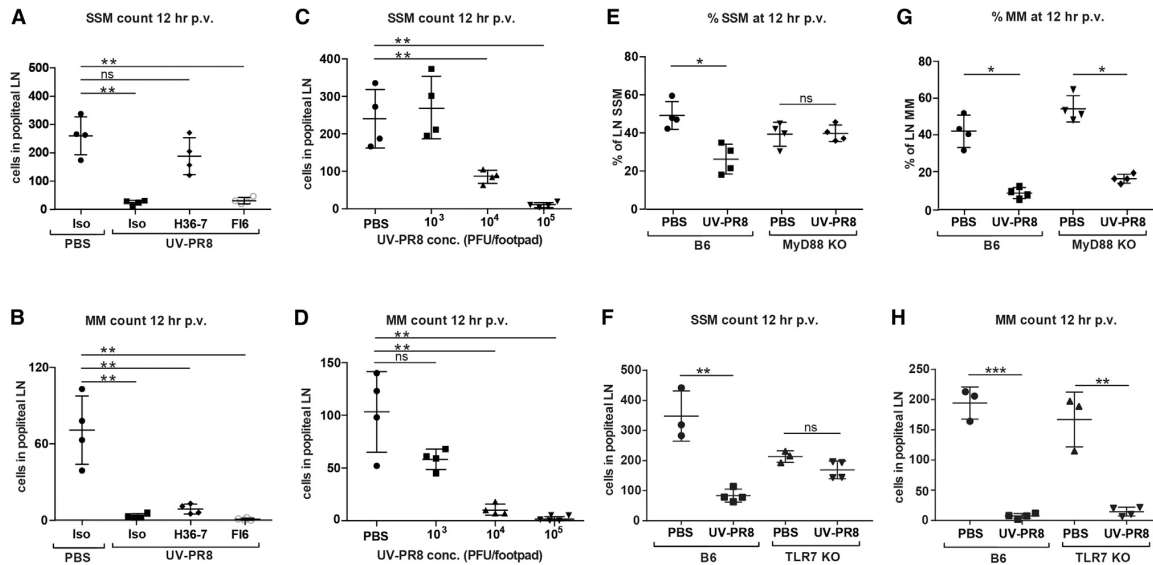


Figure 3. SSM Disappearance Requires Viral Internalization and Is Dependent on MyD88 and TLR7 Recognition, while MM Does Not (A and B) Flow cytometric analysis of SSMs (A) and MMs (B) from mice passively immunized with the influenza-neutralizing antibody H36-7 and the anti-fusion antibody F16 prior to the administration of UV-inactivated vaccine (UV-PR8). Pre-administration of H36-7 rescues SSMs from death following the administration of UV-PR8, but not MMs (A and B, respectively). (C and D) Flow cytometric analysis showing a correlation between the number of SSMs (C) and MMs (D) and influenza vaccine dosage. (E–H) Flow cytometric analysis of SSMs from MyD88 KO (E) and TLR7 KO (F) mice at 12 hr after administration of UV-PR8 showing that MyD88 and TLR7 are involved in the intracellular signaling events that lead to SSM death in response to UV-PR8, but not MM death (G and H). In all figures, the presented data are representative of at least three independent experiments ($n \geq 3$). * $p < 0.1$; ** $p < 0.01$; *** $p < 0.001$. Error bars, SD.

et al., 2008). In our work, we also observed recruitment of natural killer (NK) cells and neutrophils to the subcapsular sinus (data not shown). However, when these cells were eliminated using α NK1.1 and α Ly-6G antibodies, respectively, we found that LNM disappearance remained unaffected (Figures S2C and S2D). A possible role of migratory DCs in the disruption of the SSM layer has been reported previously (Gaya et al., 2015). We found that migratory DCs did not contribute to the observed phenotype, as vaccinated CCR7 knockout (KO) mice, which are deficient in DC recruitment to the LN (Martín-Fontecha et al., 2003), exhibited the same SSM response as B6 mice (Figure S2E).

To determine the role of the inflammasome in this process, we vaccinated mice deficient in IL-1R, IL-1 β , the adaptor protein ASC (apoptosis-associated speck-like protein with a CARD domain), or ICE (IL-1 β -converting enzyme) and assessed their SSM numbers by flow cytometry at 12 hr p.v. Contrary to a recent report that described an inflammasome-dependent SSM burst in response to vaccinia virus (Sagoo et al., 2016), we observed a consistent decrease in SSMs in all of the tested KO strains p.v., confirming that, at least in our model, the inflammasome was not involved in LNM death (Figure S2A). In support of these results, we were not able to detect any upregulation of the transcripts of IL-1 β or IL-18 during the first 24 hr p.v. (Figure S2B). In contrast, p.v. SSM disappearance was prevented in MyD88 KO mice (Figure 3E) and in Toll-like receptor

7 (TLR7) KO (Figure 3F), which confirmed that the death mechanism is dependent on viral recognition mediated by TLR7 signaling. However, MM death was not prevented in MyD88 KO (Figure 3G) or TLR7 KO (Figure 3H) mice, which suggests that death is triggered by different pathways in these cell populations.

LN Macrophages Initiate the Inflammatory Cascade that Follows Vaccine Administration

To evaluate the role that LNMs have on the initiation of the inflammatory response, we focused on the expression of different proinflammatory molecules after vaccination. Among the tested cytokines, we detected a rapid and significant secretion of IL-1 α and IFN- β in the LN within the first 90 min p.v. (Figure 4A). To evaluate the duration and magnitude of the inflammatory reaction, we examined the levels of additional inflammatory molecules in the first 24 hr p.v. We observed a significant peak in the secretion of MIG, IP-10, KC, MCP-1, MIP-1 α , and MIP-1 β at 12 hr, followed by an abrupt decrease by 24 hr p.v. (Figure 4B).

To investigate the role of macrophage death in the induction of the inflammatory response, we measured the levels of secreted IFN- β and IL-1 α in mice in which LN macrophages had been depleted with clodronate liposomes (CLLs) prior to vaccination. We observed that p.v. IFN- β secretion, which we found to be MyD88 independent, was abolished in CLL-pretreated mice (Figure 4C, left). Similarly, secretion of IL-1 α was inhibited in

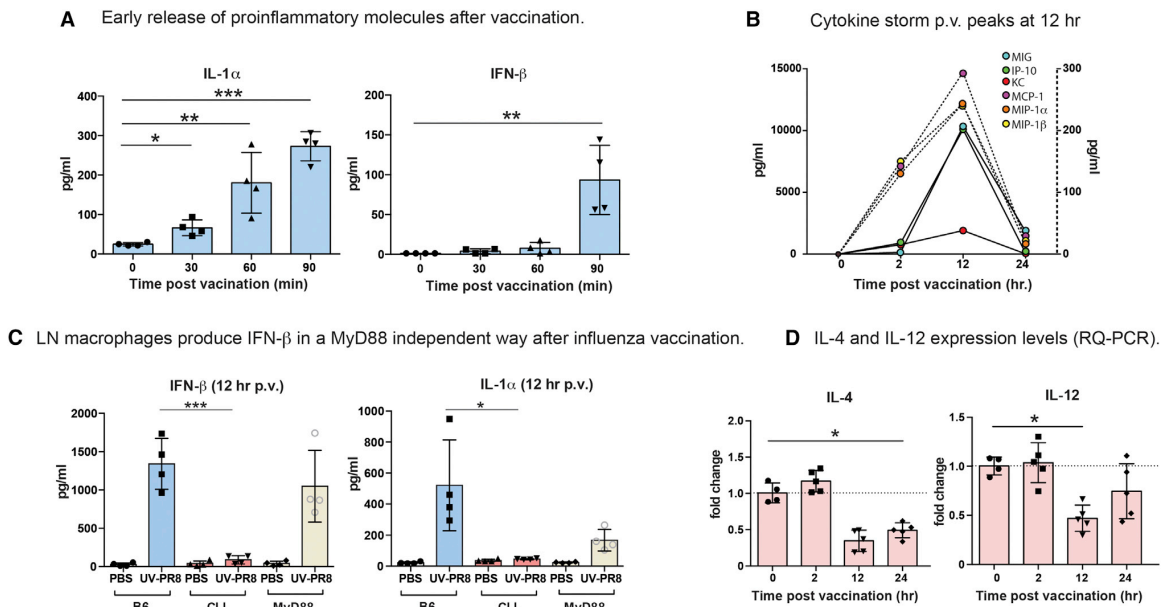


Figure 4. LNMs Are Responsible of the Initial Type I IFN Response that Follows Vaccination

(A) Secretion of the proinflammatory cytokines IL-1 α and IFN- β in the first 90 min p.v. Cytokine levels were measured in LN exudates by a cytoplex assay. (B) Levels of acute-phase cytokines MIG, IP-10, KC, MCP-1, MIP-1 α , and MIP-1 β in the LN in the first 24 hr p.v. A peak of secretion was measured at 12 hr p.v. Dotted lines refer to the right-hand axis. (C) Levels of secreted IFN- β and IL-1 α in LNs from macrophage-depleted (CLL-pretreated) and MyD88 KO mice at 12 hr p.v. The expression of these cytokines requires the existence of macrophage prior to vaccination. (D) RNA expression levels of the cytokines IL-4 and IL-12 during the first 24 hr that follows vaccination. In all figures, the presented data are representative of at least three independent experiments ($n \geq 3$). * $p < 0.1$; ** $p < 0.01$; *** $p < 0.001$. Error bars, SD.

this group, although the production of this cytokine was dependent on MyD88 (Figure 4C, right). Moreover, mRNA levels of the cytokines IL-4 and IL-12, which are important for the differentiation of naive T cells into Th2 and Th1, respectively, were found to be significantly downregulated at 12 hr p.v. (Figure 4D). Taken together, these findings suggest that, upon vaccine challenge, macrophages are key to the production of inflammatory cytokines in the draining LNs.

IFN- β Produced by MMs Triggers the IL-1 α Inflammatory Cascade

To investigate whether macrophages were the source of the type I IFN response, we performed intracellular staining of IFN- β at 2 hr p.v. Moreover, since DCs had been previously identified as a source of IFN- β in the LN (Iannacone et al., 2010), it was of interest to include them in our investigation. Flow cytometric analysis showed that both macrophages and DC produced IFN- β , but to a different extent. Although the IFN- β + cell count was similar for both LNs and DCs, at 2 hr p.v. (data not shown), the former expressed IFN- β at levels $\sim 1,000$ times higher than the latter (Figure 5A, left). Interestingly, a more detailed characterization of the macrophage subtype showed that at 2 hr p.v., the majority of IFN- β + macrophages were MMs (Figure 5B). These results were further confirmed by immunohistochemical

analysis in which we observed a prominent expression of IFN- β that was associated with CD169+ MMs located in the interfollicular and medullary areas at 2 hr p.v. (Figure 5C), compared to controls (Figure S3A). Additionally, IFN- β expression appeared to be induced in a positive feedback loop initiated by macrophages, as IFN- α/β receptor (IFNAR) KO or macrophage-depleted (CD169DTR) mice presented significantly lower IFN- β levels than B6 controls at 12 hr p.v. (Figure 5D).

To study the mechanism of action of IL-1 α and IFN- β , we examined the effect of different concentrations of their recombinant forms alone (without vaccination with UV-PR8). At 12 hr post-administration (footpad injection) of recombinant IL-1 α or recombinant IFN- β , we measured concentrations of inflammatory cytokines in the LN similar to the ones previously detected following vaccination. Interestingly, IFN- β was sufficient to induce secretion of IL-1 α , albeit at levels inversely proportional to the administered dose. Strikingly, both IL-1 α and IFN- β were sufficient to induce the expression of the chemoattractant protein MCP-1 that is involved in the trafficking of monocytes and DCs (Figure 5E).

To examine the involvement of LNs in the expression of IL-1 α , immunostaining was performed in LN sections at 2 hr p.v., and results confirmed that LN macrophages act as producers of this cytokine (Figure 5F). Additionally, intracellular

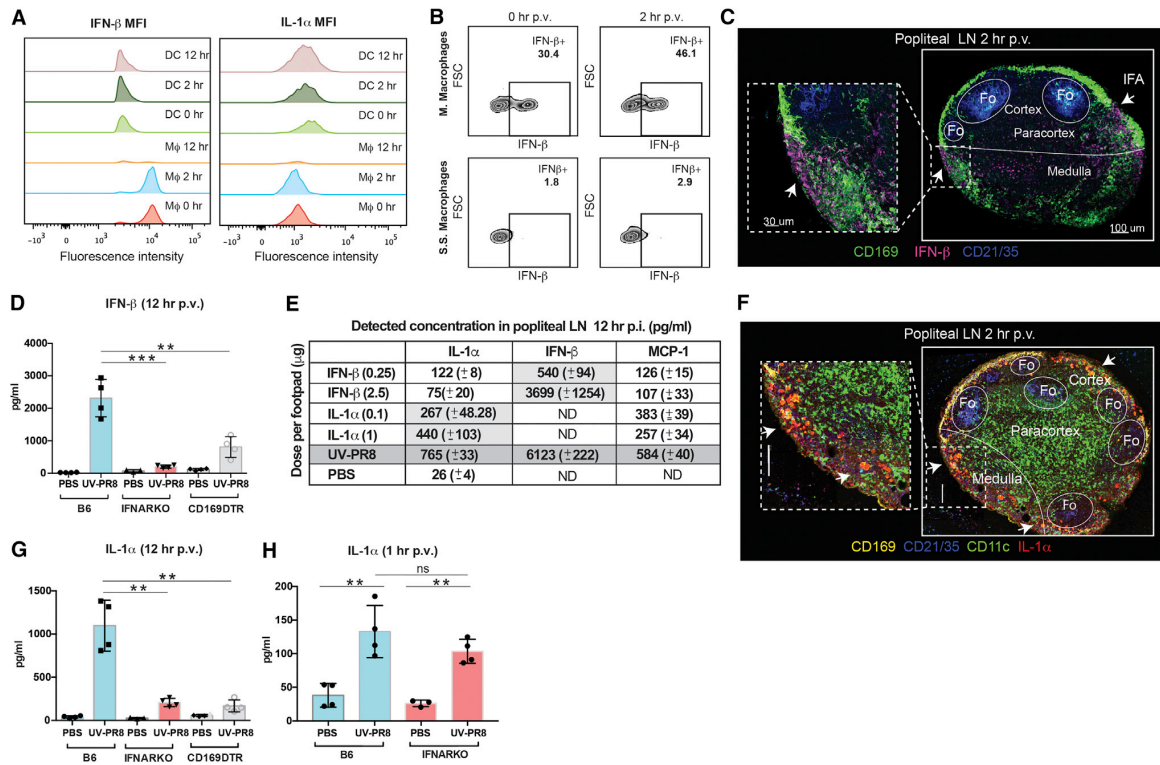


Figure 5. IFN- β Produced by MM Induces the Expression of IL-1 α after Vaccination

(A) Representative results showing intracellular quantification of IFN- β (left) and IL-1 α (right) in LNMs (gating strategy described in Figure 1) and DCs (CD3⁻/CD11c^{high}/CD169⁻) at 0, 2, and 12 hr p.v. Histograms represent fluorescence intensity that indicates the level of expression of each of the cytokines in the examined cells.

(B) Representative plots showing intracellular quantification of IFN- β in MM (up) and SSM (down) at 2 hr p.v.

(C) Confocal micrographs showing expression of IFN- β (purple) in the medullary and interfollicular areas of the LN associated with MMs (CD169⁺; green) at 2 hr p.v.

(D) Levels of IFN- β in LN from B6, IFNAR KO, and macrophage-depleted (CD169-DTR) mice at 12 hr p.v.

(E) Detected IL-1 α , IFN- β , and MCP-1 levels in the popliteal LN after administration of two concentrations of recombinant IFN- β or IL-1 α alone (without UV-PR8) compared to controls (UV-PR8 or PBS treatments). SD is indicated in brackets; ND indicates non-detectable amounts.

(F) Confocal micrographs showing the expression of IL-1 α (red) at 2 hr p.v. associated to LN macrophages (CD169⁺; yellow) in the cortical and medullary area of a popliteal LN. The follicular area was stained with anti-CD21/35-PB antibody (blue).

(G and H) Levels of IL-1 α in LN from B6, IFNAR KO, and macrophage-depleted (CD169-DTR) mice at 12 hr p.v. (G) and at 1 hr p.v. (H).

In all figures, the presented data are representative of at least three independent experiments ($n \geq 3$). * $p < 0.1$; ** $p < 0.01$; *** $p < 0.001$. Error bars, SD.

staining of IL-1 α confirmed that both LNMs and DCs are able to produce this potent cytokine at 2 hr p.v. (Figure 5A, right). Importantly, IL-1 α expression appeared to be dependent on signaling through the type I IFN receptor at 12 hr p.v., as IFNAR KO mice showed significantly lower levels than B6 controls (Figure 5G). However, the expression of IL-1 α at 1 hr p.v. was similar in B6 and IFNAR KO mice, which suggests an IFN-independent mechanism in the initial release of this cytokine (Figure 5H).

LNMs Induce the Activation and Migration of LNDCs and Influence Their Capacity to Present Antigen

Having established the necrotic nature of LNM death and their response after vaccine administration, we hypothesized that

the release of inflammatory molecules may mediate the activation of LNDCs. To investigate a possible link between LNM death and LNDC migratory dynamics, we performed 2PM 3D reconstruction analysis on CD11c-YFP mice at 12 hr p.v., which revealed an attraction of CD11c⁺ DCs toward the areas where LNMs were present (Figure 6A). The analysis of these data demonstrated a clear decrease in the distance between LNDCs (mainly located in the paracortex in non-vaccinated animals) and the LNM layer (Figure 6B). To investigate the effect of macrophage-mediated antigen capture by DCs on their capacity to stimulate CD4 T cells, we isolated DCs from CLL-pretreated and control mice at 12 hr p.v., co-cultured them in vitro with HA-specific CD4⁺ T cells, and measured the division index

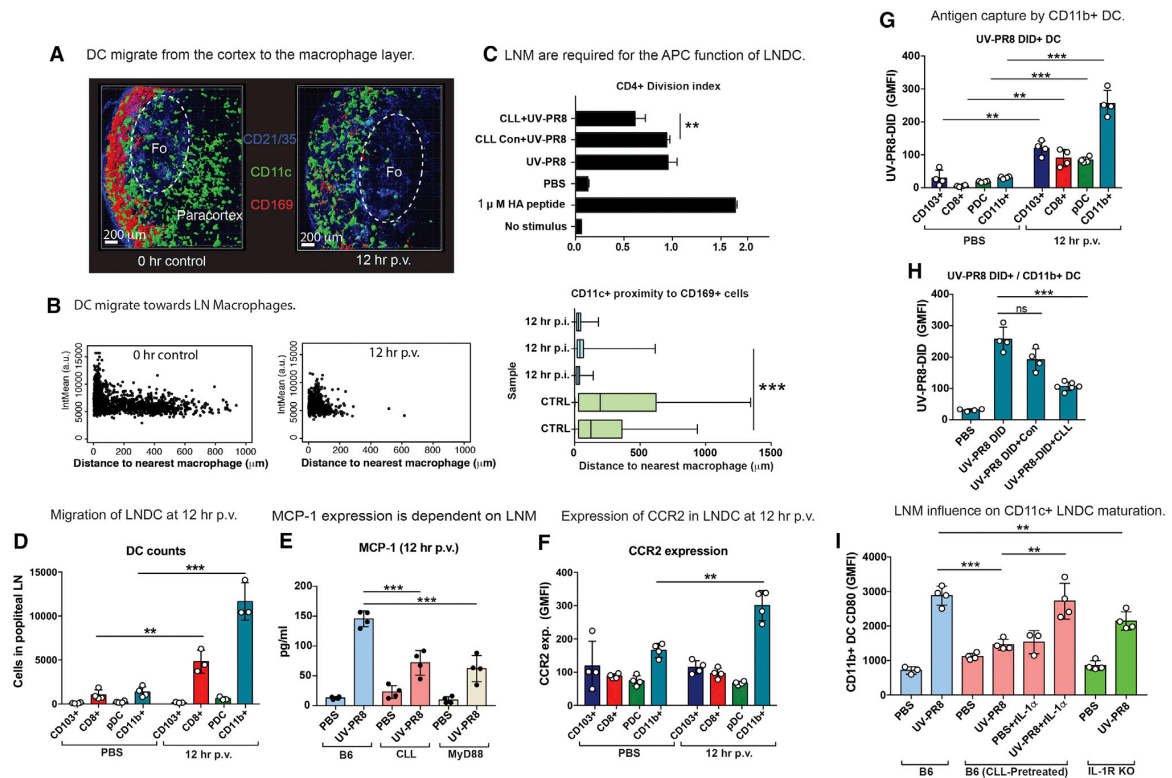


Figure 6. LNMs Induce the Activation, Migration, and Antigen Presentation Capacity of CD11b⁺ LNDCs

(A) Representative 2PM showing the position of CD11c-YFP⁺ cells in a control (left) or vaccinated mouse with respect to the LNM layer (red) at 12 hr p.v. (B) Representative dot plot of the distance between LNDCs and the nearest macrophage (μm) at 12 hr in control (left) and vaccinated (middle) mice. The y axis represents mean intensity expressed in arbitrary units (a.u.). Right: chart showing the CD11c⁺ cells in relation to CD169⁺ LNMs. (C) Flow cytometric assessment of the division index of transgenic influenza HA-specific CD4⁺ T cells after being cocultured for 72 hr with DCs isolated from mice that had received one of the following treatments: CLL or control liposomes followed by vaccination, vaccine alone, PBS, HA peptide, or no stimulus. DCs were isolated at 12 hr p.v. (left). (D) Flow cytometry data showing the number cells in four different DC subpopulations (CD103⁺, CD8⁺, pDCs, and CD11b⁺ DCs) present in the LN at 12 hr p.v. (E) Levels of secreted MCP-1 in LNMs from macrophage-depleted (CLL-treated) and MyD88 KO mice at 12 hr p.v. (F) Flow cytometry data showing expression levels of CCR2 in LNDCs at 12 hr p.v. (G) Flow cytometry data showing changes in the GMFI of the different DC subpopulations that have captured DiD-labeled UV-PR8. (H) Differences in virus uptake in CD11b⁺ DCs from mice that were administered PBS or UV-PR8-DiD and test groups that were pretreated with clodronate (CLL)- or PBS-containing liposomes (control liposomes). (I) GMFI analysis showing differences in surface expression of the costimulatory molecule CD80 at 12 hr p.v. in DCs from vaccinated or PBS-injected mice that had been pretreated with CLL and coadministered with recombinant IL-1 α . Mice deficient in IL-1 receptor were also tested (right). In all figures, the presented data are representative of at least three independent experiments ($n \geq 3$). * $p < 0.1$; ** $p < 0.01$; *** $p < 0.001$. Error bars, SD.

of the latter. We found that DCs from macrophage-depleted mice had a significantly impaired ability to stimulate CD4⁺ T cells, compared to control treatments (Figure 6C), confirming the requirement of the LNM-DC interaction for effective DC function.

To study the effect of macrophage-induced inflammation on LNDCs, we evaluated antigen capture and maturation in four groups of DCs divided according to their expression of specific surface markers (Merad et al., 2013) (Figure S4A). We confirmed that the presence of migratory CD103⁺ DCs and plasmacytoid dendritic cells (pDCs) was negligible in the draining LN at 12 hr

p.v. Interestingly, we also observed a significant increase in the number of CD8⁺ DCs and CD11b⁺ DCs at this time point (Figure 6D).

To understand the signals that directed the movement of these cells, and considering that the type I IFN response initiated by LNMs induced the release of MCP-1 (Figures 5E and 6E), we analyzed the expression of its receptor, CCR2, in the different DC subtypes. Interestingly, we observed a significant increase in the number of CD11b⁺ DCs that expressed CCR2 (data not shown) and a prominent upregulation of the expression of this receptor in these cells at 12 hr p.v. (Figures 6F and S4B).

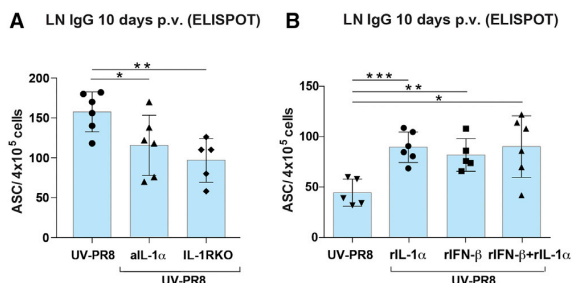


Figure 7. The Inflammation Initiated by LNMs Is Essential for the Development of an Effective B Cell Response

(A) Number of influenza-specific IgG ASC in LNs from mice pretreated with anti-IL-1 α compared with a control group vaccinated with UV-PR8 alone or deficient in the IL-1 receptor (IL-1RKO). LNs were collected at 10 days p.v. (B) Number of influenza-specific IgG ASC in LNs from mice pretreated with rIL-1 α , rIFN- β , or a combination of these cytokines compared with a control group vaccinated with UV-PR8 alone. LNs were collected at 10 days p.v. In all figures, the presented data are representative of at least three independent experiments ($n \geq 3$). * $p < 0.1$; ** $p < 0.01$; *** $p < 0.001$. Error bars, SD.

We also observed clear differences in the capacity of the different DC populations to capture virus, the CD11b⁺ DC subset being associated with the highest uptake of the vaccine (Figure 6G). Moreover, we found that the amount of labeled UV-PR8 captured by CD11b⁺ DCs in macrophage-ablated mice decreased compared to the empty liposomes or the untreated groups, as shown by geometric mean fluorescence intensity (GMFI) analysis (Figure 6H). This observation reflected either the reduction in retained quantity and availability of antigen in the LN (Gonzalez et al., 2010) due to macrophage depletion or the reduced ability of DCs to capture antigen because of the lack of macrophage-induced inflammatory signals.

Moreover, at 12 hr p.v., the expression of the costimulatory molecules CD80 and CD86 was significantly lower in CD11b⁺ DCs from CLL-pretreated mice than in the untreated group (Figures 6I and S4C, respectively). Interestingly, co-administration of IL-1 α and vaccine restored CD80 expression in CLL-pretreated mice to the same level as in mice administered UV-PR8 alone. We also confirmed that CD80 expression by CD11b⁺ DCs was lower in vaccinated IL-1R KO mice than in the equivalent B6 controls (Figure 6I).

The Inflammatory Cascade Associated with IL-1 α Release Is Essential for Humoral Immunity in the Draining LN

As mentioned previously, LN macrophages play a critical role in the initiation of the inflammatory response. Therefore, to study the effect that macrophage-dependent inflammation has on antibody production, we performed a series of immunizations in mice treated with anti-IL-1 α antibody and in mice deficient in IL-1R. We observed that at 10 days p.v., the number of influenza-specific ASC in the draining LN was significantly reduced compared to the control mice in all of the tested groups, which highlighted that macrophage-dependent IL-1 α -mediated inflammation is required for the development of an effective B cell response in this organ (Figure 7A). Moreover, to determine

whether IL-1 α and IFN- β have an adjuvant action, mice were immunized with the influenza vaccine alone or vaccine supplemented with recombinant IL-1 α , IFN- β , or both. Strikingly, at 10 days p.v. the number of ASC were significantly increased in the groups treated with the recombinant IL-1 α and IFN- β in comparison with mice treated with the vaccine alone (Figure 7B).

DISCUSSION

Since the identification of macrophage death as an immunological reaction (Barth et al., 1995), it has become apparent that this phenomenon involves the interplay of signaling cascades triggered by the presence of antigen. However, it is only recently that studies have focused on SSM rupture as an event that mobilizes innate and adaptive immunity (Gaya et al., 2015; Staudt and Gerhard, 1983).

We observed that following UV-PR8 administration, both SSMs and MMs undergo necrotic death through a process that is dependent on vaccine dosage. The mechanism we describe differs from the one presented in previous studies. Gaya and colleagues (Gaya et al., 2015) reported that SSM disappearance was dependent on the infiltration of migratory DCs. However, in our observations, infiltrated DCs did not contribute to the described phenotype, as CCR7 KO mice that are deficient in DC recruitment to the LN showed the same SSM response as mice in the B6 control group. Moreover, we observed that SSM death occurs within the first 3 hr after vaccination, much earlier than the time required for DCs to migrate to the LN (Martín-Fontecha et al., 2003), and we could not observe any recruitment of migratory DCs expressing CD103 in the LN at 12 hr p.v. Furthermore, Gerner and colleagues (Gerner et al., 2015) questioned the paradigm that T cell induction is exclusively mediated by DCs migrating from the peripheral organs, as these cells require extended periods of time to reach the draining LN. We also discarded the possibility that LNM death is affected by infiltrated innate immune cells, as depletion of NK cells or neutrophils did not prevent macrophage disappearance. Interestingly, Sagoo and colleagues (Sagoo et al., 2016) described a mechanism by which SSMs undergo inflammasome-mediated pyroptosis after administration of live vaccinia virus. In our model, although UV-irradiated influenza virus retained its ability to enter the host cell, we eliminated the possible involvement of the inflammasome pathway, given that depletion of molecules associated with this pathway did not prevent SSM death.

Importantly, pretreatment with an antibody against the SA binding site of PR8 HA prevented SSM death, while pretreatment with the F16 antibody that binds to the fusion domain of HA did not, indicating that influenza viral entry via the HA-SA interaction is required to trigger this mechanism. Once inside the cell, the single-stranded viral RNA is recognized by TLR7 and triggers SSM death in a process that is dependent of the adaptor protein MyD88. Interestingly, Gaya and colleagues recently described a mechanism in which MyD88 was also involved in SSM death following infection (Gaya et al., 2015).

Previous studies have proposed a model in which SSMs capture and shuttle intact antigen from the subcapsular sinus to

B cells in the underlying follicle (Carrasco and Batista, 2007; Junt et al., 2007). We observed that elimination of SSMs as a consequence of antigen administration occurs soon after vaccination, and SSMs remain absent for at least 1 week thereafter (Figure 2F). Therefore, it is unlikely that these cells could play a role as APCs. However, it could be possible that MMs, which reappear within the first 7 days p.v. (Figure 2G), might be involved in antigen presentation, a possibility that requires further investigation.

We propose an alternative scenario in which the contribution of LNMs to the adaptive response is associated with their role in the initiation of the inflammatory response that follows vaccination. This process is initiated by the secretion of IFN- β , which we found to be dependent on the presence of macrophages. These results are in agreement with previous reports that demonstrated an important role for macrophage-produced type I IFN in different immunological processes such as the T central memory response against virus (Sung et al., 2012) or the migration of pDCs from the deep cortex to the SCS area following viral infection (Asselin-Paturel et al., 2005; Iannacone et al., 2010). However, in this work, we demonstrated that MMs, but not SSMs, are the cells principally responsible for IFN- β secretion. This suggests that the interfollicular regions in the subcapsular sinus and the medullary part of the LN might be the most relevant areas in which cell activation and antigen presentation occur.

Type I IFNs are known to be secreted in response to UV-inactivated influenza virus in a process that is dependent on MyD88 (Diebold et al., 2004), an adaptor protein that plays a key role in the defense of the host against many pathogens (Seo et al., 2010). The role of type I IFN is to induce an antiviral state through the production of proinflammatory cytokines and instruct the adaptive immune response against the virus (Iwasaki and Pillai, 2014). Macrophage activation following recognition of virus by TLR results in the expression of nuclear factor κ B (NF- κ B)-mediated proinflammatory cytokines or the production of IRF7-mediated type I IFN (Iwasaki and Pillai, 2014; Malmgaard et al., 2004). Surprisingly, we found that vaccine-induced IFN- β production was MyD88-independent. This result was in contrast to the role of TLR7 in the induction of IFN- β and suggested an alternative mechanism that may involve other sensing molecules such as RIG-I, a previously described type I IFN inducer in infected and immune cells (Kato et al., 2005). However, we found that TLR7 recognition and MyD88 signaling were important for the induction of IL-1 α and MCP-1 in a process mediated by the recognition of influenza single-stranded RNA in the endosomal compartment of LNMs and DCs. We observed that MMs located in the interfollicular area (IFA) and medullary area of the LN were the cell type responsible for initial IFN- β secretion. From their position in the IFA, these cells could generate an IFN gradient that might contribute to the activation of nearby SSMs. Moreover, the administration of recombinant IFN- β alone was sufficient to induce secretion of IL-1 α . In addition, IL-1 α production was impaired in mice deficient in IFNAR or in mice in which macrophages had been ablated at 12 hr p.v., confirming the role of IFN- β in the observed peak in IL-1 α secretion.

Our model agrees with the “inflammatory loop” model described by Di Paolo and Shayakhmetov (Di Paolo and

Shayakhmetov, 2016) in which inflammation is initiated by stressed or damage cells via IL-1 α -dependent activation of chemokines that recruit inflammatory cells to the site of infection. Interestingly, previous reports have stressed the role of pre-stored IL-1 α as an alarmin molecule involved in the initiation of the inflammatory response in the context of sterile inflammation (Rider et al., 2011) or other physiological stimuli (Di Paolo and Shayakhmetov, 2016). To act as an extracellular alarmin, pro-IL-1 α requires the loss of plasma membrane integrity, which is indicative of necrotic cell death (Galluzzi et al., 2015). In this work, we confirmed by EM the loss of plasma membrane integrity in the LNM following influenza vaccination (Figures 1F and 1G). In addition, we observed that LNMs express substantial amounts of IL-1 α at steady state (Figure S3B). Interestingly, we observed that the initial release of IL-1 α was independent of the type I IF signal. Thus, it might be hypothesized that the early levels of this cytokine measured in the LN are associated with the necrotic death of macrophages, which constitutively express and store IL-1 α , as confirmed by immunohistochemistry and fluorescence-activated cell sorting (FACS) studies. However, the observed peak in expression of IL-1 α at 12 hr p.v. is most likely due to de novo synthesis by LNDCs, triggered by the disappearance of the LNM.

The observations in our model agree with previous studies that describe the leakage of cytosolic IL-1 α to the surrounding milieu as a result of cell death caused by injury or infection (Chen et al., 2007; Eigenbrod et al., 2008). Regarding the source of IL-1 α in the LN, although LNMs and DCs appeared to be the major producers of this cytokine, we could not discard the contribution of other myeloid or stromal cells. Similarly, we could not rule out the possibility that alternative mechanisms other than those that involve IL-1 α might affect the activation of DCs in vivo. Additionally, the direct effect of IL-1 α on LNDCs needs to be further evaluated.

In this work, we showed that the type I IFN reaction, initiated by LNMs, promotes B cell responses to influenza vaccine in the LN, given that transient treatment with an antibody against IL-1 α reduced immunoglobulin G (IgG) production significantly. Additionally, co-administration of vaccine and recombinant IL-1 α increased the humoral response in the draining LN. Our results are in agreement with other studies that suggest that IL-1 α and IL-1 β serve as mucosal adjuvants when administered with soluble protein antigens (Staats and Ennis, 1999).

Different studies have recently demonstrated the capacity of DCs to relocate to the LN interfollicular areas in which antigen is captured (Iannacone et al., 2010; Woodruff et al., 2014). However, the specific effect of the IL-1 inflammatory pathway on DC activation in the LN is not fully understood. We observed that CD11b⁺ DCs in the draining LN have a prominent role capturing influenza virus. Additionally, IL-1 α and IFN- β , initially secreted by LNMs, contribute to the maturation of this DC subset based on the effect that these molecules have on the expression of the costimulatory markers CD80 and CD86. Importantly, IL-1 α and IFN- β induced the expression of MCP-1 that attracts CCR2⁺ CD11b⁺ DCs to the areas in which antigen and DAMP from necrotic SSMs remain. Moreover, the presence of LNMs appeared to be necessary for antigen presentation between LNDCs and CD4⁺ T cells, as demonstrated by the lower capacity

of DCs isolated from macrophage-depleted mice to present antigen to influenza-specific CD4⁺ T cells.

In this study, we provide a link between LNM death in response to vaccination and the promotion of DC function in the LN through a mechanism that involves TLR7-mediated viral recognition and the release of IFN- β and the alarmin molecule IL-1 α . These cytokines activate DCs and stimulate them to secrete IL-1 α in a positive feedback loop. Importantly, secretion of MCP-1, which is also induced by the type I IFN response, attracts CCR2⁺ CD11b⁺ DCs to the areas with remaining antigen and DAMP from necrotic SSMs, ensuring effective DC activation and function.

Based on our results, we can consider the stimulation of the IL-1 α inflammatory pathway as a possible strategy for the enhancement of APC function in LNDs and the improvement of the humoral response against influenza vaccine.

EXPERIMENTAL PROCEDURES

Mice

Mice were bred in-house or acquired from Janvier Labs (C57BL/6) or Charles River Laboratories (BALB/c). The following transgenic strains were used: CX3CR1-EGFP (Jung et al., 2000), IL-1R/KO (Labow et al., 1997), IL-1 β /KO (Matsuki et al., 2006), ASC/KO (Mariathasan et al., 2004), ICE/KO (Kuida et al., 1995), MyD88/KO (Hou et al., 2008), IFNAR KO (Müller et al., 1994), LysMcre-GFP (Clausen et al., 1999), TLR-7/KO (Lund et al., 2004), and influenza HA-specific CD4 T cell receptor α/β (TCR- α/β) (Kirberg et al., 1994). All strains had the C57BL/6 background except for the HA-specific CD4 TCR that was on BALB/c. Mice were maintained in specific-pathogen-free facilities at the Institute for Research in Biomedicine, Bellinzona. Experiments were performed in accordance with the Swiss Federal Veterinary Office guidelines, and animal protocols were approved by the veterinarian local authorities.

Antigen Administration and Injections

Influenza virus strain A/PR/8/34 was grown, purified, inactivated, and labeled as described previously (Gonzalez et al., 2010). Different concentrations of inactivated virus were injected into the footpad of anesthetized mice at different time points prior to LN collection. Virion dosage ranged from 10³ to 10⁵ PFUs per footpad in a final volume of 10 μ L. For macrophage depletion, mice were injected in the footpad with 10 μ L CLL or PBS-containing (control) liposomes (Clodronateliposomes.org) at days 5 and 3 prior to immunization. For NK cell and neutrophil depletion, 300 μ g of the depletion antibodies α NK1.1 (clone PK136) and α Ly-6G (clone 1A8) (BioXCell) were administered intraperitoneally (i.p.) and intravenously (i.v.) at days 3 and 1 before vaccine administration, respectively. Macrophage, NK cell, and neutrophil disappearance following depletion treatment was assessed by FACS (data not shown). For follicular dendritic cell (FDC) and SSM labeling, mice received 0.5 μ g fluorescence-labeled α CD21/35 and α CD169 (BioLegend), respectively, which was injected into the footpad 3 to 5 hr prior to image acquisition. For cytokine blocking, the antibody α IL-1 α (clone ALF-161, BioXCell) was administered i.v. at a dose of 200 μ g/animal, as well as footpad at 61 μ g/animal, at the time of vaccination. Recombinant cytokines were injected at indicated amounts into the footpad at the time of vaccination and 6 hr p.v., except for the ELISPOT experiment, in which only one injection of 0.1 μ g rIL-1 α , 0.25 μ g of rIFN- β , or a combination of both was administered into the footpad 30 min p.v..

Flow Cytometry

Popliteal LNs were collected, disrupted with tweezers, and digested for 10 min at 37°C in an enzyme mix composed of DNase I (0.28 mg/mL, Amresco), dispase (1 U/mL, Corning), and collagenase P (0.5 mg/mL, Roche) in calcium- and magnesium-free PBS (PBS-) followed by a stop solution composed of 2 mM EDTA (Sigma-Aldrich) and 2% heat-inactivated filter-

sterilized fetal calf serum (Thermo Fisher Scientific) in PBS- (Sigma-Aldrich). Fc receptors were blocked (α CD16/32, BioLegend) followed by surface staining and analyzed by flow cytometry on an LSRFortessa (BD Biosciences). Where indicated, intracellular staining was performed (88/8824/00, eBioscience) following the manufacturer's instructions. Data were analyzed using FlowJo software (TriStar), including the calculation of division index.

Immunohistology and Microscopy

Mice were anesthetized with a mixture of ketamine (100 mg/kg bodyweight, Parke Davis) and xylazine (10 mg/kg bodyweight, Bayer) and perfused with a fixative solution made of 10 mL of 0.05 M phosphate buffer containing 0.1 M L-lysine, 4% paraformaldehyde, and 2 mg/mL NaIO₄ at pH 7.4 (PLP). Popliteal LNs were subsequently collected and incubated in 30% sucrose phosphate-buffered solution overnight. Tissues were snap frozen in O.C.T. compound (VWR Chemicals Leuven). 10- to 30- μ m sections were cut with a microtome, blocked with proper sera, and stained with the indicated antibodies (see antibody section). Immunofluorescence confocal microscopy was performed using a Leica TCS SP5 confocal microscope (Leica Microsystems). Micrographs were acquired in sequential scans and merged to obtain a multicolor image. Images were analyzed using Imaris software (Bitplane AG). Transmission electron microscopy was performed as described previously (Rooszendaal et al., 2009).

In Vivo PI Staining

To quantify necrotic SSMs following vaccination, C57BL/6J mice were injected with 10 μ L of 10⁷ PFU/mL UV-PR8 into the footpad. 1 hr later, SSM and LN follicles were labeled by footpad administration of 0.25 μ g of fluorescently labeled α CD169 and 0.5 μ g of α CD21/35 antibodies (BioLegend). 3 hr later, 20 μ g of PI (Sigma-Aldrich) was administered by footpad injection and LN were harvested immediately. 3D reconstructions of a complete follicular area and overlying SSM layer were made using two-photon intravital microscopy (150- μ m tissue depth). Quantification of necrotic SSMs was performed using Imaris software based on CD169 expression, PI signal, sphericity, and volume.

Antibodies

In this study, the following antibodies (BioLegend) were used: α B220 (RA3-6B2), α CD4 (GK1.5), α CD21/35 (7E9), α F4/80 (BM8), α CD40 (3/23), α CD80 (16-10A1), α CD11c (N418), α CD169 (3D6.112), α CD3 (17A2), α NK1.1 (PK136), α CD11b (M1/70), α CD69 (H1.2F3), α I-A/I-E (M5/114.15.2), α Ly-6G (1A8), α CD16/32 (93), α MHCI (SF1-1.1.1), α Gr-1 (RB6-8C5), α CD86 (GL-1), α Ly-6C (HK1.4), α IFN- β (PBL Assay Science), rabbit α IFN- β (Abcam), α lg(H+L)-AP, α lgG-biot, α lgM-biot (Southern Biotech), α CCR2 (R&D Systems), H36-7, F16 (HUMABS BioMed), and depletion antibodies α IL6 (MP5-20F3), α IL-1 α (ALF-161), and rat IgG1 isotype (HRPN) (all from BioXCell).

ELISPOT

Mice were immunized with different doses of UV-inactivated PR8 virus (10³ to 10⁵ PFU per footpad) subcutaneously. For enzyme-linked immunospot assay (ELISPOT), on day 10 p.v., popliteal LNs were removed aseptically, disrupted, and passed through a 40- μ m cell strainer. 4 \times 10⁵ cells were plated on UV-PR8-coated (10⁷ PFU/mL) filter plates (MultiScreen-HTS, Merck Millipore) and incubated for 16 hr at 37°C. For detection, a biotin-conjugated α lgG or α lgM was used, followed by streptavidin-conjugated horseradish peroxidase (HRP). A developing solution consisting of 200 μ L 3-amino-9-ethylcarbazole (AEC) solution (Sigma) in 9 mL sodium acetate buffer containing 4 μ L 30% H₂O₂ was subsequently added. Spots were read on a C.T.L. ELISPOT reader using ImmunoSpot 5.1 software (Cellular Technology).

In Vitro Evaluation of Hemagglutinin-Specific Transgenic CD4⁺ T Cell Responses

LN-resident DCs were isolated by digestion as described previously (Gonzalez et al., 2010). Samples were enriched for CD11c⁺ DCs by magnetic separation with microbeads (Miltenyi Biotech). Purity was evaluated by FACS and was always higher than 85%. LNs were collected from T cell antigen receptor

transgenic mice with expression of an $\alpha\beta$ T cell antigen receptor specific for influenza HA peptide, and single-cell suspensions were prepared. Following lysis of red blood cells by ammonium chloride-potassium bicarbonate buffer (BioWhittaker, Lonza), cells were labeled for 10 min with 5 μ M CFSE (Invitrogen) and washed thoroughly. HA-specific CD4⁺ T cells (2×10^5) were cultured for 72 hr together with DCs (5×10^4). Proliferation was measured by flow cytometry and presented as division index.

Cytoplex Assay

LEGENDPlex assays (Mouse Proinflammatory Chemokine Panel and Mouse Inflammation Panel; BioLegend) were performed to monitor cytokine and chemokine expression. Briefly, popliteal LNs were collected and carefully disrupted in 100 μ L ice-cold phosphate buffer, minimizing cell rupture. The suspension was centrifuged at 1,500 rpm for 5 min, and the supernatant was collected. 25 μ L supernatant was used for the protocol following the manufacturer's instructions. Samples were analyzed by flow cytometry on an LSRFortessa (BD Biosciences), and data were analyzed using LEGENDPlex software (BioLegend).

qPCR

To measure the expression levels of the cytokines IL-1 β , IL-12, IL-4, and IL-18 the following sets of primers were designed: *IL-1 β* forward, 5'-TGTTTTCCTCCTTGCCTC-3'; *IL-1 β* reverse, 5'-GCTGCCTAATGTCCCC TT-3'; *IL-12* forward, 5'-TGTGGAATGGCGTCTCTG-3'; *IL-12* reverse, 5'-CAGTTCAATGGGCAGGT-3'; *IL-4* forward, 5'-GAGCTCGTCTGTA GGGCT-3'; *IL-4* reverse, 5'-CCGAAAGAGTCTCTGCAG-3'; *IL-18* forward, 5'-GGTCCATGCTTTCTGGACT-3'; and *IL-18* reverse, 5'-GGCCAAGAG GAAGTGATTG-3'. Popliteal LNs were collected at 0, 2, 6, 12, and 24 hr p.v. and disrupted in lysing matrix D 1.4-mm ceramic sphere tubes using FastPrep-24 tissue disruption (MP Biomedicals), and RNA was isolated using an RNeasy Mini kit (QIAGEN). 1 μ g of cDNA was synthesized using a cDNA synthesis kit (Applied Biosystems) following the manufacturer's recommendations. For the qPCR reaction, a SYBR Master Mix (Applied Biosystems) was used, and samples were run on a 7900HT Fast Real-Time PCR System (Applied Biosystems). Cytokine mRNA levels were expressed relative to GAPDH expression (primers: *GAPDH* forward, 5'-ACATCATCCCTGCATC CACT-3'; *GAPDH* reverse, 5'-AGATCCACGACGGACACATT-3'). The Pfaffl method (Pfaffl, 2001) was used to calculate the relative expression of the transcripts.

Multiphoton Microscopy and Analysis

Deep tissue imaging was performed on a customized two-photon platform (TrimScope, LaVision BioTec). Two-photon probe excitation and tissue second-harmonic generation (SHG) were obtained with a set of two tunable Ti:sapphire lasers (Chameleon Ultra I, Chameleon Ultra II, Coherent) and an optical parametric oscillator that emits in the range of 1,010 to 1,340 nm (Chameleon Compact OPO, Coherent), with output wavelength in the range of 690–1,080 nm. The objectives used were a Nikon LWD 16 \times /0.80 numerical aperture (NA) W in Figure 1A and a Nikon N Plan Apo λ 4 \times /0.20 NA in Figure 5H. 3D reconstructions of whole popliteal LNs (Figure 1A) were made using a mosaic of up to 3 \times 3 adjacent field-of-view image acquisitions with a z-depth of up to 300 μ m. Images were stitched together using Fiji (Schindelin et al., 2012) together with a custom-developed script written in Beanshell to automate image processing. To automate the stitching operations, we developed a script using Beanshell programming language. The hyperstacks were subsequently imported in the software Imaris 7.7.2 (Bitplane) to obtain the 3D rendering of the LN. Cell populations were segmented (analysis in Figures 1B and 1C) by putting a threshold on the color intensity after background subtraction.

Statistics

All data are expressed as the mean \pm SD. For statistical analyses and data representation, Prism 6.0b (GraphPad Software) was used. Group comparisons were assessed using nonparametric tests. All statistical test were two-tailed, and statistical significance was defined as * $p < 0.05$, ** $p < 0.01$, and *** $p < 0.001$.

SUPPLEMENTAL INFORMATION

Supplemental Information includes four figures and one movie and can be found with this article online at <http://dx.doi.org/10.1016/j.celrep.2017.02.026>.

AUTHOR CONTRIBUTIONS

S.F.G. directed the study, designed experiments, analyzed and interpreted the results, and wrote the manuscript. N.C., Y.F., M.P.-S., R.D., D.U.P., and V.L.-K. designed and performed the experiment and analyzed results. F.S., M.U., D.C., S.J.T., A.L., and M.C.C. provided reagents and analyzed and interpreted results.

ACKNOWLEDGMENTS

We thank professors Harald von Boehmer and Shizuo Akira for providing influenza HA-specific CD4 TCR- α/β and MyD88 KO mice, respectively, and Maria Ericsson, Gabriela Danelon-Sargenti, Sara Cordeiro, and David Jarrossay for technical support. This work was supported by Swiss National Foundation (SNF) grants R'Equip (145038) and Ambizione (148183) and the Marie Curie Reintegration Grant 612742. S.F.G. was supported by a grant from the Swiss Vaccine Research Institute (SVRI). D.U.P. was supported by SystemsX.ch grant 2013/124.

Received: September 28, 2016

Revised: December 14, 2016

Accepted: February 7, 2017

Published: March 7, 2017

REFERENCES

- Asselin-Paturel, C., Brizard, G., Chemin, K., Boonstra, A., O'Garra, A., Vicari, A., and Trinchieri, G. (2005). Type I interferon dependence of plasmacytoid dendritic cell activation and migration. *J. Exp. Med.* 201, 1157–1167.
- Barth, M.W., Hendrzak, J.A., Melnicoff, M.J., and Morahan, P.S. (1995). Review of the macrophage disappearance reaction. *J. Leukoc. Biol.* 57, 361–367.
- Carrasco, Y.R., and Batista, F.D. (2007). B cells acquire particulate antigen in a macrophage-rich area at the boundary between the follicle and the subcapsular sinus of the lymph node. *Immunity* 27, 160–171.
- Chen, C.J., Kono, H., Golenbock, D., Reed, G., Akira, S., and Rock, K.L. (2007). Identification of a key pathway required for the sterile inflammatory response triggered by dying cells. *Nat. Med.* 13, 851–856.
- Chtanova, T., Schaeffer, M., Han, S.J., van Dooren, G.G., Nollmann, M., Herzmark, P., Chan, S.W., Satija, H., Camfield, K., Aaron, H., et al. (2008). Dynamics of neutrophil migration in lymph nodes during infection. *Immunity* 29, 487–496.
- Clausen, B.E., Burkhardt, C., Reith, W., Renkawitz, R., and Förster, I. (1999). Conditional gene targeting in macrophages and granulocytes using LysMcre mice. *Transgenic Res.* 8, 265–277.
- Corti, D., Voss, J., Gamblin, S.J., Codoni, G., Macagno, A., Jarrossay, D., Vachier, S.G., Pinna, D., Minola, A., Vanzetta, F., et al. (2011). A neutralizing antibody selected from plasma cells that binds to group 1 and group 2 influenza A hemagglutinins. *Science* 333, 850–856.
- Di Paolo, N.C., and Shayakhmetov, D.M. (2016). Interleukin 1 α and the inflammatory process. *Nat. Immunol.* 17, 906–913.
- Diebold, S.S., Kaisho, T., Hemmi, H., Akira, S., and Reis e Sousa, C. (2004). Innate antiviral responses by means of TLR7-mediated recognition of single-stranded RNA. *Science* 303, 1529–1531.
- Eigenbrod, T., Park, J.H., Harder, J., Iwakura, Y., and Núñez, G. (2008). Cutting edge: critical role for mesothelial cells in necrosis-induced inflammation through the recognition of IL-1 α released from dying cells. *J. Immunol.* 181, 8194–8198.
- Farrell, H.E., Davis-Poynter, N., Bruce, K., Lawler, C., Dolken, L., Mach, M., and Stevenson, P.G. (2015). Lymph node macrophages restrict murine cytomegalovirus dissemination. *J. Virol.* 89, 7147–7158.

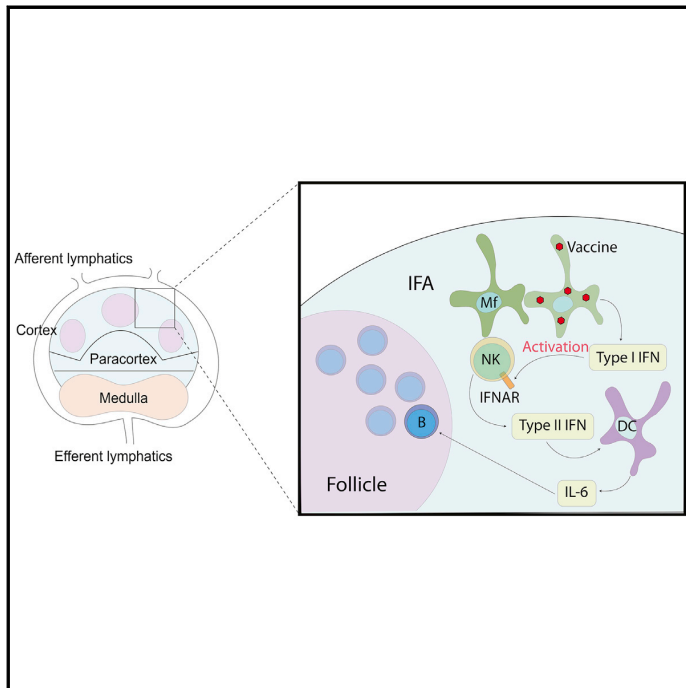
- Galluzzi, L., Bravo-San Pedro, J.M., Vitale, I., Aaronson, S.A., Abrams, J.M., Adam, D., Alnemri, E.S., Altucci, L., Andrews, D., Annicchiarico-Petruzzelli, M., et al. (2015). Essential versus accessory aspects of cell death: recommendations of the NCCD 2015. *Cell Death Differ.* **22**, 58–73.
- Gaya, M., Castello, A., Montaner, B., Rogers, N., Reis e Sousa, C., Bruckbauer, A., and Batista, F.D. (2015). Host response. Inflammation-induced disruption of SCS macrophages impairs B cell responses to secondary infection. *Science* **347**, 667–672.
- Gerner, M.Y., Torabi-Parizi, P., and Germain, R.N. (2015). Strategically localized dendritic cells promote rapid T cell responses to lymph-borne particulate antigens. *Immunity* **42**, 172–185.
- Gonzalez, S.F., Lukacs-Kornek, V., Kuligowski, M.P., Pitcher, L.A., Degen, S.E., Kim, Y.A., Cloninger, M.J., Martinez-Pomares, L., Gordon, S., Turley, S.J., and Carroll, M.C. (2010). Capture of influenza by medullary dendritic cells via SIGN-R1 is essential for humoral immunity in draining lymph nodes. *Nat. Immunol.* **11**, 427–434.
- Gray, E.E., and Cyster, J.G. (2012). Lymph node macrophages. *J. Innate Immun.* **4**, 424–436.
- Hickman, H.D., Takeda, K., Skon, C.N., Murray, F.R., Hensley, S.E., Loomis, J., Barber, G.N., Bunnick, J.R., and Yewdell, J.W. (2008). Direct priming of antiviral CD8+ T cells in the peripheral interfollicular region of lymph nodes. *Nat. Immunol.* **9**, 155–165.
- Hou, B., Reizis, B., and DeFranco, A.L. (2008). Toll-like receptors activate innate and adaptive immunity by using dendritic cell-intrinsic and -extrinsic mechanisms. *Immunity* **29**, 272–282.
- Iannacone, M., Moseman, E.A., Tonti, E., Bosurgi, L., Junt, T., Henrickson, S.E., Whelan, S.P., Guidotti, L.G., and von Andrian, U.H. (2010). Subcapsular sinus macrophages prevent CNS invasion on peripheral infection with a neurotropic virus. *Nature* **465**, 1079–1083.
- Iwasaki, A., and Pillai, P.S. (2014). Innate immunity to influenza virus infection. *Nat. Rev. Immunol.* **14**, 315–328.
- Jung, S., Aliberti, J., Graemmel, P., Sunshine, M.J., Kreutzberg, G.W., Sher, A., and Littman, D.R. (2000). Analysis of fractalkine receptor CX(3)CR1 function by targeted deletion and green fluorescent protein reporter gene insertion. *Mol. Cell. Biol.* **20**, 4106–4114.
- Junt, T., Moseman, E.A., Iannacone, M., Massberg, S., Lang, P.A., Boes, M., Fink, K., Henrickson, S.E., Shayakhmetov, D.M., Di Paolo, N.C., et al. (2007). Subcapsular sinus macrophages in lymph nodes clear lymph-borne viruses and present them to antiviral B cells. *Nature* **450**, 110–114.
- Kastenmüller, W., Torabi-Parizi, P., Subramanian, N., Lämmermann, T., and Germain, R.N. (2012). A spatially-organized multicellular innate immune response in lymph nodes limits systemic pathogen spread. *Cell* **150**, 1235–1248.
- Kato, H., Sato, S., Yoneyama, M., Yamamoto, M., Uematsu, S., Matsui, K., Tsujimura, T., Takeda, K., Fujita, T., Takeuchi, O., and Akira, S. (2005). Cell type-specific involvement of RIG-I in antiviral response. *Immunity* **23**, 19–28.
- Kirberg, J., Baron, A., Jakob, S., Rolink, A., Karjalainen, K., and von Boehmer, H. (1994). Thymic selection of CD8+ single positive cells with a class II major histocompatibility complex-restricted receptor. *J. Exp. Med.* **180**, 25–34.
- Kuida, K., Lippke, J.A., Ku, G., Harding, M.W., Livingston, D.J., Su, M.S., and Flavell, R.A. (1995). Altered cytokine export and apoptosis in mice deficient in interleukin-1 beta converting enzyme. *Science* **267**, 2000–2003.
- Kuka, M., and Iannacone, M. (2014). The role of lymph node sinus macrophages in host defense. *Ann. N Y Acad. Sci.* **1319**, 38–46.
- Labow, M., Shuster, D., Zetterstrom, M., Nunes, P., Terry, R., Cullinan, E.B., Bartfai, T., Solorzano, C., Moldawer, L.L., Chizzonite, R., and McIntyre, K.W. (1997). Absence of IL-1 signaling and reduced inflammatory response in IL-1 type I receptor-deficient mice. *J. Immunol.* **159**, 2452–2461.
- Lund, J.M., Alexopoulou, L., Sato, A., Karow, M., Adams, N.C., Gale, N.W., Iwasaki, A., and Flavell, R.A. (2004). Recognition of single-stranded RNA viruses by Toll-like receptor 7. *Proc. Natl. Acad. Sci. USA* **101**, 5598–5603.
- Malmgaard, L., Melchjorsen, J., Bowie, A.G., Mogensen, S.C., and Paludan, S.R. (2004). Viral activation of macrophages through TLR-dependent and -independent pathways. *J. Immunol.* **173**, 6890–6898.
- Mariathasan, S., Newton, K., Monack, D.M., Vucic, D., French, D.M., Lee, W.P., Roose-Girma, M., Erickson, S., and Dixit, V.M. (2004). Differential activation of the inflammasome by caspase-1 adaptors ASC and Ipaf. *Nature* **430**, 213–218.
- Martín-Fontecha, A., Sebastiani, S., Höpken, U.E., Uguccioni, M., Lipp, M., Lanzavecchia, A., and Sallusto, F. (2003). Regulation of dendritic cell migration to the draining lymph node: impact on T lymphocyte traffic and priming. *J. Exp. Med.* **198**, 615–621.
- Matsuki, T., Nakae, S., Sudo, K., Horai, R., and Iwakura, Y. (2006). Abnormal T cell activation caused by the imbalance of the IL-1/IL-1R antagonist system is responsible for the development of experimental autoimmune encephalomyelitis. *Int. Immunol.* **18**, 399–407.
- Mempel, T.R., Henrickson, S.E., and Von Andrian, U.H. (2004). T-cell priming by dendritic cells in lymph nodes occurs in three distinct phases. *Nature* **427**, 154–159.
- Merad, M., Sathe, P., Helft, J., Miller, J., and Mortha, A. (2013). The dendritic cell lineage: ontogeny and function of dendritic cells and their subsets in the steady state and the inflamed setting. *Annu. Rev. Immunol.* **31**, 563–604.
- Moseman, E.A., Iannacone, M., Bosurgi, L., Tonti, E., Chevrier, N., Tumanov, A., Fu, Y.X., Hacoheh, N., and von Andrian, U.H. (2012). B cell maintenance of subcapsular sinus macrophages protects against a fatal viral infection independent of adaptive immunity. *Immunity* **36**, 415–426.
- Müller, U., Steinhoff, U., Reis, L.F., Hemmi, S., Pavlovic, J., Zinkernagel, R.M., and Aguet, M. (1994). Functional role of type I and type II interferons in antiviral defense. *Science* **264**, 1918–1921.
- Pfaffl, M.W. (2001). A new mathematical model for relative quantification in real-time RT-PCR. *Nucleic Acids Res.* **29**, e45.
- Phan, T.G., Grigороva, I., Okada, T., and Cyster, J.G. (2007). Subcapsular encounter and complement-dependent transport of immune complexes by lymph node B cells. *Nat. Immunol.* **8**, 992–1000.
- Phan, T.G., Green, J.A., Gray, E.E., Xu, Y., and Cyster, J.G. (2009). Immune complex relay by subcapsular sinus macrophages and noncognate B cells drives antibody affinity maturation. *Nat. Immunol.* **10**, 786–793.
- Rider, P., Carmi, Y., Guttman, O., Braiman, A., Cohen, I., Voronov, E., White, M.R., Dinarello, C.A., and Apte, R.N. (2011). IL-1 α and IL-1 β recruit different myeloid cells and promote different stages of sterile inflammation. *J. Immunol.* **187**, 4835–4843.
- Rozenendaal, R., Mempel, T.R., Pitcher, L.A., Gonzalez, S.F., Verschoor, A., Mebius, R.E., von Andrian, U.H., and Carroll, M.C. (2009). Conduits mediate transport of low-molecular-weight antigen to lymph node follicles. *Immunity* **30**, 264–276.
- Sagoo, P., Garcia, Z., Breart, B., Lemaître, F., Michonneau, D., Albert, M.L., Levy, Y., and Bousso, P. (2016). In vivo imaging of inflammasome activation reveals a subcapsular macrophage burst response that mobilizes innate and adaptive immunity. *Nat. Med.* **22**, 64–71.
- Schindelin, J., Arganda-Carreras, I., Frise, E., Kaynig, V., Longair, M., Pietzsch, T., Preibisch, S., Rueden, C., Saalfeld, S., Schmid, B., et al. (2012). Fiji: an open-source platform for biological-image analysis. *Nat. Methods* **9**, 676–682.
- Seo, S.U., Kwon, H.J., Song, J.H., Byun, Y.H., Seong, B.L., Kawai, T., Akira, S., and Kweon, M.N. (2010). MyD88 signaling is indispensable for primary influenza A virus infection but dispensable for secondary infection. *J. Virol.* **84**, 12713–12722.
- Staats, H.F., and Ennis, F.A., Jr. (1999). IL-1 is an effective adjuvant for mucosal and systemic immune responses when coadministered with protein immunogens. *J. Immunol.* **162**, 6141–6147.
- Staudt, L.M., and Gerhard, W. (1983). Generation of antibody diversity in the immune response of BALB/c mice to influenza virus hemagglutinin. I. Significant variation in repertoire expression between individual mice. *J. Exp. Med.* **157**, 687–704.

- Sung, J.H., Zhang, H., Moseman, E.A., Alvarez, D., Iannacone, M., Henrickson, S.E., de la Torre, J.C., Groom, J.R., Luster, A.D., and von Andrian, U.H. (2012). Chemokine guidance of central memory T cells is critical for antiviral recall responses in lymph nodes. *Cell* *150*, 1249–1263.
- Winkelman, E.R., Widman, D.G., Xia, J., Johnson, A.J., van Rooijen, N., Mason, P.W., Bourne, N., and Milligan, G.N. (2014). Subcapsular sinus macrophages limit dissemination of West Nile virus particles after inoculation but are not essential for the development of West Nile virus-specific T cell responses. *Virology* *450-451*, 278–289.
- Woodruff, M.C., Heesters, B.A., Herndon, C.N., Groom, J.R., Thomas, P.G., Luster, A.D., Turley, S.J., and Carroll, M.C. (2014). Trans-nodal migration of resident dendritic cells into medullary interfollicular regions initiates immunity to influenza vaccine. *J. Exp. Med.* *211*, 1611–1621.

Cell Reports

Influenza Vaccination Induces NK-Cell-Mediated Type-II IFN Response that Regulates Humoral Immunity in an IL-6-Dependent Manner

Graphical Abstract



Authors

Yagmur Farsakoglu, Miguel Palomino-Segura, Irene Latino, ..., Federica Sallusto, Jens V. Stein, Santiago F. Gonzalez

Correspondence

santiago.gonzalez@irb.usi.ch

In Brief

The role of natural killer (NK) cells in the context of influenza vaccination is unclear. Farsakoglu et al. demonstrate that NK cells produce early type II IFNs and regulate IL-6 secretion by dendritic cells, which affects the local anti-viral antibody responses in the draining lymph node after influenza vaccination.

Highlights

- NK cells are activated by macrophages in a type-I-IFN-dependent manner
- Early production of IFN γ is mediated by NK cells in the draining lymph node
- NK-cell-secreted IFN γ regulates the recruitment of IL-6+ dendritic cells
- Together IL-6 and IFN γ positively regulate anti-influenza B cell responses



Farsakoglu et al., 2019, Cell Reports 26, 2307–2315
February 26, 2019 © 2019 The Authors.
<https://doi.org/10.1016/j.celrep.2019.01.104>

CellPress

Influenza Vaccination Induces NK-Cell-Mediated Type-II IFN Response that Regulates Humoral Immunity in an IL-6-Dependent Manner

Yagmur Farsakoglu,^{1,2,8} Miguel Palomino-Segura,^{1,2} Irene Latino,¹ Silvia Zanaga,¹ Nikolaos Chatziandreou,¹ Diego Ulisse Pizzagalli,^{1,3} Andrea Rinaldi,⁴ Marco Bolis,^{4,5} Federica Sallusto,^{1,6} Jens V. Stein,⁷ and Santiago F. Gonzalez^{1,9,*}

¹Institute for Research in Biomedicine (IRB), Università della Svizzera italiana, Via Vincenzo Vela 6, 6500 Bellinzona, Switzerland

²Graduate School of Cellular and Molecular Sciences, Faculty of Medicine, University of Bern, 3012 Bern, Switzerland

³Institute of Computational Science (ICS), Università della Svizzera italiana, Via Giuseppe Buffi 13, 6900 Lugano, Switzerland

⁴Institute of Oncology Research (IOR), Via Vincenzo Vela 6, 6500 Bellinzona, Switzerland

⁵Laboratory of Molecular Biology, Istituto di Ricerche Farmacologiche Mario Negri IRCCS, via Giuseppe La Masa 19, 20156 Milano, Italy

⁶Institute for Microbiology, ETH Zurich, Wolfgang-Pauli-Strasse 10, 8093 Zurich, Switzerland

⁷Theodor Kocher Institute (TKI), University of Bern, Freiestrasse 1, 3000 Bern, Switzerland

⁸Present address: Salk Institute for Biological Studies, La Jolla, CA 92037, USA

⁹Lead Contact

*Correspondence: santiago.gonzalez@irb.usi.ch

<https://doi.org/10.1016/j.celrep.2019.01.104>

SUMMARY

The role of natural killer (NK) cells in the immune response against vaccines is not fully understood. Here, we examine the function of infiltrated NK cells in the initiation of the inflammatory response triggered by inactivated influenza virus vaccine in the draining lymph node (LN). We observed that, following vaccination, NK cells are recruited to the interfollicular and medullary areas of the LN and become activated by type I interferons (IFNs) produced by LN macrophages. The activation of NK cells leads to their early production of IFN γ , which in turn regulates the recruitment of IL-6+ CD11b+ dendritic cells. Finally, we demonstrate that the interleukin-6 (IL-6)-mediated inflammation is important for the development of an effective humoral response against influenza virus in the draining LN.

INTRODUCTION

While contained inflammation enhances both humoral and cellular adaptive immunity, uncontrolled or persistent inflammation has detrimental roles associated with reduced long-lived memory cell formation and cellular exhaustion (Wherry, 2011). Therefore, it is essential to better understand the mechanisms that lead to the initiation of the inflammatory response following vaccination.

Among the different types of inflammatory molecules, type I interferons (IFNs) are critical for the effective initiation of the inflammatory response and the generation of an antiviral state (Gabay and Kushner, 1999). Additionally, they are also involved in the activation of various immune cells such as dendritic cells (DCs) and natural killer (NK) cells (Madera et al., 2016). In a previous

study, we showed that lymph node macrophages (LNMs) are one of the major producers of type I IFNs at early times post influenza vaccination. This mechanism is essential for the activation of DCs and the regulation of the local humoral responses (Chatziandreou et al., 2017). In addition, LNMs activate other innate immune cells involved in the inflammatory process, such as NK cells (Garcia et al., 2012).

NK cells play an important role in eliminating stressed and infected cells without the need for prior sensitization (Vivier et al., 2008). Moreover, they can directly recognize influenza virus via receptor NKp46 (Mendelson et al., 2010). The absence of NKp46 results in increased mortality, highlighting the importance of NK cell functions during influenza infection (Gazit et al., 2006). Previous studies have stressed the role of NK cells as one of the major producers of type II IFNs contributing to the activation of T cells (Martín-Fontecha et al., 2004), macrophages (Mosser and Edwards, 2008), DCs (Gerosa et al., 2002), and B cells (Wilder et al., 1996). Despite the fact that NK cells have been widely studied in various tissue and disease models, their role in response to vaccination needs to be investigated.

RESULTS

NK Cells Are Recruited to the LN and Undergo Type I IFN-Dependent Activation

To assess the involvement of NK cells in response to influenza vaccination at early time points (0–24 h post vaccination; p.v.), we investigated their recruitment to the draining LN after footpad injection of ultraviolet inactivated influenza virus (UVPR8). We observed a significant increase of total NK (Figure 1A) and CD69+ and GranzymeB+ NK cell numbers (Figure 1B) at 12 and 24 h p.v., which correlated with an increase in their fluorescence intensity (Figure 1C). To assess NK cell recruitment, we performed intravital two-photon microscopy (IV-2PM) in combination with epifluorescence time-lapse microscopy using *Ncr1*-GFP mice (Gazit et al., 2006). We observed that NK cells were



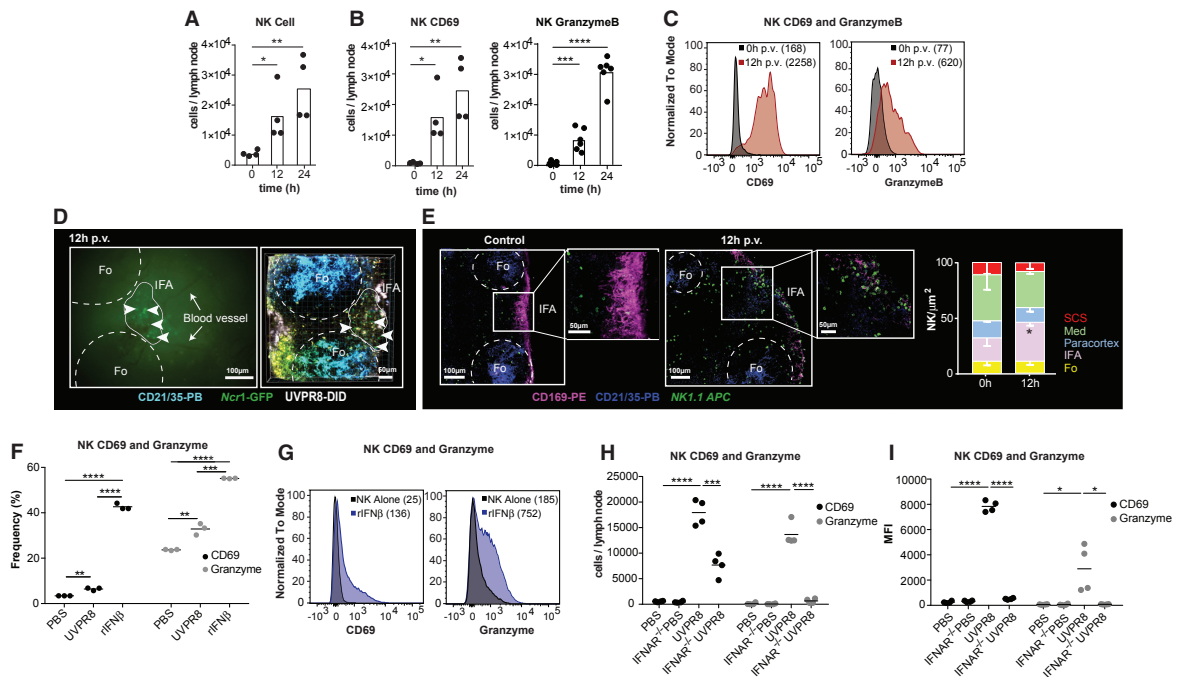


Figure 1. NK Cells Get Recruited to the Popliteal Lymph Node at Early Times after Influenza Vaccination and Are Activated by Type I IFNs (A and B) Flow cytometry showing total NK (A) and CD69+ and GranzymeB+ NK cell numbers (B) in the lymph node (LN) following vaccination at indicated time points.

(C) Representative histograms of fluorescence intensity showing upregulation of CD69 and GranzymeB at 12 h post vaccination (p.v.) in comparison with non-vaccinated controls. Median fluorescence intensity (MFI) values are indicated in parentheses.

(D) Snapshot from an epifluorescence time lapse (left) and two-photon microscopy (right) showing recruitment of NK cells (green) via blood vessels located in the interfollicular area (IFA) of the LN at 12 h p.v.

(E) Confocal micrographs showing recruitment of NK cells in the IFA of LN from control (left) and vaccinated at 12 h p.v. (middle). The right graph shows the quantification of the frequency of NK cell density in the medullary (Med), IFA, cortex, follicle (Fo), and subcapsular sinus (SCS) areas of the LN at indicated time points.

(F) Flow cytometry showing frequency of CD69+ and GranzymeB+ NK cells after 12 h culture with UVPR8 and/or recombinant IFN- β compared with control group.

(G) Representative histograms of fluorescence intensity rIFN- β -treated NK cells showing upregulation of CD69 and GranzymeB at 12 h p.v. compared to control groups. MFIs are indicated in parentheses.

(H and I) Flow cytometry showing total CD69+ NK and GranzymeB+ NK cell numbers (H) and MFI values (I) at 12 h p.v. in LN of IFNAR^{-/-} and B6 mice.

In all figures, the presented data are representative of at least three independent experiments. Results are given as mean \pm SD. ns, not significant, $p > 0.05$; * $p < 0.05$; ** $p < 0.01$; *** $p < 0.001$; **** $p < 0.0001$.

recruited via blood vessels (Figure 1D, left; Video S1) and accumulated in the interfollicular area (IFA) of the LN (Figure 1D, right). Additionally, using immunohistochemistry, we confirmed a significant increase of these cells in the IFA of the LN at 12 h p.v. (Figure 1E).

Next, we assessed the mechanism by which NK cells are recruited to the LN by evaluating their number in IL1R^{-/-}, interferon- α/β receptor (IFNAR)^{-/-}, and CXCR3^{-/-} animals. We observed that IL1R^{-/-}, IFNAR^{-/-}, CXCR3^{-/-} showed no reduction in the total number of NK cells in the LN at 12 h p.v. (Figures S1A and S1B). However, we observed that LN macrophages were involved in the recruitment of the NK cells as their depletion with clodronate liposomes (CLLs) significantly reduced the number of NK cells at 12 h p.v. (Figure S1C).

NK cells can directly recognize hemagglutinin (HA) from influenza virus via receptor NKp46 (Mandelboim et al., 2001). Thus, we tested whether influenza vaccine can directly activate NK cells *in vitro*. We cultured spleen-sorted NK cells with UVPR8 and observed a partial activation at 12 h post-culture, indicated by a significant increase of CD69+ and GranzymeB+ NK cell frequency (Figure 1F). Next, we cultured spleen-sorted NK cells in the presence or absence of recombinant IFN- β (rIFN- β). As expected, rIFN- β alone was enough to increase the CD69+ and GranzymeB+ NK cell frequency (Figure 1F), along with their expression (Figure 1G). Moreover, we observed that the numbers of CD69+ and GranzymeB+ NK cells decreased significantly in IFNAR^{-/-} mice at 12 h p.v. (Figure 1H) in concordance with the reduced median fluorescence intensity (MFI) (Figure 1I). Finally, to

evaluate if the recruitment of activated NK cells at 12 h p.v. was influenza specific, we designed a similar set of experiments using UV-inactivated DNA virus (vaccinia UVNYVAC-C). Interestingly, we observed that the immunization with vaccinia promoted a stronger NK cell recruitment at 12 h p.v. (Figure S1D). Additionally, we observed a significant increase in the total number of CD69⁺ and IFN γ ⁺ NK cells (Figures S1E and S1G, respectively) but not in the MFI levels of CD69 and GranzymeB, which were significantly reduced in animals vaccinated with vaccinia compared with influenza (Figures S1E and S1F, respectively).

Subcapsular Sinus and Medullary Macrophages Interact with NK Cells, Leading to Their Activation

To study the interaction between NK cells and LNMs, we performed IV-2PM at 12 h p.v. on the popliteal LN of *Ncr1*-GFP mice. We observed that NK cells interact with both subcapsular sinus macrophages (SSMs; CD169⁺, F4/80⁻; Figure 2A; Video S2) and medullary macrophages (MMs; CD169⁺, F4/80⁺; Figure 2B, Video S2). To further evaluate these interactions, we analyzed NK cell motion tracks in different regions of the LN. We found that the preferential direction of NK cells was higher in the IFA and the medulla compared to the subcapsular sinus area (SCS; Figure 2C). Moreover, NK cells moved slower in the medulla and SCS in comparison to the IFA, as indicated by the reduction in their mean track speed (Figure 2D). Analysis of the arrest coefficient, defined as the proportion of time in which an NK cell moves slower than 2 $\mu\text{m}/\text{min}$, demonstrated that NK cells arrested at a significantly higher rate in the medulla compared to the SCS and the IFA (Figure 2E). To evaluate the ability of LNMs to stimulate and activate NK cells *in vivo*, we eliminated LNMs by treatment with CLLs and analyzed the expression of CD11b by NK cells, as a marker of their maturation (Kim et al., 2002). We observed that CLL-treated mice had a significantly lower frequency of mature NK cells at 12 h p.v. in comparison to the CLL-untreated group (Figure 2F). In addition, the MFI levels of CD69 and GranzymeB in NK cells were significantly reduced in the CLL-treated group compared to control groups (Figure 2G), confirming the involvement of LNMs in NK cell activation.

Involvement of NK Cells in the Early Inflammatory Reaction Initiated by LNMs

Considering that NK cells are known to be one of the key players in the type II IFN response (Vivier et al., 2008), we evaluated their production of IFN γ following influenza vaccination. The analysis of LN extracts from the first 24 h following vaccination showed a prominent peak in IFN γ levels at 12 h p.v., followed by a striking reduction at 24 h p.v. (Figure 3A). We observed that the number IFN γ ⁺ NK cells peaked at 12 h p.v. (Figure 3B), correlating with their frequency (Figure 3C). Moreover, we confirmed that NK cells were the major producers of IFN γ at this time (Figures S2A and S2B) and pre-treatment with the $\alpha\text{NK1.1}$ significantly lowered the IFN γ levels in the LN (Figure 3D). In addition, confocal microscopy revealed that IFN γ ⁺ NK cells were located in the IFA of the LN at 12 h p.v. (Figure 3E). Having identified the effect of LNMs on NK cell activation, we observed a close interaction between IFN γ ⁺ cells and CD169⁺ macrophages at 12 h p.v. using IV-2PM imaging (Figure 3F). We assessed the

involvement of LNMs in NK cell production of IFN γ by depleting LNMs with CLLs. We detected a significant decrease in IFN γ ⁺ NK cell numbers in animals lacking LNMs (Figure 3G), which correlated with a significant reduction of secreted IFN γ at 12 h p.v. (Figure 3H). We further evaluated the effect of IFNAR on the production of IFN γ by NK cells. We found that the total number of IFN γ ⁺ NK cells (Figure 3I) and their MFI (Figure 3J) were significantly reduced in IFNAR^{-/-} mice compared to the control group. To further evaluate the role of NK cells in the induction of the inflammatory response, we performed real-time PCR on samples obtained from mice depleted of NK cells in comparison to the control group. We observed that the transcription levels of the inflammatory mediators IFN γ and IL-6 were significantly elevated at 12 h p.v. in comparison to PBS controls and NK-cell-depleted mice (Figures 3K and 3L). In contrast, IL-18 and IL-1 β levels were increased in mice lacking NK cells (Figures 3M and 3N).

Early IFN γ Secreted by NK Cells Is Important for the Local Production of IL-6 in the Draining LN

To confirm that the reduction of IL-6 transcripts correlated with its protein level, we measured the concentration of IL-6 in NK-cell-depleted mice in comparison to the control group. We confirmed that the absence of NK cells significantly reduced the levels of IL-6 in the draining LN (Figure 4A). Interestingly, we observed that the reduction of IL-6 was dependent on IFN γ (Figure 4A). Having shown the effects of LNMs and type I IFNs on the regulation of IFN γ production by NK cells, we examined the levels of IL-6 in CD169^{DTR} and IFNAR^{-/-} mice at 12 h p.v. We observed a prominent reduction in the levels of IL-6 (Figure 4B) in animals lacking LNMs or type I IFN signaling. Moreover, in concordance with earlier studies (Hunter and Jones, 2015), we found that IL-6 production was dependent on MyD88 signaling, as MyD88^{-/-} mice exhibited a complete reduction in secreted IL-6 at 12 h p.v. (Figure 4C). Using flow cytometry, we identified CD11b⁺ DCs as the major source of IL-6 at 12 h p.v. (Figures 4D and 4E). To investigate whether IFN γ produced by NK cells is involved either in the proliferation or recruitment of CD11b⁺ DCs, we checked their Ki-67 expression in the presence or absence of NK cells at 12 h p.v. The absence of NK cells did not affect DC proliferation (Figure S3A). However, we measured a significant decrease in the number of IL-6⁺ CD11b⁺ DCs when we eliminated NK cells or blocked IFN γ signaling (Figures 4F and 4G, respectively). Additionally, we could observe a decrease in the levels of different chemokines known to be involved in the recruitment of DC precursors to the LN (Figures S3B–S3D). Furthermore, to evaluate the capacity of IFN γ to directly stimulate IL-6 production by CD11b⁺ DCs, we sorted CD11b⁺ splenic DCs and stimulated them with recombinant IFN γ or lipopolysaccharides (LPS) for 12 h. We saw that IFN γ could directly act on CD11b⁺ DCs to induce IL-6 secretion (Figure S3E).

IL-6 Production Regulates Humoral Immunity in the Draining LN

To determine whether additional production of IL-6 occurs at later time points p.v., we examined the kinetics of IL-6 secretion in the LN in response to UVPR8. We observed that the peaks of

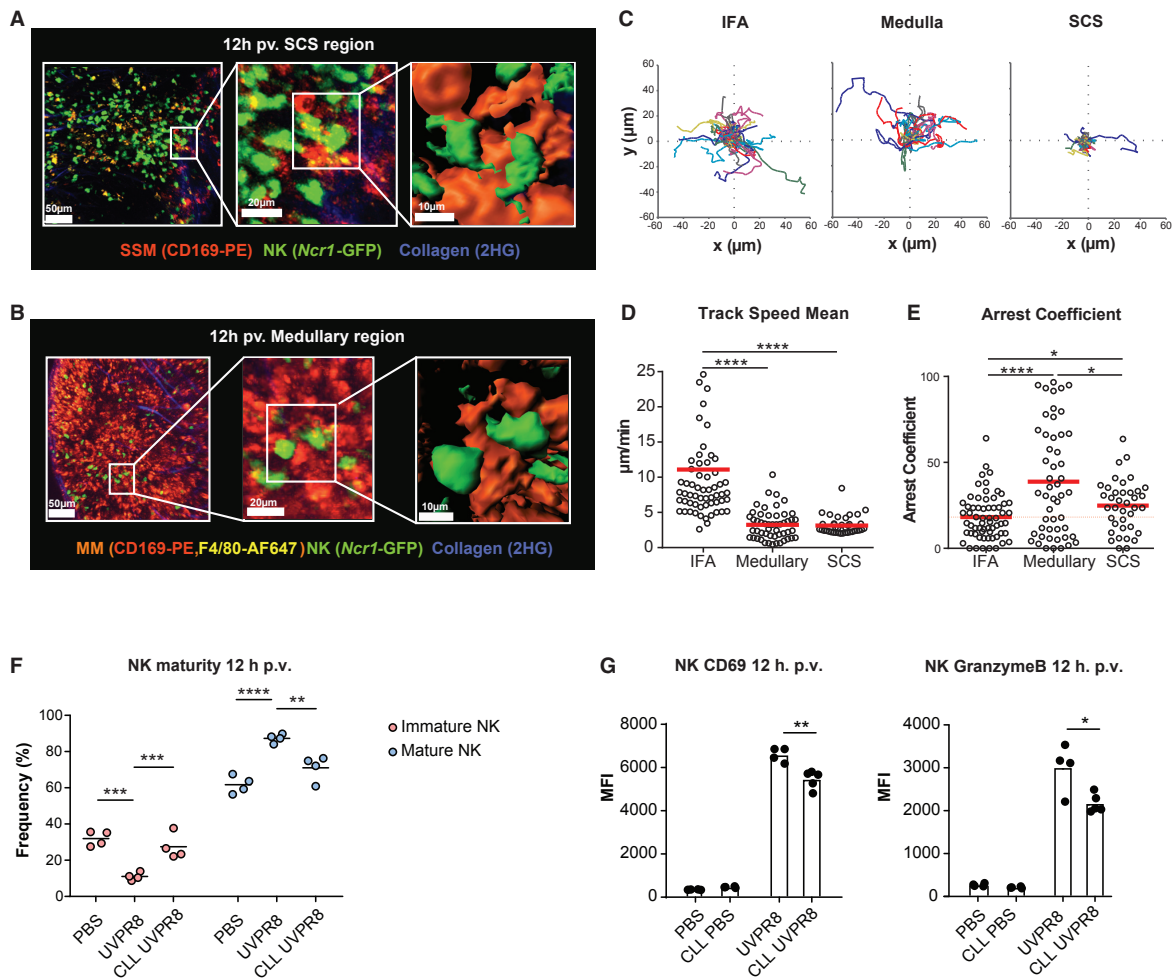


Figure 2. Subcapsular Sinus and Medullary Macrophages Interact Differently with NK, Leading to Their Activation

(A and B) Representative intravital two-photon micrograph showing close interactions between infiltrated NK cells with subcapsular sinus macrophages (SSMs) (CD169-PE) (A) and medullary macrophages (MMs; CD169-PE, F4/80-AF647) (B) in the LN at 12 h p.v. Central panels represent the magnified dotted box. Right panels demonstrated surface reconstruction of the zoomed images.

(C) Graphical representation of tracks with common origin showing preferential direction of NK cells in the interfollicular (IFA), medullary, and subcapsular sinus area (SCS).

(D and E) Representative graphs showing track speed mean (D) and arrest coefficient (E) of NK cells in the indicated regions of the LN at 12 h p.v.

(F) Flow cytometric analysis of the frequency of CD11b+ and CD11b- NK cells at 12 h p.v. in mice treated with/without CLLs compared with PBS controls.

(G) Flow cytometric quantification of CD69+ and GranzymeB+ NK cells at 12 h p.v. in mice treated with/without CLLs compared with PBS controls.

In all figures, the presented data are representative of at least three independent experiments. Results are given as mean \pm SD. ns, $p > 0.05$; * $p < 0.05$; ** $p < 0.01$; *** $p < 0.001$; **** $p < 0.0001$.

IL-6 and IFN γ occur within the first 24 h p.v. (Figures 5A and 5B, respectively). Previous studies have demonstrated that IL-6 affects B cell responses (Eto et al., 2011). Therefore, to examine the involvement of IL-6 in the regulation of the local humoral responses to influenza vaccine, we neutralized the initial IL-6 production by administrating α IL-6 antibodies at the time of vaccination. Using enzyme-linked immunospot assay (ELISPOT) analysis, we observed a significant reduction in the number of

influenza-specific antibody-secreting cells (ASCs) in the draining LN at day 10 p.v. in IL-6-neutralized mice compared to untreated controls (Figure 5C). Next, we tested whether the elimination of NK cells or the absence of the interferon-g (IFN γ R) would result in a reduction of the local B cell responses to the virus. ELISPOT analysis confirmed that the number of influenza-specific ASCs were significantly reduced in both cases, compared to the respective control groups (Figures 5D and 5E). Having validated

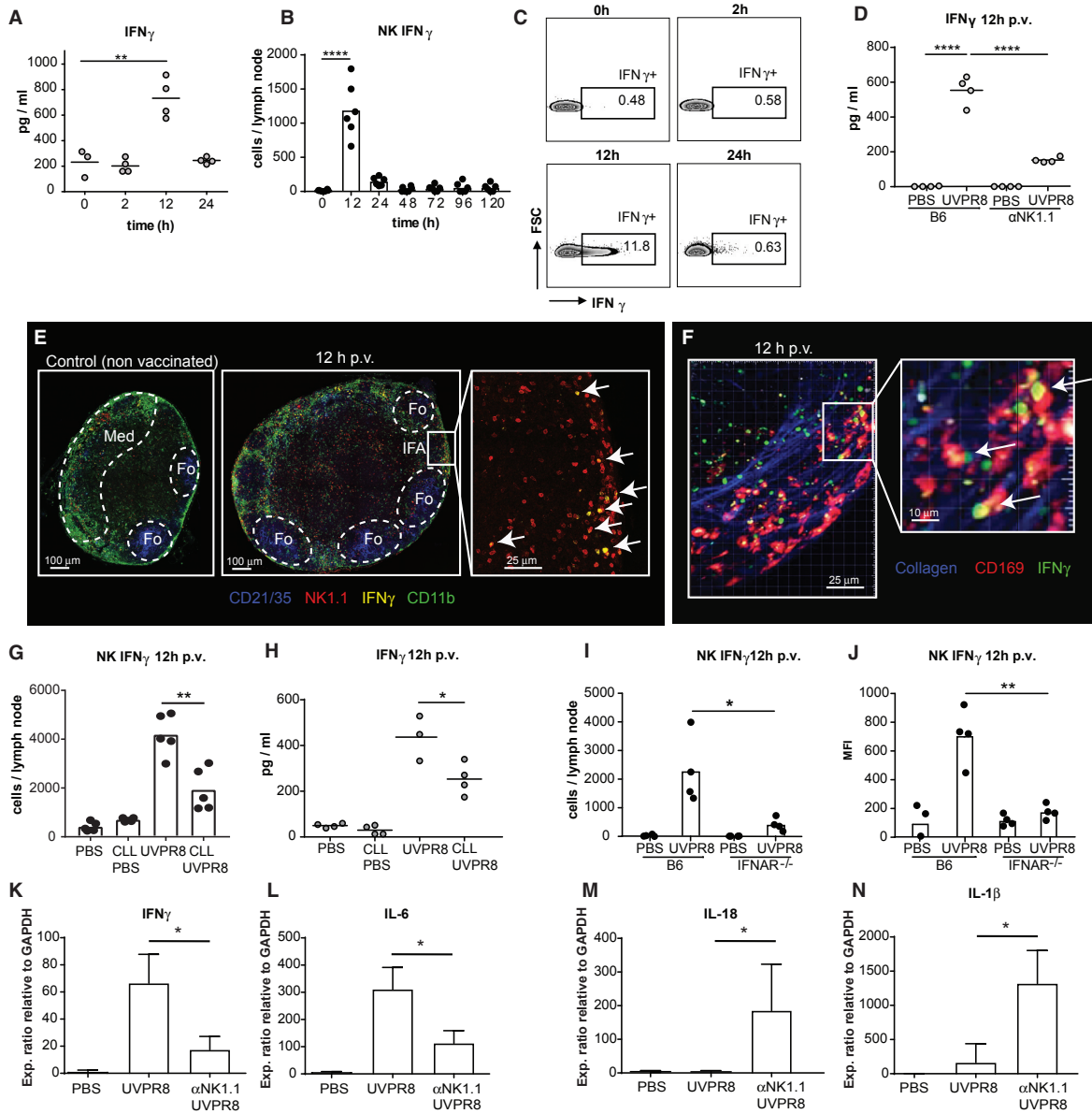


Figure 3. Early Production of IFN γ by NK Cells Is Dependent on the Type I IFN Response Initiated by LNMs

(A) ELISA showing IFN γ in the LN at indicated time points p.v.
 (B and C) Flow cytometric analysis of total IFN γ ⁺ NK cell numbers (B) and representative plots showing frequency of IFN γ ⁺ NK cells (C) at indicated time points p.v.
 (D) Cytoplex indicating IFN γ in LN of α NK1.1-treated mice and control groups at 12h p.v.
 (E) Representative confocal micrograph of popliteal LN at 12h p.v. (middle) showing IFN γ ⁺ cells (yellow), NK1.1⁺ cells (red), and IFN γ -producing NK cells (merge) located in the interfollicular area (IFA) of the LN. The left panel represent the control group, and the right panel indicates the zoomed area. Arrows indicate IFN γ ⁺ and NK cells at 12h p.v.
 (F) Representative micrograph (left) and amplification (right) showing close interactions between IFN γ ⁺ cells and LN macrophages (CD169-PE) at 12h p.v. White arrows indicate IFN γ ⁺ cells.
 (G) Flow cytometry showing IFN γ ⁺ NK total numbers at 12h p.v. in CLL-treated mice with respect to the control group.
 (H) Cytoplex showing a reduction of IFN γ levels in LN of CLL-treated mice at 12h p.v. compared to control groups.

(legend continued on next page)

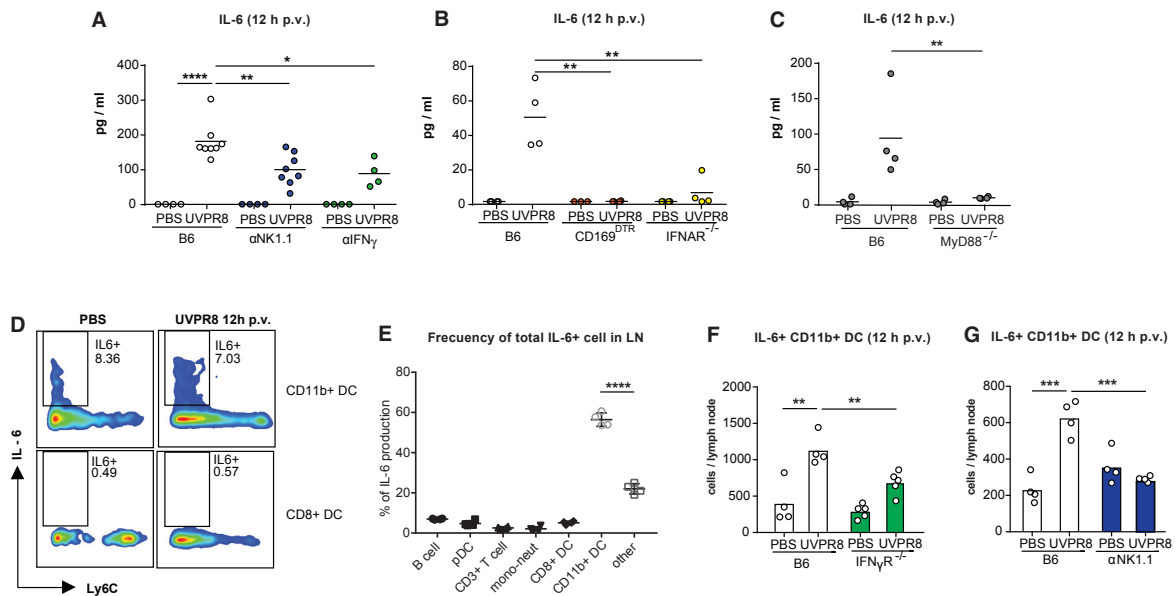


Figure 4. NK Cells Regulate DC Production of IL-6

(A) Cytoplex analysis of IL-6 in popliteal LN from anti-NK1.1-treated and anti-IFN γ -treated mice compared to the control group at 12 h p.v. (B and C) Cytoplex analysis of IL-6 in popliteal LN CD169^{DTR}, IFNAR^{-/-} (B), and MyD88^{-/-} (C) mice compared to the control group at 12 h p.v. (D) Representative flow cytometry indicating IL-6 production of CD11b+ DCs and CD8+ DCs at 12 h p.v. compared to control. (E) Flow cytometry showing the frequency of the IL-6+ cells in the LN. (F and G) Flow cytometry indicating IL-6+ DC numbers at 12 h p.v. in LN of IFN γ ^{-/-} (F) and anti-NK1.1-treated mice (G). In all figures, the presented data are representative of at least three independent experiments. Results are given as mean \pm SD. ns, $p > 0.05$; * $p < 0.05$; ** $p < 0.01$; *** $p < 0.001$; **** $p < 0.0001$.

the importance of IFN γ and IL-6 in driving influenza-specific humoral response, we investigated whether immunoglobulin G (IgG) ASC reduction was due to impairment in B cell development. We found that, while the level of IgG antibodies was reduced, germinal center and plasma cell numbers were not altered using neutralizing antibody treatments or when the type II IFN signaling was blocked (IFN γ ^{-/-}) at 12 h p.v. (Figures S4A and S4B).

DISCUSSION

In this study, we revealed that following influenza vaccination, NK cells are preferentially located at the interfollicular and medullary regions of the LN, which is in accordance with a previous report (Bajénoff et al., 2006). Additionally, we demonstrated that NK cell recruitment was independent of CXCR3 and dependent on the presence LNMs. We also demonstrated that neither type I IFNs nor IL-1 α , produced by LNMs after vaccination (Chatziandreou et al., 2017), were involved in the initial recruitment of

NK cells. It is possible that the release of other danger signals after the necrotic death of the LNMs (Chatziandreou et al., 2017) could be involved in the recruitment of NK cells. Former studies outlined that the activation of NK cells was associated with their interaction with SSMs (Coombes et al., 2012; Garcia et al., 2012). We show that MMs also interact with NK cells, forming stable contacts in the medullary area. Considering the role of type I IFNs on the functions of NK cells (Madera et al., 2016), we confirmed that IFN signaling was necessary for the effective activation of NK cells. In a previous work, we reported that LNMs are responsible for the initial production of type I IFNs following influenza vaccination (Chatziandreou et al., 2017), which could explain the close interactions of NK cells with the LNMs in these areas. We also saw that recruitment of NK cells in the IFA, together with their high speed, correlates with the presence of IFN γ ⁺ cells in this region. In fact, we have formerly shown that IFA are one of the major sites for type I IFN production (Chatziandreou et al., 2017). NK cells require several cytokines for full maturation and to perform their effector functions (Brady et al.,

(I and J) Flow cytometry of IFN γ ⁺ NK total numbers (I) and MFI values (J) in IFNAR^{-/-} and control mice at 12 h p.v. (K–N) Quantitative real-time PCR analysis of cDNA from LN of mice treated with/without anti NK1.1 compared to controls at 12 h p.v. testing the expression of inflammatory molecules IFN γ (K), IL-6 (L), IL-18 (M), and IL-1 β (N). In all figures, the presented data are representative of at least three independent experiments. Results are given as mean \pm SD. ns, $p > 0.05$; * $p < 0.05$; ** $p < 0.01$; **** $p < 0.0001$.

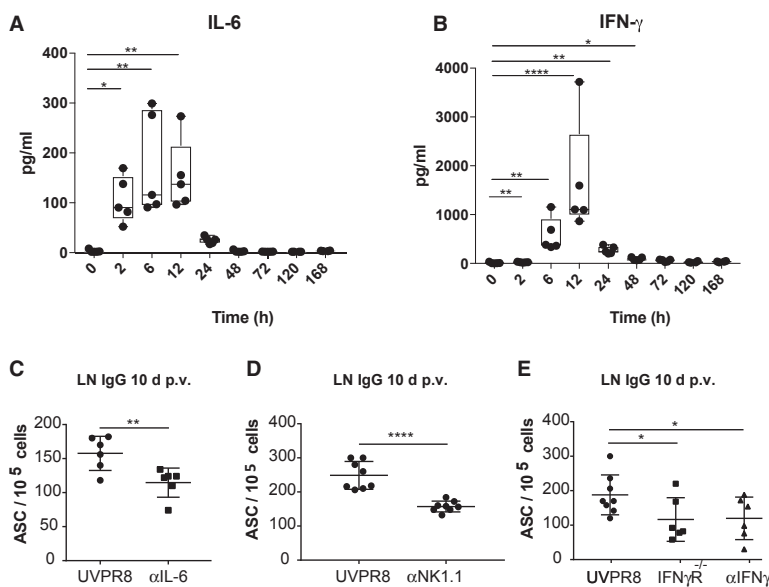


Figure 5. NK-Regulated IL-6 Production Is Involved in the Humoral Response against Influenza Vaccine

(A and B) Time course showing the secreted levels of the cytokines IL-6 (A) and IFN γ (B) in the LN at 2, 6, 12, 24, 48, 72, 120, and 168 h p.v. (C–E) ELISPOT analysis of IgG antibody-secreting cells (ASCs) from UVPR8-vaccinated, α IL-6-treated (C), α NK1.1-treated (D), and IFN γ R^{-/-}-treated and α IFN γ -treated (E) mice at 10 days p.v. In all figures, the presented data are representative of at least three independent experiments. Results are given as mean \pm SD. ns, $p > 0.05$; * $p < 0.05$; ** $p < 0.01$; **** $p < 0.0001$.

2010). The decrease of NK cell maturation, activation, and production of IFN γ observed in the interferon- α/β receptor knockout (IFNARKO) mice could be associated with the early production of this cytokine by the LNMs. However, we cannot exclude the contribution of other type-I-IFN-producing cells or alternative factors that might affect NK cell effector functions.

It was demonstrated that innate CD8+ T cells are the major producers of early IFN γ after administration of modified vaccinia virus (MVA) in the LN (Kastenmüller et al., 2012). However, we showed that following influenza vaccination, early production of IFN γ was mediated by NK cells. The observed discrepancy is most likely related to the type of pathogen studied, since vaccination with another attenuated vaccinia virus (NYVAC-C) showed that the magnitude of NK cell recruitment and their effector functions were different in both models. Further, MVA was shown to activate the inflammasome pathway, yet we could not detect the expression of inflammasome-associated molecules in our model. Interestingly, depletion of NK cells resulted in increased transcription of IL-18 and IL-1 β , which might be related with the absence of IFN γ as it was previously shown that IFN γ promotes the production of nitric oxide (NO) that prevents inflammasome assembly (Mao et al., 2013; Mishra et al., 2013).

Previous studies have described that IFN γ produced by NK cells is essential for Th1 differentiation (Martin-Fontecha et al., 2004). Prior to differentiation, CD4+ T cells need to be primed by DCs in a multi-step process that requires at least a day (Mempel et al., 2004). Although we observed an earlier release of IFN γ at 2 h p.v., the peak of IFN γ secretion occurred at 12 h p.v.; therefore, we discarded involvement of early IFN γ in Th1 differentiation. Instead, IFN γ is also known to regulate the production of various pro-inflammatory mediators, including tumor necrosis factor alpha (TNF- α) (Donnelly et al., 1995), IL-12 (Libraty et al., 1997), and IL-6 (Yi et al., 1996). In fact, the peaks of IFN γ and

IL-6 secretion coincided, and both transcript and protein levels of IL-6 were reduced in mice lacking NK cells. Further, the 2 h IFN γ release also correlated with the presence of IL-6, confirming the interdependence of the two cytokines. Importantly, neutralization of IFN γ resulted in decreased IL-6 secretion. It is important to mention that a prominent decrease in IL-6 levels observed in mice lacking

type I IFN receptors or LNMs suggests the presence of additional factors in its regulation besides NK-cell-secreted IFN γ . Among the various types of IL-6-producing cells (Hunter and Jones, 2015), we revealed that CD11b+ DCs were the major source of this cytokine at 12 h p.v. Moreover, we confirmed that IFN γ can act directly on a CD11b+ DC population to induce the secretion of IL-6, as well as contributing to their recruitment. Also, in accordance with previous studies (Naugler et al., 2007), the production of IL-6 was dependent on viral recognition by Toll-like receptors, as the absence of MyD88 signaling abolished its secretion. Interestingly, we show that the lack of NK cells or IFN γ reduced the total number of IL-6-producing DCs, which could be associated with poor monocyte differentiation into DCs caused by the absence of IFN γ (Goldszmid et al., 2012). Moreover, proliferation of IL-6+ DCs was not affected by the absence of NK cells, suggesting that the decrease is also not related with the proliferative capacity of DCs. In fact, it is known that IFN γ is essential for DC homeostasis and activation (Akbar et al., 1996). Therefore, it is possible that NK cell depletion affects the reciprocal interactions between DCs and NK cells required for DC homeostasis (Gerosa et al., 2002), leading to the observed reduction in the number of DCs. Along this line, depletion of NK cells resulted in decreased levels of macrophage inflammatory protein (MIP)-1 α , which is known to affect CD8a–CD11b+ DC maturation and activation in the LN (Bachmann et al., 2006; Trifilo and Lane, 2004). Hence, it is probable that NK cells are involved in activating DCs for IL-6 production along with their maintenance in the LN at 12 h post influenza vaccination.

We showed that the initial inflammatory peak directly affects the humoral response to influenza virus, as blocking IL-6 reduced influenza-specific ASCs in the draining LN. The mechanism by which IL-6 might influence this response is most likely

related with the regulation of the follicular helper T cells (T_{FH}) differentiation and B cell activity as previously described (Choi et al., 2013; Eto et al., 2011). Further, elimination of NK cells, hence $IFN\gamma$, may skew the overall inflammatory response, which can affect the antibody isotype class switching, leading to a reduction in IgG levels. It should also be noted that the depletion method used here also depletes natural killer T (NKT) cells. Although, we have shown that NKT cells are not involved in the initial $IFN\gamma$ secretion and that we do not detect the presence of IL-4 (Chatziandreou et al., 2017) in our vaccination model, it is possible that elimination of NKT cells affects the overall B cell responses by other means.

In this work, we show that the type I IFN response generated by LNMs is associated with the activation of NK cells, which in turn produce $IFN\gamma$ leading to the recruitment of IL-6+ CD11b+ DCs. We demonstrated that both IL-6 and type II IFNs regulate the influenza-specific local B cell responses.

STAR★METHODS

Detailed methods are provided in the online version of this paper and include the following:

- KEY RESOURCES TABLE
- CONTACT FOR REAGENT AND RESOURCE SHARING
- EXPERIMENTAL MODEL AND SUBJECT DETAILS
 - Mice
 - *In vitro* NK cell culture and $IFN\beta$ stimulation
 - *In vitro* CD11b+ DC culture and $IFN\gamma$ stimulation
- METHOD DETAILS
 - Virus production, inactivation and labeling
 - Antigen administration and injections
 - Flow cytometry
 - Immunohistology/microscopy
 - Cytoplex assay
 - ELISPOT
 - Multiphoton microscopy and analysis
 - qPCR
- QUANTIFICATION AND STATISTICAL ANALYSIS
 - Statistics

SUPPLEMENTAL INFORMATION

Supplemental Information can be found with this article online at <https://doi.org/10.1016/j.celrep.2019.01.104>.

ACKNOWLEDGMENTS

We thank Prof. M. Thelen, Prof. A. Jaworowski, and Dr. J. Abe for valuable discussions. We thank Prof. M. Esteban for providing vaccinia virus NYVAC-C, F. Thelen, D. Jarrossay, and R. D'Antuono for technical support, and Prof. Br. Horvat for providing CD119^{DTR} mice. This work was supported by the Swiss National Science Foundation (SNF) grants 176124, R'Equip (145038), and Ambizione (148183) and a Marie Curie Reintegration Grant (612742).

AUTHOR CONTRIBUTIONS

S.F.G. directed the study. S.F.G., Y.F., M.P.-S., and I.L. designed experiments, analyzed and interpreted the results, and wrote the manuscript. Y.F., M.P.-S., I.L., S.Z., N.C., and A.R. performed experiments. D.U.P. and M.B.

analyzed and interpreted results. F.S. and J.V.S. interpreted results and provided reagents.

DECLARATION OF INTERESTS

All the authors declare no competing financial interests.

Received: February 6, 2018

Revised: December 11, 2018

Accepted: January 28, 2019

Published: February 26, 2019

REFERENCES

- Akbar, S.M., Inaba, K., and Onji, M. (1996). Upregulation of MHC class II antigen on dendritic cells from hepatitis B virus transgenic mice by interferon-gamma: abrogation of immune response defect to a T-cell-dependent antigen. *Immunology* 87, 519–527.
- Bachmann, M.F., Kopf, M., and Marsland, B.J. (2006). Chemokines: more than just road signs. *Nat. Rev. Immunol.* 6, 159–164.
- Bajénoff, M., Breart, B., Huang, A.Y., Qi, H., Cazareth, J., Braud, V.M., Germain, R.N., and Glaichenhaus, N. (2006). Natural killer cell behavior in lymph nodes revealed by static and real-time imaging. *J. Exp. Med.* 203, 619–631.
- Barnden, M.J., Allison, J., Heath, W.R., and Carbone, F.R. (1998). Defective TCR expression in transgenic mice constructed using cDNA-based α - and β -chain genes under the control of heterologous regulatory elements. *Immunol. Cell Biol.* 76, 34–40.
- Brady, J., Carotta, S., Thong, R.P., Chan, C.J., Hayakawa, Y., Smyth, M.J., and Nutt, S.L. (2010). The interactions of multiple cytokines control NK cell maturation. *J. Immunol.* 185, 6679–6688.
- Chatziandreou, N., Farsakoglu, Y., Palomino-Segura, M., D'Antuono, R., Pizzagalli, D.U., Sallusto, F., Lukacs-Kornek, V., Uguccioni, M., Corti, D., Turley, S.J., et al. (2017). Macrophage Death following Influenza Vaccination Initiates the Inflammatory Response that Promotes Dendritic Cell Function in the Draining Lymph Node. *Cell Rep.* 18, 2427–2440.
- Choi, Y.S., Eto, D., Yang, J.A., Lao, C., and Crotty, S. (2013). Cutting edge: STAT1 is required for IL-6-mediated Bcl6 induction for early follicular helper cell differentiation. *J. Immunol.* 190, 3049–3053.
- Coomes, J.L., Han, S.-J., van Rooijen, N., Raulet, D.H., and Robey, E.A. (2012). Infection-induced regulation of natural killer cells by macrophages and collagen at the lymph node subcapsular sinus. *Cell Rep.* 2, 124–135.
- Donnelly, R.P., Freeman, S.L., and Hayes, M.P. (1995). Inhibition of IL-10 expression by IFN-gamma up-regulates transcription of TNF-alpha in human monocytes. *J. Immunol.* 155, 1420–1427.
- Eto, D., Lao, C., DiToro, D., Barnett, B., Escobar, T.C., Kageyama, R., Yusuf, I., and Crotty, S. (2011). IL-21 and IL-6 are critical for different aspects of B cell immunity and redundantly induce optimal follicular helper CD4 T cell (T_{fh}) differentiation. *PLoS ONE* 6, e17739.
- Gabay, C., and Kushner, I. (1999). Acute-phase proteins and other systemic responses to inflammation. *N. Engl. J. Med.* 340, 448–454.
- Garcia, Z., Lemaître, F., van Rooijen, N., Albert, M.L., Levy, Y., Schwartz, O., and Bousso, P. (2012). Subcapsular sinus macrophages promote NK cell accumulation and activation in response to lymph-borne viral particles. *Blood* 120, 4744–4750.
- Gazit, R., Gruda, R., Elboim, M., Arnon, T.I., Katz, G., Achdout, H., Hanna, J., Qimron, U., Landau, G., Greenbaum, E., et al. (2006). Lethal influenza infection in the absence of the natural killer cell receptor gene Ncr1. *Nat. Immunol.* 7, 517–523.
- Gerosa, F., Baldani-Guerra, B., Nisii, C., Marchesini, V., Carra, G., and Trinchieri, G. (2002). Reciprocal activating interaction between natural killer cells and dendritic cells. *J. Exp. Med.* 195, 327–333.
- Glaccum, M.B., Stocking, K.L., Charrier, K., Smith, J.L., Willis, C.R., Maliszewski, C., Livingston, D.J., Peschon, J.J., and Morrissey, P.J. (1997). Phenotypic

- and functional characterization of mice that lack the type I receptor for IL-1. *J. Immunol.* 159, 3364–3371.
- Goldszmid, R.S., Caspar, P., Rivollier, A., White, S., Dzutsev, A., Hieny, S., Kellsall, B., Trinchieri, G., and Sher, A. (2012). NK cell-derived interferon- γ orchestrates cellular dynamics and the differentiation of monocytes into dendritic cells at the site of infection. *Immunity* 36, 1047–1059.
- Gómez, C.E., Nájera, J.L., Jiménez, V., Bieler, K., Wild, J., Kostic, L., Heidari, S., Chen, M., Frachette, M.-J., Pantaleo, G., et al. (2007). Generation and immunogenicity of novel HIV/AIDS vaccine candidates targeting HIV-1 Env/Gag-Pol-Nef antigens of clade C. *Vaccine* 25, 1969–1992.
- Gonzalez, S.F., Lukacs-Kornek, V., Kuligowski, M.P., Pitcher, L.A., Degn, S.E., Kim, Y.-A., Cloninger, M.J., Martinez-Pomares, L., Gordon, S., Turley, S.J., and Carroll, M.C. (2010). Capture of influenza by medullary dendritic cells via SIGN-R1 is essential for humoral immunity in draining lymph nodes. *Nat. Immunol.* 11, 427–434.
- Hancock, W.W., Lu, B., Gao, W., Csizmadia, V., Faia, K., King, J.A., Smiley, S.T., Ling, M., Gerard, N.P., and Gerard, C. (2000). Requirement of the chemokine receptor CXCR3 for acute allograft rejection. *J. Exp. Med.* 192, 1515–1520.
- Huang, S., Hendriks, W., Althage, A., Hemmi, S., Bluethmann, H., Kamijo, R., Vilcek, J., Zinkernagel, R., and Aguet, M. (1993). Immune response in mice that lack the interferon- γ receptor. *Science* 260, 1742–1744.
- Hunter, C.A., and Jones, S.A. (2015). IL-6 as a keystone cytokine in health and disease. *Nat. Immunol.* 16, 448–457.
- Kastenmüller, W., Torabi-Parizi, P., Subramanian, N., Lämmermann, T., and Germain, R.N. (2012). A spatially-organized multicellular innate immune response in lymph nodes limits systemic pathogen spread. *Cell* 150, 1235–1248.
- Kim, S., Iizuka, K., Kang, H.-S.P., Dokun, A., French, A.R., Greco, S., and Yokoyama, W.M. (2002). In vivo developmental stages in murine natural killer cell maturation. *Nat. Immunol.* 3, 523–528.
- Libraty, D.H., Airan, L.E., Uyemura, K., Jullien, D., Spellberg, B., Rea, T.H., and Modlin, R.L. (1997). Interferon-gamma differentially regulates interleukin-12 and interleukin-10 production in leprosy. *J. Clin. Invest.* 99, 336–341.
- Madera, S., Rapp, M., Firth, M.A., Beilke, J.N., Lanier, L.L., and Sun, J.C. (2016). Type I IFN promotes NK cell expansion during viral infection by protecting NK cells against fratricide. *J. Exp. Med.* 213, 225–233.
- Mandelboim, O., Lieberman, N., Lev, M., Paul, L., Arnon, T.J., Bushkin, Y., Davis, D.M., Strominger, J.L., Yewdell, J.W., and Porgador, A. (2001). Recognition of haemagglutinins on virus-infected cells by NKp46 activates lysis by human NK cells. *Nature* 409, 1055–1060.
- Mao, K., Chen, S., Chen, M., Ma, Y., Wang, Y., Huang, B., He, Z., Zeng, Y., Hu, Y., Sun, S., et al. (2013). Nitric oxide suppresses NLRP3 inflammasome activation and protects against LPS-induced septic shock. *Cell Res.* 23, 201–212.
- Martín-Fontecha, A., Thomsen, L.L., Brett, S., Gerard, C., Lipp, M., Lanzavecchia, A., and Sallusto, F. (2004). Induced recruitment of NK cells to lymph nodes provides IFN- γ for T(H)1 priming. *Nat. Immunol.* 5, 1260–1265.
- Mempel, T.R., Henrickson, S.E., and Von Andrian, U.H. (2004). T-cell priming by dendritic cells in lymph nodes occurs in three distinct phases. *Nature* 427, 154–159.
- Mendelson, M., Tekoah, Y., Zilka, A., Gershoni-Yahalom, O., Gazit, R., Achdout, H., Bovin, N.V., Meninger, T., Mandelboim, M., Mandelboim, O., et al. (2010). NKp46 O-glycan sequences that are involved in the interaction with hemagglutinin type 1 of influenza virus. *J. Virol.* 84, 3789–3797.
- Mishra, B.B., Rathinam, V.A., Martens, G.W., Martinot, A.J., Kornfeld, H., Fitzgerald, K.A., and Sasseti, C.M. (2013). Nitric oxide controls the immunopathology of tuberculosis by inhibiting NLRP3 inflammasome-dependent processing of IL-1 β . *Nat. Immunol.* 14, 52–60.
- Miyake, Y., Asano, K., Kaise, H., Uemura, M., Nakayama, M., and Tanaka, M. (2007). Critical role of macrophages in the marginal zone in the suppression of immune responses to apoptotic cell-associated antigens. *J. Clin. Invest.* 117, 2268–2278.
- Mosser, D.M., and Edwards, J.P. (2008). Exploring the full spectrum of macrophage activation. *Nat. Rev. Immunol.* 8, 958–969.
- Müller, U., Steinhoff, U., Reis, L.F., Hemmi, S., Pavlovic, J., Zinkernagel, R.M., and Aguet, M. (1994). Functional role of type I and type II interferons in antiviral defense. *Science* 264, 1918–1921.
- Naugler, W.E., Sakurai, T., Kim, S., Maeda, S., Kim, K., Elsharkawy, A.M., and Karin, M. (2007). Gender disparity in liver cancer due to sex differences in MyD88-dependent IL-6 production. *Science* 317, 121–124.
- Pfaffl, M.W. (2001). A new mathematical model for relative quantification in real-time RT-PCR. *Nucleic Acids Res.* 29, e45.
- Schindelin, J., Arganda-Carreras, I., Frise, E., Kaynig, V., Longair, M., Pietzsch, T., Preibisch, S., Rueden, C., Saalfeld, S., Schmid, B., et al. (2012). Fiji: an open-source platform for biological-image analysis. *Nat Methods* 9, 676–682.
- Trifilo, M.J., and Lane, T.E. (2004). The CC chemokine ligand 3 regulates CD11c+CD11b+CD8 α - dendritic cell maturation and activation following viral infection of the central nervous system: implications for a role in T cell activation. *Virology* 327, 8–15.
- Vivier, E., Tomasello, E., Baratin, M., Walzer, T., and Ugolini, S. (2008). Functions of natural killer cells. *Nat. Immunol.* 9, 503–510.
- Wherry, E.J. (2011). T cell exhaustion. *Nat. Immunol.* 12, 492–499.
- Wilder, J.A., Koh, C.Y., and Yuan, D. (1996). The role of NK cells during in vivo antigen-specific antibody responses. *J. Immunol.* 156, 146–152.
- Yi, A.-K., Chace, J.H., Cowdery, J.S., and Krieg, A.M. (1996). IFN-gamma promotes IL-6 and IgM secretion in response to CpG motifs in bacterial DNA and oligodeoxynucleotides. *J. Immunol.* 156, 558–564.

STAR★METHODS

KEY RESOURCES TABLE

| REAGENT or RESOURCE | SOURCE | IDENTIFIER |
|---|------------------|---------------------------------|
| Antibodies | | |
| Alexa Fluor 647 α B220, clone RA3-6B2 | BioLegend | Cat# 103226 RRID:AB_389330 |
| Brilliant Violet 605 α B220, clone RA3-6B2 | BioLegend | Cat# 103244 RRID:AB_2563312 |
| PE/Cy7 α B220, clone RA3-6B2 | BioLegend | Cat# 103222 RRID:AB_313005 |
| Pacific Blue α CD21/CD35, clone 7E9 | BioLegend | Cat# 123414 RRID:AB_2085158 |
| APC/Cy7 α CD4, clone GK1.5 | BioLegend | Cat# 100414 RRID:AB_312699 |
| Alexa Fluor 488 α F4/80, clone BM8 | BioLegend | Cat# 123120 RRID:AB_893479 |
| APC/Cy7 α F4/80, clone BM8 | BioLegend | Cat# 123118 RRID:AB_893477 |
| Alexa Fluor 647 α CD11c, clone N418 | BioLegend | Cat# 117312 RRID:AB_389328 |
| APC/Cy7 α CD11c, clone N418 | BioLegend | Cat# 117324 RRID:AB_830649 |
| Brilliant Violet 711 α CD11c, clone N418 | BioLegend | Cat# 117349 RRID:AB_2563905 |
| Alexa Fluor 647 α CD169, clone 3D6.112 | BioLegend | Cat# 142408 RRID:AB_2563621 |
| PE α CD169, clone 3D6.112 | BioLegend | Cat# 142404 RRID:AB_10915697 |
| PE/Cy7 α CD3, clone 17A2 | BioLegend | Cat# 100220 RRID:AB_1732057 |
| efluor 450 α CD3, clone 17A2 | eBioscience | Cat# 48-0032-82 RRID:AB_1272193 |
| Purified α CD16/32, clone 93 | BioLegend | Cat# 101302 RRID:AB_312801 |
| APC α CD44, clone IM7 | BioLegend | Cat# 103012 RRID:AB_312963 |
| Alexa Fluor 647 α CD19, clone 6D5 | BioLegend | Cat# 115525 RRID:AB_493340 |
| APC/Cy7 α CD86, clone GL-1 | BioLegend | Cat# 105030 RRID:AB_2244452 |
| PE α CD95/FAS, clone 15A7 | eBioscience | Cat# 12-0951-81 RRID:AB_465788 |
| Alexa Fluor 488 α CD11b, clone M1/70 | BioLegend | Cat# 101217 RRID:AB_389305 |
| Alexa Fluor 647 α CD11b, clone M1/70 | BioLegend | Cat# 101218 RRID:AB_389327 |
| Brilliant Violet 421 α CD138/Syndecan-1, clone 281-2 | BioLegend | Cat# 142523 RRID:AB_2565621 |
| PE-Cy7 α CD27, clone LG.7F9 | eBioscience | Cat# 25-0271-82 RRID:AB_1724035 |
| FITC α CD69, clone H1.2F3 | BioLegend | Cat# 104505 RRID:AB_313108 |
| Alexa Fluor 488 α GL-7, clone GL-7 | eBioscience | Cat# 53-5902-82 RRID:AB_2016717 |
| Alexa Fluor 488 α Gr-1, clone RB6-8C5 | BioLegend | Cat# 108417 RRID:AB_389309 |
| Alexa Fluor 647 α GranzymeB, clone GB11 | BioLegend | Cat# 515405 RRID:AB_2566333 |
| Brilliant Violet 650 α I-A/I-E, clone M5/114.15.2 | BioLegend | Cat# 107641 RRID:AB_2565975 |
| Pacific Blue α I-A/I-E, clone M5/114.15.2 | BioLegend | Cat# 107620 RRID:AB_493527 |
| Goat α Ig (H+L)-AP | Southern Biotech | Cat# 1010-04 |
| Goat α IgG biotin | Southern Biotech | Cat# 1030-04 |
| Avidin-Peroxidase | Sigma-Aldrich | Cat# A3151 |
| Brilliant Violet 785 α IFN γ , clone XMG1.2 | BioLegend | Cat# 505838 RRID:AB_2629667 |
| PE α Ly-6C, clone HK1.4 | BioLegend | Cat# 128007 RRID:AB_1186133 |
| Brilliant Violet 711 α Ly-6G, clone 1A8 | BioLegend | Cat# 127643 RRID:AB_2565971 |
| PE α MHC class I, clone SF1-1.1 | BioLegend | Cat# 116607 RRID:AB_313742 |
| APC α IL-6, clone MP5-20F3 | BioLegend | Cat# 504508 RRID:AB_10694868 |
| Alexa Fluor 488 α NK1.1, clone PK136 | BioLegend | Cat# 108718 RRID:AB_493183 |
| APC α NK1.1, clone PK136 | BioLegend | Cat# 108710 RRID:AB_313397 |
| α NK1.1 <i>InVivo</i> Ab anti-mouse NK1.1, clone PK136 | BioXCell | Cat# BP0036 RRID:AB_1107737 |
| α IFN γ , <i>InVivo</i> Ab anti-mouse IFN γ , clone XMG1.2 | BioXCell | Cat# BE0055 RRID:AB_1107694 |
| α IL-6, <i>InVivo</i> Ab anti-mouse IL-6, clone MP5-20F3 | BioXCell | Cat# BE0046 RRID:AB_1107709 |

(Continued on next page)

ADDITIONAL CONTRIBUTION 2

| Continued | | |
|--|---|--------------------|
| REAGENT or RESOURCE | SOURCE | IDENTIFIER |
| Bacterial and Virus Strains | | |
| Influenza A virus strain A/PR/8/34 | Gonzalez et al., 2010 | N/A |
| Vaccinia Virus Strain NYVAC-C | Gómez et al., 2007 | N/A |
| Chemicals, Peptides, and Recombinant Proteins | | |
| Diphtheria Toxin from <i>Corynebacterium diphtheriae</i> | Sigma | Cat# D0564 |
| Clodronate Liposomes (CLL) /PBS control liposomes | Clodronateliposomes.com | N/A |
| Zombie Aqua Fixable Viability Kit | BioLegend | Cat# 423101 |
| Paraformaldehyde powder, 95% | Sigma | Cat# 158127-500G |
| Agarose, low gelling temperature | Sigma | Cat# A9414 |
| Tween20 | Sigma | Cat# 9005-64-5 |
| Triton-X | Sigma | Cat# 9002-93-1 |
| Bovine Serum Albumine (BSA) | Amresco | Cat# 0332 |
| Recombinant Mouse IFN- β Protein | R&D Systems | Cat# 8234-MB-010 |
| Recombinant Mouse IFN- γ Protein | Abnova | Cat# P4450 |
| LPS RB-Ultrapore | InvivoGen | Cat# tlr1-eblps |
| DiD | Thermo Fisher | Cat# D7757 |
| Ketamin Labatec | Labatec Pharma | Cat# 7680632310024 |
| Rompun 2% (Xylazine) | Bayer | Cat# 6293841.00.00 |
| 3-Amino-9-ethylcarbazole | Sigma-Aldrich | Cat# A6926 |
| Critical Commercial Assays | | |
| Intracellular Fixation & Permeabilization Buffer Set | eBioscience | Cat# 88-8824-00 |
| LEGENDplex Mouse Proinflammatory Chemokine Panel (13-plex) | BioLegend | Cat# 740451 |
| LEGENDplex Mouse Inflammation Panel (13-Plex) | BioLegend | Cat# 740150 |
| Experimental Models: Organisms/Strains | | |
| C57BL/6 | Janvier Labs | RRID:MGI:5752053 |
| IFNAR ^{-/-} mice | Müller et al., 1994 | N/A |
| CD169 ^{DTR} mice | Miyake et al., 2007 | N/A |
| IFN γ R ^{-/-} mice | Huang et al., 1993 | N/A |
| <i>Ncr1</i> -GFP mice | Gazit et al., 2006 | N/A |
| OT-II TCR mice | Barnden et al., 1998 | N/A |
| IL-1R ^{-/-} mice | Glaccum et al., 1997 | N/A |
| CXCR3 ^{-/-} mice | Hancock et al., 2000 | N/A |
| Oligonucleotides | | |
| IL-18 FW (5'-GGTCCATGCTTTCTGGACT-3') | Microsynth | N/A |
| IL-18 RV (5'-GGCCAAGAGGAAGTGATTTG-3') | Microsynth | N/A |
| IL-6 FW (5'-AGCCAGAGTCCTTCAGAG-3') | Microsynth | N/A |
| IL-6 RV (5'-GGAGAGCATTGGAAATTG-3') | Microsynth | N/A |
| IFN γ FW (5'-GAGGAAGTGGCAAAGGATG-3') | Microsynth | N/A |
| IFN γ RV (5'-GCTGATGGCCTGATTGTCTT-3') | Microsynth | N/A |
| IL-1 β FW (5'-TGTTTTCTCCTTGCTCTG-3') | Microsynth | N/A |
| IL-1 β RV (5'-GCTGCCTAATGTCCCCTG-3') | Microsynth | N/A |
| GAPDH FW (5'-ACATCATCCCTGCATCCACT-3') | Microsynth | N/A |
| GAPDH RV (5'-AGATCCACGACGGACACATT-3') | Microsynth | N/A |
| Software and Algorithms | | |
| FlowJo software (TriStar , version 10.1) | https://www.flowjo.com/ | RRID:SCR_008520 |
| Fiji software (Schindelin et al., 2012 , version 1.48k) | https://fiji.sc/ | RRID:SCR_002285 |
| Imaris software (Bitplane, version 8.4.2) | http://www.bitplane.com/ | RRID:SCR_007370 |

(Continued on next page)

| Continued | | |
|--|---|-----------------|
| REAGENT or RESOURCE | SOURCE | IDENTIFIER |
| LEGENDPlex software (Biolegend, version 7.0) | https://www.biolegend.com/legendplex/software | N/A |
| Prism software (GraphPad, version 4) | https://www.graphpad.com/scientific-software/prism/ | RRID:SCR_002798 |
| Adobe Illustrator (CC2018) | https://www.adobe.com/ | RRID:SCR_014198 |

CONTACT FOR REAGENT AND RESOURCE SHARING

Further information and requests for resources and reagents should be directed to and will be fulfilled by the Lead Contact, Santiago F. Gonzalez (santiago.gonzalez@irb.usi.ch).

EXPERIMENTAL MODEL AND SUBJECT DETAILS

Mice

Mice were bred in house or acquired from Janvier labs (C57BL/6). The following transgenic strains were used: IFNAR^{-/-} (Müller et al., 1994), CD169^{DTR} (Miyake et al., 2007), IFN γ R^{-/-} (Huang et al., 1993), *Ncr1*-GFP (Gazit et al., 2006), OT-II TCR (Barnden et al., 1998), IL-1R^{-/-} (Glaccum et al., 1997), CXCR3^{-/-} (Hancock et al., 2000). All strains had C56BL/6 background. For all the experiments young and healthy female mice between 5-7 weeks of age were used. Mice were maintained in specific pathogen-free facilities at the IRB. Experiments were performed in accordance with the Swiss Federal Veterinary Office guidelines and animal protocols were approved by the local authorities.

In vitro NK cell culture and IFN- β stimulation

NK cells were sorted by FACSAria as CD3- NK1.1+ cells from spleens of C57BL/6 female mice and cultured at 5×10^5 cells/ml in complete RPMI with/without rIFN- β 25 pg/well and/or UV-PR8 10^4 PFU/well in 96-well round bottom plates. 12 h later NK cells were surface and intracellular labeled for FACS analysis.

In vitro CD11b+ DC culture and IFN γ stimulation

Splenic CD11c+ DC were purified by magnetic cell separation according to manufacturer's instructions (Miltenyi Biotec). Pre-enriched cells were sorted by FACSAria as CD11c+ MHC-II+ CD11b+ cells and 5×10^5 splenic CD11b+ DC were plated/well into a 96-well plate in complete RPMI alone or with recombinant IFN γ (rIFN γ) (10 μ g/ml) or LPS (200 ng/ml) for 12 h. The supernatant was then taken and analyzed for cytokine production.

METHOD DETAILS

Virus production, inactivation and labeling

Influenza virus strain A/PR/8/34 and vaccinia virus strain NYVAC-C (Gómez et al., 2007) were used in this study. Influenza virus was grown for 2 days in the allantoic cavity of 10-day embryonated chicken eggs. In order to remove cellular debris, allantoic fluid was harvested and centrifuged at 3000 rpm for 30 min and virus was subsequently purified twice in a discontinuous sucrose gradient at 25,000 rpm for 90 min. The virus pellet was resuspended in PBS and aliquots were stored at -70°C . Virus stocks were quantified by plaque assays. The vaccinia virus NYVAC-C, provided by Prof. Mariano Esteban, (CNB, Madrid). To inactivate both viruses, viral suspensions were placed under the UV lamp at a distance of 15 cm for 15 min. For the labeling of UV-inactivated influenza virus, 50 μ g/ml of DiD was added to the viral suspension and incubated for 20 min at RT. After that, virus was subsequently purified by centrifugation as mentioned before. DiD-UV-inactivated virus aliquots were stored at -70°C .

Antigen administration and injections

10^6 plaque-forming units (PFU) of inactivated virus per footpad in a final volume of 10 μ L were injected into anaesthetized mice at different time points prior to LN collection. For macrophage depletion, mice were injected with 10 μ L/footpad of CLL or PBS-containing liposomes (control) (Clodronateliposomes.org) at days 5 and 3 before vaccination. Macrophage depletion from CD169^{DTR} mice was established by intraperitoneal (i.p.) injection of 30 ng of diphtheria toxin (Sigma-Aldrich) per g of mouse a day before vaccination. For NK cell depletion 300 μ g of α NK1.1 (clone PK136; BioXCell) was administered i.p. (day-3) and intravenously (i.v.) (day-1) before vaccine administration. IFN γ blocking was performed by i.v. injection of 200 μ g of α IFN γ (clone XMG1.2, BioXCell) at the time of vaccination. 4 h after vaccination 70 μ g / footpad of α IFN γ was administered in a total volume of 10 μ L. α IL-6 (clone ALF-161, BioXCell) was administered i.v. at a dose of 200 μ g/mice, as well as footpad at 120 μ g/mice, at the time of vaccination. For *in vivo* labeling of

cells, mice received 1 μ g of fluorescently labeled α CD21/35, α F4/80 and α CD169/footpad (Biolegend), 3 to 5 h before image acquisition.

Flow cytometry

Popliteal LNs were collected, disrupted with tweezers, and digested for 10 min at 37°C in an enzyme mix composed of DNase I (0.28 mg/ml, Amresco), dispase (1 U/ml, Corning), and collagenase P (0.5 mg/ml, Roche) in calcium- and magnesium-free PBS (PBS-) followed by a stop solution composed of 2 mM EDTA (Sigma-Aldrich) and 2% heat-inactivated filter-sterilized fetal calf serum (Thermo Fisher Scientific) in PBS- (Sigma-Aldrich). Fc receptors were blocked (α CD16/32, Biolegend) followed by surface staining and analyzed by flow cytometry on an LSRFortessa™ (BD Biosciences). Where indicated, intracellular and/or nuclear staining was performed according to the instructions (#88/8824/00, eBioscience, #00-5523-00, eBioscience). Dead cells were excluded using ZombieAcqua fixable viability dye (Biolegend) and data were analyzed using FlowJo software (TriStar Inc).

Immunohistology/microscopy

Mice were anesthetized with a mixture of ketamine (100 mg/kg bodyweight, Parke Davis) and xylazine (10 mg/kg bodyweight, Bayer) and perfused with a fixative solution made of 10 mL of 0.05 M phosphate buffer containing 0.1 M L-lysine, 4% paraformaldehyde (PFA), and 2 mg/mL NaIO₄ at pH 7.4 (PLP). Popliteal LN were collected and further fixed in 4% PFA at 4°C shaking for 4–6 h and embedded in 5% low gelling agarose (Sigma-Aldrich). 50–100 μ m sections were cut with Leica VT 1200S vibratome (Leica Microsystems), blocked with proper sera and stained with the indicated antibodies in 0.05% Tween-20 in 0.5% BSA PBS- for two days at 4°C shaking (see antibody section). Immunofluorescence confocal microscopy was performed using a Leica TCS SP5 confocal microscope (Leica Microsystems). Micrographs were acquired in sequential scans and merged to obtain a multicolor image. Images were processed using Imaris software (Bitplane AG).

Cytoplex assay

LEGENDPlex™ assays (Mouse Proinflammatory Chemokine Panel and Mouse Inflammation Panel; Biolegend) were performed to monitor cytokine/chemokine expression. Briefly, popliteal LNs were collected and carefully disrupted in 100 μ L ice-cold phosphate buffer, minimizing cell rupture. The suspension was centrifuged at 1,500 rpm for 5 min, and the supernatant was collected. 25 μ L supernatant was used for the protocol following the manufacturer's instructions. Samples were analyzed by flow cytometry on an LSRFortessa (BD Biosciences), and data were analyzed using LEGENDPlex software (BioLegend).

ELISPOT

For enzyme-linked immuno-spot assay (ELISPOT), on day 10 p.v., popliteal LNs were removed aseptically, disrupted, and passed through a 40- μ m cell strainer. 4 \times 10⁵ cells were plated on UV-PR8-coated (10⁷ PFU/mL) filter plates (MultiScreenHTS, Merck Millipore) and incubated for 16 h at 37°C. For detection, a biotin-conjugated α IgG was used, followed by avidin-Peroxidase (Sigma-Aldrich). A developing solution consisting of 200 mL 3-amino-9-ethylcarbazole (AEC) solution (Sigma-Aldrich) in 9 mL sodium acetate buffer containing 4 mL 30% H₂O₂ was subsequently added. Spots were read on a C.T.L. ELISPOT reader using ImmunoSpot® 5.1 software (Cellular Technology) and counted using ImageJ software.

Multiphoton microscopy and analysis

Deep tissue imaging was performed on a customized two-photon platform (TrimScope, LaVision BioTec). Two-photon probe excitation and tissue second-harmonic generation (SHG) were obtained with a set of two tunable Ti:sapphire lasers (Chameleon Ultra I, Chameleon Ultra II, Coherent) and an optical parametric oscillator that emits in the range of 1,010 to 1,340 nm (Chameleon Compact OPO, Coherent), with output wavelength in the range of 690–1,080 nm. For the *in vivo* analysis of cell movement, two-photon micrographs were acquired in full Z stacks of 50 μ m every 30 s. To analyze NK cell motion quantitatively, manual tracking was used (Imaris 7.7.2, Bitplane). For the statistical analysis of cell migration, only track durations greater than 5 min were considered.

qPCR

Popliteal LNs were collected and disrupted in lysing matrix D 1.4-mm ceramic sphere tubes using FastPrep-24 tissue disruption (MP Biomedicals), and RNA was isolated using an RNAeasy Mini kit (QIAGEN). A final amount of 0.5 μ g of cDNA was synthesized using a cDNA synthesis kit (Applied Biosystems) following the manufacturer's recommendations. For qPCR reaction, SYBR Master Mix (Applied Biosystems) was used, and samples were run on a 7900HT Fast Real-Time PCR System (Applied Biosystems). mRNA levels were expressed relative to GAPDH expression. The Pfaffl method (Pfaffl, 2001) was used to calculate the relative expression of the transcripts. Primers: IL-18 FW, 5'-GGTCCATGCTTCTTGACT-3'; and IL-18 RV, 5'-GGCCAAGAGGAAGTGATTTG-3'; IL-6 FW, 5'-AGCCAGAGTCTTCAGAG-3'; IL-6 RV, 5'-GGAGAGCATTGGAAATTG-3'; IFN γ FW, 5'-GAGGAAGTGGCAAAGGATG-3'; IFN γ RV, 5'-GCTGATGGCCTGATTGTCTT-3'; IL-1 β FW, 5'-TGTTTTCCTCCTTGCCTCTG-3'; and IL-1 β RV, 5'-GCTGCCTAATGTCCCCTG-3' GAPDH FW, 5'-ACATCATCCCTGCATCCACT-3'; GAPDH reverse, 5'-AGATCCACGACGGACACATT-3'.

QUANTIFICATION AND STATISTICAL ANALYSIS

Statistics

Results were expressed as the mean \pm standard deviation (SD). For statistical analysis Prism 4 (Graphpad Software, La Jolla, USA) was used. Data was represented using Prism software. Group comparisons were assessed using nonparametric tests. All statistical tests were two-tailed and statistical significance was defined as: * ($p < 0.05$), ** ($p < 0.01$), *** ($p < 0.001$) **** ($p < 0.0001$). The number of times each experiment was repeated, and the number of animals used per experiment, are detailed in each figure.

Protection against influenza infection requires early recognition by inflammatory dendritic cells through C-type lectin receptor SIGN-R1

Miguel Palomino-Segura^{1,2}, Laurent Perez¹, Yagmur Farsakoglu^{1,2}, Tommaso Virgilio^{1,2}, Irene Latino¹, Rocco D'Antuono³, Nikolaos Chatziandreou¹, Diego U. Pizzagalli^{1,4}, Guojun Wang^{5,6}, Adolfo García-Sastre^{5,6,7}, Federica Sallusto^{1,8}, Michael C. Carroll⁹, Olivier Neyrolles¹⁰ and Santiago F. Gonzalez^{1*}

The early phase of influenza infection occurs in the upper respiratory tract and the trachea, but little is known about the initial events of virus recognition and control of viral dissemination by the immune system. Here, we report that inflammatory dendritic cells (IDCs) are recruited to the trachea shortly after influenza infection through type I interferon-mediated production of the chemokine CCL2. We further show that recruited IDCs express the C-type lectin receptor SIGN-R1, which mediates direct recognition of the virus by interacting with N-linked glycans present in glycoproteins of the virion envelope. Activation of IDCs via SIGN-R1 triggers the production of the chemokines CCL5, CXCL9 and CXCL10, which initiate the recruitment of protective natural killer (NK) cells in the infected trachea. In the absence of SIGN-R1, the recruitment and activation of NK cells is impaired, leading to uncontrolled viral proliferation. In sum, our results provide insight into the orchestration of the early cellular and molecular events involved in immune protection against influenza.

How the innate immune system initially recognizes the replicating influenza virus is an important determinant of the infection outcome¹. However, there is limited knowledge about these early immune defence mechanisms and how they affect disease progression. The host immune system first encounters influenza virus in the upper airways to which initial virus replication is restricted². Later, infection progresses to the lower respiratory tract through the airway epithelium of the trachea; this is essential for the development of the acute phase of the disease³. Most of the knowledge about the immune response in the trachea has been gained from studies focusing on the pulmonary phase of the infection²; therefore, there is a need for better characterization of the early response in the trachea.

The immune response to airborne pathogens involves their recognition by macrophages and dendritic cells (DCs) located underneath the mucosal cell layer⁴. Tracheal DCs have been divided into subtypes according to their anatomical location and expression of surface markers^{4,5}. One of the best-studied subtypes is the resident conventional DCs (cDCs) that have an important role in initiating the adaptive response by migrating to regional lymph nodes (LNs) and presenting antigen to T cells⁶. A second group of DCs, the inflammatory DCs (IDCs), perform their function at the site of infection⁷. IDCs are an important source of cytokines such as tumour-necrosis factor (TNF) and inflammatory molecules such as nitric oxide⁸. However, the precise functions of IDCs during influenza infection have not been identified.

The activation of these cells is associated with the detection of viral components by pattern-recognition receptors commonly expressed by DCs⁹. C-type lectin receptors are pattern-recognition receptors that bind specific pathogen-associated carbohydrate structures¹⁰. The C-type lectin receptor DC-specific intercellular adhesion molecule-3-grabbing non-integrin (DC-SIGN) murine homologue SIGN-R1 is known to directly recognize bacterial¹¹, viral¹² and fungal¹³ pathogens. Previous studies have described the presence of cells expressing SIGN-R1 in the skin, lungs and in secondary lymphoid organs such as the spleen¹⁴ and LNs¹². However, the specific function of this receptor in the response against infectious virus is not known.

Here, we show that IDCs are recruited into the tracheal epithelium and recognize influenza virus via SIGN-R1. The production of inflammatory chemokines by these cells induces the recruitment of natural killer (NK) cells, which is essential for the control of viral replication in the trachea.

Results

Influenza infection induces the recruitment of IDCs to the trachea. To characterize the inflammatory response that occurs in the trachea following influenza infection, we infected mice with 200 plaque-forming units (p.f.u.) of the mouse-adapted influenza virus strain PR8. We confirmed, using confocal microscopy, that the virus was able to initially infect the tracheal epithelial cell layer

¹Institute for Research in Biomedicine, Università della Svizzera italiana, Bellinzona, Switzerland. ²Graduate School of Cellular and Molecular Sciences, Faculty of Medicine, University of Bern, Bern, Switzerland. ³Light Microscopy STP, The Francis Crick Institute, London, UK. ⁴Institute of Computational Science, Università della Svizzera italiana, Lugano, Switzerland. ⁵Department of Microbiology, Icahn School of Medicine at Mount Sinai, New York, NY, USA. ⁶Global Health and Emerging Pathogen Institute, Icahn School of Medicine at Mount Sinai, New York, NY, USA. ⁷Department of Medicine, Division of Infectious Diseases, Icahn School of Medicine at Mount Sinai, New York, NY, USA. ⁸Institute for Microbiology, ETH Zurich, Zurich, Switzerland. ⁹Program in Cellular and Molecular Medicine, Boston Children's Hospital and Harvard Medical School, Boston, MA, USA. ¹⁰Institut de Pharmacologie et de Biologie Structurale, Université de Toulouse CNRS, UPS, Toulouse, France. *e-mail: santiago.gonzalez@irb.usi.ch

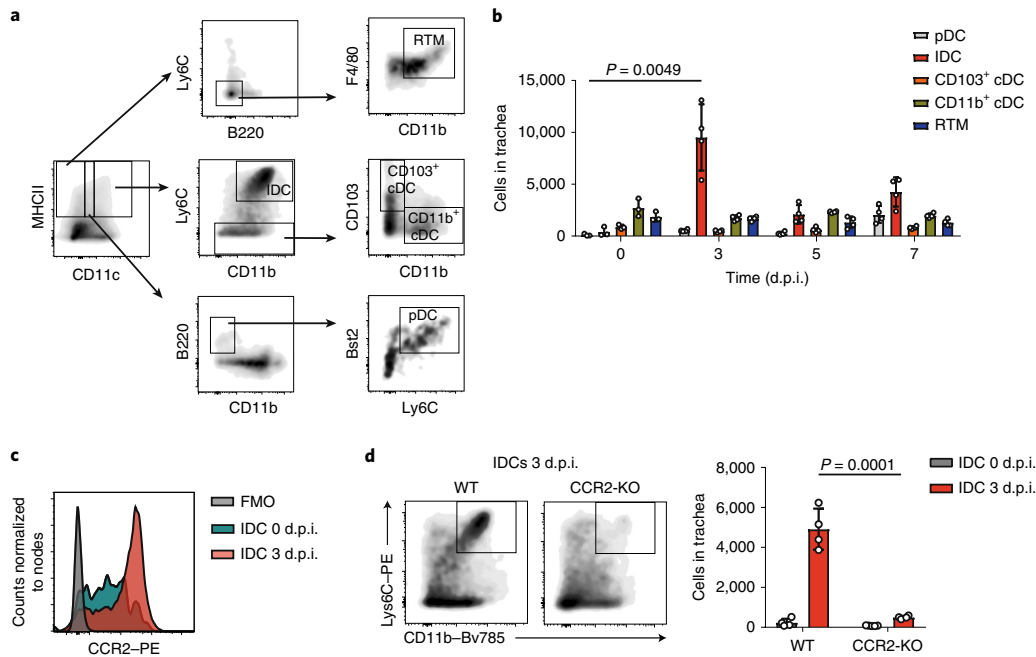


Fig. 1 | Influenza infection promotes early recruitment of IDCs to the trachea. **a**, Flow cytometric characterization of IDCs (CD45⁺MHCII⁺CD11c⁺CD11b⁺Ly6C^{high}), pDCs (CD45⁺MHCII⁺CD11c^{int}B220⁺CD11b⁻Bst2⁺Ly6C⁺), CD103⁺ cDCs (CD45⁺MHCII⁺CD11c⁻CD11b⁻Ly6C⁻CD103⁺), CD11b⁺ cDCs (CD45⁺MHCII⁺CD11c⁺CD11b⁺Ly6C⁻CD103⁻) and resident RTMs (CD45⁺MHCII⁺CD11c⁻B220⁻Ly6C⁻CD11b⁺F4/80⁺) in mouse trachea. **b**, Flow cytometric analysis of DC subsets and RTMs in trachea at 0, 3, 5 and 7 d.p.i. with influenza virus PR8 ($n=3, 4, 4$ and 4 mice per group, respectively). **c**, Representative histogram showing surface expression of the chemokine receptor CCR2 in tracheal IDCs at 0 and 3 d.p.i. **d**, Flow cytometric analysis showing a significant reduction in the number of IDCs in tracheas from CCR2-KO mice compared with the WT group at 3 d.p.i. Left: a representative scatter plot at 3 d.p.i. Right: IDC quantification ($n=4$ mice per group). Data are representative of at least three independent experiments, presented as mean \pm s.d. and analysed by two-tailed Student's *t*-test.

(Supplementary Fig. 1a). Next, using flow cytometry analysis of the expression of cell-surface markers^{4,7,15}, we characterized tracheal cell populations: IDCs, plasmacytoid DCs (pDCs), CD103⁺ cDCs, CD11b⁺ cDCs and resident respiratory tract macrophages (RTMs) (Fig. 1a). We observed a prominent recruitment of IDCs at 3 days post infection (d.p.i.) (Fig. 1b). Previous studies have reported that CCR2⁺Ly6C^{high} monocytes are precursors of IDCs¹⁶. Therefore, we confirmed the monocytic origin of these cells based on their expression of CCR2 (Fig. 1c), in contrast to the other DC subtypes (Supplementary Fig. 1b). Furthermore, we observed that, in IDCs, CCR2 is eventually downregulated, as the expression of the maturation marker major histocompatibility complex (MHC) class II increases (Supplementary Fig. 1c). Next, we studied the specific effect on IDCs when infecting CCR2-knockout (KO) mice. We confirmed by flow cytometry that, at 3 d.p.i., IDC numbers were significantly reduced in CCR2-KO mice, compared with their wild-type (WT) counterparts (Fig. 1d). However, we did not detect any significant variation in the total number of the other cell types analysed (Supplementary Fig. 1d).

Recruited IDCs are in close proximity to the tracheal epithelium during influenza infection. To study the location of the DC network in the mucosal tissue, we used confocal microscopy to produce three-dimensional (3D) reconstructions of mouse tracheas from mice expressing CD11c–yellow fluorescent protein (YFP). We observed that in uninfected mice, CD11c⁺ DCs were distributed homogeneously above the basement membrane, in proximity to the epithelial cell layer (Fig. 2a). To study the specific location of the

different subsets of DCs and RTMs before and after influenza infection, we stained explants from tracheas of CD11c–YFP mice with antibodies against CD11b and Ly6C (Fig. 2b and Supplementary Fig. 2a). Consistent with the flow cytometry data, we could not detect any IDCs in uninfected animals (Supplementary Fig. 2b). In the infected mice, we found that recruited IDCs were located towards the lumen of the trachea, unlike the other cell types, which were mainly located in the lamina propria (Fig. 2c).

Type I interferon-dependent CCL2 production recruits IDC precursors to the trachea. To characterize the antiviral response that leads to the recruitment of IDCs, we assessed the expression of type I interferon (IFN) in the trachea. We observed a significant upregulation of the transcript levels of both *Ifna* and *Ifnb* during the first 2 d.p.i. (Fig. 3a). Moreover, cytoplasm analysis confirmed that protein levels of IFN- β were significantly elevated in both WT and CCR2-KO mice at 3 d.p.i. (Fig. 3b). We also detected a significant increase in levels of RNA encoding the chemokine CCL2—a CCR2 ligand—during the first 3 d.p.i. (Fig. 3c), coinciding with an increase in CCL2 protein (Fig. 3d). RTMs, together with pDCs and IDCs, were the main producers of CCL2 (Supplementary Fig. 3a, b). Interestingly, we observed a similar pattern of expression for CCL2 and type I IFN during the first 7 d.p.i. (Supplementary Fig. 3c), concurrent with IDC recruitment to the trachea. To examine whether the expression of the two cytokines is linked, we analysed CCL2 protein levels in mice deficient in the type I IFN receptor (IFNAR). This analysis showed that signalling through IFNAR was required for secretion of CCL2 (Fig. 3d). In addition, we observed a

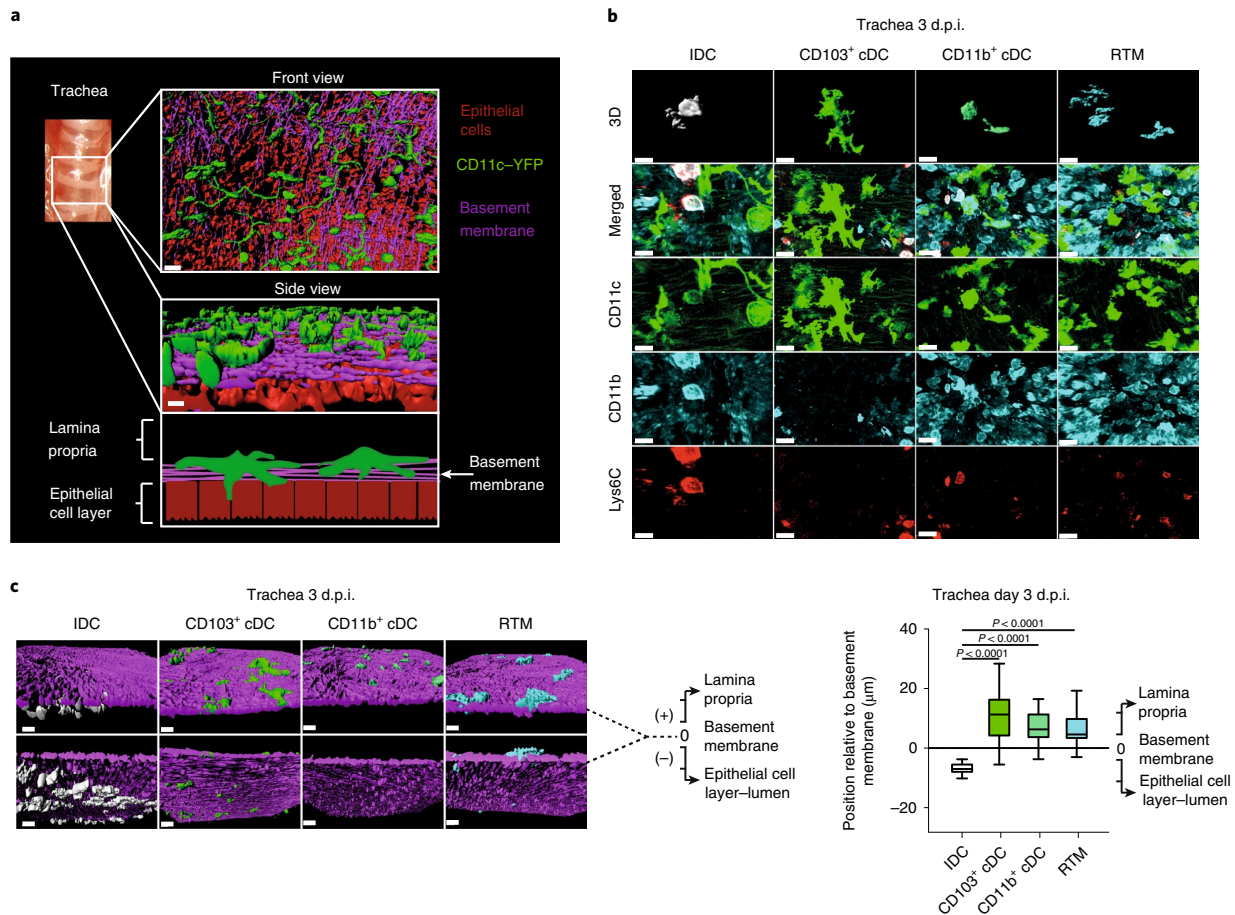


Fig. 2 | Recruited IDCs are located in close proximity to the epithelial cell layer during influenza infection. **a**, Top and middle: 3D surface reconstruction of confocal images from a trachea showing the network of CD11c⁺ cells (green) located in the lamina propria in close contact with the basement membrane (violet). Epithelial cells (red), located in the luminal part, are stained with CMTMR. Bottom: schematic indicating the anatomical distribution of the reconstructed area. Scale bars, 20 µm. **b**, Confocal micrographs showing the 3D reconstruction of the DC subsets and RTMs located in the tracheal mucosa at 3 d.p.i. Cells were characterized on the basis of expression of CD11c (green), CD11b (light blue) and Ly6C (red). IDCs, CD11c⁺CD11b⁺Ly6C⁺; CD103⁺ cDCs, CD11c⁺CD11b⁻Ly6C⁻; CD11b⁺ cDCs, CD11c⁺CD11b⁺Ly6C⁻; RTMs, CD11c⁻CD11b⁻Ly6C⁻. Scale bars, 16 µm (IDC panels); 20 µm (other panels). **c**, Left: representative 3D reconstruction from confocal micrographs of a trachea at 3 d.p.i. showing the location of IDCs (red), CD103⁺ cDCs (green), CD11b⁺ cDCs (yellow) and RTMs (light blue) in relation to the basement membrane (violet). Scale bars, 20 µm. Right: box plot representing the position of the cell subtypes in relation to the basement membrane in the tracheal mucosa at 3 d.p.i. Cells located towards the lamina propria were given positive values while cells located towards the luminal side were given negative values (data are based on the analysis of three confocal reconstructions; IDC, $n = 61$; CD103⁺ cDC, $n = 54$; CD11b⁺ cDC, $n = 40$; RTM, $n = 40$). Data are representative of at least three independent experiments. In **c**, boxes show 25th to 75th percentiles, the line represents the median and the whiskers show 5th to 95th percentiles. Data were analysed using the two-tailed Student's *t*-test.

marked decrease in the numbers of CCR2⁺ monocytes in tracheas from IFNAR-KO mice at 3 d.p.i. (Fig. 3e) and a similar reduction in the number of IDCs (Fig. 3f), consistent with the role of CCR2⁺ monocytes as IDC precursors.

IDCs express the lectin receptor SIGN-R1 that recognizes glycosylated influenza viral proteins. We assessed the expression of SIGN-R1 in the mononuclear phagocytic cell compartment of the trachea using flow cytometric analysis. We found that SIGN-R1 was highly expressed by IDCs at 3 d.p.i. (Fig. 4a,b). Moreover, 3D confocal microscopy revealed that SIGN-R1 colocalized with DiO-labelled influenza virus after 1 h of incubation (Fig. 4c), suggesting that this C-type lectin, expressed in IDCs, is able to bind influenza virus. To examine this possibility, we performed enzyme-linked

immunosorbent assay (ELISA), which confirmed that SIGN-R1 binds with high affinity to whole influenza virus (with half-maximal effective concentration, $EC_{50} = 1.67 \mu\text{g ml}^{-1}$; Supplementary Fig. 4a). To further investigate this interaction, we performed surface plasmon resonance (SPR) assays, which showed that SIGN-R1 binds the haemagglutinin (HA) glycoprotein of influenza PR8 virus with an equilibrium dissociation constant (K_D) of 142 nM (Fig. 4d, top). Next, to evaluate whether the binding of influenza virus to SIGN-R1 could be abrogated by interfering with glycosylation, we removed glycan moieties from HA using different glycosidases. We used endoglycosidase H to eliminate mannose glycosylation from HA. However, since all later oligosaccharide structures are resistant to endoglycosidase H, we also used peptide-N-glycosidase F (PNGase F), which cleaves between the innermost

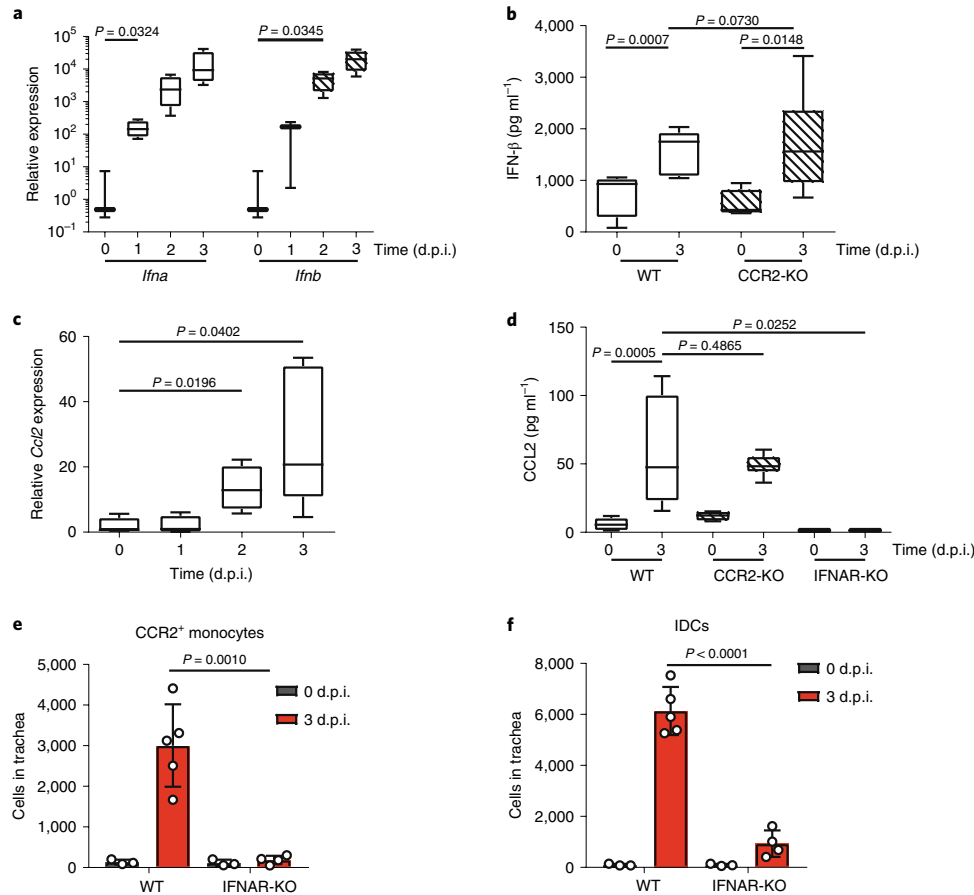


Fig. 3 | Type I IFN is required for the production of CCL2, which recruits IDC precursors to the trachea. **a**, Time course showing RNA expression (relative to *Gapdh*) of the cytokine genes *Ifna* and *Ifnb* in mouse trachea during the first three days after infection with influenza virus (*Ifna*, $n = 3, 4, 4$ and 4 ; *Ifnb*, $n = 3, 3, 4$ and 4 mice per respective time point). **b**, Levels of secreted IFN- β in trachea from CCR2-KO mice during the first three days after infection compared with WT mice (WT, $n = 5$ and 5 ; CCR2-KO, $n = 4$ and 6 mice per respective time point). **c**, Time course showing RNA expression levels of the chemokine gene *Ccl2* in trachea during the first three days after infection ($n = 4, 4, 4$ and 5 mice per respective time point). **d**, Levels of secreted CCL2 in trachea from CCR2-KO and IFNAR-KO mice at 3 d.p.i. compared with WT mice (WT, $n = 9$ and 10 ; CCR2-KO, $n = 4$ and 6 ; IFNAR-KO, $n = 3$ and 5 mice per respective time point). **e**, Quantification of total number of CCR2⁺ monocytes (CD45⁺MHCII⁻CD11c⁻CD11b⁺Ly6C^{high}Ly6G⁻CCR2⁺) in trachea from IFNAR-KO mice at 3 d.p.i. compared with uninfected controls (WT, $n = 3$ and 5 ; IFNAR-KO, $n = 3$ and 4 mice per respective time point). **f**, Quantification of total number of IDCs in trachea from IFNAR-KO mice at 3 d.p.i. compared with uninfected controls (WT, $n = 3$ and 5 ; IFNAR-KO, $n = 3$ and 4 mice per respective time point). The presented data are representative of at least three independent experiments. In **a-d**, boxes show 25th to 75th percentiles, the line represents the median and the whiskers show minimum and maximum values. In **e,f**, data are mean \pm s.d. Data were analysed using the two-tailed Student's *t*-test.

N-acetylglucosamine and asparagine residues of high-mannose glycans regardless of the complexity of the glycan. We monitored glycosylation removal by western blotting of the protein after treatment and found that PNGase F was the most efficient enzyme for removal of all *N*-linked glycans (Supplementary Fig. 4b). After *N*-linked glycans were removed from HA, we could no longer detect binding with SIGN-R1 (Fig. 4d, middle). Of note, HA still bound to the monoclonal antibody H36-7¹⁷ following removal of *N*-linked glycans (Supplementary Fig. 4c), indicating that HA remained correctly folded after PNGase F treatment. Next, we performed binding assays with different HA subtypes to investigate the possibility that SIGN-R1 recognizes other flu strains. In agreement with the affinity measurement by SPR, we observed high binding titres (EC_{50} value shown) for H1 (PR8 ($0.66 \mu\text{g ml}^{-1}$) and New Caledonia ($0.81 \mu\text{g ml}^{-1}$)), H3 ($1.19 \mu\text{g ml}^{-1}$) and H5

($1 \mu\text{g ml}^{-1}$) strains (Fig. 4e). In addition, SIGN-R1 binding was also observed with neuraminidase subtype 1 (N1) ($EC_{50} = 0.63 \mu\text{g ml}^{-1}$; Supplementary Fig. 4d). In this assay, FI6, an antibody specific for the stem region of HA¹⁸, was included to confirm that the observed binding was not due to HA contamination in the N1 purification. Of note, SIGN-R1 also bound to other respiratory viruses, such as the human respiratory syncytial virus¹⁹ (RSV; $EC_{50} = 0.98 \mu\text{g ml}^{-1}$) and the human metapneumovirus²⁰ (MPV; $EC_{50} = 1.14 \mu\text{g ml}^{-1}$) (Supplementary Fig. 4a). In sum, these results indicate that SIGN-R1 recognizes several viruses by targeting the carbohydrate moiety of glycoproteins. Moreover, we observed that addition of a SIGN-R1-blocking antibody significantly reduced the binding of DiO-labelled influenza PR8 to SIGN-R1⁺ IDCs (Fig. 4f), confirming the role of this receptor in the attachment of the virus on IDCs.

SIGN-R1 is involved in the production of inflammatory chemokines by IDCs and the recruitment of NK cells into the tracheal mucosa. To investigate the role of IDCs as inducers of the inflammatory response, we studied the production of different chemokines in tracheal lavage from CCR2-KO and SIGN-R1-KO mice at 3 d.p.i. We found that the absence of IDCs or SIGN-R1 resulted in a significant reduction in the levels of the chemokines CCL5, CXCL9 and CXCL10 (Fig. 5a,b and Supplementary Fig. 5a). Furthermore, the reduced chemokine expression in SIGN-R1-KO mice was not a result of a deficiency in DCs and RTMs relative to WT mice (Supplementary Fig. 5b). The specific expression of these chemokines by IDCs and their reduced levels in SIGN-R1-KO mice were confirmed intracellular staining and flow cytometry (Fig. 5c–f). To examine whether the observed differences were due to the direct interaction of SIGN-R1 with viral proteins, we isolated IDCs generated by intranasal administration of polyinosinic:polycytidylic acid (Poly I:C); these IDCs exhibited similar SIGN-R1 expression levels to those in tracheal IDCs at 3 d.p.i. (Supplementary Fig. 5c). We incubated these IDCs in vitro with a vaccine suspension containing HA. Twelve hours after stimulation, WT IDCs treated with HA showed increased production of CCL5 compared with untreated controls, whereas SIGN-R1-KO IDCs did not (Supplementary Fig. 5d). We also confirmed that IDCs were the main source of these chemokines in the trachea at 3 d.p.i. and that SIGN-R1 deficiency reduced chemokine expression levels only in IDCs (Fig. 5g,h and Supplementary Fig. 5e). To investigate the roles of CCL5, CXCL9 and CXCL10 in the recruitment of NK cells to the infection site²¹, we developed a flow cytometry assay (Fig. 5i) to detect the infiltration of NK cells in the trachea (Fig. 5j). We observed an early peak in the number of NK cells in the infected trachea, which coincided with the peak of IDCs at 3 d.p.i. Moreover, confocal microscopy analysis indicated that the majority of NK cells were positioned towards the luminal side, in close proximity to IDCs (average distance of 66.2 μm; Fig. 5k,l and Supplementary Fig. 5f). On average, 25.5% of the NK cells analysed established contacts with IDCs (Supplementary Fig. 5g). Furthermore, we observed that NK cells expressed the receptors CCR5 and CXCR3, which bind to the chemokines CCL5, CXCL9 and CXCL10²², but not to CCR2 (Fig. 5m). The recruitment of tracheal NK cells was partly dependent on IDCs, as demonstrated by the reduced number of these cells in CCR2-KO and SIGN-R1-KO mice (Fig. 5n).

SIGN-R1⁺ IDCs are required to control influenza infection. Next, we investigated the involvement of IDCs in the activation and functional properties of the recruited NK cells. We detected a significant decrease in the number of cells positive for the markers CD69, granzyme B, perforin, NKG2D, NKp46, CD11b and IFN-γ in CCR2-KO and SIGN-R1-KO mice relative to WT mice at 3 d.p.i. (Fig. 6a). The observed decrease also correlated with a significant decrease in the frequency of NK cells positive for the same markers and the expression levels of CD69, granzyme B, CD11b and IFN-γ, but not of perforin, NKG2D and NKp46, in NK cells from CCR2-KO and SIGN-R1-KO mice (Fig. 6b and Supplementary Fig. 6a). We detected a significant increase in the transcription levels of *Il18* in WT mice during the first 3 d.p.i. (Fig. 6c); the magnitude of this increase was significantly reduced in CCR2-KO and SIGN-R1-KO mice (Fig. 6d). To study how the absence of IDCs, NK cells or SIGN-R1 affected the progression of influenza infection, we measured viral titres in tracheas from CCR2-KO and SIGN-R1-KO mice and in mice treated with NK1.1-depleting antibody at 3 d.p.i. We observed an increase in the influenza titres in all of the examined groups relative to the WT control (Fig. 6e). These results correlated with increased mortality (Fig. 6f) and weight loss (Fig. 6g) in all of the deficient groups. Finally, we analysed the levels of influenza-specific antibodies in WT and SIGN-R1-KO mice at 5 and 10 d.p.i. (Supplementary Fig. 6b) with a sublethal dose

of influenza virus. The results show that at 5 d.p.i., the mice had very low or undetectable titres of influenza-specific antibodies and that SIGN-R1-KO mice showed no deficiency in antibody production at later time points after infection.

Discussion

In this study, we aimed to elucidate the mechanism by which IDCs contribute to the control of influenza infection. Initially, we characterized the origin of the recruited IDCs. Previous studies had confirmed Ly6C^{high}CCR2⁺ monocytes as the precursors of IDCs at the site of infection¹⁶. Here we observed that following their recruitment to the trachea, monocytes differentiated to IDCs and exhibited high expression of MHCII and CD11c and downregulation of CCR2. The prominent expression of CCR2 in IDC progenitors suggested a critical role for its ligands, CCL2 and CCL7, in the regulation of their migration to the inflamed tissue^{23,24}. The observed increase in the expression of CCL2 described in this study is probably associated with the recruitment of monocytes from the bone marrow to the bloodstream²⁵ and facilitates monocyte trafficking across an epithelial cell monolayer²⁶.

Previous studies demonstrated that type I IFN signalling is necessary for the enhancement and maintenance of CCL2 levels²⁷. Accordingly, we observed an early and pronounced expression of type I IFN in the trachea following influenza infection. Moreover, we showed that this signalling pathway was necessary for CCL2 production in the trachea, as IFNAR-KO mice exhibited a severe reduction in the levels of this chemokine. This result correlated with a complete inhibition of the recruitment of CCR2⁺ monocytes and IDCs in the infected trachea. A similar effect on CCL2 production was previously reported in the draining LN of IFNAR-KO mice after vaccination with a non-replicative ultraviolet (UV)-inactivated PR8²⁸. However, we cannot discount the possible effect that lack of viral control in IFNAR-KO mice²⁹ might have on the production of CCL2 and cell recruitment in the infected trachea.

Furthermore, we demonstrated that, following their recruitment in the trachea, IDCs are positioned in close proximity to the epithelial cell layer, which suggests a role of IDCs in sensing viral particles generated by infected epithelial cells. Moreover, it has been shown that IDCs from lungs have the capacity to internalize viral particles during influenza infection³⁰. Therefore, we might expect a similar function of IDCs capturing influenza virus in the trachea.

C-type lectin receptors have recently emerged as inducers of the expression of specific genes in response to pathogens³¹. In our investigation, we studied the expression of the C-type lectin receptor SIGN-R1 in IDCs in the trachea. Our data showed that SIGN-R1 participates in the recognition of influenza virus, as blocking of this receptor affected the capture of PR8 by IDCs. We confirmed this hypothesis using SPR and demonstrated that SIGN-R1 binding to HA is glycosylation-dependent. Moreover, SIGN-R1 was able to recognize another surface protein of influenza virus, neuraminidase, and other viruses with a comparable glycosylation pattern. These results relate to the capacity of SIGN-R1 to bind the mannose present on HA from all influenza virus subtypes. Thus, we demonstrated that SIGN-R1 is a key receptor that is able to bind a number of viral glycoproteins by targeting the carbohydrate moiety. This property could be used for the development of therapeutic agents that could block the infection of a wide range of influenza virus subtypes. In addition, it has been previously demonstrated that SIGN-R1 recognizes other airborne pathogens such as *Streptococcus pneumoniae*¹¹ or *Mycobacterium tuberculosis*³², suggesting its potential therapeutic use for controlling airborne bacterial infections.

We also demonstrated that SIGN-R1 binding to influenza virus is necessary for the secretion of inflammatory cytokines, as expression in IDCs enhanced the production of CCL5, CXCL9 and CXCL10. Furthermore, we observed that CCL5 expression was not increased in SIGN-R1-KO IDCs when they were stimulated in vitro with HA.

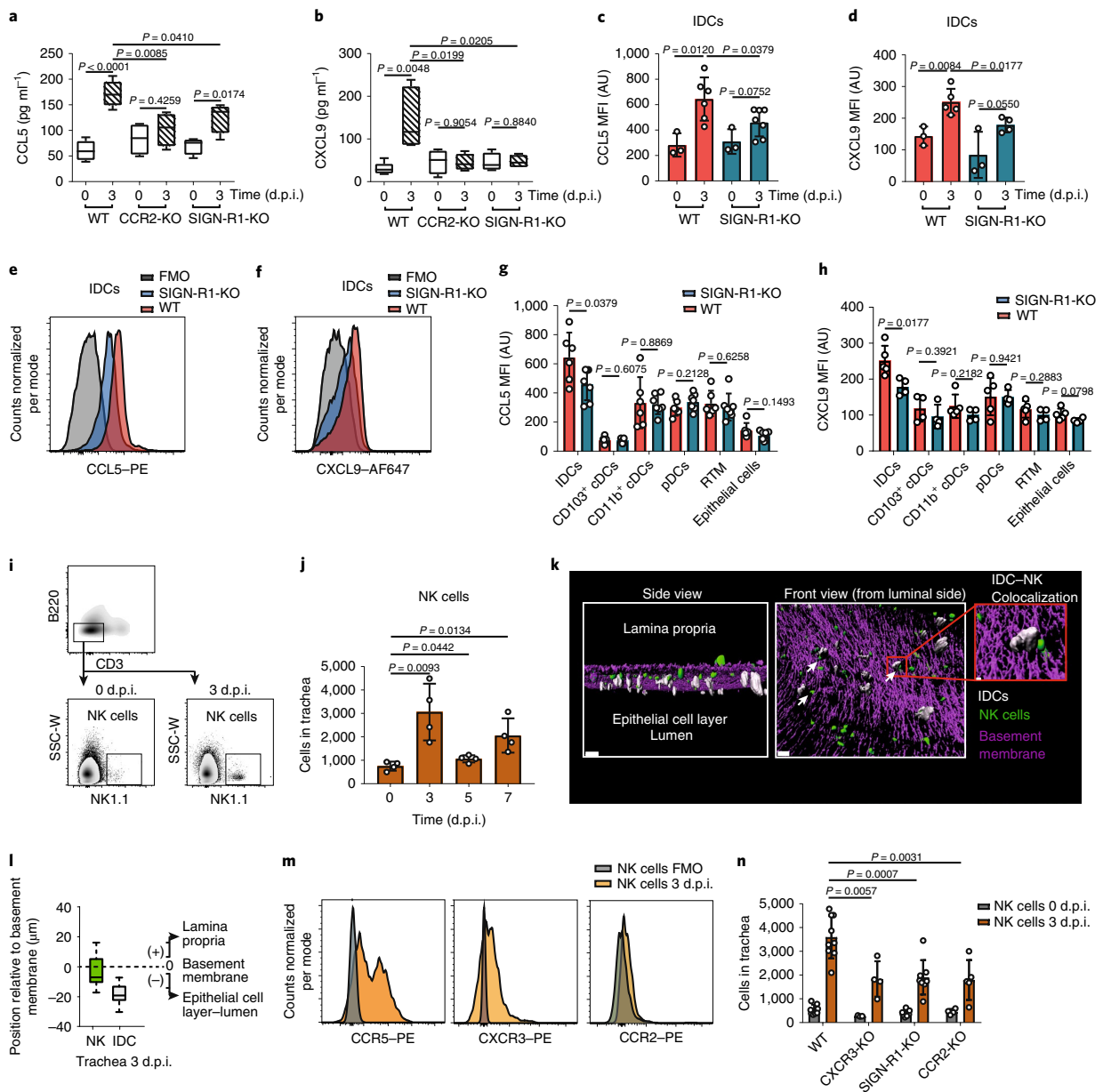


Fig. 5 | SIGN-R1 is involved in the production of inflammatory chemokines by IDCs and the recruitment of NK cells into the tracheal mucosa.

a, b, Levels of secreted CCL5 (**a**) and CXCL9 (**b**) in tracheas (WT, $n = 5$; CCR2-KO, $n = 4$; SIGN-R1-KO, $n = 4$ mice per group). **c-f**, Representative MFI of CCL5 (**c, e**; WT, $n = 3$ and 6; SIGN-R1-KO, $n = 3$ and 7 mice per time point) and CXCL9 (**d, f**; WT, $n = 3$ and 5; SIGN-R1-KO, $n = 3$ and 4 mice per time point) expression in tracheal IDCs at 3 d.p.i. **g, h**, Expression levels of CCL5 (**g**; WT, $n = 6$; SIGN-R1-KO, $n = 7$ mice per group) and CXCL9 (**h**; WT, $n = 5$; SIGN-R1-KO, $n = 4$ mice per group) by different cell types at 3 d.p.i. **i, j**, Quantification of NK cells (CD3⁺B220⁺NK1.1⁺) in mouse trachea ($n = 4$ mice per group). **k**, Three-dimensional reconstruction from confocal micrographs of a trachea at 3 d.p.i. showing the proximity of the IDCs (white) and NK cells (green) to the basement membrane (violet). White arrows indicate IDC interactions with NK cells. Scale bars, 40 µm (main panels) and 5 µm (expanded region). **l**, Box plot showing the anatomical position of IDCs (white) and NK cells (green) in relation to the basement membrane in the tracheal mucosa at 3 d.p.i. (data are based on analysis of three confocal reconstructions; IDC, $n = 63$; NK cells, $n = 102$). **m**, Surface expression of chemokine receptors in tracheal NK cells at 3 d.p.i. ($n = 3$ mice per group). **n**, Quantification of total number of NK cells in tracheas at 0 and 3 d.p.i. (WT, $n = 8$ and 9; CXCR3-KO, $n = 3$ and 4; SIGN-R1-KO, $n = 7$ and 8; CCR2-KO, $n = 4$ and 4 mice per time point). Data are representative of at least three independent experiments (**a-m**) or at least two independent pooled experiments (**n**). In **a, b** and **l**, box plots show 25th to 75th percentiles, the line represents the median and whiskers show minimum and maximum values (**a, b**) or 5th to 95th percentiles (**l**). In **c, d, g, h, j** and **n**, data are mean \pm s.d.; two-tailed Student's *t*-test.

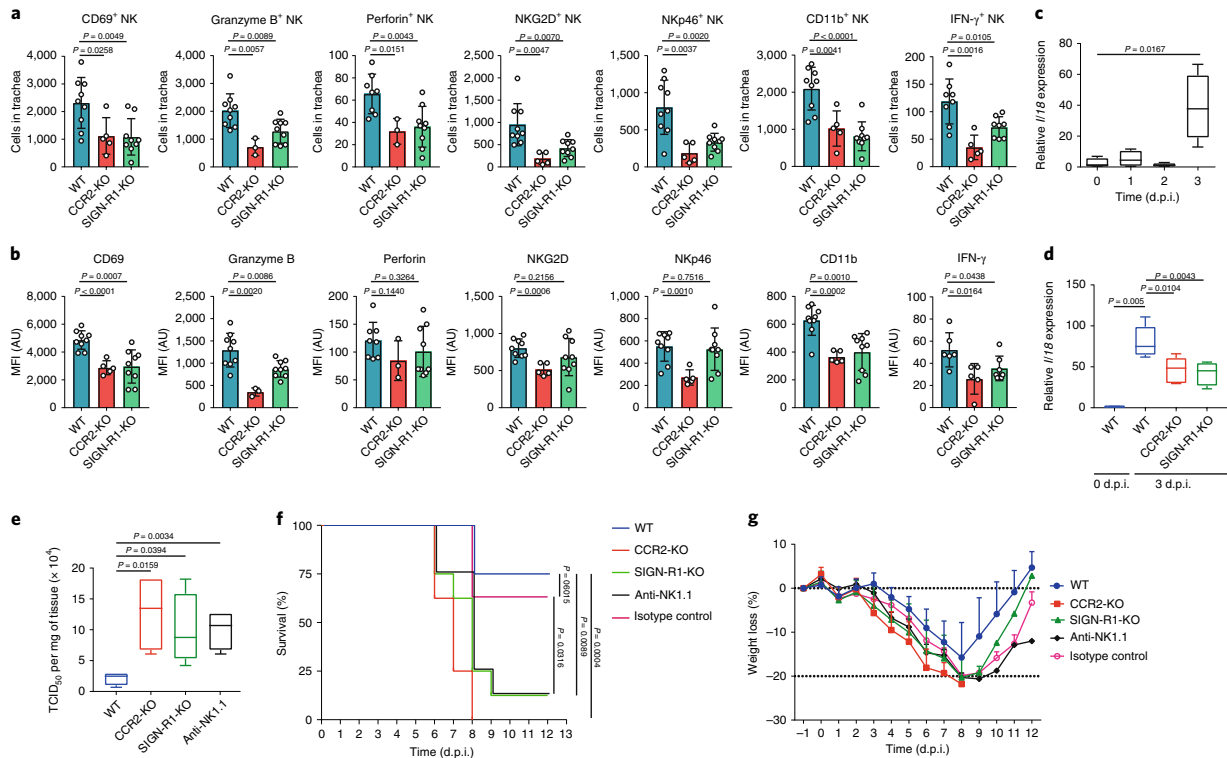


Fig. 6 | SIGN-R1⁺ IDCs are required to control influenza infection in the trachea. **a, b**, Quantification of total numbers (**a**) and MFI (**b**) of CD69⁺, granzyme B⁺, perforin⁺, NKG2D⁺, Nkp46⁺, CD11b⁺ and IFN- γ ⁺ NK cells at 3 d.p.i. (WT, $n=9$, 9, 8, 9, 9, 9 and 8; CCR2-KO, $n=5$, 3, 3, 5, 5, 5 and 5; SIGN-R1-KO, $n=9$, 9, 9, 9, 9 and 8 mice, respectively). **c**, Time course showing expression of *Ifl8* mRNA in trachea during the first three days after infection ($n=4$ mice per group). **d**, Expression levels of *Ifl8* mRNA in trachea from WT, CCR2-KO and SIGN-R1-KO mice at 3 d.p.i. (WT, $n=3$ and 5; CCR2-KO, $n=6$; SIGN-R1-KO, $n=6$ mice per group). **e**, Virus titre in trachea from WT, CCR2-KO and SIGN-R1-KO mice and mice treated with NK1.1-depleting antibody (anti-NK1.1), determined by 50% tissue culture infective dose (TCID₅₀) assay at 3 d.p.i. with influenza virus ($n=4$ mice per group). **f, g**, Mortality and morbidity analysis by determining survival (**f**) and weight loss (**g**) of WT, CCR2-KO and SIGN-R1-KO mice and mice treated with NK1.1-depleting antibody or isotype control mice after infection with influenza virus ($n=8$ mice per group). In **g**, dashed lines indicate no changes in the body weight of mice (0%) and the limit of body weight loss, after which animals are considered to have reached the experimental end point (-20%). Data are representative of at least two independent pooled experiments (**a, b**) or at least three independent experiments (**c–e**). In **a, b** and **g**, data are mean \pm s.d. In **c–e**, boxes show 25th to 75th percentiles, lines represent the median and whiskers show minimum and maximum values. Two-tailed Student's *t*-test (**a–e**); Mantel-Cox method (**f**).

However, we did not observe significant production of CXCL9 and CXCL10. This might be related to the technical limitations of the in vitro model, in which IDCs do not receive additional activation signals (such as IFN- γ) that are required for the expression of these two chemokines³³.

CCL5, CXCL9 and CXCL10 are involved in the recruitment of T cells and NK cells to the site of infection^{34,35}. In the present study, we concluded that the reduction in the number of NK cells observed in SIGN-R1-KO mice was due to the reduced expression of these cytokines as a result of the lack of activation of tracheal IDCs. However, due to limitations in the in vivo model of infection—such as the absence of a mutant influenza virus lacking glycosylation—we cannot rule out that an alternative mechanism, independent of SIGN-R1 binding to viral proteins, might be responsible for the observed phenotype. The importance of NK cells during viral infection has been previously demonstrated in humans³⁶ and in mice, where the absence of NK cells was associated with a higher susceptibility to influenza virus³⁷. In this study, we postulate that newly recruited NK cells perform effector functions intended to control the spread of the virus. In support of this hypothesis, we detected a robust expression in the recruited NK cells of the cytotoxic receptors NKG2D and Nkp46, which are involved in

the recognition of virus-associated molecules and the activation of these cells³⁸.

Furthermore, in CCR2-KO and SIGN-R1-KO mice we observed a reduced infiltration of NK cells expressing IFN- γ , granzyme B and perforin. These molecules are critical for the effector function of NK cells^{39–42}. However, we also detected a decrease in the expression levels of CD69, granzyme B, CD11b and IFN- γ , which indicates that SIGN-R1⁺ IDCs contribute to the activation of NK cells during influenza infection. Previous studies have demonstrated that IL-18 plays an important role in NK cell activation⁴³ and IDCs have the capacity to produce IL-18⁴⁴. Here we observed reduced levels of IL-18 in infected SIGN-R1-KO and CCR2-KO mice. Therefore, we believe that IDCs secrete IL-18, which promotes the activation and effector function of NK cells during influenza infection.

The increase in the viral titres observed in CCR2-KO and SIGN-R1-KO mice might be associated with a deficiency in the activation and recruitment of NK cells in these mouse models. These data support the role of IDCs in controlling the initial replication of the virus, as suggested by previous studies with influenza-infected CCR2-KO mice⁴⁵. Interestingly, CCR2-KO mice exhibited increased viral levels and increased mortality after infection compared with SIGN-R1-KO mice, which coincided with reduced chemokine

production and NK-cell activation. This could be related to the severe reduction in IDC numbers in this strain rather than a deficiency in other cell subtypes or immune mechanisms. IDCs are known to also produce other cytokines, such as TNF and nitric oxide⁸, which limit influenza virus infection^{46,47}. Conversely, other reports have observed a lower susceptibility of CCR2-KO mice compared with WT animals after infection with influenza virus^{48,49}. This discrepancy has been proposed to be related to the differences in the experimental conditions, such as the concentration of the virus used for the initial infection⁵⁰.

In conclusion, we demonstrated that IDCs have an important role in the initial events of the immune response against influenza infection through the direct recognition of viral particles by SIGN-R1 and the secretion of chemokines that recruit and activate NK cells in the tracheal mucosa. Consequently, NK cells contribute to the early elimination of virus-infected cells in the trachea (Supplementary Fig. 6c).

Methods

Mice. C57BL/6 mice were bred in-house or acquired from Janvier Labs. SIGN-R1-KO³² mice were donated by O. Neyrolles (Institut de Pharmacologie et de Biologie Structurale, Toulouse, France). The following transgenic strains with a C56BL/6 background were used: CD11c-YFP³¹, CCR2-KO³² and IFNAR-KO³³. Mice were maintained in specific pathogen-free facilities at the Institute for Research in Biomedicine, Bellinzona. Experiments were performed in accordance with the Swiss Federal Veterinary Office guidelines and animal protocols were approved by the local veterinary authorities.

Antibodies. The fluorescently labelled antibodies for cell-surface phenotypic staining, cell sorting and intracellular staining are listed in Supplementary Table 1. The following depletion antibodies were used: for NK cells, NK1.1 (PK136, BioXcell) and mouse IgG2a (C1.18.4, BioXcell) as isotype control. The following antibodies were used for ELISA: F16 (HUMABS BioMed); alkaline phosphatase AffiniPure goat anti-human IgG, Fc γ -fragment specific (Jackson ImmunoResearch); human anti-F (RSV) IgG1 (MPE8, HUMABS BioMed) as isotype control; and alkaline-phosphate-conjugated goat anti-mouse total IgG, IgG1, IgG2a, IgG2b, IgG3, IgM and IgA antibodies (Southern Biotech). For the SPR assays, monoclonal antibody H36-7¹³ was used as positive control.

Virus production, generation of recombinant influenza virus, infection and survival assay. The influenza virus strain A/PR/8/34 was grown, purified, inactivated and labelled as described previously¹². To generate the recombinant influenza virus PR8 carrying an mCherry reporter (rPR8-NS1-mCherry), a plasmid encoding the NS1 of PR8 fused with mCherry gene was constructed by overlapping fusion PCR. In brief, the NS1 open reading frame without the stop codon was fused to the N terminus of mCherry via a GSGRRQAGGT linker region (NS1-mCherry). mCherry was followed by a short GSGSG linker, a 19-amino acid 2A autoproteolytic site (ATNFSLLKQAGDVEENPGP) derived from porcine teschovirus-1 and by the nuclear export protein open reading frame. The first 147 nucleotides of the nuclear export protein were silently mutated. Silent mutations were also introduced into the endogenous splice-acceptor site in the NS1 open reading frame to prevent splicing. The rPR8-NS1-mCherry virus was rescued using standard reverse-genetics techniques. Age-matched (6–8 week old) female mice were anaesthetised with a mix of ketamine (100 mg per kg (body weight), Parke Davis) and xylazine (10 mg per kg (body weight), Bayer) and intranasally inoculated with 40 μ l (20 μ l in each nostril) containing 200 p.f.u. of influenza virus. In survival studies, mice were monitored daily for up to 12 d and sacrificed when weight loss was more than 20%. For NK-cell depletion, 200 μ g of the depletion antibody NK1.1 (see 'Antibodies') was administered intraperitoneally 2 d before infection and 1 d.p.i. For analysis of influenza-specific antibodies, mice were infected with 70 p.f.u. of influenza virus. The human RSV virus (A2 strain) was obtained from ViraTree and propagated and expanded in human epithelial type 2 (HEp-2) cells. The MPV virus (strain A1/6621/01) was propagated and expanded in rhesus monkey kidney epithelial (LLC-MK2) cells.

Flow cytometry. Tracheas were collected from the larynx to the tracheal bifurcation, mechanically disrupted with scissors and digested for 45 min at 37 °C in an enzyme mix composed of DNase I (0.28 mg ml⁻¹, Amresco) and 0.26 U ml⁻¹ Liberase TL Research Grade (Roche) in RPMI 1640 Medium (Gibco) followed by a stop solution of 2 mM EDTA (Sigma-Aldrich) and 2% heat-inactivated filter-sterilized Fetal Calf Serum (Thermo Fisher Scientific) in PBS (Sigma-Aldrich). Single-cell populations were obtained by forcing the remaining tissue pieces through a 40 μ m strainer followed by lysis of red blood cells. Fc receptors from the isolated cells were blocked (CD16/32, Biolegend) followed by surface staining and analysis by flow cytometry on a LSRFortessa (BD Biosciences).

Where indicated, intracellular staining was performed using Intracellular Fixation and Permeabilization Buffer Set (eBioscience) following the manufacturer's instructions. Dead cells were excluded using Zombie Aqua fixable viability dye (Biolegend) and data were analysed using FlowJo software (TriStar Inc.; v10.1).

SIGN-R1 blocking assays. Tracheas were processed as for flow cytometric analysis and tracheal IDCs in single-cell suspensions were sorted using a FACSAria IIIu (BD Biosciences) on the basis of their expression markers (CD45⁺CD11c⁺MHCII⁺CD11b⁺Ly6C^{high}). IDCs were dispensed into a round-bottom 96-well plate containing 5 \times 10⁴ cells in 100 μ l of RPMI 1640 Medium (Gibco) per plate and cultured for 2 h at 37 °C. Following this, cell suspensions were incubated with 1 μ g of fluorescently labelled SIGN-R1-blocking antibody or isotype control antibody for 30 min on ice (see 'Antibodies'). After washing, cell suspensions were (except for negative control wells) incubated with 5 \times 10⁵ p.f.u. of DiO-labelled UV-inactivated PR8 for 1 h on ice. Finally, after washing, IDC suspensions were surface stained using 1 μ g of fluorescently labelled SIGN-R1-blocking antibody, fixed and analysed by flow cytometric analysis.

Immunohistology of tracheal explants. Immunofluorescence confocal microscopy was performed using a Leica TCS SP5 confocal microscope using sequential acquisition to limit the signal crosstalk. For immunofluorescence images shown in Figs. 2 and 5 and Supplementary Figs. 1 and 2, tracheas were collected and fixed in 4% paraformaldehyde at 4 °C for 1 h. Then, in cases where the epithelial cell layer was stained, a solution containing 10 μ M of CellTracker Orange ((5-(and-6)-((4-chloromethyl)benzoyl)amino)tetramethylrhodamine) (CMTMR) (Thermo Fisher Scientific) or 5 μ M Cell Trace Violet (Thermo Fisher Scientific) was placed in the intraluminal space of the trachea and explants were incubated for 30 min at 7 °C and washed three times with PBS. Next, they were blocked with sera from the same host that the indicated antibodies used for staining. The antibodies used for staining were diluted in 0.01% Triton + 1% BSA in PBS and incubated with the tracheal explants for 4 h at 4 °C with shaking (see 'Antibodies'). Tracheas were cut into two halves along the long axis. Pieces were placed on a microscopy slide and embedded in Fluoromount Aqueous Mounting Medium (Sigma-Aldrich). Three-dimensional images were acquired using a HCX PL APO CS \times 20 0.7 numerical aperture oil-immersion objective (z step was 1 μ m for a total depth ranging from 50 μ m to 112 μ m). The cell populations were identified by assessing the signal intensity in the different channels as described below (or explained in the caption for Fig. 2 and Supplementary Fig. 2). In Fig. 5k, IDCs were defined as CD11c⁺Ly6C⁺NK1.1⁻ and NK cells were defined as CD11c⁻NK1.1⁺. The basement membrane was identified (in the absence of additional specific staining) by manually localizing the position of collagen fibres that generated autofluorescence signals detectable in the 412–464 nm channel after excitation with a 405 nm laser during the imaging process. For every reconstruction, 10–40 cells of each cell type were analysed. Three-dimensional surfaces shown in Figs. 2, 5 and Supplementary Fig. 2 were reconstructed using Imaris software (Bitplane; v8.4.2). Counting and localization with respect to the collagen layer of basement membrane (Figs. 2d and 5k and Supplementary Fig. 2b) was performed manually using the cell counter plugin in Fiji software (v1.48k)⁵⁴. In Supplementary Fig. 6a, the average distance between NK cells and their nearest neighbour cells in the IDC population was calculated measuring the Euclidean distance between the centres of the identified cells. In Supplementary Fig. 6b, contact between cells was calculated as described⁵⁵ and was considered when their distance (closest voxels) was less than or equal to 5 μ m.

SINGR1-PR8 colocalization. In Fig. 4, IDCs were isolated from tracheas as mentioned in the previous section and cultured in RPMI 1640 medium in μ -Slide 8 well ibiTreat (ibidi) for 3 h at 37 °C to allow them to attach to the bottom of the slide wells. Cell suspensions were subsequently incubated with 5 \times 10⁵ p.f.u. of PR8-DiO for 1 h on ice. After washing, IDC suspensions were surface stained using 1 μ g of fluorescently labelled SIGN-R1 antibody. Finally, cells were fixed, embedded with Vectashield mounting medium with DAPI (Vector Laboratories) and examined by immunofluorescence confocal microscopy. Three-dimensional images were acquired using a HCX PL APO Lambda Blue \times 63.0 1.40 numerical aperture oil-immersion objective (z step was 1 μ m for a total depth 20 μ m). Three-dimensional surfaces shown in Fig. 4 were reconstructed using Imaris software (Bitplane; v8.4.2).

Recombinant proteins and enzymatic treatment. Recombinant mouse SIGN-R1-Fc chimaera protein (SIGN-R1-Fc) extracellular domain was obtained from R&D systems. HA from influenza A H1N1 (A/Puerto Rico/8/34), influenza A H1N1 (A/New Caledonia/20/99), influenza A H3N2 (A/Victoria/361/2011), influenza A H5N1 (A/Vietnam/1194/2004) and neuraminidase from influenza A H5N1 (A/Hubei/1/2011) were obtained from Sino Biological. HA from influenza A H1N1 (A/Puerto Rico/8/34) was used for glycosylation assays using Endo H₁ (NEB) or PNGase F (NEB) according to the manufacturer's instructions.

Western blotting. Recombinant HA was treated with glycosidase and boiled in reducing SDS-PAGE loading buffer, separated by SDS-PAGE and analysed by western blotting. Detection was performed with an His-tag antibody (Thermo

Fisher Scientific, clone 4E3D10H2/E3) in 1% BSA for 2 h and secondary goat anti-mouse IgG (H+L)-HRP conjugated (Thermo Fisher Scientific).

SIGN-R1 ELISA. Maxisorp (Nunc) ELISA plates were coated with 50 μ l of UV-inactivated virus (1 mg ml⁻¹ of PR8, RSV or MPV), recombinant HA (2 μ g ml⁻¹) or N1 (2 μ g ml⁻¹) at 4 °C overnight. The plates were washed with PBS, blocked with 1% BSA in PBS for 1 h at room temperature and incubated with dilutions of recombinant mouse SIGN-R1-Fc chimaera protein (SIGN-R1-Fc, R&D systems). For plates coated with N1, FL6 antibody and the isotype control human anti-F (RSV) IgG1 (see 'Antibodies') were added to the wells. After incubation for 1 h at room temperature, plates were washed and 50 μ l of alkaline phosphatase AffiniPure goat anti-human IgG, Fc γ -fragment specific (see 'Antibodies') diluted 1:1,000 in 1% BSA in PBS was added to each well. After 1 h incubation at room temperature and washing, 50 μ l of 1.0 mg ml⁻¹ para-nitrophenylphosphate in 0.2M Tris buffer (prepared with SIGMAFAST para-nitrophenyl phosphate tablets (Sigma-Aldrich) in deionized water was added to each well, followed by incubation at room temperature for 45 min. Absorbance was read on a Biotek PoweWave 340 (Biotek) microplate reader at 405 nm. EC₅₀ values were inferred from fitting binding curves using GraphPad Prism 7 software.

Influenza-specific serum antibody ELISA. After infection, blood was collected at 5 and 10 d.p.i. and serum was obtained. ELISAs were performed as previously described³⁶. Absorbance was read on a Biotek PoweWave 340 (Biotek) microplate reader at 405 nm.

Tracheal cytoplex assay. LEGENDPlex assays (Mouse Proinflammatory Chemokine Panel and Mouse Inflammation Panel; Biolegend) were performed to monitor cytokine and chemokine expression. In brief, tracheas were collected and the luminal side was washed five times with 100 μ l of ice-cold PBS. Tracheal washes were centrifuged at 1,500 r.p.m. for 5 min and the supernatant was collected. Supernatants (25 μ l aliquots) were processed following the manufacturer's instructions. Samples were analysed by flow cytometry on LSRFortessa (BD Biosciences) and data were analysed using LEGENDPlex software (Biolegend; v7.0).

Generation of IDCs and in vitro culture with influenza HA. IDCs were generated by intranasal administration of 40 μ g of polyinosinic:polycytidylic acid to mimic the replication intermediates present in cells infected with RNA viruses in the lungs³⁷. After 2 d of administration, lungs were collected, IDCs were sorted as described in Flow cytometry and SIGN-R1 blocking assays, and 5 \times 10⁴ cells were plated per well into a round-bottom 96-well plate in 65 μ l complete RPMI medium alone or RPMI + Inflixal V (60 μ l of medium + 5 μ l of vaccine solution) medium. After 12 h, 25 μ l of supernatant was used to perform Mouse Proinflammatory Chemokine Panel LEGENDPlex assay.

PCR with reverse transcription. For cytokine expression in whole tissue, trachea were collected at the specified time after infection in 700 μ l of TRIzol reagent (Thermo Fisher Scientific), disrupted in lysing matrix D 1.4 mm ceramic sphere tubes using FastPrep-24 tissue disruption (MP Biomedicals) and RNA was isolated using a RNeasy Mini kit (Qiagen). For analysis of cytokine expression of IDCs and epithelial cells, tracheas were collected at 0 and 3 d.p.i., single-cell suspensions were obtained, and IDCs (CD45⁺CD11c⁺MHCII⁺CD11b⁺Ly6C^{high}) and epithelial cells (CD45⁻EpCam⁺) were sorted as described above, and RNA was isolated using a RNeasy Mini kit (Qiagen). Due to the absence of IDCs at 0 d.p.i., RNA was extracted from uninfected tracheal DCs (CD45⁺CD11c⁺MHCII⁺). After RNA isolation, 0.5–1 μ g of cDNA was synthesized using a cDNA synthesis kit (Applied Biosystems) following the manufacturer's recommendations. For the PCR reaction, SYBR Master Mix (Applied Biosystems) was used and samples were run on a 7900HT Fast Real-Time PCR System (Applied Biosystems). To measure expression levels of the cytokines IFN- α , IFN- β , CCL2, IL-18, CCL5, CXCL9 and CXCL10, the sets of primers listed in Supplementary Table 2 were used. The Pfaffl method³⁸ was used to calculate the relative expression of the transcripts.

Viral titres. Influenza titres from trachea homogenates were measured using a TCID₅₀ assay. In brief, tracheas were aseptically removed from mice, weighed and disrupted in 1 ml of ice-cold sterile PBS. The determination of TCID₅₀ was carried out using 96-well plates containing confluent Madine-Darby canine kidney (MDCK) cell monolayers. The MDCK cells were incubated with serial threefold dilutions of influenza virus culture supernatant in infection medium (Minimum Essential Medium Eagle+ GlutaMAX-1 (Gibco) with antibiotics and 1 μ g ml⁻¹ of TPCK-Treated Trypsin (Sigma-Aldrich) without FCS) at 37 °C. After 1 h, the monolayer was rinsed with PBS, overlaid with infection medium and incubated at 37 °C for 4 d. To identify influenza virus-positive wells, the monolayers were stained with crystal violet (Sigma-Aldrich) in 70% methanol. Titres were expressed as the dilution of tracheal extract at which 50% of the MDCK cultures revealed virus growth, as calculated by the Spearman and Karber method.

SPR. The experiments were carried out at 25 °C on a ProteON XPR-36 instrument (Bio-Rad Laboratories) in PBS (GIBCO, Thermo Fisher Scientific) and 0.05% Tween-20 (Sigma). The indicated proteins were immobilized on a ProteON GLM

sensor chip (Bio-Rad Laboratories) surface through amine coupling at 100 nM and a blank surface with no protein was created under identical coupling conditions for use as a reference. Analyte proteins (HA with different glycosylation patterns), were injected at a flow rate of 100 μ l min⁻¹, at concentrations of 100, 75, 50, 25 and 12.5 nM in different sensor channels. The data were processed using Proteon Manager software (v3.1) and double-referenced by subtraction of the blank surface and buffer-only injection. k_a , k_d and K_D were calculated by two-state fitting.

Statistics. Prism 7 (GraphPad) was used for statistical analyses and data presentation. Group comparisons were assessed using the unpaired two-tailed Student's *t*-test. For statistical analysis between survival curves the Mantel-Cox method was used.

Reporting Summary. Further information on research design is available in the Nature Research Reporting Summary linked to this article.

Data availability

All data from this study are available from the corresponding author upon request.

Received: 10 May 2018; Accepted: 6 June 2019;

Published online: 29 July 2019

References

- Eichelberger, M., Allan, W., Zijlstra, M., Jaenisch, R. & Doherty, P. C. Clearance of influenza virus respiratory infection in mice lacking class I major histocompatibility complex-restricted CD8⁺ T cells. *J. Exp. Med.* **174**, 875–880 (1991).
- Pulendran, B. & Maddur, M. S. Innate immune sensing and response to influenza. *Life Sci. J.* **6**, 23–71 (2014).
- Rello, J. & Pop-Vicas, A. Clinical review: primary influenza viral pneumonia. *Crit. Care* **13**, 235 (2009).
- Wikstrom, M. E. & Stumbles, P. A. Mouse respiratory tract dendritic cell subsets and the immunological fate of inhaled antigens. *Immunol. Cell Biol.* **85**, 182–188 (2007).
- GeurtsvanKessel, C. H. et al. Clearance of influenza virus from the lung depends on migratory langerin⁺CD11b⁻ but not plasmacytoid dendritic cells. *J. Exp. Med.* **205**, 1621–1634 (2008).
- Brimmes, M. K., Bonifaz, L., Steinman, R. M. & Moran, T. M. Influenza virus-induced dendritic cell maturation is associated with the induction of strong T cell immunity to a coadministered, normally nonimmunogenic protein. *J. Exp. Med.* **198**, 133–144 (2003).
- GeurtsvanKessel, C. H. & Lambrecht, B. N. Division of labor between dendritic cell subsets of the lung. *Mucosal Immunol.* **1**, 442–450 (2008).
- Serbina, N. V., Salazar-Mather, T. P., Biron, C. A., Kuziel, W. A. & Pamer, E. G. TNF/iNOS-producing dendritic cells mediate innate immune defense against bacterial infection. *Immunity* **19**, 59–70 (2003).
- Iwasaki, A. & Medzhitov, R. Toll-like receptor control of the adaptive immune responses. *Nat. Immunol.* **5**, 987–995 (2004).
- Monteiro, J. & Lepenies, B. Myeloid C-type lectin receptors in viral recognition and antiviral immunity. *Viruses* **9**, 59 (2017).
- Kang, Y. et al. The C-type lectin SIGN-R1 mediates uptake of the capsular polysaccharide of *Streptococcus pneumoniae* in the marginal zone of mouse spleen. *Proc. Natl Acad. Sci. USA* **101**, 215–220 (2004).
- Gonzalez, S. F. et al. Capture of influenza by medullary dendritic cells via SIGN-R1 is essential for humoral immunity in draining lymph nodes. *Nat. Immunol.* **11**, 427–434 (2010).
- Taylor, P. R. et al. The role of SIGNR1 and the β -glucan receptor (dectin-1) in the nonopsonic recognition of yeast by specific macrophages. *J. Immunol.* **172**, 1157–1162 (2004).
- Parent, S. A. et al. Molecular characterization of the murine SIGNR1 gene encoding a C-type lectin homologous to human DC-SIGN and DC-SIGNR. *Gene* **293**, 33–46 (2002).
- Davies, L. C., Jenkins, S. J., Allen, J. E. & Taylor, P. R. Tissue-resident macrophages. *Nat. Immunol.* **14**, 986–995 (2013).
- Auffray, C., Sieweke, M. H. & Geissmann, F. Blood monocytes: development, heterogeneity, and relationship with dendritic cells. *Annu. Rev. Immunol.* **27**, 669–692 (2009).
- McKean, D. et al. Generation of antibody diversity in the immune response of BALB/c mice to influenza virus hemagglutinin. *Proc. Natl Acad. Sci. USA* **81**, 3180–3184 (1984).
- Corti, D. et al. A neutralizing antibody selected from plasma cells that binds to group 1 and group 2 influenza A hemagglutinins. *Science* **333**, 850–856 (2011).
- Khan, W. H., Shrugaram, R. V. L. N., Broor, S. & Parveen, S. Glycosylation studies of G protein of group B human respiratory syncytial virus (hRSV) in eukaryotic system. *Int. J. Curr. Microbiol. Appl. Sci.* **3**, 107–113 (2014).
- Yang, C. F. et al. Human metapneumovirus G protein is highly conserved within but not between genetic lineages. *Arch. Virol.* **158**, 1245–1252 (2013).

21. Gregoire, C. et al. The trafficking of natural killer cells. *Immunol. Rev.* **220**, 169–182 (2007).
22. Turner, M. D., Nedjai, B., Hurst, T. & Pennington, D. J. Cytokines and chemokines: at the crossroads of cell signalling and inflammatory disease. *Biochim. Biophys. Acta Mol. Cell Res.* **1843**, 2563–2582 (2014).
23. Deshmane, S. L., Kremlev, S., Amini, S. & Sawaya, B. E. Monocyte chemoattractant protein-1 (MCP-1): an overview. *J. Interf. Cytokine Res.* **29**, 313–326 (2009).
24. Jia, T. et al. Additive roles for MCP-1 and MCP-3 in CCR2-mediated recruitment of inflammatory monocytes during *Listeria monocytogenes* infection. *J. Immunol.* **180**, 6846–6853 (2008).
25. Nakano, H. et al. Blood-derived inflammatory dendritic cells in lymph nodes stimulate acute TH1 immune responses. *Nat. Immunol.* **10**, 394–402 (2009).
26. Herold, S. et al. Alveolar epithelial cells direct monocyte transepithelial migration upon influenza virus infection: impact of chemokines and adhesion molecules. *J. Immunol.* **177**, 1817–1824 (2006).
27. Pattison, M. J., MacKenzie, K. F., Elcombe, S. E. & Arthur, J. S. C. IFN β autocrine feedback is required to sustain TLR induced production of MCP-1 in macrophages. *FEBS Lett.* **587**, 1496–1503 (2013).
28. Chatziandreou, N. et al. Macrophage death following influenza vaccination initiates the inflammatory response that promotes dendritic cell function in the draining lymph node. *Cell Rep.* **18**, 2427–2440 (2017).
29. Tate, M. D. & Hertzog, P. J. P109 The role of the type I interferon receptor during influenza virus infection. *Cytokine* **59**, 554–555 (2012).
30. Helft, J. et al. Cross-presenting CD103⁺ dendritic cells are protected from influenza virus infection. *J. Clin. Invest.* **122**, 4037–4047 (2012).
31. Geijtenbeek, T. B. H. & Gringhuis, S. I. Signalling through C-type lectin receptors: shaping immune responses. *Nat. Rev. Immunol.* **9**, 465–479 (2009).
32. Tanne, A. et al. A murine DC-SIGN homologue contributes to early host defense against *Mycobacterium tuberculosis*. *J. Exp. Med.* **206**, 2205–2220 (2009).
33. Schroder, K., Hertzog, P. J., Ravasi, T. & Hume, D. A. Interferon- γ : an overview of signals, mechanisms and functions. *J. Leukoc. Biol.* **75**, 163–189 (2004).
34. Taub, D. D. et al. Recombinant human interferon-inducible protein 10 is a chemoattractant for human monocytes and T lymphocytes and promotes T cell adhesion to endothelial cells. *J. Exp. Med.* **177**, 1809–1814 (1993).
35. Hickman, H. D. et al. CXCR3 Chemokine receptor enables local CD8⁺ T cell migration for the destruction of virus-infected cells. *Immunity* **42**, 524–537 (2015).
36. Biron, C. A., Byron, K. S. & Sullivan, J. L. Severe herpesvirus infections in an adolescent without natural killer cells. *N. Engl. J. Med.* **320**, 1731–1735 (1989).
37. Stein-Streilein, J. & Guffee, J. In vivo treatment of mice and hamsters with antibodies to asialo GM1 increases morbidity and mortality to pulmonary influenza infection. *J. Immunol.* **136**, 1435–1441 (1986).
38. Jost, S. & Altfeld, M. Control of human viral infections by natural killer cells. *Annu. Rev. Immunol.* **31**, 163–194 (2013).
39. He, X.-S. et al. T cell-dependent production of IFN- γ by NK cells in response to influenza A virus. *J. Clin. Invest.* **114**, 1812–1819 (2004).
40. Ge, M. Q. et al. NK cells regulate CD8⁺ T cell priming and dendritic cell migration during influenza A Infection by IFN- and perforin-dependent mechanisms. *J. Immunol.* **189**, 2099–2109 (2012).
41. Hwang, I. et al. Activation mechanisms of natural killer cells during influenza virus infection. *PLoS ONE* **7**, e31858 (2012).
42. Verbist, K. C., Rose, D. L., Cole, C. J., Field, M. B. & Klonowski, K. D. IL-15 Participates in the respiratory innate immune response to influenza virus infection. *PLoS ONE* **7**, e37539 (2012).
43. Chaix, J. et al. Cutting edge: priming of NK cells by IL-18. *J. Immunol.* **181**, 1627–1631 (2008).
44. Haerberlein, S., Sebald, H., Bogdan, C. & Schleicher, U. IL-18, but not IL-15, contributes to the IL-12-dependent induction of NK-cell effector functions by *Leishmania infantum* in vivo. *Eur. J. Immunol.* **40**, 1708–1717 (2010).
45. Dawson, T. C., Beck, M. A., Kuziel, W. A., Henderson, F. & Maeda, N. Contrasting effects of CCR5 and CCR2 deficiency in the pulmonary inflammatory response to influenza A virus TL-156. *Am. J. Pathol.* **156**, 1951–1959 (2000).
46. Rimmelzwaan, G. F., Baars, M. M., de Lijster, P., Fouchier, R. A. & Osterhaus, A. D. Inhibition of influenza virus replication by nitric oxide. *J. Virol.* **73**, 8880–8883 (1999).
47. Seo, S. H. & Webster, R. G. Tumor necrosis factor alpha exerts powerful anti-influenza virus effects in lung epithelial cells. *J. Virol.* **76**, 1071–1076 (2002).
48. Lin, K. L., Suzuki, Y., Nakano, H., Ramsburg, E. & Gunn, M. D. CCR2⁺ monocyte-derived dendritic cells and exudate macrophages produce influenza-induced pulmonary immune pathology and mortality. *J. Immunol.* **180**, 2562–2572 (2008).
49. Lin, S.-J. et al. The pathological effects of CCR2⁺ inflammatory monocytes are amplified by an IFNAR1-triggered chemokine feedback loop in highly pathogenic influenza infection. *J. Biomed. Sci.* **21**, 99 (2014).
50. Pamer, E. G. Tipping the balance in favor of protective immunity during influenza virus infection. *Proc. Natl Acad. Sci. USA* **106**, 4961–4962 (2009).
51. Lindquist, R. L. et al. Visualizing dendritic cell networks in vivo. *Nat. Immunol.* **5**, 1243–1250 (2004).
52. Boring, L. et al. Impaired monocyte migration and reduced type 1 (Th1) cytokine responses in C-C chemokine receptor 2 knockout mice. *J. Clin. Invest.* **100**, 2552–2561 (1997).
53. Müller, U. et al. Functional role of type I and type II interferons in antiviral defense. *Science* **264**, 1918–1921 (1994).
54. Schindelin, J. et al. Fiji: an open-source platform for biological-image analysis. *Nat. Methods* **9**, 676–682 (2012).
55. Palomino-Segura, M. et al. Imaging cell interaction in tracheal mucosa during influenza virus infection using two-photon intravital microscopy. *J. Vis. Exp.* **138**, e58355 (2018).
56. Gonzalez, S. E., Jayasekera, J. P. & Carroll, M. C. Complement and natural antibody are required in the long-term memory response to influenza virus. *Vaccine* **26**, 186–193 (2008).
57. Harris, P. et al. Double-stranded RNA induces molecular and inflammatory signatures that are directly relevant to COPD. *Mucosal Immunol.* **6**, 474–484 (2013).
58. Pfaffl, M. W. A new mathematical model for relative quantification in real-time RT-PCR. *Nucleic Acids Res.* **29**, e45 (2001).

Acknowledgements

We thank D. Jarrossay for the provision of technical support and M. Uguccioni for critical discussion of the manuscript; J. Paulson (The Scripps Research Institute) for initially providing KO mice; D. Corti (Humabs) for providing the antibody F16 and Core G of the Consortium for Functional Glycomics (S. Orr) for mouse phenotyping. This work was supported by the Swiss National Foundation grants, Réquipt (145038), Ambizione (148183) and grant 176124 to S.F.G., the European Commission Marie Curie Reintegration Grant (612742), and SystemsX.ch for a grant to D.U.P. (2013/124). This work was partly supported by Center for Research on Influenza Pathogenesis and National Institute of Allergy and Infectious Diseases-funded Center of Excellence on Influenza Research and Pathogenesis (contract number HHSN272201400008C).

Author contributions

M.P.-S. and S.F.G. conceived the project, designed experiments and analysed and interpreted the results. M.P.-S. performed most of the experiments. L.P. designed, performed and analysed in vitro SIGN-R1–HA-interaction experiments with help from S.F.G. and M.P.-S. T.V. helped to perform confocal microscopy experiments. I.L. helped to study the in vitro chemokine production of IDCs. R.D. and D.U.P. analysed confocal microscopy data. G.W. and A.G.-S. generated the recombinant influenza virus. Y.F., N.C., E.S., M.C.C. and O.N. advised on the experiments, interpreted results, helped to develop protocols and contributed with reagents. S.F.G. and M.P.-S. wrote the manuscript with the help of N.C., L.P. and O.N. S.F.G. directed the study.

Competing interests

The authors declare no competing interests.

Additional information

Supplementary information is available for this paper at <https://doi.org/10.1038/s41564-019-0506-6>.

Reprints and permissions information is available at www.nature.com/reprints.

Correspondence and requests for materials should be addressed to S.F.G.

Publisher's note: Springer Nature remains neutral with regard to jurisdictional claims in published maps and institutional affiliations.

© The Author(s), under exclusive licence to Springer Nature Limited 2019

Reporting Summary

Nature Research wishes to improve the reproducibility of the work that we publish. This form provides structure for consistency and transparency in reporting. For further information on Nature Research policies, see [Authors & Referees](#) and the [Editorial Policy Checklist](#).

Statistics

For all statistical analyses, confirm that the following items are present in the figure legend, table legend, main text, or Methods section.

- | | |
|-----|-----------|
| n/a | Confirmed |
|-----|-----------|
- The exact sample size (*n*) for each experimental group/condition, given as a discrete number and unit of measurement
 - A statement on whether measurements were taken from distinct samples or whether the same sample was measured repeatedly
 - The statistical test(s) used AND whether they are one- or two-sided
Only common tests should be described solely by name; describe more complex techniques in the Methods section.
 - A description of all covariates tested
 - A description of any assumptions or corrections, such as tests of normality and adjustment for multiple comparisons
 - A full description of the statistical parameters including central tendency (e.g. means) or other basic estimates (e.g. regression coefficient) AND variation (e.g. standard deviation) or associated estimates of uncertainty (e.g. confidence intervals)
 - For null hypothesis testing, the test statistic (e.g. *F*, *t*, *r*) with confidence intervals, effect sizes, degrees of freedom and *P* value noted
Give P values as exact values whenever suitable.
 - For Bayesian analysis, information on the choice of priors and Markov chain Monte Carlo settings
 - For hierarchical and complex designs, identification of the appropriate level for tests and full reporting of outcomes
 - Estimates of effect sizes (e.g. Cohen's *d*, Pearson's *r*), indicating how they were calculated

Our web collection on [statistics for biologists](#) contains articles on many of the points above.

Software and code

Policy information about [availability of computer code](#)

- | | |
|-----------------|---|
| Data collection | <ol style="list-style-type: none"> 1. FACSDiva™ software (BD Biosciences, version 6.2) was used to collect the flow cytometry data. 2. SDS Standard Core software (Applied Biosystems, version 2.4.1) was used for data collection in RQ-PCR assays. 3. LAS AF software (Leica Microsystems, version 27.9723.3) was used to acquire immunofluorescence confocal images. 4. Gen5 software (BioTek, version 1.11) was used to read ELISA plates. 5. ProteON Manager Software (Bio-Rad Laboratories) was used for SPR data collection. |
| Data analysis | <ol style="list-style-type: none"> 1. FlowJo software (TriStar Inc., version 10.1) was used to analyse flow cytometry data. 2. FIJI software (Schindelin et al., 2011, version 1.48k) was used to count and locate cells in confocal immunofluorescence images. 3. Imapris software (Bitplane, version 8.4.2) was used to generate 3D surfaces from immunofluorescence images of murine tracheas and in vitro cell cultures. 4. LEGENDPlex™ software (Biolegend, version 7.0) was used to analyse data from Cytoflex assays. 5. Prism software (GraphPad, version 7.00) was used for statistical analyses and data presentation. 8. Microsoft excel (2010 edition) was used to process raw numerical data for entry into Prism software. |

For manuscripts utilizing custom algorithms or software that are central to the research but not yet described in published literature, software must be made available to editors/reviewers. We strongly encourage code deposition in a community repository (e.g. GitHub). See the Nature Research [guidelines for submitting code & software](#) for further information.

Data

Policy information about [availability of data](#)

All manuscripts must include a [data availability statement](#). This statement should provide the following information, where applicable:

- Accession codes, unique identifiers, or web links for publicly available datasets
- A list of figures that have associated raw data
- A description of any restrictions on data availability

Data are available from the corresponding author upon request.

Field-specific reporting

Please select the one below that is the best fit for your research. If you are not sure, read the appropriate sections before making your selection.

Life sciences Behavioural & social sciences Ecological, evolutionary & environmental sciences

For a reference copy of the document with all sections, see [nature.com/documents/nr-reporting-summary-flat.pdf](https://www.nature.com/documents/nr-reporting-summary-flat.pdf)

Life sciences study design

All studies must disclose on these points even when the disclosure is negative.

| | |
|-----------------|--|
| Sample size | Sample size was reported in the figure legends. To protect animal welfare, a minimal number of animals were used (4-5 mice were used per group for the majority of experiments). For in vitro studies, 3-4 replicates per condition were used for the majority of experiments. No statistical methods were used to predetermine sample size, which were empirically determined to optimize numbers based on our previous experience with equivalent experiments. |
| Data exclusions | N/A, no data has been excluded. |
| Replication | All other All experiments were repeated at least 2 or 3 times with similar results. |
| Randomization | No randomization was used in this study. Mice used in this study had a C57BL/6 background and were age- and gender-matched, bred in-house or acquired from Janvier labs. Mice were distributed in similar size groups under the same conditions at the start of each experiments. Therefore any differences found in the study are due to the genotype of the mice or experimental conditions. |
| Blinding | No blinding was performed for animal studies. |

Reporting for specific materials, systems and methods

We require information from authors about some types of materials, experimental systems and methods used in many studies. Here, indicate whether each material, system or method listed is relevant to your study. If you are not sure if a list item applies to your research, read the appropriate section before selecting a response.

| Materials & experimental systems | | Methods | |
|-------------------------------------|---|-------------------------------------|--|
| n/a | Involvement | n/a | Involvement |
| <input type="checkbox"/> | <input checked="" type="checkbox"/> Antibodies | <input checked="" type="checkbox"/> | <input type="checkbox"/> ChIP-seq |
| <input type="checkbox"/> | <input checked="" type="checkbox"/> Eukaryotic cell lines | <input type="checkbox"/> | <input checked="" type="checkbox"/> Flow cytometry |
| <input checked="" type="checkbox"/> | <input type="checkbox"/> Palaeontology | <input checked="" type="checkbox"/> | <input type="checkbox"/> MRI-based neuroimaging |
| <input type="checkbox"/> | <input checked="" type="checkbox"/> Animals and other organisms | | |
| <input checked="" type="checkbox"/> | <input type="checkbox"/> Human research participants | | |
| <input checked="" type="checkbox"/> | <input type="checkbox"/> Clinical data | | |

Antibodies

| | |
|-----------------|--|
| Antibodies used | <ol style="list-style-type: none"> 1. αLy-6C; Clone: HK1.4; Colour: PE, Biotin; Manufacturer: Biolegend. Dilution: 1/500. 2. αF4/80; Clone: BM8; Colour: APC/Cy7, AF488; Manufacturer: Biolegend. Dilution: 1/200. 3. αB220; Clone: RA3-6B2; Colour: AF647, PE/Cy7, BV605; Manufacturer: Biolegend. Dilution: 1/300. 4. αCD103; Clone: 2E7; Colour: AF647, AF488; Manufacturer: Biolegend. Dilution: 1/300. 5. αCD11b; Clone: M1/70; Colour: AF488, BV785, AF647; Manufacturer: Biolegend. Dilution: 1/300. 6. αI-A/I-E (MHCII); Clone: M5/114.15.2; Colour: Pacific Blue, BV650; Manufacturer: Biolegend. Dilution: 1/500. 7. αEpCAM; Clone: G8.8; Colour: PE/Cy7; Manufacturer: eBioscience. Dilution: 1/200. 8. αCD45; Clone: 30-F11; Colour: AF700; Manufacturer: Biolegend. Dilution: 1/300. 9. αCD45.2; Clone: 104; Colour: PE/Cy7; Manufacturer: Biolegend. Dilution: 1/300. |
|-----------------|--|

10. α CD11c; Clone: N418; Colour: AF647, APC/Cy7, Bv711; Manufacturer: Biolegend. Dilution: 1/300.
 11. α CCL2; Clone: 2H5; Colour: Pacific Blue[™]; Manufacturer: BioXcell. Dilution: 1/300.
 12. α SIGN-R1; Clone: 22D1; Colour: CF405M^{**}, Atto647^{***}; Manufacturer: BioXcell. Dilution: 1/200.
 13. Armenian hamster IgG (α SIGN-R1 isotype control); Colour: Pure; Manufacturer: BioXcell. Dilution: 1/200.
 14. α CCL5; Clone: 2E9/CCL5; Colour: PE; Manufacturer: Biolegend. Dilution: 1/200.
 15. α CXCL9; Clone: MIG-2F5.5; Colour: AF647; Manufacturer: Biolegend. Dilution: 1/200.
 16. α CD3e; Clone: eBio500A2; Colour: eFluor450; Manufacturer: eBioscience. Dilution: 1/300.
 17. α NK1.1; Clone: PK136; Colour: AF488, PerCP-Cy5.5; Manufacturer: Biolegend, eBioscience. Dilution: 1/200.
 18. α CCR5; Clone: HM-CCR5; Colour: PE; Manufacturer: Biolegend. Dilution: 1/300.
 19. α CXCR3; Clone: CXCR3-173; Colour: PE; Manufacturer: Biolegend. Dilution: 1/300.
 20. α CCR2; Clone: 475301; Colour: PE; Manufacturer: R&D Systems. Dilution: 1/300.
 21. α CD69; Clone: H1.2F3; Colour: FITC; Manufacturer: Biolegend. Dilution: 1/300.
 22. α GranzymeB; Clone: GB11; Colour: AF647; Manufacturer: Biolegend. Dilution: 1/300.
 23. α Perforin; Clone: eBioOMAK-D; Colour: PE; Manufacturer: eBioscience. Dilution: 1/200.
 24. α XKG2D; Clone: CX5; Colour: APC; Manufacturer: Biolegend. Dilution: 1/300.
 25. α NKp46; Clone: 29A1.4; Colour: eFluor450; Manufacturer: eBioscience. Dilution: 1/300.
 26. α IFN- γ ; Clone: XMG1.2; Colour: BV785; Manufacturer: Biolegend. Dilution: 1/200.
 27. α Ly-6G; Clone: 1A8; Colour: BV711; Manufacturer: Biolegend. Dilution: 1/300.
 28. α CD16/32; Clone: 93; Colour: Pure; Manufacturer: Biolegend. Dilution: 1/200.
 29. α Gr-1; Clone: RB6-8C5; Colour: AF488; Manufacturer: Biolegend. Dilution: 1/300.
 30. α NK1.1; Clone: PK136; Manufacturer: BioXcell. Dilution: specified in methods.
 31. Mouse IgG2a, κ ; Clone: C1.18.4; Manufacturer: BioXcell. Dilution: specified in methods.
 32. Fl6; Manufacturer: HUMABS BioMed. Dilution: specified in methods/results.
 33. Alkaline Phosphatase AffiniPure Goat Anti-Human IgG, Fc γ fragment specific; Manufacturer: Jackson ImmunoResearch. Dilution: specified in methods.
 34. Isotype mouse IgG1 α -CMV pp72; Clone: 6E1; Manufacturer: Santa Cruz Biotechnology. Dilution: specified in methods/results.
 35. α CD317 (BST2); Clone: 927; Manufacturer: Biolegend. Dilution: 1/300
 36. Alkaline phosphate-conjugated goat anti-mouse total IgG, IgG1, IgG2a, IgG2b, IgG3, IgM and IgA antibodies; Manufacturer: Southern Biotech. Dilution: specified in methods
 37. H36-7; Manufacturer: HUMABS BioMed. Dilution: specified in methods/results.
 38. anti-His tag antibody; Clone: 4E3D10H2/E3; Manufacturer: Thermo Fisher Scientific. Dilution: specified in methods/results.
 39. Goat anti-Mouse IgG (H+L)-HRP conjugated; Clone: G-21040; Manufacturer: Thermo Fisher Scientific. Dilution: specified in methods/results.
- * In-house labelled with Pacific Blue[™] Antibody Labeling Kit (ThermoFisher Scientific), ** In-house labelled with CF405M Mix-n-Stain[™] Antibody Labeling Kit (Biotium), *** In-house labelled with Atto 647 NHS ester (Atto-Tec).

Validation

1. α Ly-6C; Application: Flow cytometry and Immunofluorescence Microscopy; Citation: Makaroff LE, et al. 2009. P. Natl. Acad. Sci. USA 106:4799.
2. α F4/80; Application: Flow cytometry; Citation: Kobayashi M, et al. 2008. J. Leukoc. Biol. 83:1354.
3. α B220; Application: Flow cytometry; Citation: Shih FF, et al. 2006. J. Immunol. 176:3438.
4. α CD103; Application: Flow cytometry; Citation: LeFrancois L, et al. 1994. Eur. J. Immunol. 24:635.
5. α CD11b; Application: Flow cytometry and Immunofluorescence Microscopy; Citation: Tan SL, et al. 2006. J. Immunol. 176:2872. (FC), Allen LA and Aderem A. 1996. J. Exp. Med. 184:627 (IF).
6. α I-A/I-E (MHCII); Application: Flow cytometry; Citation: Matte-Martone C, et al. 2008. Blood 111:3884.
7. α EpCAM; Application: Flow cytometry; Citation: Pardo-Saganta A, et al. 2015. Nature. 597-601.
8. α CD45; Application: Flow cytometry; Citation: Haynes NM, et al. 2007. J. Immunol. 179:5099.
9. α CD45.2; Application: Flow cytometry; Citation: Kohlmeier JE, et al. 2008. Immunity. 29:101.
10. α CD11c; Application: Flow cytometry and Immunofluorescence Microscopy; Citation: Cervantes-Barragan L, et al. 2007. Blood 109:1131. (FC), Chin RK, et al. 2006. J. Immunol. 177:290 (IF).
11. α CCL2; Application: blocking antibody; Citation: Brunner, P. M., et al. (2015). Exp Dermatol 24(7): 522-528.
12. α SIGN-R1; Application: Flow cytometry, blocking antibody and Immunofluorescence Microscopy; Citation: Kang, Y. S., et al. (2004). Proc Natl Acad Sci U S A 101(1): 215-220.
13. Armenian hamster IgG (α SIGN-R1 isotype control); Application: Flow cytometry; blocking antibody and Immunofluorescence Microscopy; Citation: Kang, Y. S., et al. (2004). Proc Natl Acad Sci U S A 101(1): 215-220.
14. α CCL5; Application: Flow cytometry; Citation: Schall TJ. 1991. Cytokine 3:165.
15. α CXCL9; Application: Flow cytometry; Citation: Thapa M et al. 2008. J. Immunol. 180(2):1098.
16. α CD3e; Application: Flow cytometry; Citation: Renand A et al. 2013. PLoS One. 8(12):e85589.
17. α NK1.1; Application: Flow cytometry; Citation: Bankoti J, et al. 2010. Toxicol. Sci. 115:422.
18. α CCR5; Application: Flow cytometry; Citation: Mao A, et al. 2005. J. Immunol. 175:5146.
19. α CXCR3; Application: Flow cytometry; Citation: Sharma R. 2009. J. Immunol. 183:3212.
20. α CCR2; Application: Flow cytometry; Citation: F Sasaki, et al. 2017. PLoS ONE, 2017;12(9):e0185133.
21. α CD69; Application: Flow cytometry; Citation: Lee JW, et al. 2006. Nature Immunol. 8:181.
22. α GranzymeB; Application: Flow cytometry; Citation: Pachnio A, et al. 2016. PLoS Pathog. 12: 1005832.
23. α Perforin; Application: Flow cytometry; Citation: Konjar S, et al. 2010. Immunology, 131:257.
24. α XKG2D; Application: Flow cytometry; Citation: Li Y, et al. 2014. PLoS One. 9:86927.
25. α NKp46; Application: Flow cytometry; Citation: Lehmann CHK, et al. 2017. J Exp Med (5):1509-1528.
26. α IFN- γ ; Application: Flow cytometry; Citation: Ferrick D, et al. 1995. Nature 373:255.
27. α Ly-6G; Application: Flow cytometry; Citation: Daley JM, et al. 2008. J. Leukocyte Biol. 83:1.
28. α CD16/32; Application: Flow cytometry (Fc block); Citation: Oliver AM, et al. 1999. Hybridoma 18:113.
29. α Gr-1; Application: Flow cytometry; Citation: Dzhagalov I, et al. 2007. Blood 109:1620.
30. α NK1.1; Application: depletion antibody; Citation: Sentman CL, et al. 1989. J. Immunol. 142:1847.
31. Mouse IgG2a, κ ; Clone: C1.18.4; Application: depletion antibody; Citation: Carmi, Y., et al. 2015. Nature 521(7550): 99-104.
32. Fl6; Application: ELISA; Citation: Corti, D. et al. 2011. Science 333, 850-856.
33. Alkaline Phosphatase AffiniPure Goat Anti-Human IgG, Fc γ fragment specific; Application: ELISA; Citation: Baer, J., Santiago,

F., et al.. 2010.Vaccine; 28(4): 907.
 34. Human Anti-F (RSV) IgG1 (MPE8); Application: ELISA; Citation: Corti, D. et al 2013. Nature, 501(7467), 439-443.
 35. α CD317 (BST2); Application: Flow cytometry; Citation: Blasius AL, et al. 2006. J. Immunol. 177:3260.
 36. Alkaline phosphate-conjugated goat anti-mouse total IgG, IgG1, IgG2a, IgG2b, IgG3, IgM and IgA antibodies; Application: ELISA; Citation: Dubovsky JA, 2013. Blood. 122:2539-49.
 37. H36-7; Application: SPR; Citation: McKean et al 1984. Proc. Natl. Acad Sci. 81 (10): 3180-4.
 38. anti-His tag antibody; Application: Western blot; Citation: Jeffrey A. Schneider et. al 2018. Nat Commun. 9 (1): 4396.
 39. Goat anti-Mouse IgG (H+L)-HRP conjugated; Application: Western blot; Citation: Karner CM, et. al 2009. Nat Genet. 41(7):793-9.

Eukaryotic cell lines

Policy information about [cell lines](#)

| | |
|--|---|
| Cell line source(s) | Madine-Darby canine kidney (MDCK) was purchased from ATCC® (CCL-34, Lot:60245139). HEp-2 cells were obtained from ATCC® (CCL-23). LLC-MK2 were obtained from ATCC® (CCL-7). |
| Authentication | HEp-2 and LLC-MK2 cells were authenticated by analysis of Short Tandem Repeat (STR) loci at ATCC. MDCK cells were not authenticated. |
| Mycoplasma contamination | All cell lines were tested negative for mycoplasma contamination using MycoAlert® Mycoplasma detection kit (Lonza, LT07-118). |
| Commonly misidentified lines (See CLAC register) | No commonly misidentified cell lines were used in this study. |

Animals and other organisms

Policy information about [studies involving animals](#); [ARRIVE guidelines](#) recommended for reporting animal research

| | |
|-------------------------|--|
| Laboratory animals | C57BL/6 mice were bred in-house or acquired from Janvier labs. SIGNR1-KO, mice were kindly donated by Dr. Olivier Neyrolles. The following transgenic strains with a C57BL/6 background were used: CD11c-YFP, CCR2-KO, IFNAR-KO. Mice were maintained in specific pathogen-free facilities at the Institute for Research in Biomedicine, Bellinzona. Experiments were performed in accordance with the Swiss Federal Veterinary Office guidelines and animal protocols were approved by the local veterinarian authorities. For experiments, female mice of 6–8 weeks old were used. |
| Wild animals | This study did not involve wild animals. |
| Field-collected samples | No samples collected from the field. |
| Ethics oversight | Experiments were performed in accordance with the Swiss Federal Veterinary Office guidelines and animal protocols were approved by the local veterinarian authorities. |

Note that full information on the approval of the study protocol must also be provided in the manuscript.

Flow Cytometry

Plots

Confirm that:

- The axis labels state the marker and fluorochrome used (e.g. CD4-FITC).
- The axis scales are clearly visible. Include numbers along axes only for bottom left plot of group (a 'group' is an analysis of identical markers).
- All plots are contour plots with outliers or pseudocolor plots.
- A numerical value for number of cells or percentage (with statistics) is provided.

Methodology

| | |
|--------------------|--|
| Sample preparation | Trachea was collected from the larynx to the tracheal bifurcation, mechanically disrupted with scissors and digested for 45 min at 37°C in an enzyme mix composed of: DNase I (0.28 mg/ml, Amresco), and 0.26 units / ml of Liberase TL Research Grade (Roche) in RPMI 1640 Medium (Gibco) followed by a stop solution of 2 mM EDTA (Sigma Aldrich) and 2 % heat-inactivated filter-sterilised Fetal Calf Serum (Thermo Fisher Scientific) in PBS (Sigma Aldrich). Single cell populations were obtained by forcing the remaining tissue pieces through a 40- μ m strainer followed by lysis of red blood cells. |
| Instrument | LSRFortessa™ (BD Biosciences) was used for data collection. |
| Software | FACSDiva™ software (BD Biosciences, version 6.2) was used to collect the flow cytometry data. FlowJo software (TriStar Inc., version 10.1) was used to analyse flow cytometry data. LEGENDPlex™ software (Biolegend, version 7.0) was used to analyse data from Cytoplex assays. |

Cell population abundance

Tracheas were processed as for flow cytometry analysis and tracheal IDC and Ep. cells were sorted using a FACSAria IIIu (BD Biosciences) accordingly with their expression markers (IDC: CD45+ / CD11c+ / MHCII+ / CD11b+, Ly6chi; Ep.cells: CD45-, EpCAM+).

Gating strategy

A figure exemplifying the gating strategy is provided within the manuscript. Singlets, viable cells and CD45+ cells were always identified for the analysis. Positive and negative staining cells were defined accordingly to signal in Fluorescent-minus-one (FMO) controls. The α CD317 (BST2) antibody was used only to identify pDC in Figure 1A.

Tick this box to confirm that a figure exemplifying the gating strategy is provided in the Supplementary Information.

Video Article

Imaging Cell Interaction in Tracheal Mucosa During Influenza Virus Infection Using Two-photon Intravital Microscopy

Miguel Palomino-Segura^{*1,2}, Tommaso Virgilio^{*1,2}, Diego Morone¹, Diego U. Pizzagalli^{1,3}, Santiago F. Gonzalez¹

¹Faculty of Biomedical Sciences, Institute for Research in Biomedicine, Università della Svizzera italiana (USI)

²Graduate School of Cellular and Molecular Sciences, Faculty of Medicine, University of Bern

³Institute of Computational Science, Università della Svizzera italiana (USI)

*These authors contributed equally

Correspondence to: Santiago F. Gonzalez at santiago.gonzalez@irb.usi.ch

URL: <https://www.jove.com/video/58355>

DOI: [doi:10.3791/58355](https://doi.org/10.3791/58355)

Keywords: Immunology and Infection, Issue 138, Two-Photon Intravital Microscopy, Trachea, Influenza virus, Neutrophil, Dendritic Cell, Cell-to-Cell interactions

Date Published: 8/17/2018

Citation: Palomino-Segura, M., Virgilio, T., Morone, D., Pizzagalli, D.U., Gonzalez, S.F. Imaging Cell Interaction in Tracheal Mucosa During Influenza Virus Infection Using Two-photon Intravital Microscopy. *J. Vis. Exp.* (138), e58355, doi:10.3791/58355 (2018).

Abstract

The analysis of cell-cell or cell-pathogen interaction *in vivo* is an important tool to understand the dynamics of the immune response to infection. Two-photon intravital microscopy (2P-IVM) allows the observation of cell interactions in deep tissue in living animals, while minimizing the photobleaching generated during image acquisition. To date, different models for 2P-IVM of lymphoid and non-lymphoid organs have been described. However, imaging of respiratory organs remains a challenge due to the movement associated with the breathing cycle of the animal.

Here, we describe a protocol to visualize *in vivo* immune cell interactions in the trachea of mice infected with influenza virus using 2P-IVM. To this purpose, we developed a custom imaging platform, which included the surgical exposure and intubation of the trachea, followed by the acquisition of dynamic images of neutrophils and dendritic cells (DC) in the mucosal epithelium. Additionally, we detailed the steps needed to perform influenza intranasal infection and flow cytometric analysis of immune cells in the trachea. Finally, we analyzed neutrophil and DC motility as well as their interactions during the course of a movie. This protocol allows for the generation of stable and bright 4D images necessary for the assessment of cell-cell interactions in the trachea.

Video Link

The video component of this article can be found at <https://www.jove.com/video/58355/>

Introduction

Two-photon intravital microscopy (2P-IVM) is an effective technique for real time imaging of cell-to-cell interactions as they occur in their natural environment¹. One of the main advantages of this method is that it allows the study of cellular processes at a greater specimen depth (500 μ m to 1 mm) compared with other traditional imaging techniques². At the same time, the use of two low-energy photons generated by the two-photon laser minimizes the tissue photo-damage typically associated with the image acquisition process⁷. During the last decade, 2P-IVM has been applied to study different types of cell-cell interactions in several disciplines^{3,4,5}. These studies have been especially relevant to investigate immune cells, which are characterized by their high dynamism and the formation of prominent contacts following the signals generated by other cells and the environment. 2P-IVM has been also applied to study the interactions between pathogen and host⁶. Indeed, it has been previously shown that some pathogens can alter the type and duration of the contacts between immune cells, hampering, as a result, the immune response⁷.

The airway mucosa is the first site in which the immune response against airborne pathogens is generated⁸. Therefore, *in vivo* analysis of pathogen-host interactions in this tissue is critical to understand the initiation of the host defense mechanisms during infection. However, 2P-IVM of the airways is challenging mainly due to the artifacts produced by the breathing cycle of the animal, which compromises the process of image acquisition. Recently, different surgical models have been described for imaging murine trachea^{9,10,11,12} and lungs^{13,14,15,16}. Tracheal 2P-IVM models represent an excellent set-up to visualize the initial phase of the immune reaction in the upper airways, while lung-alveoli 2P-IVM models are more suitable to study the late phase of infections. The developed lung models present a limitation associated with the presence of air-filled alveoli, which restrict the optical penetration of the laser and make the mucosal layer of the intrapulmonary airways inaccessible for *in vivo* imaging¹⁷. Conversely, the structure of the trachea, formed by a continuous epithelium, facilitates image acquisition.

Here, we present a protocol that includes a detailed description of the steps required to perform influenza infection, surgical preparation of the animals, and 2P-IVM of the trachea. In addition, we describe a specific experimental set-up for the visualization of neutrophils and dendritic cells (DC), two immune cell types that play an important role as mediators of the defense mechanism against influenza virus^{18,19}. Finally, we describe

a procedure to analyze neutrophil-DC interactions. These contacts have been shown to modulate DC activation and, subsequently, to affect the immune responses against pathogens²⁰.

Protocol

All animal procedures involving mice were performed in accordance with the Swiss Federal Veterinary Office guidelines and animal protocols were approved by the local veterinarian authorities.

1. Influenza Infection of CD11c-YFP Mice

1. Biosafety

NOTE: The mouse adapted strain of influenza A/Puerto Rico/8/34 H1N1 (PR8) was grown in fertilized eggs, purified and titrated as previously described²¹. All the steps involving infected animals or biological samples were carried out under a biosafety cabinet according to biosafety level (BSL) 2 conditions.

1. Clean the biosafety cabinet with a 70% ethanol solution before and after the infection procedure.
2. Discard all waste materials produced during this procedure following proper WHO biosafety guidelines (<http://www.who.int/csr/resources/publications/biosafety/Biosafety7.pdf>). Discard solid waste in autoclavable bins and contaminated liquids in plastic bags filled with 70% ethanol solution or medical disinfectant.

2. Influenza intranasal infection

NOTE: B6.Cg-Tg(Ilgax-Venus)1Mnz/J (CD11c-YFP)²² on a C57BL/6J background were used in this study. Mice were maintained in the specific pathogen-free facility at the Institute for Research in Biomedicine.

1. Place a maximum of 5 age- and sex-matched (six to eight-week-old) CD11c-YFP mice per cage. Wait for at least two days for mice acclimation to housing conditions before the infection procedure.
2. Defrost PR8 stock and prepare the corresponding dilution using cold 1x Dulbecco's phosphate buffer saline modified without calcium chloride and magnesium chloride (PBS) to obtain a final concentration of 200 plaque forming units (PFU) in 30 μ L. Keep virus dilution on ice during the whole procedure.

NOTE: Titration of every batch of influenza virus prior to its use is recommended to ensure a precise infection dose.

3. Inject a dose of ketamine (100 mg/kg) and xylazine (10 mg/kg) intraperitoneally (i.p.) using a 26 G needle 1 mL syringe.
4. Wait until the mouse is fully anesthetized (complete loss of both righting and pedal withdrawal reflex). Deep anesthesia is necessary for an optimal infection, since not-fully anesthetized mice will swallow or expel the virus inoculum, leading to variations in the infection dose.
5. Place the anesthetized mouse in a supine position. Collect 15 μ L of virus inoculum. Place the pipette tip close to the mouse left nostril and dispense the viral inoculum drop by drop. As drops must be inhaled, do not pipette them directly inside the nose cavity.
6. Wait 2–5 min and place the pipette tip containing the remaining 15 μ L of virus inoculum in the right nostril.
7. Check that the mouse is correctly breathing and place it in a cage in lateral *decubitus*. Monitor mouse breathing and anesthesia recovery (approximately 60 min after induction).

NOTE: It is possible to infect more than 1 mouse at the same time. In this case, administer viral inoculum in the left nostril of all mice in a sequence, wait for 2–5 min and then administer the virus in the right nostril. To avoid variability between individuals, infect no more than 3 mice at the same time.

8. Monitor animal health status and weight loss daily.
9. Euthanize mice according to the humane endpoint determined by the authority guidelines. The euthanasia method has to be approved by the animal experimentation authorities and must respect local ethical regulations. After two-photon experiments, euthanize mice by administration of an overdose of ketamine/xylazine followed by cervical dislocation. In all the other experiments, use CO₂ inhalation as a method for euthanasia.

NOTE: To measure the viral titers of the infected trachea, 50% tissue culture infective dose (TCID₅₀) assay or real time polymerase chain reaction (RT-PCR) assay can be performed as previously described²³.

3. Evaluation of neutrophil recruitment in trachea by flow cytometry

NOTE: This part of the protocol is optional. It aims to evaluate neutrophil recruitment in tracheal mucosa following influenza infection.

1. Euthanize infected and uninfected control mice at day 3 post-infection (p.i.) by CO₂ inhalation.
NOTE: In order to prevent tracheal damage, avoid using cervical dislocation to euthanize animals. Additionally, perfusion of euthanized mice is advisable to avoid contamination from blood neutrophils.
2. Spray the mouse neck with 70% ethanol solution and perform a skin incision using surgical scissors from the chest to the chin.
3. Separate the salivary glands using forceps and expose the trachea.
4. Dissect the muscles around the trachea using forceps and scissors.
NOTE: This step must be performed carefully since trachea could be easily damaged during the procedure.
5. Hold the trachea with forceps and carefully detach the esophagus by dissection.
6. Holding the intrathoracic part of the trachea with forceps, make an incision at the beginning of the bronchial tree. Then detach the trachea from the larynx and carefully remove any musculature left.
7. Place the organ in a 1.5 mL tube containing RPMI 1640 + HEPEs medium (RPMI) on ice.
8. Prepare the enzyme mixture for trachea digestion, containing 0.26 units/mL of collagenase (I and II) and 0.2 mg/mL of DNase I in RPMI.
9. Place the dissected trachea in a 6-well plate containing 1 mL of enzyme mixture.
10. Cut the organ into small pieces with the help of forceps and scissors. Keep the plate on ice during this step.
11. Incubate at 37 °C for 45 min. During this time, shake the plate every 15 min.
12. Stop the enzyme digestion by adding 1 mL of FACS washing buffer (2 mM EDTA and 2% heat-inactivated filter-sterilized fetal bovine serum (FBS)) in PBS.

13. Resuspend the solution with a 1 mL pipette to help to disassociate the partially undigested pieces of tissue.
14. Transfer the solution to another well by passing the content through a 40 μ m strainer. Then, gently smash the remaining pieces of the organ trapped on top of the strainer using a 2 mL syringe plunger.
NOTE: Smashing partially undigested pieces of trachea over the strainer is a critical step to obtain an optimal number of cells during flow cytometric analysis.
15. Wash the well and the strainer with FACS washing buffer and transfer the suspension in a 5 mL tube kept on ice.
16. Centrifuge the tubes at 166 x g for 5 min at 4 °C. Discard the supernatant and resuspend the cells in 100 μ L of FACS washing buffer.
17. Proceed with antibody surface staining for flow cytometry. Briefly, block Fc receptors of the isolated cells using an antibody against CD16/32, followed by surface staining. To correctly identify neutrophils, the flow cytometry panel should contain the following antibodies: α Ly6G, α CD11b, α CD45, as well as a viability dye to exclude dead cells.
18. Run the whole content of the samples on a flow cytometer and analyze the data.
 1. To get an optimal number of immune cells, run the single cell suspension at a speed not higher than 3,000 events/s. This will reduce the number of events excluded during the acquisition. Using this protocol, it should be possible to obtain 1 to 2 million of cells per trachea.

2. Isolation and Injection of Neutrophils

NOTE: In this procedure, B6.129(ICR)-Tg(CAG-ECFP)CK6Nagy/J mice (CK6-ECFP) were used²⁴. These animals express CFP in all cell types under the human β -actin promoter. Alternatively, it is also possible to use C57BL/6J mice to isolate cells and stain them according to the protocol described in step 2.6. The purification and manipulation of neutrophils may increase their activation status, potentially altering their migratory and functional properties.

1. Euthanize the animal by CO₂ inhalation.
2. Remove both femurs and tibias and gently clean them using forceps.
3. Cut bone epiphyses and flush the bone marrow using a 1 mL syringe filled with sterile cold PBS, in a 50 mL tube kept on ice.
4. Resuspend the cells with an 18 G needle and filter the cell suspension with a 40 μ m strainer. Wash once with PBS at 110 x g for 5 min at 4 °C and resuspend cells in 2 mL of cold PBS.
5. **Dilute 100% Percoll 9:1 in 10x PBS and prepare gradient solutions of percoll 72%, 64% and 52% using 1x PBS. Carefully layer 2 mL of each of the three gradients in a 15 mL tube, starting from the most concentrated one.**
 1. Add carefully 2 mL of the bone marrow cell suspension on top of the gradients and centrifuge at 1,100 x g for 30 min at room temperature (RT) without acceleration and brake.
6. Carefully remove the band at the interface between 64% and 72% and wash it once at 200 x g for 5 min at 4 °C with cold PBS. Resuspend cells in a volume of 100 μ L of PBS and keep them on ice. The purity of the neutrophils is expected to be higher than 90%.
7. Optionally, label neutrophils with a cell proliferation kit using the manufacturer's protocol. Add the dye to the cell suspension to a final concentration of 10 μ M in a volume of 1 mL, incubate at 37 °C for 30 min and wash (166 x g, 5 min).
8. Estimate cell concentration using a hemocytometer and inject intravenously 5 x 10⁶ cells in a maximum volume of 100 μ L in the previously infected CD11c-YFP⁺ mice using a 26 G needle 1 mL syringe, 12 h before imaging.

3. Preparing the Mouse for Imaging

1. **Anesthesia**
 1. Anesthetize infected CD11c-YFP⁺ mice at day 3 p.i. according to step 1.2.3.
 2. Once mice are deeply anesthetized, prepare a catheter for anesthesia re-dosing.
 1. Remove a 30 G needle from a syringe using forceps.
 2. Insert the needle to a 20 cm piece of PE-10 medical silicon tubing.
 3. Insert a 30 G needle syringe filled with ketamine/xylazine mixture on the other side of the tube.
 4. Remove the air inside of the tube.
 3. Prepare a 20 G catheter connected to a tube from an oxygen insufflating machine to maintain automated ventilation (**Figure 1Ai**). Set it on a breath ratio of 130 beats per minute (b.p.m.) with a tidal volume of 0.2 mL using a 100% oxygen gas supply.
2. **Prepare the mouse for surgery**
 1. Keep the mouse on a specific customized surgical board (**Figure 1Aii-iii**) over a heated plate or a heated surgical bench set at 37 °C for all the time of the surgery.
 2. Shave the hair from the neck of the mouse using an electric razor and a depilatory cream (**Figure 1Bi**).
 3. Place the mouse above the plastic mouse positional (**Figure 1Aii-a**), keeping the animal head outside of the positional (**Figure 1Bii**) to create an angle that facilitates the intubation of the trachea.
 4. Fix the forelimbs, the paws, and the tail with surgical tape, moisten mouse eyes with a vitamin A enriched gel and disinfect the mouse neck (**Figure 1Bii**).
3. **Surgery**
 1. Prepare properly autoclaved items, namely, scissors, microsurgical scissors, and forceps.
 2. Perform a small incision on the long medial axis of the neck, approximately 1 cm long, in the middle area between the upper chest and the line passing through the lower point of the mandible (**Figure 1Biii**).
 3. Move laterally the skin patches and the salivary glands and visualize the trachea, covered by the muscles. Then, dissect the tracheal muscles carefully using the forceps (**Figure 1Biii**).
 4. Intubate the mouse with a catheter and start artificial ventilation (**Figure 1Biv**).

NOTE: The catheter is composed of an external plastic part, which protects the tracheal mucosa, and an inner iron needle. The presence of the needle represents the ideal solution to extend and stabilize the trachea and to regulate its exposition. Artificial ventilation through the catheter will guarantee proper breathing of the mouse.

5. Immediately start the artificial ventilation to monitor mouse breathing.
6. Fix the catheter height and orientation using a surgical hook (**Figure 1Bv**) connected to the specific rod on the surgical board (**Figure 1Aii-b**). Expose the trachea at the same height of the chin.
7. Encircle the trachea with petroleum jelly and cover it with a few drops of pre-heated PBS to guarantee proper hydration to the organ (**Figure 1Bvi**).
8. Mount the coverslip on top of the preparation. For this step, glue a coverslip on a metal holder (**Figure 1Bvii**), which will be screwed to the XYZ translator (**Figure 1Aii-c**). Adjust the XYZ translator to place the coverslip on top of the surgical preparation.
9. Place the catheter for the administration of the anesthesia intraperitoneally (**Figure 1Bviii**).
10. Inject 50% of the initial dose of ketamine/xylazine mixture every 30 min.

NOTE: Re-dosing from 50% to 25% of the initial ketamine/xylazine mixture is a safe and valid alternative²⁵. However, since this protocol is terminal and a strict immobilization of the animal is required during the whole procedure, use higher dosages to maintain a deep surgical plane of anesthesia.

4. In Vivo Time-lapse Imaging

NOTE: Image acquisition was performed with an upright two-photon microscope, equipped with two Ti:Sa lasers, temperature-controlled incubation chamber, and a 25X/NA 1.1 water immersion objective. The photomultipliers (PMT) used for image acquisition were either hybrid detectors or high sensitivity GaAsP.

1. Place the surgical board with the anesthetized mouse inside the microscope incubation chamber (pre-heated at 37–38 °C) and add a drop of water on the coverslip.
2. Center and find focus on the tracheal tissue.
3. **Set the scanning frequency to 800 Hz, with 520 x 520 pixels, a field of view of 440 x 440 μm^2 and line average 1.**
 1. Tune Ti:Sa laser to 830 nm to excite second harmonic generation (SHG) from collagen, with an indicative power at source of 150 mW. Tune the second Ti:Sa laser at 920 nm with 94 mW at source, to excite both CFP and YFP.
 2. Set-up the 3D and timelapse acquisition mode with simultaneous excitation

NOTE: Keep the laser powers as low as possible to minimize photobleaching and phototoxicity.
4. Record fluorescence using two channels in non-descanned mode, with a master dichroic mirror at 560 nm. In the set-up used in this protocol, a second dichroic mirror split the signal at 495 nm to separate channel 1 (emission filter 475/50) from channel 2 (emission filter 525/50) (**Figure 2A**). This configuration collects SHG light from collagen in the first channel, while CFP emission is collected in both channels 1 and 2 and YFP is collected only in channel 2.
5. Define a range 50 μm along the Z axis, with a step size of 3 μm (voxel size 0.86 μm x 3 μm). Record images every 30 s for a total duration of 30 min.
6. If desired, acquire multiple regions. Before running more acquisitions, check vital signs and reinject anesthesia through the catheter if needed (see step 3.3.10).
7. At the end of the imaging process, euthanize the mouse through ketamine/xylazine overdose followed by cervical dislocation.

5. Image Processing and Quantitative Analysis of Neutrophil-DC Motility and Interaction

NOTE: In this protocol, a specialized imaging software was used for analyzing the microscopy data.

1. After 4D image acquisition is completed, transfer the files (data and metadata) on a workstation with sufficient computational resources (suggested minimum system requirements: 32 GB RAM, fast solid-state-drives, recent CPU, dedicated GPU based on a massively parallel architecture).
2. Open the files in the imaging software.
3. Play the video and ensure that the cells of interest are clearly visible and that imaging artifacts are absent.

NOTE: To this end, verify that both the movement of the sample and the brightness variation are sufficiently confined. Indeed, these represent challenges for the automatic analysis²⁶. If the movement of the sample between adjacent frames is excessive, apply a drift correction method, using for instance the SHG channel as a fixed reference. This allows to better measure the movement of the cells rather than the movement of the sample. Additionally, in the presence of bright background or debris, prune the reconstructed surfaces using volume as a selection parameter.
4. Generate a co-localization channel specific for CFP⁺ cells, in order to separate the signal between CFP and the collagen (SHG). To this end, denote a gating polygon (**Figure 2Bi**) that selects only the voxels having a positive intensity both in the green channel and in the blue channel.

NOTE: This procedure may vary according to the filter set of the microscope and the staining of the cells. It can be achieved by selecting only voxels with sufficient intensity in both the green and the blue channels. Amongst the available tools, the “coloc” functionality can be used to automatically compute the colocalization channel based on intensity thresholding. Additionally, methods based on machine learning can be used for this step with the supervision of an expert²⁷.
5. Detect and track CFP⁺ cells, using automatic surface reconstruction and tracking (surface tool) over the appropriate co-localization channel.

NOTE: Manual curation of eventual tracking errors and exclusion of tracks with a duration shorter than a defined threshold (*i.e.*, 150 s) may be required.
6. Generate a co-localization channel specific for CD11c-YFP⁺ cells, in order to separate CFP and YFP signals. To this end, denote a gating polygon (**Figure 2Bii**) that selects only the voxels having a positive intensity in the green channel but a low intensity in the blue channel.

NOTE: Representative micrographs showing the signals from channel 1, channel 2, the co-localization channel for CFP, the co-localization channel for YFP, and the combination of all channels can be found in **Figure 2Biii**.

7. Reconstruct the surface of the CD11c-YFP⁺ cells and track their position over time (surface tool).
NOTE: Manual correction of eventual tracking errors is not required for this step. Indeed, due to the complex spatio-temporal dynamics of DC, reconstructing their precise surface from 2P-IVM data is a challenging task that cannot be achieved with available segmentation software. Amongst the reasons that make this task challenging, thin protrusions and brightness variations do not allow for the usage of certain image-processing techniques, such as smoothing filters or static thresholding. Moreover, in a network of DC, it is difficult to separate single cells based only on their appearance in 2P-IVM data. For these reasons, rather than attempting an accurate segmentation by tuning software parameters, we propose to reconstruct non-accurate surfaces of DC. Then, handle the possible errors by means of robust metrics as described in 5.8.
8. **Measure cell migration.**
 1. Export the classical migration measures for both CFP⁺ and CD11c-YFP⁺ cells. Amongst these, the “track speed mean” indicates the average migratory velocity of the cells while the “track straightness” indicates the directionality of the cells. These measures can be exported as a spreadsheet file from the imaging software.
 2. In the exported spreadsheet files, compute the “corrected track straightness” (also referred to as corrected confinement ratio) for both CFP⁺ and CD11c-YFP⁺ cells, which is defined as “track straightness” multiplied by the square root of “track duration” divided by the square root of the video duration. This measure is more robust than “track straightness” in the presence of short tracks²⁸, originating for instance from tracking errors.
NOTE: only videos of the same length can be compared with this measure.
9. **Measure cell interaction.**
 1. Define a contact between a CFP⁺ cell and a CD11c-YFP⁺ cell if their distance (closest voxels) is less or equal than a threshold (*i.e.*, 2 μ m).
NOTE: This threshold should be sufficiently strict to detect a contact only when cells are in close proximity. However, we encourage to keep this threshold greater than 0, ideally N times bigger than the voxel radius (N > 2), because border smoothing can make the reconstruction of cells smaller than the actual cell size.
 2. Count the number and the duration of contacts between CFP⁺ and CD11c-YFP⁺ cells. In the imaging software this can be done for instance by executing a “kiss and run” plug in. These measures can be exported as a spreadsheet file from the statistics tab.
10. Import the previously computed measures in a statistical software, generate the plots and perform statistical tests.

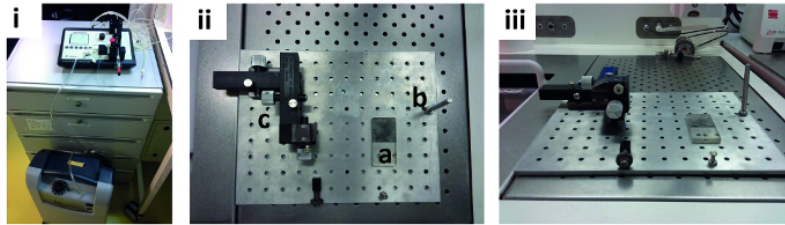
Representative Results

In this work, we described a detailed protocol to study *in vivo* the motility and the interactions between neutrophils and DC during influenza infection in murine trachea (**Figure 3A**). To this purpose, we isolated CFP⁺ neutrophils (92% purity; **Figure 3B**) from CK6-ECFP mice and we adoptively transferred them into a CD11c-YFP mouse infected with influenza. After that, we performed 2P-IVM of the trachea at day 3 p.i. At this time point we observed a clear recruitment of neutrophils in the infected area, as shown by flow cytometric analysis (**Figure 3C**). The 2P-IVM protocol requires the use of a specific surgical board and an oxygen supplier for rodents (**Figure 1A**). Supplying oxygen through a cannula inserted in the trachea helped the animal breathing, facilitated the exposition of the trachea, and controlled the organ movement associated with breathing (**Figure 1B**). Following this experimental set-up, we acquired stable 4D images *in vivo* in the infected trachea during a period of 30 min (**Figure 3D, Movie 1**).

The analysis of the acquired 4D images through specialized imaging software allowed to measure the migration of cells and to quantify the spatio-temporal dynamics of neutrophils and DC. Regarding cell motility, we observed significant differences between the movement of DC and the recruited neutrophils, which showed a significantly faster speed than the latter (**Figure 4A**). This result confirms the dynamic nature of neutrophils, previously described as highly motile cells capable of migrating towards a chemoattractant source²⁹. Regarding directionality, we concluded that complex morphology of the DC yielded frequent errors in cell tracking, which in turn produced tracks with decreased duration and increased variance of the measured directional behavior (**Figure 4B**). For this reason, we computed a robust metric that is able to measure directionality by considering track duration. Using this metric, we observed a significant difference in the directionality of neutrophils vs DC (**Figure 4C**).

Additionally, the computation of the distance between neutrophils and DC allowed to detect and to analyze their contacts over time. In this experimental model, we observed some neutrophils that formed multiple-brief contacts with DC and others that did not form any contact during the imaged period (**Figure 4D**). Moreover, the study of the average trend of the distance between neutrophils and DC over time allowed us to study the overall positioning of the studied cells (**Figure 4E**), while the investigation of the trend in specific cells allowed to characterize the behavior of each single-cell (**Figure 4F, Movie 2**).

A Custom-built imaging platform and oxygen supplier



B Steps for preparing the mouse for imaging

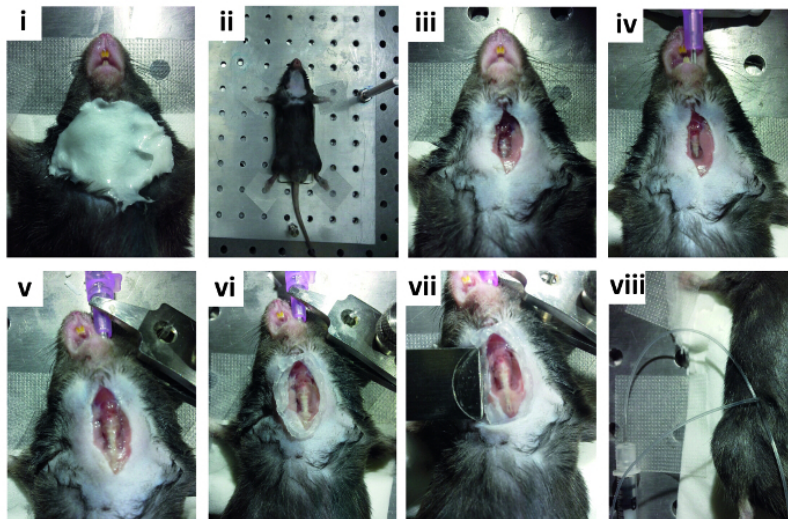
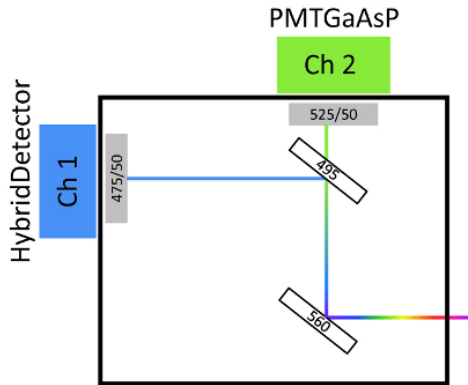


Figure 1: Equipment and steps for 2P-IVM of murine trachea. (Ai) The portable animal anesthesia system in charge of the automated ventilation is connected to a pump that supplies oxygen to the mouse. Front view (Aii) and side view (Aiii) of the custom-made surgical board used for the tracheal model. The board is composed of a metal stage with a plastic mouse positional (Aii-a), a rod for holding a movable clamp (Aii-b), and a fine tunable XYZ translator (Aii-c). (B) Sequential steps of the tracheal surgical model: (Bi) hair removal of the surgical area, (Bii) positioning of the anesthetized mouse in the surgical board, (Biii) surgical exposition of the trachea, (Biv) intubation with a catheter with artificial ventilation, (Bv) fixation of the catheter, (Bvi) addition of PBS to the exposed trachea, (Bvii) mounting of the coverslip, and (Bviii) placement of a catheter with anesthesia. [Please click here to view a larger version of this figure.](#)

A PMT and filter set-up of 2PM



B Generation of co-localization channels

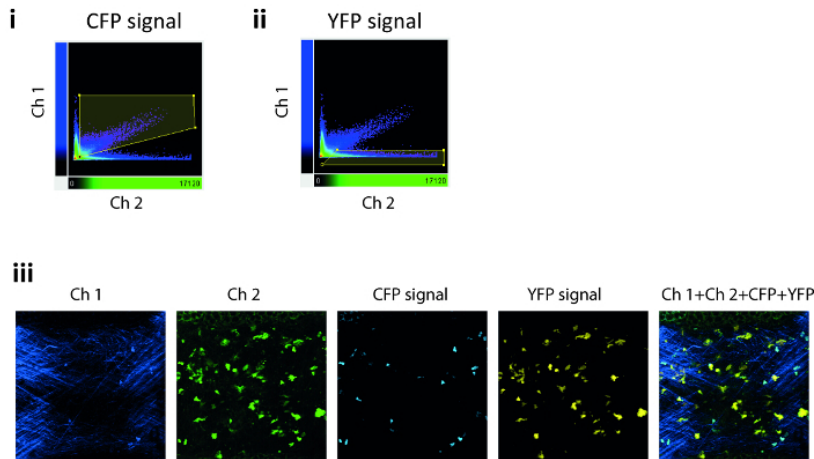
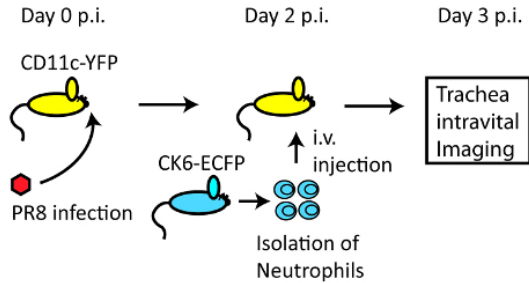
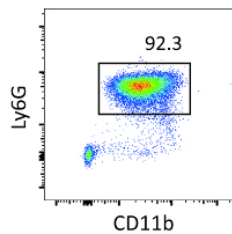


Figure 2: Fluorescent signal detection during 2P-IVM. (A) Schematic representation of the microscope detection filter set-up and corresponding channels. Dichroic mirror at 560 nm separates blue/green from red/far red emissions. Additional dichroic mirror at 495 nm is used to further recognize the different subregions of the emission spectrum. Channel 1 employs a hybrid detector (emission filter 475/50), while channel 2 uses high sensitivity GaAsP PMT (emission filter 525/50). (B) Representative scatter dot plots of 2P signals showing the gating strategy for the generation of the colocalization channels for the identification of signal coming from the CFP (Bi) and the YFP (Bii) fluorophores. (Biii) Representative micrographs showing the specific signals from channel 1 (Ch 1, dark blue), channel 2 (Ch 2, green), the co-localization channel for CFP (light blue), the co-localization channel for YFP (yellow), and the combination of all channels (Ch 1+Ch 2+CFP+YFP). [Please click here to view a larger version of this figure.](#)

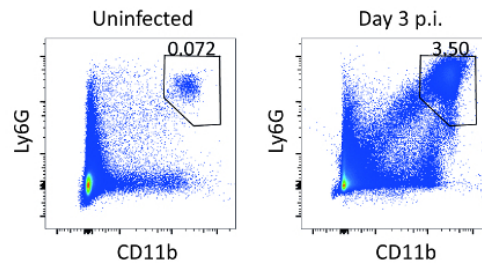
A Experimental outline



B Purity of isolated Neutrophils



C Neutrophils in trachea at day 3 p.i.



D 2P-IVM imaging of murine trachea

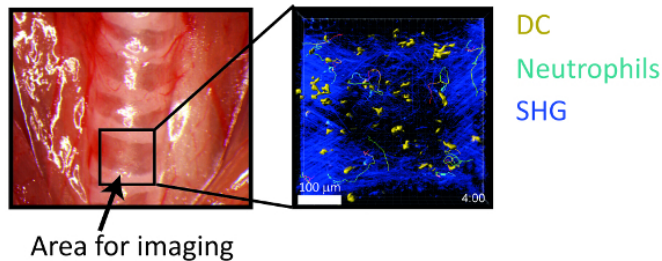


Figure 3: Intravital 4D imaging of neutrophils and DC in an influenza infected trachea. (A) Schematic outline of the protocol. **(B)** Representative flow cytometric scatterplot showing the percentage of neutrophils with respect to the total CD45+ cells in a cell suspension isolated from murine bone marrow using the Percoll gradient method. **(C)** Representative flow cytometric scatterplots showing an increase in the frequency of neutrophils in tracheas from uninfected mice compared to mice infected with influenza virus at day 3 p.i. **(D)** (Left panel) Anatomical image of a murine trachea showing the area selected for image acquisition. (Right panel) Representative 3D projection of a 2P-IVM micrograph showing the surface reconstruction of neutrophils (light blue) and DC (yellow) together with their tracks at day 3 p.i. SHG signal is shown in dark blue. Scale bar = 100 μm. [Please click here to view a larger version of this figure.](#)

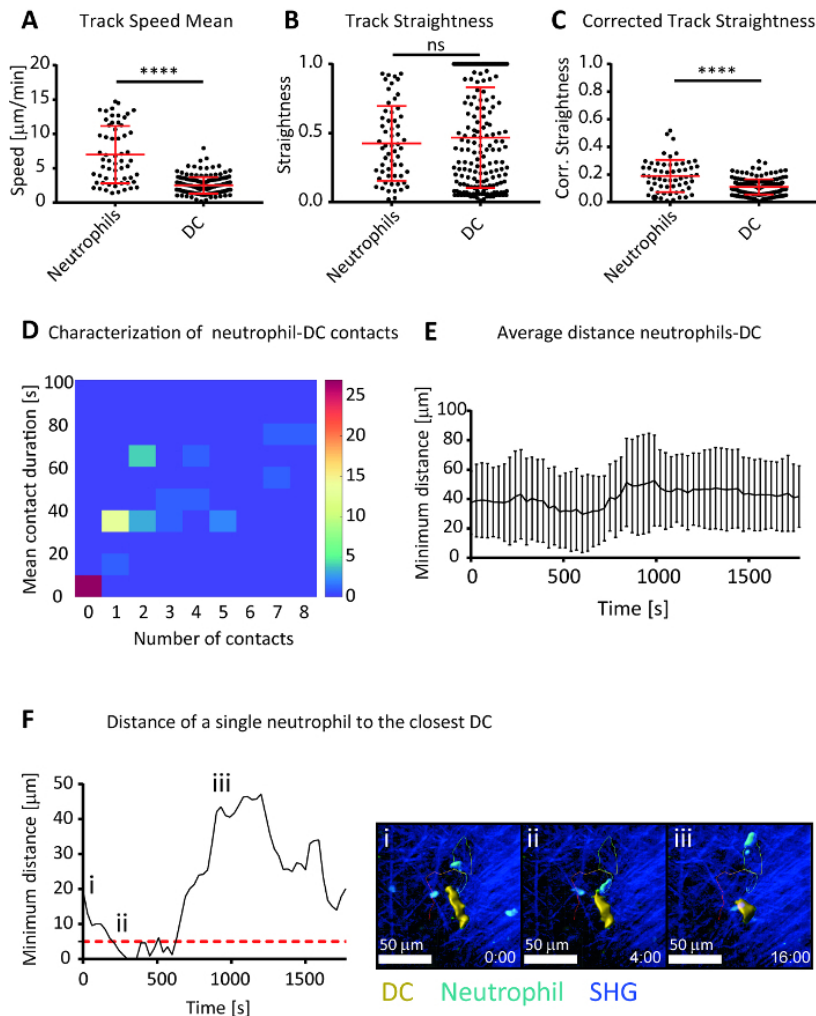
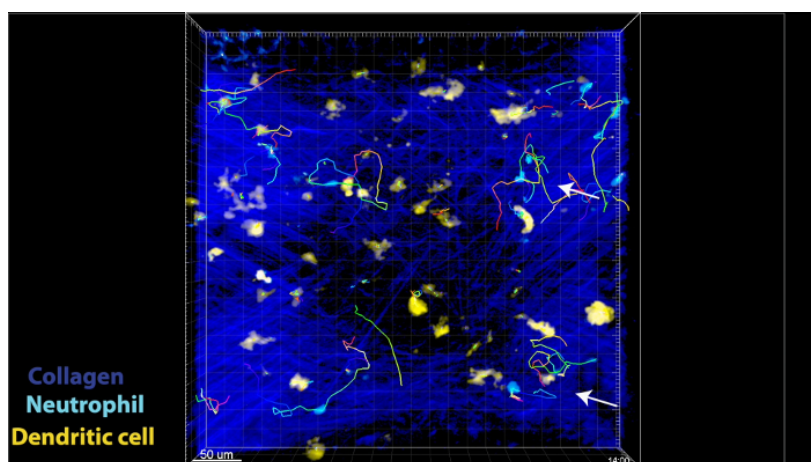
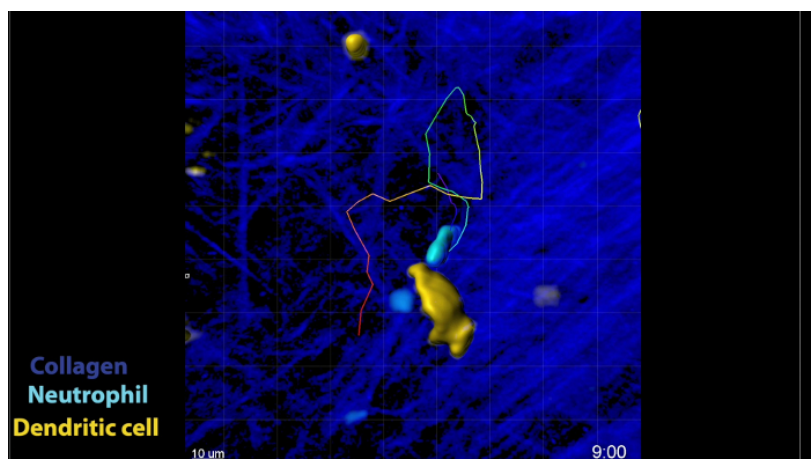


Figure 4: Characterization of neutrophil and DC migration and interaction dynamics in influenza infected trachea. Representative plots showing the track speed mean (A), track straightness (B), and corrected track straightness (C), as defined by Beltman and colleagues (2009)²⁸, of neutrophils and DC in trachea at day 3 p.i. with influenza virus. The corrected track straightness measurement exhibits robustness to tracking errors. (D) 2D histogram showing the frequency of neutrophil according to their number of contacts with DC and the mean contact duration. (E) Average distance of neutrophils to the closest DC during the duration of the movie. (F) (Left) Analysis of the distance of a representative neutrophil to the closest DC in time. The dotted red line indicates the distance threshold to consider that a neutrophil established a contact with a DC. (Right i-iii) Micrographs acquired at different time points representing the migration of a neutrophil (light blue) towards a DC (yellow). Cell tracks are shown as a multicolored line that changes color from blue to red to represent time. SHG signal from fibrillary collagen is shown in dark blue. Scale bar = 50 µm. In all figures, the presented data are representative of at least three independent experiments. Results are given as mean ± SD. Statistics by Welch's test. ns p > 0.05; ****p < 0.0001. [Please click here to view a larger version of this figure.](#)



Movie 1: Neutrophils and DC dynamics in trachea during influenza infection. 30 min time-lapse 3D image showing interaction dynamics between neutrophils (light blue) and DC (yellow) as well as their respective tracks with respect to the collagen network (dark blue) of the trachea. Representative neutrophil-DC interactions are indicated by white arrows. Cell tracks are shown as a multicolored line that changes color from blue to red to represent time. Scale bar = 50 μm . [Please click here to view this video.](#) (Right-click to download.)



Movie 2: Representative short-term neutrophil-DC interaction in the trachea during influenza infection. 30 min time-lapse 3D image showing a representative interaction between a neutrophil (light blue) and a DC (yellow) and their respective tracks. Cell tracks are shown as a multicolored line that changes color from blue to red to represent time. SHG signal from collagen is shown in dark blue. Scale bar = 10 μm . [Please click here to view this video.](#) (Right-click to download.)

Discussion

This work presents a detailed protocol for the generation of 4D images showing the migration of adoptively transferred neutrophils and their interactions with DC during an influenza infection in the mouse trachea. The described 2P-IVM model will be relevant to study immune cell dynamics during an infection in the airways.

Recently, several models based on the visualization of cell dynamics in the airways have been developed^{9,10,11,12,13,14,15,16}. However, *in vivo* imaging of the lung is still challenging, considering the anatomic position of this organ and the technical difficulties to minimize the movement during the breathing cycle³⁰. To overcome these problems, some authors have proposed the use of a custom-built circular suction chamber, which needs to be surgically inserted in the thorax^{13,14}. However, this procedure requires an invasive intervention that could compromise the results, especially in those studies that have focused on the investigation of the inflammatory response. Furthermore, lung surgical models present a limitation for deep tissue imaging due to the light refraction originated by the air in the alveoli¹⁷. Conversely, different tracheal models have been recently employed to study cell dynamics in the airway epithelium. Imaging of this organ presents clear advantages compared to lung, such as the relatively simple surgery required to expose and immobilize the organ, as well as the higher accessibility to the tracheal epithelium. The proposed tracheal model is also relevant to investigate the initiation of the response against airway pathogens, such as influenza virus, since the trachea is one of the first sites of viral replication during the course of an influenza infection⁸.

Interestingly, a study showing an alternative intubation-free method for imaging the trachea has been recently published¹². This method is characterized by a decreased inflammation and shows clear advantages in studies where the mucociliary function of the epithelial cells needs

to be preserved. However, this method does not guarantee sufficient stability and the acquisition of brighter signals necessary to study cell-cell contacts in a range of a few μm . Conversely, the method presented in the current protocol provides better immobilization of the organ thanks to the intubation, and allows the detection of stronger fluorescence signals as a result of the shorter distance between the organ and the coverslip¹².

Accomplishing tissue immobilization during *in vivo* 2P-IVM image acquisition is the most critical step to generate optimal data. Some crucial measures that contribute to the stability of the presented method include: an appropriate mouse anesthesia; a correct mouse intubation; and a surgical exposition of the trachea that allows an easy access to the organ by the coverslip. Additionally, imaging the right number of cells (ideally 30 cells per field of view) will strengthen the obtained results. The recruitment of the optimal number of cells will depend to a large extent on the viral infection dose, which is very much influenced by the proper administration of the viral inoculum.

Another critical step of the protocol is the surgical exposition of the trachea. Different measures can be adopted to minimize the damage caused to the organ during surgery. For example, the trachea should not be directly touched with surgical tools. Instead, it should be exposed by manipulating only the surrounding tissues (skin, salivary glands, and muscles). If strictly necessary, the trachea should be handled using unsharpened items. Additionally, efforts should be done to avoid blood vessel damage. Finally, to prevent organ dehydration, it is also important to cover it with PBS immediately after surgery.

Despite the unique advantages of this method over the previously described methods for the visualization of the immune cell interactions in the tracheal mucosa, the use of this model presents some limitations. As described above, the presence of inflammation associated with the tracheal surgery might represent a drawback when studying immune responses. To overcome this limitation, it is possible to administer anti-inflammatory drugs prior to the initiation of the procedure. Another limitation of this model is related to the presence of a strong autofluorescence signal existing in the airways, which is mainly generated by the resident cells and the mucus layer. This non-specific fluorescence creates artefacts that might hinder the analysis. Furthermore, misleading calculation of the track straightness parameter might be generated when comparing cell tracks of different durations and when tracking errors introduce tracks of short duration²⁶. To overcome this problem, we applied a penalty coefficient to correct track straightness. Such correction is intended to minimize the effect of miss-tracking in the results²⁸.

A crucial aspect of 2P-IVM experiments is the possibility to re-use mice that have undergone surgery and imaging. The *in vivo* imaging protocol described here does not require animal euthanasia or organ collection, thus leaving the possibility to recover and re-use mice after surgery for other procedures. Using a single mouse, for example, to perform trachea imaging at different time points could dramatically decrease the number of total animals needed in an experiment, supporting the *animal reduction* principle. Moreover, it could also reduce inter-individual variability. However, animal recovery and re-use must follow animal welfare standards that includes the administration of proper analgesic drugs and antibiotics to the animals during recovery time. All these procedures must be included in the animal experimentation protocol and approved by the local veterinarian authorities.

The described protocol can be easily adapted to the study of other immune cell types. For example, isolation and injection of (fluorescent or stained) pathogen-specific T cells might be used to study T cell activation dynamics³¹ as well as their interaction with other cells such as tracheal DC. In a similar way, the visualization of blood or lymphatic vessels could represent an interesting approach to study the recruitment of inflammatory cells into the tracheal tissue during the course of infection. Moreover, 2P-IVM of the trachea could also be applied to study the dynamics of the immune response to other airborne pathogens. Therefore, the use of transgenic fluorescent airborne pathogens, such as *Streptococcus pneumoniae*³², will create new opportunities to study their interactions with the immune system. Although this procedure focuses on measuring the dynamics of immune cells during infection, it could be also applied to different fields including cancer, asthma, or wound-healing.

Disclosures

The authors have nothing to disclose.

Acknowledgements

This work was supported by the Swiss National Foundation (SNF) grants (176124, 145038, and 148183), the European Commission Marie Curie Reintegration Grant (612742), and the SystemsX.ch for a grant to D.U.P. (2013/124).

References

- Helmchen, F., Denk, W. Deep tissue two-photon microscopy. *Nature Methods*. **2** (12), 932-940 (2005).
- Zipfel, W.R., Williams, R.M., Webb, W.W. Nonlinear magic: multiphoton microscopy in the biosciences. *Nature biotechnology*. **21** (11), 1369-77 (2003).
- Fein, M.R., Egeblad, M. Caught in the act: revealing the metastatic process by live imaging. *Disease Models & Mechanisms*. **6** (3), 580-593 (2013).
- Dombeck, D.A., Harvey, C.D., Tian, L., Looger, L.L., Tank, D.W. Functional imaging of hippocampal place cells at cellular resolution during virtual navigation. *Nature Neuroscience*. **13** (11), 1433-1440 (2010).
- Cahalan, M.D., Parker, I. Choreography of cell motility and interaction dynamics imaged by two-photon microscopy in lymphoid organs. *Annual review of immunology*. **26**, 585-626 (2008).
- Germain, R.N., Robey, E.A., Cahalan, M.D. A Decade of Imaging Cellular Motility and Interaction Dynamics in the Immune System. *Science*. **336** (6089), 1676-1681 (2012).
- Coombes, J.L., Robey, E.A. Dynamic imaging of host-pathogen interactions *in vivo*. *Nature Reviews Immunology*. **10** (5), 353-364 (2010).
- Pulendran, B., Maddur, M.S. Innate Immune Sensing and Response to Influenza. *Life Science Journal*. **6** (4), 23-71 (2014).
- Lim, K. *et al.* Neutrophil trails guide influenza-specific CD8 + T cells in the airways. *Science*. **349** (6252) (2015).

10. Kim, J.K. *et al.* In vivo imaging of tracheal epithelial cells in mice during airway regeneration. *American journal of respiratory cell and molecular biology*. **47** (6), 864-8 (2012).
11. Kretschmer, S. *et al.* Autofluorescence multiphoton microscopy for visualization of tissue morphology and cellular dynamics in murine and human airways. *Laboratory investigation; a journal of technical methods and pathology*. **96** (8), 918-31 (2016).
12. Veres, T.Z. *et al.* Intubation-free *in vivo* imaging of the tracheal mucosa using two-photon microscopy. *Scientific Reports*. **7** (1), 694 (2017).
13. Looney, M.R. *et al.* Stabilized imaging of immune surveillance in the mouse lung. *Nature methods*. **8** (1), 91-6 (2011).
14. Thornton, E.E., Krummel, M.F., Looney, M.R. Live Imaging of the Lung. *Current Protocols in Cytometry*. **60** (1) (2012).
15. Tabuchi, A., Mertens, M., Kuppe, H., Pries, A.R., Kuebler, W.M. Intravital microscopy of the murine pulmonary microcirculation. *Journal of Applied Physiology*. **104** (2), 338-346 (2008).
16. Fiore, D. *et al.* Two-photon intravital imaging of lungs during anthrax infection reveals long-lasting macrophage-dendritic cell contacts. *Infection and immunity*. **82** (2), 864-72 (2014).
17. Secklehner, J., Celso, C. Lo, Carlin, L.M. Intravital microscopy in historic and contemporary immunology. *Immunology and Cell Biology*. **95** (6), 506-513 (2017).
18. Lambrecht, B.N., Hammad, H. Lung Dendritic Cells in Respiratory Viral Infection and Asthma: From Protection to Immunopathology. *Annual Review of Immunology*. **30** (1), 243-270 (2012).
19. Camp, J. V., Jonsson, C.B. A role for neutrophils in viral respiratory disease. *Frontiers in Immunology*. **8** (MAY) (2017).
20. van Gisbergen, K.P.J.M., Sanchez-Hernandez, M., Geijtenbeek, T.B.H., van Kooyk, Y. Neutrophils mediate immune modulation of dendritic cells through glycosylation-dependent interactions between Mac-1 and DC-SIGN. *The Journal of experimental medicine*. **201** (8), 1281-92 (2005).
21. Gonzalez, S.F. *et al.* Capture of influenza by medullary dendritic cells via SIGN-R1 is essential for humoral immunity in draining lymph nodes. *Nature Immunology*. **11** (5), 427-434 (2010).
22. Lindquist, R.L. *et al.* Visualizing dendritic cell networks *in vivo*. *Nature immunology*. **5** (12), 1243-1250 (2004).
23. Li, H. *et al.* Human V γ 9V δ 2-T cells efficiently kill influenza virus-infected lung alveolar epithelial cells. *Cellular and Molecular Immunology*. **10** (2), 159-164 (2013).
24. Tran Cao, H.S. *et al.* Development of the transgenic cyan fluorescent protein (CFP)-expressing nude mouse for "technicolor" cancer imaging. *Journal of Cellular Biochemistry*. **107** (2), 328-334 (2009).
25. Jaber, S.M. *et al.* Dose regimens, variability, and complications associated with using repeat-bolus dosing to extend a surgical plane of anesthesia in laboratory mice. *Journal of the American Association for Laboratory Animal Science : JAALAS*. **53** (6), 684-91 (2014).
26. Pizzagalli, D.U. *et al.* Leukocyte Tracking Database, a collection of immune cell tracks from intravital 2-photon microscopy videos. *Scientific Data*. **In press** (2018).
27. Sommer, C., Straehle, C., Kothe, U., Hamprecht, F.A. Ilastik: Interactive learning and segmentation toolkit. *2011 IEEE International Symposium on Biomedical Imaging: From Nano to Macro*. 230-233 (2011).
28. Beltman, J.B., Marée, A.F.M., De Boer, R.J. Analysing immune cell migration. *Nature Reviews Immunology*. **9** (11), 789-798 (2009).
29. Keller, H.U. Motility, cell shape, and locomotion of neutrophil granulocytes. *Cell motility*. **3** (1), 47-60 (1983).
30. Sumen, C., Mempel, T.R., Mazo, I.B., von Andrian, U.H. Intravital Microscopy. *Immunity*. **21** (3), 315-329 (2004).
31. Lambert Emo, K. *et al.* Live Imaging of Influenza Infection of the Trachea Reveals Dynamic Regulation of CD8+ T Cell Motility by Antigen. *PLOS Pathogens*. **12** (9), e1005881 (2016).
32. Kjos, M. *et al.* Bright fluorescent Streptococcus pneumoniae for live-cell imaging of host-pathogen interactions. *Journal of bacteriology*. **197** (5), 807-818 (2015).

